RAMTM II

Proceedings of

2nd National Conference on
Recent Advancements in Manufacturing Technology
& Management

Organised by

Department of Production Engineering
Jadavpur University

Editors

Souren Mitra
Upama Dey

Co-sponsored by

RAMTM-II 2025

Proceedings of
2nd National Conference on
Recent Advancements in Manufacturing Technology & Management

Organised by

Department of Production Engineering
Jadavpur University

Editors

Souren Mitra
Upama Dey

Co-sponsored by

RAMTM-II 2025: Proceedings of 2nd National Conference on Recent Advancements in Manufacturing Technology & Management

Organised by the Department of Production Engineering
Jadavpur University

Edited by Souren Mitra, Upama Dey

© The Authors

All rights reserved, including those of translations into other languages. No part of this book be reproduced, stored in a retrieval system, or transmitted in any form, or by means, electronic, mechanical, photocopying, recording or otherwise without the written permission of the publisher.

ISBN: 978-81-986567-9-7

Published by
Jadavpur University Press
Jadavpur University
Kolkata 700032

Printed and bound by
Ficus

Layout and cover-design by
Kawshik Aki

COMMITTEES

Advisory Committee Members for RAMTM-II

J. Paulo Davim, Professor, University of Aveiro, Portugal

Eric MacDonald, Professor, University of Texas at El Paso, USA

Mustafizur Rahman, Professor, National University of Singapore, Singapore

Saleem Hashmi, Professor Emeritus, Dublin City University, Ireland

Tsanka Dikova, Professor, Medical University of Varna, Bulgaria

Bijoy Bhattacharyya, Former Professor, Jadavpur University, India

Debanik Roy, Scientist, DRHR-BARC, India

Dinesh Kumar Shukla, Chairman, AERB, India

Dipankar Bose, Professor, NITTTR Kolkata, India

Dipten Misra, Director, SLSE, Jadavpur University, India

Goutam Biswas, Professor, IIT Kanpur, India

Goutam Bose, Professor, Haldia Institute of Technology, India

Makarand Joshi, OS & Director, R & D Establishment (Engrs.), DRDO

Mantu Patra, General Manager, Tata Steel Ltd. Haldia, India

Nagahanumaiah, Director, CMTI, India

Naresh Chandra Murmu, Director, CSIR-CMERI, India

Pravin Deshpande, General Manager, Electronica Hitech Machine Tools Pvt Ltd, India

Sampad Kumar Biswas, Research Advisor, MNIT Jaipur, India

Santanu Das, Professor, Kalyani Government Engineering College, India

Subhasis Bhaumik, Professor, IIEST Shibpur, India

Sudhir Sharma, Managing Director, Dynotech Instruments Pvt Ltd, India

Vijay Kumar Jain, Professor Emeritus, IIT Kanpur, India

Vijay Kumar Meena, Sr. Principal Scientist, CSIR-CSIO, Chandigarh, India

Organizing Committee Members for RAMTM-II

Chief Patron

Vice-Chancellor, Jadavpur University

Patrons

Pro Vice-Chancellor, Jadavpur University

Dean, Faculty of Engineering and Technology, Jadavpur University

Chairman

Head, Department of Production Engineering, Jadavpur University

Organizing Secretary

Souren Mitra	Department of Production Engineering, Jadavpur University

Members

Ajoy Kumar Dutta	Department of Production Engineering, Jadavpur University
Arunanshu Shekhar Kuar	Department of Production Engineering, Jadavpur University
Biplab Ranjan Sarkar	Department of Production Engineering, Jadavpur University
Biswanath Doloi	Department of Production Engineering, Jadavpur University
Debamalya Banerjee	Department of Production Engineering, Jadavpur University
Shankar Chakraborty	Department of Production Engineering, Jadavpur University
Soumya Sarkar	Department of Production Engineering, Jadavpur University
Subir Kumar Debnath	Department of Production Engineering, Jadavpur University
Ranjib Biswas	Department of Mechanical Engineering, Jadavpur University
Asim Gopal Barman	Department of Production Engineering, Jadavpur University
Sanjib Kumar Saren	Department of Production Engineering, Jadavpur University

Sub-Committees for RAMTM-II

Aparna Duggirala	Department of Production Engineering, Jadavpur University
Kingshuk Mandal	Department of Production Engineering, Jadavpur University
Rupam Rakshit	School of Laser Science and Engineering, Jadavpur University
Souradip Paul	School of Laser Science and Engineering, Jadavpur University
Suhas Mandal	School of Laser Science and Engineering, Jadavpur University
Upama Dey	School of Laser Science and Engineering, Jadavpur University

Abhijat Paul	Department of Production Engineering, Jadavpur University
Arnab Mandal	Department of Production Engineering, Jadavpur University
Arya Bhattacharya	Department of Production Engineering, Jadavpur University
Dibakar Gupta	Department of Production Engineering, Jadavpur University
Hrisheeta Roy	Department of Production Engineering, Jadavpur University
Manish kumar	Department of Production Engineering, Jadavpur University
Maurya Samanta	Department of Production Engineering, Jadavpur University
Nirjhar Das	Department of Production Engineering, Jadavpur University
Ripan Das	Department of Production Engineering, Jadavpur University
Sagnik Mitra	Department of Production Engineering, Jadavpur University
Satapriya Das	Department of Production Engineering, Jadavpur University
Satyaky Jana	Department of Production Engineering, Jadavpur University
Sumit Mallick	Department of Production Engineering, Jadavpur University
Tahsin Azim Islam	Department of Production Engineering, Jadavpur University
Washim Ahmed	Department of Production Engineering, Jadavpur University

JADAVPUR UNIVERSITY
Kolkata 700032, INDIA

Email: deanfet@jadavpuruniversity.in

DEAN, FACULTY OF ENGINEERING AND TECHNOLOGY

MESSAGE

Date: 6th January 2025

I am delighted to congratulate the Department of Production Engineering of our University on organizing the National Conference RAMTM-II on January 16-17, 2025. This conference aims to serve as a collaborative platform for experts from all the sectors of engineering industries, academia, and research and development organizations to interact and exchange ideas. The conference seeks to foster networking among participating institutions, organizations, and industries to address shared challenges and advance manufacturing technology in these specialized fields.

For students and young researchers, this platform offers a valuable opportunity to learn from esteemed experts, explore global advancements, and contribute to innovative solutions. For industry professionals, it serves as a gateway to explore cutting-edge research and collaborate with academic innovators. Collectively, these efforts will help localize global knowledge, making it accessible and actionable for addressing regional and global challenges.

I am confident that this conference will yield impactful outcomes in research, innovation, and application, and I wish it resounding success.

Rajib Bandyopadhyay

Prof. Rajib Bandyopadhyay

যাদবপুর বিশ্ববিদ্যালয়
JADAVPUR UNIVERSITY
PRODUCTION ENGINEERING DEPARTMENT
188, Raja S. C. Mullik Road, Kolkata - 700 032, West Bengal, India.

Website : www.jaduniv.edu.in
E-mail : hod@production.jdvu.ac.in
Phone : +91 33 2414 6153
Fax : +91 33 2414 6153

Message from the Head, Department of Production Engineering and Chairman, RAMTM-II 2025

It is a great pleasure to welcome you to the inaugural function of National seminar RAMTM-II organised by Production Engineering Department, Jadavpur University on January 16-17, 2025.

Production Engineering Department was founded by Prof. Amitabha Bhattacharya, a doyen in the academic map of the world. He conceived the importance of introduction of this course in UG level during 1978 as there was radical and sea changes in the concept of manufacturing.

Under LPG (liberalization, privatization and globalization) environment, the customer is the king. There had been a paradigm shift from mass production to mass customization.

Under the utopian environment, trailblazing researches have been carried out throughout the international context. It has been felt that the market demand has become highly volatile and lead time negligibly small. To get the maximum competitive advantage, concepts of intelligent manufacturing systems, cloud manufacturing, digital manufacturing, Industry 4.0 have been widely utilized using Internet of Things (IOT), Artificial Intelligence and Machine Learning with holonic, bionic and fractal perceptions.

This national seminar will bridge the gap between Industries and Academics. The researchers, trainers and young faculty members will be immensely benefitted through mutual interactions, understanding and dissemination of cutting edge tool and leading-edge techniques being applied in the global scenario.

I wish this seminar a great success.

Bijan Sarkar

Dr. Bijan Sarkar

Professor & Head; Production Engineering Department, Jadavpur University

Chairman- **RAMTM-II 2025**

From Secretary's Desk

The manufacturing system is concerned with manufacturing technology and manufacturing management. The role of manufacturing systems in the economy and society has long been established through their wealth-creating activities. There is little doubt that it will continue to play a vital role in our lives. The experiences of the manufacturing industries in the last decades have provided a strong indication that they will face new challenges.

In today's global setting, the success of manufacturing industries can only be achieved through the optimization of manufacturing and other functions in logical association with one another. Hence, the aim of the RAMTM-II 2025 Conference is to bring together specialists and practitioners from industries, government, and academia, providing a forum for the exchange of ideas to tackle various issues and adapt to the evolving environment of technology and management.

The conference focuses on different issues related not only to manufacturing activities but also to the optimization of total manufacturing systems, which is increasingly becoming an essential tool for gaining a competitive advantage. A striking feature of the conference is the six keynote addresses to be delivered by Dr. Dinesh Kumar Shukla, Chairman, AERB; Dr. Debanik Roy, Group Head, Division of Remote Handling & Robotics, BARC (DAE); Dr. Makarand Joshi, OS & Director, R&D Establishment (Engrs.), DRDO; Dr. Vijay Kumar Meena, Sr. Principal Scientist, CSIR-CSIO, Chandigarh; Dr. Nagahanumaiah, Director, CMTI, Bangalore; and Prof. Pradip Kumar Ray, Emeritus Professor, Industrial and Systems Engineering, IIT Kharagpur.

The cross-section of delegates attending RAMTM-II 2025, from key industries, R&D organizations, and academic institutions, further highlights the importance of the conference topics. We are grateful to all the invited speakers for accepting our invitation and for their efforts in sharing the latest developments in their fields.

We would like to express our appreciation to all the authors of contributed papers who have responded to our call with great enthusiasm. We are also grateful to the reviewers, both from within and outside the university, for their diligence in reviewing the manuscripts and their revised versions. Their painstaking efforts have undoubtedly enhanced the quality of the papers and, consequently, the proceedings of the conference.

We extend our sincere gratitude to all members of the Advisory Committee for their active interest and constructive suggestions at various stages. We also acknowledge the invaluable support received from all sponsors and well-wishers.

We are grateful to the editing team, comprising faculty members and research scholars, for methodically formatting the papers and ensuring adherence to the conference template. We also extend our thanks to Jadavpur University Press, which has a distinguished track record of publishing seminal academic works, for their valuable efforts, suggestions, and inputs in making this volume a reality.

We sincerely regret any errors that might have crept in unnoticed. All comments and suggestions for the improvement of our future programs are welcome.

RAMTM-II 2025 is being held for the second time to address various issues related to technology and management on a unified platform, and we hope that its spirit will be carried forward in the coming years.

Kolkata
January 2025

Souren Mitra

Keynote Addresses

i. **Keynote address I** **Dr. Dinesh Kumar Shukla**, Chairman, AERB

Title of the Talk: Nuclear Power Plants Safety – Role of Design, Construction and Quality

ii. **Keynote address II** **Dr. Debanik Roy**, Group Head, Division of Remote Handling & Robotics, BARC (DAE)

Title of the Talk: Topology- Optimized Bio-Robots: A Journey with Miniaturized Manufacturing

iii. **Keynote address III** **Dr. Makarand Joshi**, OS & Director, R & D Establishment (Engrs.), DRDO

Title of the Talk: Design and manufacture of large multi-functional composites structures

iv. **Keynote address IV** **Dr. Vijay Kumar Meena**, Sr. Principal Scientist, CSIR-CSIO, Chandigarh

Title of the Talk: Additive Manufacturing for Automotive, Energy and Medical Applications

v. **Keynote address V** **Dr. Nagahanumaiah**, Director CMTI, Bangalore

Title of the Talk: Additive Manufacturing: Pioneering the Future of Industrial Production- Challenges and Opportunities

vi. **Keynote address VI** **Prof. Pradip Kumar Ray**, Emeritus Professor, Industrial and Systems Engineering, IIT Kharagpur

Title of the Talk: Ergonomic Design of Human-Product Interfaces with Assurance of Risk-free Environment with Automation for Improved Performance: Applications in Healthcare Systems

NUCLEAR POWER PLANTS SAFETY – ROLE OF DESIGN, CONSTRUCTION AND QUALITY

Shri Dinesh Kumar Shukla
Chairman, AERB

Abstract

Atomic Energy Regulatory Board (AERB) is the national authority for ensuring that the use of ionizing radiation and nuclear energy does not cause any undue risk to the health of workers, members of the public and to the environment. Its mandate includes overseeing the safety of Nuclear Power Plants (NPPs) across various stages: siting, design, construction, commissioning, operation, maintenance, plant life extension, and decommissioning. The AERB has developed a comprehensive set of regulatory documents outlining safety requirements at each stage of an NPP's lifecycle. This presentation provides an overview of AERB's regulatory framework and processes, focusing on the sound design and construction principles, as well as the associated quality assurance measures. Emphasis is placed on the strong safety concepts incorporated into design, the application of the highest standards in manufacturing and construction, and the roles and responsibilities of organizations to ensure product quality. Despite rigorous quality measures, failures still occur, prompting an introspective examination of the systems involved, along with my observations and reflections on the processes and challenges are covered in this talk.

TECHNOLOGY-OPTIMIZED BIO-ROBOTS: A JOURNEY WITH MINIATURIZED MANUFACTURING

Dr. Debanik Roy

Group Head, Division of Remote Handling & Robotics, BARC (DAE)

Extended Abstract

Design of compliant robotic structures in a miniaturized ensemble is quite challenging. Miniature robotics involves components that come in compact sizes. Added to this facet, the global choice for robotic applications is biased toward compliant devices. Both aspects, viz., miniaturization and compliance, are handshaking with customization. We are increasingly moving towards product-oriented development of small-sized compliant robotic devices, and the trend has been very apparent in the last decade. However, successful 'out-of-the-laboratory' type design and firmware of compliant robotic systems at the prototype level are pretty demanding. The task of such prototyping gets even more complicated when there is a need to focus on the miniaturized encapsulation of such a robotic device. By virtue of the design, compliant robots provide enhanced dexterity, easy maneuverability, a moderate level of flexibility, and compliant actuation.

Size-optimized compliant robotic devices are of importance from the stand-point of relatively critical practical applications, such as spot-inspection, general maintenance & internal surveillance of pipes, chutes and ducts in industries. Barring size effect, intricacies of the mechanical design for such miniature robots need careful attention and cohesion with respect to its pre-programmed navigation. This keynote address will unfold complete indigenous firmware of three crucial functional verticals of Bio-inspired Robotics, namely: [a] compliant robotics; [b] flexible robotics & [c] worm robotics. We will dwell on one of the tailor-made bio-robots, christened as "Compliant Universal Robotic Leech" (CURL) ~ developed in two versions chronologically. Our customized robotic leech is a sort of miniature robot with intention of being operated inside cylindrical pipes of nuclear power plants in horizontal plane, having inner diameter less than 75 mm. Our research was aimed at the design, analysis and hardware development of a compliant crawler device, modeled on the bio-mechanics of a *leech* that can grip and crawl on the object it sticks to. Unlike jointed and kinematically coupled systems, a compliant mechanism transfers and/or transform motion, force or energy, being achieved by the elastic deformation of its own members. In a way, the inherent flexibility metric of such mechanism is optimally exploited in all the prototypes that will be highlighted in the lecture. Nonetheless, we can extract engineering benefits out of a typical compliant device in the form of *redundancy* in degrees-of-freedom,

despite having lesser joints, in comparison to its quasi-rigid counterparts. The prototype CURL has been attributed with three functional sub-systems, viz. a] rolling unit; b] crawling unit and c] gripper unit, which are responsible for its planar motion. Rolling & crawling motions may occur simultaneously in certain cases in such a way so as to complement the conjugate motion of the prototype CURL, but those are not supplementary to each other.

Unlike many of the bio-robot designs available hitherto, we have integrated a novel customized parallel-jaw type miniaturized gripper with either of the two functional sub-systems of the prototype CURL. This gripper is unique not only by its design but also by its added dexterity. Besides inspection of the pipe on its internal surfaces, CURL is earmarked to perform additional task of picking / gripping of disposable objects inside the pipe. This extra task is entrusted to be performed by the customized miniature gripper. Contextually, design & firmware of a variety of such bionic grippers will be described in the lecture.

This lecture will also take us to the journey of developing a bionic type 'Rolling Capsule' and the performance parameters expected from the same under a suitable application manifold. This study focuses on designing and manufacturing miniature components capable of traversing inside ducts with relatively small cross-sections. The work reports the successful development of a tethered miniature-compliant rolling device. The rolling capsule-type miniature robot is designed to operate inside rectangular or square ducts with an inner diameter of less than 40 mm. The design consists of a multi-part external body assembly primarily composed of the retainer ring powered by a miniature motor within an enclosure. The rolling segment aims to traverse inside the duct axially by spinning in one direction. 3D printing technology is leveraged for the fabrication of prototypes. With its design freedom, metal 3D printing is an innovation that can be used to print fully functional rigid miniature components with high accuracy and speed. The robot is constructed from a modular set of components held together using a combination of screws and various lock mechanisms. The average device dimension of all the design variations is approximately 20 x 40 mm enabling the component to roll into a duct with an inner diameter as small as 30 mm, thus fulfilling the aim of the study.

The field of Flexible Robotic System (FRS) is one of the niche ensembles of present-day bio-robotic research that caters for real-time aspects like rheology (stress-strain paradigms), in-situ vibration, sensor fusion & non-linear coupled dynamics for control. As some of these features are inherent in FRS, prototyping multiple degrees-of-freedom bio-inspired flexible robot as an application-centric firmware is highly challenging. This lecture will take us into details of the relevant research towards design as well as modeling issues for the firmware of higher-order FRS, as a foundation to fully-operational & commercial version of assistive type Flexible Bionic Robots. We shall focus on the state-of-the-art research in FRS, pin-pointing novel designs & prototype hardware development of different types of multi-link (straight and gooseneck-styled)

serial-chain as well as closed-loop bionic type flexible robots fitted with miniaturized gripper(s) at the free end.

Although research on Assistive Robotics in agriculture has commenced to a limited extent in recent past, the essence of such developments was limited to solo robot, seldom bio-inspired. The concept of team robots having near-identical features, symbolizing biological off-springs was never explored in application manifolds pertaining to agriculture. The erstwhile prototypes of robotic systems targeting agricultural applications missed the feel of biology in true sense. We shall dwell on a novel assistive robotic system in this lecture having '*Mother*' and '*Daughter(s)*' for use in agricultural fields. Our design has been nucleated from a famous biological worm, namely, *Caenorhabditis elegans (C.elegans)* that has fully-developed reproductive system, notwithstanding its length (~ 1 mm.) or even the diameter (~ 50 micron). Incidentally, *C.elegans* is an interesting biological entity that evokes imagination and assertion to create miniature robotic systems, especially by mimicking its reproductive system. In this talk, we will report the technological concept designs of representative '*Mother-Daughter'* Worm Robotic system by naturally inheriting the reproductive mechanism of the biological *C.elegans* worm (notwithstanding the size effect). The said worm robot will be poised to perform various tedious jobs in an agricultural field, such as spraying pesticide & manure and/or general observation on the crop's growth.

As part of the prototype hardware of bio-inspired worm robots, e.g. Assistive Mother Daughter Robot (AMoDaR) or in short, '*AgriWorm*' the lecture will bring out the biological facet of '*Mother*' & '*Daughter*' worm in conjugate. In other words, the basic *AgriWorm* will be the '*Mother*' and it will have technological provision for 'delivering' the '*Daughter*' robot-worms in a time-bound manner following a pre-assigned sequence for such 'delivery' at the desired application-site. Our indigenous design architecture of '*AgriWorm*' is rooted with the ideation of 'Reproductive Sack' that is pretty similar to situations of the biological worm, *C. elegans*. However, unlike the case of reproduction of biological *C.elegans*, we can't have a smooth transition of the robot worm off-spring in the surrounding environment, because those 'daughter' robot-worms are not 'live' worms. Hence, we need to augment the technology for near-smooth 'ejection' of the robotic off-springs over the ground-field ('datum') surface. Ideally the 'mother' *AgriWorm* should be positioned suitably over the datum so as to ease out the 'reproduction' process, technologically. Irrespective of the static position of the 'mother' *AgriWorm*, the said robotic reproduction process will generate enough vibration in the system, which is inevitable but can be controlled via tailor-made technology. In our specific case with prototype *AMoDaR* this notion of reproductive sack has been mutated through a novel design of robotic encapsulation, wherein multiple off-springs of *AgriWorm* can be obtained sequentially. The conceptual facets and detailed schematic design of the *AMoDaR* can be entrusted to usher in successful prototyping of the *AgriWorm* in due course.

Besides mechanical design & manufacturing, study on the dynamics of real-time activation and autonomous position control of the target point of a miniature bio-robotic device is a challenging research domain. The talk will also touch upon these facets with reference to the 12 indigenous hardware of bio-inspired robots, designed & developed by the author and his research group over the past 8 years (~ 2017-2024).

DESIGN AND MANUFACTURE OF LARGE MULTI-FUNCTIONAL COMPOSITES STRUCTURES

Dr. Makarand Joshi

OS & Director, R & D Establishment (Engrs.), DRDO

Abstract

Out-of-autoclave manufacture of structural composites has been the focus of work at the Composites Research Center (CRC) at R&DE(E), DRDO, Pune. Two manufacturing processes, vacuum assisted resin transfer moulding (VARTM) and resin film infusion (RFI) have been successfully developed over the past two decades. A number of products have been designed and manufactured using these processes for various applications. Many of these structures require additional functionalities such as armour protection, radar/acoustic transparency, stealth etc. The technologies for these additional features have also been successfully developed at CRC and implemented in various products.

This presentation highlights the work carried out at CRC with emphasis on technology development.

ADDITIVE MANUFACTURING FOR AUTOMOTIVE, ENERGY AND MEDICAL APPLICATIONS

Dr. Vijay Kumar Meena

Sr. Principal Scientist, CSIR-CSIO, Chandigarh

Abstract

Additive manufacturing (AM), commonly known as 3D printing, has emerged as a disruptive technology adapting itself for usage in diverse industries, whether it is the automotive, energy, or medical. In the automotive industry, AM facilitates rapid prototyping, the production of lightweight components, and the creation of customized vehicle parts, enhancing efficiency and performance while reducing inventory. For the energy sector, AM offers innovative solutions for manufacturing complex energy electrodes, and renewable energy systems, improving durability, efficiency, and sustainability. In the medical industry, AM enables the creation of patient-specific implants, surgical equipment, and orthopaedic and maxillofacial implants, changing healthcare with customized and biocompatible solutions. AM's ability to produce complex geometries, reduce material waste, tailor mechanical properties, and shorten manufacturing time duration demonstrates its potential to change the manufacturing Industry.

ADDITIVE MANUFACTURING: PIONEERING THE FUTURE OF INDUSTRIAL PRODUCTION – CHALLENGES AND OPPORTUNITIES

Dr. Nagahnumaiah

Director, Central Manufacturing Technology Institute (CMTI), Bengaluru -560 022

Abstract

Additive Manufacturing (AM), often referred to as 3D printing, is revolutionizing industrial production by enabling unprecedented design flexibility, resource efficiency, and customization. As industries worldwide transition toward advanced manufacturing technologies, AM emerges as a key enabler of innovation and sustainable growth. This presentation will explore the transformative potential of AM as an industrial production process, focusing on its ability to redefine supply chains, reduce material waste, and accelerate product development cycles.

The session will also address critical challenges, including scalability, material limitations, cost barriers, and the need for robust standards and certifications. Furthermore, it will shed light on the emerging opportunities in leveraging AM for high-value sectors such as aerospace, healthcare, and automotive, alongside strategies for fostering an ecosystem conducive to adoption and innovation.

ERGONOMIC DESIGN OF HUMAN-PRODUCT INTERFACES WITH ASSURANCE OF RISK-FREE ENVIRONMENT WITH AUTOMATION FOR IMPROVED PERFORMANCE: APPLICATIONS IN HEALTHCARE SYSTEMS

Professor Pradip Kumar Ray
Emeritus Professor, Department of Industrial and Systems Engineering
Adviser, Vinod Gupta School of Management
Indian Institute of Technology Kharagpur
Kharagpur 721 302 West Bengal, India

Abstract

In the context of product and worksystem development in the present industrial context, development of human-product interface in the healthcare systems has been a critical issue, and depends primarily on assessment of existing interfaces from the ergonomic design perspectives as well as the technology used. While we consider design and development of an automated interface between humans and products in worksystems considering a number of ergonomic design aspects, such as postural analysis, anthropometric match, physical and mental work capacity, and impact of environmental factors on the human performance, the main objective of designing such an interface is to create a risk-free and sustainable environment for personnel working under extreme conditions and constraints.

In this talk, details of a comprehensive evaluation system for human-product/process interface and a methodology for developing an automated system for monitoring and control of the design interfaces will be presented. A number of applications of improved interfaces including automated systems ensuring risk-free environment in healthcare worksystems will be discussed.

Contributed Papers: Table of Contents

Additive Manufacturing			
Paper ID RAMTM25-	**Paper Title**	**Author List**	**Page No.**
108	Experimental Investigation of Mechanical and Tribological Properties of 3D-Printed Polymer Materials Using Variable FDM Parameters	Goutam Kumar Bose, Gairik Kumar Bose, Ritoban Maitra and Indrajeet Sen	33
109	Topology Optimization of Component for Functional Integration Using Additive Manufacturing	Subho Mukherjee, Bhushan Dewangan	44
114	Design and FEA Analysis of Lattice Structure for Biomedical Application	Muskan Rathi, Prashant Kumar, Vijay Kumar Meena, Amit Lochan Sharma	52
121	Influence of Torch Oscillation on GMAW-WAAM Fabricated Low-Carbon Steel Components	Kumar Kanishka and Bappa Acherjee	62
124	Numerical Investigation of Mechanical Behaviour of Strut-Based Lattice Structures Under Compressive Load	Souradip Paul, Vijay Kumar Meena, Souren Mitra	63
126	Surface Modification with Metal Matrix Composite Coating Involving Laser Cladding Process: A Review	Dwaipayan Gupta, Ruma Sen, Bikash Choudhury	74
128	Comparative Analysis of Mechanical Properties of ASA Parts 3D Printed with Different Infill Patterns in FDM	Asish Tripathi, Dipayan Chakraborty, Abhishek Mandal	84

Advance Machining Processes			
Paper ID RAMTM25-	**Paper Title**	**Author List**	**Page No.**
103	Study of Performance Characteristics of Ss 304 Alloy for Micro ECM Utilizing Grey Relational Analysis	Adarsh Kumar and Dipankar Bose	95
105	A Review on Machinability of Difficult to Machine (DTM) Materials Using Cryogenically Treated Cutting Tool Inserts	Sandip K Bidgar, Dr B U Sonawane and Dr B D Bachchhav	103

Advance Machining Processes			
Paper ID RAMTM25-	**Paper Title**	**Author List**	**Page No.**
107	Critical Analysis of Fiber Laser Micro-Machined Kerf Quality on Al7075 Alloy Sheet	Kajal Kumar Mandal	115
110	Parametric Analysis and Multi-Objective Optimization in WEDM of Inconel 718 Using Pareto Algorithm	Kunal Dey, Kingshuk Mandal2, Dipankar Bose	124
113	Advancements in Ultrasound-Assisted Underwater Laser Micromachining: A Review	Suhas Mandal, Arunanshu Shekhar Kuar, Bappa Acherjee	131
115	Performance Enhancement of Wire-EDM of Marine Grade Material by Supplying SIC Powder in The Dielectric Medium	Sadananda Chakraborty, Souren Mitra and Dipankar Bose	138
118	Experimental Study on The Reduction of Burr Formation Under Different Drilling Environment	Sweta Yadav, Santanu Das, Partha Pratim Saha	146
123	Analysis of The Performance of Laser Cutting on Ceramic Tiles Based on TLBO Technique	Rupam Rakshit, Swarajit Pal, Paramasivan K, Pankaj Keshari, Subhash Chandra Panja, Dipten Misra	154
125	Study of Drilling Soda-Lime Glass by Air-Abrasive Jet Using Sic Abrasive with Varying Impingement Angle	Deb Kumar Adak, Alakesh Maity and Saikat Jana	162
129	Single Objective Optimization of Laser Cutting Parameters of Glazed Ceramic Tile Using Particle Swarm Optimization	Pankaj Keshari, Rupam Rakshit, Paramasivan K., Dipten Misra	169
206	Machine Learning-Enabled Prediction of Tool Wear in CNC Milling	Jyotiraditya Roy, Sumanta Banerjee and Anindita Kundu	175
207	Parametric Optimization in En31 Alloy Steel Under MQL for Enhanced Machining Performance	Sutanu Misra and Goutam Paul	182

New Generation Forming & Welding Technology			
Paper ID RAMTM25-	**Paper Title**	**Author List**	**Page No.**
101	Micro-Friction Stir Welding (μFSW) of Aluminum Alloys Using Pinless Tool	Meghnath Sen and Asit Baran Puri	191
102	Microwave-Assisted Fusion Joining of Natural Fiber Composites	Abhijay Muliya, Himanshu Pathak, Sunny Zafar, Subhamoy Sen	198
104	Effect of Thermal Properties on Transport Phenomena During Laser Welding of Dissimilar Materials in Lap Configuration	Asish Tripathy, Himadri Chattopadhyay, Sudip Simlandi, Nilkanta Barman	201
106	Multi-Objective Optimization of FSW Parameters for Joining Dissimilar AA5230 and AA4635 Aluminium Alloys	Anubhab Basu, Ranjib Biswas, Nirmal Kumar Mandal, Dipankar Bose, Souren Mitra	212
111	An Overview of Laser-Assisted Metal-Polymer Welding: Fundamentals, Key Parameters, Quality Attributes, and Applications	Rajesh Guria, Bappa Acherjee, Souren Mitra	220
120	Study of Weldability of 304H Austenitic Boiler Quality Steels by Gas Tungsten Arc Welding	Subhodwip Saha, Santanu Das and Subrata Mondal	234
122	Optimization of Laser Welding Parameters to Minimize Heat-Affected Zone in SS304 Stainless Steel	Upama Dey, Bappa Acherjee, Souren Mitra	240

Precision & Micro-Manufacturing			
Paper ID RAMTM25-	**Paper Title**	**Author List**	**Page No.**
112	An Experimental Investigation into the Top Burr Formation in Micro-Milling Using Bulk Metallic Glass	Debajyoti Ray and Asit Baran Puri	249

Precision & Micro-Manufacturing			
Paper ID RAMTM25-	**Paper Title**	**Author List**	**Page No.**
119	Experimental Investigation on The Dielectric Effect During Electro Discharge Machining of Tin-Al2O3 Composites	Goutam Paul, Soumya Sarkar, Nagahanumaiah and Souren Mitra	256

Emerging Manufacturing Technologies			
Paper ID RAMTM25-	**Paper Title**	**Author List**	**Page No.**
116	Bibliometric Analysis of Emerging Manufacturing Technologies: A Sustainable Review	Ajoy Kumar Bhowmick, Nipu Modak	269
127	A Comprehensive Review of Cryogenic Treatment Effects on Tool Hardness, Wear Resistance, and Microstructural Transformations	Mr Mohan L Chanpur and Dr Sandeep H Wankhade	277

Green Technology & Sustainable Manufacturing			
Paper ID RAMTM25-	**Paper Title**	**Author List**	**Page No.**
212	Transforming Plastic Waste into Eco-Friendly Bricks: A Sustainable Approach to High-Density Polyethylene Recycling	Abu Supian Gazi, Ziyauddin Seikh, Mukandar Sekh	293

Safety Engineering & Management			
Paper ID RAMTM25-	**Paper Title**	**Author List**	**Page No.**
205	IOT Based Radiation Monitoring for Safe Operation of Industrial Radiography (IR) Facilities	M. K. Pathak, A. Pathak, S. Sarkar	305

Optimisation of Production Systems			
Paper ID RAMTM25-	**Paper Title**	**Author List**	**Page No.**
203	Multi-Response Optimization of Design for Tibia Fracture Fixation Plate Using Taguchi Grey Relational Analysis	Drupad Roy, Manik Chandra Das, Raja Dhason, Shubhabrata Datta	313
211	Infusion of Holonomy In Multi Criteria Decision Making	Bikash Bepari and Bipradas Bairagi	318
213	Design and Optimization of Two Stage Gear Reducer Using Real Coded Genetic Algorithm for Multiple Gear Ratios	Paridhi Rai and Asim Gopal Barman	325

Miscellaneous			
Paper ID RAMTM25-	**Paper Title**	**Author List**	**Page No.**
202	A Numerical Study on Evolution of Heat Flow During Solidification of A356 Alloy	Joydip Paul, Sudip Simlandi, and Nilkanta Barman	335

Additive Manufacturing

Experimental Investigation of Mechanical and Tribological Properties of 3D-Printed Polymer Materials Using Variable FDM Parameters

Goutam Kumar Bose[1], Gairik Kumar Bose[2], Ritoban Maitra[1] and Indrajeet Sen[1]
[1] Haldia Institute of Technology, Haldia, West Bengal, India
[2] Tata Consulting Engineers, Kolkata, West Bengal, India
gkbose@yahoo.com
gairik.bose@tce.co.in
ritoban.maitra24@gmail.com
indrajeetsen04@gmail.com

Abstract. Additive manufacturing, also known as 3D printing, is a revolutionary method used in industrial production to create lighter and stronger parts or systems. It uses data computer-aided design or 3D object scanners that deposit material for layer-by-layer geometric shapes. In this method, performance will be improved, complex geometries will be allowed, and fabrication will be easy. The Fused Deposition Modelling 3D printing method is used to provide a realistic guideline for the 3D printed commodities. It shows that optimal surface roughness could be obtained from PLA material, high printing speed, moderate temperature, and a prohibited layer height of 0.2 mm. This study deals with the characterization of the FDM process using PLA, ABS, and Nylon by investigating Compressive Strength, surface roughness, and Wear Resistance. The factors of wear resistance were the printing speed, temperature, and layer height. The optimal conditions in which maximum wear resistance is induced are associated with a large layer height and moderate to high temperatures at high-speed print. Mildness is all about achieving maximum strength and wear resistance. At 210-225°C and a speed of 60-70 mm/s, the FDM process optimizes strengths, wear resistance, and surface finishes. Nonetheless, there are trade-offs. For instance, improvements in wear resistance come at the expense of surface finish or strength.

Keywords: 3D printing, FDM, Surface Response Methodology

1 Introduction

Additive manufacturing is also commonly known as 3D printing. It is a revolutionary method in industrial production to make lighter and stronger parts or systems. It employs data computer-aided design or 3D object scanners to deposit material as the only source for creating layer-by-layer geometric shapes. Unlike traditional methods, additive manufacturing requires the removal of material through milling, machining, carving, and shaping, among others. That is to say, additive manufacturing offers improved performance, complex geometries, and simplified fabrication in the right applications and provides ample opportunity to those embracing it.
A summary of the previous literature relevant to the earlier study is provided in this section. Product manufacturing applies more advanced business models in engineering and manufacturing, presenting many production and consumption options without facing huge challenges.[1] The mechanical performance of ABS is highly dependent upon FDM parameters where the raster angle and gap influence properties; however, a negative gap shows increased performance while a positive gap lowers the performance.[2] The laser treatment on the BMGMC samples modifies the microstructure. It changes the size, morphology, and dispersion of the CuZr B2 phase into the base metal, heat-affected zone, and fusion zone. The technique was applied to document the treatment and emphasize the complexity of the thermal history of metallic AM parts/alloys.[3] The areas where Advanced Manufacturing (AM) changes the industry's face are geometry processing and material design. Because of the emergence of AM, geometry processing and material design benefits have been made available in education.[4] Gu et al. explore the utilization of powder materials in laser-based material characterization (AM) of metallic components, especially their physical properties, densification mechanisms, and the relation between the material, process, and metallurgical mechanisms. [5] Through intensive research over the last twenty years, tremendous growth has been made in the development and commercialization of new and innovative AM processes and numerous practical applications have been developed in aerospace, automotive, biomedical, energy, and other fields. Thus through intensive research, AM technology has made tremendous progress through advancing its applications in various fields and has shown significant progress in the field of research. [6] The relationship of AM processes with materials is complex and includes laser and electron beam melting. Typical microstructures

of additively manufactured steel, aluminium, and titanium that are presented go along with properties evolving under static as well as dynamic loading. [7] A comparison of cost, traditional injection moulding vs layer manufacturing techniques (stereolithography, fused deposition modelling, laser sintering), shows that in certain geometries layer manufacturing techniques can become more economical. [8] Rapid prototyping techniques develop shaped objects by iteratively adding material. These methods are distinct from shaping and material removal manufacturing processes. Ten years of research and development in rapid prototyping, focusing on process-by-process details and technological and economic trends. [9] Metallic materials fabricated by direct energy deposition and powder bed fusion are evaluated in terms of strength, toughness, and the formation of fatigue cracks.[10] Polymer processing is a crucial aspect of advanced polymer systems, particularly in additive manufacturing (AM). Techniques like sheet lamination, extrusion, and 3D bioprinting are used to create a range of polymers, including thermoplastics, thermosets, elastomers, hydrogels, functional polymers, and biological systems. These polymers are used in various applications, including lightweight engineering, architecture, food processing, optics, energy technology, dentistry, and personalized medicine. [11] This new development of a metal/polymer composite material for FDM rapid prototyping involves cost and time savings. The feedstock consists of iron particles dispersed within a nylon-type matrix. Experimental investigation has been carried out on the thermal properties in comparison to other composites. Feedstock filaments were successfully used in an unmodified FDM system for injection moulding inserts. [12]The well-ordered tissue constructs in human tissues and organs are created using computer-aided design techniques in additive manufacturing. The spatial variations of cells and biomaterials are produced in these techniques, which would speed up the process of understanding how to create tissue and its function. That is still not sufficient, though, because the availability of suitable polymers is still below expectations, and the application already needs practicality. [13] 3D printing is the additive production technique that produces an object layer by layer based on a CAD program. It improves the times of production for small parts and is flexible. Fused Deposition Modelling FDM employs plastic filament and heated extrusion nozzles. Various challenges and mechanical properties are presented in the production process with different materials. [14] The FDM technique is a critical element of 3D printing and material requirements. This part briefly discusses the pros and cons of recycled, bio-based, and blended thermoplastics, and available solutions for improving their mechanical properties before, during, and after the printing process. [15] The thermal and mechanical properties of new metal-particle-filled ABS composites developed for Fused Deposition Modeling applications are presented. DMA techniques were adopted to characterize the viscoelastic properties. It was found that the inclusion of the metallic filler in the composite improved the thermal and mechanical properties of ABS. Thus, such composite applications in various fields can help achieve high-performance prototypes on FDM platforms. [16] Additive manufacturing (AM) involves the formation of parts from powder, wire, or sheets using various techniques developed for melting or solid-state joining. Techniques are targeted at processing defects, heat transfer, solidification, solid-state precipitation, mechanical properties, and post-processing metallurgy. New efforts focus on new material developments for commercial production. [17] Additive manufacturing, also popularly known as 3D printing, is one of the popular processing methods of fibre composites, which received a great deal of attention in terms of high performance and durability. However, the inherent strength of these composites is quite lower in comparison to the conventional methods, of injection moulding. This article reviews the analysis of the performance of FDM-fabricated polymer-fibre composites during mechanical testing and the observed properties along with the effect of various processing parameters on the resultant thermal properties. [18] Layer structures as well as road structures have direct significant effects on the mesostructure and mechanical properties of polymer chains. Schemes of deposition, such as adaptive slicing and curved layer deposition, are critical to achieve the maximum connectivity and continuity of polymer chains in their network. Curved layer deposition is suggested for FDM particularly for thin shell-like parts to ensure fiber continuity. An enhancement in the mathematical models of curved slicing towards improved mechanical characteristics in printed parts has been established. [19] Recent decades have witnessed tremendous growth in Additive Manufacturing technologies, concentrating more on the evolution of engineering design and taking advantage of the possibilities of the technology while its constraint is mitigated. It provides opportunities, constraints, and economic considerations for design for AM production with key industrial applications, future challenges, and promising research directions for maximizing AM's potential in the industry. [20] Orthopaedic regenerative medicine uses the principle of mimicking the biomechanical properties of host bones in the design of bone scaffolds and implants. Porous metals offer flexible stiffness and porosity, hence enabling the in-growth of bone tissue, which further accelerates osseointegration. Additive manufacturing, a more recent manufacturing technique, now offers complex structures with customized mechanical performance. Topology optimization techniques allow porous metals to achieve specified mechanical properties, hence the implants designed by this approach of additive manufacturing are of interest. [21] Wire + Arc Additive Manufacturing is a manufacturing technology enabling large, critical components to be deposited in metals such as titanium, aluminium, and steel. This process provides higher deposition rates, low material and equipment costs, and good structural integrity for use as a replacement

for low and medium-complexity parts. [22] Additive manufacturing is revolutionising the manufacturing industry by offering strength and accuracy. Despite much research and development, additive manufacturing has become the most crucial part of the future of manufacturing despite an improvement in handling various materials. [23] The work studies characteristic features of the FDM process in producing the product using PLA, ABS, and Nylon by investigating Compressive Strength, surface roughness (Ra), and Wear Resistance by doing experimental studies on various process parametric combinations of Printing Speed (PS), Printing Temperature (PT), and Layer Height (LH). ANOVA was used to analyze this experimental data. Concerning the Taguchi Methodology, the Signal to Noise Ratio (S/N ratio) reveals how significant process parameters will affect the individual response. This experimental study aims to simultaneously produce minimum surface roughness (Ra), better compressive strength, and higher wear resistance while achieving the basic but contradictory goals by utilising a single set of optimal or nearly optimal process variables. Multi-response optimization has been done using the Response Surface Methodology.

2 Experimental plan

The present experimental study was conducted on Delta WASP 2040 Industrial X with WASP ZEN X Extruder 0.4 mm as shown in Figure 1. Three different polymer material filaments were used namely, PLA (Polylactic Acid), ABS (Acrylonitrile Butadiene Styrene) and Nylon. Figure 2 shows the product developed in different polymer materials. Other variable parameters that are considered are Printing Speed, Printing Temperature and Layer Height. Three different responses such as surface finish, compressive strength and wear resistance are measured during the experimentation following the L9 orthogonal array. The Perthometer M1 is a stylus-type profilometer produced by MahrGmbh and is used to determine the surface finish of the product which is expressed in µm as Ra. Compressive strength test is done by the objects with the help of a Universal Testing Machine of TUE-C-100. The wear resistance test is done by using a Tribotester of (TR-20LE) DUCOM make. Depending upon the capacity of the FDM machine, the control parameters and their levels are shown in Table 1 below.

Table 1: Control parameters and levels

Control Parameters	Symbols	Units	Levels		
			L1	L2	L3
Printing Speed	PS	mm/s	30	50	70
Printing Temp	PT	°C	190	210	230
Layer Height	LH	mm	0.1	0.2	0.3

Fig 1: FDM machine

Fig 2: Product in (a) PLA, (b) ABS (c) Nylon

3 Results and Discussion

The graph of the S/N ratio is an analytical tool for Response Surface Methodology. It could be applied to determine the robustness of the process, which is defined by three responses: wear resistance, surface roughness, and strength. The higher values of the S/N ratio indicate stability and lower sensitivity to parameter variability. The smaller values will account for a smoother surface with the best strength.

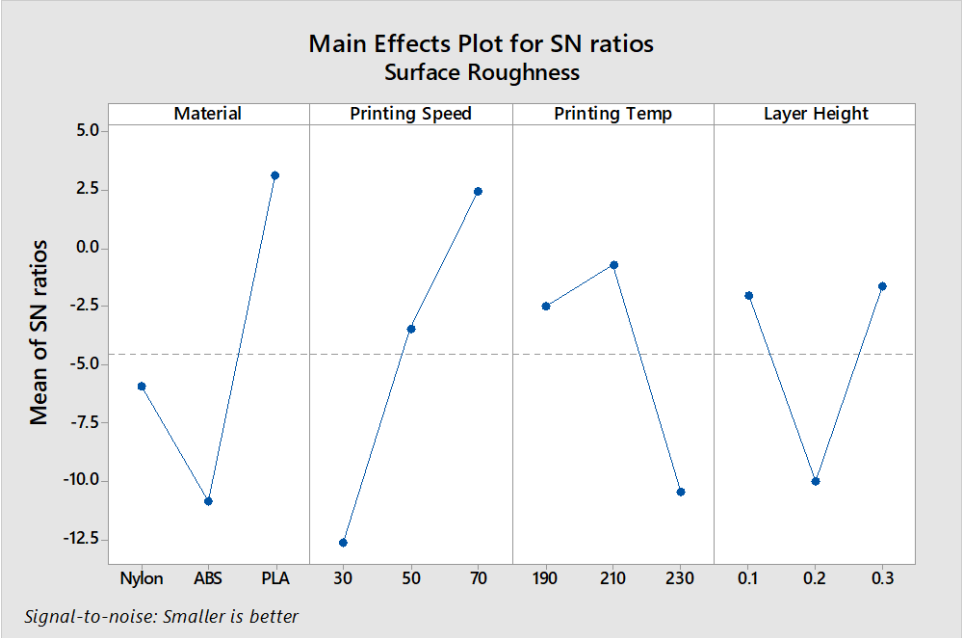

Fig 3: S/N ratio for Surface Finish

The effects plot in Fig. 3 above shows the effects of material, print speed, print temperature, and layer height on the strength of a 3D-printed part. However, the material choice has virtually no impact on strength; print speed greatly reduces the SN ratio. Print temperature elevates the maximum strength, whereas layer height has no significant effect. The SN ratio is independent of all tested values.

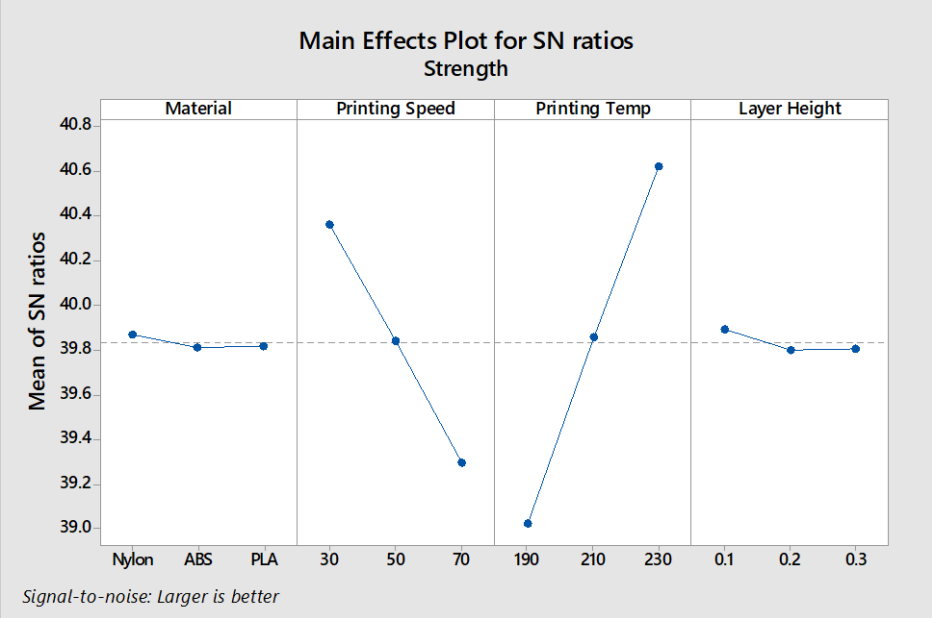

Fig 4: S/N ratio for Strength

The S/N Ratio Plot as illustrated in Fig. 4, shows how material, print speed, print temperature, and layer height affected the factors of surface roughness. Both PLA and Nylon got the best performances with high SN ratios at the same time having the roughest surfaces of ABS. Greater print speeds create smoother surfaces. The roughest surfaces were provided by the smallest SN ratio, 0.2 mm. SN ratios of 0.1 mm and 0.3 mm are more excellent for surface roughness.

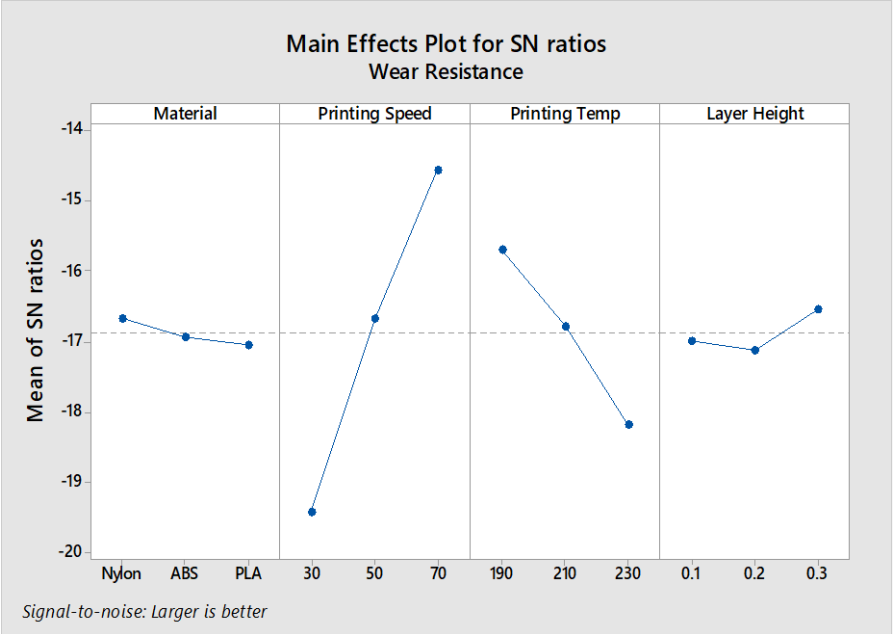

Fig 5: S/N ratio for Wear Resistance

The S/N Ratio Plot as illustrated in Fig. 5, indicates that material choice has no significant effect on the wear resistance of ABS and Nylon. The SN ratios suggest a slight improvement in Nylon but, for PLA, with the lower value obtained, material choice is not significant. Wear resistance increases as the printing speed increases from 30 to 70 mm/s. Temperature varies in a nonlinear relationship, and optimum temperatures occur at moderate values of 210°C. Layer height also varies with wear resistance performance, with 0.3 mm showing the best performance.

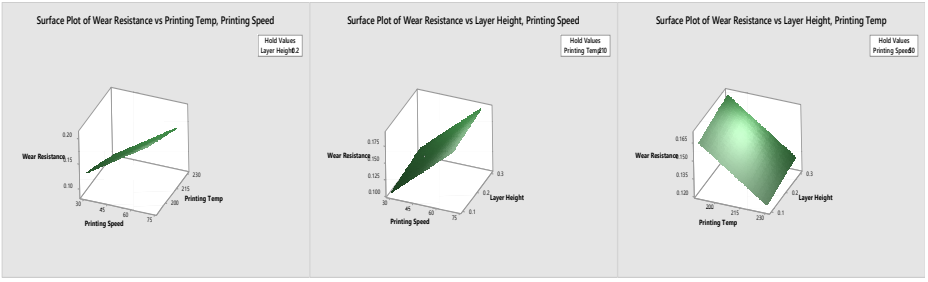

Fig 6: Response Surface Plots of Wear Resistance

The Fig. 6 shows three surface plots indicate interaction effects between different pairs of factors for the Wear Resistance. Each plot shows a 3D view, indicating how wear resistance changes with alterations in the levels of Printing Speed, Printing Temperature, and Layer Height. Therefore, in Plot 1 there is a clear positive correlation between printing speed and wear resistance although with a slight increase in wear resistance while the printing speed increases. The region of optimum wear resistance happens when the combination is a higher value of the printing speed around 70 mm/s with moderate to high temperatures of the printing process, approximately 230°C. As seen in Plot 2, the most obvious effect that layer height would have on resistance to wear is that greater layer heights relate well with higher resistance. The effect of printing speed, in this regard, also relates well with higher resistances, and its optimal region is seen to be when higher printing speeds combined with the largest layer height are used. In Plot 3, layer height is the most influential in wear resistance: Higher heights are at 0.3 mm, while larger wear resistances are evident. It is less significant for printing temperature, but the whole optimum region for wear resistance still depends on a combination of high layer height and moderate to high printing temperatures.

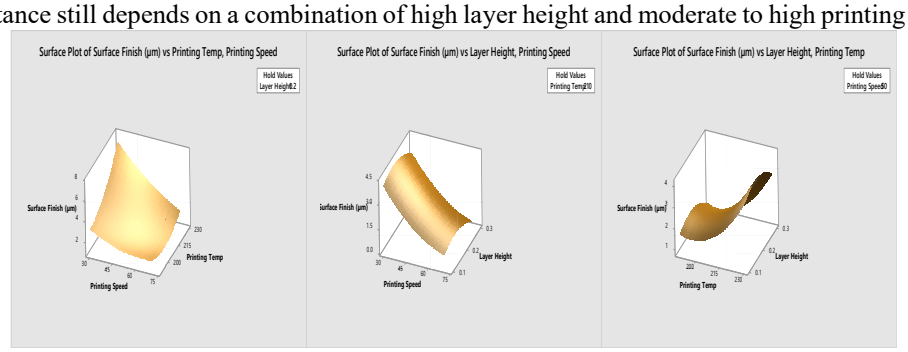

Fig 7: Response Surface Plots of Surface Finish

The surface plots demonstrated in Fig.7 show how Surface Finish, in µm, is controlled by combinations of Printing Speed, Printing Temperature, and Layer Height. Lower values on the surface finish scale are indicative of a smoother surface finish which is the desirable characteristic for most 3D printing applications. In Plot 1, The surface finish strongly depends on printing speed at which higher speeds result in a smoother finish. However, the effect of the printing temperature also impacts the resultant finishing surface as its contribution yields an improvement with increased temperatures. Thus, this region is obtained at higher temperatures and speeds for the smoothest surface finish. In Plot 2, it is evident that the surface finish depends on layer height and printing speed. The lower the layer heights, the smoother the surfaces, and the more the printing speed, the better the surface finish. The best layer height-speed combination will result in the best feasible surface finish and the best area is also a combination of two. The surface finish is affected by the layer height and the printing temperature as shown in Plot 3. Lower layer heights give a smoother surface than if layers are high. However, very rough surfaces are produced if the layers are high. High-temperature improvements for surface finish are just slight and not as strong as layer height. Low layer height and high printing temperature give a smooth surface finish.

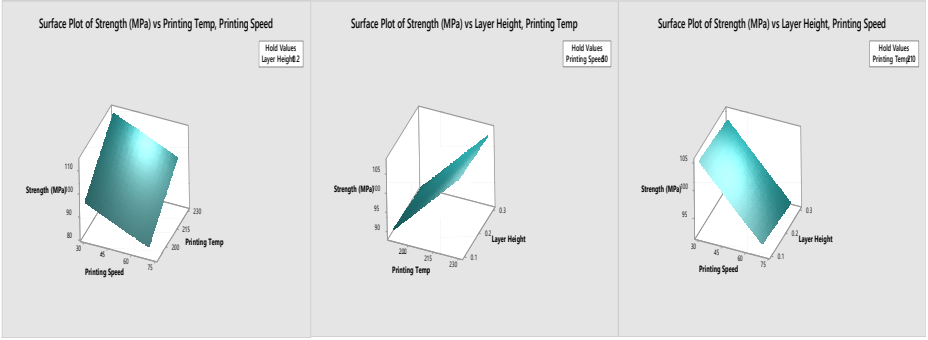

Fig 8: Response Surface Plots of Strength

The three surface plots as illustrated in Fig.8 show the Strength in MPa is a function of combinations of Printing Speed, Printing Temperature, and Layer Height. In Plot 1, the strength values correlate well with better mechanical properties values. The strength of a printing process increases strongly with increasing printing temperature, and it is apparent that the increase becomes more pronounced as the temperature approaches 230°C. The effect of printing speed is much less significant, with minor increases in strength noted at higher speeds. The optimal region for strength appears to be at 230°C and 50-70 mm/s. In Plot 2, the layer height hugely affects the strength, particularly when it comes to printing temperature. More compact layer heights, for example, 0.1 mm are stronger. High temperatures above 210°C to 230°C improve the strength. The highest strength is obtained with low layer height and with high temperature. Plot 3 demonstrates that strength decreases with increasing layer height in printing. Lower layer heights provide better mechanical properties. Strength increases slightly with higher printing speed; however, it is minimal. The optimal region for the highest strength forms through a combination of low layer height and moderate to high printing speed.

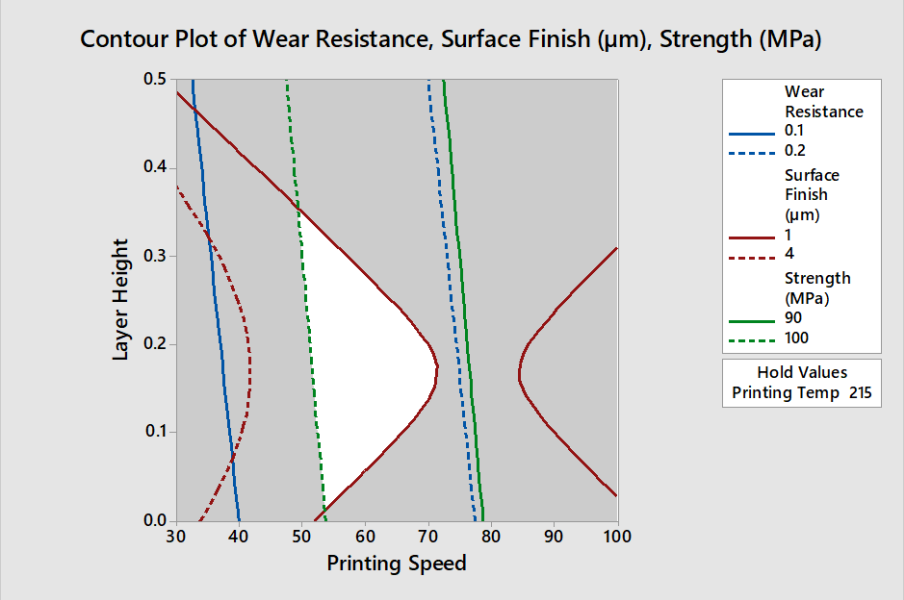

Fig 9: Contour Plot of the Responses against Layer Height and Printing Speed

The contour plot in Fig. 9 displays the effect of print speed and layer height on wear resistance, surface finish, and strength during the FDM process at 215°C. Wear resistance increases with the increased layer height and the increased printing speed, with the most wear-resistant samples found in the lower left corner. The surface finish increases at moderate printing speeds and decreases with a smaller layer height, while the rough surface appears to increase with time. Lower layer height and speed will increase strength, but the best strength feature is found in the lowest layer height and speed regions. The best strength features work well with a combination of low layer heights and lower speeds. Generally, the graph shows that these factors play a role that should be taken into consideration during the process of FDM.

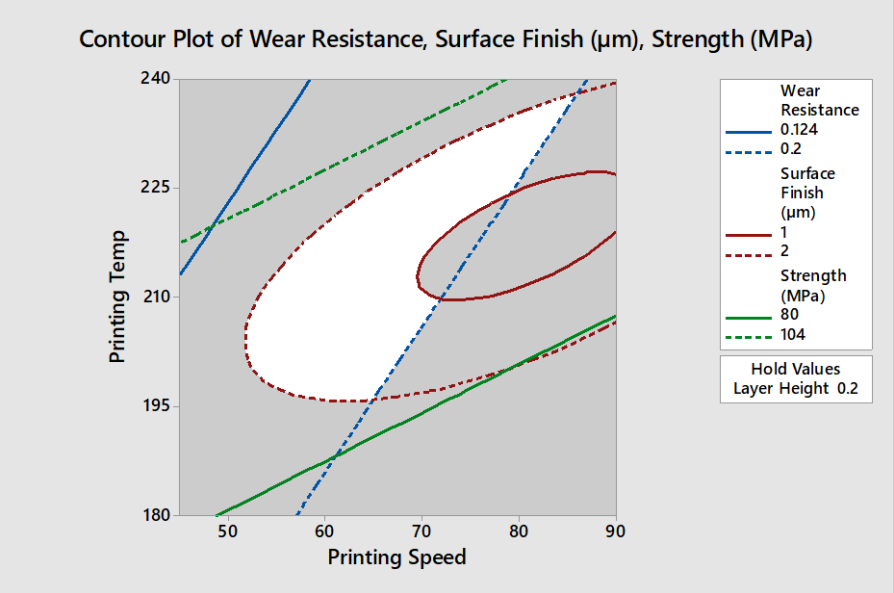

Fig 10: Contour Plot of the Responses against Printing Temp. And Printing Speed

From the contour plot, as shown in Fig. 10, the effects of print speed and temperature can be known about three aspects in Fused Deposition Modelling; wear resistance, surface finish, and strength. The highest wear resistance is higher at high temperatures and a low speed; such regions with low speeds give the best performance. The surface finish was found to be lower with a printing speed of 70 mm/s of the temperature range of 210-220°C with poorer areas often concentrated in lower temperatures and high speeds. Optimal strength is obtained at higher temperatures greater than 220°C for moderate velocities where strength increases substantially with temperature regardless of printing velocity. Maximum strength occurs at intermediate velocities and elevated temperatures greater than 220°C and will be found on the green strength lines, particularly towards the regime of 104 MPa.

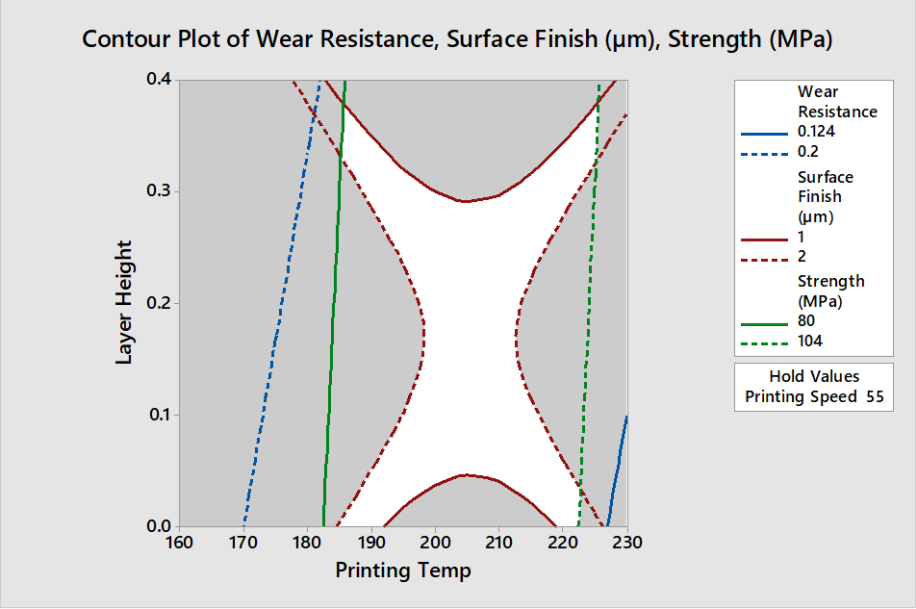

Fig 11: Contour Plot of the Responses against Layer Height and Printing Temp.

An interaction effect of print temperature and layer height on three measured responses in FDM for ABS, Nylon, and PLA materials has been depicted in a contour plot as shown in Fig. 11. Wearing resistance is found to increase with higher layers and temperatures. The surface finish or roughness is related to layer height and temperature. A better surface finish corresponds to smaller layer height and printing temperature, while the increase in surface roughness relates to an increase in layers and temperatures. Strength increases by the ascending temperature of printing and descendent heights of layers. Printing at high temperatures, above 200°C, seems to achieve optimal strength. This may be seen in ABS, PLA, and Nylon which show higher bonding strength in a high-temperature range. The graph illustrates the complex relationship of those parameters and their effect on the performance of FDM materials.

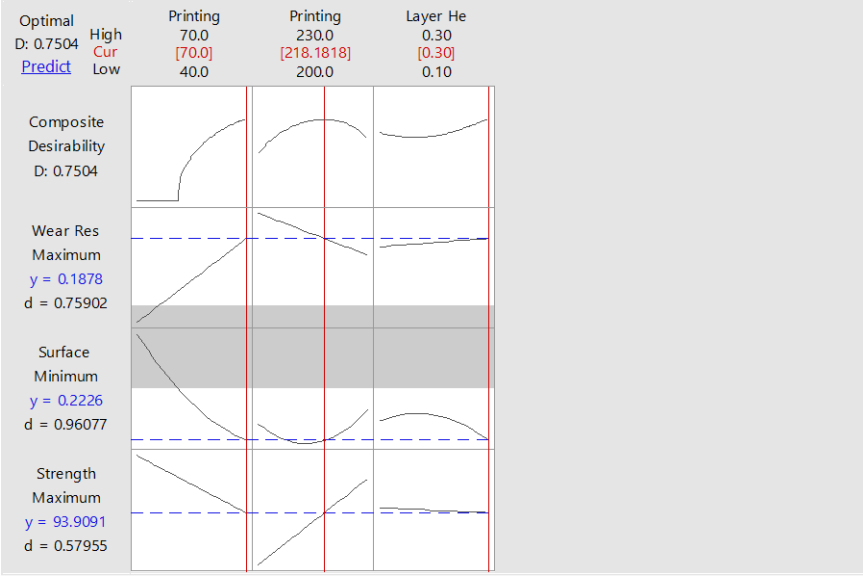

Fig 12: Response Optimiser graph for the responses

The response optimiser graph as shown in Fig. 12, allows for wear resistance, surface roughness and strength to be optimized together to produce optimal results, employing a composite desirability function when setting goals that are also conflicting. This graph helps in better understanding complex responses better. This composite desirability score (D) stands at 0.7504, which depicts a fairly good overall optimization in printing speed, temperature, and layer height. It is, therefore, an adequately optimized process but not without flaws. Wear resistance is optimized sufficiently at a maximum value which occurs at chosen values of parameters; however, still, there is room for improvement because various parameter interactions could conflict with layer height and surface finish interactions. However, this result promises more wear resistance. Surface roughness is among the most critical responses for a surface. A high desirability score of 0.96077 indicates that the model significantly reduces surface roughness, assuming other factors are in order, for example, printing speed, temperature, and layer height. This high desirability suggests that the parameters selected appropriately impact the finish. Surface roughness and wear resistance are significant parameters that determine the maximum strength of a material. The present limiting setting parameters do not allow reaching the maximum strength, but optimizing strength in tandem with surface finish can give a balance between minimizing roughness and enhancing strength. The two main variables are the surface roughness and strength. The optimal speed depends on the printing temperature with these two variables. A minimum surface roughness and maximum wear resistance are achieved with a 70 mm/s speed. At a temperature of 230°C, the wear resistance competes with the strength, while its surface roughness is minimized. In the 0.3mm layer height, both strength and finish can be balanced.

4 Conclusion

An effective and practical guideline for producing a variety of 3D printed goods by using the FDM method can be obtained from the experimental study to assess the ideal parametric combination and the ensuing impact of the parameters over the responses. PLA provides very smooth surfaces, while ABS provides rougher finishes. The best temperatures for wear resistance are around 210°C. High speeds of about 70 mm/s give smoother surfaces. The ideal selection would be to use the PLA material, high printing speed, moderate temperature, and avoid a 0.2 mm layer height for optimal surface roughness. Importantly, factors affecting wear resistance considerably include printing speed, temperature, and layer height. The higher the print speed, high temperature, and large layer height results in smoother surfaces but with lower strength. Therefore, optimal conditions for maximum wear resistance occur in a high-speed print with a large layer height and moderate to high temperatures.

It is evident from the experiment that the wear resistance depends on the rate of printing, and that mainly if coupled with higher temperatures or thicker layer heights. Low printing rates with small layer heights normally ensure optimal levels of strength, but wear resistance favours higher speeds and low layer heights. However, to attain an optimal balance in this case, layer height had to be compromised, and because it tends to weaken the material with increased speed. The FDM process has optimized strengths, wear resistance, and surface finishes at 210-225°C and a speed of 60-70 mm/s. Moderation is the key to moderate temperature against moderate speed for maximum strength and wear resistance that ensures favourable material properties.

Strengthening, wear resistance, and a surface finish: FDM maximizes such characteristics. Strength, wear resistance, and generally acceptable surface finish: the middle zone is found around 200°C. Print parameters are balanced to ensure that for the main aim, the selection strikes a balance. A contour plot helps to select the best fit of parameters for specific goals in the FDM process.

The optimization process for Fused Deposition Modelling is well-balanced, minimizing surface roughness while optimizing wear resistance and strength. The process involves compromising parameters like printing speed, temperature, and layer height to achieve desirable outcomes. However, some trade-offs remain, such as improving wear resistance at the cost of surface finish or strength. Surface roughness is highly optimized, suggesting a preference for smoother surfaces. Future research in this evolving discipline may assess these criteria and responses.

References

1. Ford, S., & Despeisse, M. (2016). Additive manufacturing and sustainability: an exploratory study of the advantages and challenges. Journal of Cleaner Production, 137, 1573–1587.
2. Taha, I., & Ebeid, S. J. (2016). Mechanical behaviour of ABS: An experimental study using FDM and injection moulding techniques. Journal of Manufacturing Processes, 21, 39–45.
3. Frazier, W. A. (2014). Metal Additive Manufacturing: A Review. Journal of Materials Engineering and Performance, 23(6), 1917–1928.
4. Gao, W., Zhang, Y., Ramanujan, D., Ramani, K., Chen, Y., Williams, C., Wang, C. C. L., Shin, Y. C., Zhang, S., & Zavattieri, P. D. (2015). The status, challenges, and future of additive manufacturing in engineering. Computer-Aided Design, 69, 65–89.
5. Gibson, I., Rosen, D. W., & Stucker, B. (2010). Additive Manufacturing Technologies. In Springer eBooks.
6. Gu, D., Meiners, W., Wissenbach, K., & Poprawe, R. (2012). Laser additive manufacturing of metallic components: materials, processes and mechanisms. International Materials Reviews, 57(3), 133–164.
7. Guo, N., & Leu, M. (2013). Additive manufacturing: technology, applications and research needs. Frontiers of Mechanical Engineering, 8(3), 215–243.
8. Herzog, D., Seyda, V., Wycisk, E., & Emmelmann, C. (2016). Additive manufacturing of metals. Acta Materialia, 117, 371–392.
9. Hopkinson, N., & Dickens, P. (2003). Analysis of rapid manufacturing—using layer manufacturing processes for production. Proceedings of the Institution of Mechanical Engineers, Part C: Journal of Mechanical Engineering Science, 217(1), 31–39.
10. Kruth, J., Leu, M., & Nakagawa, T. (1998). Progress in Additive Manufacturing and Rapid Prototyping. CIRP Annals, 47(2), 525–540.
11. Lewandowski, J. J., & Seifi, M. (2016). Metal Additive Manufacturing: A Review of Mechanical Properties. Annual Review of Materials Research, 46(1), 151–186.
12. Ligon, S. C., Liska, R., Stampfl, J., Gurr, M., & Mülhaupt, R. (2017). Polymers for 3D Printing and Customized Additive Manufacturing. Chemical Reviews, 117(15), 10212–10290.
13. Masood, S. H., & Song, W. (2005). Thermal characteristics of a new metal/polymer material for FDM rapid prototyping process. Assembly Automation, 25(4), 309–315.
14. Melchels, F. P., Domingos, M., Klein, T. J., Malda, J., Da Silva Bartolo, P. J., & Hutmacher, D. W. (2012). Additive manufacturing of tissues and organs. Progress in Polymer Science, 37(8), 1079–1104.
15. Ngo, T., Kashani, A., Imbalzano, G., Nguyen, K., & Hui, D. S. (2018). Additive manufacturing (3D printing): A review of materials, methods, applications and challenges. Composites Part B-engineering, 143, 172–196.
16. Nikzad, M., Masood, S. H., & Sbarski, I. (2011). Thermo-mechanical properties of highly filled polymeric composites for Fused Deposition Modeling. Materials in Engineering, 32(6), 3448–3456.
17. Sames, W. J., List, F. A., Pannala, S., Dehoff, R. R., & Babu, S. S. (2016). The metallurgy and processing science of metal additive manufacturing. International Materials Reviews, 61(5), 315–360.
18. Shanmugam, V., Haarith, D., Babu, K., Rajendran, S., Veerasimman, A., Marimuthu, U., Singh, S., Das, O., Khorasani, S. N., Hedenqvist, M. S., Berto, F., & Ramakrishna, S. (2021). The mechanical testing and performance analysis of polymer-fibre composites prepared through additive manufacturing. Polymer Testing, 93, 106925.
19. Singamneni, S., Roychoudhury, A., Diegel, O., & Huang, B. (2012). Modelling and evaluation of curved layer fused deposition. Journal of Materials Processing Technology, 212(1), 27–35.

20. Thompson, M. E., Moroni, G., Vaneker, T. H., Fadel, G. M., Campbell, R. I., Gibson, I., Bernard, A., Schulz, J., Graf, P., Ahuja, B., & Martina, F. (2016). Design for Additive Manufacturing: Trends, opportunities, considerations, and constraints. CIRP Annals, 65(2), 737–760.
21. Wang, X., Xu, S., Zhou, S., Xu, W., Leary, M., Choong, P. F. M., Qian, M., Brandt, M., & Xie, Y. (2016). Topological design and additive manufacturing of porous metals for bone scaffolds and orthopaedic implants: A review. Biomaterials, 83, 127–141.
22. Wang, Y., Voisin, T., McKeown, J. T., Ye, J., Calta, N. P., Li, Z., Zeng, Z., Zhang, Y., Chen, W., Roehling, T. T., Ott, R. T., Santala, M. K., Depond, P. J., Matthews, M. J., Hamza, A. V., & Zhu, T. (2018). Additively manufactured hierarchical stainless steels with high strength and ductility. Nature Materials, 17(1), 63–71.
23. Williams, S. W., Martina, F., Addison, A. C., Ding, J., Pardal, G., & Colegrove, P. A. (2016). Wire + Arc Additive Manufacturing. Materials Science and Technology, 32(7), 641–647.
24. Wong, K. V., & Hernandez, A. M. P. (2012). A Review of Additive Manufacturing. ISRN Mechanical Engineering (Print), 2012, 1–10.

TOPOLOGY OPTIMIZATION OF COMPONENT FOR FUNCTIONAL INTEGRATION USING ADDITIVE MANUFACTURING

Subho Mukherjee[1], Bhushan Dewangan[2]

[1] Department of Mechanical Engineering, Institute of Engineering & Management, Kolkata
[2] Department of Mechanical Engineering, National Institute of Technology, Rourkela

subhomukherjee2@gmail.com
erbhushandewangan@gmail.com

Abstract. Additive manufacturing, a cutting-edge production technique, allows for rapid prototyping and the creation of complex components. Coupled with topology optimization, a powerful computational tool, mechanical and structural designs can be optimized for material distribution. This synergistic approach unlocks new design possibilities, enabling the creation of innovative and efficient parts. The present work proposes topology optimization of the fire extinguisher mounting brackets for better load carrying capacity, being cost effective and making them available for application using 3D printing. The research offers validation modules for the mounting brackets considering point of application of load and holding position of bracket as constraints. Numerical simulations employing the Von Mises criterion and total deformation optimization in ANSYS Workbench aim to minimize mass. This work presents a novel approach to optimize the design of mounting brackets using topology optimization. By optimizing the material distribution, the design aims to improve strength while reducing mass and cost. Results suggest that the presented approach effectively leverages additive manufacturing for lighter and better functional strength. Different test scenarios are examined and optimum geometrical properties are selected. Important findings associated with the safe design in the context of various parameters like Von Mises stress, strain under loading and the deformation pattern of the part is reported in this research. Findings suggest that the topology optimization not only reduces mass but also cost of material as it directly affects the manufacturing cost associated with the brackets.

Keywords: Topology Optimization, Mass reduction, Additive Manufacturing, Total deformation & Von-Mises Stress Criteria.

1 Introduction

Additive manufacturing, or 3D printing, is a rapidly growing technology that creates tangible objects from digital designs [1]. 3D printing is a manufacturing process that creates physical objects from a digital model. It works by adding layers of material to build up the object. For 3D printing topology optimization minimizes material wastage. The design compliant optimized part is absolutely important for manufacturing [2]. This technology has seen rapid growth in recent years. The first commercial 3D printer was developed in 1980 by Charles Hull. Today, 3D printing is not only used for prototyping but also used to make a wide variety of products, including artificial heart pumps, jewellery, 3D printed corneas, rocket engines, steel bridges, and products for the aviation and food industries [3].

Topology optimization is used in tailoring designs for specific additive manufacturing processes, such as 3D printing, to maximize part quality and efficiency as introduced in their research by [4]. Later [5] in the research proposed the material distribution approach for topology optimization. An evolutionary algorithm for topology optimization was as presented by [6]. [7] Reviews recent advances in topology optimization with functionally graded materials. [8] Discusses the challenges and opportunities of topology optimization for additive manufacturing. Fatigue failure of parts due to cyclic loading has been the area of the interest for many of the authors. Multi material compliance minimization problem was presented by sanders et al. in their research article. [9] carried out topology optimization of a high performance aerospace bracket and validated both experimentally and analytically the increase in strength characteristics of the proposed model. The materials also play an important role when it comes to the topology optimized 3D printing parts [10]. The authors [11] presented topology optimization procedure in their research for anisotropic materials and proposed strength improvement. Authors [12] introduced penalty method of topology optimization in their research and presented different set of design considerations. Many authors have historically attempted topology optimization for multi-material continuums as proposed in their research [13]. The enhancement of the part's performance is obtained by topology optimization by [14]. Topology optimization techniques for the adaptive structures is as presented by [15].

After an insightful review of the available literatures, an attempt to optimize the geometry of the fire extinguisher bracket is proposed in the paper. This article mainly considers the application of topology-optimized structural design for improvised strength characteristics. The article is presented as follows. In Section two, the detailed design requirements of the fire extinguisher mounting bracket is presented. Section three introduces the design model of the fire extinguisher mounting bracket considering strength characteristics. This section also harbours the comparison of the various process parameters considering various loading for the bracket. In the Section four, the result and discussion is presented.

2 ANSYS Modelling

The commercial software ANSYS has been used for the structural optimization. Fig.1 represents various views for the cad model prepared in ANSYS. The static structural module has been used for analysis. Iterative solver is employed to solve the static structural for mounting bracket. The meshing method used is of mostly tetrahedrons (Quadratic element order) with patch conforming being the meshing algorithm. The selection of this element is done to maintain the stability, reduction of computation time and consideration of curvature body for effective stress prediction. Convergence criteria is being measured for equivalent stress of 2.62e+06 Pa having 8953 nodes and 5015 elements. The inner surface of the hole in the mounting brackets are selected as a boundary conditions. Fig.2 represents the flowchart for topology optimization in ANSYS workbench.
B.Cs: Remote Displacements(X,Y,Z) is Zero(m) and Rotations (R_x R_y and R_z) to be Zero(deg.).

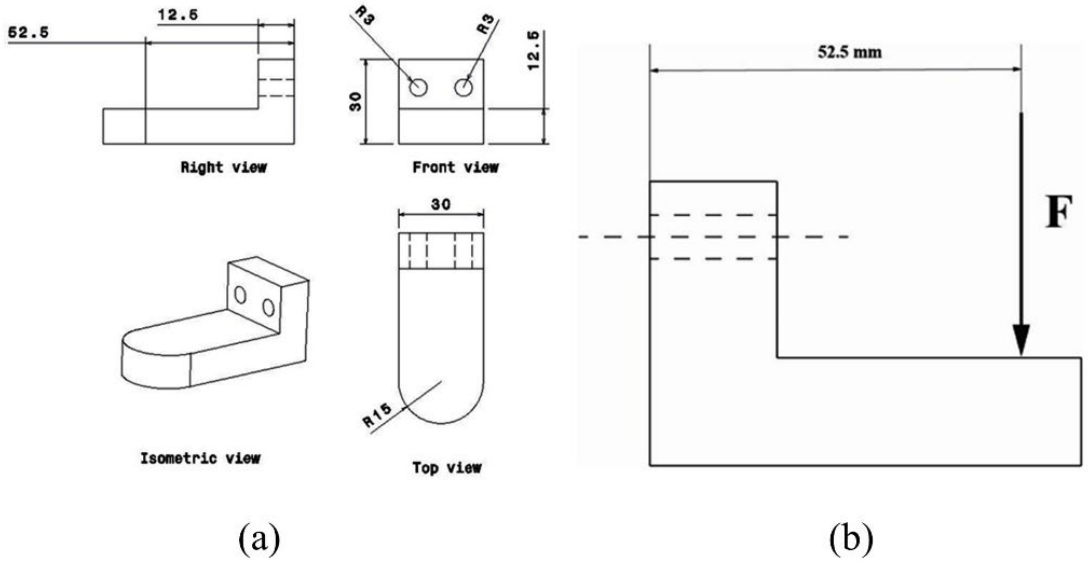

Fig. 1. (a) 2D drawing of 12.5 mm thick mounting as a base geometry for ANSYS Design Modeller (b) Load "F"

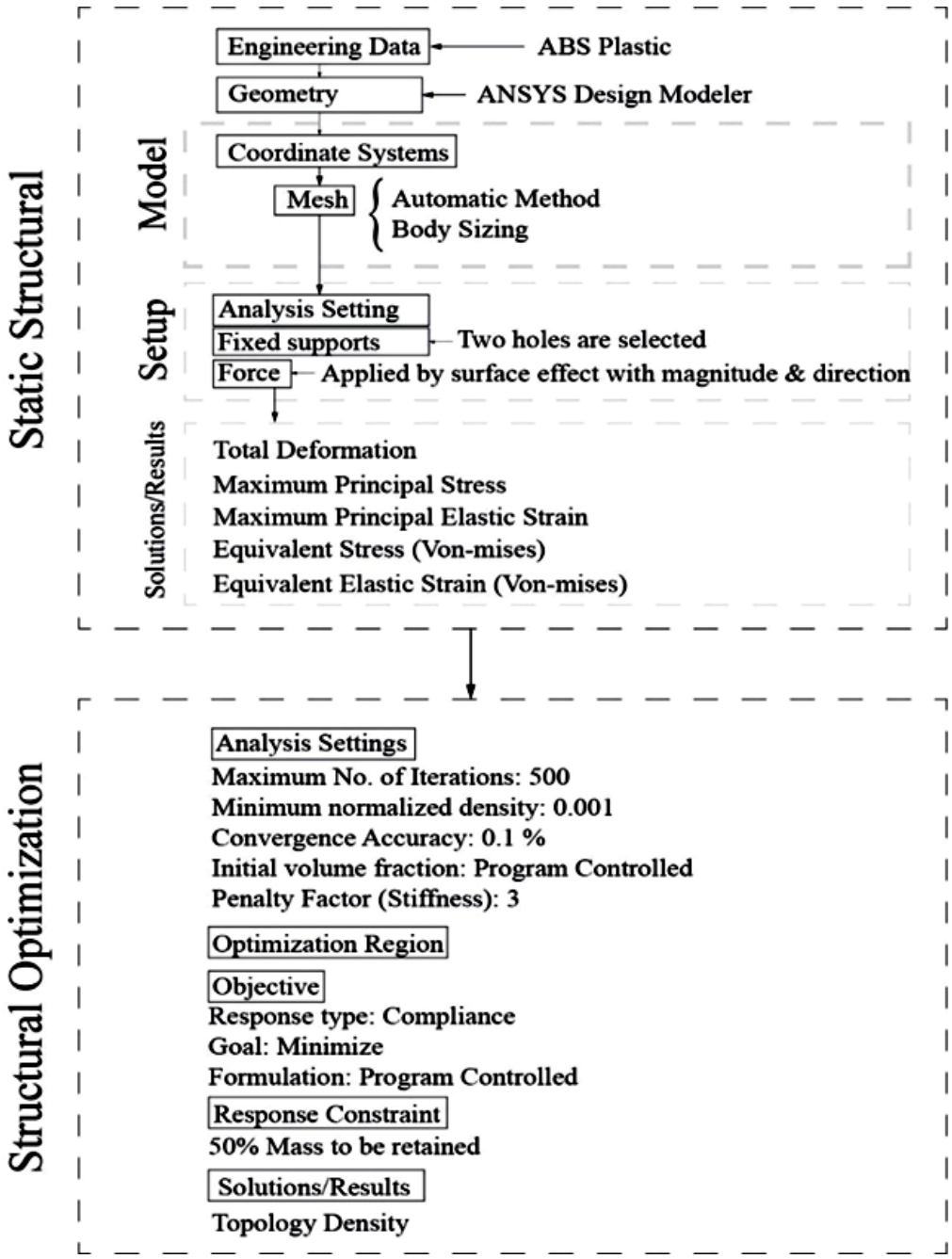

Fig. 2. Flow chart for topology optimization using ANSYS Workbench

3 Results and Discussion

Fig. 3 below represents the results obtained from the topology optimization of the proposed bracket. Fig. 3(a) denotes the model whereas 3(b) represents the optimized model after optimization showing sharp edges and discontinuous geometry. Figure 3(c) signifies the same geometry after altercation for removing the sharp edges and improving the aesthetics. Similarly, Fig. 4,5,6,7 and 8 represents the various stress, strain and deformation outline before and after optimization.

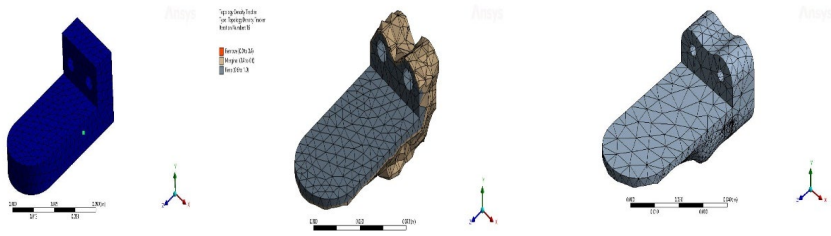

(a) (b) (c)

Fig. 3. (a) Original Mounting (b) Optimized mounting without altercation (c) Optimized mounting with altercation

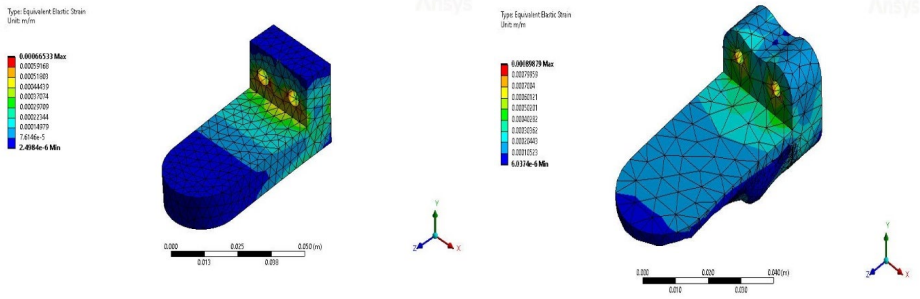

(a) (b)

Fig. 4. Equivalent elastic strain of the mounting (a) Original (b) Optimized

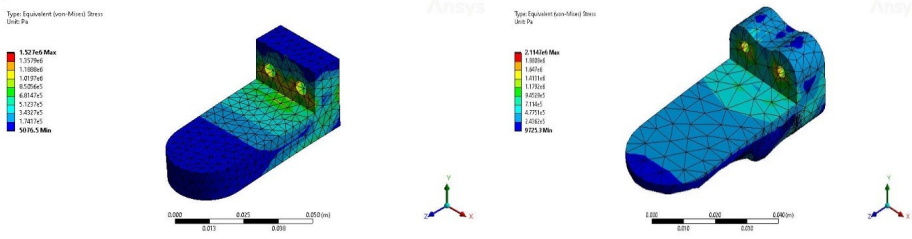

(a) (b)

Fig. 5. Equivalent (Von-mises) stress of the mounting (a) Original (b) Optimized

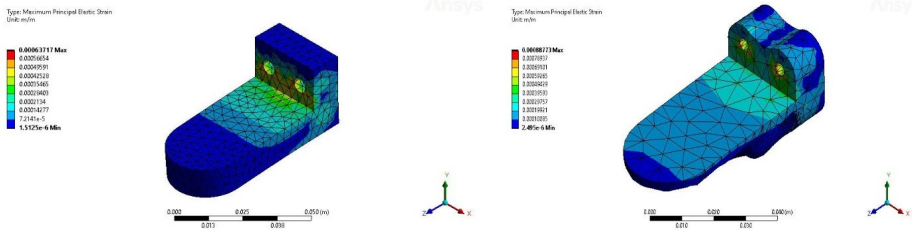

(a) (b)

Fig. 6. Maximum Principal elastic strain of the mounting (a) Original (b) Optimized

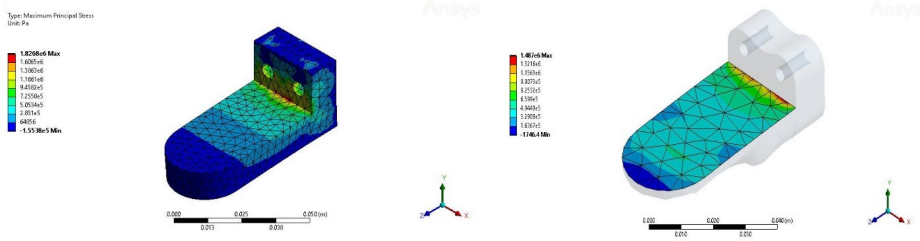

(a) (b)

Fig. 7. Maximum Principal stress of the mounting (a) Original (b) Optimized

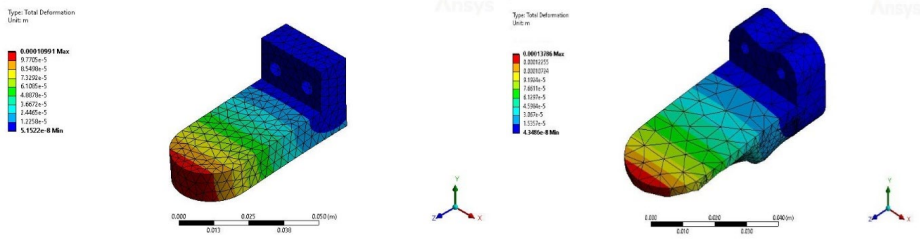

(a) (b)

Fig. 8. Total deformation of the mounting under loading and boundary conditions (a) Original (b) Optimized

Table 1,2,3,4 and 5 represents the stress, strain limitations and deformation pattern of the bracket corresponding to the various decreasing load values. Different decreasing loading values is chosen to express the safe operational characteristics in terms of stress, strain generated and deformation in the bracket.

Table 1. Stress strain and Deformation data for Load of 2.5 kg on mounting bracket

Load on the mounting bracket (2.5 kg)						
Results	**Minimum Values**		**Maximum Values**		**Average Values**	
	Original	**Optimized**	**Original**	**Optimized**	**Original**	**Optimized**
Maximum Principal Stress (Pa)	-1.55e+005	-1.75e+003	1.83e+006	1.49e+006	1.44e+005	4.54e+005
Equivalent Stress (Von-Mises) (Pa)	5.08e+003	9.73e+003	1.53e+006	2.11e+006	2.83e+005	3.67e+005
Total deformation (m)	5.15e-008	4.35e-008	1.1e-004	1.38e-004	3.41e-005	3.42e-005
Maximum Principal Elastic Strain (m/m)	1.51e-006	2.49e-006	6.37e-004	8.88e-004	8.69e-005	9.69e-005
Equivalent Elastic Strain (Von-Mises) (m/m)	2.5e-006	6.04e-006	6.65e-004	8.99e-004	1.32e-004	1.64e-004

Table 2. Stress strain and Deformation data for Load of 2.0kg on mounting bracket

Load on the mounting bracket (2 kg)						
Results	**Minimum Values**		**Maximum Values**		**Average Values**	
	Original	**Optimized**	**Original**	**Optimized**	**Original**	**Optimized**
Maximum Principal Stress (Pa)	-1.24e+005	-1.4e+003	1.46e+006	1.19e+006	1.15e+005	3.64e+005
Equivalent Stress (Von-Mises) (Pa)	4.06e+003	7.79e+003	1.22e+006	1.69e+006	2.26e+005	2.94e+005
Total deformation (m)	4.12e-008	3.48e-008	8.79e-005	1.1e-004	2.73e-005	2.74e-005
Maximum Principal Elastic Strain (m/m)	1.21e-006	2.e-006	5.1e-004	7.11e-004	6.95e-005	7.76e-005
Equivalent Elastic Strain (Von-Mises) (m/m)	2.e-006	4.83e-006	5.32e-004	7.2e-004	1.06e-004	1.31e-004

Table 3. Stress strain and Deformation data for Load of 1.5kg on mounting bracket

Load on the mounting bracket (1.5 kg)						
Results	**Minimum Values**		**Maximum Values**		**Average Values**	
	Original	**Optimized**	**Original**	**Optimized**	**Original**	**Optimized**
Maximum Principal Stress (Pa)	-9.32e+004	-1.05e+003	1.1e+006	8.93e+005	8.64e+004	2.73e+005
Equivalent Stress (Von-Mises) (Pa)	3.05e+003	5.84e+003	9.16e+005	1.27e+006	1.7e+005	2.21e+005
Total deformation (m)	3.09e-008	2.61e-008	6.59e-005	8.28e-005	2.05e-005	2.06e-005
Maximum Principal Elastic Strain (m/m)	9.07e-007	1.5e-006	3.82e-004	5.33e-004	5.21e-005	5.82e-005
Equivalent Elastic Strain (Von-Mises) (m/m)	1.5e-006	3.63e-006	3.99e-004	5.4e-004	7.95e-005	9.85e-005

Table 4. Stress strain and Deformation data for Load of 1.0kg on mounting bracket

Load on the mounting bracket (1 kg)						
Results	**Minimum Values**		**Maximum Values**		**Average Values**	
	Original	**Optimized**	**Original**	**Optimized**	**Original**	**Optimized**
Maximum Principal Stress (Pa)	-6.22e+004	-6.99e+004	7.31e+005	5.95e+005	5.76e+004	1.82e+005
Equivalent Stress (Von-Mises) (Pa)	2.03e+003	3.89e+003	6.11e+005	8.47e+005	1.13e+005	1.47e+005
Total deformation (m)	2.06e-008	1.74e-008	4.4e-005	5.52e-005	1.36e-005	1.37e-005
Maximum Principal Elastic Strain (m/m)	6.05e-007	9.99e-007	2.55e-004	3.55e-004	3.48e-005	3.88e-005
Equivalent Elastic Strain (Von-Mises) (m/m)	9.99e-007	2.42e-006	2.66e-004	3.6e-004	5.3e-005	6.56e-005

Table 5. Stress strain and Deformation data for Load of 0.5kg on mounting bracket

Load on the mounting bracket (0.5 kg)						
Results	**Minimum Values**		**Maximum Values**		**Average Values**	
	Original	**Optimized**	**Original**	**Optimized**	**Original**	**Optimized**
Maximum Principal Stress (Pa)	-3.11e+004	-3.50e+004	3.65e+005	2.98e+005	2.88e+004	9.09e+004
Equivalent Stress (Von-Mises) (Pa)	1.02e+003	1.95e+003	3.05e+005	4.23e+005	5.66e+004	7.35e+004
Total deformation (m)	1.03e-008	8.71e-009	2.2e-005	2.76e-005	6.82e-006	6.86e-006
Maximum Principal Elastic Strain (m/m)	3.02e-007	5.e-007	1.27e-004	1.78e-004	1.74e-005	1.94e-005
Equivalent Elastic Strain (Von-Mises) (m/m)	5.e-007	1.21e-006	1.33e-004	1.8e-004	2.65e-005	3.28e-005

4 Conclusion

3D printing offers vast possibilities for manufacturing, while topology optimization is crucial for designing light-weight, high-performance structures. This paper proposes combining these technologies to design and manufacture a fire extinguisher mounting bracket that prioritizes performance. The practice of topology optimization is achieved by intricate modelling and utilisation of important design methodology for safe design. The design optimization of the bracket is implemented in terms of equivalent elastic strain, von-mises strain and deformation pattern. Later a comparison between the stress strain and deformation under the action of various loading on the optimized bracket is presented in the paper. The tables presented in the results and discussion sections indicates significant improvement of the load carrying capabilities of the bracket. The topology optimization approach is employed to redesign the material distribution of the part and is obtained through analytical simulations. The analysis concludes that the optimized part is the ideal solution in terms of both design and strength. Table 6 below presents a quantitative comparison between the reduction of both mass and cost of the optimized bracket. This research validates the part's suitability for safe operation and demonstrates its cost-effectiveness by reducing material usage.

Table 6. Comparison between the original and optimized Bracket

Mass of the Bracket		**Cost of the Bracket**		**Percentage change**	
Original (gm)	Optimized (gm)	Original (Rs.)	Optimized (Rs.)	Mass of Bracket (%)	Cost Of Bracket (%)
31.1	22.1	28	19.89	-28.94	-28.96

References

1. ISO/PRF 17296-1, (2015), "Additive manufacturing -- General principles -- Part 1: Terminology".
2. Sigmund O., (1997), On the design of compliant mechanisms using topology optimization, *International Journal of Solids and Structures*, vol.34(9), pp.1151-1166.

3. Yuanbin W., Blache, and Xun X., (2017.), Selection of additive manufacturing processes, Rapid Prototyping Journal, vol. 23(2), pp. 434-447,
4. Bendsoe M. P., and Kikuchi N. (1988). Generating optimal topologies in structural design, *Computer Methods in Applied Mechanics and Engineering*, vol.71(3), pp.197-224.
5. Bendsøe M. P., (1989), Optimal shape design as a material distribution problem. *Structural Optimization*, vol.1(2), pp.193-202.
6. Huang X., and Xie Y. M., (2009). Evolutionary topology optimization for minimum compliance and stress minimization. *Computer Methods in Applied Mechanics and Engineering*, vol.198(45-46), pp.3478-3494.
7. Zhou M., Wang G., and Xia L., (2016), Topology optimization with functionally graded materials: A review, *Applied Mechanics Reviews,* vol.68(4), pp.408-417.
8. Guo X., Zhang W., and Liu X., (2018), Topology optimization for additive manufacturing: A review. *Additive Manufacturing*, vol.23, pp.325-340.
9. Chen Y., Wang Q., Wang C., Gong P., Shi Y., Yu Y., and Liu Z., (2021), Topology Optimization Design and Experimental Research of a 3D-Printed Metal Aerospace Bracket Considering Fatigue Performance, Applied Science, vol. 11, pp.66-71.
10. Shahrubudin N., Lee T.C., Ramlan R., (2019), An Overview on 3D Printing Technology: Technological, Materials and applications, Procedia Manufacturing, vol. 35, pp.1286–1296
11. Zou J. and Xia X., (2023), Topology optimization for additive manufacturing with strength constraints considering anisotropy, Journal of Computational Design and Engineering, vol. 10, pp. 892–904.
12. Liu S., Li Q., Hu J., Chen W., Zhang Y., Luo Y., Wang Q., (2024), A Survey of Topology Optimization Methods Considering Manufacturable Structural Feature Constraints for Additive Manufacturing Structures Additive Manufacturing Frontiers vol. 3(2), pp.200-223.
13. E Sanders D.E, Miguel A., Paulino A.G.H., (2018), Multi-material continuum topology optimization with arbitrary volume and mass constraints, Computer Methods in Applied Mechanics and Engineering, vol.340, pp.798-823.
14. Mallaiah M and Hanush S.S,(2022),Topology optimization of aerospace part to enhance the performance by additive manufacturing process Materials Today Proceedings, vol. 62(7),pp. 7373-7378.
15. Senatore G. and Wang Y.,(2024),Topology Optimization of Adaptive Structures: New Limits of Material Economy Computer Methods in Applied Mechanics and Engineering Volume 422, pp.116-129.

Design and FEA Analysis of Lattice Structure for Biomedical Application

Muskan Rathi[1*], Prashant Kumar[2], Vijay Kumar Meena[2], Amit Lochan Sharma[1 2]

[1]Academy of Scientific and Innovative Research (AcSIR), Ghaziabad, India
[2]Central Scientific Instruments Organisation, Chandigarh, India
*muskan.csio23a@acsir.res.in

Abstract. Solid titanium implants are conventionally used to replace lost bone or regain joint functionality. The stiffness of these solid titanium implants is much higher than that of bone, which leads to bone resorption due to stress shielding. The stiffness of these implants must be reduced to reduce the effect of stress shielding. This can be achieved by fabricating porous implants with various lattice structures. In this study, three types of lattice structures, gyroid, Voronoi open, and Voronoi closed, with varying pore sizes from 0.3 mm to 1.2 mm with a variation of 0.3 mm and constant strut thickness were designed. A total of 12 lattice configurations were designed, and the FEA of the uniaxial static compression test was performed under a 1500 N load. It was found that with an increase in porosity, the deformation and maximum compressive stress increased, whereas the stiffness of the lattice structure decreased. The FEA results indicate a significant reduction in the stiffness of the lattice structures. The compression results showed that configurations 'GY 0.3' and 'VC 0.3' are suited for orthopaedic implants, as their maximum compressive stress closely aligns with the compressive strength of the femur. The results also indicated that all configurations with a pore size of 0.6 mm exhibited comparable mechanical properties.

Keywords: Orthopaedic implants, Finite Element Analysis, Lattice structure

1 Introduction

With the growing elderly population worldwide, the cases of osteoporosis and osteoarthritis are increasing, leading to an increased demand for orthopaedic implants [1][2]. Titanium alloy (Ti-6Al-4V) implants are most frequently used in load-bearing applications because of their superior mechanical properties, strong resistance to corrosion, and biocompatibility [3].

The success rate of orthopaedic procedures is determined by bonding between the implant and host bone. However, this bonding weakens in the case of solid metallic implants owing to bone resorption in response to stress shielding [4]. Stress shielding occurs due to the higher stiffness of metallic implants compared with that of natural bone. Surveys revealed that 79% of revision surgeries were performed because of implant loosening due to stress shielding [5]. Measures like incorporating porous structures in implants are being explored to bring the stiffness of metal implants closer to that of the host bone and avoid stress shielding [6]. Porous implants also encourage the growth of bone cells and improve bone-implant integration. As reported in the literature, pore sizes ranging from 0.1 to 0.8 mm are suitable for osteointegration [7][8]. Pore sizes higher than 1 mm were found to be suitable for fibrous tissue growth [9]. Lattice structures can be incorporated into the implants to introduce controlled porosity.

Lattices are cellular structures consisting of interconnected networks of struts or plates [10]. Lattices are designed to create stiff, strong, lightweight, load-bearing structures with as little material as possible [11]. Based on the arrangement of unit cells, lattice structures are divided into two categories: periodic and stochastic lattices [12]. In periodic lattice structures, the unit cells are arranged in a regular repeating fashion with a certain shape, design, size, and topology, whereas the cells in stochastic lattice structures are distributed randomly in the design space and have different sizes and topologies [13]. The gyroid structure is a well-known example of a periodic lattice, more specifically, a TPMS (Triply Periodic Minimal Surface) lattice, whereas the Voronoi lattice is a strut-based stochastic lattice [14] [15]. Voronoi lattices can be further classified into two types: open and closed. In Voronoi open lattices, the struts are not connected on the surface, creating an open-cell structure. Conversely, Voronoi closed lattices feature closed cells, where the struts are connected [16]. Owing to their complex geometry, lattice structures can be fabricated using additive manufacturing (AM) processes only. AM, commonly known as 3D printing, is a process that creates objects by adding material layer by layer based on digital models [17].

Various studies have been performed on TPMS gyroid and Voronoi lattices and it was found that gyroid structures offer high strength-to-weight ratios, improved bone ingrowth, and enhanced mechanical properties such as reduced stress shielding and better fatigue resistance [18][19]. Zatul Faqihah Mohd Salaha et al., in their study, showed that Voronoi lattice structures in hip implants yield the lowest von Mises stress and displacement values

[20]. However, studies have not been performed on the effect of pore size on the mechanical properties of lattice structures with constant strut thickness.

This study focuses on the design and finite element analysis (FEA) of three different types of lattices: gyroid, Voronoi open, and Voronoi closed, with varying pore sizes ranging from 0.3 mm to 1.2 mm with a variation of 0.3 mm and constant strut thickness of 0.4 mm. The lattice structures were initially designed using nTopology software, followed by meshing in 3Matic software to prepare the models for analysis. Subsequently, uniaxial compression tests were performed on all 12 lattice models in Abaqus software, enabling a detailed evaluation of their mechanical behaviour under uniaxial compressive loading. From deformation results obtained in FEA, percentage reduction in stiffness was calculated. In addition, maximum compressive stress is found from von Mises stress distribution using FEA. This work aims to evaluate and compare the mechanical properties of different lattice structures to identify the most suitable design for orthopaedic applications. By analysing their performance under compressive loading, this study aims to determine the optimal lattice structure that balances load-sharing characteristics and stiffness. Previous studies often examined the effects of porosity on mechanical properties of lattices by changing both the pore size and strut thickness, making it difficult to isolate their individual impacts. In this work, we take a different approach by keeping the strut thickness constant and varying only the pore size. This allows us to understand better how pore size alone influences mechanical properties, such as stiffness and maximum compressive stress, providing fresh insights that were not explored in earlier research.

2 Methodology

2.1 Lattice design

A cube with dimensions of 10 mm × 10 mm × 12 mm was first designed in nTopology software. Using this cube as the base geometry, three types of lattice structures - gyroid, Voronoi open, and Voronoi closed were designed. These structures were selected based on their application in orthopaedic implants due to their ability to optimize mechanical properties, mimic natural bone architecture, and facilitate tissue ingrowth [21]. To investigate the effect of pore size on mechanical performance, four different pore sizes (0.3 mm, 0.6 mm, 0.9 mm, and 1.2 mm) were incorporated into each lattice design while uniformly maintaining a strut thickness of 0.4 mm for all lattices, as shown in Figure 1. Along with the lattice structures, a solid block is also designed to compare its mechanical properties with those of the lattices designed. All the studied design configurations are tabulated in Table 1.

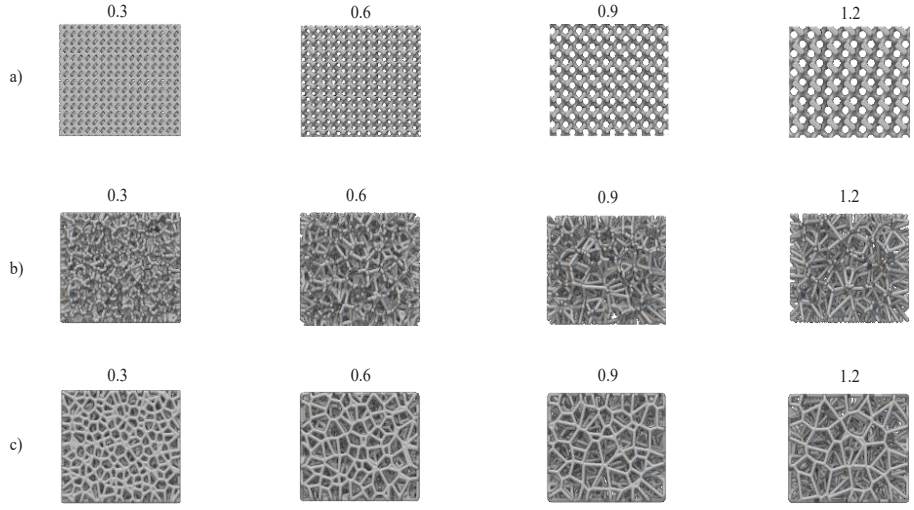

Fig. 1. Lattice structures with different pore sizes a) Gyroid b) Voronoi open c) Voronoi closed

Gyroid structures were created using the 'TPMS (Triply Periodic Minimal Surface)' block, and the pore size was controlled by changing cell size and mid-surface offset values. The designed lattices were subsequently imported into the 3Matic software to accurately measure their pore size and strut thickness, ensuring that they met the specified requirements. Both types of Voronoi lattices were designed using the 'Voronoi Volume Lattice' block by randomly distributing seed points within the structure. The average pore size was controlled by adjusting the point spacing values. All lattice structures were subsequently surface-meshed and exported in the STL format.

Table 1. Overview of design configurations for the comparative study

Configurations	Design Variation
SB	Solid block with no pores
GY 0.3	Gyroid with pore size 0.3 mm
GY 0.6	Gyroid with pore size 0.6 mm
GY 0.9	Gyroid with pore size 0.9 mm
GY 1.2	Gyroid with pore size 1.2 mm
VO 0.3	Voronoi open with average pore size 0.3 mm
VO 0.6	Voronoi open with an average pore size 0.6 mm
VO 0.9	Voronoi open with average pore size 0.9 mm
VO 1.2	Voronoi open with average pore size 1.2 mm
VC 0.3	Voronoi closed with average pore size 0.3 mm
VC 0.6	Voronoi closed with average pore size 0.6 mm
VC 0.9	Voronoi closed with average pore size 0.9 mm
VC 1.2	Voronoi closed with average pore size 1.2 mm

2.2 Porosity Calculation

The designed lattice structures were imported into 3Matic software, where the volume of each lattice was determined from the properties section to calculate the porosity. The formula used to calculate the porosity is given in Equation 1, where Vs and Vl are the volumes of the solid block and lattice structure, respectively. The calculated porosity percentages of the designed lattice structures are presented in Table 2.

$$Porosity = \frac{V_s - V_1}{V_s} * 100 \qquad (1)$$

Table 2. Porosity percentage of designed configurations

Configurations	Volume of solid block (mm^3)	Volume of Lattice (mm^3)	Porosity (%)
SB	1200	N/A	0
GY 0.3	1200	893.161	25.570
GY 0.6	1200	459.896	61.675
GY 0.9	1200	267.571	77.702
GY 1.2	1200	239.467	80.044
VO 0.3	1200	730.09	39.159
VO 0.6	1200	420.371	64.969
VO 0.9	1200	264.351	77.971
VO 1.2	1200	182.100	84.825
VC 0.3	1200	770.402	35.800
VC 0.6	1200	459.486	61.709
VC 0.9	1200	295.529	75.373
VC 1.2	1200	208.732	82.606

2.3 Assembly Model and Volume Mesh Generation

An assembly model consisting of the lattice structure sandwiched between two cylindrical plates was then designed and meshed with tetrahedral elements, as shown in Fig. 2. The Mesh density was carefully controlled, with finer elements applied to areas where the model was in contact with the cylindrical plate to capture the detailed stress and deformation behaviour. All assembly meshes were subsequently exported in INP format to ensure compatibility with Abaqus software for further analysis.

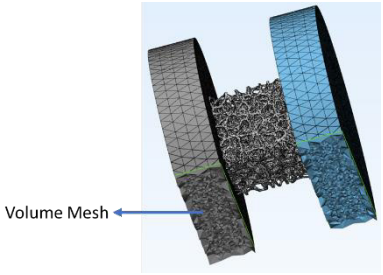

Fig. 2. Assembly Model showing Volume Mesh

2.4 Finite Element Analysis (FEA)

The assembly mesh was imported into the Abaqus software for finite element analysis (FEA). The top and bottom plates were assigned the material properties of steel, whereas the lattice structures were assigned the properties of Ti-6Al-4V alloy. The material properties for the FEA study are provided in Table 2. The assembly was constrained at the lower surface of the bottom plate. A uniaxial compressive load of 1500 N was applied to the upper surface of the top plate. The loading and boundary conditions were maintained consistently across all the design configurations, as shown in Fig. 3. In Abaqus, the primary equation governing the analysis is the equilibrium equation (Equation 2), where K represents the global stiffness matrix, u denotes the nodal displacement vector, and F is the external force vector. Stress is calculated using the constitutive relationship (Equation 3), where σ and ε are the stress and strain tensors, respectively, and D is the material stiffness matrix. For evaluating compressive stress, Abaqus commonly employs the Von-mises stress criterion to determine the equivalent stress (σvm) under complex loading conditions with σ1, σ2, and σ3 representing the principal stresses [22].

$$\sigma = D \cdot \varepsilon \qquad (2)$$

$$Ku = F \qquad (3)$$

$$\sigma_{vm} = \sqrt{\frac{1}{2}[(\sigma_1 - \sigma_2)^2 + (\sigma_2 - \sigma_3)^2 + (\sigma_3 - \sigma_1)^2]} \qquad (4)$$

On completion of FEA, the contour plots of compression and deformation were obtained. From the obtained deformation values, the stiffness was calculated.

Table 3. Properties of Material used in Finite Element Simulation

Components	Young's Modulus (MPa)	Poisson Ratio
Titanium [23]	106000	0.3
Stainless Steel [24]	200000	0.3

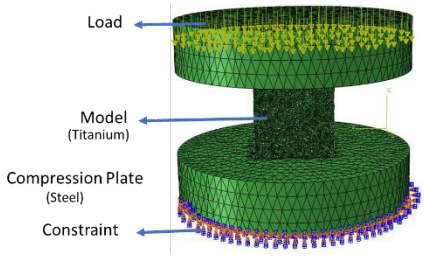

Fig. 3. FEA on Assembly Model

3 Result and Discussion

In this study, the finite element method is used to analyse the mechanical properties of three different types of lattice structures with varying pore sizes and uniform strut thickness. In addition to the lattice structures, a solid block was subjected to the same uniaxial compression test for comparative analysis. For the solid block, the maximum compressive stress and maximum deformation were recorded as 56.46 MPa and 2.55 µm, respectively.

Additionally, the stiffness of the solid block was calculated to be 588.23 kN/mm. These results provide a critical reference point for comparing the mechanical properties of the lattice structures with the solid structure. This comparison highlights how introducing porosity and lattice architecture affects the mechanical rigidity of the material. The maximum stress and deformation values obtained from FEA and the stiffness of all configurations are documented in Table 7. The table also constitutes the percentage reduction in stiffness of the lattice structures compared to the solid structure. The formula used to calculate stiffness is given in Equation 5, where 'F' is the load applied and 'δ' is the deformation. The strength of the femur bone is 103 to 238 MPa, as studied by Kellar et al. in 1990 [25].

$$Stiffness = \frac{F}{\delta} \qquad (5)$$

The results showed that increasing the pore size of the lattice structures decreased their stiffness. The FEA results of different lattice structures are discussed below. The values of maximum stress (Von-Mises) on lattice structures varied from 154.1 MPa for 'VC 0.3' to 1405 MPa for 'VO 1.2'.

3.1 TPMS Gyroid

The stress and deformation distribution results on a gyroid lattice with different pore sizes and uniform strut thickness are shown in Table 4. The values of maximum stress and maximum deformation on the gyroid lattice are 1364.3 MPa and 4.27 µm, respectively, for 'GY 1.2' under uniaxial compression. 'GY 0.3', having a maximum compressive strength of 156.3 MPa, can safely withstand the applied load without reaching failure as the strength of the femur is in the range of 103 – 238 MPa. Compressive stress is increased with the increase in pore size as larger pores lead to higher local stress concentrations as there is less material to distribute the load.

Table 4. The Von-Mises stress distribution and displacement distribution of gyroid lattices with different pore sizes.

Configurations	Von Mises Stress Distribution	Displacement Distribution
GY 0.3	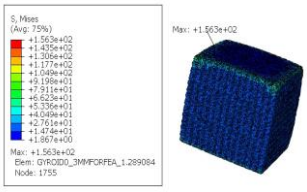	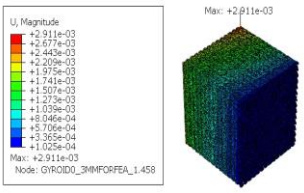
GY 0.6	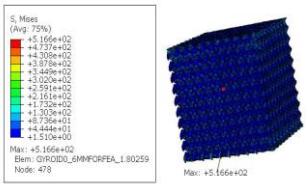	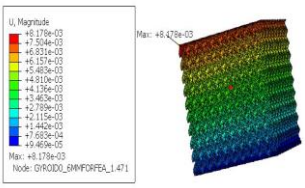
GY 0.9	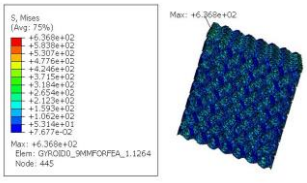	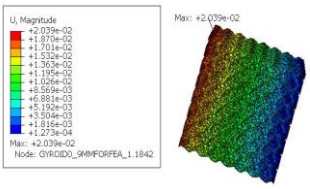
GY 1.2	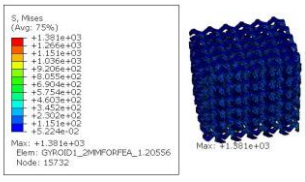	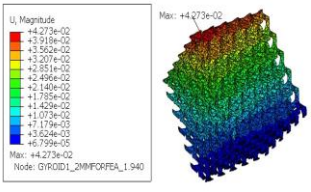

3.2 Voronoi Open

The stress and deformation distribution results on Voronoi open lattice with different pore sizes and uniform strut thickness are shown in Table 5. The maximum recorded compressive stress for the Voronoi open lattice is 1405 MPa for configuration 'VO 1.2', while the corresponding maximum deformation is 8.19 µm. Out of all the configurations of Voronoi open, 'VO 0.3' is the most suitable one for use in orthopaedic implants.

Table 5. The Von-Mises stress distribution and displacement distribution of Voronoi open lattices with different pore sizes.

Configurations	Von Mises Stress Distribution	Displacement Distribution
VO 0.3	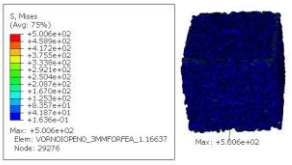	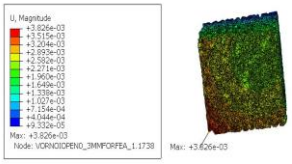
VO 0.6	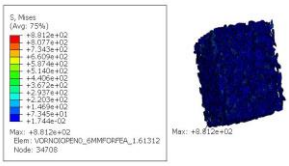	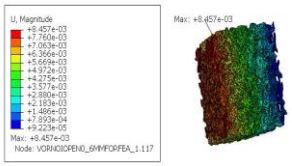
VO 0.9	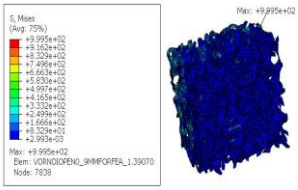	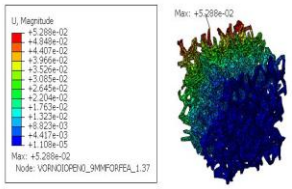
VO 1.2	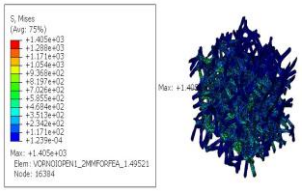	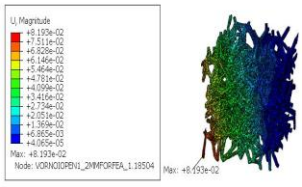

3.3 Voronoi Closed

The distribution of stress and deformation for the Voronoi open lattice structures with varying pore sizes and uniform strut thickness is presented in Table 6. The values of maximum stress and maximum deformation on the Voronoi closed lattice are 1355.5 MPa and 4.15 µm, respectively, for 'VC1.2' under uniaxial compression. 'VC 0.3', having a maximum compressive strength of 154.1 MPa, can safely withstand the applied load without reaching failure when compared to the human femur, having strength in the range of 103 – 238 MPa.

Table 6. The Von-Misses stress distribution and displacement distribution of voronoi closed lattices with different pore sizes.

Configurations	Von Mises Stress Distribution	Displacement Distribution
VC 0.3	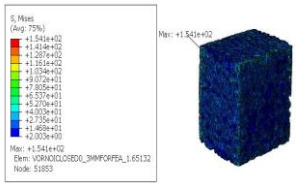	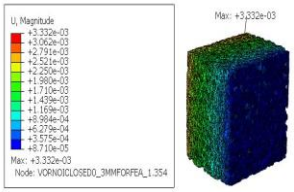
VC 0.6	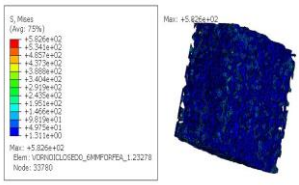	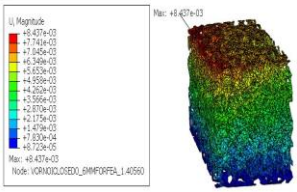
VC 0.9	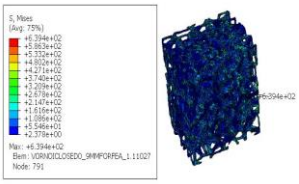	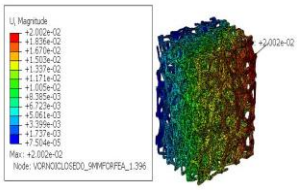
VC 1.2	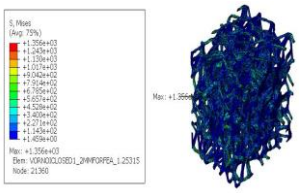	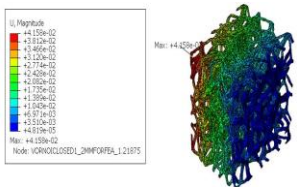

Table 7. Maximum Von-Mises stress and deformation value under uniaxial compression of 1500 N

Configurations	Maximum Compressive Stress (MPa)	Maximum Deformation (µm)	Stiffness (kN/mm)	% Reduction in stiffness
SB	56.46	2.55	588.23	N/A
GY 0.3	156.3	2.91	514.46	12.58
GY 0.6	516.6	8.17	183.59	68.82
GY 0.9	636.8	2.03	73.80	87.45
GY 1.2	1364.3	4.27	35.12	94.03
VO 0.3	500.6	3.82	392.67	33.24
VO 0.6	881	8.45	177.51	69.82
VO 0.9	999.5	5.28	28.40	95.17
VO 1.2	1405	8.19	18.31	96.89
VC 0.3	154.1	3.33	450.45	23.42
VC 0.6	582.5	8.43	177.93	69.75
VC 0.9	656.7	2.00	75.00	87.25
VC 1.2	1355.5	4.15	36.14	93.86

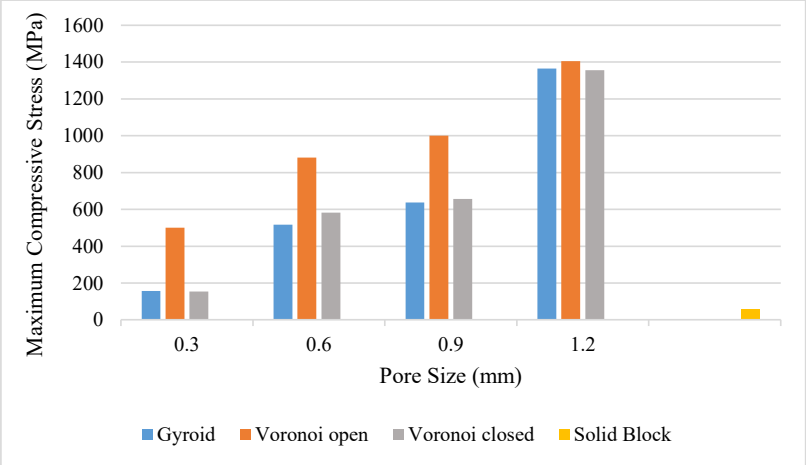

Fig. 4. Maximum compressive stress on different configurations

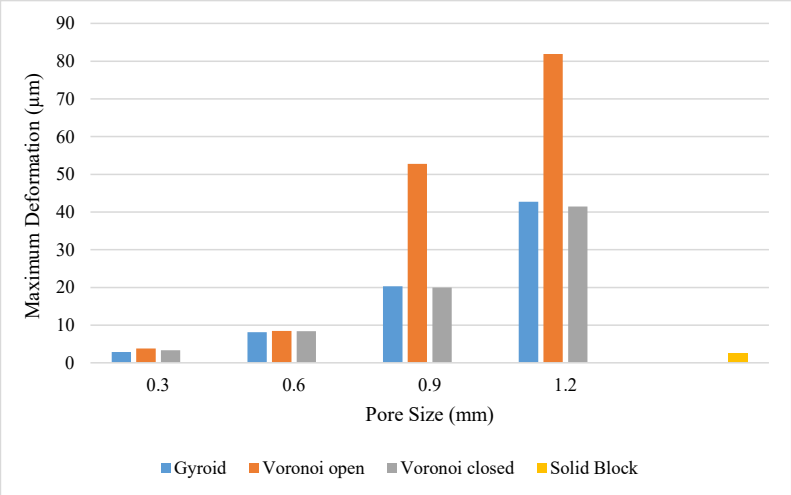

Fig. 5. Maximum deformation of different configurations

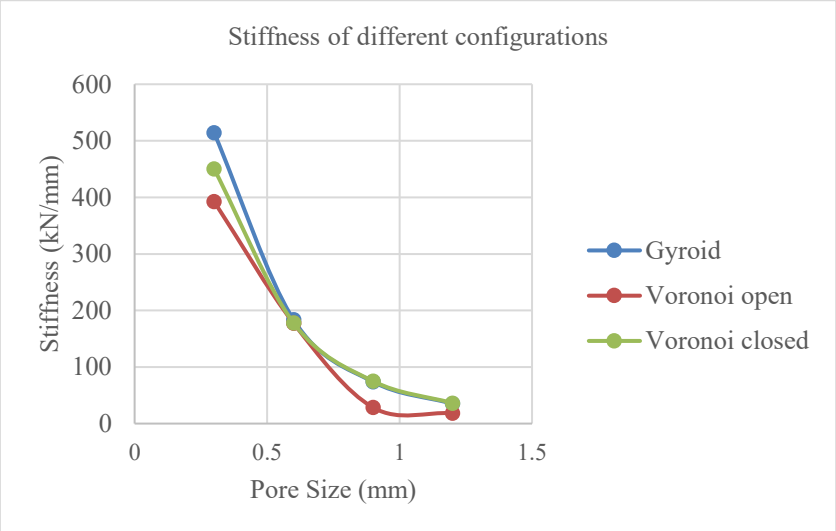

Fig. 6. Stiffness of different configurations

4 Conclusions

In this work, a comparison of three different types of lattice structures – gyroid, Voronoi open, and Voronoi closed with different pore sizes ranging from 0.3 mm to 1.2 mm with a variation of 0.3 mm and a constant strut thickness of 0.4 mm is made. The stress distribution and deformation results of these lattice structures have been deduced using uniaxial compressive FEA under 1500 N load. The stiffness of all configurations is calculated using different pore sizes. The following conclusions were drawn from this study:

i) The values of the maximum compressive stress, maximum deformation, and stiffness of the gyroid and Voronoi closed lattices are almost the same for the same pore-size structures. Since both structures were designed with the same pore sizes, the overall porosity and lattice volume are nearly the same. This results in similar stress responses and stiffness, as both structures have comparable load-bearing capacities for the same volume of material.

ii) For the same pore sizes, the stiffness of the Voronoi open lattice is significantly less than that of the Voronoi closed lattice because the additional material in the Voronoi closed lattices that closes the cells on the surfaces enhances the resistance to deformation.

iii) Configurations 'GY 0.3' and 'VC 0.3' are suitable for use as an orthopaedic implant under the applied load of 1500 N as their maximum compressive stress is less than the strength of the human femur which is in the range of 103 – 238 MPa.

iv) All configurations with a pore size of 0.6 mm exhibited comparable mechanical properties under uniaxial compression testing. As a result, their selection for practical applications will primarily depend on their osteointegration potential.

This study is beneficial for engineers in choosing the correct configuration of the lattice type and pore size for designing porous orthopaedic implants.

References

[1] A.-M. Wu et al., 'Global, regional, and national burden of bone fractures in 204 countries and territories, 1990–2019: a systematic analysis from the Global Burden of Disease Study 2019', Lancet Healthy Longev., vol. 2, no. 9, pp. e580–e592, Sep. 2021, doi: 10.1016/S2666-7568(21)00172-0.

[2] 'The Lancet: New study reveals the most common form of arthritis, osteoarthritis, affects 15% of the global population over the age of 30 | Institute for Health Metrics and Evaluation'. Accessed: Sep. 11, 2024. [Online]. Available: https://www.healthdata.org/news-events/newsroom/news-releases/lancet-new-study-reveals-most-common-form-arthritis

[3] 'Titanium-Based alloys and composites for orthopedic implants Applications: A comprehensive review - ScienceDirect'. Accessed: Oct. 21, 2024. [Online]. Available: https://www.sciencedirect.com/science/article/pii/S0264127524002235

[4] 'Stress-Related Bone Resorption | 19 | Joint Replacement and Bone Resor'. Accessed: Dec. 03, 2024. [Online]. Available: https://www.taylorfrancis.com/chapters/edit/10.1201/b14138-19/stress-related-bone-resorption-bobyn-tanzer-glassman

[5] H. Malchau, P. Herberts, and L. Ahnfelt, 'Prognosis of total hip replacement in Sweden: Follow-up of 92,675 operations performed 1978–1990', Acta Orthop. Scand., vol. 64, no. 5, pp. 497–506, Jan. 1993, doi: 10.3109/17453679308993679.

[6] G. Ryan, A. Pandit, and D. Apatsidis, 'Fabrication methods of porous metals for use in orthopaedic applications', Biomaterials, vol. 27, no. 13, pp. 2651–2670, May 2006, doi: 10.1016/j.biomaterials.2005.12.002.

[7] S. Arabnejad, R. Burnett Johnston, J. A. Pura, B. Singh, M. Tanzer, and D. Pasini, 'High-strength porous biomaterials for bone replacement: A strategy to assess the interplay between cell morphology, mechanical properties, bone ingrowth and manufacturing constraints', Acta Biomater., vol. 30, pp. 345–356, Jan. 2016, doi: 10.1016/j.actbio.2015.10.048.

[8] C. Wang et al., 'Effect of Pore Size on the Physicochemical Properties and Osteogenesis of Ti6Al4V Porous Scaffolds with Bionic Structure', ACS Omega, vol. 5, no. 44, pp. 28684–28692, Nov. 2020, doi: 10.1021/acsomega.0c03824.

[9] A. I. Itälä, H. O. Ylänen, C. Ekholm, K. H. Karlsson, and H. T. Aro, 'Pore diameter of more than 100 μm is not requisite for bone ingrowth in rabbits', J. Biomed. Mater. Res., vol. 58, no. 6, pp. 679–683, Jan. 2001, doi: 10.1002/jbm.1069.

[10] L. J. Gibson, 'Modelling the mechanical behavior of cellular materials', Mater. Sci. Eng. A, vol. 110, pp. 1–36, Mar. 1989, doi: 10.1016/0921-5093(89)90154-8.

[11] M. F. Ashby, 'The properties of foams and lattices', Philos. Trans. R. Soc. Math. Phys. Eng. Sci., vol. 364, no. 1838, pp. 15–30, Jan. 2006, doi: 10.1098/rsta.2005.1678.

[12] L. J. Gibson and M. F. Ashby, Cellular solids: structure and properties, 2nd ed. in Cambridge solid state science series. Cambridge ; New York: Cambridge University Press, 1997.

[13] G. Dong, Y. Tang, and Y. F. Zhao, 'A Survey of Modeling of Lattice Structures Fabricated by Additive Manufacturing', J. Mech. Des., vol. 139, no. 10, p. 100906, Oct. 2017, doi: 10.1115/1.4037305.

[14] S. C. Kapfer, S. T. Hyde, K. Mecke, C. H. Arns, and G. E. Schröder-Turk, 'Minimal surface scaffold designs for tissue engineering', Biomaterials, vol. 32, no. 29, pp. 6875–6882, Oct. 2011, doi: 10.1016/j.biomaterials.2011.06.012.

[15] S. Gómez, M. D. Vlad, J. López, and E. Fernández, 'Design and properties of 3D scaffolds for bone tissue engineering', Acta Biomater., vol. 42, pp. 341–350, Sep. 2016, doi: 10.1016/j.actbio.2016.06.032.

[16] C. Pan, Y. Han, and J. Lu, 'Design and Optimization of Lattice Structures: A Review', Appl. Sci., vol. 10, no. 18, p. 6374, Sep. 2020, doi: 10.3390/app10186374.

[17] S. A. Kumar and R. V. S. Prasad, 'Basic principles of additive manufacturing: different additive manufacturing technologies', in Additive Manufacturing, Elsevier, 2021, pp. 17–35. doi: 10.1016/B978-0-12-822056-6.00012-6.

[18] Á. É. Kovács et al., 'Comparative Analysis of Bone Ingrowth in 3D-Printed Titanium Lattice Structures with Different Patterns', Materials, vol. 16, no. 10, p. 3861, May 2023, doi: 10.3390/ma16103861.

[19] A. Yánez, A. Herrera, O. Martel, D. Monopoli, and H. Afonso, 'Compressive behaviour of gyroid lattice structures for human cancellous bone implant applications', Mater. Sci. Eng. C, vol. 68, pp. 445–448, Nov. 2016, doi: 10.1016/j.msec.2016.06.016.

[20] Z. F. M. Salaha et al., 'Biomechanical Effects of the Porous Structure of Gyroid and Voronoi Hip Implants: A Finite Element Analysis Using an Experimentally Validated Model', Materials, vol. 16, no. 9, p. 3298, Apr. 2023, doi: 10.3390/ma16093298.

[21] C. M. Suryawanshi, S. Sagar, R. Bhallamudi, and S. Mishra, 'Effective design and mechanical response of Gyroid lattice scaffold for orthopedic implants', Manuf. Lett., vol. 35, pp. 493–501, Aug. 2023, doi: 10.1016/j.mfglet.2023.07.015.

[22] 'ABAQUS Theory Manual (v6.6)'. Accessed: Dec. 04, 2024. [Online]. Available: https://classes.engineering.wustl.edu/2009/spring/mase5513/abaqus/docs/v6.6/books/stm/default.htm?startat=ch02s01ath13.html

[23] 'Clinical Spine Surgery'. Accessed: Sep. 21, 2024. [Online]. Available: https://journals.lww.com/jspinaldisorders/abstract/2004/04000/analysis_of_the_effect_of_lumbar_spine_fusion_on.10.aspx

[24] M. F. Ashby, H. Shercliff, and D. Cebon, Materials: Engineering, Science, Processing and Design. Butterworth-Heinemann, 2018.

[25] 'Young's modulus, bending strength, and tissue physical properties of human compact bone - Keller - 1990 - Journal of Orthopaedic Research - Wiley Online Library'. Accessed: Nov. 29, 2024. [Online]. Available: https://onlinelibrary.wiley.com/doi/abs/10.1002/jor.1100080416

Influence of Torch Oscillation on GMAW-WAAM Fabricated Low-Carbon Steel Components

Kumar Kanishka[1][0000-0002-6543-2176] and Bappa Acherjee[2][0000-0003-0286-6038]

[1,2] Department of Production and Industrial Engineering, Birla Institute of Technology: Mesra, Ranchi – 835215, India
kanishkbvp@gmail.com, bappa.rana@gmail.com

Abstract. Wire arc additive manufacturing (WAAM) is a promising technique for producing and repairing large, complex metal components with cost-effectiveness and high deposition rates. This study investigates the influence of torch oscillation on the bead profile, microstructure, and mechanical properties of low-carbon steel fabricated via gas metal arc welding (GMAW)-WAAM. The experimental setup employs a CLOOS® GMAW welding unit with a six-axis robotic arm, using ER70S-6 low-carbon, low-alloy steel wire as filler material. The effects of torch oscillation on the deposition characteristics are examined, with a focus on bead width, height, penetration, surface roughness, and microstructure. Results show that torch oscillation enhances bead width and surface quality but reduces bead height and penetration compared to non-oscillated deposition. Microstructural analysis reveals fine-grained ferritic phases and uniform grain distribution in oscillated samples. Hardness, tensile strength, and elongation are also analyzed in the GMAW-WAAM fabricated wall, showing improved mechanical properties with oscillation. These findings highlight the significant role of torch oscillation in optimizing WAAM for better bead quality and mechanical performance.

Keywords: Wire arc additive manufacturing, GMAW, torch oscillation, low-carbon steel, bead profile, mechanical properties.

Numerical investigation of mechanical behaviour of Strut-based lattice structures under compressive load

Souradip Paul[1], Vijay Kumar Meena[2], Souren Mitra[3]

[1] School of Laser Science and Engineering, Jadavpur University, India
[2] Central Scientific Instrument Organization, India
[3] Department of Production Engineering, Jadavpur University, India
paulsoura2012@gmail.com

Abstract. Nature presents a remarkable array of mesoscopic or microscopic cellular structures such as bone, wood, honeycomb, shell and sea urchin. These can have exceptional mechanical properties including high load-bearing capacity and remarkable energy absorption capabilities. Different lattice structures were generated to mimic the structures to get enhanced mechanical properties. In this study, stress distribution and elastic modulus of two strut-based lattices: FCC and Octet were investigated using numerical simulation varying porosity and unit lattice size. The results established a nuanced understanding of the behaviour of elastic modulus with varying the structural parameters such as porosity and unit lattice size within the examined range, thereby providing critical insights into the design and optimization of advanced lattice materials.

Keywords: Additive Manufacturing, Lattice structure, Numerical Simulation.

1 Introduction

Additive manufacturing, commonly known as 3D printing, represents a new age manufacturing process that allows direct fabrication of complex geometric structures by depositing materials layer by layer. Additive manufacturing encompasses a variety of processing techniques that enable the fabrication of 3D components using various5 material classes, including metals, polymers, and ceramics [1-4]. It provides design freedom to create intricate geometries like lattice structures that were previously impossible through conventional manufacturing processes. Lattice structures gained significant attention in advance engineering applications due to their good specific stiffness, specific strength, and great energy absorption capability [5]. Naturally available lattice structures are irregular in shape and size resulting unsatisfactory performance in mechanical applications [6]. To improve the performance, periodic and regular shaped lattice structures were generated. Lattice structures can be mainly classified into two primary categories: Triply Periodic Minimal Surface (TPMS) lattices and strut-based lattices. TPMS lattices are characterized by smooth, continuous geometries and mathematically specified minimal surfaces extended in 3D with zero mean curvature. Strut-based lattices are composed of discrete interconnected beam-like elements arranged in periodic configurations [7,8]. Recent researches are carried out on different aspects of TPMS lattice structures [9-11] and strut-based lattice structures like Body Centered Cubic (BCC) [12-14]. There are very limited researches available for the strut-based lattice structures of Face Centered Cubic (FCC) and Octet. This study aims to investigate the mechanical behaviour of the FCC and Octet lattice under the compressive load varying the porosity and the unit size of the lattice structures by numerical simulation.

2 Materials and Method

2.1 Design of samples

In this study a solid cube with dimensions of 10 mm per side was selected as the base geometry for investigating lattice structural configuration. Lattice structures were implemented into the cube using Ntopology software. Two distinct strut-based lattice structures: Face Centered Cubic (FCC) and Octet were selected for this study. Two different sets of design constraints are selected for this study. Firstly, 5 mm x 5 mm x 5 mm unit lattice was chosen and systematically varying the strut thickness, different porosity level designs were achieved for both the lattice structures. In the second set keeping the porosity constant at 65%, the unit lattice size was varied for both the lattice structures. Comprehensive design parameters are presented in Table 1 and corresponding designs are illustrated in Fig 1.

Table 1. Design parameters

a. FCC lattice structure with 5 mm x 5 mm x 5 mm unit lattice size			
Porosity level	60%	70%	80%
Strut thickness (mm)	1.47	1.23	0.97
Solid volume (mm3)	402.49	301.86	201.11
Relative density	40.25%	30.19%	20.11%
b. Octet lattice structure with 5 mm x 5 mm x 5 mm unit lattice size			
Porosity level	60%	70%	80%
Strut thickness (mm)	1.04	0.87	0.68
Solid volume (mm3)	402.95	301.71	198.29
Relative density	40.30%	30.17%	19.83%
c. FCC lattice structure with 65% porosity level			
Unit lattice size	2.5 x 2.5 x 2.5	5 x 5 x 5	10 x 10 x 10
Strut thickness (mm)	0.67	1.35	2.7
Solid volume (mm3)	347.4	351.57	351.51
Relative density	34.74%	35.16%	35.15%
d. Octet lattice structure with 65% porosity level			
Unit lattice size	2.5 x 2.5 x 2.5	5 x 5 x 5	10 x 10 x 10
Strut thickness (mm)	0.48	0.95	1.9
Solid volume (mm3)	354.48	348.48	348.73
Relative density	35.45%	34.85%	34.87%

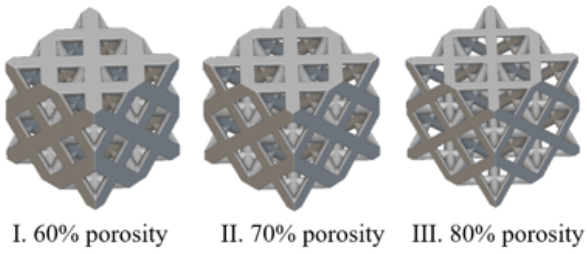

a. FCC lattice structure with 5 mm x 5 mm x 5 mm unit lattice size

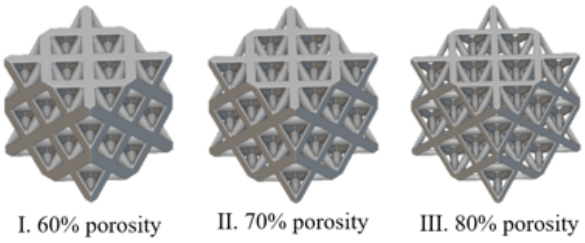

b. Octet lattice structure with 5 mm x 5 mm x 5 mm unit lattice size

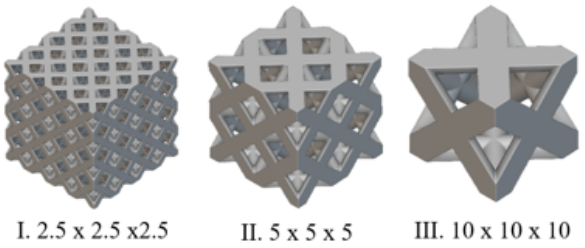

c. FCC lattice structure with 65% porosity level

d. Octet lattice structure with 65% porosity level

Fig. 1. Lattice Structure Designs: FCC and Octet Geometrical Representations

2.2 Materials Used

In this paper Ti-6Al-4V alloy is used to develop the FEM model. The alloy has the elastic Modulus of 110GPa and poisons ratio of 0.30 [15,16]. This is a light weight high strength corrosive resistant material which is extensively used in biomedical implants [17-19], aerospace [20], automobile, [21] marine [22] and structural applications. Ti-6Al-4V is powder is also suitable for 3D printing using Selective Laser Metal method.

2.3 Numerical Simulation

In this section, FEM analysis of the lattice structures set up was discussed to determine the elastic modulus of them. The FEM analysis was carried out in the Ntopology Software. The material considered as an elastic isotropic material i.e. the stress strain curve will be linearly increasing and the property of the material remains same in every direction. Mesh was generated using tolerance level 0.1mm and 0.05 mm min feature size [Fig. 2]. The minimum feature was kept low to increase the accuracy of the analysis. At the top surface of the lattice 10000N load was applied and the bottom surface was fixed for the compression test simulation. [Fig. 3].

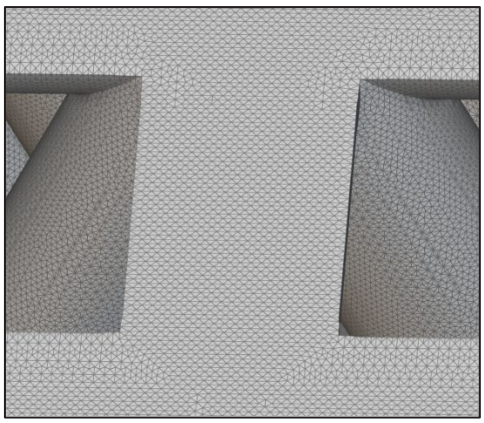

Fig. 2. Mesh characteristic of the lattice

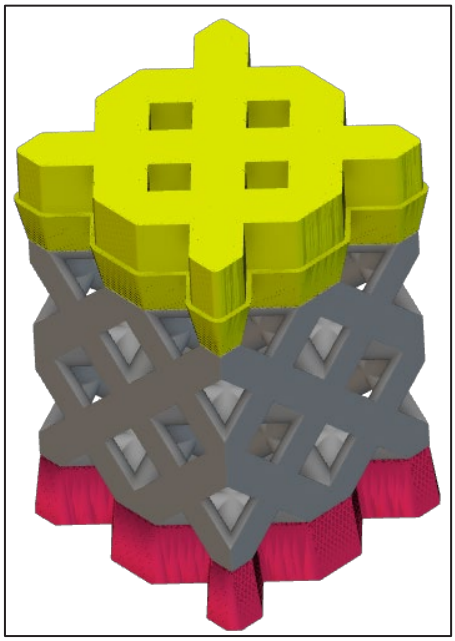

Fig. 3. Simulation set up for the compression test

3 Results and Discussion

This section presents and compares all the numerical simulation results of all the lattice types. It is divided into two parts: the results and analysis for varying porosity with same unit lattice size of FCC and Octet lattices and the results and analysis for varying unit lattice size with same porosity of FCC and Octet lattices.

3.1 Results and analysis for varying porosity with constant unit lattice size

The von Mises stress distribution of varying porosity of FCC lattices structures are shown in the Fig 4 and von Mises stress distribution of varying porosity of Octet lattices are presented in the Fig 5. It can be observed that joints tend to have the highest stress concentration and the middle of struts has comparatively lower stresses. Titanium alloys generally show maximum strain limit of 2% in the elastic zone [23,24]. Stress strain plots of elastic zone of FCC lattices presented in Fig 6. and Octet lattices presented in Fig 7. It is evident from the plot that elastic modulus in both the lattices i.e. slope of the line decreases from the 60% porosity to 70% porosity then increases when the porosity is 80%. The elastic modulus from the stress strain plot is shown in the Table 2.

Table 2. Elastic modulus of FCC and Octet lattices with varying porosity

Porosity	60%	70%	80%
FCC	2.21 x 10^{11} Pa	2.06 x 10^{11} Pa	2.87 x 10^{11} Pa
Octet	2.22 x 10^{11} Pa	1.92 x 10^{11} Pa	2.49 x 10^{11} Pa

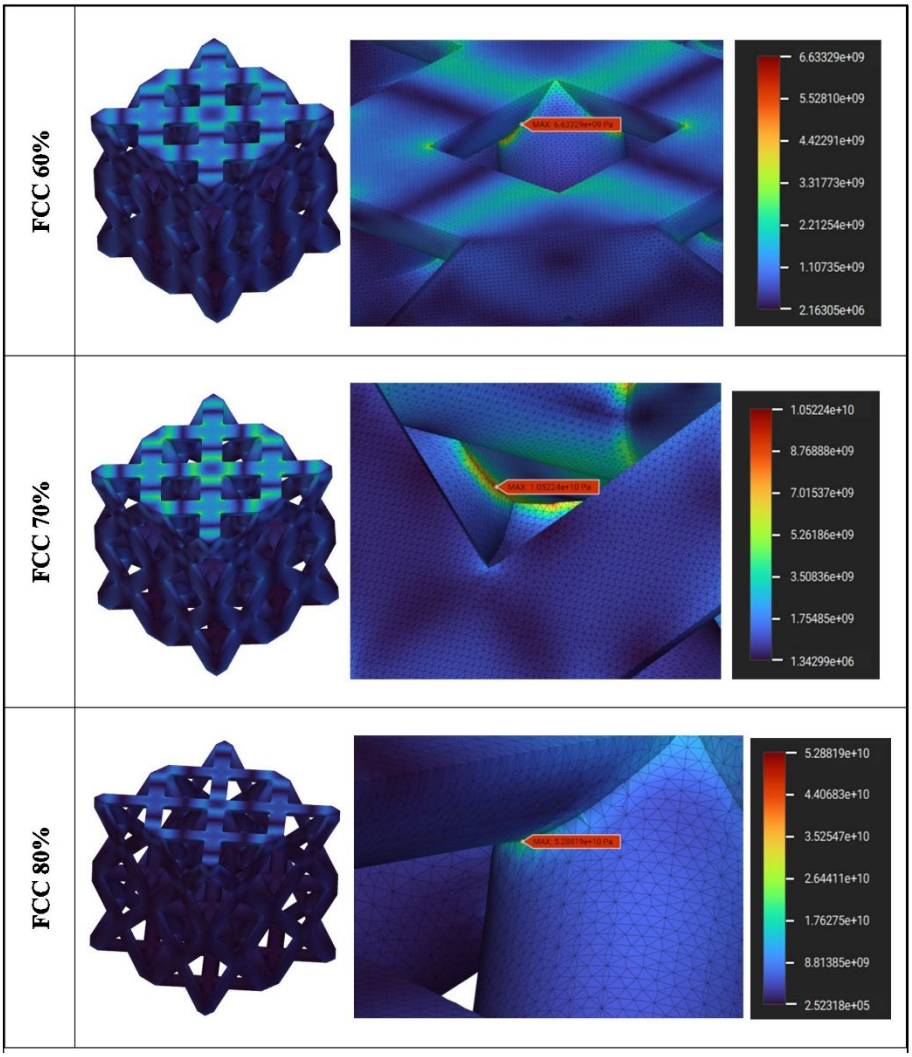

Fig. 4. Von Mises stress distribution in FCC lattice structure with different porosity under compressive loading

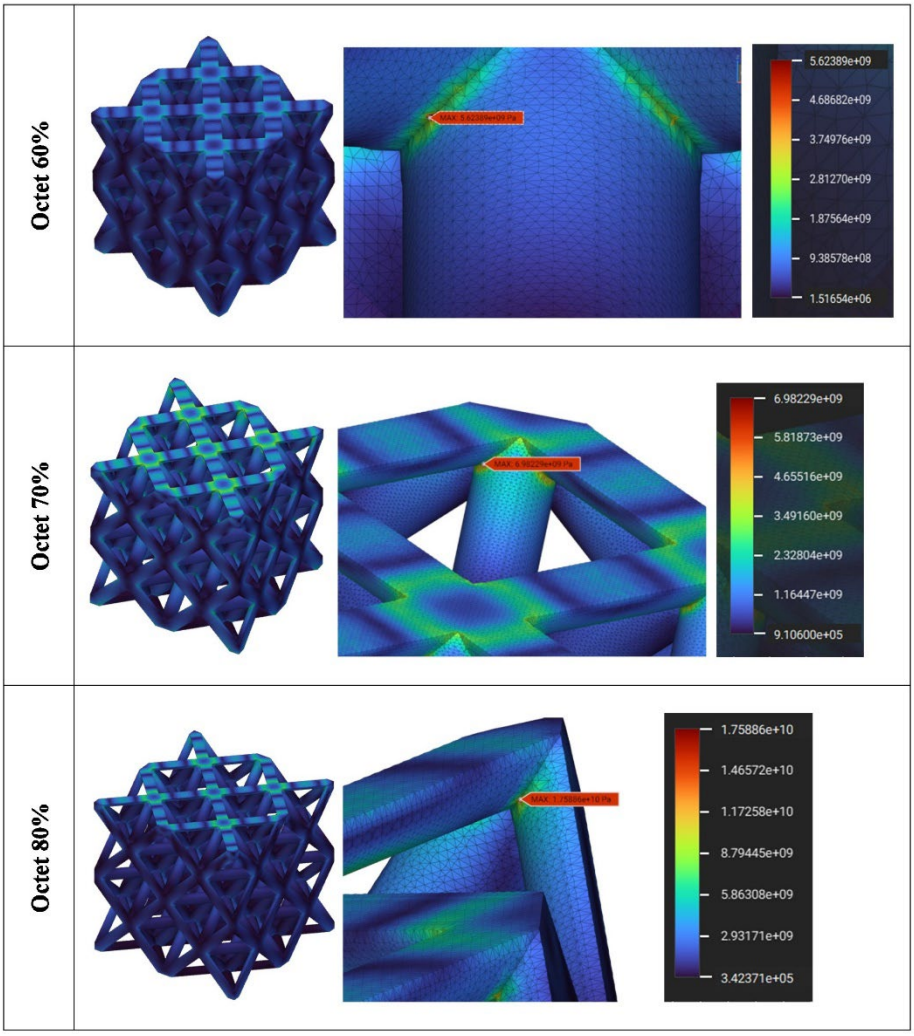

Fig. 5. Von Mises stress distribution in Octet lattice structure with different porosity under compressive loading

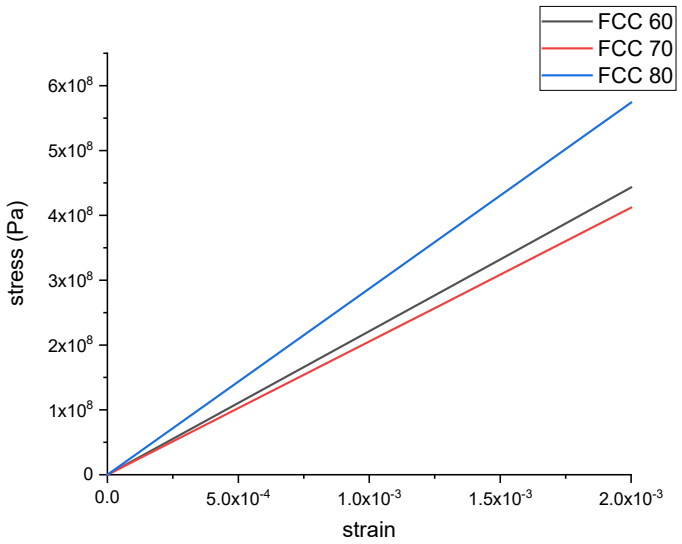

Fig. 6. Stress strain diagram of FCC Lattice Structure with different porosity under compressive loading

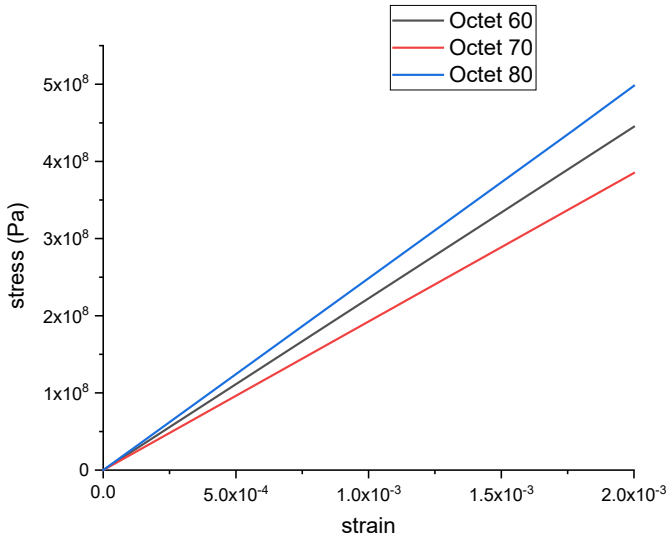

Fig. 7. Stress strain diagram of Octet Lattice Structure with different porosity under compressive loading

3.2 Results and analysis for varying unit lattice size with constant porosity level

The von Mises stress distribution of varying unit lattice size keeping the porosity constant of FCC lattices structures are shown in the Fig 8 and von Mises stress distribution of varying unit lattice sizes with unit lattice size constant of Octet lattices are presented in the Fig 9. It is evident from the stress distribution images that the stress concentration is much higher at the joint compare to the middle of the struts. From the stress strain plots presented in Fig 10,11 it can be observed that the elastic modulus is increasing with increasing the unit lattice size for both type of lattices. The elastic modulus calculated from the plot is presented in Table 3.

Table 3. Elastic modulus of FCC and Octet lattices with varying unit size

Porosity	2.5 mm x 2.5 mm x 2.5 mm	5 mm x 5 mm x 5 mm	10 mm x 10 mmx 10 mm
FCC	1.66 x 10^{11} Pa	2.10 x 10^{11} Pa	3.15 x 10^{11} Pa
Octet	1.74 x 10^{11} Pa	2.21 x 10^{11} Pa	3.06 x 10^{11} Pa

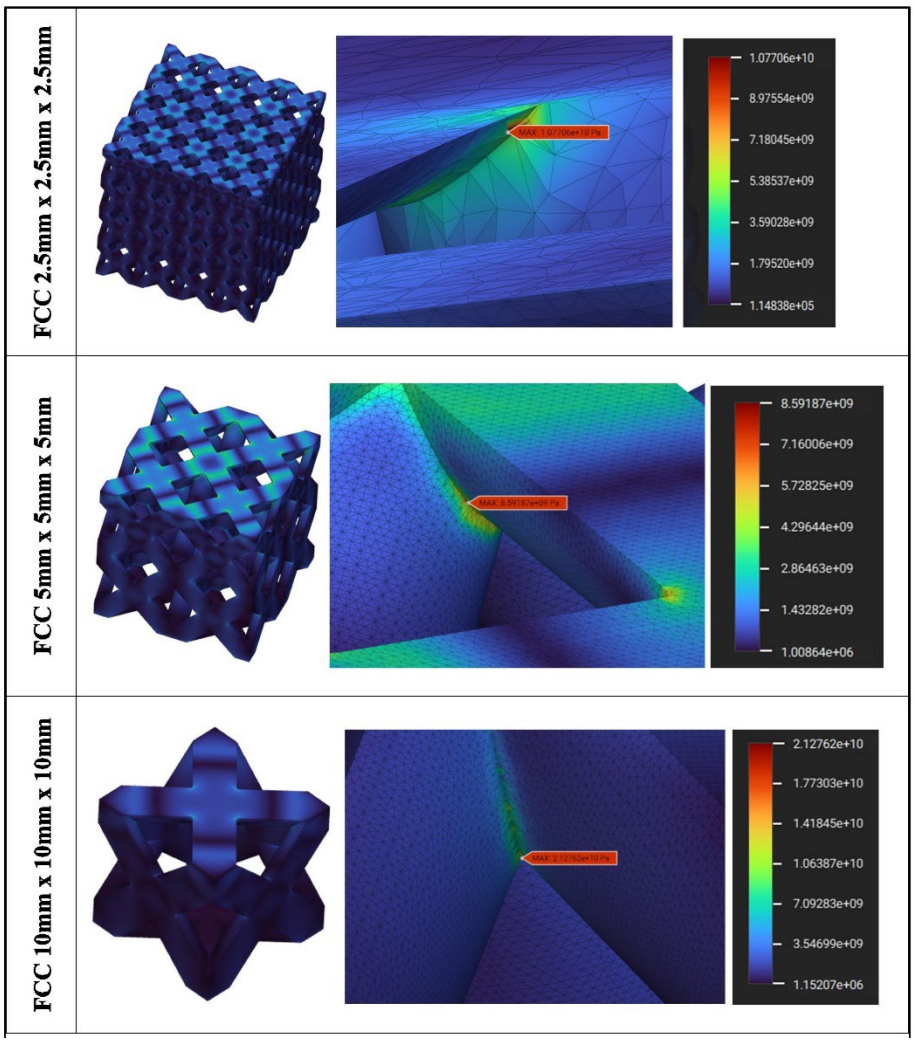

Fig. 8. Von Mises stress distribution in FCC lattice structure with different unit lattice size under compressive loading

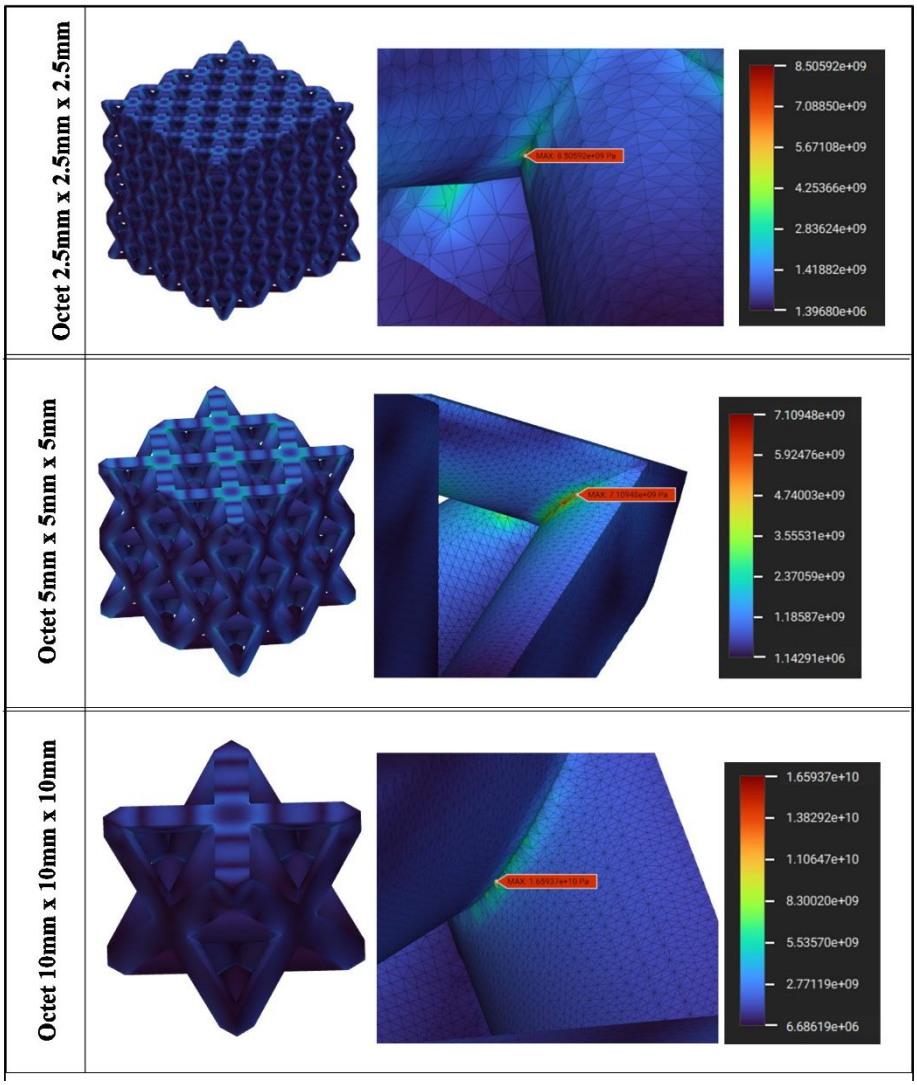

Fig. 9. Von Mises stress distribution in Octet lattice structure with different unit lattice size under compressive loading

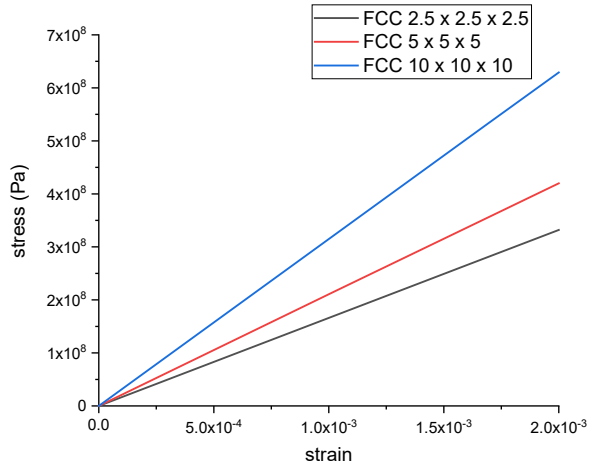

Fig. 10. Stress strain diagram of FCC lattice Structure with different unit lattice size under compressive loading

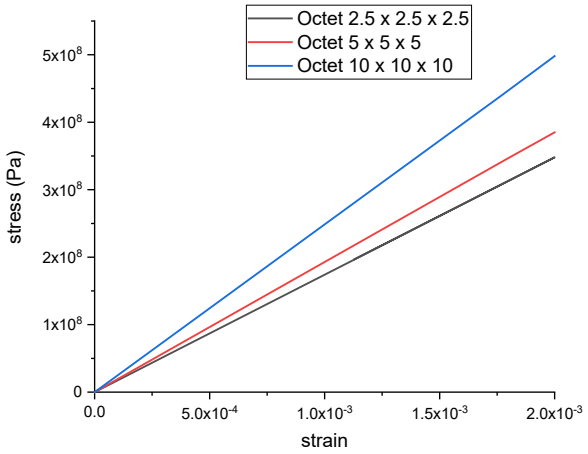

Fig. 11. Stress strain diagram of Octet lattice Structure with different unit size under compressive loading

4 Conclusion

In the present research, a comprehensive study was done to analyze the mechanical behaviour of the FCC and Octet lattice structure under compressive load. The conclusion can be drawn from the study are

- Both the lattices showed similar trends when porosity and unit lattice size varied.
- Elastic modulus decreases when porosity increases from 60% to 70% and again increases when the porosity further increased to 80%.
- Elastic modulus increases when unit lattice size increases.
- At 5 mm x 5 mm x 5 mm unit lattice size, FCC lattice with 80% porosity showed the highest elastic modulus. At 65% porosity level, FCC lattice with 10 mm x 10 mm x 10 mm unit lattice showed the best elastic modulus.
- At 5 mm x 5 mm x 5 mm unit lattice size, Octet lattice with 70% porosity showed the lowest elastic modulus and at 65% porosity level, FCC lattice with 5 mm x 5 mm x 5 mm showed the lowest elastic modulus.

References

1. Gibson, I., Rosen, D., & Stucker, B. Additive Manufacturing Technologies. In *Springer eBooks*. https://doi.org/10.1007/978-1-4939-2113-3 (2014).
2. Abdulhameed, O., Al-Ahmari, A., Ameen, W., & Mian, S. H. Additive manufacturing: Challenges, trends, and applications. *Advances in Mechanical Engineering*, *11*(2). https://doi.org/10.1177/1687814018822880 (2019).
3. Stavropoulos, P., & Foteinopoulos, P. Modelling of additive manufacturing processes: a review and classification. Manufacturing Review, 5, 2. https://doi.org/10.1051/mfreview/2017014 (2018).
4. Frazier, W. E. Metal Additive Manufacturing: a review. Journal of Materials Engineering and Performance, 23(6), 1917–1928. https://doi.org/10.1007/s11665-014-0958-z (2014).
5. W. Tao and M. C. Leu, "Design of lattice structure for additive manufacturing," *International Symposium on Flexible Automation (ISFA)*, Cleveland, OH, USA, 2016, pp. 325-332, doi: 10.1109/ISFA.2016.7790182 (2016).
6. Song, S.; Xiong, C.; Zheng, J.; Yin, J.; Zou, Y.; Zhu, X. Compression, Bending, Energy Absorption Properties, and Failure Modes of Composite Kagome Honeycomb Sandwich Structure Reinforced by PMI Foams. Compos. Struct. 277, 114611 (2021)
7. Pan, C., Han, Y., & Lu, J. Design and Optimization of Lattice Structures: A review. Applied Sciences, 10(18), 6374. https://doi.org/10.3390/app10186374 (2020).
8. Li, Y., Jiang, D., Zhao, R., Wang, X., Wang, L., & Zhang, L. High mechanical performance of lattice structures fabricated by additive manufacturing. Metals, 14(10), 1165. https://doi.org/10.3390/met14101165 (2024).
9. Chatzigeorgiou, C., Piotrowski, B., Chemisky, Y., Laheurte, P., & Meraghni, F. Numerical investigation of the effective mechanical properties and local stress distributions of TPMS-based and strut-based lattices for biomedical applications. Journal of the Mechanical Behavior of Biomedical Materials/Journal of Mechanical Behavior of Biomedical Materials, 126, 105025. https://doi.org/10.1016/j.jmbbm.2021.105025 (2021).
10. Viet, N., Karathanasopoulos, N., & Zaki, W. Mechanical attributes and wave propagation characteristics of TPMS lattice structures. Mechanics of Materials, 172, 104363. https://doi.org/10.1016/j.mechmat.2022.104363 (2022).

11. Guo, X., Zheng, X., Yang, Y., Yang, X., & Yi, Y. Mechanical behavior of TPMS-based scaffolds: a comparison between minimal surfaces and their lattice structures. SN Applied Sciences, 1(10). https://doi.org/10.1007/s42452-019-1167-z (2019).
12. Kamranfard, M. R., Darijani, H., Rokhgireh, H., & Khademzadeh, S. Analysis and optimization of strut-based lattice structures by simplified finite element method. Acta Mechanica, 234(4), 1381–1408. https://doi.org/10.1007/s00707-022-03443-9 (2022).
13. Boniotti, L., Foletti, S., Beretta, S., & Patriarca, L. Analysis of strain and stress concentrations in micro-lattice structures manufactured by SLM. Rapid Prototyping Journal, 26(2), 370–380. https://doi.org/10.1108/rpj-10-2018-0270 (2019).
14. Guo, S., Ma, Y., Liu, P., & Chen, Y. Mechanical Properties of Lattice Structures with a Central Cube: Experiments and Simulations. Materials, 17(6), 1329. https://doi.org/10.3390/ma17061329 (2024).
15. Frosch, K., Barvencik, F., Viereck, V., Lohmann, C. H., Dresing, K., Breme, J., Brunner, E., & Stürmer, K. M. Growth behavior, matrix production, and gene expression of human osteoblasts in defined cylindrical titanium channels. Journal of Biomedical Materials Research Part A, 68A(2), 325–334. https://doi.org/10.1002/jbm.a.20010 (2003).
16. Zhu, H., Zhong, W., Zhang, P., Liu, X., Huang, J., Liu, F., & Li, J. Biomechanical evaluation of autologous bone-cage in posterior lumbar interbody fusion: a finite element analysis. BMC Musculoskeletal Disorders, 21(1). https://doi.org/10.1186/s12891-020-03411-1 (2020).
17. Meena, V. K., Kalra, P., & Sinha, R. K. Finite element study on the influence of pore size and structure on stress shielding effect of additive manufactured spinal cage. Computer Methods in Biomechanics & Biomedical Engineering, 25(5), 566–577. https://doi.org/10.1080/10255842.2021.1970142 (2021).
18. 24. Guo, A. X., Cheng, L., Zhan, S., Zhang, S., Xiong, W., Wang, Z., Wang, G., & Cao, S. C. Biomedical applications of the powder-based 3D printed titanium alloys: A review. Journal of Material Science and Technology, 125, 252–264. https://doi.org/10.1016/j.jmst.2021.11.084 (2022).
19. Popov, V. V., Muller-Kamskii, G., Kovalevsky, A., Dzhenzhera, G., Strokin, E., Kolomiets, A., & Ramon, J. Design and 3D-printing of titanium bone implants: brief review of approach and clinical cases. Biomedical Engineering Letters, 8(4), 337–344. https://doi.org/10.1007/s13534-018-0080-5 (2018).
20. Karkun, M. S., & Dharmalinga, S. 3D printing technology in aerospace industry – a review. International Journal of Aviation Aeronautics and Aerospace. https://doi.org/10.15394/ijaaa.2022.1708 (2022).
21. R. Endymion Grosious, Natrayan Lakshmaiya, "Advancements in automotive production: exploring the role of 3D printing and selective laser sintering," Proc. SPIE 13188, International Conference on Medical Imaging, Electronic Imaging, Information Technologies, and Sensors (MIEITS 2024), 1318819; https://doi.org/10.1117/12.3030833 (2024)
22. Mohammed, J. S. Applications of 3D printing technologies in oceanography. Methods in Oceanography, 17, 97–117. https://doi.org/10.1016/j.mio.2016.08.001 (2016).
23. Ozan, S., Lin, J., Li, Y., Ipek, R., & Wen, C. Development of Ti–Nb–Zr alloys with high elastic admissible strain for temporary orthopedic devices. Acta Biomaterialia, 20, 176–187. https://doi.org/10.1016/j.actbio.2015.03.023 (2015).
24. Stapleton, A. M., Raghunathan, S. L., Bantounas, I., Stone, H. J., Lindley, T. C., & Dye, D. Evolution of lattice strain in Ti–6Al–4V during tensile loading at room temperature. Acta Materialia, 56(20), 6186–6196. https://doi.org/10.1016/j.actamat.2008.08.030 (2008).

Surface modification with metal matrix composite coating involving laser cladding process: A review

Dwaipayan Gupta[1,2], Ruma Sen[3], Bikash Choudhury[3]

[1] Doctor of Philosophy scholar, University of Engineering and Management, Kolkata
[2] Asst. Professor, Budge Budge Institute of Technology, Kolkata
[3] Associate Professor, Institute of Engineering and Management, Kolkata
dwaipayanguptame@gmail.com

Abstract. Laser cladding process for surface treatment has been a topic of interest amongst the researchers for quite a while. Laser cladding process is a very efficacious process for coating onto the areas too small or too large. Metal matrix composites (MMCs) are typically strong materials capable of withstanding severe working condition. Deposition of these materials onto different substrates by laser cladding process can produce high quality coatings. These coatings can significantly enhance the microhardness of the surface and thereby making it scratch resistant, reduce the rate of wear and coefficient of friction and can improve the corrosion properties. Coatings of MMCs through laser cladding are also done to change the magnetic property of surfaces. This article describes the laser cladding process of MMC coating onto a substrate. The effect of laser cladded deposition of MMCs on the microhardness, wear resistance and corrosion resistance of different MMC-Substrate systems are described here.

Keywords: Metal matrix composites, Laser power, Powder feed rate, Micro hardness, Surface wear, Corrosion

1 Introduction

Surface engineering has been an integral part of materials engineering for quite a while. Surface engineering enables to modify the nature of the surface of a substrate in order to increase its properties like hardness, toughness, corrosion resistance, durability etc. so that the substrate could be used in difficult conditions like extreme environment, extreme temperature or severely high pressure under the water. Surface properties could be modified by different methods like surface hardening through heat treatment, vapour deposition, coating etc. Lately coating process has drawn significant attention amongst the researchers across the globe. Surface coating is performed by depositing a layer of another material with enhanced properties like hardness, toughness etc. onto the surface of a substrate [1]. Metal matrix composites (MMCs) are considered such materials suitable for coating on the surface of a substrate to increase its surface quality [2]. Metal matrix composites have typically high strength and hardness which make them fit for use in difficult conditions. In metal matrix composites, reinforcements of several kinds like ceramics or other metals in different shapes and forms like fibers, particulates or whiskers are introduced into a matrix of a pure metal. However in case of surface engineering particulate MMCs are used. In this case the reinforcement is sprayed along with the laser beam onto the surface of a substrate and is deposited the surface of the substrate by creating a molten pool of material which forms the composite material at the surface[1]. Laser cladding is one of the highly recommended processes for such purpose. Laser cladded materials significantly increase the corrosion and wear properties of the substrate surfaces [1-3]. Bartkowski et al.[1] investigated the effects of Fe/WC coating on low carbon steel using Yb-YAG laser cladding process. The experimented with power feeding rates of 600, 700 and, 800 W while keeping the laser scanning speed same. With low power feeding rate, nucleated dendritic carbide formation was observed on the WC. The increased power feeding rates however changes the shape of the carbides with formation of secondary carbide. The highest microhardness and corrosion resistance was observed for the powder flow rate of 12.50 g/min. Riquelme et al.[2] investigated the result of coating of Al/SiC on the ZE41 magnesium alloy using laser cladding method. They have observed the tendency of formation of Al4C3, intermediate phase during laser deposition. This would definitely result in some uneven hardness on the surface of the material. They experimented with different alloying proportion of Si and Ti to the Al matrix to prevent the intermediate phase. There are some dilutions of magnesium from ZE41 substrate to the Al matrix as well. Zhang et al.[3] experimented on MMC coating using high power direct diode laser to develop a layer of vanadium carbide (VC), tungsten carbide (WC) and titanium carbide (TiC) mixed with AISI 420 Stainless steel on A36 mild steel substrate. They tested the erosion characteristics of the MMC using abrasive waterjet at angles 30˚, 45˚ and 90˚ impact angles. They observed the improvement in the erosion properties at 30˚and ,

45˚ impact angles after the addition of the mentioned carbides. At normal impact angle, VC and TiC improves the erosion properties significantly. Carbides of vanadium and titanium cause ductile erosion behaviour with maximum loss of material taken place at 45˚ erosion angle. For all kinds of coatings VC alone proves to be the best for erosion resistance on SS420 substrate. Muvvala et al.[4] detected during the process through online monitoring the changes in microstructure of Inconel 718/TiC coating in-situ in by laser cladding process. They described exhaustively the process of dilution of grains due to undercooling or the dendrite formation by coalescence of floating TiC particles due to slow cooling. Excessive dilution causes changes in composition those results in shifting of solidification shelf location. Dendritic growth of TiC causes embrittlement of the coating. In order to enhance the cooling rate their experiment was carried out in power modulated mode. Yang et al. [5] studied the influence on the magnetic properties of WC-FeNiCr MMC in laser cladding process. They coated the MMC on the surface of N1310 non-magnetic steel sample. Content of WC and laser power has significant effect on the magnetic property. Formation γ-austenitic Fe-Ni layer has been observed in the laser cladded layer. Muvvala et al. [6] investigated the decomposition of TiC through laser cladding MMC coating in process. They mentioned that with increase in molten pool time, there is a sustained reaction layer of TiC and the matrix material that initiate the strong bonding. Nevertheless with extended molten pool lifetime the TiC layer decomposes with greater degree and causes dendrite formation through heterogeneous nucleation. This modified structure induces embrittlement with reduced wear quality which results in fracture and chipping of the coating during wear test. Tan et al. [7] explored the dry sliding behaviour of Al2O3-M7C3/Fe MMC coating prepared through laser cladding, when the particles are strengthened. They coated the MMC onto a steel substrate with different mixtures of Fe alloys and Thermit mixture of Al/Fe2O3. The percentage of Thermit mixture governs the proportion of ceramic Al2O3 and carbide M7C3 in the coated layer which would strengthen the layer. The higher proportion of Thermit mixture increases the microhardness alongside the wear resistance of the composite coat. Yakovlev et al. [8] published their study on wear resistance of laser cladded MMC coatings. They mentioned that the ductile matrices like Cu or Sn acts as the solid lubricants which are strengthened by ceramic phases as reinforcement could act like good wear resistant coating with low coefficient of friction. They produced a functionally graded material (FGM) coating with coefficient of friction 0.12. Li et al. [9] observed the properties and grain-orientation structure of Ni/WC/La2O3 coating produced by ultra-sonic vibrator assisted laser cladding treatment. Normally WC powder gets concentrated at the bottom layer of the coating. This causes significant downfall of the surface hardness. This problem is mitigated with ultra-sonic vibration power of 800 W. With ultra-sonic vibration associated laser cladded coating, flaking and pitting is observed in the direction of the sliding.

2 Process description

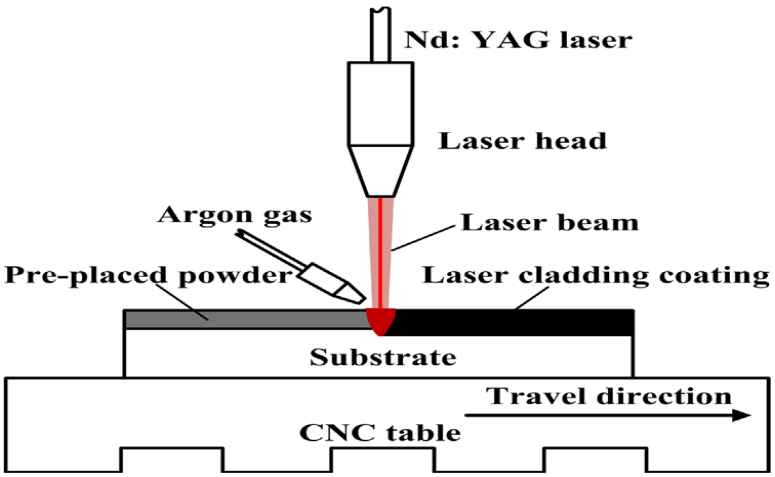

Fig. 1. Schematic representation of laser cladding process using Nd-YAG laser beam [7]

In this process the mixture of matrix and reinforcement in the powdered for is placed at the surface to be coated of the substrate. Then high energy density laser beam is applied on the mixture to create a molten material pool which would eventually get bonded with the substrate material and forms a deposition or coating. The substrate is always maintained with a constant feed in the normal direction of the applied laser beam. Vilar [10] stated that Laser cladding process deposits hard layers on the surface of substrate to a depth typically ranges from 50μm to 2mm. This process could be used for coating a larger area as well as intricate small portions. The ability to deposit materials on a smaller section makes this process very useful actually. A wide range of materials could be used as

coating material in this process. Whatever be the material is t needs to be used in powdered form [1-3,10]. Liang et al. [11] mentioned in their article that scanning speed of laser beam has significant effect on the heat input to the substrate. Laser power, scanning speed and powder feed rate are the three key process parameters for the process. Their article also suggests that the size of the molten pool decides the pores formation in the coating. As this is a dynamic equilibrium system, the material flow rate hugely influences the stability of the molten pool. More concentrated powder flow rate enables splash free coating process. For a successful coating process the interaction between the laser and the powder mixture and the interaction between the molten pool and substrate is an important parameter to taken into account [11, 12].

3 Effect of laser cladded coatings on surface microhardness

When Fe/WC coating is made through laser cladding on low carbon steel, it has been observed that with powder feed rate of 6.25g/min, the near to surface microhardness ranges from 1150-1200 HV 0.05. Laser beam power hardly alters the microhardness value. Nevertheless the microhardness decreases with an increase in depth of coating. The formation of bar shaped carbides and dendritic carbides could be held responsible for the produced microhardness. The highest microhardness for Fe/WC coating on low carbon steel has been observed for 800 W laser power associated with a scanning speed of 600 mm/min and powder flow rate of 12.5 g/min [1]. When ductile matrices like Cu/Sn is with reinforced ceramics like WC/Co are used to prepare MMC for coating, at 300 g load, the microhardness of the coating of WC/Co, Cu/Sn and satellite has two characteristics values one account for the core and the other for solid lubricant which is due to ductile matrix of Cu/Sn [8]. When Al2O3-M7O3/Fe MMC coating is used with strengthened particle, the Thermit mixture (Al2O3) percentage has significant effect on the microhardness of the substrate. The hardness value is observed at 676.4 HV at 5% mixture proportion, which increases to 708.6 HV at 10%. This increased hardness is primarily due to dispersive distribution of Al2O3 and M7O3 carbide [7]. When coating is produced from Ni/WC/La2O3 in ultra-sonic vibration assisted laser cladding, it has been observed that the ultrasonic power can alter the hardness of the coated substrate. The variation is not uniform though. The highest hardness is observed 800 W powers, which is 55 HRC and it is 47.94 HRC at 600 W and 46.2 HRC at 900 W [9]. When VC and TiC coating is applied in 420 SS the microhardness of the substrate significantly increases. This increase in hardness occurs in two ways. At first the precipitation of VC and TiC lifts the hardness and then the Cr of the SS forms intermediate phase carbide with the C from the carbide coatings [3]. When Al/SiC coating is used on ZE41 Mg alloy, for different percentages of Al/SiC mixture, the hardness does not changes significantly except the addition of Ti in the coating mixture. This reduces the hardness to a greater extent however not as low as pure ZE41 substrate [2]. When WC is coated on Ni based alloy through laser cladding process, it is found that the size of WC powder has proportional relation with the surface hardness. This is due to formation of lamellar carbides [13].

4 Effect of laser cladded coatings on surface wear rate

Laser cladded MMC coatings have significant effects on the reduction in surface wear rate and coefficient of friction. It has been observed that when Cu/Sn alloy is reinforced with WC/Co and Cr is added to the sample, as earlier mentioned the microhardness gets reduced as well as the coefficient of friction significantly to 0.25 from 0.32 which is obtained without Cr. The lowest coefficient of friction is obtained for the MMC coating where stellite is added to Cu/Sn matrix as another alloying agent and reinforced with WC/Co. The magnitude of coefficient of friction, in this case is found to be 0.12 [8]. When strengthened particles of thermit mixture is coated on AISI 4140 steel, it is found that the wear mass loss remains unaltered with thermit mixture quantity. Higher hardness evidently reflects higher wear resistance. It has been found that the relative wear resistance with 0%, 5% and 10% Thermit mixture are 4.057, 8.075 and 11.639 respectively.

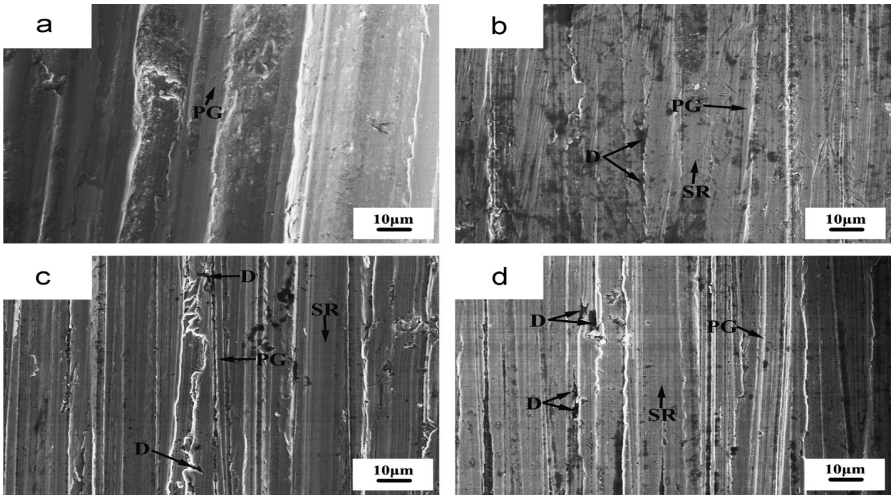

Fig. 2. Morphology of worn surfaces for a)Pure substrate b) 0% thermit mixture c) 5% thermit mixture and d) 10% thermit mixture [7]

It is evident from the Fig 2 that the coated surfaces Fig 2.b), Fig 2.c) and Fig 2.d) offer greater resistance to plastic wears like ploughing wear as seen in the pure substrate AISI 4140 steel. Composite coated surfaces show groove like wear patterns. These shallow grooves increases with increase in Thermit mixture proportion which is clearly visible in Fig 2.c) and Fig 2.d). Tan et al. [7] said that, this increase in shallow grooving is probably due to the in situ synthesization of Al2O3 and M7C3 carbide at the coating site. This actually reduces the tendency for micro ploughing of the surface. The Austenitic matrix of Fe provides better strength to the MMC coating which could reduce the rate of wear of the surface when coating is produced from high speed scanning.

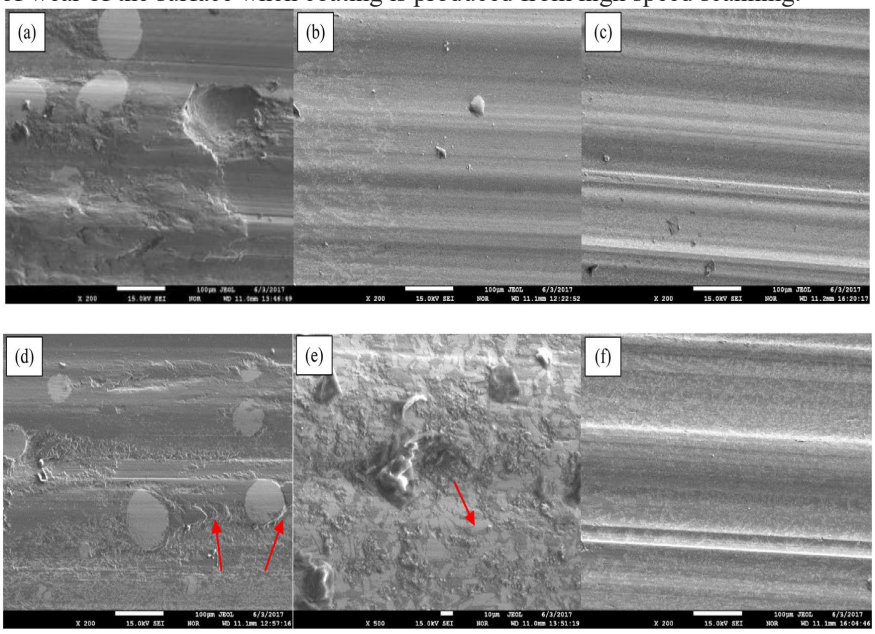

Fig. 3. Morphologies of worn surfaces a) Without ultra-sonic vibration b) With ultra-sonic vibration power of 600 W c) With ultra-sonic vibration power of 700 W d), e) and f) are for 800 W ultra-sonic vibration power and g) Ultra-sonic power 900 W [9]

Ni/WC/La2O3 in ultra-sonic vibration assisted laser cladding; it is observed that the loss of weight of the composite coating is lowest at 800 W ultra-sonic powers. At this level, as mentioned earlier, the hardness is also appreciable. This study [9] shows that without ultra-sonic vibration Ni/WC/La2O3 the coating produces flaking and mico-cracks. Fig 3 shows the different surface morphologies at different ultra-sonic vibration power inputs. At 0 power, there are a lots of ploughings and pits formation in the coating, which diminishes with the increase in ultra-sonic vibration power. The relatively better distribution of WC carbide powder increases the wear resistance to the substrate as seen in Fig 3.d). Fig 3.f) shows some abundance of precipitated carbides in the cladding reion which increases the wear resistance [9]. When Inconel 718/TiC coating is done through laser cladding on AISI

304 Austenitic steel, it has been found during in process investigation that the wear rate and molten pool lifetime increases with a lower in the scanning

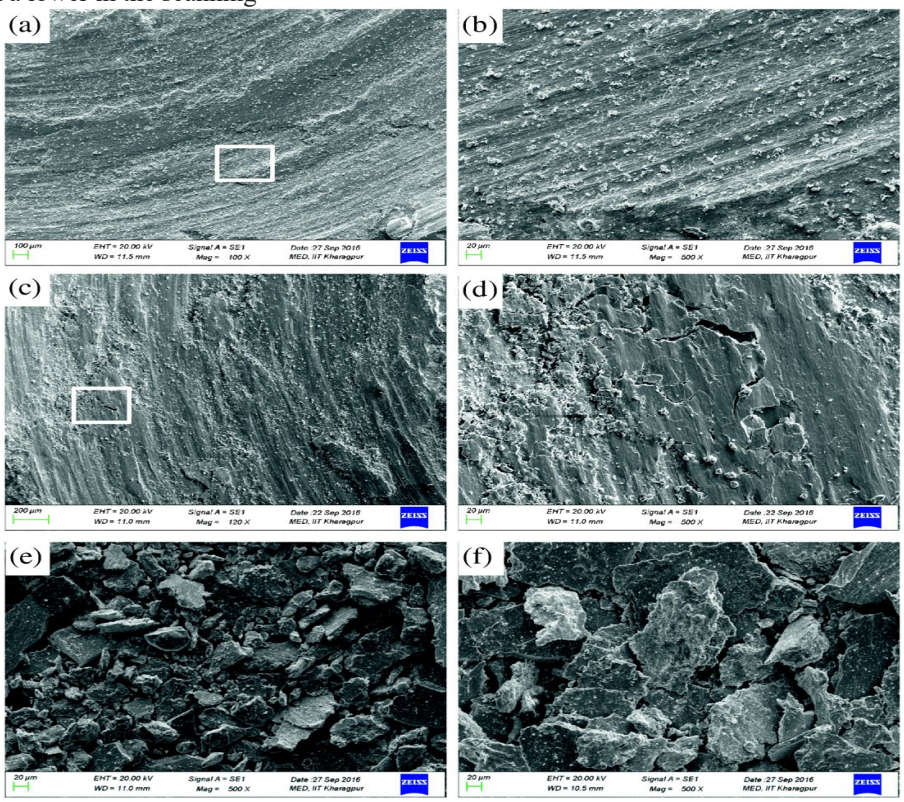

Fig. 4. Surface morphology and worn surfaces at 1200 W laser power and scanning speed of a),b) 1200mm/min; c),d) 400mm/min and e),f) the corresponding debris. [6]

Fig 4 shows the worn out surface characteristics of cladding done with 1200 W laser power and scanning speeds 1200mm/min and 400mm/min respectively. It can be seen that at 400mm/min scanning speed, tracks are found with fractures and spalling. At 1200mm/min this is not seen. Muvvala et al. [6] stated that this is due to the decomposition of TiC results in strengthened matrix and that reduces the wear. Muvvala et al. [4] also stated that the TiC present in the coating acts as the stopper for the ploughing effect during the wear. At a very low to moderate scanning speed the wear debris are found to be very large due to brittle nature of the fracture. When VC, WC and TiC reinforced in AISI 420 SS matrix and coated on A36 mild steel and subject to erosion testing [3], it is seen that the weight loss of the coating shows a linear relation for all the mentioned three reinforcements at 30˚ erosion angle. The coating of 420 SS with VC reinforcement has highest erosion resistant character with lowest wear rate. The coating of 420-WC offers least wear resistance while TiC reinforcement fall in between. Fig 5 shows the erosion wear characteristics of VC, WC and TiC reinforced 420 SS coating on A36 mild steel with respect different erosion angles.

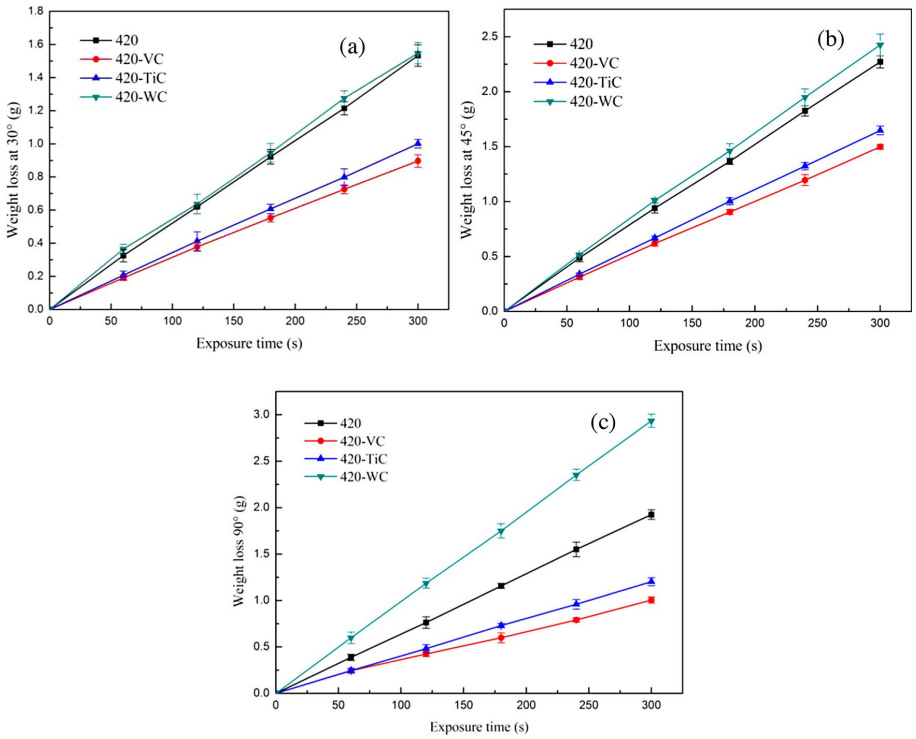

Fig. 5. Accumulated weight loss of coating at erosion angles a) 30˚. b) 45˚ and c) 90˚ [3]

The erosion behaviour for 90˚ erosion angle is very different from that occurred for 30˚ and 45˚ erosion angles. The weight loss of 420-WC is excessively high for 90˚ erosion angles. 420-VC still shows the highest resistance to weight loss and better wear property regardless. When B4C reinforced Ti6Al4V matrix put under investigation with 3, 6 and 7 wt% of B4C reinforcement, it has been observed that there are in-situ formations of TiC, TiB phases alongside α-Ti and remaining B4C phase. This resulted in increased wear resistance. Abrasive wear has been identified as the dominant wear time. At 7 and 9 wt%, wear resistance increases significantly and these is due to the enhanced load transfer ability of TiC and TiB phases [17].

5 Effect of laser cladded coatings on surface corrosion

Laser cladded coating of MMCs on the substrates has notable positives effects on corrosion resistance of the surfaces. Mostly MMCs are non responsive to a greater degree towards corrosive agents [1-4]. When 5% NaCl solution atmosphere is used to investigate the corrosion behaviour of Fe/WC coated low carbon steel, it is found that powder feeding rate and laser beam power has significant effect on the corrosion resistance. Bartkwoski et al. [1] stated that an increased laser beam power degrades the corrosion resistance due to remelting of the substrate. This results in the thickening of iron and addition of iron in the coating which reduces the corrosion resistance ability of the substrate. Increasing the powder feeding rate increases the amount of tungsten which increases the corrosion resistance. However some other experiments suggest that increased percentage of WC reduces corrosion resisting ability. This may be due to the dissolution of WC which makes the stellite matrix more susceptible to 3.5% NaCl solution atmosphere.

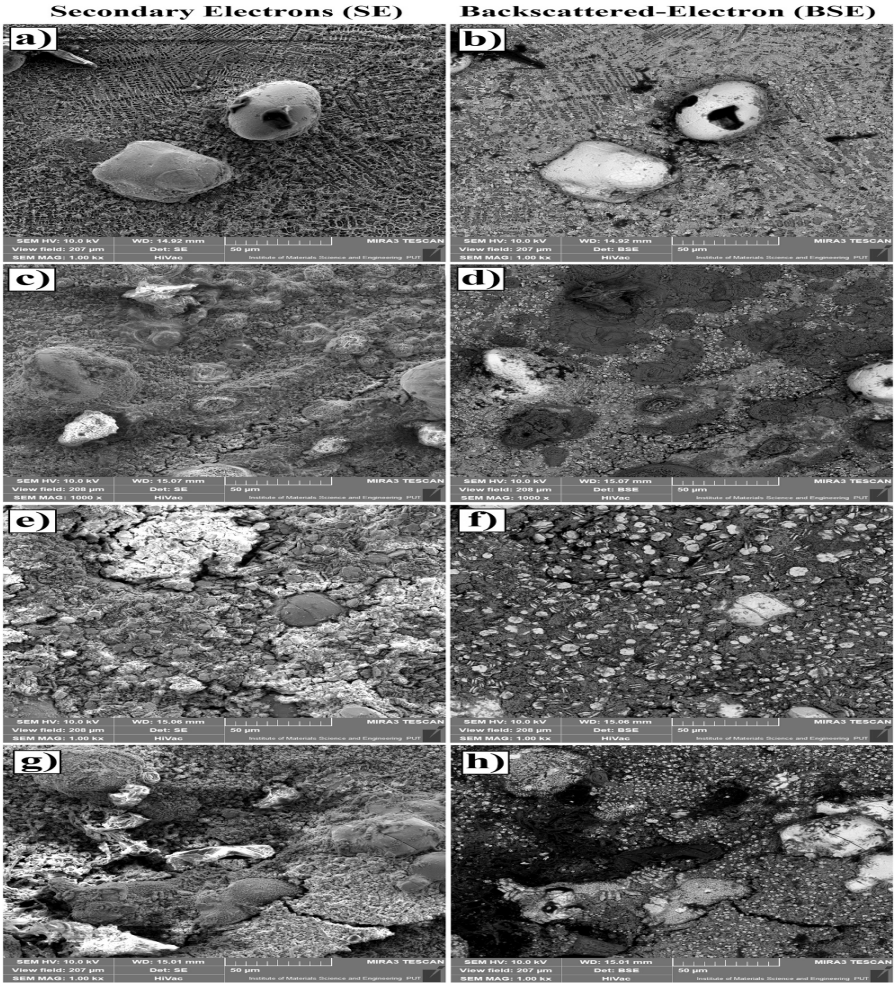

Fig. 6. Morphology of Fe/WC coating after corrosion. a) 600 W, 12.5 g/min, SE b) 600 W, 12.5 g/min, BSE c) 600 W, 6.25 g/min, SE, d) 600 W, 6.25 g/min, BSE, e) 800 W, 12.5 g/min, SE f) 800 W, 12.5 g/min, BSE g) 800 W, 6.25 g/min, SE h) 800 W, 6.25 g/min, BSE [1]

Fig 6 shows that coatings created at 600 W laser beam power suffer less corrosion and less amount of crater is seen this case. 800 W laser beam power reduces corrosion resistance as described earlier, due to remelting of the substrate and addition of more iron into the coating [1]. Fig 6.e) and Fig 6.h) suggests that there is a high rate of corrosion when WC powder feeding rate is reduced. There is a formation of many new phases during the crystallization of the coating. At these sights electro-chemical corrosion sets in. Ni, Cr and Co based coatings show significant resistance towards wet corrosion. Ni, Cr based materials exposed to air to molten sulphate-vanadate compound shows equivalent or may be better character. During hot corrosion, the surface morphology represents dense reaction layers [14].

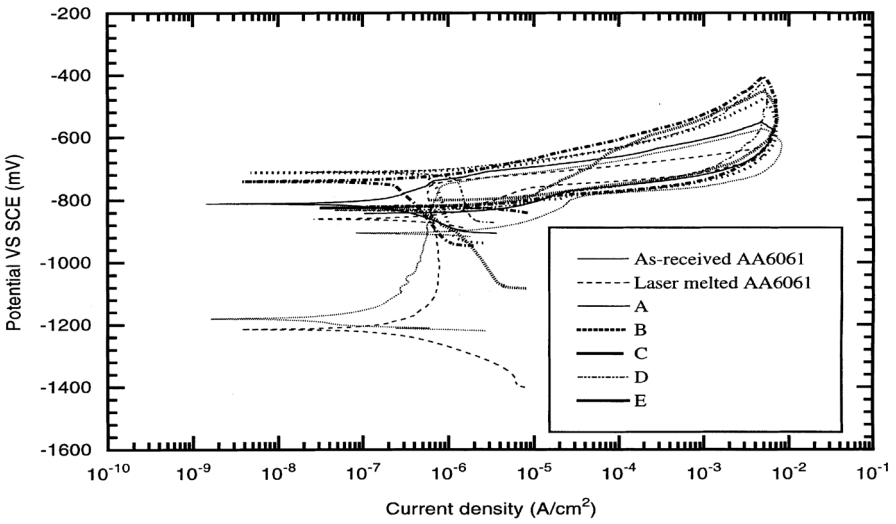

Fig. 7. Potentiodynamic polarisation curve of as received AA6061 specimen and laser cladding coated specimen in air free NaCl solution at 23˚C

When laser cladded coating of SiC and Si3N4 is deposited on AA6061 Al alloy, and the specimen is subjected to 3.5% NaCl solution at 23˚C temperature, it has been observed that there are pitting effects on the as received specimen of AA6061. The laser coated specimen requires more 32mV for the incipient corrosion. Man et al. [15] suggested that this occurs due to the dissolution of precipitation on the resolidified surface. There is no notable change of pitting potential has been found. When binary composite coatings of HA/TiO2 and HA/ZrO2 are developed on the surface of Ti-6Al-V alloy, it has been observed that there is a significant improvement of corrosion of the titanium alloy. Ti alloys release metallic ions into the bloodstream and increases corrosion. HA (hydroxyapetite) based coating has pronounced effect on the corrosion resistant of Ti alloy. HA/TiO2 and HA/ZrO2 produces crack free surfaces, which in turns result in corrosion free durable surface [16].

6 Discussions

From the above discussions it is evident that laser cladding is a very suitable process for the surface coating in order to obtain hard, wear and corrosion resistant surface [1-3]. This process is a very good tool for coating on to small and large anomalies on a substrate surface [10]. Metal matrix composites are generally regarded as strong materials capable of withstanding large stress, friction and a wide range of corrosive agents. Process parameters like laser beam power, powder feeding rate, laser scanning speed etc. have pronounced effect on the coating qualities [2]. Surface microhardness largely depends on the rate of carbide formation both in the form of nucleated or dendrite [3, 7, 9]. The wear rate largely depends upon the laser beam power and scanning speed. Low scanning speed and low power provide better wear properties due to prevention of softening of the substrate [6]. A good coated surface shows shallow grooving when subjected to wear [7]. Corrosion behaviour of laser cladded MMC coatings in certain atmospheres depends on the laser beam power and powder flow rate. Low powder flow rate enhances the corrosion of the substrate. Ferrous substrates succumb to corrosion when coated with higher laser power, due to addition of Fe metal into the coating. Addition of Fe to the coating leads to more corrosion of the entire system [1]. Ni, Cr based materials can reduce the corrosion to a significant extent both in wet and hot corrosion condition [14]. Si3N4, SiC ceramics have pronounced effect on the corrosion resistance of AA6061 substrate. The addition of the mentioned ceramics can increase the corrosion potential by significant degrees [15].

7 Future Challenges

Composite coating using laser cladding process is a very promising topic in the context of surface engineering. Nevertheless there are several gray areas need to be addressed. Laser cladding process is a direct energy deposition (DED) process also called the laser metal deposition (LMD) process [7]. When composites prepared as coatings on the substrate surfaces, several problems arise there even if the process has positive impacts on the microstructure characteristics, mechanical properties wear and corrosion resistance. The challenges and possible mitigation processes are mentioned as follows:

i. Laser cladding process may have adverse effects on the substrate materials in bulk. This changes the microstructure and property of the materials which could be diminished by using suitable scanning speed, laser power and powder feeding rate [1].

ii. Laser cladding process has positive impact on microhardness. Increased microhardness of the surface causes difficulties in machining of the material. Inverse laser scanning may assist the machining processes by imparting uniform heat distribution to the matrix and reinforcements which would in turn improve the machinability of the material. [18].

iii. Fe based substrate under the influence of laser energy, gets melted and enters into the coating at the surface. Fe increases corrosion and thereby damage of the material is inevitable. Increased powder feeding rate, where the powders are typically W/Co types could help in mitigating this challenge.

8 Conclusions

From the above discussion, it could be inferred that laser cladding coating method is one of the favourite methods of surface treatment. MMCs have been stood out promising candidates to be coated on the substrate surfaces due to their enhance characteristics. MMCs could be coated onto a large range of substrates. MMC coating could not only alter the microhardness, wear and corrosion properties which are discussed in this article, but they can also affect the magnetic susceptibility of the system.

i). MMC coating through laser cladding affects positively the microhardness of a substrate if applied with proper laser beam power, powder feeding rate and scanning speed.

ii). These coatings with enhanced hardness can reduce the coefficient of friction and wear rate of the substrate. If dissolution of coating could be controlled properly, good wear resistant layers could be imparted onto a substrate.

iii). Higher powder feeding rate with lower laser beam power results in better corrosion resistant layer. Degree of intermediate phase formation and dissolution of coatings can alter the corrosion properties of a coated system.

References

1. Bartkowski D, Bartkowska A, Jurči P. Laser cladding process of Fe/WC metal matrix composite coatings on low carbon steel using Yb: YAG disk laser. Optics & Laser Technology. 2021 Apr 1;136:106784.
2. Riquelme A, Rodrigo P, Escalera-Rodríguez MD, Rams J. Characterisation and mechanical properties of Al/SiC metal matrix composite coatings formed on ZE41 magnesium alloys by laser cladding. Results in Physics. 2019 Jun 1;13:102160.
3. Zhang Z, Kovacevic R. Laser cladding of iron-based erosion resistant metal matrix composites. Journal of Manufacturing Processes. 2019 Feb 1;38:63-75.
4. Muvvala G, Karmakar DP, Nath AK. In-process detection of microstructural changes in laser cladding of in-situ Inconel 718/TiC metal matrix composite coating. Journal of Alloys and Compounds. 2018 Apr 5;740:545-58.
5. Yang J, Liu F, Miao X, Yang F. Influence of laser cladding process on the magnetic properties of WC–FeNiCr metal–matrix composite coatings. Journal of Materials Processing Technology. 2012 Sep 1;212(9):1862-8.
6. Muvvala G, Karmakar DP, Nath AK. Online assessment of TiC decomposition in laser cladding of metal matrix composite coating. Materials & Design. 2017 May 5;121:310-20.
7. Tan H, Luo Z, Li Y, Yan F, Duan R, Huang Y. Effect of strengthening particles on the dry sliding wear behavior of Al2O3–M7C3/Fe metal matrix composite coatings produced by laser cladding. Wear. 2015 Feb 15;324:36-44.
8. Yakovlev A, Bertrand P, Smurov I. Laser cladding of wear resistant metal matrix composite coatings. Thin solid films. 2004 Apr 1;453:133-8.
9. Li M, Zhang Q, Han B, Song L, Cui G, Yang J, Li J. Microstructure and property of Ni/WC/La2O3 coatings by ultrasonic vibration-assisted laser cladding treatment. Optics and Lasers in Engineering. 2020 Feb 1;125:105848.
10. Vilar R. Laser cladding. Journal of laser applications. 1999 Apr 1;11(2):64-79.
11. Liang Y, Liao ZY, Zhang LL, Cai MW, Wei XS, Shen J. A review on coatings deposited by extreme high-speed laser cladding: processes, materials, and properties. Optics & Laser Technology. 2023 Sep 1;164:109472.
12. Nurminen J, Näkki J, Vuoristo P. Microstructure and properties of hard and wear resistant MMC coatings deposited by laser cladding. International Journal of Refractory Metals and Hard Materials. 2009 Mar 1;27(2):472-8.
13. Janicki D. High power diode laser cladding of wear resistant metal matrix composite coatings. Solid State Phenomena. 2013 Jun 5;199:587-92.
14. Tuominen J. Engineering coatings by laser cladding-the study of wear and corrosion properties.
15. Man HC, Kwok CT, Yue TM. Cavitation erosion and corrosion behaviour of laser surface alloyed MMC of SiC and Si3N4 on Al alloy AA6061. Surface and Coatings Technology. 2000 Oct 1;132(1):11-20.
16. Kumari R, Kumar S, Das AK, Murmu AM, Kanchan K. Microstructural characterization and corrosion analysis of HA/TiO2 and HA/ZrO2 composite coating on Ti-alloy by laser cladding. Applied Surface Science Advances. 2024 Dec 1;24:100655.

17. Liu D, He D, Li H, Li N, Ma L, Li H, Xu Y, Yu J. Multi-ceramic phases synergistically reinforced titanium matrix composite coating deposited by laser cladding: Effect of B4C content on the microstructure and wear properties. Surface and Coatings Technology. 2024 Dec 9:131648.
18. Mypati O, Panzer J, Robles-Linares JA, Zan S, Liao Z, Axinte D. Modelling and experimental study of laser-assisted milling of fibre reinforced SiC/Ti-6Al-4V metal matrix composite. Materials & Design. 2024 Jan 1;237:112552.

Comparative Analysis of Mechanical Properties of ASA Parts 3D Printed with Different Infill Patterns in FDM

Asish Tripathi[1], Dipayan Chakraborty[2], Abhishek Mandal[3]

[1,3] Department of Mechanical Engineering, Jadavpur University, Kolkata, West Bengal 700032, India
[2] Department of Mechanical Engineering, Indian Institute of Technology, Tirupati, 517619, India
amandal.mech@jadavpuruniversity.in

Abstract. Fused Deposition Modeling (FDM) is among the earliest methods in the history of additive manufacturing (AM). Due to its cost-effectiveness, it remains one of the most widely used AM techniques globally, particularly for processing polymers and their composites. However, selecting optimal process parameters during printing is crucial for producing high-quality parts. This paper examines the effects of two different infill patterns, double dense and hexagonal, on mechanical responses, specifically tensile strength and surface roughness, while keeping other parameters constant. The results indicate that acrylonitrile styrene acrylate (ASA) parts printed with the hexagonal infill pattern exhibit superior tensile strength compared to those printed with the double dense infill pattern, whereas the double dense pattern offers better surface quality. It also investigates the impact of various process parameters, including shell thickness, orientation, and infill density, on the mechanical properties.

Keywords: Fused deposition modelling (FDM), Double dense pattern, Hexagonal pattern, Shell thickness, Orientation angle, Infill density, Tensile strength, Surface roughness.

1 Introduction

Additive manufacturing is an innovative and powerful technology that hugely impacts today's industrial manufacturing hub. Additive manufacturing, as the name implies, can be a consecutive layer-based production technology. Additive manufacturing (AM) or 3D printing is a new emerging technique that blows our minds with customer satisfaction with the highest integrity. It enables the production of complex geometries, customization, rapid prototyping, and on-demand manufacturing. The technology finds applications in various industries, including aerospace, healthcare, automotive, consumer products, and architecture. As additive manufacturing continues to advance, new materials, techniques, and applications are being developed, pushing the boundaries of what can be achieved in manufacturing and design [1-4]. Depending on the criteria used, there are several classification methods for additive manufacturing. Fig. 1 shows the common classification of AM based on the process.

The utilization of extrusion-based additive manufacturing (AM) has gained significant popularity in the recent fabrication of three-dimensional prototypes and components, even those with intricate shapes. Fused Deposition Modeling (FDM) is among the earliest and most popular additive manufacturing techniques for producing three-dimensional thermoplastic components. Renowned for its versatility, ease of use, and cost-effectiveness, FDM is one of the most widely adopted 3D printing methods. The process begins with designing a 3D model in CAD software, which is then converted into a compatible file format using slicing software. This software divides the model into thin horizontal layers, ready for printing [6-8]. During the printing process, a spool of thermoplastic filament, such as acrylonitrile butadiene styrene (ABS), acrylonitrile styrene acrylate (ASA), or polylactic acid (PLA), feeds into the FDM printer. Filaments reinforced with carbon fiber for added strength or conductive properties for

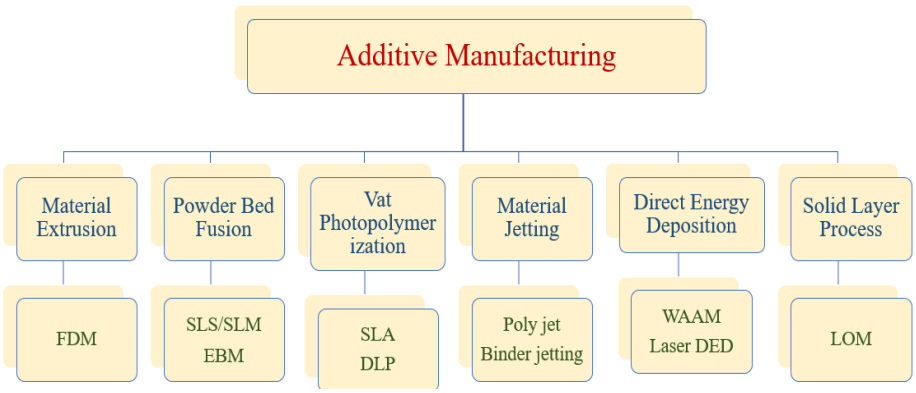

Fig. 1. Process-based classification of additive manufacturing [5]

electronic applications are also available. The filament is heated until it reaches its melting point, then extruded through a heated nozzle that moves along a predefined path, depositing the material layer by layer onto a build platform. Each layer solidifies quickly, bonding to the layer below, enabling complex and detailed structures to be created with precision. As each layer is completed, the build platform lowers to make space for the next layer. Fig. 2 presents a schematic of the FDM process, illustrating each stage of the printing sequence.

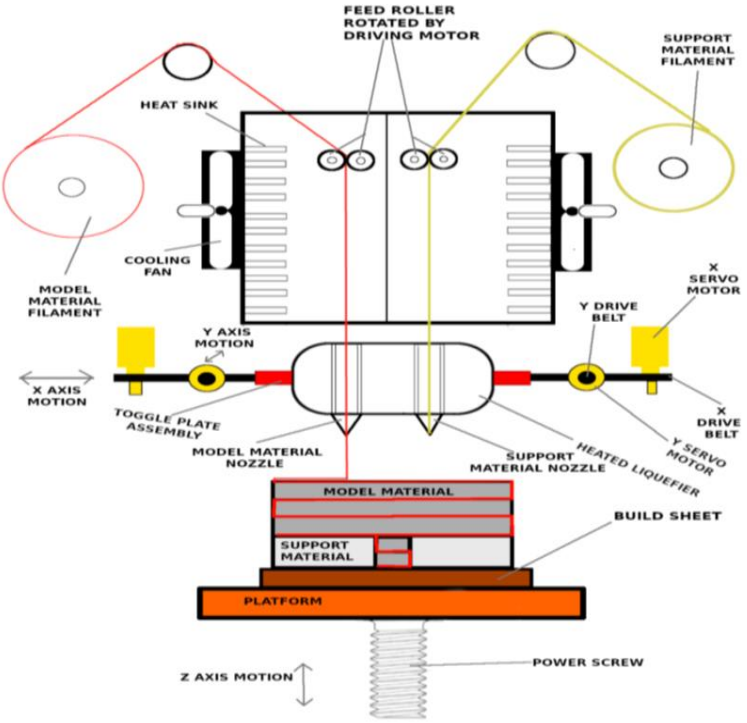

Fig. 2. Process schematic of the fused deposition modelling process [5]

The diagram shows how the filament is fed into the FDM printer, heated to its melting point, and extruded through a nozzle that deposits material layer by layer onto the build platform. The build platform lowers incrementally after each layer is completed, allowing the object to gradually take shape as each layer bonds with the previous one [5]. A variety of filaments with diverse mechanical, thermal, and aesthetic characteristics are available, allowing users to tailor prints to specific requirements. This adaptability makes FDM ideal for a wide range of applications, from prototyping and product development to, in some cases, final-use parts. Fig. 3 outlines the key process parameters involved in FDM, each significantly impacting the quality, accuracy, and mechanical properties of the printed parts. These parameters include factors such as extrusion temperature, layer height, print speed, infill density, infill pattern and nozzle diameter, among others. By carefully controlling these variables, users can optimize the FDM process to achieve desired surface finishes, dimensional accuracy, and material strength in the final printed object.In Fused Deposition Modeling (FDM), the choice of infill pattern is a crucial factor influencing the mechanical and surface properties of printed parts. The infill pattern, which defines the internal structure within the part, determines how forces are distributed, affecting overall strength,

stiffness, impact resistance, and flexibility. Different infill geometries, such as honeycomb, grid, and gyroid, enable a balance between material usage and structural integrity, making them essential for optimizing part performance. Beyond mechanical properties, infill patterns also impact the surface quality and appearance of FDM parts. Higher-density patterns can lead to smoother top surfaces by providing better support for each layer, while specific patterns can enhance aesthetic appeal, especially in transparent or translucent materials where internal geometry is visible. By understanding the effects of infill patterns, designers can tailor FDM prints to meet specific functional and visual requirements, creating parts that are both efficient and reliable for various applications [9-11].

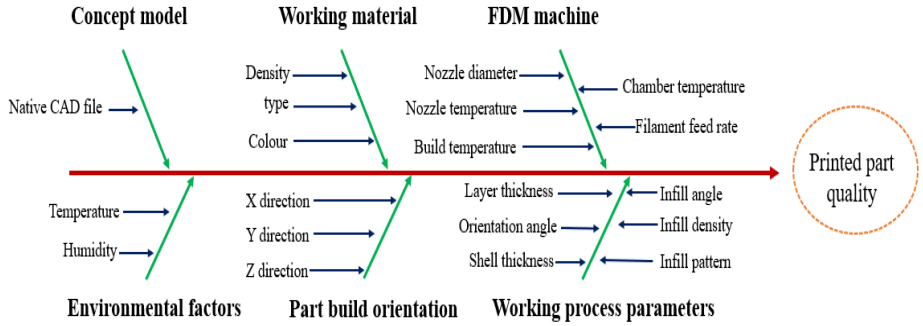

Fig. 3. Fishbone diagram for FDM process parameters [5]

Studies show that denser, structured infill patterns, like honeycomb and grid, yield stronger and stiffer FDM parts compared to sparse or line-based patterns. According to Lee et al.[12], honeycomb infill demonstrates higher load-bearing capacity due to its hexagonal geometry, which distributes stress more effectively. Similarly, grid patterns create a rigid structure that enhances the part's compressive and tensile strength [13]. Infill patterns can also influence a part's ability to withstand impact. Triangular or gyroid infill patterns have been found to provide better energy absorption, which enhances impact resistance [14]. The gyroid pattern, in particular, has been recognized for its unique structure, offering a balance between strength and energy dissipation. Sparse infill patterns, such as line or zigzag, introduce more void spaces within the structure, which can improve flexibility by allowing slight deformation under load [15]. This quality is advantageous for parts that require some degree of elasticity or compressive flexibility. Higher infill densities generally correlate with improved surface smoothness, as they reduce sagging and layer deformation by providing better support [16, 17]. In contrast, low-density patterns may lead to uneven cooling and shrinkage, especially in large parts, leading to surface distortions. Research by Tortorich et al. [18] highlights the versatility of FDM infill customization, showing how specific patterns can be selected based on the application's functional requirements. The infill pattern is a significant determinant of an FDM part's mechanical performance and surface finish, with each pattern presenting distinct advantages depending on load requirements, flexibility, and visual quality. As the studies reviewed indicate, selecting the appropriate infill pattern is essential to achieving optimal performance and aesthetics, particularly for applications that require customized structural or surface properties. The primary objectives of this study focus on advancing the mechanical properties and surface quality of components by investigating the influence of double-dense and hexagonal infill patterns. These patterns are explored for their potential to enhance structural integrity and achieve superior surface finishes. To systematically analyze their impact, key process parameters—specifically orientation angle, shell thickness, and infill density—are meticulously studied. These parameters are critical because they directly affect tensile strength, which determines the load-bearing capacity of the components, and surface roughness, which is vital for aesthetic appeal and functional performance. By holding the infill pattern constant, the study isolates the effects of these parameters, ensuring a focused and precise understanding of their roles in optimizing mechanical and surface characteristics. This approach provides valuable insights into designing robust, high-quality components in additive manufacturing and related fields.

2 Experimental Procedure

The material used in this study is acrylonitrile styrene acrylate (ASA), a thermoplastic polymer known for its high impact resistance, toughness, and heat resistance. ABS is widely used across various industries, including automotive, electronics, home applications, due to its exceptional mechanical properties. A dog-bone-shaped (Fig. 4a)tensile specimen (ASTM D638-Type 4) and a 20 × 20 × 8 mm³ block (Fig. 4b) are fabricated using the

Stratasys F170 FDM 3D printing machine(Fig. 4c) to study the tensile properties and surface roughness respectively. The process parameters and their respective levels are detailed in Table 1.

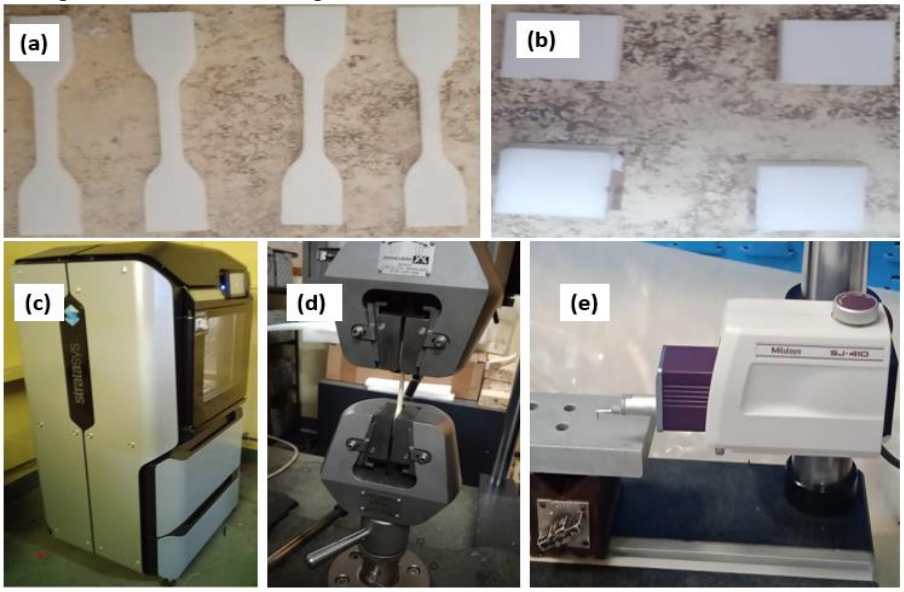

Fig. 4. Printed **(a)** dog-bone shape specimen for tensile test, **(b)** rectangular block for surface roughness test, **(c)** Stratasys F170 FDM machine, **(d)** Instron 100 KN UTM, **(e)** Mitutoyo surface roughness teste

Table 1. Process parameters and its levels

Sl. No	Parameters	Low	High
1	Shell thickness (mm)	0.05	0.12
2	Orientation angle (°)	20	60
3	Infill density (%)	40	60

The design of experiment (DOE) is prepared by central composite design (CCD), shown in Table 2 and each sample is printed for double dense and hexagonal infill pattern to study and optimize their effect on mechanical and surface properties. The nozzle temperature is maintained at a constant 220°C, with the chamber heated to 90°C. SCA-1200 HT cleaning system is used to remove support material (QSR) after printing. Tensile test of the specimens are performed using Instron 100 KN UTM (Fig. 4d) and Mitutoyo tester (Fig. 4e) is used to measure the surface roughness.

Table 2. Design of experiment (DOE) for the experiment

Sl. No	Shell thickness (mm)	Orientation angle (˚)	Infill density (%)
1	0.120000	60.0000	40.0000
2	0.050000	60.0000	60.0000
3	0.120000	20.0000	40.0000
4	0.085000	73.6359	50.0000
5	0.085000	40.0000	50.0000
6	0.050000	20.0000	60.0000
7	0.085000	6.3641	50.0000
8	0.085000	40.0000	50.0000
9	0.143863	40.0000	50.0000
10	0.085000	40.0000	50.0000
11	0.085000	40.0000	66.8179
12	0.050000	60.0000	40.0000
13	0.120000	60.0000	60.0000
14	0.085000	40.0000	50.0000
15	0.085000	40.0000	33.1821
16	0.026137	40.0000	50.0000
17	0.085000	40.0000	50.0000
18	0.050000	20.0000	40.0000
19	0.120000	20.0000	60.0000
20	0.085000	40.0000	50.0000

3 Result and Discussion

3.1 Tensile Strength

Specimens with both double-dense and hexagonal infill patterns are printed according to the design of experiments (DOE). Table 4 presents the maximum load each sample can withstand before failure for both infill patterns. Among the double-dense pattern samples, Sample 12 has the highest load capacity at 765.2361 N (Fig. 5a), while Sample 6 has the lowest at 679.352 N. For the hexagonal pattern samples, Sample 2 exhibits the highest load capacity at 790.73 N (Fig. 5b), whereas Sample 17 shows the lowest load capacity at 690.11 N.

Table 3. Maximum load sustained by each double dense pattern sample before failure

Sl. No	ST (mm)	OA (˚)	ID (%)	Load (N) for double dense pattern	Load (N) for hexagonal pattern
1	0.05	60	40	705.3	740.2889
2	0.085	40	50	739.08	790.7308
3	0.12	20	40	714.3148	748.4021
4	0.085	40	50	743.8039	772.4313
5	0.12	60	40	748.3503	780.0346
6	0.026137	40	50	679.352	705.235
7	0.085	6.364143	50	699.1	722.25
8	0.085	73.63586	50	730.31	760
9	0.085	40	50	757.2125	772.1041
10	0.085	40	66.8179	760.3752	768.7938
11	0.05	60	60	709.7	752.7
12	0.12	60	60	765.2361	789.633
13	0.12	20	60	720.7992	759.974
14	0.085	40	60	744.3895	772.3251
15	0.085	40	50	742.8451	771.3218
16	0.14	40	50	722.8593	790.6826
17	0.05	20	40	694.2	698.1119
18	0.085	40	50	727.9	760.9
19	0.05	20	60	689.9918	712.9538
20	0.085	40	33.1820	764.2543	775.9831

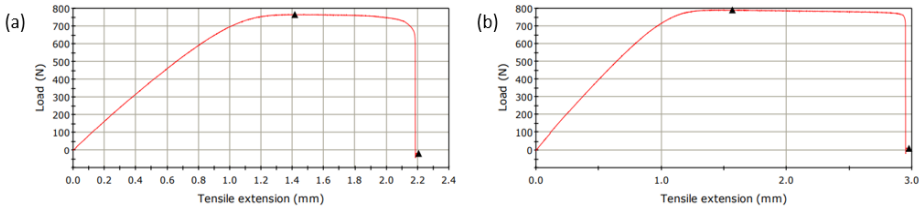

Fig. 5. Load vs extension plot for **(a)** sample 12 – double dense infill pattern and **(b)** sample 2 - hexagonal infill pattern

Comparing all the values it is observed that the honeycomb infill pattern offers better tensile strength in FDM-printed parts compared to a double-dense structure for the same other process parameters. It is because of its efficient hexagonal geometry, which naturally distributes tensile loads across the entire part. This pattern's interconnected cells absorb and redirect stress uniformly, minimizing weak points and reducing the risk of stress concentration, which can lead to fractures. Additionally, the honeycomb structure's design provides just the right amount of flexibility, allowing it to deform slightly under load without compromising overall integrity.

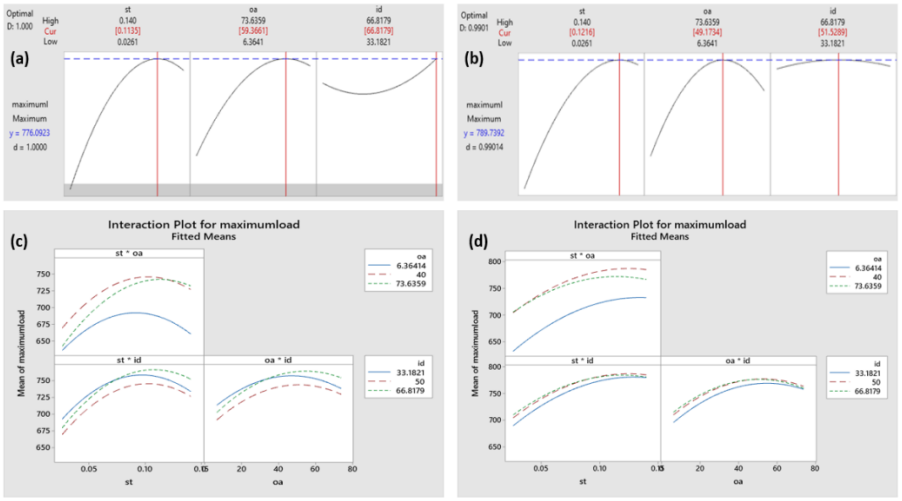

Fig. 6. Load optimization plot and two-way interaction plot for **(a)** and **(c)** double dense structure and, **(c)** and **(d)** honeycomb structure

In contrast, a double-dense structure often results in a rigid, brittle part that lacks the energy-absorbing capacity of a honeycomb, making it more susceptible to cracking under tensile forces. Thus, honeycomb infill achieves a superior balance of strength and material efficiency, enhancing tensile performance without adding unnecessary weight. Optimizing other process parameters, such as shell thickness (ST), orientation angle (OA), and infill density (ID), is crucial for achieving maximum tensile strength. For the sample with a double-dense infill pattern, the optimized parameters for maximum tensile load are ST = 0.1135 mm, OA = 59.36°, and ID = 66.8179% (Fig. 6a). For the sample with a hexagonal infill pattern, the optimal parameters are ST = 0.1216 mm, OA = 49.17°, and ID = 51.52% (Fig. 6b).The tensile strength of FDM FDM-printed specimen strongly depends upon its process parameters. Increasing the shell thickness enhances the part's external strength by adding more material to the outer layers, which directly bears the applied tensile forces. Thicker shells provide greater resistance to deformation and failure, improving overall tensile strength. The outer layers of a printed part typically play a critical role in maintaining structural stability under load, and thicker shells reduce the risk of failure at the surface. The orientation of the printed layers relative to the applied tensile load is crucial. The tensile strength of FDM-printed parts tends to increase initially and then decrease as the orientation angle changes from 5° to 75° due to the relationship between layer bonding, stress distribution, and the alignment of printed layers relative to the applied load. When the orientation angle is between 0° and 45°, the printed layers align in a manner that optimizes interlayer bonding. The material in the part is deposited in a way that enhances the load transfer between adjacent layers, leading to stronger connections between them. As the orientation angle increases, the layers start to align in directions that are more favorable for load-bearing, resulting in better tensile strength. The alignment also reduces the likelihood of delamination, a common failure mode when layers are not bonded strongly. After reaching an optimal orientation angle, typically around 45°, further increasing the orientation angle (from 45° to 75°) leads to reduced tensile strength. As the angle becomes steeper, the printed layers are less aligned with the applied tensile load, which weakens the bonding between layers. At higher angles, the tensile forces are applied more across the layers rather than along them, leading to poor load transfer and increased risk of delamination or cracking between layers. Tensile strength increases with infill density also.

Higher infill density means more material is used inside the part, which increases the internal support and overall stiffness. Denser infills provide more continuous material throughout the structure, reducing void spaces and enhancing load-bearing capacity. This increases the tensile strength by minimizing the chances of failure due to insufficient material in areas of high stress. A higher infill density also improves the uniformity of the part, making it less likely to have weak zones that could fail under tensile loading. The ANOVA analysis reveals that shell thickness, orientation angle, and infill density are the key process parameters that significantly affect the load-carrying capacity during the tensile test. Additionally, two-way interactions, such as ST×OA, ST×ID, and ID×OA, also play an important role in influencing tensile strength (Fig. 6 c & d) for both the sample printed with different infill pattern. A thicker shell provides external strength, while a favorable orientation angle ensures optimal interlayer bonding. Increasing the infill density improves internal structural support, further enhancing load distribution. The optimal combination will vary depending on the specific application and design requirements, but generally, thicker shells, moderate to high infill density, and an orientation angle that aligns the layers with the tensile load will result in the best tensile performance.

3.2 Surface Roughness

Surface roughness is an important parameter in manufacturing and additive processes, as it influences the performance, aesthetic quality, and functional properties of a part. In FDM, surface roughness plays a critical role in determining how a printed part performs in its application, particularly regarding friction, wear, and surface contact. Table 4 shows the average surface roughness (Ra) value for both double dense and hexagonal pattern printed samples. For double dense infill pattern sample number 3 with ST = 0.12 mm, OA = 20˚and, ID = 40% show minimum surface roughness (Ra) value (0.558 µm). For hexagonal infill pattern, sample number 17 with ST = 0.05 mm, OA = 20˚and, ID = 40% shows lowest Ra value (0.549 µm). Optimized surface roughness value explain that for same optimized input parameter, printed parts with double dense infill pattern show better surface quality compared to parts with hexagonal infill pattern. Because the double-dense pattern.

Table 4. Average surface roughness values for double dense and hexagonal infill pattern printed specimens

Sl. No	ST (mm)	OA (˚)	ID (%)	Ra (µm) for double dense pattern	Ra (µm) for hexagonal pattern
1	0.05	60	40	0.676	1.67
2	0.085	40	50	1.234	0.913
3	0.12	20	40	0.588	2.463
4	0.085	40	50	1.413	0.692
5	0.12	60	40	0.987	0.707
6	0.026137	40	50	1.887	0.954
7	0.085	6.364143	50	1.786	2.22
8	0.085	73.63586	50	0.651	0.681
9	0.085	40	50	1.156	1.003
10	0.085	40	66.81793	1.041	0.982
11	0.05	60	60	0.589	1.069
12	0.12	60	60	0.551	0.719
13	0.12	20	60	0.659	1.051
14	0.085	40	60	0.95	0.886
15	0.085	40	50	1.1	0.667
16	0.14	40	50	0.755	0.719
17	0.05	20	40	1.847	0.549
18	0.085	40	50	0.985	0.872
19	0.05	20	60	2.215	1.03
20	0.085	40	33.18207	0.962	1.08

Fig. 7 shows the optimization plots and two way interaction plots for double dense infill pattern (Fig. 7 a & c) and hexagonal infill pattern (Fig. 7b & d). With double-dense infill pattern, surface roughness increase with decreasing shell thickness. With thinner shells, fewer outer layers are available to form a smooth, continuous surface. This lack of thickness makes the surface more susceptible to variations and inconsistencies from the underlying infill pattern. Since the shell is thinner, the outer surface of the part may not have enough material to fully smooth out the irregularities created by the infill structure, leading to a rougher surface finish. Again, A double-dense infill is a tightly packed structure that can create distinct edges and contact points near the outer shell. When the shell is thin, these contact points are closer to the surface, making the outer layer conform more closely to the infill's pattern. This conformity can result in a “textured” appearance where the infill pattern subtly impacts the outer surface, increasing surface roughness. It is obseved that, for FDM parts printed with a hex-

agonal infill pattern, surface roughness can increase with increasing shell thickness due to the unique interaction between the hexagonal pattern and the outer shell layers. Hexagonal infill patterns are structured with open, honeycomb-like cells that may not provide continuous support for the outer shell. As shell thickness increases, more layers are added on top of this infill, but the lack of a consistent base from the hexagonal pattern can lead to uneven support. The outer shell layers may not be perfectly aligned with the infill structure, which can result in slight sagging or irregularities in the topmost layers, increasing surface roughness. s more shell layers are deposited on top of the hexagonal infill, localized stresses can accumulate due to the repetitive heating and cooling cycles during printing. These stresses can cause minor warping or distortions in the shell layers, particularly where the shell does not have full support from the hexagonal cells. This warping effect is more pronounced with thicker shells, leading to an uneven surface finish and increased roughness. Optimized results confirmed that surface roughness decreases with decreased orientation angle. This is because At lower orientation angles, the printed layers are more aligned with the horizontal plane. This alignment allows the nozzle to deposit layers in a flatter, more consistent manner, reducing visible layer lines. The smoother stacking of layers helps create a more uniform surface, thereby reducing surface roughness.

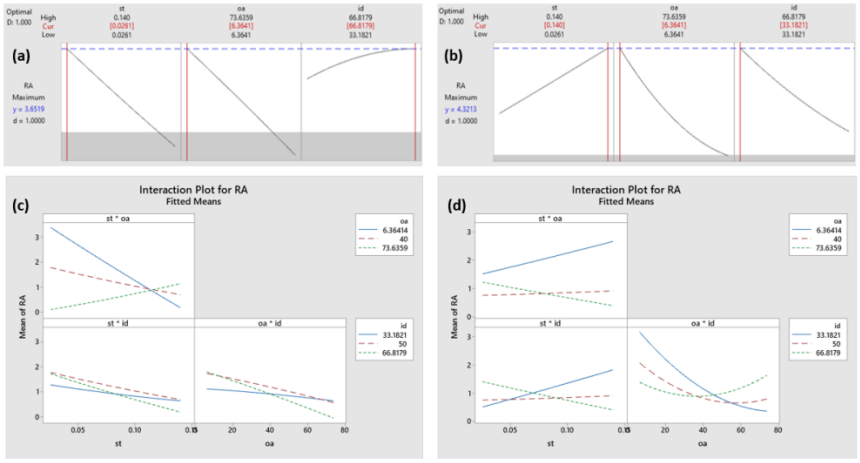

Fig. 7. Surface roughness optimization plot and two-way interaction plot for **(a)** and **(c)** double dense structure and, **(c)** and **(d)** honeycomb structure

Again, Higher orientation angles cause the layers to "step" more prominently, especially on inclined or curved surfaces. This stair-stepping effect becomes less noticeable at lower orientation angles, where the layers sit more flush with each other, leading to a smoother finish. The reduced stair-stepping minimizes the texture on the part's surface, improving overall surface quality. At low orientation angles, each new layer has a larger surface area of contact with the previous layer. This enhanced contact helps improve bonding between layers, leading to a more continuous, cohesive outer surface with fewer gaps or irregularities that can contribute to roughness. A high infill density is crucial for achieving a better surface finish in FDM parts, especially when using double-dense or hexagonal infill patterns. Higher density increases the internal support for the top layers, reducing the likelihood of surface sagging or deformation between infill sections.

4 Conclusion

The main objective of this study is to examine how two distinct infill patterns, i.e., double dense and hexagonal in the FDM process, affect mechanical properties, specifically tensile strength and surface roughness. It is concluded that the hexagonal infill pattern generally offers better tensile strength for FDM-printed ASA parts compared to the double-dense infill pattern because of its highly efficient, honeycomb-like structure that distributes stress evenly throughout the part. This geometry mimics natural, load-bearing structures like beehives, where each hexagon shares its load with adjacent cells, creating an interconnected network that resists deformation under tension. This allows the hexagonal pattern to absorb and distribute forces more uniformly, improving the overall structural integrity. In contrast, the double-dense pattern, though providing closer support for surface quality, lacks this interlocking, stress-distributing design, making it less effective at withstanding tensile loads throughout the part's bulk. But, the double-dense infill pattern offers better surface quality for FDM-printed parts compared to the hexagonal pattern because it provides more closely spaced support points directly beneath the outer layers. This consistent support reduces the risk of surface sagging or gaps, which can lead to smoother, more even top layers. Since the double-dense pattern minimizes unsupported areas between infill lines, it helps

achieve a flatter, more uniform surface, reducing visible layer lines and imperfections. This study also investigates the impact of various process parameters, including shell thickness, orientation angle, and infill density, on tensile strength and surface quality. These parameters play a critical role in influencing the mechanical performance of the parts. High shell thickness and infill density, combined with an optimized orientation angle, contribute to enhanced tensile strength in FDM parts printed with both infill patterns. To achieve improved surface roughness, the orientation angle should be minimized.

References

1. Kyle Raney, Eric Lani, Devi K.Kalla, "Experimental characterization of the tensile strength of ABS parts manufactured by fused deposition modeling process," MaterialsToday, Proceedings 4, pp: 7956–7961, 2017.
2. Wang K, Ho C-C, Zhang C, Wang B. A review on the 3D printing of functional structures for medical phantoms and regenerated tissue and organ applications. Engineering 2017;3:653–62
3. Divyathej M V, Varun M, Rajeev P; "Analysis of mechanical behavior of 3D printed ABS parts by experiments", International Journal of Scientific & Engineering Research, Volume: 7, 2016.
4. Jiang J. A novel fabrication strategy for additive manufacturing processes. J Clean Prod 2020; 272:122916.
5. Chakraborty, D., Mandal, A., Prajapati, A., Kumar, A. "Effect of Process Parameters on Mechanical Performances of 3D-Printed ABS Parts", Volume 1, PFAM 2023 Springer Proceedings in Materials, vol 52. Springer, Singapore. https://doi.org/10.1007/978-981-97-5959-0_3.
6. Shilpesh R. Rajpurohit, Harshit K. Dave; "Effect of process parameters on tensile strength of FDM printed PLA part", Rapid Prototyping Journal, Vol. 24 No. 3, pp. 1317-1324, 2018.
7. Pazhamannil RV, Govindan P, Sooraj P. Prediction of the tensile strength ofpolylactic acid fused deposition models using artificial neural network technique. Mater Today Proc 2020.
8. Kenny L. Alvarez C., Rodrigo F. Lagos C., and Miguel Aizpun; "Investigating the influence of infill percentage on the mechanical properties of fused deposition modelled ABS parts," IngenIería e InvestIgacIón,Volume 36, 2016.
9. Kyle Raney, Eric Lani, Devi K.Kalla, "Experimental characterization of the tensile strength of ABS parts manufactured by fused deposition modeling process," MaterialsToday, Proceedings 4, pp: 7956–7961, 2017.
10. Divyathej M V, Varun M, Rajeev P; "Analysis of mechanical behavior of 3D printed ABS parts by experiments", International Journal of Scientific & Engineering Research, Volume: 7, 2016.
11. C.A. Griffiths, J. Howarth, G. de-Almeida Rowbotham, A. Rees, "Effect of build parameters on processing efficiency and material performance in fused deposition modelling," ProcediaCIRP 49, pp :28– 32, 2016.
12. Lee, J. H., et al. (2017). Structural performance of different infill pattern for additive manufacturing. *Journal of Mechanical Science and Technology*, 31(8), 3949–3954.
13. Ahn, S.-H., Montero, M., Odell, D., Roundy, S., & Wright, P. K. (2002). Anisotropic material properties of fused deposition modeling ABS. *Rapid Prototyping Journal*, 8(4), 248–257.
14. Farouk, O., et al. (2020). Investigating the Effect of Infill Pattern on Mechanical Properties of PLA Parts Made by FDM. *Materials Research Express*, 7(4), 045309.
15. Górski, F., et al. (2019). Influence of Infill Patterns on Mechanical Properties of Parts Manufactured Using FDM Technology. *Procedia Manufacturing*, 38, 1257–1263.
16. Tanikella, N. G., et al. (2021). Improving the Surface Quality of FDM Parts Using Infill Optimization Techniques. *3D Printing and Additive Manufacturing*, 8(4), 173–183.
17. Pham, B., et al. (2018). The Effect of Infill Density and Pattern on the Mechanical Properties and Surface Finish of FDM Parts. *Additive Manufacturing*, 21, 21–26.
18. Tortorich, R., et al. (2021). Optimization of Infill Patterns for FDM to Balance Strength and Aesthetics in Product Design. *Procedia CIRP*, 100, 324–32

Advanced Machining Processes

Study of Performance Characteristics of SS 304 Alloy for Micro ECM utilizing Grey Relational Analysis

Adarsh kumar[1], Dipankar Bose[1]

[1]Dept. of Mechanical Engineering National Institute of Technical Teachers Training and Research, Kolkata

Abstract. Grey relational optimization of micro Electrochemical Machining parameters during machining SS 304 Alloy. The chief goals of this study included increasing material removal rate (MRR), refining the surface roughness (SR) and minimizing radial overcut (RO). The relationship between performance characteristics and process parameters (voltage, feed rate, and current) was established by conducting a grey relational analysis (GRA). In this study, the experimental design was made utilizing the Taguchi L9 (3) orthogonal array for investigation and Grey relational grade (GRG) was measured to determine optimal parameter settings. Results indicated that the current significantly influenced MRR, while voltage, feed rate and current played a crucial role in surface roughness improvement. Additionally, voltage, feed rate and current were found to affect radial overcut. The optimized parameters were validated through confirmatory experiments, demonstrating a significant improvement in all three performance measures. This research contributes to the optimization of micro ECM processes for SS304 machining, offering insights into enhancing productivity and surface quality in precision manufacturing application.

Keywords: SS 304, Micro ECM, MRR, Surface roughness, Radial overcut, Grey relational technique, Optimization.

1 Introduction

Micro electrochemical machining (Micro-ECM) is an accurate material removing technique that can create micro tasks of good quality into different materials including stainless steel 304 (SS 304) alloy [1]. EDM is accomplished by initially placing a workpiece and a tool electrode in an electrolytic solution holding the two with respects to each other at proper distance. These performance measures are the MRR, SR and RO and it is important to optimize them for high machining accuracy, efficiency in Micro-ECM. The optimization of MRR, SR, and ROC in Micro-ECM of SS 304 alloy is a complex problem due to the interdependent nature of these performance measures. Traditional optimization techniques, like as the Taguchi method and response surface methodology, have limitations in handling such complex problems [2]. Therefore, advanced optimization techniques, such as the Grey Relational Analysis (GRA), have been proposed to optimize multiple performance measures simultaneously. GRA is a mathematical approach that can handle complex optimization problems with multiple performance measures by converting them into a single grey relational grade (GRG) [3]. The GRG represents the degree of correlation between the ideal and actual performance measures, and its maximization leads to the optimization of all performance measures simultaneously. This paper aims to optimize the MRR, SR, and ROC for Micro-ECM of SS 304 alloy utilizing the GRA technique. The experimental design and results, as well as the optimization of performance measures, are presented and discussed in detail. The findings of this study can provide valuable insights into the optimization of Micro-ECM of SS 304 alloy and contribute to the development of advanced machining techniques for micro-feature production.

2 Materials and Methods

Work material is selected as stainless steel 304 for this research. Design of Experiments: Design of experiment (L9 orthogonal arrays) has been used and since this work is in the range, the description of work material is 90 mm length, 40 mm width with a thickness of 0.5 mm. The weight percentage chemical composition of stainless Steel 304 alloy material obtained from [4], [5] has been given in Table 1.

Fig. 1. Micro ECM Experimental setup

Table 1. SS 304 Alloy chemical

Element	Fe	Cr	Ni	Mn	Si	N	C	P	S
Minimum (%)	66.74	17.5	8	-	-	-	-	-	-
Maximum (%)	71.24	19.5	10.5	2	1	0.11	0.07	0.05	0.03

[4][5

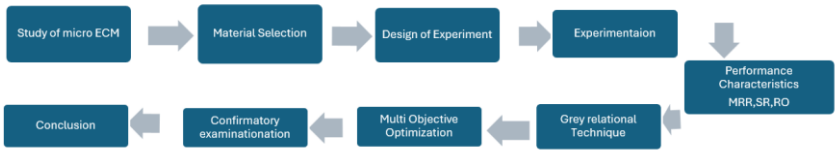

Fig. 2. Representation of Methodology Investigation

2.1 Design of Experiments

Design of Experiments methodology using Taguchi technique has been successfully employed in several research works based on aluminum alloys and composites. The Taguchi method has been demonstrated to reduce the number of tests necessary to develop a response over that needed in traditional full factorial design. This method has two significant advantages: the first is that it allows us to pinpoint potential crosstalks between different parameters[6], [7]; Design of Experiments is an important quality tool, which can be applied in various types of investigations e.g., to discover competitive factor in a process, effect of each factor on outcomes, analyze external sources of variation and identify patterns to fix machine problems; determine optimal parameters for new processes. The industry uses this tool to improve the competitiveness of products in the world, both to create and manufacture better quality products that have a certain reliability as well. Through well-planned and statistically rigorous experiments, it becomes feasible to simultaneously evaluate multiple variables, explore interrelationships, and uncover interactions [8], [9]. In this present research study, the input variables parameters considered in the experiments are voltage (V), current (A), feed rate (f) and other parameters has been kept constant. Input parameters and its various levels are represented in Table 2 and Table 3.

Table 2. Taguchi array

Taguchi Array	L9(3^3)
Factors	3
Runs	9

Table 3. Levels of selected input variables

Sl. no	Process Parameters	1st Level	2nd Level	3rd Level
I.	Voltage (V)	8	10	12
II.	Tool feed rate (mm/min)	0.096	0.12	0.144
III.	Current (amp)	30	40	50

2.2 Grey relational technique

In grey relation analysis, come first experimental or measured responses that thereafter are normalized in 0-1 range. This is what the process of it being done is referred to as grey relation generation. Grey relation coefficients (GRC) are calculated so as to interpret the correlation of normalized actual experimental data versus the ideal or best experimental data obtained out of this experiment. Average of all grey relation coefficient of selected responses: the grey relation grade(GRG) [10]. The evaluation of the (GRG) determines the overall quality characteristics of the multi-response process. Using datasets the (GRC) are calculated and then the grey relation rank is estimated. We will describe this Protocol further in this section: The Initial data is pre-processed before determining the normalized response values based on formulas (1) and (2), which correspond to the predictor variables' output [11]. For MRR, higher values are preferable, while surface roughness and radial overcut should be lower. Generally, higher normalized values indicate stronger output qualities.

Higher the better (HB) $A_{pq} = \frac{Bpq - Min(Bpq)}{Max(Bpq) - Min(Bpq)}$ (1)

Lower the better (LB) $A_{pq} = \frac{Max(Bpq) - Bpq}{Max(Bpq) - Min(Bpq)}$ (2)

The significant difference between the normalized highest possible value and individual normalized each value is determined using equation (3). Equations (4) and (5) are subsequently employed to compute the grey relation grade and rank.

$\emptyset pq = | Y^*_{pq} - Y_{pq} |$ (3)

Grey relation grade, $0pq = \frac{min(\emptyset pq) + (0.5 \times max(\emptyset pq))}{\emptyset pq + (0.5 \times max(\emptyset pq))}$ (4)

Grey relation grade, $yj = \frac{\sum_{i=1}^{n} \theta pq}{n}$ (5)

3 Results and Discussion

The design of experiments has been optimized via 3-level L9 Taguchi orthogonal array design. Design was compiled using the minitab 22 statistical software to run that. Three factors at three levels:- During the experiment 'throughout' is not tolerated; rather, over as a synonym. Work material after Machining as per Figure 3

Fig. 3. Stainless steel 304 Alloy

Equations (6) and (7) are used to calculate the MRR and overcut. Before machining and final weights of the workpiece material were determined by an automated measurement system accurate up to 0.001 g. The roughness of machine workpieces was tested with Mitutoyo SJ-410 surface roughness test device, diameter specimens — using optical microscope. Table 4 shows the measured MRR, SR, and overcut values.

Material Removal Rate (MRR) = $\frac{\text{original weight} - \text{after machining material weight}}{\text{density} \times \text{machining time}}$ (6)

Radial overcut (RO) = machined diameter hole — tool diameter size (7)

Table 4. MRR, SR and overcut values of experimental results

	Voltage (V)	Tool feed Rate (mm/min)	Current (amp)	MRR (mm^3/min)	SR (Rq) (μm)	RO (mm)
01	8	0.096	30	26.60	0.655	0.566
02	8	0.120	40	42.87	0.712	0.623
03	8	0.144	50	63.55	1.307	0.551
04	10	0.096	40	42.11	0.689	0.650
05	10	0.120	50	58.00	0.854	0.517
06	10	0.144	30	45.39	0.459	0.646
07	12	0.096	50	47.16	0.772	0.631
08	12	0.120	30	49.81	1.031	0.725
09	12	0.144	40	52.33	1.159	0.603

3.1 Impact of operating conditions on the observed outcomes

The Taguchi method of testing is a way to conduct fewer tests in order to evaluate the effect of input variables. As it can be seen this is a quick and easy way to approach different technical challenges [12], [13]. One of the worst possible methods to apply material properties and hence cut heavy metal-contaminated material such as stainless steel 304 alloy is the Taguchi testing model that suffers heavily on MRR. An accurate tool to investigate the machining efficiency is by characterizing the material removal rate, this justifies regarding how assessable micro ECM would be at improvement of stainless steel 304 alloy through comprehension towards machining parameters. The best response output variable among the voltage and current is feed rate, as shown in table 5 representing material removal rate responses. Figure 4 shows when the voltage, tool feed rate and current increase the MRR values also increase.

Table 5. MRR response

Level	Voltage (V)	Tool feed rate (mm/min)	Current (amp)
1st	32.40	31.49	31.86
2nd	33.63	33.95	33.17
3rd	33.93	34.53	34.93
Delta	1.53	3.04	3.07
Rank	3rd	2nd	1st

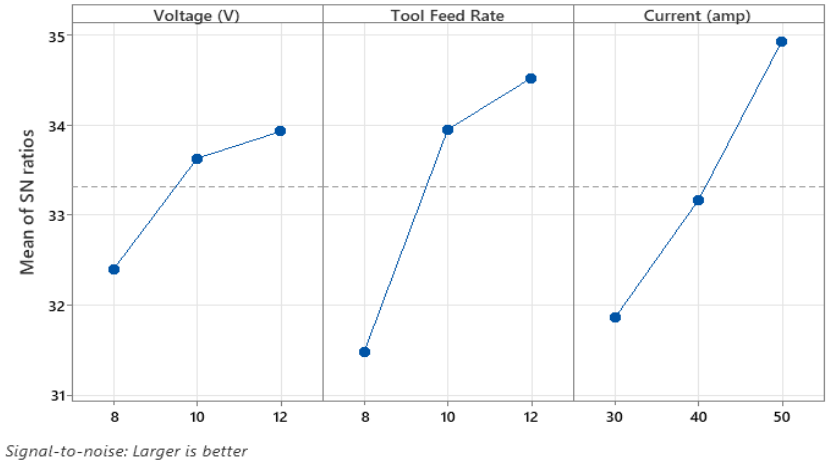

Fig. 4. Displays the main effects plot for MRR

The SR and machining process can be determined from the roughened surfaces created. The high-quality surface texture achieved during machining eliminates the need for additional finishing procedures on the workpiece. Table 6 highlights that voltage is the key parameter influencing SR, as displays in Figure 5's main effect plot. Figure 5 displays the main effect plot for SR. When the voltage, feed rate and current increases the SR is increases.

Table 6. SR response

Level	Voltage (V)	Tool feed rate (mm/min)	Current (amp)
1st	1.4334	3.0528	3.3912
2nd	3.7901	1.3520	1.6348
3rd	0.2336	1.0522	0.4348
Delta	3.5565	2.0006	2.9603
Rank	1st	3rd	2nd

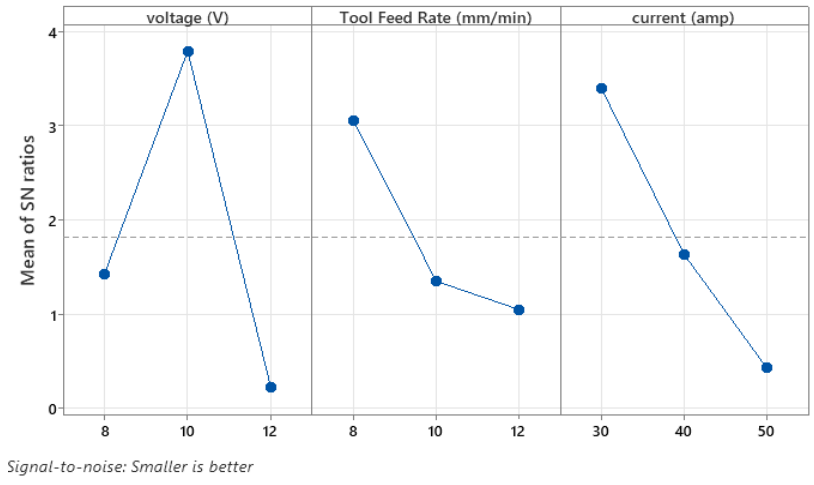

Fig. 5. Displays the main effect plot for SR

Tests has been conducted using an stereo optical microscope. The main effect plot for RO can be observed in Figure 6. it displays that when the current and tool feed rate increase the RO values also increase, but there is a deviation in voltage.

Table 7. RO response

Level	Voltage (V)	Tool feed rate (mm/min)	Current (amp)
1st	4.744	4.228	3.844
2nd	4.422	4.211	4.082
3rd	3.729	4.455	4.969
Delta	1.015	0.244	1.125
Rank	2nd	3rd	1st

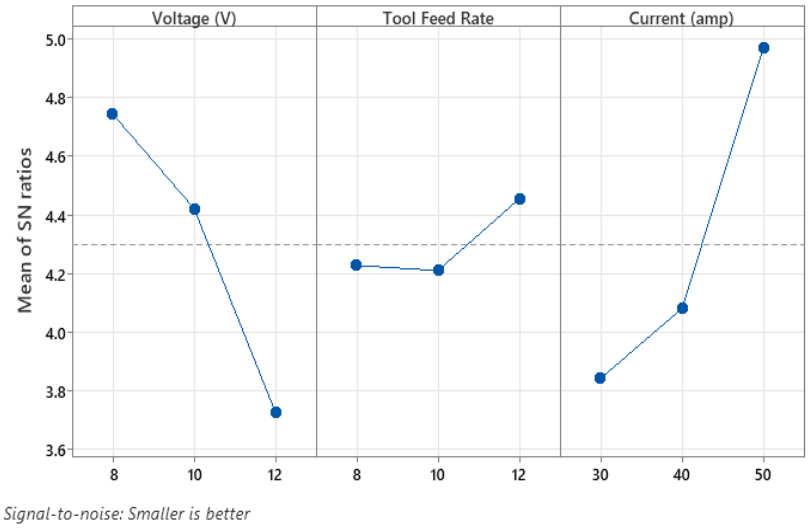

Fig. 6. Displays the main effect plot for RO

3.2 Multi objective optimization

Table 8 displays the calculated GRG for individual run, with the highest value identified as rank 1. The optimum value found in sample 05 at voltage is 10 volts, feed rate is 0.120 mm/min and current is 50 amp.

Table 8. GRG and the experimental runs rank

Ex. No.	Volt-age (V)	Tool Feed Rate (mm/min)	Current (amp)	Grey relational grade (GRG)	Rank
01	8	0.096	30	0.5652	**4**
02	8	0.120	40	0.5315	**6**
03	8	0.144	50	0.6953	**2**
04	10	0.096	40	0.5169	**8**
05	10	0.120	50	0.7655	**1**
06	10	0.144	30	0.6512	**3**
07	12	0.096	50	0.5281	**7**
08	12	0.120	30	0.4455	**9**
09	12	0.144	40	0.5541	**5**

The graph in Figure 7 illustrates the relationship between Grey Relational Grade (GRG) and the number of experimental trials. It was determined that experimental sample number 05, conducted with 10 Voltage, 0.120 mm/min feed rate, and 50 amp current, yielded the most favorable outcomes.

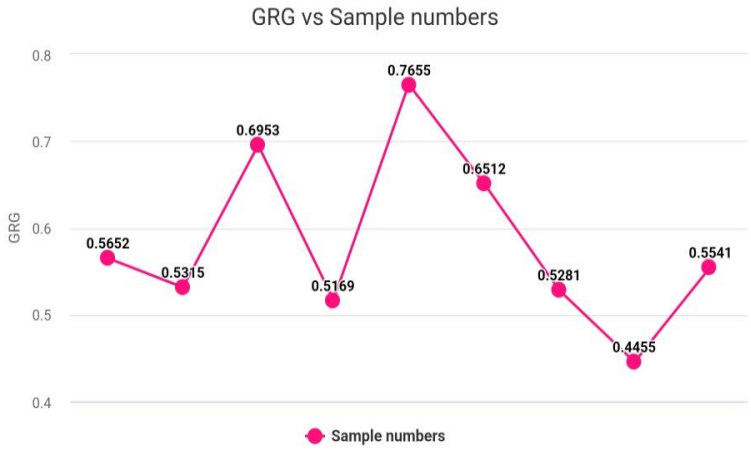

Fig. 7. Graph of GRG vs Sample numbers

3.3 Confirmatory examination

The overall grey relation grade is employed for evaluating the impact of optimal control parameter effect. After determining the optimality of the state, a confirmatory test is conducted to prove that measurement and demonstrate results with MRR, (SR) & (RO). Where, Table 18 Shows the currently field values and optimal field values of the grey relation grades for all input variable. From the actual trial run number 1 and the optimized trial run number 2, there is a grey ratio uptrend 0.2403. It showed a trend to coincide with the optimal values, suggesting that there is still space for enhancement in the machining process.

Table 9. Result of confirmatory examination

Parameter	Actual value (Run 1)	Optimum value (Run 2)	Percentage of enhancement (%)
MRR (mm^3/min)	26.60	58.00	118.04 %
SR (μm)	0.655	0.854	30.38 %
RO (mm)	0.566	0.517	8.65 %
Grey relational grade (GRG)	0.5252	0.7655	45.94
Grey relation grade improvement			0.2403

4 Conclusion

This study as focused on optimizing the micro electrochemical machining process of SS 304 alloy through a multi-objective approach using Grey Relational Analysis based on Taguchi methodology. The research findings were derived from a comprehensive analysis and testing conducted in the relevant study. After that study the following features have been found,

- For an answer to the plan case the general parameters will be provided as output, current one is the primary way that should happen for all of them.
- The current is essential to all necessary output parameters.
- All the results show that with increasing voltage, tool feed rate and current mrr values are also increases.
- Surface roughness decreasing with higher voltage, feed rate and current.

- When the voltage increase the radial overcut decreases but the radial overcut increases during the tool feed rate and current increases.
- Optimum values of sample 05 (voltage 10 volts, feed rate 0.120 mm/min and current is 50 amps.) (Table 8)
- The confirmatory test was also conducted to justify the outcomes received by employing grey relational technique. This is because for the initial run number 1, the grey ratio value was at 0.1586 whereas in the best worst-run: number 05, the value increased to 0.2403 as shown in the results of investigations carried out with its determination presented in Figure-8 (a). (Table 9)
- The results of this current study emphasized a key factor for manufacturers to enhance both productivity and quality when working with stainless steel 304 alloy through micro-electrochemical machining.

References

1. Sathish, T. "Experimental investigation of machined hole and optimization of machining parameters using electrochemical machining." Journal of Materials Research and Technology 8.5 (2019): 4354-4363.
2. Jeyapaul, R., P. Shahabudeen, and K. Krishnaiah. "Quality management research by considering multi-response problems in the Taguchi method–a review." The International Journal of Advanced Manufacturing Technology 26 (2005): 1331-1337..
3. Tong, Lee-Ing, Chi-Chan Chen, and Chung-Ho Wang. "Optimization of multi-response processes using the VIKOR method." The International Journal of Advanced Manufacturing Technology 31 (2007): 1049-1057.
4. "AISI 304 stainless steel," Matmatch. [Online]. Available: https://matmatch.com/learn/material/aisi-304-stainless-steel. [Accessed: 15-Sep-2024].
5. "Stainless steel 304 (1.4301)," Thyssenkrupp Materials (UK) Ltd. [Online]. Available: https://www.thyssenkrupp-materials.co.uk/stainless-steel-304-14301.html. [Accessed: 15-Sep-2024].
6. Radhika, N., and R. Subramaniam. "Wear behaviour of aluminium/alumina/graphite hybrid metal matrix composites using Taguchi's techniques." Industrial lubrication and tribology 65.3 (2013): 166-174.
7. Girish, B. M., et al. "Optimization of wear behavior of magnesium alloy AZ91 hybrid composites using taguchi experimental design." Metallurgical and materials transactions A 47 (2016): 3193-3200.
8. Rajurkar, K. P., and R. R. Bishu. "Design of experiments to study and optimize process performance." International Journal of Quality & Reliability Management 16.1 (1999): 56-71.
9. Dey, A., S. Debnath, and K. M. Pandey. "Optimization of electrical discharge machining process parameters for Al6061/cenosphere composite using grey-based hybrid approach." Transactions of Nonferrous Metals Society of China 27.5 (2017): 998-1010.
10. Manikandan, N., S. Kumanan, and C. Sathiyanarayanan. "Multiple performance optimization of electrochemical drilling of Inconel 625 using Taguchi based Grey Relational Analysis." Engineering Science and Technology, an International Journal 20.2 (2017): 662-671.
11. Madhankumar, S., et al. "Optimization of micro electrochemical machining of Inconel 625 using Taguchi based grey relational analysis." International journal of applied engineering research 13.9 (2018): 6771-6779.
12. Madhankumar, S., et al. "Fabrication of Al6063 alloy, silicon carbide and boron glass powder metal matrix composites in stir casting process and analysis the impact of process variables on mechanical properties." Materials Today: Proceedings 42 (2021): 529-535.
13. Rajesh, S., S. Madhankumar, and M. Harikrishnan TV. "Effect of Processing Parameters on Metal Matrix Composites in Stir Casting Process Using Taguchi Technique." Int. J. Res. Appl. Sci. Eng. Technol. 6.1 (2018): 1610-1615.

A Review on Machinability of Difficult to Machine (DTM) Materials using Cryogenically Treated Cutting Tool Inserts

Sandip K Bidgar [1], Dr B U Sonawane [2], Dr B D Bachchhav [3]

[1]Research Scholar, COEP Technological University, Pune - 411005, Maharashtra, India
Assistant Professor, Department of Production Engineering, AISSMS COE, Pune - 411001, Maharashtra, India
[2]Associate Professor, Department of Manufacturing Engineering and Industrial Management, COEP Technological University, Pune - 411005, Maharashtra, India
[3]Professor, Department of Mechanical Engineering, AISSMS COE, Pune - 411001, Maharashtra, India
skbidgar@gmail.com

Abstract. The machinability of difficult-to-machine (DTM) materials, such as titanium combinations, nickel-based superalloys, and solidified steels, face challenges in advanced manufacturing forms due to their inherent properties, counting high strengths, hardness, and low thermal conductivity. These materials frequently lead to quick apparatus wear, destitute surface wrap up, and heavy machining costs. Recent advances in cryogenic treatment of cutting tools have improved machinability by extending tool life, reducing wear, and enhancing surface quality. This work basically analyzes the current state of inquire about on the utilize of cryogenically treated cutting tools for machining DTM materials. The survey includes different viewpoints of cryogenic treatment, including the treatment process parameters, their impacts on instrument fabric microstructure, and resultant mechanical properties. It investigates the components through which cryogenic treatment upgrades instrument execution, such as stage change, remaining stretch lessening, and carbide precipitation. Besides, the survey highlights exploratory thinks about and mechanical applications that illustrate enhancements in apparatus life, surface keenness, and dimensional exactness. The paper also examines the financial and natural suggestions of utilizing cryogenically treated instruments, emphasizing cost-effectiveness and supportability in fabricating. Challenges such as treatment consistency, prepare optimization, and the improvement of standardized conventions are recognized as key zones for future investigate. Moreover, the potential integration of cryogenic innovation with other progressed machining procedures, such as high-speed machining and dry machining, is investigated to advance improve the execution and maintainability of fabricating forms. Cryogenic treatment of cutting tools is an effective way to improve the machinability of DTM materials, showing openings for development and progression within the field of fabricating engineering. This survey points to supply a comprehensive understanding of the benefits, challenges, and future headings of this promising innovation.

Keywords: Cryogenic Treatment, Difficult-to-Machine Materials, Tool Wear Reduction, Surface Integrity, Machinability Enhancement.

1 Introduction

A big problem in the area of manufacturing engineering is how to make materials that are difficult-to-machine (DTM). More and more, high-performance use materials like titanium alloys, nickel-based super alloys, and strengthened steels as they have great mechanical qualities, such as high strength, resistance to wear, and great thermal stability. Because of these qualities, they work great in industries like aircraft, automobile, and biomedicine, where parts have to withstand harsh conditions and meet strict performance standards. Due to these same qualities, DTM materials are extremely hard to machine [1]. This often results in fast tool wear, bad surface finishes, and high costs for cutting. As businesses try to make their output more efficient and high-quality, making these products easier to work has become a top concern [2]. Within the past, high-performance cutting instruments and progressed machining strategies, like high-speed machining, were utilized to work with DTM materials. This was done to reduce the harm caused by the high temperatures and strengths that were made amid the cutting tool. Shockingly, these strategies do not continuously work since standard apparatus materials aren't continuously great sufficient for the cruel conditions that come up when DTM materials are machined. Within the past few years, cryogenic treatment has ended up a potential way to form cutting devices work way better [3]. In this handle, the device fabric is cooled to cryogenic temperatures, which are more often than not come to with fluid nitrogen. It is at that point kept at these temperatures for a certain sum of time, recently gradually rising to room temperature [4], [5]. The method changes the design of the apparatus fabric in a great way, which makes it harder to wear, more strong, and superior at exchanging warm. Figure 1 shows the Overview of direction for DTM Materials. Cryogenic treatment of cutting device embeds might be very supportive for working with DTM materials since it amplifies the life of the devices and progresses the quality of the surface, which brings down the overall taken a toll of generation [6].

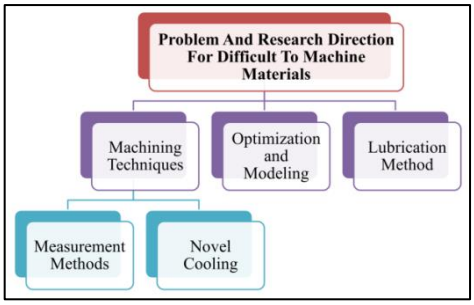

Fig. 1. Overview of direction for difficult to Machine Materials

The process improves the microstructural properties of tool materials, like carbide precipitation and matrix change. These properties then affect the tools' mechanical properties and how well they work when they are being machined. For illustration, cold treatment can alter remaining austenite into martensitic and cause little carbides to make, which makes the device harder and more safe to wear. Within the same way, cold treatment can move forward the hardness of high-speed steel instruments by refining the microstructure and bringing down inside stresses [7]. A part of inquire about has been done on utilizing cutting apparatuses that have been treated with cryogens to machine DTM materials. Many considers have appeared that this strategy works to create the materials simpler to machine. Cryogenically treating instruments has been appeared to have way better surface wraps up, lower wear rates, and more exact estimations compared to apparatuses that have not been treated. It is since the instrument materials have way better qualities presently, which lets them handle the tall warm and energetic loads that come up when DTM materials are being machined. Utilizing instruments that have been treated with cryogens can moreover lower cutting powers and temperatures by a huge sum. This brings down the chance of warm harm to the question and increments the tool's life [8].

Cryogenically treating cutting devices has benefits for the economy and the environment in expansion to its logical benefits. The longer device life and superior cutting execution can lower the taken a toll of apparatuses and boost generation. Cryogenic treatment is also a clean and ecologically inviting strategy since it doesn't utilize any harmful chemicals or make any destructive exhaust. It may be a great choice for businesses that need to be more economical and less hurtful to the soil in their generation strategies. Indeed in spite of the fact that the comes about see good, there are still a few issues that ought to be settled some time recently cryogenically treated cutting instruments can be broadly used in industry. The lack of uniform strategies for the cold treatment prepare is one of the most issues. This could cause contrasts in how well the treatment works. Cryogenic treatment innovation may too be difficult to utilize since it is costly and difficult to understand, especially for little and medium-sized businesses [9]. To urge comes about that are steady and simple to rehash, more ponder ought to be done to discover the leading cooling rate, splashing time, and setting conditions. In the future, cold treatment might be combined with other advanced machining methods, like high-speed machining, dry machining, and mixed processes, to make the process even better and last longer [10]. This combination could lead to the creation of cutting tools that are very resistant to wear, have less of an effect on the environment, and are more cost-effective. Additionally, looking into how cold treatment could be used on other tool materials and tasks could make it more useful and applicable in more production processes. Table 1 shows the summary of approaches in using cryogenically treated cutting tool.

Table 1. Summary of approaches in using cryogenically treated cutting tool

Method	Approach	Type of Material	Cutting Tools	Remark
Cryogenic Treatment [11]	Deep cryogenic treatment (DCT)	Titanium Alloys	Carbide Inserts	Significant improvements in tool wear resistance and surface finish.
Cryogenic Cooling [12]	Liquid nitrogen as a cooling medium	Nickel-Based Superalloys	CBN Tools	Enhanced tool life and reduced thermal damage.
Cryogenic Treatment and Coating [13]	DCT combined with TiAlN coating	Hardened Steels	Coated Carbide Tools	Improved surface quality and reduced cutting forces.
Hybrid Cryogenic-MQL [14]	Minimum quantity lubrication combined with cryogenic cooling	Titanium Alloys	PVD Coated Inserts	Reduced tool wear and increased process efficiency.
Cryogenic Assisted Machining [15]	Internal cryogenic cooling through tool	Nickel-Based Superalloys	PCBN Tools	Enhanced tool performance and reduced tool wear.
Cryogenic Treatment and Micro-blasting [16]	DCT followed by micro-abrasive blasting	Hardened Steels	Ceramic Inserts	Increased tool life and better control of dimensional accuracy.
Cryogenic Treatment [17]	Sub-zero temperature treatment	Titanium Alloys	Uncoated Carbide Inserts	Improved toughness and reduced tool breakage.
Advanced Cryogenic Treatment [18]	Multi-stage cryogenic treatment process	Nickel-Based Superalloys	HSS Tools	Significant reduction in cutting temperatures and tool wear.
Hybrid Cooling Techniques [19]	Combination of cryogenic cooling and conventional flood cooling	Hardened Steels	CVD Coated Tools	Better tool wear management and improved surface finish.
Cryogenic Machining [20]	External cooling with liquid nitrogen spray	Titanium Alloys	Diamond Tools	Enhanced tool life and cutting efficiency.
Cryogenic Hardening [21]	Enhanced hardening through cryogenic processing	Nickel-Based Superalloys	Carbide Inserts	Improved cutting performance and reduced work hardening effect.
Integrated Cryogenic Processing [22]	Combined heat and cryogenic treatment	Hardened Steels	Cermet Tools	Enhanced tool life and precision.
Cryogenic Treatment and Laser [23]	Laser-assisted cryogenic machining	Titanium Alloys	PCBN Inserts	Improved tool wear resistance and surface quality.
Cryogenic Treatment Optimization [24]	Optimization of cryogenic process parameters	Nickel-Based Superalloys	PVD Coated Carbide Tools	Maximized tool life and reduced machining costs.

2 Difficult-to-Machine (DTM) Materials

2.1 Characteristics and applications of DTM materials

Some of the mechanical qualities that make materials difficult to machine (DTM) are their high strength, hardness, and resistance to wear and rust. Because of these qualities, they are very useful in tough situations, but they are also very hard to machine. DTM materials are often used in fields like aircraft, automotive, power generation, and healthcare, where parts are put through harsh conditions and need to keep their performance and structural integrity [25].

1. Titanium Alloys

Titanium metals are known for having a high strength-to-weight ratio, not rusting, and being able to handle high temperatures. Because of these qualities, they are perfect for use in aircraft, like in plane parts and engine parts, where efficiency and weight reduction are very important. However, they are hard to machine because they don't conduct heat well and respond quickly with chemicals at high temperatures. Because it doesn't transfer heat well, heat builds up at the cutting edge, which speeds up tool wear and makes the surface finish less smooth [26]. The reaction with tool materials can also lead to built-up edges, which makes the cutting process even more difficult.

2. Nickel-Based Superalloys

Nickel-based superalloys are designed to stay strong and stable at high temperatures. This makes them necessary for turbine blades, exhaust valves, and other high-temperature uses in the aircraft and power generation industries, overview illustrate in figure 2. It is very hard to machine these metals because they don't easily change shape or rust, which is good for working conditions. Because they are hard and tend to work-harden during grinding, cutting forces are higher and tool wear happens faster. Furthermore, the presence of rough carbide phases in these metals speeds up the wear and tear on tools.

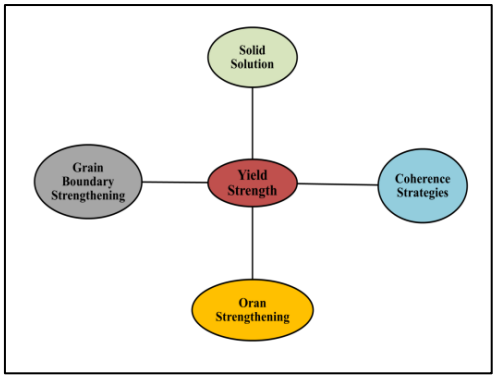

Fig. 2. Strengthening mechanisms in polycrystalline Ni-based Material

3. Hardened Steels

The car and metalworking industries use hardened steels a lot because they are very hard and don't break down easily. This is made possible by heat treatment methods. When accuracy and longevity are important, these materials are used in things like tools, molds, and bearing parts. Machining sharpened steels is hard because they are very strong and don't bend easily. This means that cutting forces are higher and tools are more likely to break. Also, using advanced grinding methods and high-performance cutting tools is needed to keep tolerances tight and make the surface smooth on sharpened steels [27]. To get around the problems that come with making these DTM materials, you need to come up with new ways to do things and use more advanced tools. Cryogenic treatment of cutting tools has become an interesting way to improve machinability by making tools last longer and work better with these materials. Understanding how each DTM material works and the problems that come up when you try to machine it is important for coming up with good ways to process them more efficiently in industrial settings.

2.2 Common challenges in machining these materials

Because they have special physical and mechanical qualities, difficult-to-machine (DTM) materials are hard to work with. These problems have a big effect on how efficiently and cost-effectively manufacturing processes work, so new tools and methods have to be created to get around them.

1. High Tool Wear

Tool wear is very fast, which is one of the main problems when working with DTM materials. Some materials, like titanium alloys, nickel-based superalloys, and strengthened steels, are very hard and rough, which makes tools break down quickly. Extreme pressures and temperatures are put on the cutting tool during the grinding process. These causes wear processes like abrasion, adhesion, and diffusion. Titanium metals, for instance, don't let heat move through them very well, so heat builds up at the cutting edge and speeds up tool wear. Nickel-based superalloys and strengthened steels have hard carbide bits that make tool wear worse by wearing away at the metal. Having to replace old tools all the time causes more downtime and lowers total output, which raises the cost of making things [28].

2. Bad Finish on the Surface

Another big problem when working with DTM materials is getting a good surface finish. The hardness and work-hardening properties of these materials often cause flaws and irregularities on the surface. One example is that when titanium metals are machined, the edges tend to build up, which makes the surface finish rough [29]. Nickel-based Superalloys tend to work-harden, which can make the surface tear and become rough if they are not made with the right parameters. High cutting forces and tool movement cause shaking and instability during grinding, which makes the surface even less smooth. A bad surface finish not only makes the part look bad and not work right, but it also lowers its fatigue strength and wear resistance, so it's important to fix this problem for important uses.

3. High costs for machining

When you have both high tool wear and a rough surface, the cost of cutting goes up in the end. More frequent tool changes and machine downtime lead to higher costs for workers and running the business. Table 2 compares the machinability of different difficult-to-machine (DTM) materials.

Table 2. Compares the machinability of different difficult-to-machine (DTM) materials

Parameter	Titanium Alloys	Nickel-Based Superalloys	Hardened Steels
Material Properties [1]	High strength-to-weight ratio, excellent corrosion resistance, low thermal conductivity	High temperature resistance, excellent mechanical strength, oxidation resistance	High hardness and wear resistance due to heat treatment
Applications [2]	Aerospace components, medical implants, automotive parts	Turbine blades, exhaust valves, high-temperature aerospace and power generation applications	Dies, molds, and bearing components in the automotive and tooling industries
Machining Challenges [3]	Rapid tool wear, poor surface finish due to chemical reactivity, and heat concentration at the cutting edge	High tool wear and surface defects due to hardness and work-hardening, leading to high cutting forces	Tool breakage and difficulty in maintaining tolerances due to high strength and reduced ductility
High Tool Wear [4]	Caused by heat concentration and chemical reactivity	Caused by abrasive carbide phases and work-hardening	Caused by high hardness and abrasiveness
Poor Surface Finish [5]	Built-up edge formation leads to rough surfaces	Surface tearing and roughness due to work-hardening	Vibration and high cutting forces lead to poor surface quality
High Machining Costs [6]	Frequent tool replacement and process optimization efforts increase costs	Advanced tooling and high energy consumption contribute to costs	Specialized tools and processes increase operational expenses
Cryogenic Treatment [7]	Enhances tool wear resistance and reduces chemical reactivity	Improves tool life and reduces surface defects by minimizing work-hardening effects	Increases tool toughness and reduces vibration for better surface finish
Tool Life Improvement [8]	Significant improvement in tool life due to reduced heat impact	Extended tool lifespan due to reduced abrasive wear and thermal impact	Enhanced wear resistance leads to longer tool life
Surface Quality [9]	Enhanced surface finish with reduced built-up edge and better heat management	Improved surface finish through reduced work-hardening and smoother machining processes	Achieves better surface quality by reducing vibration and improving dimensional accuracy
Economic Benefits [10]	Lower production costs due to reduced tool wear and extended tool life	Cost savings from longer tool life and improved machining efficiency	Reduced tooling costs and improved productivity due to better tool performance

The cost of making DTM materials goes up even more because of the need for specialized cutting tools and advanced machine technologies, like precise machining centres and covered tools. Because these materials are so

hard to work with, it often takes a lot of process improvement and trial-and-error to get the results that are wanted, which raises the cost of the whole process. In addition, grinding uses more energy and resources, which raises the cost of output and has an effect on the environment.

3 Cryogenic Treatment of Cutting Tools

3.1 Description of the Cryogenic Treatment Process

By putting cutting tools through very low temperatures, cryogenic treatment is a high-tech way to improve their performance. There are two major steps in the process: cooling and soaking. During the cooling process, the tools are slowly cooled down to very cold temperatures. Liquid nitrogen, which can hit -321°F (-196°C), is usually used for this. This managed and slow cooling keeps the temperature of the tool material from changing quickly, which can cause damage, process shown in figure 3. When the right temperature is reached, the tools are kept in a frozen state during the soaking phase for a set amount of time, which can be anywhere from a few hours to more than 24 hours, based on the material and the qualities that are wanted. The tools are slowly brought back to room temperature through a controlled heat process after being soaked [30]. This is very important to keep them from stressing out and breaking. A lot of different tool materials and parts are often treated with cryogenics. A lot of the time, materials like high-speed steels, carbide tools, and cobalt-based metals are handled to make them harder, tougher, and less likely to break down. The process works especially well for cutting tools that are used to work with difficult-to-machine (DTM) materials because it improves their performance and durability by making the material's substructure and mechanical qualities better.

3.2 Microstructural Changes Induced by Cryogenic Treatment

The cryogenic treatment method causes big changes in the microstructure of the materials that are treated. These changes improve the mechanical qualities that are important for cutting.

1. Modifications of Phase

Changes in phase are one of the most important changes in microstructure. Cryogenic treatment makes it easier for residual austenite, a phase that is soft and bendable, to change into martensite, a phase that is much harder and less likely to wear down. The general strength and physical stability of the tool material are improved by this change, which greatly lowers wear during cutting operations. The change happens because of the low temperatures reached during cryogenic cooling, which help the crystal lattice structure move around.

2. Residual Stress Reduction

Putting something through cryogenic treatment also helps lower any remaining stresses in the material. There can be leftover pressures in cutting tools when they are being made and machined because of fast cooling, grinding forces, and heat expansion. These pressures can cause tools to bend, crack, and break before they should. The process relieves stress on the tools by cooling them to freezing temperatures and letting them slowly return to room temperature. This makes the tool structure more stable and strong. This lowers the leftover stresses, which makes the tool last longer and work better under the high heat and mechanical loads that are common in DTM cutting.

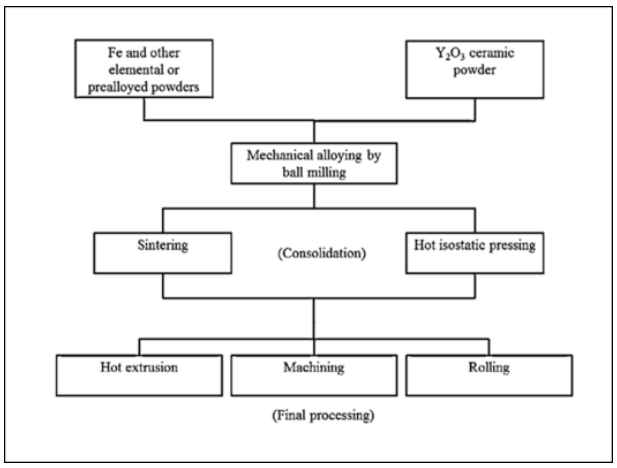

Fig. 3. Representation of workflow of mechanical alloying process model

3. Carbide Precipitation

Cryogenic treatment not only changes the phases of materials but also lowers stress and encourages carbide production in tool steels and other alloys. Low temperatures make it easier for fine carbides to form that are spread out evenly in the microstructure. These carbides are like tiny building blocks that make the tool material stronger, harder, and more resistant to wear. Cobalt particles spread out evenly in the tools make them better at cutting. They can keep their sharp edges and handle rough wear while they're being machined. Table 3 shows the cryogenic treatment process and the materials and tools commonly treated.

Table 3. Cryogenic treatment process and the materials and tools commonly treated

Parameter	Titanium Alloys	Nickel-Based Superalloys	Hardened Steels
Cooling Rate [31]	Moderate cooling rate to prevent thermal shock	Gradual cooling to reduce thermal stresses	Controlled cooling to minimize thermal gradients
Minimum Temperature [32]	Typically reaches -196°C for optimal treatment	Similar temperatures to ensure uniform treatment	Achieves -196°C to promote microstructural changes
Soaking Duration [33]	8 to 24 hours depending on tool material and size	12 to 24 hours for effective phase transformation	10 to 24 hours for stress relief and transformation
Warming Process [34]	Slow return to ambient temperature to avoid cracks	Gradual warming to prevent residual stress build up	Controlled warming to maintain dimensional stability
Commonly Treated Materials [35]	Carbide and high-speed steel tools used for machining	Cobalt-based alloys and high-performance carbides	Tool steels and cermets for precision applications
Targeted Tools [36]	Inserts, end mills, and drills for aerospace parts	Turbine blade tools, high-temperature machining	Dies, molds, and precision tools in automotive

3.3 Mechanical property enhancements in tool materials

The mechanical features of cutting tools can be improved by freezing them. This makes them better for cutting materials that are hard to machine (DTM). Hardness, stiffness, and heat conductivity all get much better as a result of the process. This makes the tools work better and last longer, composition discussed in table 4.

1. Increased Hardness

Cryogenic treatment makes cutting tools much harder by changing the austenite that is still present into martensite, which is a much harder phase. This phase change is very important because martensite gives the cutting tool the hardness it needs to handle the rough and high-stress conditions that come up during grinding, different properties of cutting material is represent it figure 4. The tool material also gets even harder during the cold process, when small carbides form on top of others. The higher sharpness makes the tool last longer and wear less, so it can be used for longer amounts of time without having to be changed out often. This improvement is especially helpful when cutting DTM materials, which are known for being very hard and not easily, deformed [30].

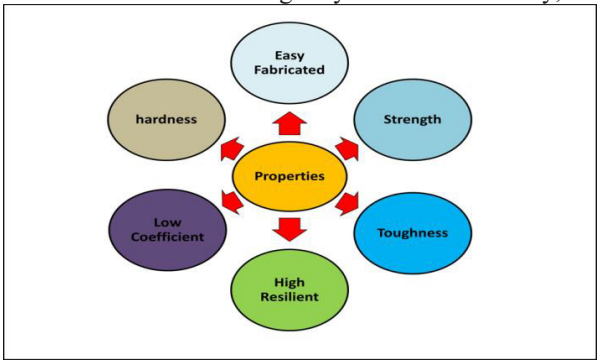

Fig. 4. Representation of different Properties of cutting tool materials

2. Improved Toughness

Along with hardness, toughness is an important mechanical trait that shows how well a tool can absorb energy and not break when it's under load. By improving the architecture of the tool material and lowering internal stresses, cryogenic treatment makes it tougher. The alter of leftover austenite and the creation of carbides offer assistance make the microstructure stronger and normal, which makes the instrument superior able to handle affect and rotational stresses amid cutting. Harder materials make it less likely that apparatuses will break or chip, which is critical for keeping machine execution relentless and getting the surface wrap up you need on workpiece.

3. Enhanced Thermal Conductivity

Cutting devices can too be made way better at exchanging warm when they are solidified. Cryogenic treatment makes it less demanding for warm to elude from the cutting zone by bringing down the sum of leftover austenite and expanding the consistency of the microstructure. This enhancement is particularly vital when working with titanium metals or other materials that do not conduct warm well, since as well much warm can cause apparatuses to wear out rapidly. The temperature contrast between the apparatus and the workpiece is reduced when the warm conductivity is superior. This makes the cutting conditions more steady and the surface quality superior [28], [37]. Table 4 shows the composition Ranges of Alloy Elements.

Table 4. Composition Ranges of Alloy Elements

Ele-ment	Min. wt% (at.%)	Min. patent wt% (at.%)	Max. patent wt% (at.%)	Max. wt% (at.%)
Cr	0.11	14.46	15.26	30.11
Co	0.11	14.11	19.11	24.11
Mo	0.11	4.36	5.36	6.11
Al	1.51	2.96	3.26	6.11
Ti	0.11	3.56	4.26	6.11
Ta	0.11	1.46	2.26	4.11

3.4 Comparison with untreated cutting tools

The qualities of the fabric and the cleaning strategies utilized on the devices have a enormous impact on how well they work with difficult-to-machine (DTM) materials. Cryogenic treatment has gotten to be a progressive strategy that essentially moves forward the mechanical qualities of cutting apparatuses compared to those that have not been treated. This leads to way better machine proficiency and longer device life.

1. Tool Wear and Longevity

When working with DTM materials, cutting instruments that haven't been cleaned frequently wear out rapidly since of the tall temperatures, unpleasantness, and mechanical powers at the cutting edge. This wear causes devices to have to be supplanted more frequently, which increments downtime and costs more to run. Cryogenically treated instruments, on the other hand, are safer to wear. Amid cold treatment, leftover austenite changes to martensitic and little carbides frame. This makes the fabric harder, brings down the rate of wear, and increments the tool's life. Considers have appeared that instruments that have been cryogenically treated can final up to 50% longer than apparatuses that have not been treated. This increases efficiency and lowers the costs of replacing tools [34].

2. Surface Finish and Dimensional Accuracy

Machining DTM materials with tools that haven't been handled often leads to rough surfaces and problems keeping the dimensions correct. These problems are caused by things like built-up edges, shaking, and heat growth. With their higher hardness and lower leftover loads, tools that have been cryogenically treated keep their cutting edges sharper for longer. This leads to smoother surfaces, less chatter, and better stability in the dimensions during cutting. In fields where accuracy and surface quality are very important, like aircraft and medical device making, being able to make surfaces that are smoother and hold their shape better is very important.

3. Taking Care of Heat

Better thermal conductivity is one of the main benefits of cryogenically treated tools. This makes it easier for heat to escape during cutting operations. Tools that haven't been cleaned often have trouble with heat buildup, which can damage both the tool and the workpiece. Cryogenically treating tools makes them better at transferring heat, which lowers the temperature in the cutting zone. This stops thermal expansion from hurting the surface finish and tool wear. This better control of heat makes it easier to get uniform results when milling materials like titanium metals that don't conduct heat well and tend to hold it [21].

4. Properties of Matter
Tools that haven't been handled may have good mechanical qualities at first, but when they're used to machine DTM materials, they often lose their performance very quickly. The architecture of cutting tools gets stronger when they are frozen, which makes them harder and tougher [14]. Cryogenically treated tools can handle higher cutting forces and impact loads without breaking because they are both hard and tough. Because of this, these tools are more reliable and can handle harsh cutting conditions, which makes them more efficient and productive.

5. Cost-Effectiveness
Cryogenic treatment may cost more up front than using tools that haven't been treated, but the long-term benefits are much greater than the costs. Manufacturing processes save a lot of money because the tools last longer, need to be changed less often, produce better surfaces, and work more efficiently. The cost benefits of using cryogenically treated tools over raw ones are also shown by the fact that they need less upkeep and repair.

Table 5. Comparing the performance of cryogenically treated cutting tools with untreated cutting tools when machining difficult-to-machine (DTM) materials

Parameter	Untreated Cutting Tools	Cryogenically Treated Cutting Tools
Tool Wear	Rapid wear due to high temperatures and mechanical stresses, requiring frequent tool changes.	Significantly reduced wear rates due to increased hardness and carbide precipitation, extending tool life.
Tool Longevity	Short tool life, leading to increased downtime and higher operational costs.	Up to 50% longer tool life, resulting in improved productivity and cost savings.
Surface Finish	Poor surface finish due to built-up edge, vibration, and thermal expansion.	Improved surface finish with reduced chatter and better dimensional accuracy.
Dimensional Accuracy	Difficult to maintain due to thermal expansion and tool deformation.	Enhanced dimensional stability, producing smoother surfaces with tighter tolerances.
Thermal Management	Poor heat dissipation leads to thermal damage to the tool and workpiece.	Improved thermal conductivity facilitates better heat dissipation, reducing temperature at the cutting zone.
Mechanical Properties	Initial good properties degrade rapidly under extreme conditions.	Enhanced hardness and toughness allow for better handling of high cutting forces and impact stresses.
Cost-Effectiveness	Higher costs due to frequent tool maintenance and replacement.	Long-term cost savings through extended tool life, reduced maintenance, and improved machining performance.
Performance Consistency	Inconsistent performance due to rapid degradation and frequent tool changes.	Consistent performance with longer-lasting cutting edges and reliable machining results.
Application Suitability	Limited suitability for high-precision and high-performance applications.	Ideal for high-precision applications requiring excellent surface integrity and dimensional control.

4 Economic and Environmental Implications

Utilizing cutting apparatuses that have been taken care of with cryogens to work with (DTM) materials is sweet for both the economy and the environment. As businesses attempt to create their forms more proficient whereas too having less of an impact on the environment, cryogenic treatment stands out as a game-changing innovation that can do both. Cutting instruments that have been solidified are a cost-effective way to do mechanical errands, particularly when working with DTM materials. Cold treatment and durable tools may cost more initially, but the long-term benefits far outweigh these expenses. Devices that have been cryogenically treated wear less rapidly and keep working well for longer, which suggests they have to be changed and supplanted less regularly. This lower rate of device wear leads to lower costs for instruments and less downtime for machines, which increments the by and large productivity of cutting forms [12]. Cryogenically treating tools can also make them work better, which can allow for faster cutting speeds and higher feed rates. This makes production even more efficient and output high.
Cryogenically treating tools improves production efficiency by keeping performance stable and reducing downtime. These tools can handle the tough conditions of cutting DTM materials because they have been treated with cryogenics, which makes them harder and tougher. Cryogenically treating tools also improves the surface finish

and accuracy of measurements, which means they don't need to be used for extra processes like cutting or sharpening, this saves time and resources. Shorter production cycles and higher output rates are made possible by this increase in cutting efficiency. This lets makers meet tight deadlines and get goods to the market faster. Besides being good for business, cold treatment is also very good for the environment according to [35]. One of the biggest benefits for the environment is that less dangerous chemicals are used than in traditional ways of cooling and lubricating. Cutting solutions often contain chemicals that are bad for people and the environment, but cryogenic treatment reduces the need for them. By using these chemicals less often, cryogenic treatment makes the workplace safer and reduces the damage that getting rid of them does to the earth. It also helps cut down on pollution and trash by using cold treatment. Because cold treatment makes tools last longer, they don't need to be replaced as often. This means that fewer tools are thrown away, which lowers waste. Cryogenically treating tools also makes them work better, which means they can use materials more efficiently, which lowers the amount of scrap and trash. This drop in trash and pollution is in line with the growing focus on ecology and resource saving in modern industry.

5 Challenges and Future Research Directions

Cryogenic treatment has a lot of benefits for cutting DTM (difficult-to-machine) materials, but there are some problems that need to be fixed before it can be widely used. Getting past these problems and looking into possible future study lines are very important if we want to make the most of this technology's uses in different industries.

A. Barriers to Widespread Adoption

Even though cryogenically treated tools seem to have a lot of benefits, they are not widely used in the industrial business for a number of reasons. One big problem is that treatment methods are not always the same [28]. The cooling rate, soaking time, and heat process are all controlled by certain parameters in the cryogenic treatment process. These parameters can change depending on the tool material and the qualities that are wanted. Because there aren't any standard methods, treatment results aren't always the same. This makes it hard for makers to safely use this technology in a range of tasks and tool types. Setting up uniform processes and standards would give producers the confidence they need to use cold treatment in a way that works every time. The high cost and difficulty of the tools needed for cryogenic treatment is another reason why it is not widely used. Specialized tools, like cryogenic tanks and precise temperature control systems, are needed for the process. These tools can be pricey to buy and keep up. Small and medium-sized businesses (SMEs) may not be able to afford the initial investment, which would stop them from using cold treatment. Because the equipment is so complicated, it needs skilled workers and repair staff, which adds to the costs of running the business. Creating cold treatment systems that are less expensive and easier to use could help solve these problems and allow more makers to use the technology [36].

B. Potential Solutions and Areas for Further Research

Centered investigate and improvement endeavors are required to urge freed of the things that halt individuals from receiving. One possible option is to discover the finest treatment settings. It may be conceivable to create treatment plans that give reliable and anticipated comes about in case we do in-depth ponders that see at how distinctive components influence distinctive sorts of instrument materials. Producers might fine-tune the method for distinctive employments by utilizing progressed models and computer tools to guess what would happen amid diverse sorts of cold treatment. Putting together cold treatment with progressed cutting strategies is another curiously region that needs more ponder. It may well be conceivable to urge superior execution and economy by combining cold treatment with methods like high-speed cutting, least amount oil (MQL), and cross breed cooling frameworks. One case is that utilizing less cutting liquid and more cryogenic cooling with MQL can cut down on tool wear and progress surface wrap up. Looking into these sorts of combinations might make cryogenic treatment more valuable and permit it to be utilized in more generation circumstances.

C. Exploration of Cryogenic Treatment for Other Materials and Applications

Cryogenic treatment might be utilized on other materials and in other fabricating forms other than the DTM materials it is as of now utilized on. Scientists might see into how cold treatment can offer assistance non-metallic materials like amalgams and plastics, which are being utilized more and more in high-performance uses. Looking into what happens after you solidify these materials may make strides their designing highlights and open up more employments for them. It would moreover be interesting to memorize more almost how cold treatment can be utilized in added substance fabricating (AM). Parts that are made utilizing AM strategies, like 3D printing, frequently have remaining weights and gaps in them. Putting AM parts through a cold process could make them more grounded and way better at what they do, making them superior for critical employments within the restorative, air ship, and car businesses.

6 Conclusion

Using cryogen-treated cutting tools for difficult-to-machine (DTM) materials marks significant progress and new possibilities in advanced manufacturing. Since they are so solid, difficult, and safe to warm, DTM materials like titanium amalgams, nickel-based super alloys, and fortified steels are exceptionally troublesome to work with. These issues often cause rapid tool wear, poor surface quality, and higher cutting costs. Cryogenic treatment could be a progressive strategy that moves forward the execution and life of cutting instruments. This makes it a valuable way to bargain with the particular issues that come with DTM materials. By changing the microstructure of the tool, cryogenic treatment makes its qualities way better. These improvements lead to higher hardness, better toughness, and better heat conductivity. Together, these factors lower tool wear, improve surface quality, and boost production efficiency. When it comes to money, using tools that have been cryogenically treated is worth it because they last longer and require less downtime and tool changes. In terms of the environment, cryogenic treatment cuts down on the use of dangerous cutting fluids and lowers trash and emissions. This is in line with current industrial goals for sustainability. Even though it has benefits, there are still problems with standardizing treatment plans and getting the expensive and complicated tools that is needed. It is recommended that future study focus on finding the best treatment settings, combining cold treatment with advanced cutting methods, and looking into how this can be used with other materials and production processes.

References

1. Korkmaz, M.E.; Gupta, M.K.; Çelik, E.; Ross, N.S.; Günay, M. A sustainable cooling/lubrication method focusing on energy consumption and other machining characteristics in high-speed turning of aluminum alloy. Sustain. Mater. Technol. 2024, 40, e00919.
2. Çakır Şencan, A.; Şirin, Ş.; Selayet Saraç, E.N.; Erdoğan, B.; Koçak, M.R. Evaluation of machining characteristics of SiO2 doped vegetable based nanofluids with Taguchi approach in turning of AISI 304 steel. Tribol. Int. 2024, 191, 109122.
3. Gao, S.; Wang, H.; Huang, H.; Kang, R. Molecular simulation of the plastic deformation and crack formation in single grit grinding of 4H-SiC single crystal. Int. J. Mech. Sci. 2023, 247, 108147.
4. Zhai, S.; Lyu, Y.; Cao, K.; Li, G.; Wang, W.; Chen, C. Seismic behavior of an innovative bolted connection with dual-slot hole for modular steel buildings. Eng. Struct. 2023, 279, 115619.
5. Panchagnula, K.K.; Sharma, J.P.; Kalita, K.; Chakraborty, S. CoCoSo method-based optimization of cryogenic drilling on multi-walled carbon nanotubes reinforced composites. Int. J. Interact. Des. Manuf. 2023, 17, 279–297.
6. Mallick, R.; Kumar, R.; Panda, A.; Sahoo, A.K. Current Status of Hard Turning in Manufacturing: Aspects of Cooling Strategy and Sustainability. Lubricants 2023, 11, 108.
7. Maruda, R.W.; Szczotkarz, N.; Wojciechowski, S.; Gawlik, J.; Królczyk, G.M. Metrological relations between the spray atomization parameters of a cutting fluid and formation of a surface topography and cutting force. Measurement 2023, 219, 113255.
8. Guo, K.; Gou, G.; Lv, H.; Shan, M. Jointing of CFRP/5083 Aluminum Alloy by Induction Brazing: Processing, Connecting Mechanism, and Fatigue Performance. Coatings 2022, 12, 1559.
9. Silva, F.J.G.; Sousa, V.F.C.; Pinto, A.G.; Ferreira, L.P.; Pereira, T. Build-Up an Economical Tool for Machining Operations Cost Estimation. Metals 2022, 12, 1205.
10. Işık, A.T.; Çakıroğlu, R. Investigation of Workpiece and Tool Surface Quality in Electro Discharge Machining of Al 5083 Alloy Produced by Powder Metallurgy. Manuf. Technol. Appl. 2022, 3, 47–58.
11. Yurtkuran, H.; Günay, M. Analyzing the Effects of Cutting Parameters on Machinability Criteria in Milling of 17-4PH Stainless Steel under Dry Environment. Manuf. Technol. Appl. 2022, 3, 8–19.
12. Şen, N.; Şirin, Ş.; Kıvak, T.; Civek, T.; Seçgin, Ö. A new lubrication approach in the SPIF process: Evaluation of the applicability and tribological performance of MQL. Tribol. Int. 2022, 171, 107546.
13. Gupta, M.K.; Etri, H.E.; Korkmaz, M.E.; Ross, N.S.; Krolczyk, G.M.; Gawlik, J.; Yaşar, N.; Pimenov, D.Y. Tribological and surface morphological characteristics of titanium alloys: A review. Arch. Civ. Mech. Eng. 2022, 22, 72.
14. Ghosh, S.; Rao, P.V. Comparison between sustainable cryogenic techniques and nano-MQL cooling mode in turning of nickel-based alloy. J. Clean. Prod. 2019, 231, 1036–1049.
15. Vishal, R.; Nimel Sworna Ross, K.; Manimaran, G.; Gnanavel, B.K. Impact on machining of AISI H13 steel using coated carbide tool under vegetable oil minimum quantity lubrication. Mater. Perform. Charact. 2019, 8, 527–537.
16. Krolczyk, G.M.; Maruda, R.W.; Krolczyk, J.B.; Wojciechowski, S.; Mia, M.; Nieslony, P.; Budzik, G. Ecological trends in machining as a key factor in sustainable production—A review. J. Clean. Prod. 2019, 218, 601–615.
17. Ross, K.N.S.; Manimaran, G. Effect of cryogenic coolant on machinability of difficult-to-machine Ni–Cr alloy using PVD-TiAlN coated WC tool. J. Braz. Soc. Mech. Sci. Eng. 2019, 41, 44.
18. Kumar, S.; Ahmed, M.R.; Lokesha, M.; Manjunath, L.H. Investigation of machinability characteristics on C45 steel with cryogenically treated M2 HSS tool using statistical technique. Int. J. Simul. Multidiscip. Des. Optim. 2019, 10, A5.

19. Zaman, P.B.; Dhar, N.R. Design and evaluation of an embedded double jet nozzle for MQL delivery intending machinability improvement in turning operation. J. Manuf. Process. 2019, 44, 179–196.
20. [20] Gill, S.S.; Singh, J.; Singh, H.; Singh, R. Investigation on wear behaviour of cryogenically treated TiAlN coated tungsten carbide inserts in turning. Int. J. Mach. Tools Manuf. 2011, 51, 25–33.
21. Krolczyk, G.M.; Maruda, R.W.; Nieslony, P.; Wieczorowski, M. Surface morphology analysis of Duplex Stainless Steel (DSS) in Clean Production using the Power Spectral Density. Meas. J. Int. Meas. Confed. 2016, 94, 464–470.
22. Özbek, N.A.; ÇİÇek, A.; GülesİN, M.; Özbek, O. Application of deep cryogenic treatment to uncoated tungsten carbide inserts in the turning of AISI 304 stainless steel. Metall. Mater. Trans. A 2016, 47, 6270–6280.
23. Akincioğlu, S.; Gökkaya, H.; Uygur, İ. A review of cryogenic treatment on cutting tools. Int. J. Adv. Manuf. Technol. 2015, 78, 1609–1627.
24. Dhokey, N.B.; Dandawate, J.V.; Rawat, R. Effect of cryosoaking time on transition in wear mechanism of M2 tool steel. ISRN Tribol. 2013, 2013, 408016.
25. Das, D.; Ray, K.K. On the mechanism of wear resistance enhancement of tool steels by deep cryogenic treatment. Philos. Mag. Lett. 2012, 92, 295–303.
26. Nath, C.; Kapoor, S.G.; DeVor, R.E.; Srivastava, A.K.; Iverson, J. Design and evaluation of an atomization-based cutting fluid spray system in turning of titanium alloy. J. Manuf. Process. 2012, 14, 452–459.
27. Sola, R.; Giovanardi, R.; Parigi, G.; Veronesi, P. A novel method for fracture toughness evaluation of tool steels with post-tempering cryogenic treatment. Metals 2017, 7, 75.
28. Krolczyk, G.M.; Nieslony, P.; Maruda, R.W.; Wojciechowski, S. Dry cutting effect in turning of a duplex stainless steel as a key factor in clean production. J. Clean. Prod. 2017, 142, 3343–3354.
29. Moore, K.; Collins, D.N. Cryogenic treatment of three heat-treated tool steels. Key Eng. Mater. 1993, 86–87, 47–54.
30. Alparslan, C.; Bayraktar, Ş. Tool Wear in Machining of Wrought and Cast Aluminium Alloys: Literature Review. Manuf. Technol. Appl. 2021, 2, 34–46.
31. Liu, N.; Liu, B.; Jiang, H.; Wu, S.; Yang, C.; Chen, Y. Study on vibration and surface roughness in MQCL turning of stainless steel. J. Manuf. Process. 2021, 65, 343–353.
32. Yaşar, N.; Korkmaz, M.E.; Gupta, M.K.; Boy, M.; Günay, M. A novel method for improving drilling performance of CFRP/Ti6AL4V stacked materials. Int. J. Adv. Manuf. Technol. 2021, 117, 653–673.
33. Krolczyk, G.M.; Maruda, R.W.; Wojciechowski, S.; Powalka, B.; Klos, S.; Szczotkarz, N.; Matuszak, M.; Khanna, N. Evaluation of turning with different cooling-lubricating techniques in terms of surface integrity and tribologic properties. Tribol. Int. 2020, 148, 106334.
34. Yilmaz, B.; Uzun, G.; Güllü, A. The Effects of Cutting Parameters on the Thrust Force, Cutting Moment and Cutting Temperature in Drilling Process Applied to Ti6Al4V Material. Manuf. Technol. Appl. 2020, 1, 1–8.
35. Singla, A.K.; Singh, J.; Sharma, V.S. Processing of materials at cryogenic temperature and its implications in manufacturing: A review. Mater. Manuf. Process. 2018, 33, 1603–1640.
36. Reddy, T.V.S.; Sornakumar, T.; Reddy, M.V.; Venkatram, R.; Senthilkumar, A. Turning studies of deep cryogenic treated p-40 tungsten carbide cutting tool inserts–technical communication. Mach. Sci. Technol. 2009, 13, 269–281.

Critical Analysis of Fiber Laser Micro-machined Kerf Quality on Al7075 alloy sheet

Kajal Kumar Mandal[0000-0003-2561-0924]

NERIST, Itanagar, India
Kajal_mandal@email.com

Abstract. The advancement of technology and invention of newer material leads the manufacturing process towards non-conventional i.e. non-traditional way of machining. Laser beam machining is one of them, important manufacturing method. Due to impingement of photons high quantity of thermal energy is generated, helps to remove the material from work through melting even vaporization at very elevated temperature. Al7075 is one of the important aluminium alloy where main alloying element is zinc. This alloy is so strong that it can be comparable to many steels. Inspite of it's average machinability property, it has high specific strength and high fatigue strength in addition toughness and durability properties. Al7075 alloy has wide applications, like, rock climbing equipment, hang gliding airframes, medical instruments, automobiles, aerospace, etc. Mitsubishi A6M0 Fighter is fabricated using this alloy in mass scale. In the present research, diode pumped fiber laser machine is utilized to carry out micro-machining on Al7075 alloy. Here, process parameters are laser beam power, pulse frequency & scanning speed, whereas output parameters are kerf depth, kerf width & heat affected zone. Design of experiment is done by response surface methodology. After performing the laser micro-machining operation, responses are critically analyzed through main effect plots and response surface plots.

Keywords: Diode pumped fiber laser, Laser micro-machining, Al7075 alloy, response surface methodology.

1 Introduction

Nowadays, laser beam machining is getting importance among all non-traditional subtractive manufacturing methods. It has a wide applications, e.g. welding, cladding, surface treatment, etc. Al7075 alloy is as strong as many steels with high specific strength and enough fatigue strength. Mitsubishi A6M0 Fighter was fabricated at first in mass scale using this alloy. Conventional manufacturing may be applicable for macro-machining, however micro-machining is possible by non-conventional machining like laser beam machining. There are lot of research work going on micro-machining using various laser machine for different material. Kuar et al. [1] performed the experiment of micro-drilling on ZrO_2 ceramic using pulsed Nd:YAG laser following RSM. Authors aimed to optimize the responses through controlling lamp current, pulse frequency (PF), air pressure and pulse width. Selected responses were HAZ thickness and hole taper. Mandal et al. [2] did a parametric study for hole taper of copper sheet by Nd:YVO_4 laser. Four input parameters namely, laser beam power (LBP), PF, scanning speed (SS) and number of passes (NP) were considered to study and analyze the influence on taper hole. Sharma and Yadava [3] performed the experiment on thin Al-alloy sheet using Nd:YAG laser & multi-objective optimization based on hybrid perspective of Taguchi methodology (TM) and grey relational analysis (GRA). Authors selected four process parameters; oxygen pressure, pulse width, PF & cutting speed, and two output parameters; kerf taper & surface roughness based on hybrid modelling of TM & response surface methodology (RSM). Biswas et al. [4] laser microdrilled on alumina-aluminum composite using pulsed Nd:YAG laser machine using central composite design (CCD) based on RSM. Authors optimized the process parameters like lamp current, PF and air pressure to observe influence on hole taper. ANOVA test was also done for the result verification. Mandal et al. [5] utilized pulsed Nd:YVO_4 laser to micro-drill on copper sheet for purpose of process optimization using GRA. Authors performed the analysis on hole taper and HAZ width as the effect of LBP, SS, PF and NP. Muthuramalingam et al. [6] studied influence of nozzle distance, focal length, gas pressure and power on hole diameter both at entry and exit. For this purpose, experiment was done on sheet of Titanium (Ti-6Al-4V) alloy by TRUMPF TLC 1005 5-axis flow laser. Wang et al. [7] investigated the cut quality i.e. surface roughness including temperature of fiber laser cut on Inconel 625 super alloy. They also performed the square model and 3D levels using RSM and verified the result with ANOVA. Result was satisfactory. Mandal et al. [8] investigated the effect of LBP, PF and SS on kerf width (KW), HAZ and surface roughness (SR) of Al7075 alloy using Nd:YVO_4 laser. Taguchi method was used for DoE and ANOVA was performed for the verification of results. Kar et al. [9] studied on micro-drilling

on Al 6061 alloy by using fiber laser. They observed influence of SS, LBP, PF and NP on hole circularity and spatter size following L16 array. Pramanik et al. [10] invented a new approach of laser sawing on Titanium alloy (Ti6Al4V). Authors chosen the process parameters as sawing angle, power, duty cycle, PF and SS to investigate the effect on kerf taper and HAZ. ANOVA was done to verify the experimental results. Chenrayan et al. [11] did experiment on nitinol material for studying the SR after laser micro-machining using a femtosecond laser. Authors selected the input parameters as LBP, SS and PF. Saleh [12] investigated on the laser micro-fabrication for miniaturized and intricate feature including micro-machining on various materials varying the machining parameters. Sharma et al. [13] performed both theoretical and experimental approach for the heating effect during laser machining process. For the simulation purpose, they used FEM and for validation, picosecond pulsed laser was used to machine micro-pillars of Al & Si. It was then followed by SEM and EBSD scans for better understanding of surface quality. Nolasco et al. [14] studied effect of laser micro-machining on CVD diamond at various wavelengths. Authors utilized femto-second laser with 216 fs pulses to determine minimum damage fluence value through incubation period. They also used theoretical for electron density formation by a single fs-pulse to calculate main light absorption mechanism.

From these research work, it is observed that lot of work have been done by many researchers in the field of laser cutting and drilling on various materials by different laser machine. Very few research works is available on Al7075 alloy and fiber laser. So there is scope for further research with this material and machine. In this present work, diode pumped fiber laser set-up is utilized for micro-machining of Al7075 alloy which is a combination between material and machine. After completing the experiment, critical analysis has been done of the processing parameters related to the kerf qualities. Here, process parameters are LBP, PF and SS; whereas kerf qualities are KD, KW and HAZ. Design of experiment is done by RSM.

2 Material and Experimental Procedure

2.1 Material

Present research work is performed on 2 mm thin sheet of Al7075 alloy. The main alloying element is zinc with of 5.66% including magnesium of 2.15%, copper of 1.32%, iron of 0.45%, silicon of 0.35%, manganese of 0.08%, chromium 0.15% with few others. It is strong enough as like as many steels. It has the density of 2.81 gm/cc, tensile strength of upto 570 MPa. In the year of 1943 Sumitomo Metal of Japan developed this alloy first time.

2.2 Experimental Procedure

Due to reflectivity property of Al7075 alloy, laser with low power and short wavelength is preferred to avoid the counteraction with the input parameters. Experimental work is done by low-power diode-pumped fiber laser (manufactured by M/S SLT) with peak power of 50 W, focal length of 77 mm, wavelength of 1064 nm, pulse duration 120 ms and spot beam diameter 21 μm. Three process parameters viz. LBP, PF & SS are selected to analyze effect on the responses like KD, KW and HAZ. Range of the parameters are selected through trial experiment. Levels of each parameters are selected based on design of experiment following CCD model of RSM. The values for 5 levels of every input parameters with 20 different combination and corresponding responses are shown in Table 1.

3 Experimental Results

Here, responses i.e. KD, KW and HAZ are measured, corresponding to different machining combinations, by an optical microscope manufactured by Olympus (STM 6). The measured values are the average of three for every conditions. Responses thereby calculated at corresponding process parameters, are listed in a tabular form, as shown in Table 1.

Table 1. Experimental result (average of three observations).

Input Parameters			Output Parameters		
LBP (W)	PF (kHz)	SS (mm/s)	KD (µm)	KW (µm)	HAZ (µm)
70	70	1.5	38.3	64.44	120.06
90	70	1.5	41.82	77.22	127.16
70	90	1.5	33.25	77.28	115.75
90	90	1.5	26.9	82.97	138.75
70	70	3.5	40.05	56.36	95.56
90	70	3.5	47.77	60.37	93.72
70	90	3.5	41.03	57.78	84.41
90	90	3.5	39.8	58.69	102.58
63.18	80	2.5	41.3	56.75	87.89
96.81	80	2.5	43.35	65.82	107.95
80	63.18	2.5	46	61.41	100.22
80	96.81	2.5	34.57	67.61	102.99
80	80	0.81	31.65	83.41	136.77
80	80	4.18	43.4	55.89	83.66
80	80	2.5	43.3	63.4	103.64
80	80	2.5	42.8	61.73	103.39
80	80	2.5	42.47	61.23	102.45
80	80	2.5	41.8	63.13	102.91
80	80	2.5	43.15	63.13	103.06
80	80	2.5	42.32	62.53	103.24

4 Analysis of experimental result

4.1 Analysis of experimental result through main effects plot

Main effects plot signifies individual influence of an input parameter on a certain response. It also compares the significance of all the input parameters on that certain response individually.

Fig. 1 represents the main effects plot of kerf depth i.e. comparative significance of LBP, PF and SS on kerf depth. This figure reveals that with the increase of LBP, kerf depth is increases slowly; increase of PF leads to decrease the kerf depth at very fast, whereas increase of SS leads to increase upto certain value then decrease the kerf depth at very fast. So, it is concluded that PF and SS are more significant and LBP is less significant.

Fig. 2 shows main effects plot for kerf width, i.e. comparative significance of LBP, PF and SS on kerf width. It is observed the kerf width increases with increase of LBP and PF, decreases with increase of SS at fast rate as compared to others. It can be concluded that SS is most significant and other two are less significant.

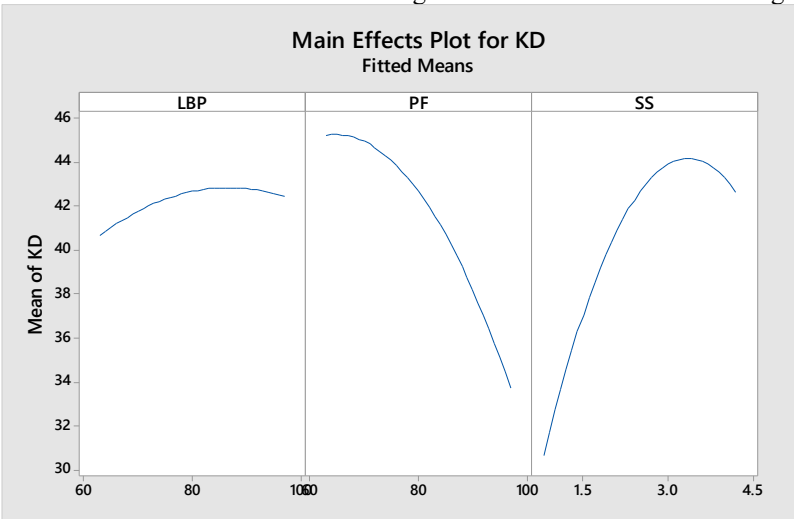

Fig. 1. Main effects plot of kerf depth.

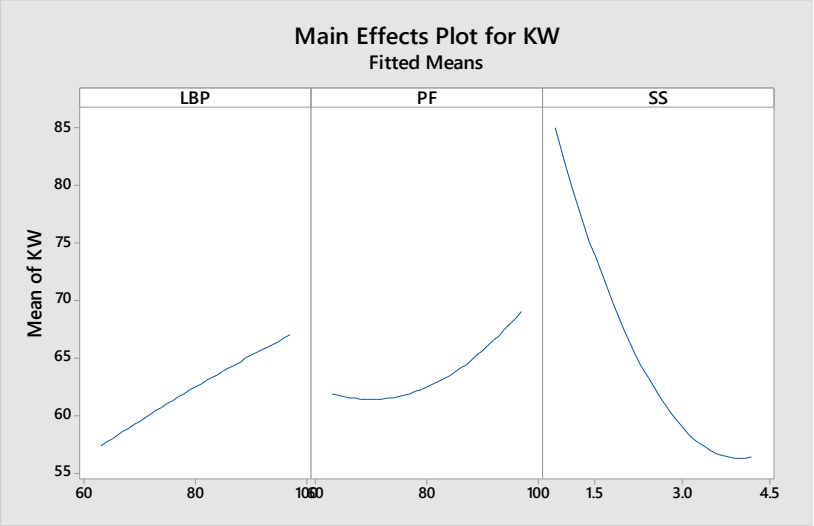

Fig. 2. Main effects plot of kerf width.

Comparative significance of LBP, PF and SS on HAZ are represented by Fig. 3, i.e. main effect plot of HAZ. It is observed that the HAZ increases with the increase of LBP and PF at different proportion, but decreases with the increase of SS very fast as compared to others. So, it can be concluded that SS is most significant, LBP is moderately significant and SS is less significant.

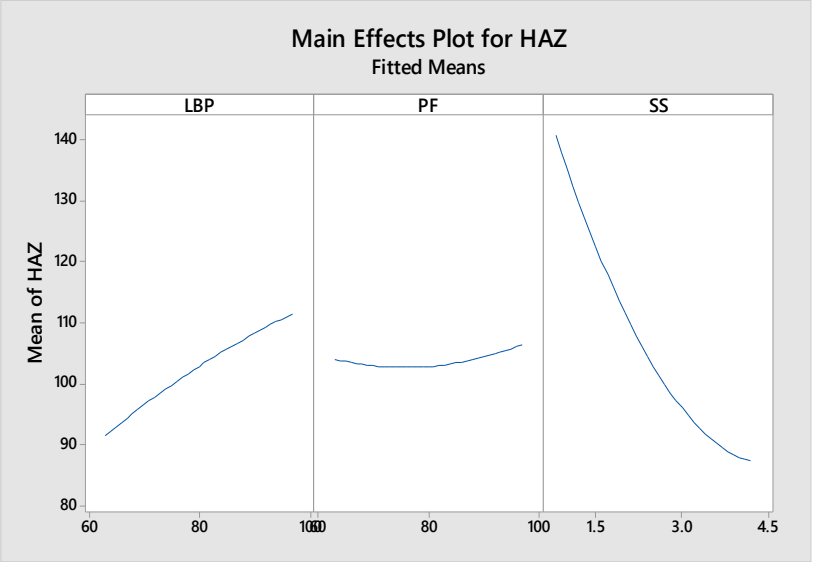

Fig. 3. Main effects plot of heat affected zone.

4.2 Analysis of experimental result through response surface plot

The response surface plot represents combined effects of two input parameters on an output parameter. These plots are drawn following response surface methodology (RSM). It is a statistical approach proposed by George E. P. Box and K. B. Wilson. RSM explores the relationship between two process variables and one response. So, basically it is 3-dimentional pictorial graph representing effects of the two parameters on a response individually.

Fig. 4 reveals the combined effects of LBP and PF at constant SS of 2.5 mm/sec on kerf depth. It is observed that due to increase of LBP, KD is increased gradually as a result of more heat generation; but due to increase of PF, KD increases as the result of less interaction of heat with the work surface. So, there is lees variation of nature due to combined effect of LBP and PF.

Combined effect of PF and SS at constant LBP of 80% of the peak power (Watts) on kerf depth is shown in Fig. 5. It reveals that due to the increase of PF, KD decreases very fast; whereas, due to increase of SS, KD increases fast. So there is certain value of both PF and SS where improved value of KD is available. It is also clear that for lower level of PF and higher level of SS, the value of KD remains in the higher range.

Fig. 6 represents the combined effect of SS and LBP on kerf depth at constant PF of 80 kHz. From this plot it is clear that KD increases due to increase of both SS and LBP as a result of more heat generation and more interaction of heat with the work surface. Combined effect will influence further.

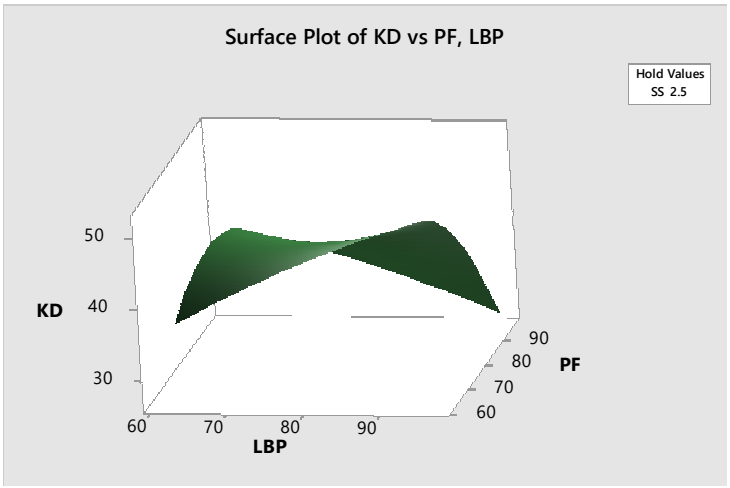

Fig. 4. Combined effects of LBP and PF at constant SS on kerf depth.

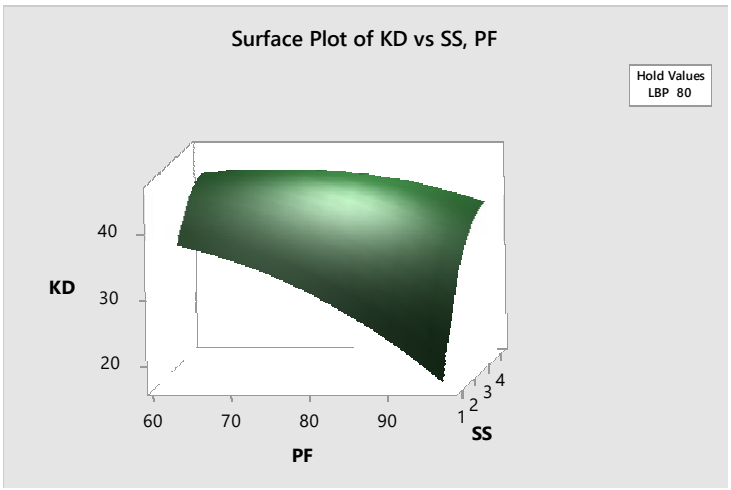

Fig. 5. Combined effect of PF and SS at constant LBP on kerf depth.

Combined effect of LBP and PF on kerf width at constant SS of 2.5 mm/sec is shown in Fig. 7. It is observed from this plot that for the lower value of LBP and PF, KW is minimum but for the higher value of PF and with the increase of LBP, KW is approximately same and become optimum level.

Fig. 8. represents combined effect of SS and PF on KW at constant laser beam power of 80% of peak power (watts). It is clear that increase of both the parameter, KW decreases; which means lower the better for both scanning speed and pulse frequency to get better KW. This is happened due to decrease of interaction of heat with the work.

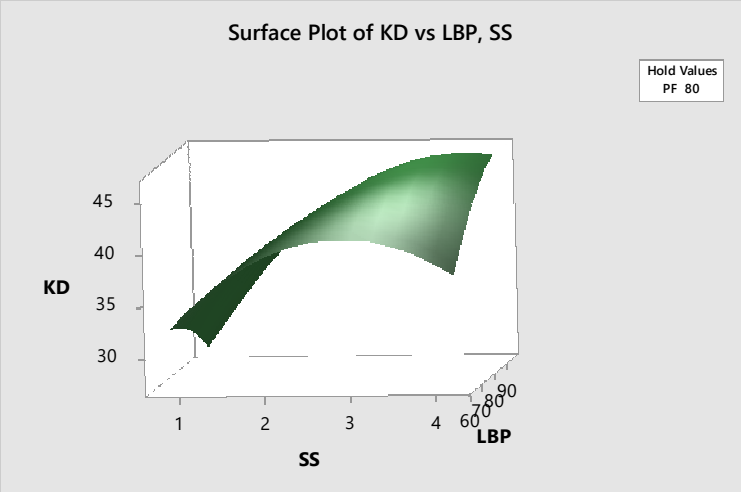

Fig. 6. Combined effect of SS and LBP on kerf depth at constant PF.

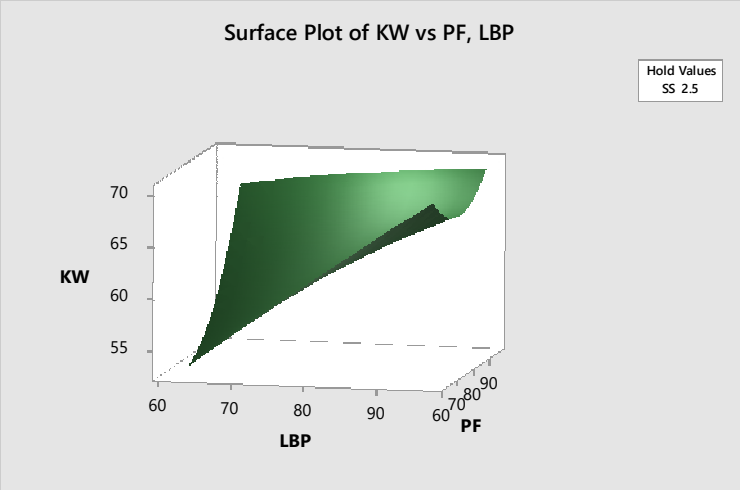

Fig. 7. Combined effect of LBP and PF on kerf width at constant SS.

Fig. 9. Shows combined effect of LBP and SS on KW at constant PF of 80 kHz. The plot reveals that KW increases slowly due to increase of LBP, decreases sharply with the increase of SS.

Combined influence of LBP and PF on heat affected zone at constant scanning speed of 2.5 mm/sec is represented by Fig.10. This plot shows that HAZ increases due to increase of both LBP at slow rate and pulse frequency at comparatively higher rate; and both the process parameters are in the higher range then HAZ increases abruptly.

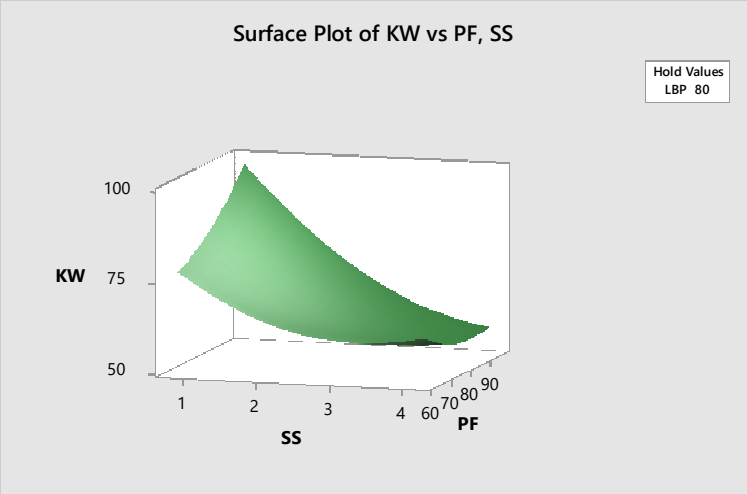

Fig. 8. Combined effect of SS and PF on kerf width at constant LBP.

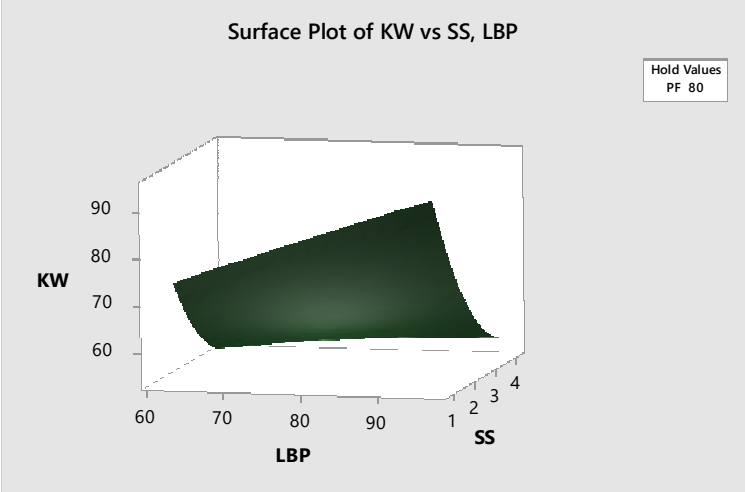

Fig. 9. Combined effect of LBP and SS on kerf width at constant PF.

Combined effect of SS and PF on heat affected zone at constant laser beam power of 80% of peak power (watts) is pictorially represented by Fig.11. In this case HAZ is greatly improved i.e. decreased with the increase of SS but there is very little change due to change of PF though combine effect is shown.

Fig. 12. Represents combined effect of SS and LBP on heat affected zone at constant pulse frequency of 80 kHz. From this plot, it is concluded that HAZ is improved i.e. decreased with the increase of SS at faster rate. But, HAZ increased gradually with the increase if LBP.

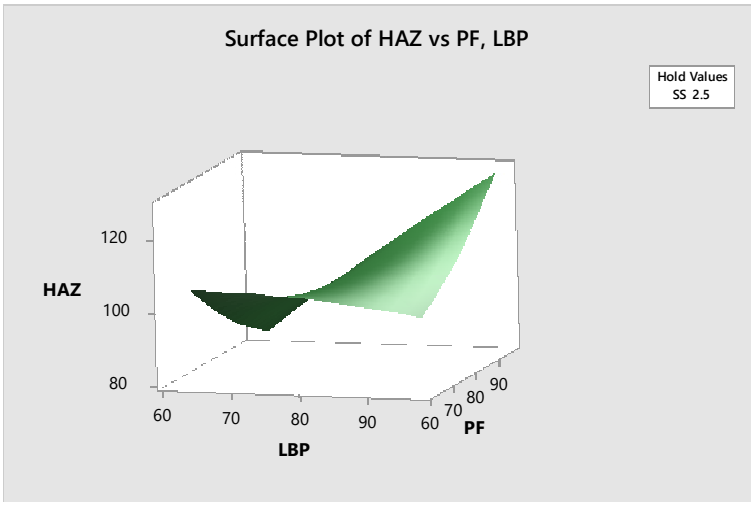

Fig. 10. Combined effect of LBP and PF on heat affected zone at constant SS.

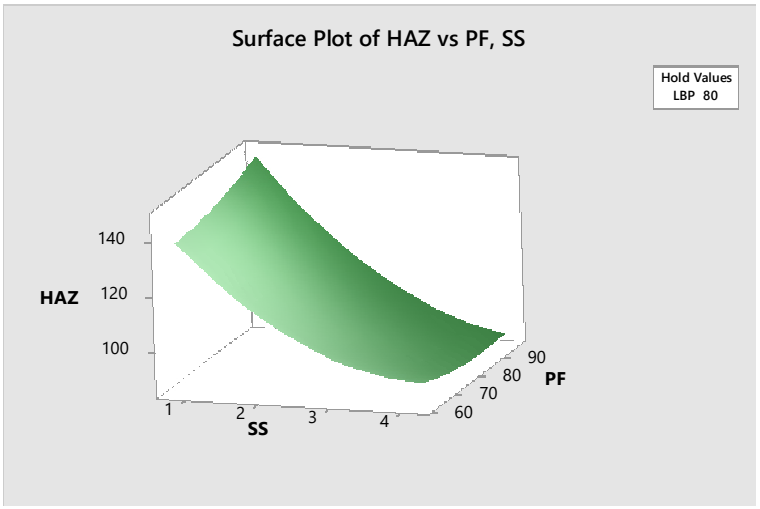

Fig. 11. Combined effect of SS and PF on heat affected zone at constant LBP.

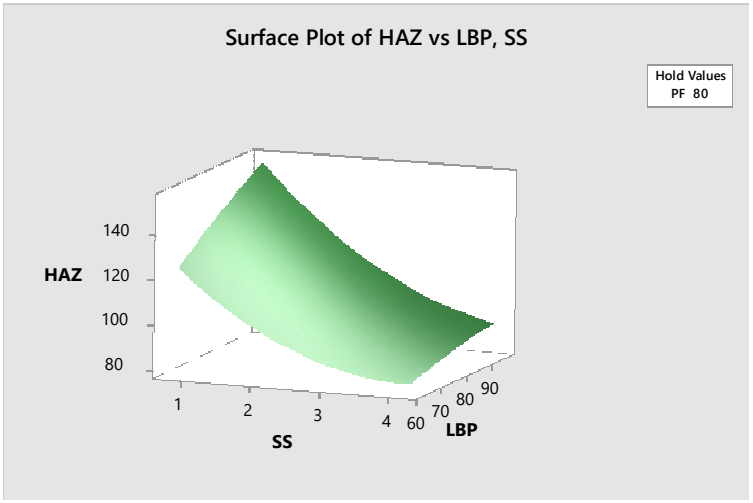

Fig. 12. Combined effect of SS and LBP on heat affected zone at constant PF.

5 Conclusions

Micro-machining of Al7075 alloy has been performed successfully irrespective of reflectivity property by using low power diode pumped fiber laser. RSM is utilized for design of experiment, analysis of experimental result through pictorial plot; both main effects polt and surface response plot. In addition to these, following conclusions may be made based on present work:

(a) Though Aluminium is highly reflective material, Al7075 alloy is well machinable by the low power fiber laser,
(b) Kerf depth; increases slowly with the increase of laser beam power, decreases sharply with the increase of pulse frequency and increases initially – reaches highest value & then decreases with increase of SS,
(c) Kerf width; increases linearly with the increase of LBP, increases gradually with the increase of PF and decreases sharply with the increase of SS,
(d) Heat affected zone; increases gradually but slow with the increase of LBP, increases very slowly with the increase of PF and decreases sharply with increase of SS,
(e) Critical analysis of main effects plot and response surface plot shows that they are all in well agreement to each other.

References

1. Kuar, A. S., Doloi, B., Bhattacharyya, B.: Modelling and analysis of pulsed Nd:YAG laser machining characteristics during micro-drilling of Zirconia (ZrO_2). International Journal of Machine Tools & Manufacture, 46(12-13), 1301–1310 (2006).
2. Mandal, K. K., Chatterjee, B., Kuar, A. S. Mitra. S.: Parametric study of hole taper in laser micro-drilling of copper sheet. International Journal of Emerging Trends in Science and Technology, 03(05), 502-508 (2016).
3. Sharma, A., Yadava, V.: Modelling and optimization of cut quality during pulsed Nd:YAG laser cutting of thin Al-alloy sheet for straight profile. Optics & Laser Technology 44, 159-168 (2012).
4. Biswas, R., Kuar, A. S., Mitra, S.: Process optimization in Nd:YAG laser microdrilling of alumina-aluminum interpenetrating phase composite. Journal of Materials Research and Technology 4(3), 323-332 (2015).
5. Mandal, K. K., Kuar, A. S., Mitra, S.: Taguchi-based grey relational analysis of hole taper and heat affected zone (HAZ) width for laser micro-drilling of copper sheet. In: Ahuja, B. B., Basu, S. K., Rajiv, V. (1st) 6th International and 27th All India Manufacturing Technology, Design and Research 2016, College of Engineering Pune INDIA, vol. 1, pp. 425-429. Excel India Publishers, New Delhi (2016).
6. Muthuramalingam, T., Moiduddin, K., Akash, R., Krishnan, S., Mian, S. H., Ameen, W., Alkhalehah, H.: Influence of process parameters on dimensional accuracy of machined Titanium (Ti-6Al-4V) alloy in laser beam machining process. Optics and Laser Technology 132, 1-8 (2020).
7. Wang, J., Sun, Z., Gu, L. Azimy, H.: Investigating the effect of laser cutting parameters on the cut quality of Inconel 625 using response surface method (RSM). Infrared Physics and Technology 118, 1-8 (2021).
8. Mandal, K. K., Kuar, A. S., Mitra, S.: Experimental investigation on laser micro-machining of Al 7075 alloy. Optics and Laser Technology 107, 260-267 (2018).
9. Kar, T., Deshmukh, S. S., Datta, S., Goswami, A.: An experimental study of low power fiber laser micro drilling of Aluminium 6061 alloy. Material Today: Proceedings 82, 96-102 (2023).
10. Pramanik, D., Roy, N., Kuar A. S., Sarkar, S., Mitra, S.: Experimental investigation of sawing approach of low power fiber laser cutting of Titanium alloy using particle swarm optimization technique. Optics and Laser Technology 147, 1-8 (2022).
11. Chenrayan, V., Vaishav, V., Shahapurkar, K., Dhanabal, P., Kalayarasan, M., Raghunath, S., Mano, M.: The effect of fs-laser micromachining parameters on surface roughness, bio-corrosion and biocompatibility of nitinol. Optics and Laser Technology 170, 110220 (2024).
12. Saleh, T.: Laser beam micromachining its challenges and oppurtunities. Comprehensive Materials Processing (Second Edition) 10, 362-372 (2024).
13. Sharma, A., Zhang, S., Fu, J., Marla, D.: Investigation of thermal effects of laser micromachining for APT and TEM specimen preparation: A modeling and experimental study. Ultramicroscopy 265, 114009 (2024).
14. Nolasco, L. K., Couto, F. A., Andrade, M. B., Mendonca, C. R.: Femtosecond laser micromachining study with multiple wavelength in CVD diamond. Diamond and Related Materials 131, 1-18 (2023).

Parametric analysis and multi-objective optimization in WEDM of Inconel 718 using Pareto Algorithm

Kunal Dey[a], Kingshuk Mandal[b], Dipankar Bose[c]

a Institute of Engineering & Management, University of Engineering and Management, Kolkata

b Jadavpur University, Kolkata

c NITTTR, Kolkata

Abstract. This study explores the effects of key parameters—namely peak current, pulse-on time, pulse-off time, and gap voltage—on the material removal rate (MRR) and surface roughness (SR) during machining of Inconel 718 in Wire-cut Electrical Discharge Machining process. Depending on the results from the experiments, a mathematical relationship has been established between MRR & SR. Analysis of Variance (ANOVA) confirmed the statistical significance of pulse-on-time and peak current, as these parameters have the most substantial impact on both MRR and SR. Multi-objective optimization was carried out to balance conflicting objectives: maximizing MRR and minimizing SR. The Pareto optimization algorithm identified a set of non-inferior solutions, suggesting 15 optimal parametric combinations. The Pareto optimization plot and the relationship serve as valuable guidelines for machining Inconel 718, assisting operators in selecting parameter settings that balance productivity with surface quality.

Keywords: WEDM, Inconel 718, ANOVA, Pareto Optimization

1 Introduction

Wire Electrical Discharge Machining (WEDM) is a specialized non-conventional machining technique known for its ability to achieve precise and intricate cuts on electrically conductive materials. This process has become increasingly popular in various sectors due to its capability to produce highly accurate parts and excellent surface finishes, particularly when working with tough and high-strength materials such as superalloys, tool steels, and titanium. Since its introduction, WEDM has been extensively employed in different industries like aerospace, automotive, medical devices, and tool and die manufacturing [1]. The ability to produce components with tight tolerances and intricate profiles makes it invaluable for the production of critical parts like turbine blades, injection molds, and medical implants. WEDM continues to evolve with advancements in technology, including improvements in wire materials, power supplies, and control systems. These advancements have expanded the range of materials and applications suitable for WEDM, reinforcing its role as a key technology in modern manufacturing. In this research, Inconel 718 has been considered as workpiece material because of its successful engineering application and also due to its poor machinability by conventional methods. Chen et al. [2] predicted cutting speed, roughness average, and maximum roughness in WEDM of pure tungsten using BPNN, with SAA applied for optimal settings. Yang et al. [3] analyzed MRR, surface roughness, and deviation at corner in WEDM of pure tungsten using a hybrid RSM and BPNN method with Simulated Annealing Algorithm (SAA). Ramakrishnan et al. [4] investigated the impact of pulse-on time, time delay, wire feed speed, and ignition current on MRR and surface roughness of Inconel 718, optimized using ANN models. Newtown et al. [5] studied the influence of WEDM parameters on the formation of the recast layer in Inconel 718, demonstrating that the energy per spark notably enhances the thickness of the recast layer. Muthukumar et al. [6] Utilized Accelerated Particle Swarm Optimization (APSO) to optimize process parameters for maximizing Material Removal Rate (MRR), improving surface finish, and minimizing kerf width during the WEDM machining of AISI D3 die steel. Kumar et al. [7] modeled removal rate, surface roughness, dimensional deviation, and wire wear ratio in WEDM of pure titanium through Box–Behnken design approach. Trauth et al. [8] examined the surface integrity and fatigue strength of Inconel 718 machined by WEDM, with machine hammer peening applies to improve its fatigue performance. Huang et al. [9] analyzed the effect of machining factors on surface roughness and MRR in WEDM of high-hardness steel employing the Taguchi approach. Kosaraju et al. [10] optimized machining parameters for Inconel 600 using Taguchi analysis. Midthur et al. [11] investigated machining of Inconel 800 (Incoloy) using RSM to optimize parameters for MRR and SR. Akar et al. [12] optimized machining parameters (MRR, SR, Kerf Width, White layer thickness) for Ni55.8Ti superalloy applying Artificial Neural Networks and Particle Swarm Optimization.

Literature reveals that most research in Wire Electrical Discharge Machining (WEDM) emphasizes the influence of process parameters on performance characteristics. Given the numerous control factors in WEDM

that impact outcomes, operators must consider an optimal setting of parameters for maximizing the MRR while minimizing the surface roughness. This study addresses both characteristics—maximizing MRR and minimizing surface roughness— RSM to establish a quantitative relationship between input and output parameters from the experimental results. Additionally, the Pareto optimization algorithm is employed to identify optimal responses, balancing the trade-offs between performance measures effectively. Pareto optimization algorithm also employed to establish a relation between those two responses This approach enables a comprehensive evaluation of process parameters, ensuring an optimized and practical solution for achieving desired machining quality in WEDM. By incorporating Pareto optimization, the study provides a robust framework for operators to achieve high efficiency and precision in WEDM processes.

2 Experimental procedure

The present research uses Inconel-718 as the workpiece material, sized 210 mm × 75 mm × 4 mm. Inconel-718 is selected for its mechanical properties, i.e. high strength, hardness, and wear resistance across a wide temperature range, making it ideal for tool and die applications. Brass wire (0.25 mm in diameter) is selected as the cutting tool, and deionized water serves as the dielectric medium. A total of 31 experiments were conducted on an EZEECUT PLUS CNC wire-cut EDM machine. Other input parameters such as wire feed rate (60 m/min), group pulse (0), and sensitivity (5) remained constant throughout the experiments. The chemical composition and physical characteristics are shown in Table 1 & 2. The properties of the Dielectric medium is tabulated in Table 3.

Table 1. Composition of Inconel 718 [14]

Inconel	Elements (% by mass)														
	Ni	Cr	Fe	Mo	Nb	Co	Mn	Cu	Al	Ti	Si	C	S	P	B
718	50-55	17-21	balance	2.8-3.3	4.75-5.5	1	0.35	0.2-0.8	0.65-1.15	0.3	0.35	0.08	0.015	0.015	0.006

Table 2. Characteristics of Inconel 718 [14]

Density (g/cm^3)	Melting point	Thermal Conductivity (W/m-K)	Co-Efficient of thermal expansion (µm/m.ºC)	Hardness
8.2	1260-1340 ºC	11.4	13	≤ 363 HB

Table 3. Electrical, thermal and mechanical properties of dielectrics

Properties Medium	Dielectric Strength	Dynamic Viscosity	Thermal Conductivity	Specific heat capacity
De-ionized water	13 MV/m	0.92 g/m-s	0.610 W/m-K	4.21 J/g-K
Kerosene	14-22 MV/m	1.64 g/m-s	0.150 W/m-K	2.20 J/g-K
Air	3 MV/m	0.019 g/m-s	0.026 W/m-K	1.00 J/g-K

2.1 Process parameter identification & Experimental data collection:

In the present investigation the controllable parameters chosen are: Peak current (1-5 A), Pulse-on-time (30-70 µsec), Pulse-off-time (2-10 µsec), Gap voltage (30-70 V). The controllable parameters actual and decided ranges along with the different levels are shows Table 4 presents the controllable parameters, their different ranges, and corresponding levels. The experiment is conducted on Inconel-718 material with brass wire as per design of experiments (DOE) with a random order. Central Composite Design (CCD) has been considered for the DOE in this investigation. Table 5 presents the values of MRR and R_a obtained from the experiments for the tested materials and wire respectively. In every experiment the output/response are measured.

Table 4. Controllable parameters and their limits

Controllable parameters	Units	Actual range	Decided range	Levels/ Limits				
				-2	-1	0	1	2
Peak current	A	1-5	1-5	1	2	3	4	5
Pulse-on-time	µ sec	1-100	30-70	30	40	50	60	70
Pulse-off-time	µ sec	1-15	2-10	2	4	6	8	10
Gap voltage	Volts	1-100	30-70	30	40	50	60	70

Table 5. Experimental values for WEDM of Inconel-718

Run	I_P	T_{on}	T_{off}	V_g	MRR	R_a	Run	I_P	T_{on}	T_{off}	V_g	MRR	R_a
1	2	40	8	40	1.92	2.33	17	3	50	6	50	2.2	2.93
2	2	60	4	40	2.76	3.15	18	3	50	10	50	1.37	2.72
3	4	60	4	60	2.9	3.17	19	3	50	6	70	1.86	3.54
4	2	60	8	60	1.36	3.86	20	2	40	8	60	1.56	2.99
5	4	60	4	40	2.93	2.85	21	2	60	4	60	2.52	2.47
6	4	60	8	60	1.72	4.29	22	3	50	6	50	2.2	2.93
7	2	40	4	40	2.68	3.06	23	2	60	8	40	1.78	3.18
8	4	60	8	40	1.87	4.57	24	5	50	6	50	2.45	3.53
9	3	50	6	50	2.2	2.93	25	4	40	4	40	2.71	4.52
10	3	30	6	50	2.49	2.86	26	3	50	6	30	2.21	2.62
11	1	50	6	50	1.62	2.19	27	4	40	4	60	2.54	3.54
12	3	70	6	50	2.25	3.05	28	3	50	2	50	3.43	2.77
13	4	40	8	40	2.13	3.91	29	3	50	6	50	2.2	2.93
14	4	40	8	60	1.86	3.66	30	3	50	6	50	2.2	2.93
15	2	40	4	60	2.32	3.46	31	3	50	6	50	2.2	2.93
16	3	50	6	50	2.2	2.93							

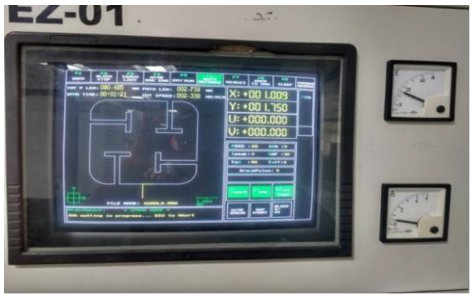

Figure 1. Programmed Path

Figure 2. Machined Profiles

3 Results & analysis

This study focuses on developing a mathematical model to predict Material Removal Rate (MRR) and Surface Roughness (Ra) in WEDM using the Pareto optimization algorithm. Through analysis of the model, the optimal combination of process parameters that yield the best responses is identified. These models play a crucial role in forecasting machining performance and also usuful in optimizing the process. The analysis and model development were conducted using Minitab-16 software, ensuring the best fit for the data. Model adequacy was evaluated through ANOVA, which is also performed in Minitab-16 to confirm its reliability and accuracy.

Table 6. ANOVA for MRR

Source	DF	Adj SS	Adj MS	F	P
Regression	14	6.66464	0.476045	486.95	0.0
Linear	4	0.03765	0.009413	9.63	0.0
Ip	1	0.00066	0.000663	0.68	0.022
Ton	1	0.01429	0.014295	14.62	0.001
Toff	1	0.01015	0.010149	10.38	0.005
Gap vol	1	0.00469	0.004687	4.79	0.044
Square	4	0.29828	0.07457	76.28	0.0
$(Ip)^2$	1	0.04841	0.048412	49.52	0.0
$(Ton)^2$	1	0.06144	0.061444	62.85	0.0
$(Toff)^2$	1	0.1033	0.103302	105.67	0.0
$(Gap\ vol)^2$	1	0.05447	0.054474	55.72	0.0
Interaction	6	0.21814	0.036356	37.19	0.0
Ip*Ton	1	0.00181	0.001806	1.85	0.093
Ip*Toff	1	0.00141	0.001406	1.44	0.048
Ip*Gap vol	1	0.03901	0.039006	39.9	0.0
Ton*Toff	1	0.15801	0.158006	161.63	0.0
Ton*Gap vol	1	0.00526	0.005256	5.38	0.034
Toff*Gap vol	1	0.01266	0.012656	12.95	0.002
Residual Error	16	0.01564	0.000978		
Lack-of-Fit	10	0.01564	0.001564		
Pure Error	6	0.0	0.0		

$R^2 = 99.77\%$ predicted $R^2 = 98.65\%$ adjusted $R^2 = 99.56\%$

The major impacts of all the process parameters; their quadratic effects; and the interaction effects between these variables are the main factors influencing the MRR, according to the ANOVA results in Table 6. Table 6 details the model's adequacy, demonstrating statistical relevance of 95% confidence level ($p < 0.05$) using metrics such adjusted R^2 and predicted R^2.

Table 7. ANOVA for surface roughness

Source	DF	Adj SS	Adj MS	F	P
Regression	14	6.74667	0.48191	238.90	0.000
Linear	4	2.16299	0.54075	268.07	0.000
Ip	1	0.10213	0.10213	50.63	0.000
Ton	1	0.51151	0.51151	253.57	0.000
Toff	1	1.57783	1.57783	782.19	0.000
Gap vol	1	0.17891	0.17891	88.69	0.000
Square	4	0.59959	0.14990	74.31	0.000
$(Ip)^2$	1	0.12472	0.12472	61.83	0.000
$(Ton)^2$	1	0.26377	0.26377	130.76	0.000
$(Toff)^2$	1	0.01939	0.01939	9.61	0.007
$(Gap\ vol)^2$	1	0.32918	0.32918	163.19	0.000
Interaction	6	2.97580	0.49597	245.87	0.000
Ip*Ton	1	0.16000	0.16000	79.32	0.000
Ip*Toff	1	0.17223	0.17223	85.38	0.000
Ip*Gap vol	1	0.21622	0.21622	107.19	0.000
Ton*Toff	1	2.20523	2.20523	1093.22	0.000
Ton*Gap vol	1	0.00122	0.00122	0.61	0.447
Toff*Gap vol	1	0.22090	0.22090	109.51	0.000
Residual Error	16	0.03227	0.00202		
Lack-of-Fit	10	0.03227	0.00323		
Pure Error	6	0.00000	0.00000		

$R^2 = 99.52\%$ predicted $R^2 = 97.26\%$ adjusted $R^2 = 99.11\%$

According to the ANOVA results in Table 7, the primary effects of Peak Current, Pulse-on-Time, Pulse-off-Time, and Gap Voltage, as well as their quadratic and interaction effects, have a significant impact on surface roughness. The model shows strong adequacy having a 95% confidence level for statistical relevance ($p < 0.05$).

3.1 Response Optimization

Pareto optimization of responses:

Pareto optimization, also known as multi-objective optimization, is a powerful method for optimizing multiple conflicting objectives simultaneously. Pareto optimization is a method used in multi-objective optimization where multiple conflicting goals (e.g., minimum surface roughness with maximum MRR in wire-cut EDM) need to be balanced. In machining optimization, this approach facilitates the adjustment of machining process parameters, such as Peak Current, Pulse-on Time, Pulse-off Time, and Gap Voltage, to optimize performance metrics like surface finish, MRR, tool wear etc. Pareto optimal solution [13] is a set of non-inferior solutions that represent the best possible outcome for multiple objectives simultaneously. In this Pareto analysis, a relationship between MRR and surface roughness is established, showing that MRR is directly proportional to surface roughness. Pareto algorithm evaluates 15 combinations based on the conflicting objectives: MRR and surface roughness. Out of 625 possible parameter combinations, 15 optimized combinations are presented in Table 10 and these 15 combinations cover the entire range of trade-offs, providing a useful subset for practical reference. The Pareto chart and corresponding plot serve as valuable guidelines for machining Inconel 718, assisting operators in selecting parameter settings that balance productivity with surface quality. This analysis enables better decision-making in WEDM processes by highlighting the trade-off between MRR and surface roughness for optimized machining outcomes.

Table 8. Optimal parametric settings for Inconel 718

Sl. No.	I_p	T_{on}	T_{off}	V_g	MRR	R_a
1	1	30	4	60	0.25	0.877
2	1	30	4	60	0.57	0.980
3	1	30	4	60	0.97	1.020
4	1	40	4	60	1.21	1.064
5	1	40	4	60	1.51	1.087
6	3	40	4	50	1.89	1.235
7	3	50	4	50	2.01	1.282
8	3	50	4	50	2.27	1.370
9	3	50	6	50	2.68	1.639
10	3	60	6	50	2.97	1.923
11	5	60	6	40	3.22	2.222
12	5	60	6	40	3.61	2.857
13	5	70	6	40	3.93	3.448
14	5	70	6	40	4.05	3.846
15	5	70	6	40	4.31	4.762

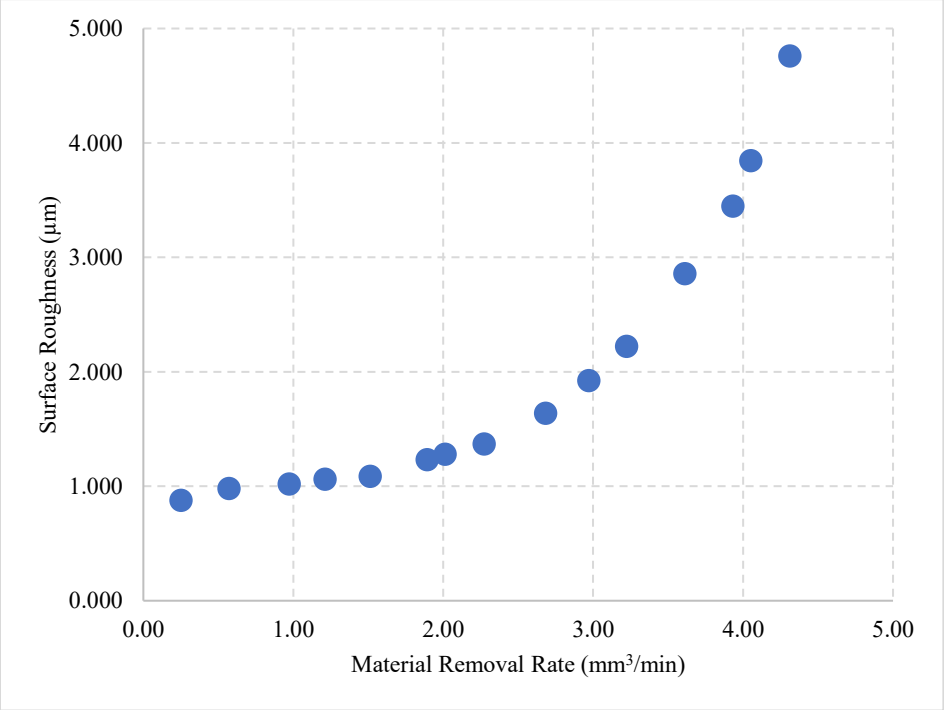

Figure 3. Pareto optimal plot for MRR vs. Surface Roughness

In this Pareto analysis, considering a 3rd order polynomial the nonlinear relationship between MRR and surface roughness for machining of Inconel 718 is expressible as -

$$R_a = 0.1084\ (MRR)^3 - 0.4029(MRR)^2 + 0.6354(MRR) + 0.7189$$

4 Conclusions

The investigation centres around the study of the impact of process parameters on the performance measures and to minimize the surface roughness. This work advances the creation of a Pareto-based model that predicts the intended machining quality in terms of outputs.

The following conclusion has been drawn on the basis of the present investigation:

1. The parametric analysis indicates that MRR is mostly influenced by pulse-on time and peak current. Surface roughness is mostly influenced by peak current, pulse-on time.
2. A relationship has been established through Pareto optimization algorithm between MRR and surface roughness.
3. Among 625 combinations, the pareto chart suggest only 15 combinations for getting the optimum responses while machining of Inconel 718
4. ANOVA results shows that R^2 value is very close to 1 for both MRR and surface roughness justifying the model adequacy.
5. Surface roughness can be enhanced by reducing the duration of pulse as well as the discharge current.
6. The pareto optimal plot and the relationship may be adopted as a technical guideline during machining of Inconel 718.

References

[1] Chen, Z., Huang, Y., Huang, H., Zhang, Z., Zhang, G., "Three-dimensional characteristics analysis of the wire-tool vibration considering spatial temperature field and electromagnetic field in WEDM", *International Journal of Machine Tools & Manufacture*, 92 (2015) 85–96.

[2] Chen, H. C., Lin, J. C., Yang, Y. K. and Tsai, C. H., "optimization of WEDM for pure tungsten using a neural network integrated simulated annealing approach", *Expert Systems with Applications*, Vol. 37, No. 1, pp. 7147-7153, 2010.

[3] Yang, R. T., Tzeng, C. J., Yang, Y. K. and Hsieh, M. H., "Optimization for wire electrical discharge machining process parameters for cutting tungsten", *International Journal of Advance Manufacturing Technology*, Vol. 60, No. 1, pp. 135-147, 2012.

[4] Ramakrishnan, R. and Karunamoorthy, L., "Modelling and multi-response optimization of Inconel 718 of CNC WEDM process", *Journal of Materials Processing Technology*, Vol. 207, No. 1-3, pp. 343-349, 2008.

[5] Newtown, T. R., Melkote, S. N., Watkins, T. R., Trejo R. M., and Reister, L., "Investigation of the effect of process parameters on the formation and the characteristics of recast layer in wire-EDM of Inconel 718", *Materials Science and engineering*, Vol. 513, pp.208-215, 2009.

[6] Muthukumar, V., Venkatasamy, R., Babu, A. S. and Kumar, N. S., "An Accelerated Particle Swarm Optimization Algorithm on Parametric Optimization of WEDM of Die-Steel", *Journal of The Institution of Engineers India Series C*, Vol. 96, No. 1, pp. 49–56, 2015.

[7] Kumar, A., Kumar, V. and Kumar, J., "Multi-response optimization of process parameters based on response surface methodology for pure titanium using WEDM process", *International Journal of Advance Manufacturing Technology*, Vol. 68, No. 9, pp. 2645–2668, 2013.

[8] Trauth, D., Klocke, F., Welling, D., Terhorst, M., Mattfeld, P. and Klink, A., "Investigation of the surface integrity and fatigue strength of Inconel718 after wire EDM and machine hammer peening", *International Journal of Material Forming*, Vol. 5, pp. 253-264, 2015.

[9] Huang, Y., Ming, W., Guo, J., Zhang Z., Liu, G., Li, M. and Zhang, G., "Optimization of cutting conditions of YG15 on rough and finish cutting in WEDM based on statistical analyses", *International Journal of Advance Manufacturing Technology*, Vol. 69, No. 5, pp. 993-1008, 2013.

[10] Kosaraju, S., Babu Bobba, P., Salkuti, S.R., "Optimization and microstructural studies on the machining of Inconel 600 in WEDM using untreated and cryogenically treated zinc electrodes", *Materials* 16 (8) (2023) 3181.

[11] Khan, M.A.S., Senthilkumar, c., "Investigation of wire-cut EDM process parameters on Nimonic 90 made by wire arc additive manufacturing process", *International Journal on Interactive Design and Manufacturing (IJIDeM)* (2023) 17:859–867.

[12] Akar, S., Seyedzavvar, M., Boga, C., "A study on the μwire-EDM of $Ni_{55.8}Ti$ shape memory superalloy: an experimental investigation and a hybrid ANN/PSO approach for optimization", *Journal of the Brazilian Society of Mechanical Sciences and Engineering* (2023) 45:171.

[13] Sarkar S., Mitra S., Bhattacharyya B., "Parametric analysis and optimization of wire electrical discharge machining of γ-titanium aluminide alloy", *Jo,urnal of Materials Processing Technology,* 159 (2005) 286–294

[14] Inconel 718, Special Metal Services Ltd., http://www.specialmetals.com.

Advancements in Ultrasound-Assisted Underwater Laser Micromachining: A Review

Suhas Mandal[1][0009-0008-5603-9293] · Arunanshu Shekhar Kuar[2][0000-0002-1740-3442] · Bappa Acherjee[3][0000-0003-0286-6038]

[1] School of Laser Science and Engineering, Jadavpur University, India
[2] Production Engineering Department, Jadavpur University, India
[3] Production and Industrial Engineering department, Birla Institute of Technology, Mesra, India

Abstract. In many industrial applications, ultrasound assisted underwater laser micromachining (UWLM) has proved itself as a feasible technology for accurate material processing. This paper provides a general analysis of recent developments, obstacles and potential future directions in the field of UWLM. It starts with the basics of UWLM and emphasizes how ultrasound and laser-material interaction work in concept to improve the surface quality and material removal efficiency. Also, the several approaches and configurations used for UWLM. In addition, the difficulties and constraints related to UWLM are discussed, including problems like damage caused by cavitation.

The conclusion provides insights into developing trends and future possibilities for research in UWLM. To sum up, this review compiles state-of-the-art information on UWLM and offers scholars and industry professionals insightful information to direct future developments and uses of this micromachining method.

Keywords: Underwater Laser Micromachining, Laser Micromachining, Ultrasound Assisted Underwater Laser Micromachining

1 Introduction

Over the past years, laser micromachining (LM) has become an interesting technology for both industries as well as for researchers. LM is a type of machining in which a high-intensity laser beam is used to cut materials. This method has many advantages over conventional machining processes, like it produces very precise and accurate grooves as the laser beam is incident on a tiny spot from where the ablation is required. LM is a non-contact method. Also, it provides a large range of flexibility with its parameters such as wavelength, frequency, pulse duration, etc.

Small features in the range of microns are made with the use of LM in industries where it is required, like electronics, automobile, aerospace, medical and many others. LM is performed in many mediums like air, vacuum, water etc. In this paper, we will be discussing about underwater laser micromachining (ULM). In this process, the material is dipped in water such that the water layer thickness is as per the requirement [1]. After that, the surface of the material is hit through the water medium with a laser beam, which results in material removal [2]. The main objective for applying ULM is to reduce the recast layers and heat-affected zone more efficiently, which is evident because the laser is a heat source [3].

Throughout the years, researchers have been improving the process of ULM to reduce heat-related problems. Processes like underwater laser micromachining in still water, in flowing water and hybrid laser waterjet technology, were introduced. Initially, the machining was performed in still water in a confined container, where the water volume was kept constant with no movement [4]. Later, the water was flown with a fixed flow rate, which enabled the bubbles created by the laser beam to flush away from the site of machining to some extent, which was used to deviate and create irregular machining [7].

Hybrid laser waterjet technology represents an ultrafast laser machining technique that involves material removal in its soft solid state, combining both laser ablation and vaporization [16]. In this method, the laser is applied to the material surface to soften it, followed by the gradual removal of the softened material using a water jet. The water jet is directed off-axially with an angle, facilitating effective material removal [17]. Applying high laser power, low water velocity, and frequency resulted in a deeper and wider cavity [18]. Moreover, this process demonstrated time and cost savings in post-processing, as the high-water jet velocity effectively broke down recast layers.

Although the problems related to thermal and surface morphologies were reduced to some extent, but it has not been eliminated. So, ultrasound-assisted underwater laser micromachining was developed, which is discussed below.

2 Methodologies and Setup Configurations

This process was introduced by Benxin Wu and a patent was also filed in 2014 [9]. UWLM comprises different setups and methodologies assigned to specific characteristics of material and requirements for machining. The selection of a proper setup is very important in determining surface quality, precision and efficiency.

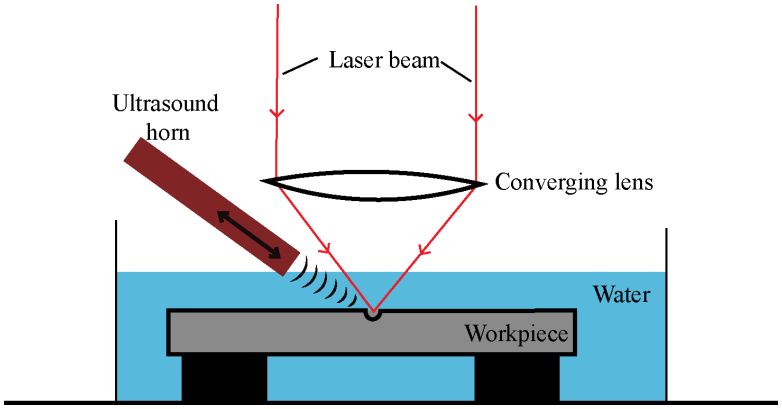

Fig. 1. Ultrasound-assisted underwater Laser micromachining directly on the site

This process involves underwater machining with the added application of ultrasound waves [12]. In this technique, the workpiece is submerged in water, and a laser beam is directed onto its surface, while an ultrasonic horn is aimed directly at the laser-workpiece interaction point (see Fig. 1) or from beneath, which travels through the water to the workpiece (see Fig. 2). An ultrasonic transducer was setup on the bottom side of chamber, where the anti-vibration rubber was placed in between the transducer and workpiece support to allow only water vibration during the process [10].

The transducer design crucially affects the intensity and distribution of ultrasound waves. The most commonly used transducer is a piezoelectric transducer, which produces ultrasound with precise amplitude and frequency [19]. To get an enhanced cavitation intensity and uniform ultrasound field distribution, the optimization of acoustic horn, transducer arrays and focusing mechanisms is needed. The parameters like power and frequency affect the ultrasound wave production and propagation, and also the geometry and material [19].

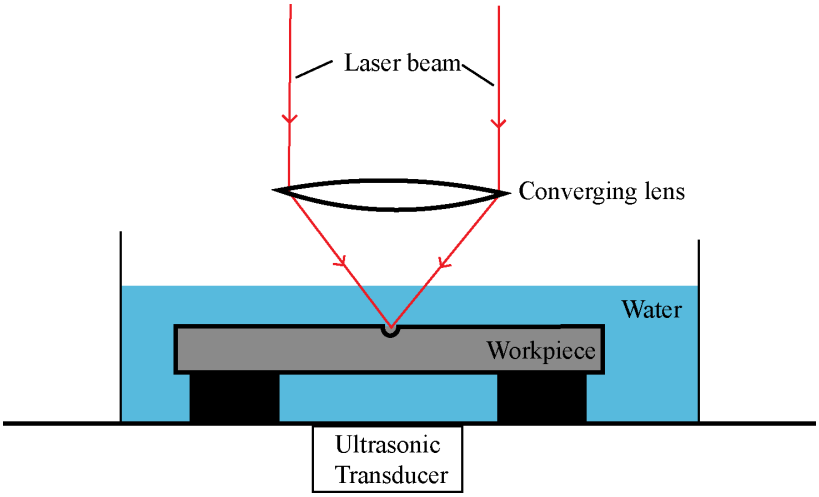

Fig. 2. Ultrasound-assisted underwater laser micromachining by indirect use of the transducer

Ultrasound played a crucial role in washing away cut debris and melted materials from the machined surface, providing rapid cooling and resulting in improved machining [11]. This approach was expected to yield less debris and a higher material removal rate (MRR) when compared to laser machining in either air or without ultrasound in water [9]. Recently, Wisan Charee *et al* introduced a method called lateral ultrasound-assisted underwater laser micromachining. Here, they located the ultrasonic transducer parallel (see Fig. 3) to the surface of the material [26].

Micro-fractures on the surface were attributed to cavitation caused by bubbles [13]. The addition of ultrasound proved particularly effective for cutting thermally sensitive materials that are challenging to ablate [10].

Lasers like Nd:YAG, CO_2 or fiber laser with high-power pulses are commonly used in UWLM [10-12]. The laser beam is generally irradiated on the surface of the workpiece with focusing mirrors and lenses to obtain the desired energy density beam spot size. The combination of laser delivery systems with real-time time monitoring and feedback mechanisms helps in optimizing performance and makes the process consistent [11].

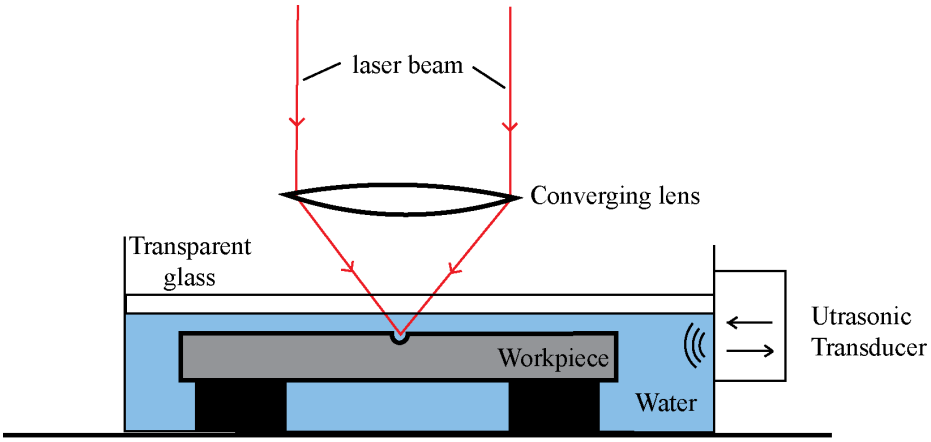

Fig. 3. Ultrasound-assisted underwater laser micromachining by lateral use of the transducer

In UWLM, a proper machining environment is necessary to ensure thermal management, flushing of debris, and process stability. Here, water-based fluids like deionized water are generally used because of their cooling effect and acoustic coupling properties [20]. Also, if additives or surfactants are used, then the efficiency can be increased by modifying cavitation intensity [15].

3 Fundamentals of Ultrasound-Assisted Underwater Laser Micromachining

UWLM combines the principles of ultrasound, laser ablation, and cavitation dynamics to achieve precise material removal in a submerged environment. Understanding the fundamental mechanisms underlying UWLM is important for optimizing process parameters and enhancing machining efficiency.

3.1 Ultrasound Generation and Cavitation

At the centre of UWLM the generation of ultrasonic waves is located, generally in the range of kHz to a few MHz. Ultrasound is generated through piezoelectric transducers, where mechanical vibrations are converted from electrical energy, which travels through water as compressions and rarefactions.

When the laser beam hits the surface of the material, a plasma is created, which eventually transforms into a plasma-induced bubble and gets bigger with time [20]. Also, the laser beam travelling through water leaves small bubbles along its path (see Fig. 4). These create obstruction in the path of the upcoming laser beams by scattering them. Then, the ultrasound waves are applied simultaneously to the plasma-induced bubble, which results in the bursting of the bubble. This creates a shockwave which drives the small bubbles away from the path of the laser beam [20]. This facilitates UWLM to perform precisely with less power loss.

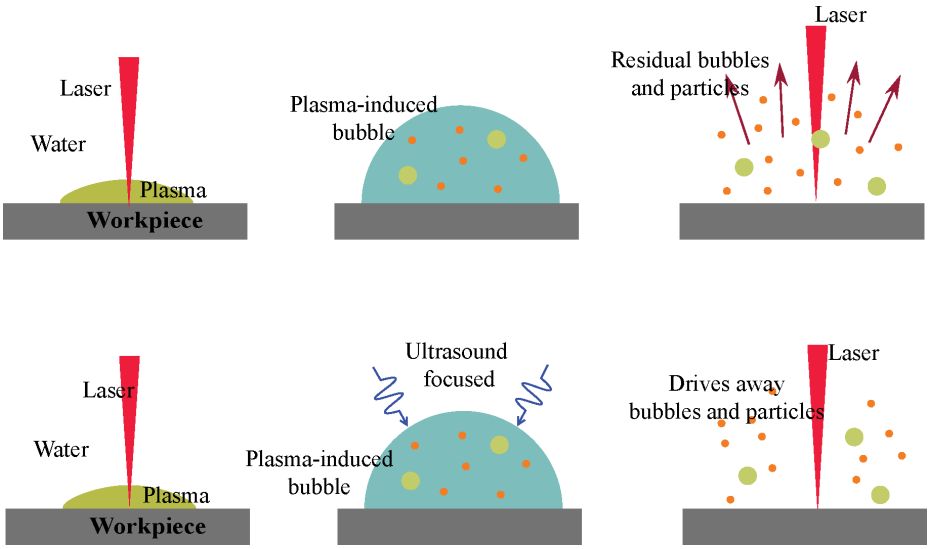

Fig. 4. Fundamental mechanism per pulse for UWLM (the bottom row) and underwater laser micromachining with no ultrasound (the top row).

3.2 Laser Ablation Dynamics

As mentioned above, the laser beam projects focused energy on the site of machining, resulting in high heating and vaporization. The material absorbs the laser energy, and a plasma plume is formed, followed by the removal of vaporized materials and molten materials. The laser creates a bubble at the site of the laser material interaction point, which is called a cavitation bubble.

Now, a phenomenon called cavitation or acoustic cavitation occurs, which is defined by the generation, growth and collapsing of the cavitation bubble when the high-intensity laser beam interacts with the ultrasonically disturbed water [5]. These bubbles expand rapidly and burst, resulting in the formation of localized shockwaves and microjets (see Fig. 5), which induce mechanical forces to the near materials [6]. These microjets and waves remove small bubbles and debris away from the site, which helps in achieving smooth grooves [5].

The effects of both laser ablation and ultrasound largely affect the material removal in UWLM. Acoustic streaming helps in removing debris and increases the cooling at the site of machining, hence decreasing thermal defects [12]. Also, even in the case of materials that are difficult to machine, like composites and ceramics, the localized pressure induced by the cavitation bubbles highly contributes to material removal. Using these combined effects, UWLM gets advantages over other underwater laser machining processes. However, for getting the optimal performance, the optimization of different process parameters is essential.

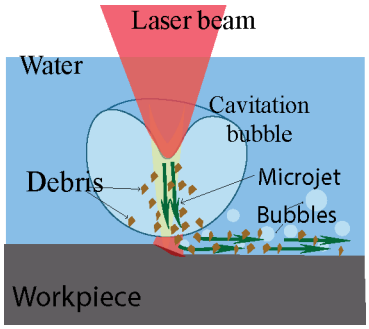

Fig. 5. Formation of laser induced cavitation bubble and microjet.

4 Applications in Various Industries

In the aerospace industry, strict requirements of reliability, precision and weight reduction are important. UWLM can be useful in manufacturing important components like fuel nozzles, aerospace alloys and turbine blades [22]. UWLM can improve fuel efficiency by enhancing aerodynamic performance and reducing frictional losses with

microscale features and precise surface texturing. Also, it can be used to manufacture composite and light materials for aircraft interiors, unmanned aerial vehicles and satellites [25].

In medical and biomedical engineering, UWLM can be used in the fabrication of biomedical scaffolds with tailored mechanical and surface properties, implants and miniaturized devices [22]. Biodegradable materials like biodegradable polymers, titanium alloys and stainless steel might be used to develop patient-specific implants, tissue engineering constructs and drug delivery systems [4]. Also, it can be used in fabricating diagnostic devices with high reproducibility, microfluidic channels and microneedles.

UWLM can be used in manufacturing integrated circuits and microelectromechanical systems for high precision with miniature features. These features include microscale patterns, interconnects and vias on ceramic materials, semiconductor substrates and glass [4]. Also, it can provide an advantage for machining flexible electronics, printed circuit boards and organic semiconductors, which helps in the development of the Internet of Things, wearable electronics and flexible displays.

In the automotive sector, UWLM can be used in manufacturing precise components, mold inserts with fine surface finish and complex geometry and tooling. Manufacturing engine components, fuel injectors and lightweight structures of advanced materials like high-strength steel, aluminium alloys and carbon fibre composites can also be done with UWLM [25].

Advanced manufacturing industries have been increasingly demanded to achieve high throughput in the mass production of micro parts for electronic, optoelectronic, and photovoltaic applications [10]. A great impact to the laser micromachining of difficult-to-machine and thermal-sensitive materials could be viable for a wide range of industrial applications [8].

5 Challenges and Limitations of UWLM

It is evident that cavitation enhances the efficiency of UWLM, yet it can lead to unwanted surface damages like surface roughness, microcracks and pitting [21]. As the cavitation bubble collapses, it creates localized microjets and shockwaves, resulting in mechanical stresses that are more than the material's strength, especially in brittle materials such as glass and ceramics [6]. In order to attenuate damage due to cavitation, we need to optimize the ultrasound parameters, such as duty cycle, intensity, and frequency, to stabilize material removal while preserving surface integrity [20].

As the ultrasound waves travel through the water, the intensity decreases, which results in a reduction in cavitation intensity and transfer of energy at longer distances. Because of this, it is necessary to use focused beams of ultrasound to get the desired cavitation effects. However, the challenge occurs in getting precise focusing of the beam and maintaining uniform cavitation distribution along big workpieces, especially for applications involving complex geometry and extended machining areas [14]. Therefore, adaptive focusing mechanisms and innovative transducer designs maximize machining efficiency and optimize cavitation dynamics.

The material properties like thermal conductivity, mechanical strength and optical absorption affect the cavitation dynamics and laser material interactions [50]. Also, UWLM faces difficulty in machining layered structures or heterogeneous materials of varying material properties [17]. Hence, to accommodate various geometries and material compositions, comprehensive optimization of process parameters, material characterization and adaptive machining approach is recommended, like laser-induced microjet assisted ablation [17].

6 Strategies for enhancing efficiency

Optimization of process parameters like ultrasonic vibration amplitude, pulse frequency, laser power and gas pressure are important as they affect the cavitation intensity, MRR and laser-material interaction [19]. With statistical optimization techniques and experimentation, we can get combinations of optimal parameters, maximizing machining efficiency and minimizing thermal and surface defects [23]. Also, advanced modeling tools help predictive process optimization, facilitating parameter sensitivity analysis and virtual experimentation [12,13].

In UWLM configurations, cavitation intensity, acoustic field homogeneity, and energy transfer efficiency are improved by creating novel transducer designs and acoustic coupling techniques [20]. The water flow produced by transducers when applied parallelly to the surface of the material pushes the bubbles away from the machining area [26].

Combining complementary machining techniques like abrasive jet machining, waterjet machining or electrochemical machining with UWLM can give combined effects and extend the overall machining process [23]. For example, integrating with abrasive jet machining can enhance MRR by cavitation-induced material fragmentation and abrasive particle impact, resulting in reduced surface roughness and faster machining rates [6]. Research has

also been conducted on UWLM with the assistance of magnetic field, which can increase the processing efficiency [27].

UWLM processes become more stable, dependable, and consistent when real-time process monitoring and feedback control mechanisms are put in place [11]. Dynamic modifications to optimize machining conditions are made possible by the early detection of process irregularities by parameter monitoring, including cavitation intensity, workpiece temperature, laser energy deposition, and acoustic emissions. Proportional-integral-derivative (PID) controllers, fuzzy logic systems, and adaptive neural networks are examples of advanced control algorithms that enable closed-loop control of important process variables, guaranteeing optimal performance and reducing the impact of material variations and environmental disturbances [24]. Moreover, predictive maintenance, anomaly detection, and performance optimization are made possible by the integration of sensor technologies and data analytics platforms, which maximizes uptime and productivity in UWLM operations.

7 Future Directions

Surface polish, quality and geometric complexity may all be improved by combining UWLM with additive manufacturing methods, including direct energy deposition, selective laser melting, and laser powder bed fusion [23]. Challenges with internal stress concentrations, surface roughness, and dimensional accuracy can be overcome by using UWLM for surface finishing and post-processing of additively manufactured components. This leads to parts with better mechanical qualities and functional performance. Furthermore, by combining UWLM with hybrid additive manufacturing techniques like laser-aided direct writing or laser metal deposition, it is possible to fabricate multilateral structures and functional gradients with greater precision and customization, opening up new possibilities for the aerospace, biomedical and automotive industries.

When it comes to decreasing energy usage, material waste, and environmental impact, UWLM is better than traditional machining methods. Waste creation, energy consumption, and the need for hazardous chemicals can be reduced with UWLM operations by utilizing the efficiency of cavitation-induced material removal and water-based machining fluids. Including assistance of multiple energy fields like magnetic field, ultrasound, gas and chemical solutions can provide better results [27]. The sustainability of UWLM process can be further improved by investigating other acoustic coupling material and adjusting process parameters for less environmental effect.

8 Conclusion

UWLM holds great promise for precision manufacturing in many industries. Higher MRR, better surface quality and increased geometric flexibility are just a few of the advantages that UWLM offers over traditional machining techniques as a result of the combination of ultrasound-induced cavitation and laser ablation. Manufacturers may precisely fabricate complicated geometries, surface modifications, and microstructures in a variety of materials, such as metals, ceramics, polymers, and composites, by utilizing UWLM's capabilities.

Although UWLM has several advantages, there are drawbacks as well, like cavitation-induced damage, acoustic attenuation, and complexity in process optimization. Innovative approaches are needed to overcome these obstacles, such as the use of hybrid process integration, process control systems, and sustainable manufacturing techniques.

Future directions and developing trends in UWLM include multi-scale and multi-material machining, sustainability, real-time process monitoring and adaptive control, and integration with additive manufacturing technologies. Through the adoption of these patterns and the investigation of novel avenues for UWLM research and development, scholars and professionals can fully realize the possibilities of this micromachining method and propel advancements in the field of precision manufacturing.

References

1. Shao, K., Zhou, Q., Chen, Q., Liu, Y., Wang, C., & Li, X. (2022). Research progress of water–laser compound machining technology. Coatings, 12(12), 1887
2. Lu, J., Xu, R. Q., Chen, X., Shen, Z. H., Ni, X. W., Zhang, S. Y., & Gao, C. M. (2004). Mechanisms of laser drilling of metal plates underwater. Journal of applied physics, 95(8), 3890-3894
3. Choo, K. L., Ogawa, Y., Kanbargi, G., Otra, V., Raff, L. M., & Komanduri, R. (2004). Micromachining of silicon by short-pulse laser ablation in air and under water. Materials Science and Engineering: A, 372(1-2), 145-162
4. Muhammad, N., & Li, L. (2012). Underwater femtosecond laser micromachining of thin nitinol tubes for medical coronary stent manufacture. Applied Physics A, 107, 849-861

5. Qiao, H., Zhihe, C., Jianfeng, C., & Zhao, J. (2021). Experimental study on water jet guided laser micro-machining of mono-crystalline silicon. Optics & Laser Technology, 140, 107057
6. Guo, Y., Qiu, P., Xu, S., & Cheng, G. J. (2022). Laser-induced microjet-assisted ablation for high-quality microfabrication. International Journal of Extreme Manufacturing, 4(3), 035101
7. Wee, L. M., Ng, E. Y. K., Prathama, A. H., & Zheng, H. (2011). Micro-machining of silicon wafer in air and under water. Optics & Laser Technology, 43(1), 62-71
8. Tangwarodomnukun, V., Likhitangsuwat, P., Tevinpibanphan, O., & Dumkum, C. (2015). Laser ablation of titanium alloy under a thin and flowing water layer. International Journal of Machine Tools and Manufacture, 89, 14-28
9. Ultrasound-assisted water-confined laser micromachining: A novel machining process, Ze Liu, Yibo Gao, Benxin Wu, Ninggang Shen, Hongtao Ding
10. Ultrasonic-assisted underwater laser micromachining of silicon, W. Charee, V.Tangwarodomnukun, C. Dumkum
11. Ultrasound-assisted water-confined laser micromachining (UWlaser micromachining) of metals: Experimental study and time-resolved observation, Ze Liua, Benxin Wua, Avik Samanta, Ninggang Shenb, Hongtao Ding b, Rong Xua, Kejie Zhao
12. Study on the mechanism of ultrasonic-assisted water confined laser micromachining of silicon, Jia Zhou, Rongwei Xu, Hui Jiao, Jia-ding Bao, Qing-yuan Liu, Yu-hong Long
13. The mechanism of micro-cracks formation in ultrasonic-assisted water confined laser micromachining silicon, Jia Zhou, Hui Jiao, Yu-xing Huang, Yu-huan Zhao, Qing-yuan Liu, Yu-hong Long, Zhi-xian Zhong, Jia-ding Bao
14. Grooving of Metals by High-Intensity Focused Ultrasound-Assisted Water-Confined laser micromachining, Ze Liu, Benxin Wu, Rong Xu, Kejie Zhao
15. Cavitation bubble removal by surfactants in Laser-Induced Plasma Micromachining, Suman Bhandari, Putong Kang, Jihoon Jeong, Jian Cao, Kornel Ehmann
16. Heating and material removal process in hybrid laser-waterjet ablation of silicon substrates, V. Tangwarodomnukun, J. Wang, C.Z. Huang, H.T. Zhu
17. Study on water-assisted laser ablation mechanism based on water layer characteristics, Jia Zhou, Yu-xing Huang, Yao-wu Zhao, Hui Jiao, Qing-yuan Liu, Yu-hong Long
18. Cavity formation and surface modeling of laser milling process under a thin-flowing water layer, Viboon Tangwarodomnukun
19. Empirical modeling and optimization of process parameters in ultrasonic assisted laser micromachining of Ti-6Al-4V, Hossein Abdollahi, Saeid Shahraki, Reza Teimouri
20. Nanosecond laser grooving of water-immersed silicon carbide assisted by high intensity focused ultrasound (HIFU), Weidong Liu, Benxin Wu
21. Experimental investigation on effects of water-based ultrasonic vibrations, transverse magnetic field and water temperatures on percussion laser drilling performance, Houxiao Wang, Sukai Zhu, Ye Xu, Naifei Ren
22. Experimental investigation of underwater laser beam micromachining (UW-LBμM) on 304 stainless steel, Rasmi Ranjan Behera, Mamilla Ravi Sankar, J.Swaminathan, Indrajeet Kumar, Ashwini Kumar Sharma, Alika Khare
23. Laser-based hybrid micromachining processes: A review, Ashish Kumar Sahu, Jitin Malhotra, Sunil Jha
24. Real time adaptive probabilistic recurrent Takagi-Sugeno-Kang fuzzy neural network proportional-integral-derivative controller for nonlinear systems, A. Aziz Khater, Eslam M. Gaballah, Mohammad El-Bardin, Ahmad M. El-Nagar
25. Alahmari, A. M., Ahmed, N., & Darwish, S. (2016). Laser beam micro-machining under water immersion. The International Journal of advanced manufacturing technology, 83, 1671-1681
26. Charee, W., Qi, H., Zhu, H., & Saetang, V. Lateral Ultrasound-Assisted Underwater Laser Micromachining Process. Available at SSRN 4881936
27. Wei, T., Sun, S., Zhang, F., Wang, X., Wang, P., Liu, X., & Wang, Q. (2024). A review on laser drilling optimization technique: parameters, methods, and physical-field assistance. The International Journal of Advanced Manufacturing Technology, 131(12), 5691-5710.

Performance enhancement of Wire-EDM of marine grade material by supplying SiC powder in the dielectric medium

Sadananda Chakraborty[1*] (0000-0001-6162-0316), Souren Mitra[2] (0000-0003-2641-9646) and Dipankar Bose[3] (0000-0001-6505-0330)

[1] Indian Maritime University, Kolkata Campus -700088, India
[2] Production Engineering Department, Jadavpur University, Kolkata -700032, India
[3]Mechanical Engineering Department, NITTTR, Kolkata -700106, India
[1*]sadananda116@gmail.com

Abstract. Since its inception, wire electric discharge machining (WEDM) has significantly benefited industries such as die, mould, automotive, and aerospace by offering an efficient resolution for machining hard-to-cut materials and complex geometries. However, traditional EDM faces inherent challenges in achieving high machining rates and fine surface finishes. The development of powder mixed wire electric discharge machining (PMWEDM) has not only improved productivity and surface finish quality. Still, it has also created new possibilities for its use in surface modification. This process enables simultaneous machining and surface modification, often requiring expensive post-treatment steps. This study explores the effect of SiC powder characteristics and WEDM inputs like pulse on time, pulse off time and peak current on performance outcomes such as surface roughness and corner inaccuracy for Inconel 625 material. Additionally, it reviews the most commonly employed methods for optimising the PMWEDM process, along with future research directions, challenges, and trends from the past decade. The effects of each individual parameters has been determined by developing the regression model.

Keywords: PMWEDM, SiC powder, kerosene, Surface Roughness, Corner Inaccuracy, RSM.

1 Introduction

The crucial factors in any machining process are accuracy and precision, especially in precision manufacturing, which is highly valued in aerospace and aeronautical industries. Globally, wire electrical discharge machining (WEDM) is one of the most popular methods used across various manufacturing sectors. Traditional machining processes like grinding, milling, and drilling often struggle to produce geometrically complex or intricate shapes. In contrast, WEDM has gained widespread acceptance for machining various materials, particularly advanced engineering materials like superalloys, ceramics, and composites [1]. WEDM is indispensable for cutting intricate shapes in difficult-to-machine metals without expensive grinding or cutting tools. The WEDM process is highly complex, involving many parameters such as discharge current intensity, discharge frequency, and pulse duration. Machining performance is often measured by cutting rate and surface roughness. Past research has shown that dropping discharge energy increases surface finish while maintaining high energy efficiency, essential to confirm an enhanced machining rate without wire breakage. Studies explored the performance of the tools and examined the impact of machining accuracy and costs. In WEDM, proper input selection is the key to optimising outcome values such as machining speed, material removal rate, and surface roughness. Extensive research has determined the relationship between process parameters and the formation of recast layers on the machined surface, particularly in the machining of Inconel 625 alloy [2]. Findings indicate that increasing energy per pulse, pulse current duration, and peak discharge current results in thicker recast layers with an average 5 to 9 µm thickness. However, factors like spark cycle and wire diameter have little effect on recast layer thickness, while surface roughness tends to increase slightly with energy per spark and wire diameter.

The Inconel 625 alloy holds numerous desired properties, such as high strength, toughness, excellent corrosion resistance, and cryogenic capabilities. These excellent mechanical properties make it appropriate for aerospace, marine applications, and various corrosive environments. However, processing these alloys using traditional methods is a challenging task [3]. Despite the extreme characteristics of conductive material, WEDMed surfaces often exhibit a lot of imperfections like micro-cracks and micro-pores. These issues can be solved by the hybrid approach of WEDM process named as Powder mixed WEDM. The powder creates a

bridging effect during machining causing an early explosion and enlarging the spark gap that helps to modify the plasma zone. As a result, debris is clearly removed from plasma zone and provides better responses.

Chakraborty et al. [4] studied that adding powders with dielectric can reduce surface roughness, with the powder's size, concentration, and electrical conductivity playing key roles in surface enhancement. Singh et al. [5] found that additives with high thermal and electrical conductivity are more likely to produce a smoother surface. Chavan [6] focused on understanding the characteristics of the plasma channel in powder-mixed EDM, while Alhodaib, A. et al. [7] explored the effect of silicon powder on the machining rate of Nimonic-90 superalloy. To further minimise surface roughness, author conducted experiments using powder-mixed WEDM on titanium alloys, building on the basic principles of electrical discharge machining [8].

In this study, WEDM has been carried out using kerosene as the working fluid, mixed with a specific proportion of abrasive powder. Material removal was primarily achieved through spark erosion, with abrasive plasma modifying aiding the process, resulting in a reduction in surface roughness [9]. The objective of the study is to enhance the machining performance of Inconel 625 using a magnetic stirring mixed-abrasive particles WEDM method. Silicon carbide (SiC) was selected as the abrasive particle. During electrical discharge, it is anticipated that Si and C will decompose from both the dielectric and powder, transferring to the workpiece surface to improve the machined surface quality and at the same time contentious spark at a point help to improve corner inaccuracy in the curvature profile.

2 Material and Methods

The entire experiment was conducted on the EZEECUT PLUS wire-cut electrical discharge machine. The detailed view of the experimental set-up for the present work is shown in Figure 1. The figure shows a detailed view of all components of wire-cut EDM.

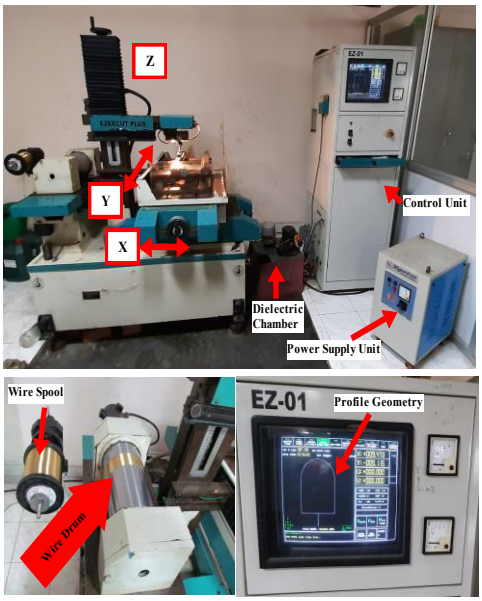

Figure 1 Photographic view of experimental set-up (EZEECUT PLUS wire cut EDM)

The dielectric chamber (20 liters capacity) with a starring unit was prepared to supply dielectric fluid. Top section, bottom section, magnate assisted section and stir and pump unit were the major parts of the dielectric chamber. One filter with mesh size 35 on the top portion is used for filtering the dielectric and preventing bubble formation in the pump. Figure 2 shows the full setup of the dielectric chamber. In the present study, Kerosene is used as a dielectric medium. Brass was the first logical alternative to copper in the EDM process, and it quickly became the most widely used electrode material for the general purpose of wire EDM. Brass wire is a grouping of zinc and copper, naturally alloyed in the range of 63% Cu and 37% Zn used as a tool material. Inconel 625, which is 5 mm thick, has been used as workpiece material. The composition of Inconel 625 was 58% nickel, 21.6% chromium, 9% molybdenum, 5% iron, 3.6% niobium+tantalum, 0.5% manganese, 0.5% silicon and 0.5% silver and remain others material. SiC abrasive with 10 µm size was added to the dielectric medium during machining. The levels of each parameter are chosen on the basis of a trial run. Selected inputs with their levels have been shown in Table 1. A total of 31 experiments have been conducted based on the

central composite design (full factorial) in RSM methodology. The other parameters of the WEDM process are kept constant throughout the experimentation.

Table 1 Machining parameters and their levels

Machining Parameters	Units	Levels				
		-2	-1	0	1	2
Pulse-on-time	µs	30	45	60	75	90
Pulse-off-time	µs	3	5	7	9	11
Peak Current	A	1	2	3	4	5
Powder Concentration	gm/lit	2	4	6	8	10

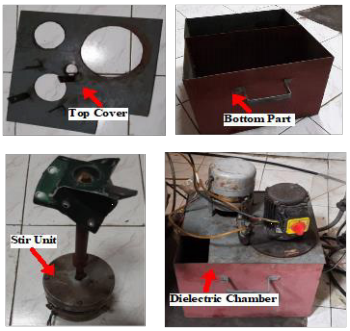

Figure. 2 The dielectric chamber fitting parts

3 Result and Discussion

Figure 3 and Figure 4 show the results obtained for surface roughness and corner inaccuracy using 31 sets of parametric combination. The figure reveals the indication of observation no to the design setting of the CCD method. Understanding the relationship between inputs and outputs is crucial. The quadratic mathematical model has been made to understand and achieve minimum surface roughness and corner inaccuracy. The regression analysis can determine the significant factors. Two outputs of surface roughness and corner inaccuracy have been modelled as in Eq. no (1) and Eq. no (2)

SR = 0.646 + 0.07944 Ton + 0.1928 Toff -1.672 Ip + 0.2871 PC - 0.000457 Ton*Ton - 0.01328 Toff*Toff + 0.0251 Ip*Ip + 0.02422 PC*PC -0.002792 Ton*Toff + 0.008867 Ton*Ip - 0.003758 Ton*PC + 0.09731 Toff*Ip - 0.01609 Toff*PC + 0.02731 Ip*PC (1)

CI = 77930 - 162.6 Ton - 5805 Toff - 11547 Ip - 8979.8 PC + 1.8312 Ton*Ton + 425.48 Toff*Toff+ 527.0 Ip*Ip + 707.91 PC*PC - 25.679 Ton*Toff + 10.98 Ton*Ip + 19.287 Ton*PC+ 578.6 Toff*Ip + 27.16 Toff*PC + 518.9 Ip*PC (2)

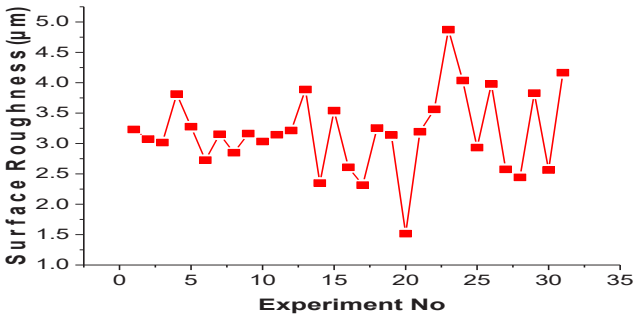

Figure. 3 Experimental data on surface roughness

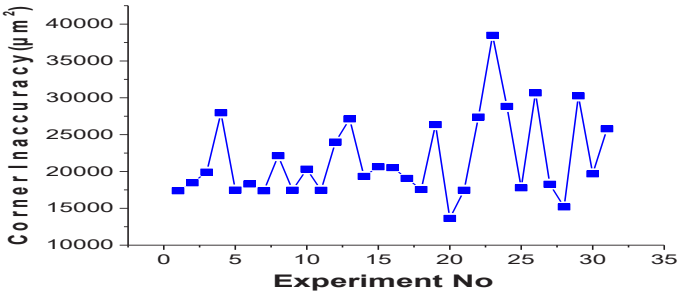

Figure 4 Experimental data of Corner Inaccuracy

3.1 ANOVA for Surface Roughness

F test and P test values of analysis of variance (ANOVA) outcomes can authenticate the regression model. The obtained F test value must be greater than the critical P ratio, and the significance level must be higher than the P test value. Table 2 and Table 3 show ANOVA outcomes of surface roughness and corner inaccuracy. The confidence level of the critical F ratio has been set at 95 % for considered outputs. P values for all considered regression responses are to be less than 0.05.

Table 2 ANOVA for Surface Roughness

Source	DF	Adj SS	Adj MS	F-Value	P-Value
Model	14	13.0516	0.93226	319.24	0
Linear	4	0.9926	0.248152	84.98	0
Ton	1	0.2932	0.293241	100.42	0
Toff	1	0.6136	0.613572	210.11	0
Ip	1	0.0163	0.016305	5.58	0.031
PC	1	0.0695	0.069489	23.8	0
Square	4	0.7465	0.186621	63.91	0
Ton*Ton	1	0.3025	0.302549	103.6	0
Toff*Toff	1	0.0807	0.08066	27.62	0
Ip*Ip	1	0.0181	0.018073	6.19	0.024
PC*PC	1	0.2684	0.268447	91.93	0
2-Way Interaction	6	1.3188	0.219793	75.27	0
Ton*Toff	1	0.1122	0.112225	38.43	0
Ton*Ip	1	0.283	0.283024	96.92	0
Ton*PC	1	0.2034	0.203401	69.65	0
Toff*Ip	1	0.6061	0.606062	207.54	0
Toff*PC	1	0.0663	0.066306	22.71	0
Ip*PC	1	0.0477	0.047742	16.35	0.001
Error	16	0.0467	0.00292		
Lack-of-Fit	10	0.0302	0.003024	1.1	0.474
Pure Error	6	0.0165	0.002748		
Total	30	13.0984			

S=0.0540392, R-sq=99.64%, R-sq(adj)=99.33%, R-sq(pred)= 98.50%

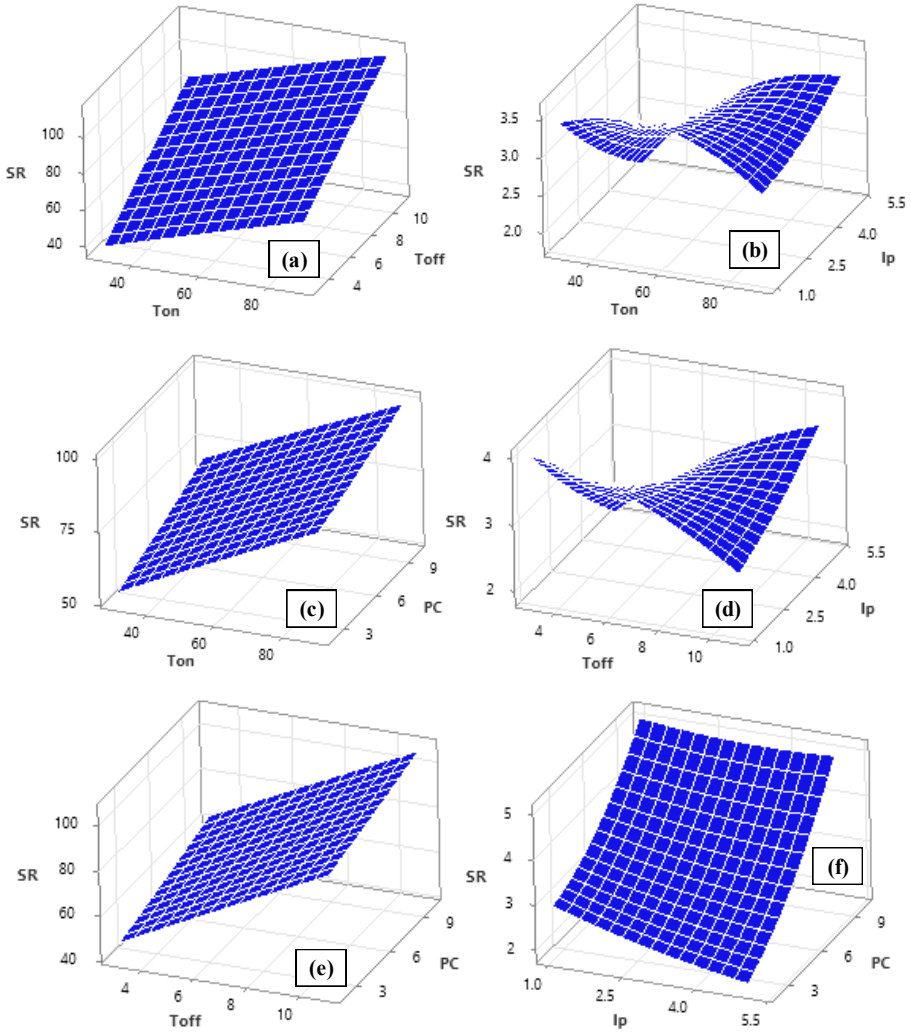

Figure. 5 Interaction Plot for Surface Roughness

The interaction effect of significant inputs of Ton, Toff and PC on surface roughness is shown in Figure 5 (a), (c) and (e). The pattern for each of the graphs is similar in nature. As the Ton and Toff increase, the surface roughness also increases. On the other hand, during an increase in Ton and Toff together, followed by an increase in PC, the surface roughness also increases. This is due to the increment pulse energy, which is directly involved in producing gas explosion and ion generation. High pulse energy eroded more material from the workpiece, causing high MRR and creating more recast layer formation. Powder mixed with dielectric in the WEDM process causes a bridging effect in the machining channel, which has more impact on modifying the plasma channel and early explosion during machining. The graph shows an increase in powder concentration, an increment in MRR, and the combined metallic formation on the machined surface. As a result, surface roughness increased. The lower value of all three inputs provides a better result. From Figure 5 (b), (d) and (f), it is clear that Ip and PC, followed by Ton and Toff, have a greater impact on surface roughness. From Figure 5 (b) and (d), the middle value of Ton and Toff showed lower surface roughness. As Ip and PC increase, the surface roughness also increases. This is due to the higher peak current producing higher discharge energy and the maximum time availability for a higher Toff value. Debris particles can not be removed smoothly from the machining zone and are attached to the machining surface during the lower Toff value. Higher Toff values cause wire breakage, leading to higher surface roughness.

3.2 Analysis of Variance for Corner Inaccuracy

Based on the ANOVA result of corner inaccuracy as in Table 3, all the inputs have less than 0.05 of p-value, which indicates the considered input settings are highly significant towards the response, i.e., corner inaccuracy.

The interaction effect of all inputs on corner inaccuracy is required to be explained in order to understand the WEDM process behaviour.

The surface plot for corner inaccuracy has been illustrated in Figure 6. Figures 6(a), (c), and (e) show an increment of corner inaccuracy during an increase in pulse on time and pulse off time. During machining in the corner sections, a low pulse setting is highly required to avoid dimensional shifts. A higher pulse on time leads to the generation of higher bubble formation, which causes wire deflection. As a result, a higher amount of uncut area is seen in the corner section. Toff value of 7 µs a better corner accuracy is seen. After that it increases corner inaccuracy. Toff is involved in reducing the spark frequency, which minimises gas exploration. Also, it provides the time to remove debris from the machining area. Due to this, up to a certain limit of Toff gives better accuracy, and due to a higher cooling rate, it can also maximise the corner inaccuracy. From Figure 6 (b), (d) and (f), it is clear that corner inaccuracy first decreases and then increases. The lower discharge current and the continuous smooth spark provide a better corner profile. It is essential to find the optimal solution for the responses.

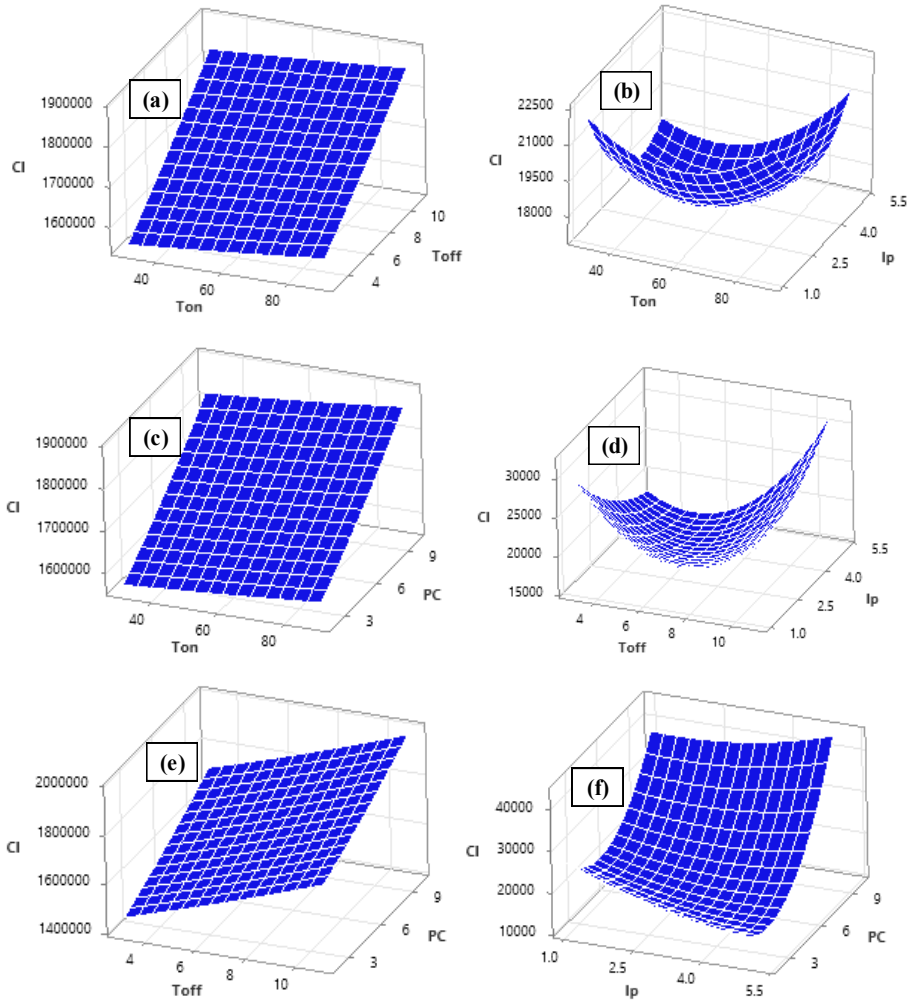

Figure. 6 Interaction Plot for Corner Inaccuracy

Table 3 ANOVA for Corner Inaccuracy

Source	DF	Adj SS	Adj MS	F-Value	P-Value
Model	14	938484910	67034636	6403.54	0.000
Linear	4	50514681	12628670	1206.36	0.000
Ton	1	470367	470367	44.93	0.000
Toff	1	22085166	22085166	2109.71	0.000
Ip	1	7793758	7793758	744.51	0.000
PC	1	20165390	20165390	1926.32	0.000
Square	4	286302986	71575746	6837.34	0.000
Ton*Ton	1	4854587	4854587	463.74	0.000
Toff*Toff	1	82826708	82826708	7912.10	0.000
Ip*Ip	1	7942675	7942675	758.73	0.000
PC*PC	1	229287882	229287882	21902.93	0.000
2-Way Interaction	6	54132930	9022155	861.85	0.000
Ton*Toff	1	9495642	9495642	907.08	0.000
Ton*Ip	1	433622	433622	41.42	0.000
Ton*PC	1	5356910	5356910	511.72	0.000
Toff*Ip	1	21423012	21423012	2046.45	0.000
Toff*PC	1	188790	188790	18.03	0.001
Ip*PC	1	17234952	17234952	1646.38	0.000
Error	16	167494	10468		
Lack-of-Fit	10	145903	14590	4.05	0.050
Pure Error	6	21591	3598		
Total	30	938652404			

S=102.315, R-sq=99.98%, R-sq(adj) =99.97% R-sq(pred)= 99.91%

3.3. Multi-objective Optimization

Based on the RSM methodology optimization technique, the result values have been determined by using model equations no (1) and (2), as shown in Figure 7. The d value (linear desirability function) remains the same for all the inputs within the specified limit. Minimum surface roughness and corner inaccuracy have been determined as 1.054 µm and 13589µm^{2,} respectively. Minimum outcomes are acheived from the input setting, such as Ton =30 µs, Toff =3 µs Ip=5, and PC =3.13 gm/lit.

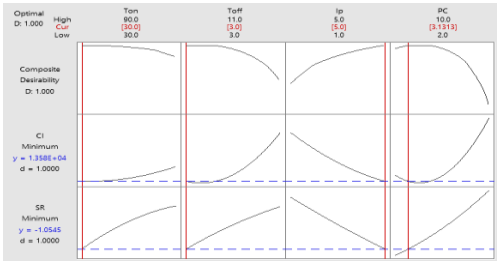

Figure 7 Multi-objective optimisation

After five sets of confirmation tests using the same inputs, an error has been determined as 4.7 % for surface roughness and 3.5% for corner inaccuracy. SEM analysis has been done on the basis of taking the middle values of all inputs and the optimum setting condition. The pictorial view of SEM analysis has been illustrated in Figure 8. It is clear that the optimum setting provides a better result of lesser recast formation and crack-free surface.

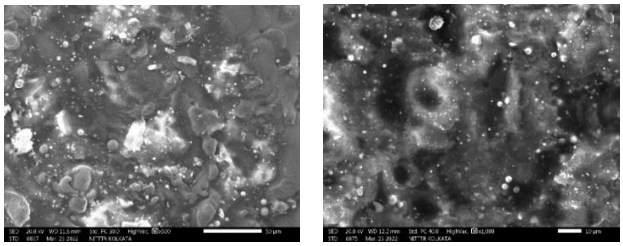

Figure 8 SEM photograph of machined sample (a) Machining setting at Ton =60 µs, Toff =7 µs Ip=3, and PC 6 gm/lit. (b) Ton =30 µs, Toff =3 µs Ip=5, and PC=3.13 gm/lit.

4 Conclusions

Due to the difficulties of the process behaviour of powder mixed WEDM, making complex shapes with high accuracy is a challenging task. The present study concentrates on powder-mixed WEDM for machining the Inconel 625 alloy. Machining inputs are analysed and optimised with the RSM approach to characterise enhanced outputs SR and corner accuracy. Based on the parametric study, it is concluded that the most significant parameters are peak current and powder concentration. The estimated outcomes under the optimal condition are fitted with the predicted value.

References

1. Vijayakumar, R., et al. Investigation in µ-WEDM of Inconel 625 superalloy using RSM-CCD technique. Materials and Manufacturing Processes, 38(4), 449–460, (2022).
2. Sonawane, S. A., and Kubade, P. R.. Optimization of WEDM of Inconel 625 by employing MABAC, MARKOS and PIV practices: a comparative study. International Journal on Interactive Design and Manufacturing, (2024).
3. Sunil, B., Goyal, A., Kumar, L., Sonia, P., Saxena, K. K., Bandhu, D., Kaur, K., Chandrashekar, R., & Ansari, M. A. (2024b). Optimizing wire electrical discharge machining performance of Inconel 625 with genetic algorithms & particle swarm optimization. Journal of Materials Research and Technology, 31, 555–569.
4. Chakraborty, S. et al. Evaluation of response characteristics using sensitivity analysis and TLBO technique of powder mixed wire EDM of Ti6Al4V alloy. CIRP Journal of Manufacturing Science and Technology, 47, 260–272, (2023).
5. Singh, G., et al. Surface morphology and microhardness behavior of 316l in HAP-PMEDM. Facta Universitatis Series Mechanical Engineering, 17(3), 445, (2019).
6. Chavan, V. Study on Effect of Blended Powder Mixed Dielectric Fluids in Wire EDM Process. International Journal for Research in Applied Science and Engineering Technology, 9(VIII), 589–599, (2021).
7. Alhodaib, A.,et al. Experimental investigation on Silicon Powder Mixed-EDM of Nimonic-90 superalloy. Metals, 11(11), 1673, (2021).
8. Chakraborty S. Performance characterization of powder mixed wire electrical discharge machining technique for processing of Ti6Al4V alloy. IMeche, Part E: Journal of Process Mechanical Engineering. 236, (4):1283-1295, (2022).
9. Srivastava S. Vishnoi M. Gangadhar MT. Kukshal V. An insight on Powder Mixed Electric Discharge Machining: A state of the art review. IMeche, Part B: Journal of Engineering Manufacture. 237(5):657-690 (2023).

Experimental study on the reduction of burr formation under different drilling environment

Sweta Yadav[1[0009-0000-4165-3946]], Santanu Das[2[0000-0001-9085-3450]], Partha Pratim Saha[3[0000-0003-3967-0581]]

[1,2]Kalyani Govt. Engineering College, Kalyani- 741235, Nadia, West Bengal, India. [3]Kanchrapara Railway Workshop, Eastern Railway, West Bengal- 743145, India. sdas.me@gmail.com

Abstract. In traditional machining process, undesirable presence of materials at the edge is often detected that are known as burrs. Burrs create problem in assembly operation. Burrs need be removed from any component. For eliminating burr, deburring operation is obligatory. Supplementary deburring process raises production tariff and it may subscribe as far as thirty percent of the entire production cost. Moreover, deburring ordinarily requires a remarkable length of time. To avoid or reduce extensive supplementary de-burring operation, some drilling experiments are carried out in the present work using dry environment and edible soyabean oil environment to reduce burr. Experiment has been accomplished in Radial Drilling Machine. From the experiment, it is observed that in some of the conditions, with increasing feed burr thickness initially decrease and then increase or vice versa. In some cases, drill cap is being observed. It can be finally inferred that at some conditions of experiments under the cutting environment of edible soybean oil give the maximum reduction of burr thickness. The objective of the work is to find out the minimum amount of drilling burr produced on AISI 316 stainless steel workpiece using Dry and Wet environment with refined soya bean oil in SQL condition under varying cutting condition. Full Factorial sign with 2-factor and 3-level is designed for the present experiment.

Keywords: Machining, Drilling, Burr, Dry Condition, Refined Soya bean Oil.

1 Introduction

Nowadays, in production, there are numerous materials which are based on the particular application and various technique that requires specific tools to make the required ultimate shapes. Operations such as drilling, milling, turning and all which are much used in practices, drive a crucial role in manufacture of convoluted part. One of the frequent production practices is drilling and it entails around thirty-five percent of production methods. Reduction or elimination of burrs created through drilling operation is essential. Occurrence of burr can generate numerous problems like functional problems, injury to assemblers and so on claiming a further deburring operation for their eradication. Outlay that is linked with removing burrs may take a share of cost of production even up to 30%. Categorization of burrs and different types of burrs during drilling operations are shown in Fig. 1 and 2.Varatharajulu et al. [1] carried out an experiment to explore the influence of speed and feed on size of burr. Analysis of Variance (ANOVA) was made to find out the significance of the machining parameters on the response. An experiment was done by Chang et al. [2] for reducing burr size in drilling. They used uncoated and TiN-coated drills. The effect of ultrasonic assistance could be seen on burrs size. Under appropriate ultrasonic vibration, burr size could be lowered remarkably. Sathiyamurthy and Ramamoorthy [3] pointed out that minimization of cost of the product plays a key role in the present scenario of manufacturing industries. Burrs are formed in most of the drilling operation. The objective of their research work was to develop a 3D FEM for simulating the mechanism of forming drilling burr. The FEM simulation demonstrated the effect of feed on drilling burr formation under varying the feed.

Mangala and Kumar [4] did an experiment on drilling burr using Taguchi's, Orthogonal Array. Cutting velocity, feed and point angle were varied. Using ANOVA and MINITAB software, optimal conditions levels for a low burr could be evolved. All trial runs were carried out unaccompanied by coolant at various coalition of selected drilling specification. Minimum cutting speed and feed and intermediate point angle yielded a low burr height. Modeling drilling burr formation in a ductile material was done in a work by Dornfeld and Kim [5]. The principle of energy conservation and metal cutting theory was proposed in this model. Prediction of drilling burr size could be done with the analytical model. Considering work material, drill geometry and process condition. Kim and Lee [6] did an experiment on Al-7075 work piece. Formation of uniform burr, uniform burr with cap, and transient burr was reported. Artificial intelligence (AI) and Convolution neural network (CNN) were applied by them to predict the types of burr.

Lee and Dornfeld [7] did an experiment on 304 stainless steel workpiece using tungsten-carbide cutter to look into burr formation. Effect of feed, cutting speed and cutting-edge radius was investigated on micro-burr

formation. Drilling burr and hole were explored titanium and aluminium alloys workpiece by Soo et al. [8].For an aluminium workpiece, CVD coated carbide tools and uncoated carbide tools for titanium material were used to find out the influence of cutting conditions on burr and quality of hole. They also reported that feed rate was the key factor for reduction of the size of exit burr. Dornfeld and Min [9] performed an extensive overview on formation of burr in metal cutting. They reported that burr might be eliminated or reduced by choosing suitable tool, process parameter and tool and part design. According to Ko et al. [10], by varying the step angle and point angle of the step drill, the burr dimensions could be changed. They introduced a step drill for reducing the extent of burr formation.

Gaitonde et al. [11] accomplished experiments using the Taguchi Optimization Method to determine the effect of varying cutting conditions and drill geometry on size of burr. They reported that cutting velocity, feed and lip clearance angle not to be dependent on drill diameter to control burr. Kim et al. [12] experimented on optimization and control of drilling burr with the help of drilling burr control charts. They used HSS Split point twist drill. Accordingly, one could reduce the total cost associated with burr formation in two ways: one by increasing feed and speed and decreasing size of burr thereby lowering debarring time. Burr type and its size could be well estimated through the control chart. Karnik et al. [13] did an experiment on austenitic stainless steel to control burr formation. They modelled drilling burr utilizing ANN and genetic algorithm (GA). To find out the suitable condition for substantial reduction of burr, larger point angle corresponding to bigger size drill was reported by them to reduce burr. Using a cryogenic cooling process a new burr minimization approach for drilling operations was introduced by Bermann and Hartmann [14]. In this investigation, they used 34CrNiMo6 and AlMgSi as a workpiece and also used carbon dioxide as a cooling medium. It is observed that instead of dry machining, cryogenic cooling can be used. Choi et al. [15] adopted FEA to model burr formation of specimens with multiple layers for the optimization of drilling process. Simulation revealed presence of inter-layer burr accompanied with burr at entry edge during drilling. Burr formation mechanism in the feed direction had been done in an experimental study by Toropov et al. [16]. Tool and workpiece orientation considered as well as cutting conditions were to find their influence on burr dimensions. For various stages of burr formation, an experiment was done using a laser measurement system.

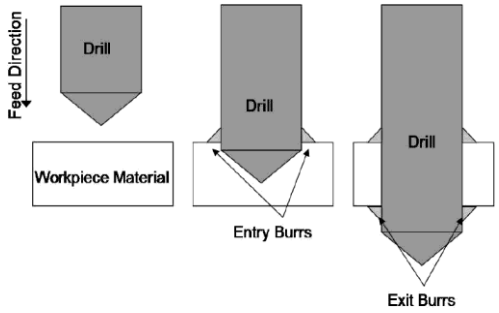

Fig. 1. Burr Formation at (a) Entry position (b) Exit position [3]

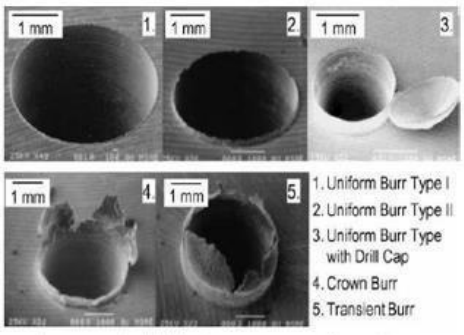

Fig. 2. Drilling Burr's types [31]

Creation of burr during making of intersecting holes was explored by Heisel and Schaal [17]. Intersecting holes were examined by them and they found the angle between drill wall and exit surface to be quite important for burr formation. Burr size could be predicted satisfactorily for short intersecting holes. With a new concept drill, Ko and Lee [18] developed a numerical model for analysing drilling burr formation. Considering the geometry of drills, each type of drill was analysed for burr formation mechanism. They made three changes such as length of chisel edge, increasing point angle, and incorporating a specific geometry to the flute. From the experiment, it was concluded that larger point angle with small corner radius could reduce burr height and cap thickness tangibly, and there was no remarkable effect on feed. Bakkal et al. [19] conducted drilling of Zr- based

bulk metallic glass (BMG) and observed burr. They observed that Size of burr at the exit end was usually more than that in the entry side. High feed reduced size of burr. It also indicated that WC–Co tool-material performance showed better than HSS drill bit.

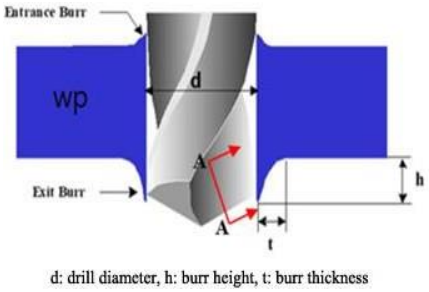

Fig. 3. The definition of drilling burr height and burr thickness [6]

Mondal et al. [20] did an experiment to suppress or eliminate burr at the exit side of low alloy steel flats. Different machining conditions were performed with dry and wet environment. Taper Shank with non-coated 14 mm diameter HSS twist drills were used for penetration to spot burr height. Back-up support on and exit edge bevel could suppress burr formation at the exit ends both in dry and wet conditions ANN was applied to model experimental results. The value obtained from model showed a close matching with the experiential results with minor alteration.

Mondal et al. [21] did an experiment on aluminium alloy to minimize burr height and thickness. They used the methodology of L_{27} orthogonal array of response surface methodology (RSM) in their experiment. Minimum burr height is obtained at a cutting velocity of 10 m/min, feed of 0.08 mm/rev, and depth of hole within backup support of 0.2 mm, whereas burr thickness is the lowest in this work at a cutting velocity of 3.9 m/min, a feed rate of 0.095 mm/rev and depth of hole inside backup support of 0.56 mm developed multi objective functions of burr height and thickness are optimized through GA. These results are useful to implement in manufacturing practice.

Mondal et al. [22] carried out their experiments on drilling on an aluminum 6061 T6 plate. They selected three factors and three levels of process parameters like drill diameter, point angle and spindle speed. Two predictive models, namely, adaptive neuro-fuzzy inference system and support vector regression, were developed using experimental data to estimate burr height and burr thickness. It was seen that both models were able to predict burr size and thickness with good accuracy, while the adaptive neuro-fuzzy inference system was found to perform better than support vector regression. Presence of a beveled work edge was reported to lower burr height experienced in milling and drilling operations [23-25] due to gradually decreasing depth of cut and the reducing need of backup support. Kim and Lee [26] did an experiment on Al-7075 workpiece that is utilized in aerospace and automobile sector. The definition of drilling burr was reported by them as shown in Fig. 3. Artificial intelligence (AI) was also applied by them to identify the types of burr. Convolution neural network (CNN) was enacted and was found useful in predicting drilling burr well. CNN model showed better prediction than the BP ANN model. The objective of the work is to study the effect of drilling burr formation on AISI 316 stainless steel workpiece using Dry and Wet environment with refined soya bean oil under varying cutting condition. Full Factorial degree of experiment with 2-factor and 3-level is designed for the present experiment.

2 Burr Formation Mechanism in Drilling Operation

The formation of burr very much depends on chip formation mechanisms. Negative shear is responsible for exit failure of cutting tools, and foot formation in milling [27]. The main reason for formation of burrs are-

i) Lateral flow of material. It occurs whenever a solid is compressed.
ii) Bending of material (such as chip roll over)
iii) Tearing of chip from workpiece.
iv) Redeposition of material.
v) Incomplete cut-off.
vi) Flow of material into cracks.

For burr formation in drilling, constant ratio between burr height and undeformed chip thickness may be a fundamental property of work material for a particular tool geometry. This occurs in regions of unreformed chip thickness, where tool performs machining rather than machining rather than plowing. Due to plastic deformation at the end of a cutting process and high compressive force, exit surface geometry changes. Depending on angular position of exit surface, effective surface angle changes. A small negative exit surface angle leads to early initiation of bending mechanism resulting in large burr. Thinner parts of a workpiece may have larger burr

[28, 29, 30]

3 Experimental Investigation

To observe the nature of burr formation, experiment is carried out in the present work using different drill diameters under varying conditions and environment. Reducing burr size can also be explored in this condition. For the experiments, Radial Drilling Machine is used. Experimental set-up detail and Machining Conditions is given in Table 1.

Under various cutting conditions, to see the effects of burr formation with different drill diameters, experimental investigation is carried out in two sets: dry condition (Set-I), and refined soya bean oil Condition (Set-II). Cutting velocity, feed and cutting environment are the parameters chosen. By changing the rotational speed and drill diameter with different cutting velocity is carried out in the experiments. To have Minimum or negligible burr formation, experiments are carried out for measuring burr thickness under different machining conditions for exp. for dry condition and refined soya bean oil condition as detailed in Table 2. Burr thickness has been measured on a Stereo Microscope. Different types of burrs are observed with different cutting velocity as shown in Fig. 3& 4 of experiment Set-I (in dry condition) &Set-II (in refined soya bean oil condition). Results observed in experiment under the dry working environment and refined soya bean oil which are shown in Table 2. Experimental results are also depicted in Fig. 5, 6 &7.

Table 1. Details of Experimental Set Up and Machining Conditions

Machine Tool	Radial Drilling Machine, Make: Energy Machine Tool Pvt. Ltd. Jamnagar, India Model: RDH 32/930, Machine No: 9903112
Tool Holder	R/L265,2-125ME-20AL(Sandvik)
Cutting Tool	HSS twist drill, Make: Addison & Co. Ltd., Chennai, India Diameter:12mm,16mm
Job Material	AISI316StainlessSteel(0.07%C,2.0%Mn,16.5%/Cr,1.0%Si, 2.25%Mo, 8.0%Ni, 0.04%P, 0.11%N, Remaining is Fe with some impurities)
Machining condition	✓ Drill Diameters: 12 mm and 16 mm. ✓ Cutting Velocity: 280 m/min and 560 m/min. ✓ Feed: 0.032, 0.05 and 0.08mm/rev. ✓ Environment: Dry and Refined soyabean oil Condition.

Table 2. Observation of burr thickness with 14m/min, 21 m/min and 28m/min Vc in Dry condition and Refined Soya bean Oil Condition

Expt. Sl. No.	Drill Diameter (mm)	Cutting velocity (m/min)	Feed (mm/rev)	Observation of burr	
				Average Burr Thickness (mm) for Exp. Set-I	Average Burr Thickness (mm) for Exp. Set-II
1	16	14	0.032	0.44	0.40
2			0.05	0.72	0.26
3			0.08	0.46	0.55
4	12	21	0.032	0.31	0.33
5			0.05	0.44	0.31
6			0.08	0.36	0.15
7	16	28	0.032	0.44	0.36
8			0.05	0.34	0.39
9			0.08	0.44	0.31

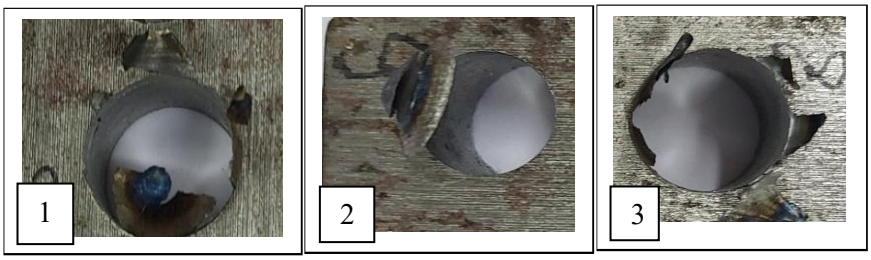

Fig. 4. Different types of Exit burrs bserved with Vc of 14m/min (1 for 16 mm drill bit), Vc of 21 m/min (2 for 12 mm drill bit) and Vc of 28 m/min (3 for 16 mm drill bit) in Expt. Set-I..

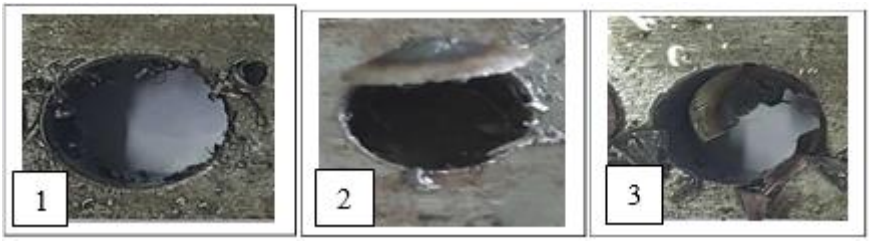

Fig. 5. Different types of Exit burrs observed with Vc of 14 m/min (1 for 16 mm drill bit), Vc of 21m/min (2 for 12 drill bit) and Vc of 28m/min (3 for 16 mm drill bit) in Refined Soyabean Oil Condition in Expt. Set-II.

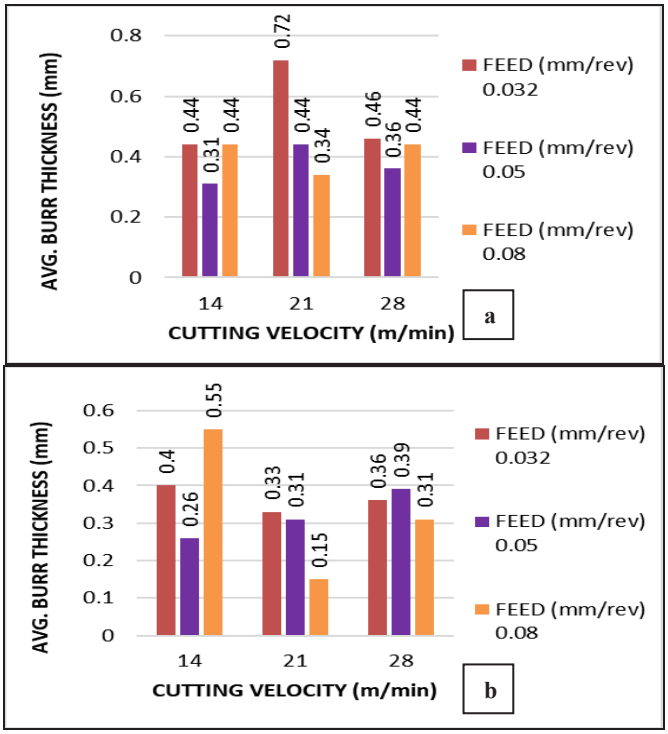

Fig. 6. Variation of average burr thickness (a) with cutting velocity at varying feed in dry environment and (b) with cutting velocity at varying feed in refined soya bean oil environment.

4 Results and Discussion

4.1 Discussion on the Observation on variation of Drilling Burr Thickness at Dry Condition (Set-I) and Refined Oil Condition (Set-II) with cutting velocity

Experimental results are presented in Table 2 for experiment Set-I (in dry condition) and experiment Set-II (in refined soya bean oil condition) as shown in Fig 5(a) & 5(b). From Fig. 5(a), variation is noticed as the average burr height boosts with boost in cutting velocity at varying cutting feed observed at drill with a diameter of 16 mm and a 12 mm drill bit which is used for drilling holes with cutting velocity of 14 and 21 m/m in respectively, but there is no trend observed for cutting velocity of 28m/min in both of the cases. However, for 16 mm of drill diameter, average burr height minimizes with rise in cutting velocity of 14 and 21 m/min correspondingly at varying feed but again trend is set for cutting velocity which increases for 28 m/min.

It is observed from Fig. 5(b) as growth is being observed for mean burr height with surge in feed at varying feed observed at drill diameter of 16 mm with cutting velocity of 14m/min and a trend is observed at 21 m/min where it decreases and again increases for cutting velocity of 28m/min. For the drill bit of 12mm with cutting velocity of 21m/min, change is observed as average burr height rises with rise in cutting velocity. However, drill diameter of 16 mm with cutting velocity of 28m/min where the average burr height immensely decreases with cutting velocity of 21m/min but again trend is set at 28 m/min where the value slightly increases.

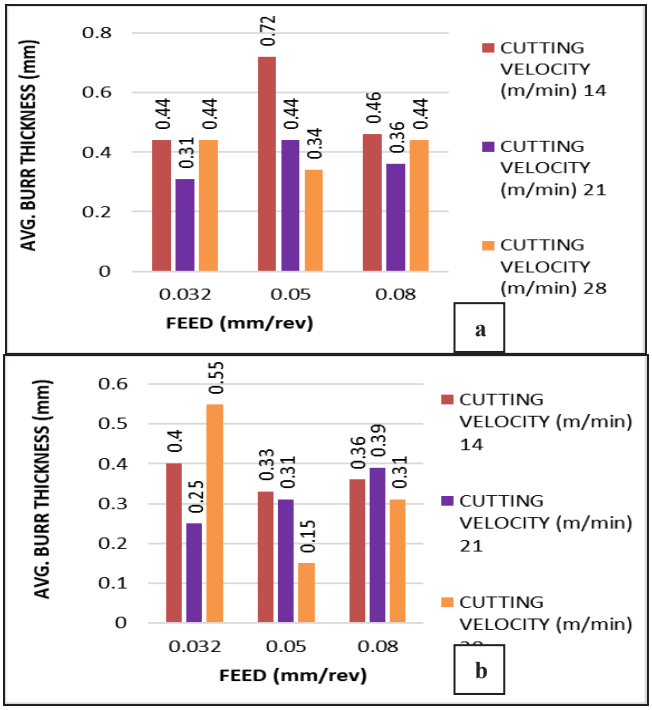

Fig. 7. Variation of average burr thickness (a) with feed at varying cutting velocity in dry environment and (b) with feed at varying cutting velocity in refined soya bean oil environment.

4.2. Discussion on the Observation on variation of Drilling Burr Thickness at Dry Condition (Set-I) and Refined Oil Condition (Set-II) with feed

Experimental results are presented in Table 2 for experiment Set-I (in dry condition) and experiment Set-II (in refined soya bean oil condition) as shown in Fig 6(a) & 6(b). From Fig. 6(a) variation is seen as the average burr height rises with rise in feed at varying cutting velocity observed at 16 mm of drill diameter with a cutting velocity of 14m/min and for drill bit which make 12 mm diameter with a cutting velocity of 21m/min at 0.032 and 0.05mm/rev feed respectively but there is no trend observed for feed of 0.08 mm/rev in both of the cases. However, for drill with a diameter of 16mm with a cutting velocity of 28m/min, reduction in average burr height with increase in feed of 0.032, 0.05 mm/rev respectively at varying cutting velocity is being observed but for feed of 0.08mm/rev where it increases.

It is noticed from Fig. 6(b), variation is seen as the mean burr height rises with rise in feed at varying cutting velocity, is observed at ϕ16 mm with cutting velocity of 14m/min, and a trend is observed for 0.05 mm/rev where it decreases and again increases for feed of 0.08mm/rev. For diameter of drill is12mm with cutting velocity of 21m/min, there is upsurge observed for average burr height with up surge in feed. However, drill diameter of 16 mm with a speed of 560 rpm, the average burr height immensely decreases feed at 0.05 mm/rev but again trend is set for feed which slightly increases at 0.08mm/rev.

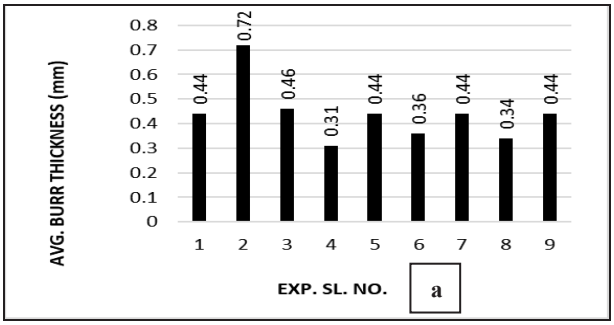

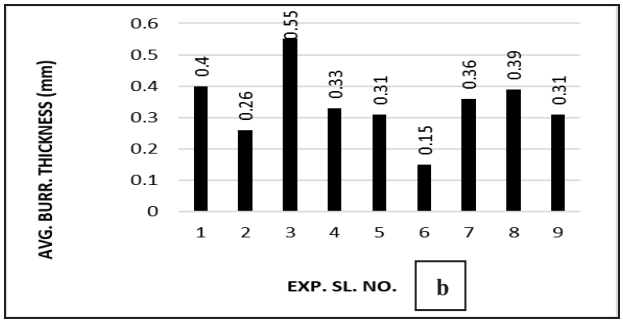

Fig. 7. Variation of average burr thickness (a), and (b) with maximum and minimum deviation in dry and refined soya bean oil environment.

4.3 Discussion on the Observation on variation of Drilling Burr Thickness with maximum and minimum deviation at Dry Condition (Set-I) and Refined Oil Condition (Set-II)

Observation on burr thickness with respect to maximum and minimum in dry Condition (Set-I) is presented in Fig. 7(a) and values are taken from Table 2. Variation of burr thickness is noticed at 16 mm drill bit is used for drilling holes with cutting velocity of 14m/min, drill diameter of 12mm with cutting velocity of 21m/min and drill diameter of 16 mm with cutting velocity of 28m/min of 0.032,0.05,0.08mm/rev feed respectively. The variation for each value with the average burr thickness was found to be within the range of 0.31-0.72mm. It is observed in case of diameter of drill at 16 mm with cutting velocity of 14m/min where average thickness of burr is maximum at 0.05 mm/rev. The maximal value is obtained in experiment 2 as 0.72 and the least value is obtained in experiment 4 as 0.31.

Experiment Set-II is conducted in refined soya bean oil condition. The experiment results are plotted in Fig.7(b) showing the burr thickness with respect to maximum and minimum values. Variation is found as ϕ16mm with cutting velocity of 14m/min, drill bit of 12mm with cutting velocity of 21m/min and diameter of drill 16 mm with cutting velocity of 14m/min at 0.032, 0.05, 0.08 mm/rev feed respectively. Variation for each value with average burr thickness was found to be within the range of 0.15 – 0.55mm. It is observed in case of ϕ16 mm with cutting velocity of 14m/min the average thickness of burr is maximum at 0.08mm/rev. The maximal value is obtained in experiment 3 as 0.55 and the minimize value is obtained in experiment 6 as 0.15.

5 Conclusions

From the experimental results, it is observed that the minimum burr thickness of 0.26 mm is observed at a cutting velocity, 14 m/min with the use of 16 mm drill bit under refined soya bean oil condition. Therefore, it can be stated that with the use of 16 mm drill bit with refined soya bean oil condition, remarkable reduction in burr thickness can be obtained. With the use of refined soya bean oil as llubricant, remarkable reduction in size of burr is achieved with compared to that dry condition. Lubricant can reduce the formation of burrs (plastically deformed material adhered to the entry/exit edge of the workpiece) by reducing the compressive stress and heat produced in the cutting zone. As the temperature of the material rises due to machining, it becomes more malleable and forms chips, which can affect the size of the burr. That is why the burr formed during the use of lubricant is becomes less.

References

[1] Varatharajulu, M., Loganathan, C., Baskar, N.: Influence of Cutting Parameters on Burr Height and Burr Thickness in Drilling of Duplex 2205 Using Solid Carbide. International Journal of Chem Tech Research, 8(2), 768-777(2015).
[2] Chang, S.S.F., Bone, G.M.: Burr Size Reduction in Drilling by Ultrasonic Assistance, robotics and Computer Integrated Manufacturing. 21, 442-450, (2005).
[3] Sathiyamurthy, S., Ramamoorthy M.: Dynamic Analysis of Drilling Burr Formation Process. 5, (2016).
[4] Mangla, S. K., Kumar, D.: Operational Modelling for Optimizing Burr Height in Mild Steel Drilling Using Taguchi Technique. 2, (2012).
[5] Kim, J., Dornfeld, D.A: Development of an Analytical Model for Drilling BurrFormation in Ductile Materials. Journal of Engineering Materials and Technology, 124, (2022).
[6] Kim, H., Lee, S. H.: Prediction of Burr Types in Drilling of Al-7075 Using Acoustic Emission and Convolution Neural Networks. IEEE Access,10, (2022).
[7] Lee, K., Dornfeld, D.A.: Micro-Burr Formation and Minimization through Process Control, Precision Engineering. 246-252, (2005).

[8] Abdelhafeez, A.M., Soo, S.L., Aspinwali, D.K., Dowson, A., Arnold, D.: Burr Formation and Hole Quality when Drilling Titanium and Aluminium Alloys, Procedia CIRP. 37, 230-235, (2015).
[9] Dornfeld, D., Min, S.: A Review of Burr Formation in Machining, Laboratory for Manufacturing and Sustainability. DOI 10.1007/978-3-642-00568-8_1, (2010).
[10] Ko, L., Changa, J.E., Yang, G.E.: Burr Minimizing Scheme in Drilling, Journal of Materials Processing Technology. 140, 237-242, (2003).
[11] Gaitonde,V.N.,Karnik,S.R.,Achyutha,B.T.:MethodologyofTaguchiOptimizationfor Multi-Objective Drilling Problems to Minimize Burr Size, International Journal of Advance Manufacturing Technology. 34, 1- 8, (2006).
[12] Kim, J., Min, S., Dornfield, D.A.: Optimization and Control of Drilling Burr Formation of AISI304L and AISI4118 Based on Drilling Burr Control Charts, International Journal of Machine Tools & Manufacture. 41, 923- 936, (2001).
[13] Gaitonde, V.N., Karnik, S.R., B. Siddeswarappa, B.T. Achyutha: Integrating Box- Behnken Design with Genetic Algorithm to Determine the Optimal Parametric Combination for Minimizing Burr Size in Drilling of AISI 316L Stainless Steel, International Journal of Advance Manufacturing Technology. 37, 230-240, (2008).
[14] Biermann, D., Hartmann, H.: Reduction of Burr Formation in Drilling Using Cryogenic Process Cooling, Institute of Machining Technology. 3, 85-90, (2012).
[15] Avila, M.C., Choi, J., Dronfield, D.A: Deburring of Cross-Drilled Hole Intersections by Mechanized Cutting, International Conference on Deburring and Edge Finishing, University of California, Berkeley. 379- 389, (2004).
[16] Toropov, A., Ko, S.L., Kim, B.K: Experimental Study of Burrs Formed in Feed Direction when Turning Aluminium alloy Al6061-T6, International Journal of Machine Tools&Manufacture.45,1015–1022, (2005).
[17] Heisel, U, Schaal, M:Burr Formation in Intersecting Holes, Production Engineering Research and Development. 2, 55-62, (2008).
[18] Ko, S.L., Lee, J.K: Analysis of Burr Formation in Drilling with a New Concept of Drill, Journal of Material Processing Technology. 113, 392-298, (2001).
[19] Bakkal, M., Shihb, A.J., McSpadden, S.B., Liu, C.T., Scattergood, R.O.: Light Emission, Chip Morphology and Burr Formation in Drilling the Bulk Metallic Glass, International Journal of Machine Tools & Manufacture. 45, 741-752, (2005).
[20] Mondal, N., Sardar, B. S., Halder, R. N., Das, S.: Observation of Drilling Burr and Finding out the Condition for Minimum Burr Formation, International Journal of Manufacturing. Article ID 208293,(2014).
[21] Mondal, N., Mandal, S., Chandra, M. M., Das, S., Halder, B.: Intelligent Methods and Systems in Production Engineering, 335, 180-195, (2022).
[22] Mondal, N., Mandal, M.C., Dey, B., Das, S.: Journal of Engineering Manuf., 234 (5), 956-968, (2020).
[23] Pratim, S. P., Das, S.: Burr Minimization in Face Milling: an Edge Bevelling Approach, Proceedings of the Institution of Mechanical Engineering B: Journal of Engineering Manufacture, 225 (9), 1528-1534, (2011).
[24] Saha, P.P., Das, S.: An Investigation on the Effect of Machining Parameters and Exit Edge Bevelling on Burr Formation in Milling, Journal of Mechatronics and Intelligent Manufacturing, 2 (1/2), 73-84, (2011).
[25] Roy, K., Mukherjee, P., Hansda, U.K.: An Experimental Investigation on Drilling Burr Formation, In Proceedings of Poster Presentation of the 3rd International and 24th AIMTDR Conference, Visakhapatnam, India, 211-216, (2010).
[26] Kim, H., Lee, H.: Prediction of Burr Types in Drilling of Al-7075 Using Acoustic Emission and Convolution Neural Networks, IEEE Access, 10, (2022).
[27] Gillespie, Bolter, P.T. : The Formation and Properties of Machining Burrs, ASME J., Engineering India, 98(1), 66-74, (1976).
[28] Pilny, L., Chiffre, L.D., Piska, M., Villumsen, M.F.: Hole Quality and Burr Reduction in Drilling Aluminium Sheets, Technical University of Denmark, Department of Mechanical Engineering, Kgs. Lyngby, Denmark, (2011).
[29] Schein, H.: Electrochemical Deburring, Technical Paper, Society of Manufacturing Engineers, 77-451, (1977).
[30] Aurich, J.C., Dornfeld, D., Arrazola, P.J., Franke, V., Leitz, L., Min, S.: Burrs Analysis Control and removal, CIRP Annals-Manufacturing Technology, 58, 519-542, (2009).
[31] Sreenivasulu, Srinivasa Rao, C. : Overview on Burr Formation, Simulation and Experimental Investigation of Burr Size-Based on Taguchi Designs of Experiments during Drilling of Aluminium 7075 Alloy, AKGEC, International Journal of Technology, 7(1), (2015).

Analysis of the performance of laser cutting on ceramic tiles based on TLBO technique

Rupam Rakshit*[1], Swarajit Pal[1], Paramasivan K[1], Pankaj Keshari[1], Subhash Chandra Panja[1], Dipten Misra[1]

[1] School of Laser Science and Engineering, Jadavpur University, Kolkata, India, 700032

*Corresponding author email: rupambiet91@gmail.com

Abstract. Excellent durability, strength, hardness, wear resistance, chemical stability, electrical and thermal insulation make ceramics a suitable choice in aerospace, automotive, and electronics industries. Machining of ceramics using conventional processes is very difficult due to its hardness and brittleness. Laser beam machining is a preferred technique to cut ceramics as it is a non-contact, thermal energy-based machining process. In this paper, laser cutting process of 7 mm thick ceramic glazed floor tile is experimentally investigated. Laser power, scanning speed, pulse frequency and assist gas pressure have been taken as process parameters to explore their effects on top kerf width and machining cost. Response surface methodology (RSM) based on Central composite design (CCD) has been adopted in the design of experiment. Based on experimental results, regression equation with analysis of variance (ANOVA) have been developed. Teaching Learning based optimization (TLBO) technique has been used to find the optimum conditions of the response, i.e. top kerf width. This work shows that lowest value of machining cost and top kerf width can be reached with the combination of lower power and higher gas pressure, frequency, and scanning speed.

Keywords: Fiber laser cutting, ceramic tiles, response surface methodology, Teaching Learning based optimization, machining cost, top kerf width

1 Introduction

Tool wear, complex shape manufacturing limitations, low dimensional accuracy, etc., pose some restrictions for conventional machining processes which lead to development of non-conventional machining or advanced machining processes like electro-discharge machining, beam machining process (laser beam machining, electron beam machining), jet machining process (water jet machining, abrasive jet machining, abrasive water jet machining), chemical machining process, electrochemical machining process, although each of these non-traditional processes has some limitations regarding material selection, sample dimension, etc [1]. Laser beam machining (LBM) is a thermally induced process where required materials can be removed with a high energy density laser beam focused on the job surface. The material removal process is achieved by the irradiation of the workpiece with the cutting source remaining at a distance and so absence of mechanical cutting force is responsible for generating zero tool wear, machine vibration, and machine noise. Materials are degraded by melting and vaporization processes in the LBM process. The quality of cutting by laser depends more on the optical and thermal properties of the workpiece than its mechanical properties. The cutting process is sustained through an energy balance between thermal conduction, incident laser energy and energy loss from the job to the surrounding. There are a variety of laser sources; however only CO2 and Nd:YAG lasers are extensively used for machining purposes. High-power fiber lasers can be utilized for the requirement of high peak value in varied applications. Fig. 1 represents a schematic of a laser cutting process.

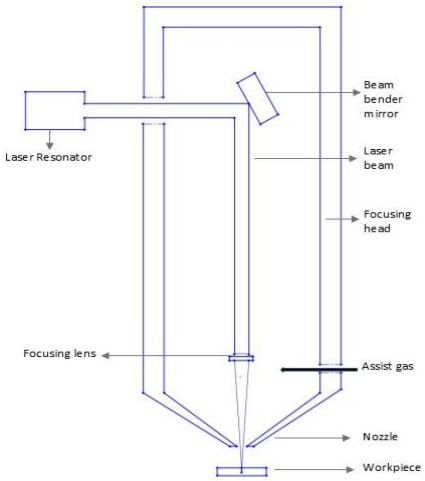

Fig. 1: Schematic of a laser cutting process

The laser after passing through the lens, is focused onto the workpiece. There is no requirement for a tool as it is a non-contact machining operation. The use of assist gases like nitrogen, oxygen, argon, etc. has great advantages like swiping away the debris from contact zone, minimizing the heat around the laser head, sometimes enhancing the cutting process through an exothermic reaction, protect the lens from back spatter and gas plume. Numerous investigations have been conducted in the field of laser machining to explore the effects of process parameters on machining quality. Haddadi et al. [2] used a CO2 laser for cutting polystyrene sheets of 3 mm thickness. They stated that increasing the laser power & velocity can minimize the heat-affected zone, also a covering gas is required to control the HAZ in laser-based cutting work. The cutting velocity is the most significant factor deciding the angle of cut and the ratio between top & bottom kerf widths. The optimized outcomes of this work were a laser power of 60 W and cutting velocity of 14 mm/sec. Moradi et al. [3] numerically studied the CO2 laser cutting process on a 3.2 mm thick polycarbonate sheet in terms of kerf taper, heat-affected zone, ratio of upper to lower kerf width by varying laser power, cutting speed, focal length with a constant assist gas pressure of 3 bar. They found that by decreasing laser power from 50 W to 20 W and increasing scanning speed from 4 mm/sec to 20 mm/sec, the HAZ is minimized and to reduce the kerf, the cutting speed was maintained at 20 mm/sec. Girish and Pandey [4] studied the teaching learning based optimisation technique which was used for machining of 1.25 mm Kevlar-29 fiber-reinforced polymer composite sheet with the help of an Nd:YAG laser. The input parameters were lamp current, pulse width, pulse frequency, air pressure, and cutting speed. The analysis demonstrates that cutting speed has a 52% contribution to the deviation of top kerf whereas lamp current has a 47% contribution to deviation of bottom kerf. Naresh and Khatak [5] have presented a work about the CO2 laser cutting of thermoplastic polymers, metal sheet cutting, polypropylene (PP), and polycarbonate (PC) by varying material thicknesses. They studied the effect of different input parameters such as scanning speed, pulse frequency, gas pressure, etc. on dross formation, severance energy, kerf width, and surface roughness. FEA, quality management, and software nesting also have been used to make cost-competitive products. Muangpool and Pullteap [6] stated a review work on the application of laser technology for industrial purposes. Precision with speed and ensuring quality end-product are some impressive advantages in this technology. They suggested a few measures, such as spreading awareness regarding beneficial aspects of laser machining, incentives through tax benefits, research collaboration with industries, as means for promotion of laser as machining tool. Quintero et al. [7] presented a theoretical model for pulsed laser cutting of ceramics. Ejection of molten material due to assist gas and recoil pressure and liquid material evaporation was investigated. At the end of the work, proposed theoretical model was validated and it was concluded that pulse length and frequency have significant effects on the cutting process.

As can be seen from the literature review that only a limited number of works on laser machining of ceramic tiles have been carried out so far, and there no published literature based on total cutting cost analysis of ceramic tiles. In this sense, top kerf width and a detailed machining cost analysis based on laser cutting of ceramic tiles have been investigated and regarding outcomes, a parametric optimization has been performed to find out the optimum combination of operating parameters (power, frequency, scanning speed, gas pressure) for a low-cost laser cutting of ceramic tile.

2 Experimental Framework

Ceramics are inorganic, crystalline, non-metallic, hard, amorphous materials, thermally stable at high temperatures, less dense than metals, brittle, more elastic than metallic conductors, and have a high melting point, including excellent electrical and thermal insulation properties. The excessive temperature gradients that occur during laser machining may create cracking due to thermal stress generation. Excellent thermal properties make laser a prominent choice in the machining process.

Experimental analysis of laser cutting on ceramic tile has been carried out and for experimentation purposes, a fiber laser (RFLC500/B/15/W, Make: Mehta Cad Cam Systems) with 50 µm laser spot diameter at focus, maximum power 500 W, and a wavelength of 1080 nm has been used. A 7 mm thick glazed ceramic tile has been chosen to cut. 0.6 mm distance between the workpiece and laser output nozzle and 20 ms piercing time has been taken as fixed during experimentation. During machining, an 8 mm gap is maintained between each cutting channel so that there is no overlap of thermal effects of each cutting zone [8]. The input process parameters have been taken as power (380 to 430 W), scanning speed (2 to 4 mm/s), gas pressure (8 to 12 bar), and frequency (300 to 650 Hz) for the study. Central composite design (CCD) based response surface methodology (RSM) has been used to generate the design of experiment (DOE) and it is furnished in Table 1. ZEISS Stemi 508 stereo microscope has been used to explore and measure the top kerf width of the machined surface. As per DOE, 30 numbers of experiments have been performed.

3 Results and Discussions

The effect of top kerf width, which is top surface width of the cut, and the total machining cost for every machined sample, has been investigated and taken as responses.

Table 1. Designed layout with experimentally obtained responses

No.	Laser power (W)	Scanning speed (mm/s)	Gas pressure (bar)	Pulse frequency (Hz)	Top kerf width (μm)	Machining cost (Rupees)
1	440	3	10	475	109.895	45.42
2	405	3	12.8	475	70.795	48.70
3	430	2	8	650	108.297	59.88
4	380	2	12	300	96.033	67.80
5	430	2	8	300	114.793	59.88
6	430	2	12	650	100.715	68.07
7	405	3	10	720	73.122	45.29
8	430	4	12	300	88.617	38.20
9	380	2	8	300	95.134	59.60
10	380	2	12	650	90.109	67.80
11	405	1.6	10	475	106.783	77.63
12	380	4	8	300	80.891	33.97
13	380	4	12	300	72.892	38.06
14	370	3	10	475	85.073	45.16
15	380	4	8	650	73.274	33.97
16	405	3	10	475	85.326	45.29
17	405	3	10	475	86.421	45.29
18	405	3	7.2	475	81.988	41.20
19	405	3	10	230	96.939	45.29
20	405	3	10	475	85.717	45.29
21	405	3	10	475	85.716	45.29
22	430	4	8	650	100.143	34.10
23	380	2	8	650	95.184	59.60
24	405	4.4	10	475	76.203	33.53
25	405	3	10	475	87.329	45.29
26	380	4	12	650	68.413	38.06
27	430	4	12	650	82.027	38.20
28	430	2	12	300	108.739	68.07
29	430	4	8	300	106.834	34.10
30	405	3	10	475	88.457	45.29

3.1 Machining cost

Cost calculation is an important aspect of an engineering work and performing the laser cutting process at low cost can be a significant task. Machining efficiency, machining time per job, energy cost, manpower cost, and gas cost have been explored to calculate the machining cost for each job. 1000 mm cut length has been considered to conduct this cost calculation. The maximum efficiency of this fiber laser cutting system has been taken as 25% [9]. Electricity bill per unit has been assumed as 10 Rs. per unit and it can be varied based on electricity supply agency. Manpower cost per hour for performing the operation has been considered as 240 Rs. per job [10]. Energy

cost, total manpower cost, gas cost has been calculated by generating the equation 1, 2, and 3 respectively. Nitrogen gas cylinder with 51 kg capacity has been used to perform the operation and the cost of each cylinder has been taken as 500 Rs. based on telephonic survey and it can be varied as per supplier. The calculated values of machining cost respect to each process parameters have been furnished in Table 1.

Energy cost = [Laser power ÷ machine efficiency] X machining time X per unit electricity cost (1)

Total manpower cost = Manpower cost per hour X machining time (2)

Gas cost = [Gas flow per hour X machining time] X [500 ÷ 51] (3)

3.2 Top kerf width

Top of the kerf width has been measured with the help of above-mentioned microscope. The values of the top kerf width have been given in Table 1. From the given Table it has been observed that 68.418 µm was the minimum top kerf width which was generated at the combination of 380 W power, 4 mm/s scanning speed, 12 bar gas pressure, and at 650 Hz frequency.

After measuring the top kerf width, a parametric analysis was performed. Fig. 2 illustrates graphically how process variables affect the response. Process parameters are represented on x-axis and top kerf width values are shown on y-axis. An upward trend was observed for laser power (P) while a decreasing trend was seen for scanning speed (SS), gas pressure (GP), and pulse frequency (f) of the main effect plot with increasing of top kerf width. At higher laser power, more incidence energy was delivered on the workpiece which developed a high material removal rate. Top kerf width dropped as scanning speed increased because faster scanning resulted in less contact time, or lower surface energy absorption and a drop-in temperature. This graph indicated that the gas pressure first helped to increase the kerf width on the upper surface until it reached a limit, after which it started to decrease as the gas pressure increased. Initially, gas pressure helped to build up more heat at the desired zone, which had a favorable effect up to a certain point. Once the limit was reached, increased gas pressure aided in reducing the heat conduction of the melted material and resulted in narrowed top kerf width. As the frequency of the laser pulse increased, its off-time became very short and because of this, the molten material had less time to solidify, resulting in a lower kerf width which has been presented in this main effect plot.

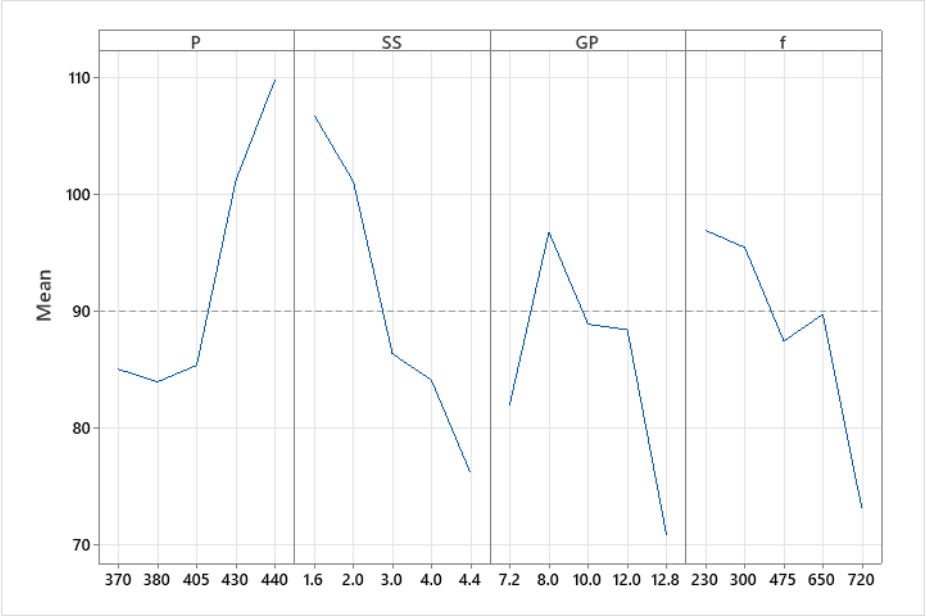

Fig. 2. Main effects of process variables on top kerf width

To quantify the effects of these parameters and determine their statistical significance, regression analysis and Analysis of Variance (ANOVA) were performed.

Regression Analysis and ANOVA results: The relations between the process parameters and the response, i.e. top kerf width has been evaluated in the form of second-order regression equation. MINITAB®18 has been used to develop and validate the equation. The equation regarding kerf width has been presented in equation 4. Regression equation is valid within the range of parameters considered in the present study. Analysis of variance (ANOVA) test has been done to explore the influence of the independent variables on the dependent variable. Table 2 furnished the ANOVA results for the top kerf width which justified the significance of the results. P, SS, GP, and f of these equations are represented as laser power, scanning speed, gas pressure, and pulse frequency respectively.

The regression equation of top kerf width,

$$1551 - 8.08 * P - 46.7 * SS - 38.12 * GP + 0.0358 * f + 0.01075 * P^2 + 3.66 * SS^2 - 1.011 * GP^2 + 0.000012 * f^2 + 0.0652 * P * SS - 0.0412 * P * SS - 0.0412 * P * GP - 0.000140 * P * f - 0.981 * SS * GP - 0.00178 * SS * f - 0.00076 * GP * f \quad (1)$$

Table 2. Analysis of variance of top kerf width

Source	Sum of Squares	Degrees of freedom	Mean Square	F-value	p-value
Model	4644.54	14	331.753	28.83	0.000
P-Power	342.34	1	342.341	29.75	0.000
SS-scanning speed	96.99	1	96.986	8.43	0.011
GP-gas pressure	203.43	1	203.432	17.68	0.001
f-frequency	1.80		1.800	0.16	0.698
P*P	406.86	1	406.858	35.36	0.000
SS*SS	120.85	1	120.854	10.50	0.005
GP*GP	147.38	1	147.379	12.81	0.003
f*f	1.20	1	1.196	0.10	0.752
P*SS	42.47	1	42.468	3.69	0.074
P*GP	67.79	1	67.786	5.89	0.028
P*f	6.04	1	6.041	0.52	0.480
SS*GP	61.55	1	61.548	5.35	0.035
SS*f	1.55	1	1.552	0.13	0.719
GP*f	1.14	1	1.136	0.10	0.758
Error	172.60	15	11.507		
R^2= 0.96; Adjusted R^2= 0.93; Predicted R^2= 0.82					

.

3.3 Teaching learning based optimization

Teaching learning based optimization (TLBO), presented by Rao *et al.* [11], is an algorithm encouraged by teaching and learning process. The algorithm works in two modes: teacher mode and learner mode. This optimization is a population-based technique where learners of a class are considered as the population size and the different subjects taught in a class are referred to as design variables. The teacher is considered the best among the population and so the outcome relies on the quality of the teacher. The grades of the learners are considered as the output of the algorithm [12, 13].

This optimization technique has been used in this work to find out the optimum conditions where the desired values (small top kerf width and low machining cost) can be obtained. MATLAB-based single-objective TLBO code has been generated to perform this parametric optimization. The fitness values (response) for each of the iterations are plotted and presented in Fig. 3. The first ten iteration values of top kerf width and machining cost has been also furnished in Table 3. A total of 100 iterations have been carried out to find the optimum values. The optimized value of top kerf width is 53.52 μm at 390.01 W power, 4.4 mm/s cutting speed, 12.8 bar gas pressure and 720 Hz frequency.

Table 3. Results of first ten iterations for top kerf width

Iteration number	Laser power (W)	Scanning speed (mm/s)	Gas pressure (bar)	Pulse frequency (Hz)	Top kerf width (μm)
1	393.3495	4.4	12.8	438.6898	65.9989
2	376.4707	4.4	12.8	697.0553	55.8523
3	393.3129	4.1869	12.8	695.0385	54.5803
4	388.6841	4.2667	12.8	720	53.5832
5	390.0118	4.4	12.8	720	53.5202
6	392.1903	4.4	12.8	720	53.5202
7	391.3157	4.4	12.8	720	53.5202
8	391.6874	4.4	12.8	720	53.5202
9	391.6874	4.4	12.8	720	53.5202
10	391.6874	4.4	12.8	720	53.5202

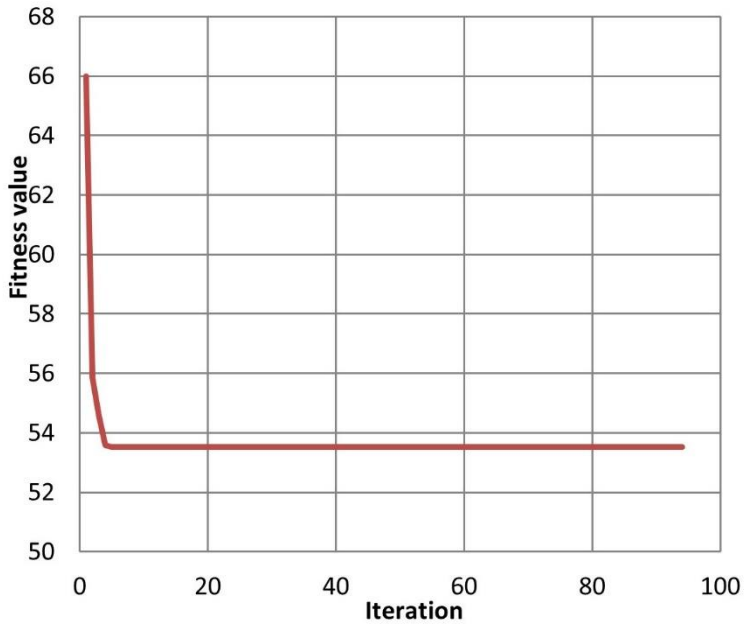

Fig. 3. Variation of Fitness Value over Iterations for top kerf width

4 Conclusions

In this work, a fiber laser machine has been used to cut a glazed ceramic tile to explore the effects of process parameters on top kerf width and machining cost. The cost of each cut has been calculated to explore the parametric values where the machining can be done under economic conditions. Laser power, frequency, scanning speed, and assist gas (nitrogen) pressure have been considered as variables. Teacher learner based optimization technique has been used in MATLAB to find out the optimized condition for the top kerf width. From this experimental work, the following points can be concluded:

- Laser power is the most significant parameter regarding top kerf width while frequency is the least significant factor within the range that has been considered.
- Lower value of top kerf width can be achieved when the laser power is at minimum but frequency, scanning speed, and assist gas pressure are set at their respective maximum. At lower power, the incident energy is less and at maximum scanning speed the interaction time between laser and workpiece is minimum leading to the lower kerf width. Maximum frequency results in minimum pulse off time which leads to less time for the molten metal to solidify, resulting in lower kerf width. Higher gas pressure means a lower rate of heat conduction from the molten metal to the adjacent solid which leads to a narrow kerf width.
- In terms of machining cost, the most important parameter is laser power and the least affected parameter is pulse frequency.
- The lowest value of machining cost can be reached with the combination of lower power and higher gas pressure, frequency, and scanning speed within the range. Laser power is directly proportional to the energy cost and at higher scanning speed, gas pressure and pulse frequency lead to a narrow kerf width at less time to complete the job, and the total cost is also directly proportional to the cycle time of machining.

References

1. Dubey, A. K., & Yadava, V. Laser beam machining - A review. International Journal of Machine Tools and Manufacture, 48(6), 609-628 (2008).
2. Haddadi, E., Moradi, M., Ghavidel, A. K., Ghavidel, A. K., & Meiabadi, S. Experimental and parametric evaluation of cut quality characteristics in CO2 laser cutting of polystyrene. Optik, 184, 103-114 (2019).
3. Moradi, M., Moghadam, M. K., Shamsborhan, M., Beiranvand, Z. M., Rasouli, A., Vahdati, M., & Bodaghi, M. Simulation, statistical modeling, and optimisation of CO2 laser cutting process of polycarbonate sheets. Optik, 225, 164932 (2021).
4. Gautam, G. D., & Pandey, A. K. Teaching learning algorithm basedoptimisation of kerf deviations in pulsed Nd: YAG laser cutting of Kevlar-29 composite laminates. Infrared Physics & Technology, 89, 203-217 (2018).
5. Khatak, P. Laser cutting technique: A literature review. Materials Today: Proceedings, 56, 2484-2489 (2022).
6. Muangpool, T., &Pullteap, S. Reviews on laser cutting technology for industrial applications. In Third International Conference on Photonics Solutions (ICPS2017) (Vol. 10714, pp. 184-191). SPIE (2018, March).
7. Quintero, F., Varas, F., Pou, J., Lusquiños, F., Boutinguiza, M., Soto, R., & Pérez-Amor, M. Theoretical analysis of material removal mechanisms in pulsed laser fusion cutting of ceramics.Journal of Physics D: Applied Physics,38(4), 655 (2005).
8. Kalvettukaran, P., Keshari, P., & Misra, D. Parametric study of laser cutting of glazed ceramic tiles. Journal of the Brazilian Society of Mechanical Sciences and Engineering,45(6), 333 (2023).
9. https://en.raycuslaser.com/upload/20210820/1fdgo1jo3734191vo.pdf.
10. https://www.hindcam.com/what-is-running-cost-of-metal-laser-cutting-machine.
11. Rao, R. V., Savsani, V. J., & Vakharia, D. P. Teaching–learning-based optimisation: a novel method for constrained mechanical design optimisationproblems.Computer-aided design,43(3), 303-315 (2011).
12. Pramanik, D., Singh, T., Roy, N., Biswas, R., Kuar, A. S., Sarkar, S., & Mitra, S. Analysis of performance characteristics with artificial intelligence based TLBO technique for laser drilling of Monel superalloy. Optics & Laser Technology, 164, 109554 (2023).
13. Tiwari, A., & Pradhan, M. K. Applications of TLBO algorithm on various manufacturing processes: AReview. Materials Today: Proceedings, 4(2), 1644-1652 (2017).

Study of Drilling Soda-lime Glass by Air-abrasive Jet using SiC Abrasive with Varying Impingement Angle

Deb Kumar Adak[1][0000-0001-7111-1267], Alakesh Maity[2][0009-0008-1328-5566] and Saikat Jana[3][0009-0004-0989-0713]

[1,2,3] College of Engineering and Management, Kolaghat, Purba Medinipur, West Bengal, India, PIN-721171.
debkumaradak1968@gmail.com

Abstract. Industries always face challenges to manufacture goods using difficult-to-conventional-machine materials with difficult shape maintaining required dimensional accuracy. In this situation, a non-traditional machining process such as Abrasive Jet Machining (AJM) seems to be used effectively. Moreover, development of such working setup at lower cost will be a good choice for industrial applications. Abrasive jet has diversified applications during pre-processing, main processing and post-processing of certain product through machining. The present work aims at effective abrasive jet drilling of soda-lime glass material used extensively among different glass materials. Due to better erosion machining, silicon carbide is used as abrasive. Objectives of this study are to find out the ranges of input parameters to have optimum process response such as material removal rate (MRR). Three process input parameters i.e., stand-off distance (SOD), abrasive grain size and impingement angle of nozzle with work-piece, in three levels at a constant 8 kg/cm^2 system pressure are used to observe MRR. Regression equation is found out from analysis of variance (ANOVA) to check the experimental model adequacy. Design of experiments (DOE) is obtained from Box-Behnken design technique of response surface methodology (RSM) with Minitab software.

Keywords: Abrasive jet machining, response surface methodology, Impingement angle, Regression equation.

1 Introduction

In manufacturing sector, some of the machining/ micro machining operations are still very conveniently be done with one of the advanced machining processes e.g., air abrasive jet machining due to its low-cost, simple operating principle. Abrasive grains ejected from nozzle are made to strike on work piece with high velocity at certain impingement angle. Jet of abrasive grains is formed with compressed air or gas mixed with suitable type and size of abrasive particles when allowed to pass through a converging nozzle [1]. Thus, high velocity stream of abrasives is generated [2]. With respect of work-piece, direction of abrasive is controlled either by tilting nozzle or work-piece with certain impingement angle. Abrasive grains with high velocity when strikes on work piece, material is removed in tiny chips by micro-abrasion action as well as by brittle fracture from work-piece as shown in Fig. 1 [3]-[5]. Abrasive jet is used for multiple applications in manufacturing industry. It is used for surface preparation, cleaning, etc., as pre-processing; drilling, cutting, surface hardening, etc., as main processing and as post-processing like, hard surface removal of cast surface, dry polishing, deburring etc. [6]. It is reported, abrasive jet machining (AJM) is practiced in Germany as early as from 1931 using dust suspended in smoke. In AJM, a localized force is applied, resulting in less heat generation compared to traditional machining processes [7].

Earlier erosion models were developed from the assumption that the volume of material removed by a single particle is proportional to the cylindrical volume obtained by radius of lateral crack (c) and its depth (h), as shown in Fig. 2 [8]. Compared to conventional machining, no shear stress and heat are generated both on work piece and cutting tool. Absence of thermal distortion is usually experienced in AJM in contrast to PAM (plasma arc machining) and LBM (laser beam machining). On the other hand, [9] - [11] provided hot abrasive air jet to machine variety of ceramic materials, polymeric materials as well as metallic materials. Alumina and silicon carbide abrasives were widely employed in AJM [12]. An effective dust-collecting system is used for smooth operation of AJM and it minimises environmental pollution issues [13-16]. Based on work piece material, abrasive particles are chosen and various machining parametric effects on required surface roughness are observed [17 &18]. Application of AJM can not be avoided for effective surface roughening, surface finishing with close dimensional tolerance corrosion removing etc. Replacing carrier medium with water i.e., water abrasive jet machining also plays an important role in advanced machining process.

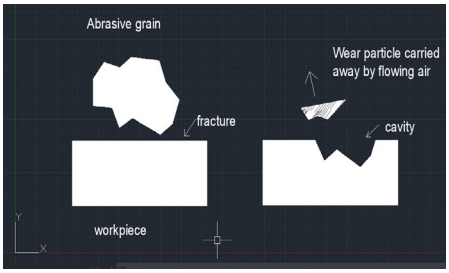

Fig. 1. Material removal in AJM [2]

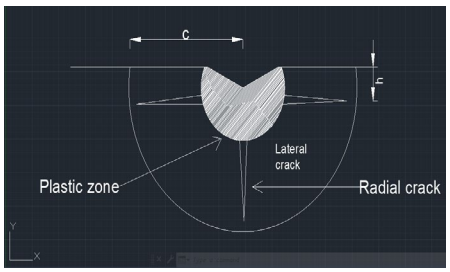

Fig. 2. Crack developed with indenter [8]

One of the purposes of this experiment is to develop a low-cost abrasive jet machining set up with dust proof machining chamber for machining materials like alumina, glass, tiles, other ceramic materials, which are otherwise difficult to machine. For this non-traditional machining process, machining chamber is important for minimising health hazard and work place pollution issues. Otherwise cost of presently available commercial AJM set up is high and added with costly nozzles.

As per literature, cost of this institute level fabricated AJM set up is only around 25-40% of commercially available similar setup. Average energy consumption for this non-traditional machining process is nominal, in terms of intermittent running cost of air compressor and a 0.5 hp AC motor. It is found, average consumption of SiC abrasive is 15-20 g/s. Minimum level of noise is associated with such as intermittent air compressor, small AC motor and abrasive jet. Jet sound is reduced by carrying out machining inside a machining chamber. Use of machining chamber reduces air-abrasive pollution level to a large extent. Through some filtering element, abrasive free air is allowed to pass to environment. Separated used abrasive is again reused after segregating in different sizes for additional machining purpose. For continuous operation statistical process control (SPC) can be incorporate for quality improvement, though the use of sensor system in abrasive rich surroundings is little bit difficult. ANOVA is being used to analyse process performance to find out best possible parametric combination so that optimum response is achieved. SEM is used in some of the work related to surface preparation in terms of average surface roughness for laser coating, thermal cladding etc., on advanced material like SS 316.

Objective of this work is to find out a suitable ranges of process variables during abrasive jet drilling operation on soda-lime glass so as to achieve desired MRR. Low-cost indigenously fabricated AJM set up with unique type of abrasive mixing chamber along with dust proof machining chamber is used as shown in Fig. 3 and Fig.4. Abrasive mass flow rate is measured effectively following a simple methodology. Measured quantity of SiC abrasive is allowed to strike alumina like hard material with definite system pressure and abrasive mixing chamber rotor rpm. Striking abrasive on alumina produces a light glow. Measuring the duration of light glow while machining, abrasive mass flow rate is calculated.

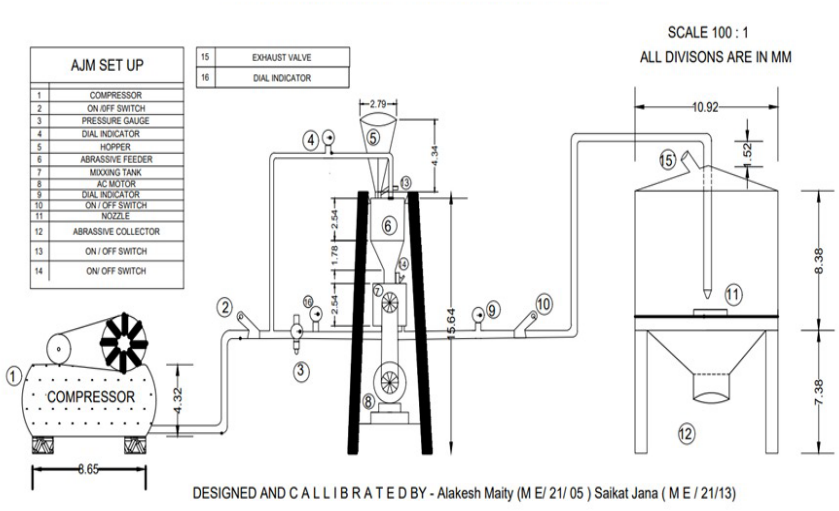

Fig. 3. Abrasive jet machining setup with machining chamber

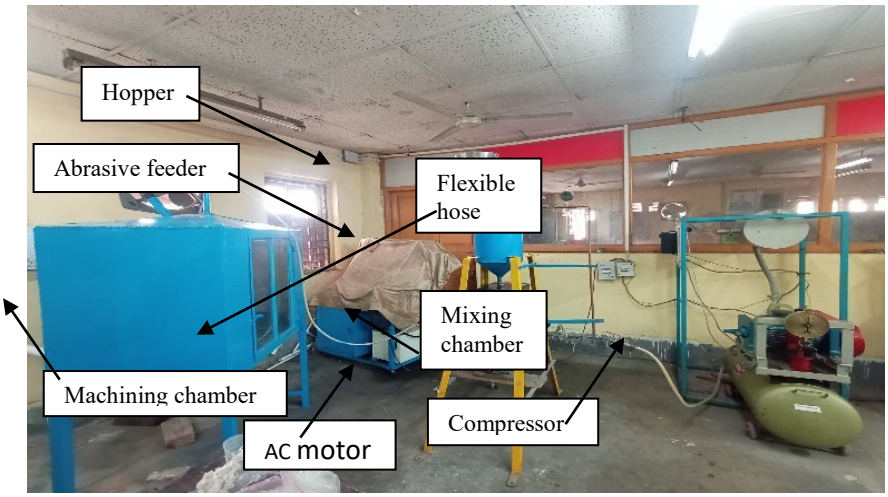

Fig. 4. Working abrasive jet machining setup with machining chamber

2 Experimental Procedure

AJM set up is used to carry out experiments on 2.57 mm thickness soda-lime glass. SiC with better cutting ability is used as abrasive particle. Three process parameters in three levels are decided for having DOE with the Box-Behnken design (BBD) strategies in RSM. Three levels of stand-off distance (SOD) are 3 mm, 5 mm and 7 mm. Three levels of abrasive grain sizes are 120µm, 185 µm and 250 µm. Similarly, three levels of impingement angle are 60˚, 75˚ and 90˚ shown in Table 1. As per DOE, 15 experiments are carried out. Detail of individual experimental run and their corresponding responses in terms of MRR are presented in Table 2. All the 15 experimental runs are carried out keeping system pressure constant at 8 kg/cm^2.

Fig. 5. Distance piece for ensuring SOD

For setting SOD properly, three distance pieces are prepared and shown in Fig. 5. Soda-lime glass sample machined with abrasive jet is shown in Fig. 6.

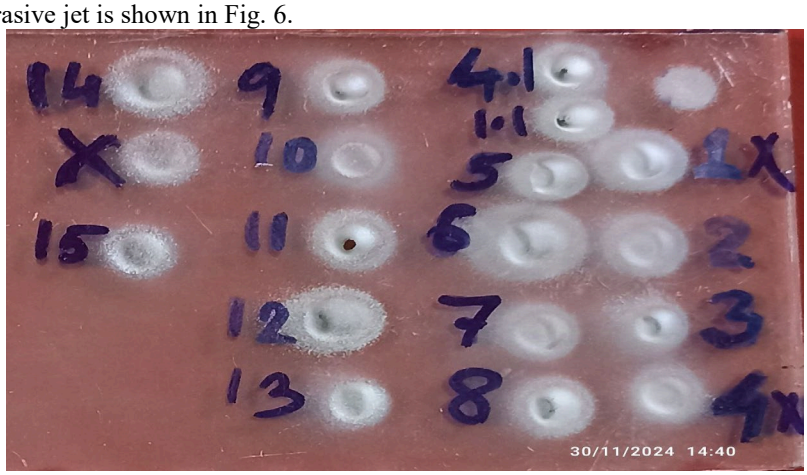

Fig. 6. Experimental sample

Table 1. Process parameters in their three level

Parameters	Lower level	Mid-level	Higher level
SOD (mm)	3	5	7
Impingement angle (˚)	60	75	90
Grain size (µm)	120	185	250

Table 2. Design of experiments with grain size, SOD and impingement angle and corresponding response as material removal rate (MRR)

Std Order	Run Order	Grain Size (µm)	SOD (mm)	Impingement angle	MRR (g/min)
1	3	120	3	75	0.789
2	8	250	3	75	1.25
3	2	120	7	75	0.678
4	5	250	7	75	2.469
5	13	120	5	60	0.743
6	11	250	5	60	2.163
7	1	120	5	90	0.814
8	4	250	5	90	1.423
9	14	185	3	60	0.935
10	15	185	7	60	1.98
11	10	185	3	90	0.583
12	7	185	7	90	1.467
13	12	185	5	75	1.41
14	6	185	5	75	0.597
15	9	185	5	75	1.319

3 Results and discussion

As per design of experiment, experiments are carried out. Response in terms of MRR is obtained and shown in Table 2. Analysis of variances (ANOVA) is performed with respect of MRR. For MRR, R-Sq value of 89.99% is obtained from ANOVA. This value is close to 90% signifies about adequacy of the experimental model.

Table 3. ANOVA for MRR at constant system pressure of 8 kg/cm^2

Source	DF	Adj SS	Adj MS	F-value	p-value
Model	9	4.42394	0.49155	4.99	0.046
Linear	3	3.73794	1.24598	12.66	0.009
Grain size d	1	2.29087	2.29087	23.28	0.005
Impingement angle Ɵ	1	0.29414	0.29414	2.99	0.144
SOD δ	1	1.15292	1.15292	11.71	0.019
Square	3	0.07287	0.02429	0.25	0.861
Grain size*Grain Size	1	0.04983	0.04983	0.51	0.509
Impingement angle *Implement angle	1	0.0137	0.0137	0.14	0.724
SOD *SOD	1	0.01896	0.01896	0.19	0.679
2 - Way Interaction	3	0.61314	0.20438	2.08	0.222
Grain size *Impingement Angle	1	0.16443	0.16443	1.67	0.253
Grain Size *SOD	1	0.44223	0.44223	4.49	0.088
Impingement Angle *SOD	1	0.00648	0.00648	0.07	0.808
Error	5	0.49212	0.09842		
Lack -of -fit	3	0.09527	0.03176	0.16	0.915
Pure Error	2	0.39684	0.19842		
Total	14	4.91606			

Individual, square or interactive parametric relationships are obtained in regression equation (1). Coefficient of each term in the equation signifies the relative share of contribution for achieving desired MRR.

MRR = 1.48 + 0.0009 Grain size - 0.362 SOD - 0.008 Impingement Angle
+ 0.000027 Grain size*Grain size + 0.0179 SOD*SOD
+ 0.000271 Impingement Angle*Impingement Angle + 0.00256 Grain size*SOD
- 0.000208 Grain size*Impingement Angle - 0.00134 SOD*Impingement Angle (1)

Significant parametric contribution towards process responses is judged with their corresponding least p-values. It is seen in ANOVA table, some of the terms such as model, linear, grain size, SOD, have p-values of 0.046, 0.009, 0.005, 0.019 respectively which are less than 0.05, and hence, are significant for MRR as shown in Table 3. Least p-value of lack of fit is 0.915. This signifies that fitness least p-value of the model is less than 10%. Therefore, fitness of ANOVA model is significant.

From ANOVA, effects of individual process parameters are shown in Fig. 7. Plots shows, MRR is increased with increase of grain size and SOD and decreased with impingement angle.

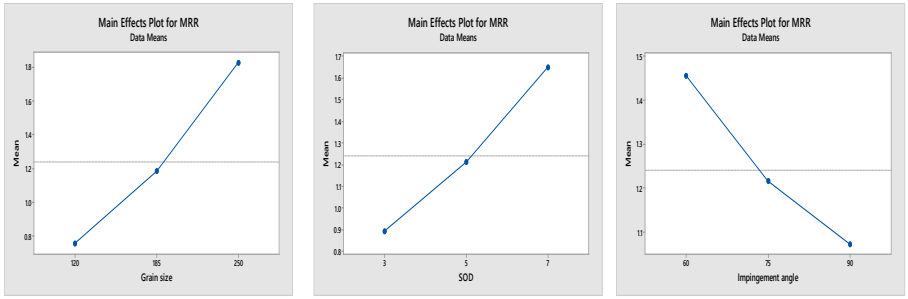

(A) (B) (C)

Fig. 7. Main Effects plot for MRR with (A) grain size (B) SOD (C) impingement angle

Relationship of MRR with interactive effects of input variables are shown in Fig. 8 through Fig. 10 in the form of contour and surface plot.

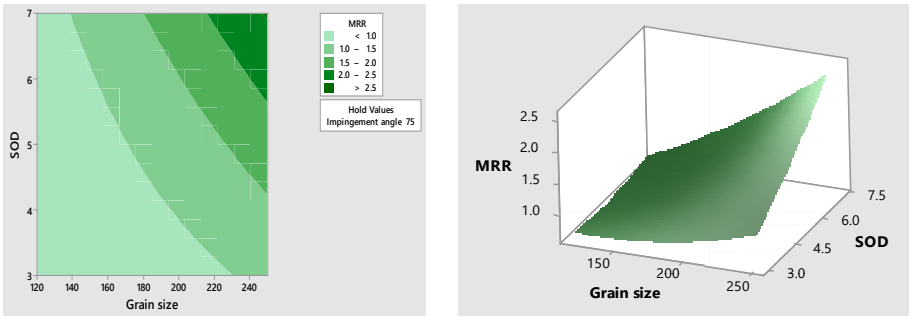

Fig. 8. Contour and surface plots of MRR vs. grain size and SOD at hold value of impingement angle 75 degree

In Fig. 8, MRR is increased with increase of grain size and SOD. As grain size is increased, mass of particle increases thus kinetic energy increases. MRR increases due to impact of abrasive particle with higher kinetic energy on substrate material. Similarly, with initial increase of SOD, exit velocity of jet increases due to acceleration, thus kinetic energy increases. MRR increases due to impact of abrasive particle with higher kinetic energy on substrate material.

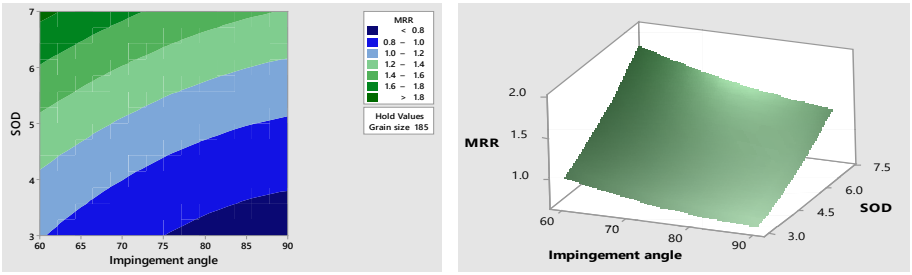

Fig. 9. Contour and surface plots of MRR vs. impingement angle and SOD at hold value of grain size 185 µm

In Fig. 9, MRR increases due to impact of abrasive particle with higher kinetic energy on substrate material. Similarly, with initial increase of SOD, exit velocity of jet increases due to acceleration, thus kinetic energy increases. MRR increases due to impact of abrasive particle with higher kinetic energy on substrate material. MRR decreases with increase in impingement angle i.e., the direction at which abrasive particles strike on work material. This may be due to increase of impingement angle, accumulation of abrasive grains inside the machined hole increases which reduces further erosion. Thus, MRR is decreased.

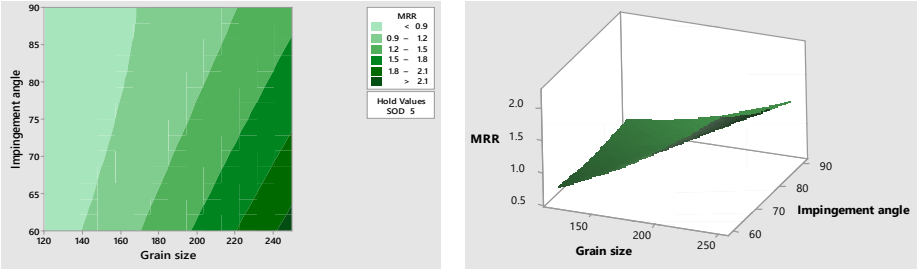

Fig. 10. Contour and surface plots of MRR vs. impingement angle and grain size at hold value of SOD 5 mm

In Fig. 10, MRR increases with increase of grain size. As grain size increases, mass of individual particle increases thus kinetic energy of each particle increases. MRR increases due to impact of abrasive particle with higher kinetic energy on substrate material. MRR decreases with increase in impingement angle through which abrasive particles strike on work material. Again, this may be due to increase of impingement angle, accumulation of abrasive grains inside the machined hole increases which reduces further erosion. Thus, MRR is decreased.

4 Conclusions

Conclusions can be drawn from this work:

- Newly developed abrasive jet machining chamber is working satisfactory without leaking of abrasives during jet machining. Therefore, pollution issue of abrasive jet machining mitigated.
- MRR is increased with increase of abrasive grain size.
- MRR is increased with increase of stand-off distance (SOD).
- MRR is decreased with impingement angle

5 Future work

Initial development of AJM setup is carried out with a grand allocated from The Institution of Engineers (India). Later on, complete AJM setup is developed with the abrasive jet machining chamber with the fund allocated through R & D cell of College of Engineering and Management, Kolaghat. Proper experimental work is carried out in the category in advanced manufacturing technology. Future modification can be carried out for hot air abrasive jet machining. Then effects of hot air abrasive jet machining can be assessed.

Acknowledgement

Development of abrasive jet machining set up is carried out from the fund granted from The Institution of Engineers (India). Later on, machining chamber is developed from the fund granted by Research and Development Cell, College of Engineering and Management, Kolaghat.

References

1. Mishra, P.K.: Abrasive jet machining: non-conventional machining. The Institution of Engineers (India) Text Book Series, Kolkata, 18th Reprint, 12-13 (2014).
2. Hassan, A., Hofy, G.E.: Advanced machining processes. Mechanical Engineering Series, McGraw-Hill Publisher (2005).
3. Srikanth, D.V., Rao, M.S.: Application of optimization methods on abrasive jet machining of ceramics. Industrial Engineering and Technology 4(3), 23-32 (2014).

4. Madhu, S., Balasubramanian, M.: A review on abrasive jet machining process parameters. Applied Mechanics and Materials 766-767, 629-634 (2015).
5. Haldar, B., Adak, D.K., Ghosh, D., Karmakar, A., Habtamu, E., Ahmed, M., Das, S.: Present status and some critical issues of abrasive jet materials processing: a review. Procedia Manufacturing 20, 523-529 (2018).
6. Finnie, I.: Erosion of surfaces by solid particles. Wear 3, 87-103 (1960).
7. Chastagner, M.W., Shih, A.J., Arbor, A.: Abrasive Jet Machining for edge generation. Transaction of NAMRI/SME 35, 359-366 (2007).
8. Wakuda, M., Yamauchi, Y., Kanzaki, S.: Effect of work piece properties on machinability in abrasive jet machining of ceramic materials. Precision Engineering Journal of the International Societies for Precision Engineering and Nanotechnology 26, 193-198 (2002).
9. Gradeen, A.G., Spelt, J.K., Papini, M.: Cryogenic abrasive jet machining of poly-dimethyl-siloxane at different temperatures. Wear 274-275, 335-344 (2012).
10. Srikanth, D.V., Rao, M.S.: Response surface methodology for optimization of process parameters in abrasive jet drilling of composites. Mechanical and Civil Engineering 11 (3), 20-26 (2014).
11. Pradhan, S., Das, S.R., Nanda, B.K., Jana, P.C., Dhupal, D.: Experimental investigation on machining of hard stone quartz with modified AJM using hot silicon carbide abrasives. The Brazilian Society of Mechanical Sciences And Engineering 42 (11), 1-22 (2020).
12. Bharadwaj, S.R., Adithya, V.S., Suryasathvik, S., Rahul, D.B., Chengappa, U.N., Mohan, K.G., Nanjundeswaraswamy, T.S.: Process parameters of abrasive jet machining. Journal of Engineering Research and Applications 9 (11), 46-51 (2019).
13. Ghara, T., Ansari, R., Adak, D.K., Ahmed, M., Das, S., Haldar, B.: Abrasive jet drilling of porcelain tiles and soda lime glass under different conditions. Proceeding of the 1st International Conference on Mechanical Engineering, Jadavpur University, Kolkata, India, January 4-6,189-208 (2018).
14. Hebda, M., Kaczor, P., Miernik, K.: Vacuum brazing of stainless steel depending on the surface preparation method and temperature of the process. Archives of Metallurgy and Materials64, 5-11 (2019).
15. Lankiewicz, K., Babul, T., Baranowski, M., Kowalski, S.: The study of the impact of surface preparation methods of Inconel 625 and 718 nickel-base alloys on wettability by BNi-2 and BNi-3 brazing filler metals. Archives of Metallurgy and Materials 60 (2),739-745 (2015).
16. Thakare, G.J., Pandey, C., Mulik, S.R., Mahapatra, M.M., Narang, K.H.: Effect of grit blasting and thermal spraying on microstructure evolution of P91 weldment. Archives of Metallurgy and Materials 63 (4), 1725-1734 (2018).
17. Melentiev, R., Fang, F.: Recent advances and challenges of abrasive jet machining. Cirp Journal of Manufacturing Science and Technology 22, 1-20 (2018).
18. Adak, D.K., Pal, V., Das, S., Ghara, T., Joardar, H., Alrasheedi, N., Haldar, B.: Surface Preparation for Coating and Erosion MRR of SS 304 Using Silicon Carbide Abrasive Jet. Lubricants 11 (10), 11010010/1-18 (2023).

Single objective optimization of laser cutting parameters of glazed ceramic tile using particle swarm optimization

Pankaj Keshari[1], Rupam Rakshit[1], Paramasivan K.[1], Dipten Misra[1]

School of Laser Science and Engineering, Jadavpur University, Kolkata, India
Kesharipankaj1992@gmail.com

Abstract. Cutting of ceramics using conventional machining is a bit challenging due to its brittle and hardness nature. Now days, laser cutting becomes popular due to its robust nature. The quality of machining is influenced by factors such as kerf width, quality of cut edge, and smoothness. In this work, a parametric analysis of laser cutting of ceramic tiles is investigated with four process parameters such as laser power, frequency, scanning speed, and gas pressure on the kerf width of the top surface of tiles. It has been noted that laser power has a positive impact on kerf width, frequency, and scanning speed has negative impact and initially, kerf width increases with gas pressure up to a certain limit after that it decreases with increasing gas pressure. A single objective particle swarm optimization was used to determine the minimum value of top kerf width and its value is evaluated as 47.1083 μm and it can be achieved at the combination of 395.76 W laser power, 5 mm/s scanning speed, 2 bar gas pressure, and 300 Hz pulse frequency.

Keywords: Ceramic Tile cutting, Kerf width, Fiber laser cutting, Particle swarm optimization

1 Introduction

Ceramics are widely used in electronics, automobile, and biomedical industries, due to their versatile properties, which have high electrical & heat resistance, excellent chemical stability, and hardness. Ceramics are employed as piezoelectric sensors, ferromagnetic substances, and superconductive materials due to their excellent insulating, dielectric as well as thermal properties [1]. Due to their biocompatibility, durability, and chemical stability, these are used in many medical applications such as dental implants, hip and knee replacement, surgical Instruments, and prosthetics [2-5]. Cutting of ceramics from traditional machining techniques is a bit challenging including mechanical mounting, wire saw cutting, etc. due to their brittleness and hardness. Traditional machining is slower, noisier, and less precise than non-traditional machining such as laser cutting. In this non-contact process, which reduces thermal stress and prevents cracking, a common issue with brittle ceramics [6]. In this decade, the consequence of the basic input parameters on the machining quality in terms of kerf width has been the subject of numerous studies conducted in the field of laser machining. Samat and Dahotre [7] presented a review of brief idea on laser machining for understanding physics and complex phenomena of quality of machining. Rakshit and Das [8] proposed an overview of cutting ceramic materials with different cutting techniques that improve machinability. Wang et al. [9] investigated the cutting of alumina substrate by femtosecond laser and analyzed the process parameter such as focus position, transverse speed, etc., on the kerf width, taper, surface profile, and crack formation during laser cutting. Quintero et al. [10] experimentally investigated the effect of input parameters including cutting speed and gas pressure on the kerf width of the upper and lower face by 500W pulsed optical fiber guided Nd: YAG laser. Kalvettukaran et al. [11] experimented with the influence of input process variables on glass formation width on the bottom surface, taper angle, and kerf widths on both top and bottom surfaces of the glazed ceramic tiles. Black and Chua [12] investigated cutting of thick ceramic tiles using 〖CO〗_2 laser of variable cutting speed and laser modes with different shield gases on the cut quality. Ghosh et al. [13] investigated the effect of process factors including focal position, cutting speed, average power, and assist gas on the surface morphology of SiC〖Al〗_2 O_3 by 2 kW quasi-continuous wave laser. Cao et al. [14] experimented with and analyzed the surface roughness, and chip morphology during the cutting process with the help of response surface methodology to obtain a regression equation to predict the optimization analysis of responses. Kalvettukaran et al [15] investigated and optimized the process parameters of laser and gas pressure through the particle swarm optimization technique for minimize glass formation and taper angle of the cutting zone.

As can be seen from the past literature, with regard to ceramics cutting, there are few literatures proving the influence of process parameters on the kerf width. On account of the brittle and hard nature of ceramics, cut a narrow kerf width is very difficult to achieve by laser machining. The quality of cut edge and smoothness is affected by kerf width. The primary aim of this investigation is to reduce the kerf width to get a good quality

cut. In this regard, a parametric analysis and optimization are conducted to evaluate the associations between the process parameters and the kerf width on the top surface.

2 Experimental Procedure

A fiber laser cutting machine of wavelength 1080 nm along with nitrogen gas as an assist gas and an average power of up to 500 W are used for the experiments [11]. In this investigation, 7 mm thick glazed ceramic tiles were selected. The laser beam is concentrated to a 50 µm diameter at focus on the job. The space between the nozzle and the workpiece remains constant at 0.6 mm during each experiment. An optical microscope, The ZEISS stemi 508, is used to measure the kerf width of the top as a response. With the help of the Response surface approach, design of experiment (DOE) has been generated. The names of the process parameters with their levels are given in Table 1[11].

Table 1. Process variables and their units and limits [11]

Parameter	Notation	Unit	Low value	High value
Laser power	P	W	380	430
Scanning speed	V	mm/s	5	15
Gas pressure	g_p	bar	2	4
Frequency	f	Hz	300	650

3 Result and Discussion

Kerf width is a key parameter in laser cutting of ceramics due to their brittle nature. The quality of cut edge and smoothness is affected by kerf width. A wider kerf width indicates materials are removed beyond the cut lines, which can result in rough edges, chipping, or uneven cuts. A wider kerf width occurs due to high energy input leading to an increase in the heat-affected zone, which can lead to micro-cracks. The primary aim of this investigation is to reduce the kerf width to get a good quality cut. A parametric analysis of laser cutting of ceramic tiles has been investigated and kerf width on the top surface taken as a response. Values of measured output with respective process parameters are given in Table 2. Table 2 shows that the kerf width on the top surface is maximum (109.895 µm) at a laser power of 440 W, scanning speed at 3 mm/s, frequency at 475 Hz, and gas pressure at 10 bar, and minimum (68.413 µm) at a laser power of 380W, scanning speed at 4 mm/s, frequency at 650 Hz, and pressure of 12 bar.

Table 2. Design layout with the numerically measured response

Sl. No.	Laser power P(W)	Scanning speed V(mm/s)	Gas pressure g_p(bar)	Frequency f (Hz)	Kerf width on the top surface (µm)
1	440	3	10	475	109.895
2	405	3	12.8	475	70.795
3	430	2	8	650	108.297
4	380	2	12	300	96.033
5	430	2	8	300	114.793
6	430	2	12	650	100.715
7	405	3	10	720	73.122
8	430	4	12	300	88.617
9	380	2	8	300	95.134
10	380	2	12	650	90.109
11	405	1.6	10	475	106.783
12	380	4	8	300	80.891
13	380	4	12	300	72.892
14	370	3	10	475	85.073
15	380	4	8	650	73.274
16	405	3	10	475	85.326
17	405	3	10	475	86.421
18	405	3	7.2	475	81.988
19	405	3	10	230	96.939
20	405	3	10	475	85.717
21	405	3	10	475	85.716
22	430	4	8	650	100.143
23	380	2	8	650	95.184
24	405	4.4	10	475	76.203
25	405	3	10	475	87.329
26	380	4	12	650	68.413
27	430	4	12	650	82.027
28	430	2	12	300	108.739
29	430	4	8	300	106.834
30	405	3	10	475	88.457

3.1 Impact of process parameters on top surface kerf width

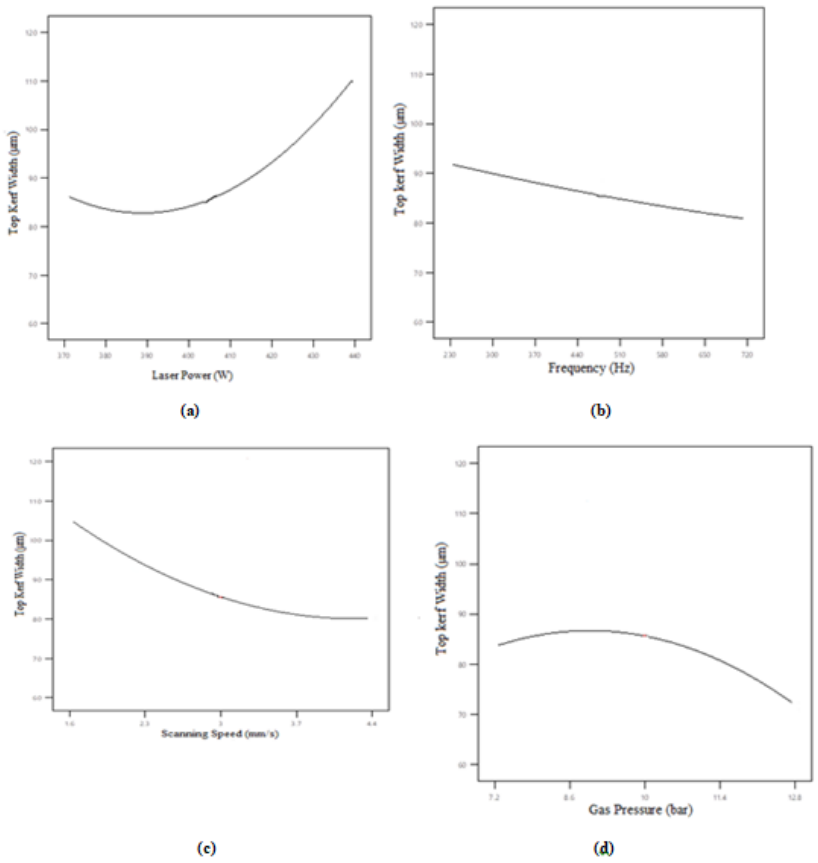

Fig. 1. Impact of process parameters on the kerf width on top surface

The impact of laser power on top kerf width is given in Fig.1(a). In this plot, fixed frequency, gas pressure, and scanning speed have been taken at 475 Hz, 10 bar, and 3 mm/s respectively. The graph shows that laser power has a constructive impact on top surface kerf width. Due to high laser power, more energy is delivered on the surface which develops a high peak temperature to melt the surface faster. So, the volume of melt increases with increasing laser power. The influence of frequency on kerf width is shown in Fig. 1(b) and to plot it, laser power, gas pressure, and scanning speed have been taken as fixed at 405 W, 3 mm/s, and 10 bar respectively. It can be concluded from this graph that the frequency has a negative impact on kerf width. When laser pulse frequency enhanced, pulse on time increases in one cycle of pulse duration, which decreases the off time of pulses by which the molten material has less time to solidify, which leads to a narrower kerf width. The relation between the scanning speed and top kerf width is furnished in Fig. 1(c). A fixed value of laser power (405 W), gas pressure (10 bar), and frequency (475 Hz) has been taken to plot this graph. The graph shows that scanning speed has a negative impact on kerf width. The temperature developed on the surface is directly proportional to the interaction period between the laser pulses and the sample. More scanning speed leads to less interaction time i.e. low energy absorbed by the surface leads to a decrease in temperature, that's why kerf width decreases with increasing scanning speed. The impact of gas pressure on the upper kerf width is plotted in Fig.1(d). In this plot, laser power, frequency, and scanning speed have been reserved at 405 W, 3 mm/s, and 475 Hz respectively. It can be concluded from this graph that; the gas pressure initially assists in growing the kerf width on the top surface up to a certain limit, after that kerf width decreases with increasing gas pressure. Initially, gas pressure has a positive impact up to a certain limit, because it assists in accumulating more heat at the targeted zone. After the limit, more gas pressure helps to decrease the heat conduction of melt material and increases the removal rate which can reduce the kerf width.

3.2 Prediction of the objective using regression equation

The present study used the regression equation, shown in equation 1 which furnished the relationship between input parameters, i.e. laser power (P), scanning speed (V), assist gas pressure (gp), and pulse frequency (f), and response as kerf width on the top surface. This equation is valid for the range of parameters taken for this work.

$$\text{Top kerf width} = 1550.89994 - 8.07644\times P - 46.68196\times V + 38.11755\times g_p + 0.035836\times f + 0.065168\times P\times V - 0.041166\times P\times g_p - 0.000140\times P\times f - 0.980656\times V\times g_p - 0.001780\times V\times f - 0.000761\times g_p\times f + 0.010749\times P^2 + 3.66148\times V^2 - 1.01084\times g_p{}^2 + 0.000012\times f^2 \quad (1)$$

3.3 Particle swarm optimization

Particle swarm optimization (PSO) is a stochastic algorithm introduced by Eberhart and Kennedy [16,17], which is inspired by the concept of the social behavior of birds. At the start of the algorithm, a position of particles is randomly created, and every single particle offers a potential solution for the given problem. A velocity is assigned to how fast each particle moves through a search space. After each iteration, particles move to a new position in the search space, and the best position reached by any individual particle is called the "personal best" whereas the best position among the "personal best" is referred to as "global best" [18]. After certain iterations are completed, a maximize or minimize function (depending upon the specific task) that is the updated global best will be obtained as output [19].

In this present study, Single objective PSO was used to minimize the kerf width of the top surface in MATLAB-online. In this work, 100 number of particles, 1.5 as a cognitive component, 2 as a social component, and 0.7 as inertia weight have been taken as PSO parameters. 100 number of iterations have been run to take the output. As per the PSO result, 47.1083 µm kerf width on the top surface was achieved as a fitness value at the combination of 395.76 W laser power, 5 mm/s scanning speed, 2 bar gas pressure, and 300 Hz pulse frequency. The relation between function fitness value and updating iteration is shown in Fig. 3.

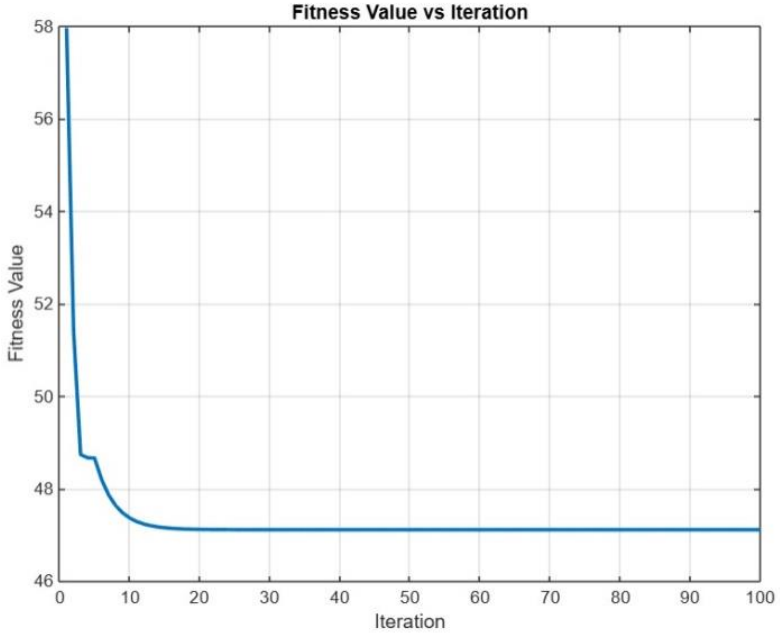

Fig. 2. Fitness function value vs. updating iteration

4 Conclusion

Based on the range of parameter values taken into consideration, the study's conclusions can be summarized as follows:

1. The kerf width on the top surface is positively impacted by laser power.
2. The kerf width on the top surface is found to be negatively impacted by scanning frequency and speed.

3. It is observed that the gas pressure initially assists in growing the kerf width on the top surface up to a certain limit, after that kerf width decreases with increasing gas pressure.
4. A single objective PSO has been done to explore the minimum value of top kerf width and its value is evaluated as 47.1083 µm and it can be achieved at the combination of 395.76 W laser power, 5 mm/s scanning speed, 2 bar gas pressure, and 300 Hz pulse frequency.

References

1. Rödel, J., Kounga, A. B., Weissenberger-Eibl, M., Koch, D., Bierwisch, A., Rossner, W. & Schneider, G. (2009). Development of a roadmap for advanced ceramics: 2010–2025. Journal of the European Ceramic Society, 29(9), 1549-1560.
2. Galante, R., Figueiredo-Pina, C. G., & Serro, A. P. (2019). Additive manufacturing of ceramics for dental applications: A review. Dental materials, 35(6), 825-846.
3. Rahaman, M. N., Yao, A., Bal, B. S., Garino, J. P., & Ries, M. D. (2007). Ceramics for prosthetic hip and knee joint replacement. Journal of the American Ceramic Society, 90(7), 1965-1988.
4. Kelly, J. R. (1997). Ceramics in restorative and prosthetic dentistry. Annual Review of Materials Science, 27(1), 443-468.
5. Merkert, P., & Kuntz, M. (2006). Future applications in ceramics. In Bioceramics and Alternative Bearings in Joint Arthroplasty: 11 th BIOLOX® Symposium Rome, June 30–July 1, 2006 Proceedings (pp. 283-288). Steinkopff.
6. Schaaf, P. (Ed.). (2010). Laser processing of materials: fundamentals, applications and developments (Vol. 139). Springer Science & Business Media.
7. Samant, A. N., & Dahotre, N. B. (2009). Laser machining of structural ceramics—A review. Journal of the European ceramic society, 29(6), 969-993.
8. Rakshit, R., & Das, A. K. (2019). A review on cutting of industrial ceramic materials. Precision Engineering, 59, 90-109.
9. Wang, X. C., Zheng, H. Y., Chu, P. L., Tan, J. L., Teh, K. M., Liu, T., ... & Tay, G. H. (2010). High quality femtosecond laser cutting of alumina substrates. Optics and Lasers in Engineering, 48(6), 657-663.
10. Quintero, F., Pou, J., Lusquinos, F., Larosi, M., Soto, R., & Perez-Amor, M. (2001). Cutting of ceramic plates by optical fiber guided Nd: YAG laser. Journal of laser Applications, 13(2), 84-88.
11. Kalvettukaran, P., Keshari, P., & Misra, D. (2023). Parametric study of laser cutting of glazed ceramic tiles. Journal of the Brazilian Society of Mechanical Sciences and Engineering, 45(6), 333.
12. Black, I., & Chua, K. L. (1997). Laser cutting of thick ceramic tile. Optics & Laser Technology, 29(4), 193-205.
13. Ghosh, P., Nix, J., Elkington, H., Smith, B., & Marimuthu, S. (2024). High Power Laser Cutting of SiC-Al2O3 Ceramic Matrix Composites. Procedia CIRP, 123, 340-345.
14. Cao, C., Zhao, Y., Zhang, G., Li, Z., Zhao, C., Yu, H., ... & Dai, D. (2024). Experimental study of plastic cutting in laser-assisted machining of SiC ceramics. Optics & Laser Technology, 169, 110098.
15. KALVETTUKARAN, P., CHAKRAVARTY, A., & MISRA, D. (2024). Multi-objective Optimization of Laser Cutting Parameters Using Particle Swarm Optimization (PSO). Lasers in Engineering (Old City Publishing), 57.
16. Eberhart, R., & Kennedy, J. (1995, October). A new optimizer using particle swarm theory. In MHS'95. Proceedings of the sixth international symposium on micro machine and human science (pp. 39-43). Ieee.
17. Kennedy, J., & Eberhart, R. (1995, November). Particle swarm optimization. In Proceedings of ICNN'95-international conference on neural networks (Vol. 4, pp. 1942-1948). ieee.
18. Dehkordi, M. H. R., Jasim, D. J., Al-Rubaye, A. H., Akbari, M., Bagherzadeh, S. A., Ghazi, M., & Mohammadkarimi, H. (2023). Modeling and multiobjective optimization of thermal effects of fiber laser cutting of Inconel 600 sheet by employing the ANN and multi-objective PSO algorithm. Journal of Laser Applications, 35(4).
19. Marini, F., & Walczak, B. (2015). Particle swarm optimization (PSO). A tutorial. Chemometrics and Intelligent Laboratory Systems, 149, 153-165.

Machine Learning-enabled Prediction of Tool Wear in CNC Milling

Jyotiraditya Roy[1], Sumanta Banerjee[2] and Anindita Kundu[3]

[1]Computer Science and Engineering Department, Heritage Institute of Technology, Kolkata 700107, India
[2]Mechanical Engineering Department, Heritage Institute of Technology, Kolkata 700107, India
[3]School of Computer Science and Engineering (SCOPE), VIT Vellore 632014, India

sumanta.banerjee@heritageit.edu

Abstract. The present study investigates the application advantages of machine learning (ML) techniques to predict tool wear during CNC machining processes. Advanced ML methods have been employed for feature selection, and the Boruta algorithm applied to identify the most relevant features. The model performance improved significantly through enhanced interpretability and reduced noise. A decision tree model was trained on the selected features, which achieved high accuracy on both training and testing datasets. In addition, logistic regression was performed with 4-fold cross-validation, which revealed variability in model performance and underscored the importance of robust evaluation techniques, in addition to the need for larger datasets. Preliminary trials were also conducted with Long Short-Term Memory (LSTM) networks with an aim to identify temporal dependencies in CNC machining data. The findings highlight the utility of ML approaches to adopt optimum predictive maintenance strategies in machining applications. The study also demonstrates the need for effective feature selection and model evaluation in achieving accurate predictions of tool wear during machining.
Keywords: CNC Machining, Machine Learning, Logistic Regression, LSTM.

1 Introduction

CNC milling is one of the most widely-used metal-removal techniques that spans across modern, state-of-the-art industries, in particular, the automotive and aerospace sectors. Known for its versatility, CNC milling facilitates multipoint cutting tools to follow tool-paths of complex geometries, and approach the workpiece from multiple directions. Based on the type of milling operations that span across a wide range of workpiece geometries, tolerances, and materials, machining parameters can vary significantly.

Tool wear is an inevitable aspect of manufacturing processes (e.g. milling, turning, and drilling). Factors that influence its rate include the process parameters (e.g., depth of cut, feed rate and cutting speed), the cutting tool geometry, and the material properties of the tool and the workpiece [1]. In a CNC milling center, the cutting tool gradually wears down and gets blunt (i.e. lose out sharpness) due to factors like attrition, thermal fracturing, abrasion, diffusion, plastic deformation, grain pull-outs (in fracture-induced mechanical wear), and chemical wear. This affects the machining process adversely, as wear-induced vibrations leads to dimensional inaccuracies, poor surface finish, and inferior-quality products. In severe cases, the tool may even break during cutting operation. Tool failure leads to sudden release of the cutting forces, and the resultant inertia effects generate irreparable zones of stress concentration within the workpiece and the machining center. Monitoring tool wear is, therefore, necessary for optimizing machining parameters (e.g. depth of cut, feed rate and cutting speed), or deciding for tool replacement. Though Taylor's equation provides a basic approximation for tool-life expectancy, advancements in sensor technology and the seamless integration of sensors in modern CNC machines have enabled precise tool-wear predictions, using measured data collected during machining processes. State-of-the art manufacturing systems use online monitoring systems that tracks tool wear continuously during machining [1, 2].

In the era of smart manufacturing, manufacturers need predictive models to estimate the remaining useful life (RUL) of components and forecast failures. Model-based or physics-based prognostics require the development of analytical models. However, detailed knowledge of system behavior is often unavailable for complex manufacturing processes. To address this limitation, data-driven methods are gaining traction, which leverage the power of AI and ML tools in system prognostics and health management (PHM). The objective of ML is to build predictive models from training data, and apply these (models) to make reliable predictions on test data. These approaches improve reliability and efficiency without relying solely on mathematical models. A number of published studies on intelligent predictive maintenance, as reviewed in [3], focus on cutting tool health, with the tool wear accounting for 20% of machining downtime and 25% of total machining costs [3].

Data-driven prognostics utilize statistical methods and ML algorithms to train predictive models. These include regression analysis, decision trees, support vector machines (SVMs), artificial neural networks (ANNs), and autoregressive models. These approaches do not require knowledge of system physics, and proves effective

in predicting tool wear, improving machining accuracy, and prolonging equipment longevity. These models, when integrated with CNC machining, enable precise, reliable, and efficient system operations through tool wear predictions and facilitating proactive tool management. ML algorithms can analyze large datasets (collected from sensors) to model the wear progression of multipoint milling cutting tools. To enable reliable wear predictions, these models are trained on historical data to recognize patterns associated with tool wear. These facilitate construction of realistic data-driven predictive models. Real-time monitoring and prediction allows operators to adjust and/or preemptively replace tools before significant wear occurs. Based on tool wear predictions, ML can help in optimizing machining parameters (e.g. depth of cut, feed rate and cutting speed), minimize machine downtime and disruptions during machining, and maximize tool life and productivity ([4], [5]). In this work, ML models have been trained and tested on published data of milling operations, on workpieces (blocks) made of machinable wax.

2 Methodology

2.1 Dataset

3 **Table 1.** Dataset of CNC milling with different attributes

	No.	Material	feedrate	Clamp pressure	Tool condition	Machining finalized	Passed Visual Inspection
0	1	Wax	6	4.0	unworn	Yes	Yes
1	2	Wax	20	4.0	unworn	Yes	Yes
2	3	Wax	6	3.0	unworn	Yes	Yes
3	4	Wax	6	2.5	unworn	No	Nan
4	5	Wax	20	3.0	unworn	No	Nan
5	6	Wax	6	4.0	worn	Yes	No
6	7	Wax	20	4.0	worn	No	Nan
7	8	Wax	20	4.0	worn	Yes	No
8	9	Wax	15	4.0	worn	Yes	No
9	10	Wax	12	4.0	worn	Yes	No
10	11	Wax	3	4.0	unworn	Yes	Yes
11	12	Wax	3	3.0	unworn	Yes	Yes
12	13	Wax	3	4.0	worn	Yes	Yes
13	14	Wax	3	3.0	worn	Yes	Yes
14	15	Wax	6	3.0	worn	Yes	Yes
15	16	Wax	20	3.0	worn	No	Nan
16	17	Wax	3	2.5	unworn	Yes	Yes
17	18	Wax	3	2.5	worn	Yes	Yes

The dataset (shown in Table 1) consists of CNC machining data collected from 18 experiments conducted on rectangular wax blocks (each of dimensions $2" \times 2" \times 1.5"$), using a CNC milling machine (Data courtesy: SMART lab, University of Michigan). Milling wax blocks simulates material behavior during machining processes. Machinable wax is inexpensive, easier to machine, and enables visualization of tool wear, cutting forces, and chip formation. Machining operations on machinable wax can provide valuable insights into toolpath optimization, machine behavior, and process dynamics [7]. The experiments varied in tool condition (i.e. “unworn” and “worn” tools), feed rate, and the clamping pressure. General data from each experiment, which includes material type (wax), feed rate, clamp pressure, and tool condition, is available in “*train.csv”*. Moreover, the outcome of each experiment (“passed visual inspection”) is recorded. Detailed time series data, sampled at time intervals of 100 ms, is provided in separate files (“experiment_01.csv to “experiment_18.csv”, which include measurements procured from four motors (X, Y, Z axes, and spindle) of the CNC machine. These time series files capture active machining routines (operations), which are labeled as "Layer 1 Up", "Layer 1 Down", "Layer 2 Up", "Layer 2 Down", "Layer 3 Up", and "Layer 3 Down". This information allows for either one of two types of analysis: treating each measurement as an independent observation, or considering the entire time series from each experiment for classification.

3.1 Data Preprocessing

When dealing with complex datasets generated from sensor feedbacks in machining processes, **Feature selection** is a critical (initial) step. For Decision Tree and Random Forest implementation, the “Feature selection” criterion has been used in predictive analysis. In multi-featured data, the Boruta algorithm is a robust

method for identifying important features. Unlike traditional techniques (e.g. PCA), which focuses on variance of a dataset, the former assesses the relevance of each feature in relation to the target variable(s). In this study, the Boruta algorithm is applied to the multi-featured (milling) dataset. The accrued insights are essential for improving model accuracy and reducing omitted variable bias [8]

Traditional ML algorithms (e.g. decision trees, logistic regression) typically require the input data to be in a 2-D format, where each feature is represented as a distinct column in a dataset. When working with complex datasets (generated from CNC milling), the dimensionality can exceed (beyond 2-D). To address this, **dimensionality transformation techniques** have been employed to condense high-dimensional data into manageable format, while preserving the essential information (necessary for predictive modelling).

An effective step in dimensionality transformation is the extraction of statistical features from multi-dimensional data. This method involves summarizing the data by identifying the key statistical measures that capture the main characteristics of the dataset. For example, in a 3-D dataset obtained from machining processes, one might compute the following statistical features: (1) **Minimum (Min)**, or the lowest observed value in a dataset, identifynig the lowest performance or quality metric recorded during the process; (2) **Maximum (Max),** or the highest observed value, which indicates the upper limits of the data and potential outlier conditions; (3) **Mean (Average)**, or the average value (of the dataset) that serves as a central tendency measure and can highlight general trends in the process; (4) **Median**, i.e. the middle value when the data is sorted, offering a robust measure against outliers and skewed distributions; and (5) **Standard deviation**, which measures the extent of variation or dispersion within a set of values, thereby indicating the consistency of the process. For the **LSTM** approach, since the experiments (on CNC milling) produced time series data of unequal lengths, the data have been padded with "-1" values to ensure uniformity across all experiments, using the length of the longest time series as the standard. After padding, standard scaling was applied to normalize the values across the experiments. This approach allows for consistent comparison and analysis, either by treating each CNC measurement as an independent observation, or go for time series classification after considering the entire time series from each experiment.

In addition, this work has applied **label encoding** to the non-numeric features in this dataset to convert them into a format that is suitable for ML models. This process involves assigning a unique integer to each category in a categorical feature, transforming the data into a form that models can process. For example, categorical features such as tool condition (e.g., "unworn" and "worn") and machining operations (e.g., "Layer 1 Up", "Layer 1 Down", etc.) were encoded into integers. Label encoding helps ensure that all input data, which includes (originally) non-numeric features, are integrated into the modeling process without losing critical information.

3.2 Models

The following paragraphs outline the basic attributes of ML methods used in this study.

Decision Tree is a versatile algorithm used for both classification and regression tasks. It works by recursive splitting of data into subsets, based on the value of input features, forming a tree-like structure. Each internal node denotes a feature, with each branch representing a decision rule. Each leaf node represents an outcome or prediction. Decision Trees are favored for their interpretability and ease of visualization, as they allow for straightforward decision-making processes [8].

Logistic Regression is a linear model used for binary classification, and predicts the probability of a binary outcome (e.g., "unworn" or "worn" tool condition). It uses a logistic function to map input features onto a probability field between 0 and 1, making it suitable for tasks where the response variable represents two classes. The model finds the best-fitting parameters by minimizing a loss function, often using techniques like regularization to avoid overfitting and improve generalization.

In order to assess model performance, the **K-fold cross-validation** technique splits a dataset into equal parts (folds). At first, the model is trained on $(K-1)$ folds, and then tested on the remaining fold. The process is repeated K times, with a different test fold each time. The results from all K iterations are averaged to provide a more reliable estimate of the model's performance. This approach helps ensure that the evaluation metrics reflect the model's ability to generalize to new data, making it more robust against overfitting.

Long Short-Term Memory (LSTM) networks are a type of recurrent neural network (RNN) designed to effectively learn from sequences of data (as shown in Table 1). Unlike traditional RNNs, LSTMs can capture long-range dependencies and mitigate the vanishing gradient problem, making them particularly well-suited for tasks involving time series and other sequential data.

The LSTM model used in this study consisted of the following layers: (1) **Input Layer**: The model was designed to accept the 3D input shaped as "(batch_size, time_steps, features)". This input structure allows the model to learn temporal patterns across sequences; (2) **LSTM Layers**: Multiple LSTM layers were stacked in order to enhance the model's ability to capture complex dependencies. The architecture typically included the **First LSTM Layer**, which was configured with 128 units and "return_sequences = True" to pass the sequence

output to the next layer, and **Subsequent LSTM Layers**, which are layers down the sequence with decreasing units (e.g., 64, 32) and "return_sequences" set according to the requirement to maintain or reduce the dimensionality of the output; and the (3) **Dense Layers**. After the LSTM layers, fully connected (Dense) layers were added to interpret the LSTM outputs. The final layer used a sigmoid activation function for binary classification.

3.3 Model Development and Training

In this analysis, the **Decision Tree** model development process began with feature selection, using the Boruta algorithm, to identify the most important features related to predicting the tool condition ("unworn" or "worn"). After selecting the key features, the data was scaled to ensure consistency across features and improve model training. The scaled data was then used to train a Decision Tree classifier from the "sklearn" library, with the selected features as inputs and the "tool condition" as the target variable. The training was conducted using the scaled "X_train data", focusing on the most relevant features, to leverage the Decision Tree's ability to capture the (non-obvious) complex relationships and improve prediction accuracy.

In the second model development process, the **Logistic Regression** tool was combined with **K-fold cross-validation** to ensure a robust evaluation of the model's performance. After selecting the most important features using the Boruta algorithm and scaling the data, the scaled features were used to train a Logistic Regression model from the "sklearn" library. The target variable was the "tool condition" (unworn or worn), and the scaled feature set served as the input. The **K-fold cross-validation** was applied to the Logistic Regression model to better assess its generalization performance. The dataset was divided into K subsets (or folds), with the model being trained on $(K-1)$ of these folds and tested on the remaining one. This process was repeated K times, each time using a different fold as the test set, and the performance metrics from each iteration were averaged to provide a comprehensive evaluation of the model. The use of K-fold cross-validation helped ensure that the Logistic Regression model's accuracy, precision, recall, and F1 score were not overly-dependent on any single subset of the data, making the evaluation more reliable and reducing the likelihood of overfitting. The final model used was the **LSTM Network**, which is good at handling sequential dependencies. It uses a neural network approach. While the **LSTM Branch** processed the sequential (time-series) data, a series of LSTM layers with gradually decreasing units (128, 128, 64, 32) helped the model learn long-term dependencies, and gradually compress the information. The "return_sequences" parameter was set to "True" for the intermediate layers, in order to ensure that the full sequence information was passed through. The output of the final LSTM layer is a fixed-size representation vector, summarizing the learned sequence features, particularly useful for capturing temporal patterns in the time-series data. To incorporate additional features of the dataset, preprocessing was done to improve model accuracy and robustness.

Additional Features Preprocessing: A separate **dense layer** was used to process the additional features of "clamp_pressure" and "feed_rate". This layer applied a non-linear transformation to the input, allowing the model to learn interactions within these features. The outputs of the LSTM layers and the dense layer (for additional features) were merged using the **concatenate layer**. By merging the compressed sequence representation from the LSTM branch and the transformed static features (attribute of **fully connected layers**), the model was enabled to make predictions using both types of information. After concatenation, a dense layer further combined the information, followed by a dropout layer to prevent overfitting. The final dense layer (or **output layer**) used a sigmoid activation function for binary classification, making the model suitable for predicting the target variable.

Compilation: The "binary_crossentropy" was used as the **loss function**, a standard for binary classification problems. The **Adam optimizer** with a learning rate of "0.001" was chosen for its efficiency in gradient descent optimization, especially with non-stationary data. The "accuracy" was used as the **evaluation metric** to monitor how well the model performs during training and validation.

Training with Early Stopping: The technique of **early stopping** was employed to avoid overfitting, by stopping the training when the validation loss no longer improved for 10 consecutive epochs, restoring the best weights. Moreover, as part of the protocol of **validation split**, 20% of the training data was reserved for validation, helping to monitor the model's performance on unseen data during training.

4 Result and Discussion

After applying the Boruta algorithm, the top 10 features (most relevant to our predictive model) were identified [9]. The Boruta algorithm effectively distinguishes essential features by comparing their importance with randomized shadow features, retaining only those that contribute significantly. This selection led to reduced overfitting, improved interpretability, and faster training times, making the model more efficient and better at

generalizing to new data. Using these selected features, the study could achieve a balance between model simplicity and performance, emphasizing the importance of effective feature selection in data-driven modelling.

Feature Selection Results: The top 10 features identified by the Boruta algorithm are S1 (System Inertia), Z1 (Current Feedback), Z1 (DC Bus Voltage), Z1 (Output Current), Z1 (Output Voltage), Z1 (Command Acceleration), S1 (Command Acceleration), Machining Process, Y1 (Actual Velocity), and Y1 (Command Acceleration). These features were deemed the most important for the predictive model, based on their relevance scores.
Thereafter, the feature of "dimensionality reduction" was applied, by selecting the following key statistical features: "mean", "min", "max", "median", and "standard deviation (SD)", which resulted in a two-dimensional (2D) dataset generally required for decision tree and logistic regression. A decision tree model was then applied to the selected features, achieving 100% accuracy on both the training and testing data. The high accuracy score shows that the decision tree model effectively captured the patterns in the training data, and could perfectly classify the test samples. However, such perfect accuracy often raises concerns about potential overfitting, especially with a small test set.

Overfitting Analysis: The decision tree's 100% accuracy (refer to Fig. 1) suggests that the model may have memorized the training data, instead of generalizing to new data. The undesired attribute of "overfitting" occurs for complex models, whereby underlying patterns tend to get overshadowed by noise or specific features/details in the training data. Given that the model achieved perfect accuracy with a limited dataset, it is likely that the decision tree overfitted, resulting in a lack of flexibility when faced with unseen data [10].

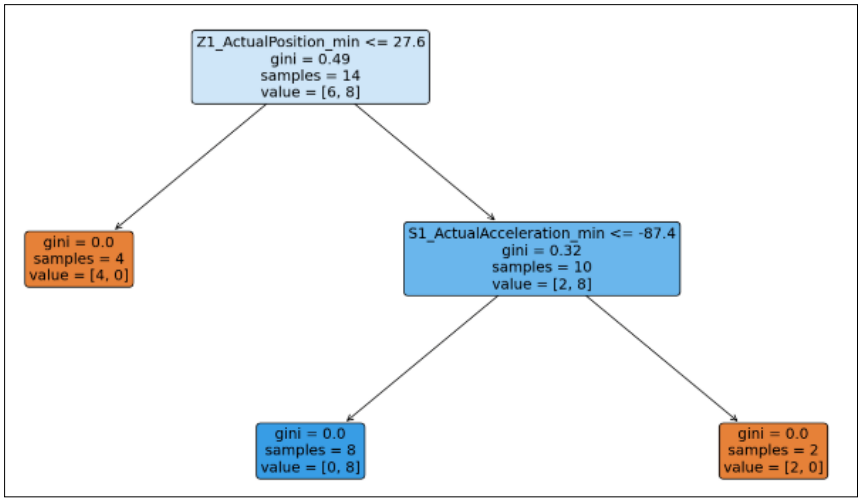

Fig. 1. The Decision Tree of the Model

The decision tree diagram visualizes how the dataset is split, based on the features **Z1_ActualPosition_min** and **S1_ActualAcceleration_min**, with splits determined by **Gini impurity** values. At the root node, the decision is based on Z1_ActualPosition_min ≤ 27.6, leading to two child nodes. One branch represents a subset with zero impurity (Gini = 0.0), indicating perfect classification for four samples. The other branch further splits based on S1_ActualAcceleration_min ≤ -87.4, achieving perfect classification in both resulting branches with Gini = 0.0. Next, a **4-fold cross-validation using logistic regression** was applied on the selected feature set. The accuracy results across the folds were as follows: 0.33, 0.33, 0.667, and 1.

Analysis of Results (Logistic regression):

Variability across Folds: The accuracy scores was observed to vary significantly, from 0.33 to 1. This suggests that the model's performance is highly dependent on the specific training and testing splits used in each fold.

Potential Overfitting in some Folds: The perfect accuracy of 1 in one fold indicates that the model might have fit the data exceptionally well for that particular subset, potentially memorizing the training data rather than generalizing.

Underperformance in Other Folds: The lower scores (0.33) in some folds suggest that the model struggled to generalize, possibly due to variability in the distribution of data between training and validation sets.

Finally, the **LSTM model** was trained and evaluated on the CNC milling data, with the following key results:

Training Accuracy: The model's training accuracy varied across the epochs, gradually improving from **66.67%** in the initial epochs to peaks of **91.67%** and **83.33%**.
Validation Accuracy: The validation accuracy was initially **0%**, indicating difficulty in learning from the data, but later stabilized around **33.33%** and **66.67%** in the later epochs.
Test Accuracy: The final test accuracy achieved by the model was **66.67%**, with a loss of **0.6550**.

Analysis of Results (LSTM):

Performance Insights: The fluctuating accuracy during training and validation phases suggests that the LSTM model had challenges in learning stable patterns from the limited dataset. The initial low validation accuracy indicates overfitting to the training data. A peak in training accuracy followed by dips and then improvements shows that the model was adjusting to the nuances of the dataset, but it struggled to generalize effectively due to the small sample size.
Data Limitation: With **18 sequential experimental samples** (12 training, 3 validation, and 3 testing), the dataset size proved a key constraint in achieving consistent model performance. The LSTM models typically require larger datasets to properly learn temporal patterns, which would help in improving the model's ability to generalize and avoid overfitting.
Model Overfitting: The pattern of higher training accuracy, relative to validation and testing, indicates that the model may be overfitting to the training data, memorizing the data instead of generalizing. Improving generalization could be possible with data augmentation techniques or using regularization methods (such as dropout layers).

Validation:

In the study by Parwala, V., et al. [11], logistic regression was applied using only the mean as a feature, thereby achieving 72% accuracy. While this approach showed promising results, chances of undermining other salient aspects of the data cannot be ruled out. The present study, in contrast, offers the following advantages: (1) **Feature Selection**, whereby the top 10 features were identified using the Boruta algorithm, which reduced noise and overfitting errors. This made the working model more generalizable, as compared to a single-feature approach (as in [11]); (2) **Dimensionality Reduction**, whereby multiple statistical features (mean, min, max, median, SD) were selected, offering a richer dataset for modelling (unlike the mean-only approach in [11]); (3) **Model Performance**: The modelled decision tree achieved 100% accuracy, although at the risk of overfitting. Moreover, Logistic regression with 4-fold cross-validation showed varying results (0.33 to 1), indicating sensitivity to data splits and a more thorough evaluation than [11]; (4) **LSTM Exploration**: The authors have also trained an LSTM that, in spite of challenges with a small dataset, suggested potential for deeper learning. This analysis was broader than the focus of analysis in [11]. From the foregoing discussions, it can be concluded that the present approach of tool wear estimation provides richer insights, better feature selection, and a more robust evaluation of models.

5 Conclusion and Future Scope

This research focusses on application of advanced ML techniques for feature selection, dimensionality reduction, and model evaluation to predict tool wear in a CNC milling process. The Boruta algorithm was applied to select the most relevant features, which significantly improved model performance by reducing noise and enhancing interpretability. Although the chosen decision tree model achieved perfect classification on both training and testing datasets, it simultaneously raises concerns about overfitting. The variability in logistic regression cross-validation results underscore the need for robust evaluation techniques and highlight the sensitivity of model performance to data splits. This attribute also indicates a strong requirement for diverse, reliable, publicly available datasets to support comprehensive training and improve generalization across different contexts.

It is relevant to note that the results of this analysis cannot always be directly extended to practical work-tool combinations involving harder materials. This is because machinable wax differs significantly in mechanical properties like hardness, thermal conductivity, and wear resistance. Thus, the model's performance and interpretability may not directly translate to practical scenarios without additional validation using diverse, real-world datasets. However, the data from wax machining is useful for debugging CNC programs, refining toolpaths, and testing tool geometries, which can then be adapted and applied with adjustments for real materials. Furthermore, while this study was limited to a dataset of only 18 samples and did not involve direct testing in practical scenarios, the results suggest that the approach could potentially be effective when scaled.

Future research will focus on testing the method in real-world settings with larger and more diverse datasets to evaluate its practical utility and robustness. Further research should focus on hyperparameter tuning, particularly for LSTM models. Utilizing techniques like the “Grid search” and “Bayesian optimization” can help

identify optimal configurations. Additionally, refining LSTM architectures will be crucial for effectively capturing temporal dependencies. Cross-departmental collaboration can also enhance the modelling process by integrating diverse expertise and historical data, enriching the research context. As mentioned, expanding the global availability of publicly accessible datasets will be essential for advancing research, as larger, varied datasets allow for more robust training and validation. By addressing these and allied areas, one can enhance the effectiveness of predictive models and drive innovation in machine learning applications across various fields of production and manufacturing engineering.

References

1. Wu, D., Jennings, C., Terpenny, J., Gao, R. X., & Kumara, S.: A comparative study on machine learning algorithms for smart manufacturing: tool wear prediction using random forests. Journal of Manufacturing Science and Engineering, 139(7), 071018 (2017).
2. Ghosh, N., Ravi, Y. B., Patra, A., Mukhopadhyay, S., Paul, S., Mohanty, A. R., & Chattopadhyay, A. B.: Estimation of tool wear during CNC milling using neural network-based sensor fusion. Mechanical Systems and Signal Processing, 21(1), 466-479 (2007).
3. Soori, M., Arezoo, B., & Dastres, R.: Machine learning and artificial intelligence in CNC machine tools, a review. Sustainable Manufacturing and Service Economics, 2, 100009 (2023).
4. Wu, D., Jennings, C., Terpenny, J., Kumara, S., & Gao, R. X. (2018). Cloud-based parallel machine learning for tool wear prediction. Journal of manufacturing science and engineering, 140(4), 041005.
5. Von Hahn, T., & Mechefske, C. K.: Machine learning in CNC machining: Best practices. Machines, 10(12), 1233 (2022).
6. Brillinger, M., Wuwer, M., Hadi, M. A., & Haas, F.: Energy prediction for CNC machining with machine learning. CIRP Journal of Manufacturing Science and Technology, 35, 715-723 (2021).
7. Adivarekar, M., & Liou, F.: Developing a General Postprocessor for Multi-Axis CNC Milling Centers. Computer-Aided Design & Applications, 57-68 (2012).
8. Mongan, P. G., Hinchy, E. P., O'Dowd, N. P., McCarthy, C. T., & Diaz-Elsayed, N.: An ensemble neural network for optimising a CNC milling process. Journal of Manufacturing Systems, 71, 377-389 (2023).
9. Kursa, M., Jankowski, A., Rudnicki, W.: Boruta - A system for feature selection. Fundamenta Informaticae 101, 271–285 (2010)
10. Patel, H.H., Prajapati, P.: Study and analysis of decision tree-based classification algorithms. In: International Journal of Computer Sciences and Engineering, vol. 6, no. 10, pp. 74–77, Indore (2018).
11. Parwala, V., Routa, B.K.: Machine learning based approach for process supervision to predict tool wear during machining. In: 28th CIRP Conference on Life Cycle Engineering, pp. 1–10. CIRP, Jaipur (2021).

Parametric optimization in EN31 alloy steel under MQL for enhanced machining performance

Sutanu Misra[1][0000-1111-2222-3333] and Goutam Paul [1][1111-2222-3333-4444]

[1] Institute of Engineering and Management (IEM), University of Engineering and Management Kolkata.
sutomechanical@gmail.com

Abstract. This research examines the rarely investigated use of liquid CO_2-assisted Minimum Quantity Lubrication (MQL) in the machining operation with an intermediate flow rate, bridging traditional MQL and reduced flow methods. Flow rate is one of the important parameter, which helps to analyze the effectiveness of machining operation. Liquid CO_2, with a lower specific heat (0.709 kJ/kgK) than air and higher density (1.98 kg/m³), increases cooling and lubrication, entering the tool-workpiece gap more efficiently than air. This work investigates EN31 alloy steel machining, with process parameters optimized via Response Surface Methodology (RSM). Analysis of variance (ANOVA) and regression models indicated high fitness, with R^2 values above 90% for Material Removal Rate (MRR) and surface roughness (Ra). Results demonstrate that MRR increases with depth of cut, speed, and feed rate, with flow rate influencing outcomes gradually. Similarly, Ra increases linearly with these parameters. Optimal flow rate selection under liquid CO_2-assisted MQL is critical to achieving better product quality, and enhanced machining performance.

Keywords: MQL, MRR, Response surface method.

1 Introduction

The rapid evolution of manufacturing created difficulties for industries as demand continues to grow dynamic environment. Sustainable manufacturing has emerged as an essential approach for modern industries, ensuring high product quality and production efficiency in recent years [1]. Sustainable manufacturing aims to minimize environmental impacts as it reduces energy consumption and increases efficiency, providing long-term benefits. Machining is a primary process in manufacturing, to get the desired dimensions of material by removing excess material from a raw workpiece [2]. During turning operations, the main cutting parameters cutting speed, feed rate, and depth of cut significantly influence surface roughness and energy consumption [3]. Roughness generally increases with higher feed rates but decreases with increased cutting speed and larger nose radius [4]. Heat-generated cutting tool interface due to friction is managed by cutting fluids, which reduce friction, enhance tool life, and maintain product quality.

Minimum Quantity Lubrication (MQL) has gained prominence as it drastically reduces the use of coolants compared to traditional wet cooling. MQL minimizes environmental impact by reducing health risks, extending tool life, and creating a cleaner working environment. While the heat-removal capacity of air-assisted MQL can be limited in high-energy machining operations. MQL using vegetable oils is more efficient than mineral oils, as vegetable oils have a higher lubricating and cooling effect [5]. Additionally, adding nanoparticles in MQL increases lubrication, minimizing friction and further enhancing sustainability. Continuous advancements in cutting tools with hard, nano-composite coatings indicated improved performance, especially at high speeds under MQL conditions, increasing tool life by 10-25% [6]. Optimization techniques like the Grey-Taguchi method have been used, highlighting the critical role of cutting speed in managing friction, temperature, and chip morphology [7]. For challenging materials like super duplex stainless steel, MQL improves machinability and the risk of crack formation due to high-temperature exposure. Deiab et al. [8] explored the effects of various cooling conditions, including cryogenic and MQL-assisted technology when machining Titanium Ti-6Al-4V alloy. Cryogenic cooling attained a positive outcome in tool wear and surface roughness but required higher energy than MQL. Similarly, in studies by Stanford et al. [9], cryogenic cooling using liquid nitrogen during turning operations decreased flank wear by 55% and 30%, respectively.

While MQL and cryogenic cooling are common, the use of liquid CO_2-assisted MQL in turning processes with varied flow rates remains underexplored. Typical MQL flow rates range from 0.33 ml/min to 1 ml/min, whereas reduced-flow techniques generally operate within 250 ml/min. This research adopts a unique approach, selecting a flow rate intermediate between traditional MQL and reduced-flow rates to enhance machining efficiency. This study focuses on optimizing machining parameters using liquid CO_2-assisted MQL for EN31 alloy steel. The chosen flow rate bridges the gap between conventional MQL and reduced flow, aiming to improve product quality while reducing costs and production time.

2 Experimentation

The experimental work focuses on turning EN31 alloy steel with specific Ø16mm × 300 mm dimensions, cutting tools, conditions, parameters, and measuring devices. The cutting tool used was a coated carbide insert with a 0.03 mm nose radius and the machining operation was performed on a precision lathe. Figure 1 illustrates a photographic view of the experimental setup. EN31 alloy, known for its use in automotive applications such as axles, spindles, and mandrels, is also used in mold dies [10]. Liquid carbon dioxide (CO_2) was maintained at a high pressure of 5 kg/cm² to ensure it remained liquid within the cylinder. As it exited the nozzle, sudden pressure drop has been occurred due to phase transformation. The conventional setup was modified where the regular tool holder was replaced by a computerized dynamometer to enhance efficiency. Material removal rate (MRR) was calculated using the weight differential before and after machining, divided by the machining time, whereas Surface roughness (Ra) was measured using a portable Talysurf device.

Table 1: Limits of Cutting Parameter

Parameters	Notification	Unit	Values		
			-1	0	1
Flow Rate	A	ml/min	10	11	12
Spindle speed	B	rpm	230	775	1200
Depth of cut	C	mm	0.3	0.7	0.9
Feed rate	D	mm/min	20	30	40

Fig. 1: Experimental setup

3 Results and Analysis

The current research consists of RSM based modelling of surface roughness, MRR, Temperature of rake surface and cutting force and followed by multi-objective optimization based on desirability function. Response surface methodology is applicable, i.e. influenced by input parameters [11]. The developed second-order regression equations are shown in **Eqn (1):**

$$Y = \beta_0 + \beta_1(A) + \beta_2(B) + \beta_3(C) + \beta_4(D) + \beta_{11}(A^2) + \beta_{22}(B^2) + \beta_{33}(C^2) + \beta_{44}(D^2) + \beta_{12}(AB) + \beta_{13}(AC) + \beta_{14}(AD) + \beta_{23}(BC) + \beta_{24}(BD) + \beta_{34}(CD) + \varepsilon \quad (1)$$

Where, $Y =$ output responses ; ε = error term

Table 1 depicts the values of the coded and actual value of each process variables. These levels as set by trial run and within the available range of parameters. Equations in terms of coded factors are also acceptable [12].

Based on the experimental results, second-order regression equations are modelled for surface roughness, and material removal rate. These equations are valuable for identifying the relative influence of the factors by

comparing their coefficients. RSM is applicable in the different real-life application such as the medical industry, automotive industry, electronic industry, where the optimum response is required. The ANOVA is implemented on experimental data to identify the significant cutting parameters influencing the responses under the application of liquid CO_2 assisted MQL to check the quality of the model [13]. If P-values in the table are below 0.05, then the associated variable is recognized statistically significant [14]. ANOVA mainly concentrates on analyzing the developed model with prior checking the accuracy of the process parameters, so that relevant results obtain [15].

3.1 Material Removal Rate

Table 2 represents the quadratic type of model accepted for prediction. The model is significant as the F-value is 15.15. A 0.01% chance of error due to noise occurs. Model terms are significant as **P-values** less than 0.0500 [16]. **Table 3** represents the corresponding ANOVA test results. Here, B, C, AC, B^2, C^2 are significant model terms. Here R^2 value is 93.81%. **Predicted R^2** of 84.35% aligns well with the **Adjusted R^2** of 87.625; i.e. the difference is less than 0.2. **Model Precision** indicates the signal to noise ratio with ratio greater than 4 is favourable. The ratio of 15.193 implies a sufficient signal, simplifies that the model can be used to explore the design space.

Table 2: Fit Summary for material removal rate

Source	Sequential p-value	Lack of Fit p-value	R^2	Adjusted R^2	Predicted R^2	Remarks
Linear	< 0.0001	0.6149	0.6013	0.6907	0.6082	
2FI	0.511	0.5929	0.5231	0.6835	0.4317	
Quadratic	**0.0014**	**0.9969**	0.9381	**0.8762**	**0.8435**	**Suggested**
Cubic	0.9965	0.7847	0.7445	0.7487	0.04	Aliased

The developed regression equation showing the relationship between the material removal rate and process parameter is as follows (Eqn 2):

MRR (gm/min) = 2.20046 + -0.088475 * A + 0.388533 * B + 0.486658 * C + -0.0587167 * D + -0.04505 * AB + -0.23285 * AC + 0.126425 * AD + -0.09925 * BC + -0.00825 * BD + 0.134875 * CD + 0.108133 * A^2 + 0.193045 * B^2 + -0.250442 * C^2 + -0.060355 * D^2 (2)

Table 3: Analysis of variance for material removal rate

Source	Sum of Squares	df	Mean Square	F-value	p-value	Remarks
Model	6.11	14	0.4366	15.15	<0.0001	significant
A-A	0.0939	1	0.0939	3.26	0.0926	
B-B	1.81	1	1.81	62.85	<0.0001	
C-C	2.84	1	2.84	98.61	<0.0001	
D-D	0.0414	1	0.0414	1.44	0.2508	
AB	0.0081	1	0.0081	0.2817	0.6039	
AC	0.2169	1	0.2169	7.52	0.0159	
AD	0.0639	1	0.0639	2.22	0.1586	
BC	0.0394	1	0.0394	1.37	0.2618	
BD	0.0003	1	0.0003	0.0094	0.924	
CD	0.0728	1	0.0728	2.52	0.1344	
A^2	0.0758	1	0.0758	2.63	0.1271	
B^2	0.2417	1	0.2417	8.39	0.0117	

C^2	0.4068	1	0.4068	14.12	0.0021	
D^2	0.0236	1	0.0236	0.8198	0.3806	
Residual	0.4035	14	0.0288			
Lack of Fit	0.0927	10	0.0093	0.1193	0.9969	Not significant
Pure Error	0.3108	4	0.0777			
Cor Total	6.52	28				

From 3D surface plot as highlighted in **Fig. 2** it has been detected that the MRR increases as depth of cut, cutting speed and feed rate increases but it changes very slowly with flow rate that means the flow rate is one of the important factors that need to be optimized. Also from **Fig. 3** it has been observed that the predicted result from RSM and actual results are in well agreement. The residuals also lie within lower and upper control limits. That means the experimental results are acceptable.

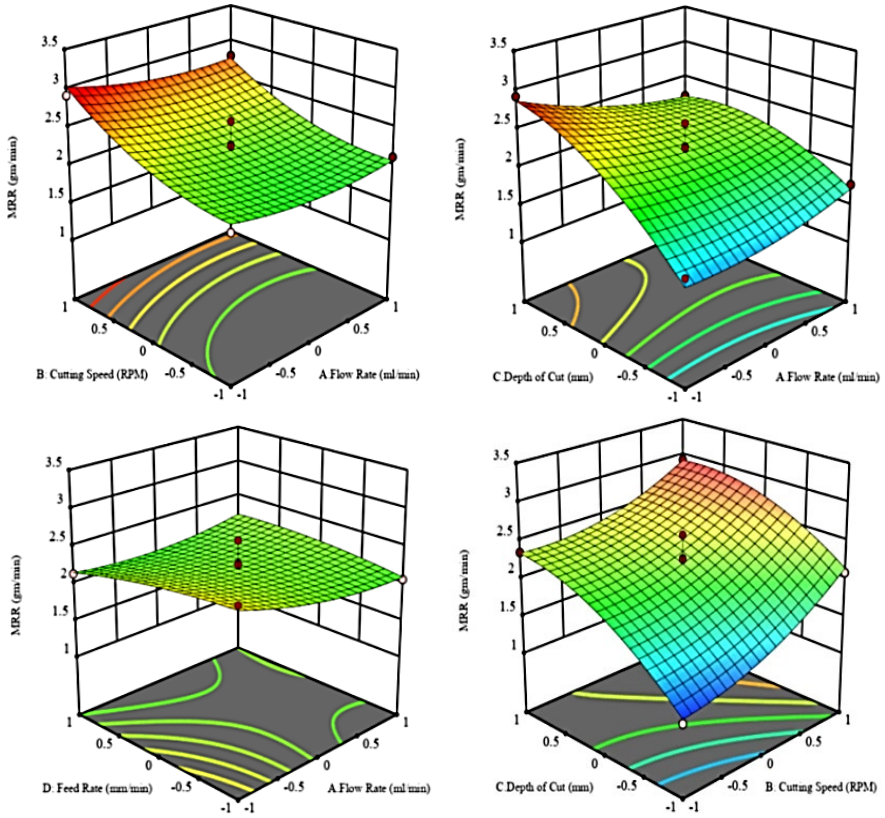

Fig. 2: 3D surface plot along with contour for MRR

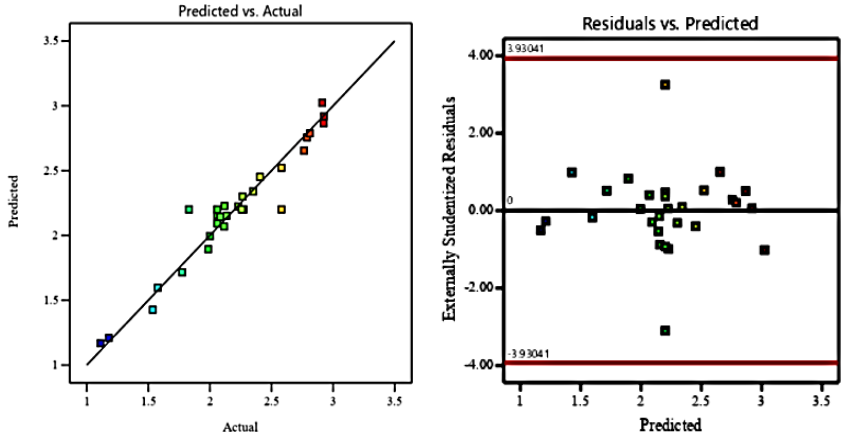

(a) (b)

Fig. 3: Plots for MRR (a) predicted versus actual, (b) residuals versus predicted

3.2 Surface Roughness

Here the linear model (as shown in **Table 4**) best suited for prediction of CLA values. The R^2 value is 99.75% indicates, it is very close to 1 so that the model is determined efficiently. **Table 5** depicts the ANOVA table where the F value of 639.25 shows the significance of the model. Here cutting speed, feed, depth of cut and flow rate all are the effective parameters on the surface roughness. Lack of fit is non-significant that means the acquired data are appropriate to fit the model. Here the signal to noise ratio is 89.064, indicates it lies in the desirable limit. The final regression equation for surface roughness is given in **Eqn (3).**

Table 4: Fit Summary for Surface Roughness

Source	Sequential p-value	Lack of Fit p-value	R^2	Adjusted R^2	Predicted R^2	Remarks
Linear	**< 0.0001**	**1.0000**	**0.9975**	**0.9982**	**0.9983**	**Suggested**
2FI	1.0000	1.0000	0.9967	0.9976	0.9983	
Quadratic	0.9999	1.0000	0.9934	0.9969	0.9975	
Cubic	1.0000	0.9993	0.9921	0.9927	0.9975	Aliased

Table 5: Analysis of variance for Surface Roughness

Source	Sum of Squares	df	Mean square	F-value	p-value	Remarks
Model	15.22	14	1.09	639.25	<0.0001	significant
A	0.0972	1	0.0972	57.15	<0.0001	
B	14.08	1	14.08	8280.25	<0.0001	
C	0.6769	1	0.6769	397.97	<0.0001	
D	0.3640	1	0.3640	214.02	<0.0001	
AB	0.0000	1	0.0000	0.0000	1.0000	
AC	0.0000	1	0.0000	0.0000	1.0000	
AD	0.0000	1	0.0000	0.0000	1.0000	
BC	0.0000	1	0.0000	0.0147	0.9052	
BD	0.0000	1	0.0000	0.0147	0.9052	
CD	0.0000	1	0.0000	0.0000	1.0000	
A^2	7.207E-07	1	7.207E-07	0.0004	0.9839	
B^2	0.0000	1	0.0000	0.0179	0.8955	
C^2	5.450E-06	1	5.450E-06	0.0032	0.9557	
D^2	5.450E-06	1	5.450E-06	0.0032	0.9557	
Residual	0.0238	14	0.0017			
Lack of Fit	0.0001	10	9.167E-06	0.0015	1.0000	not significant
Pure Error	0.0237	4	0.0059			
Cor Total	15.25	28				

CLA value (µm) = 7.834 + -0.09 * A + -1.08333 * B + 0.2375 * C + 0.174167 * D + 5.07044e-15 * AB + 2.3573e-16 * AC + 1.38981e-17 * AD + -0.0025 * BC + 0.0025 * BD + -6.75318e-17 * CD + -0.000333333 * A^2 + 0.00216667 * B^2 + 0.000916667 * C^2 + 0.000916667 * D^2 (3)

From 3D surface plots are displayed in **Fig. 4** it has been identified that the Ra increases linearly with increase of feed rate, depth of cut and cutting speed. Ra also changes linearly but very slowly with flow rate. The optimum levels of these input parameters require to be optimized.

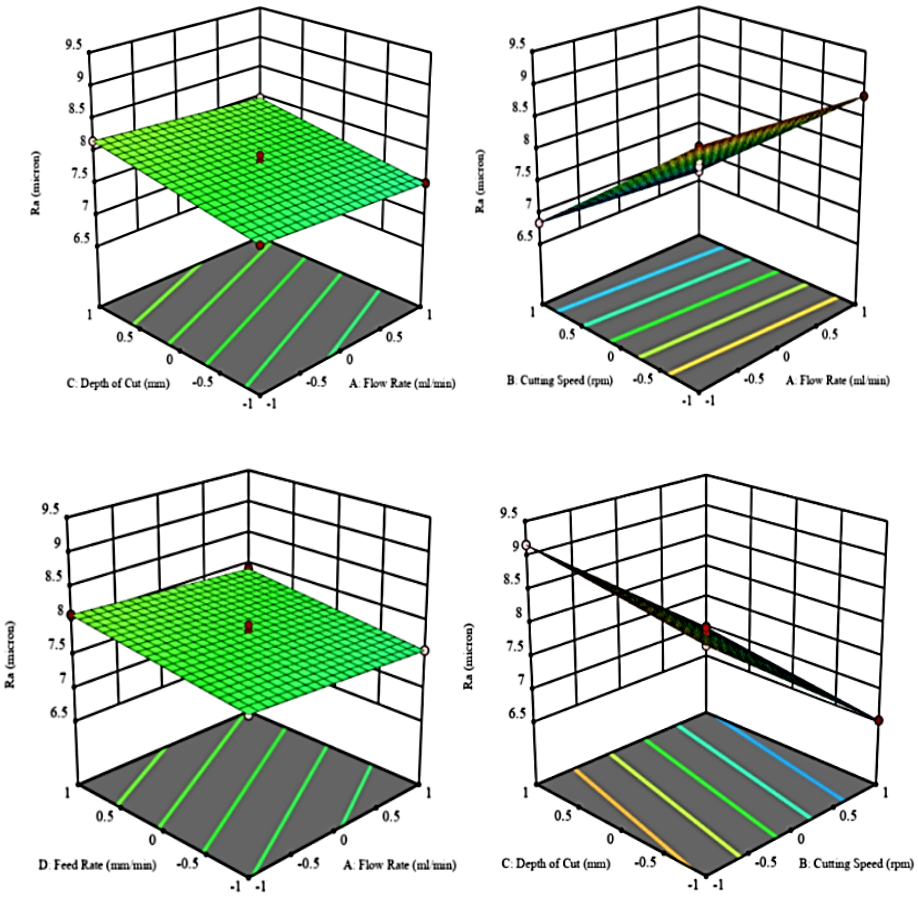

Fig. 4: 3D surface plot along with contour for Surface roughness

Also, from **Fig. 5** it has been observed that the predicted results and actual results are in well agreement. The residuals except one value also lies within lower and upper control limits. That means the experimental results are acceptable. The optimum level setting of the input process parameters are needed to optimise the MRR which is a larger the better type criteria corresponding to smaler the better type criteria CLA value is needed to synchronise the contradictory responses as well as to understand the process well.

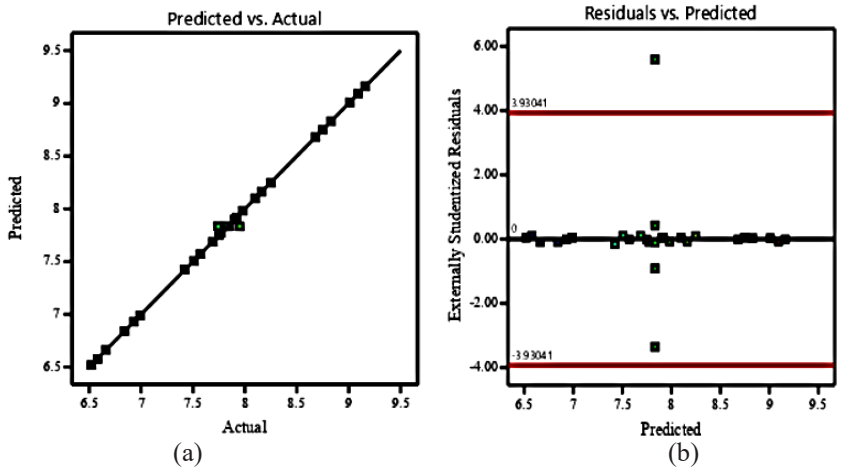

(a) (b)

Fig. 5: Plots for Ra (a) predicted versus actual, (b) residuals versus predicted

4 Conclusion

Some of the conclusions are drawn from this study-

a) The selected levels were applied in the design of experiments based on response surface methodology. Here 29 number of experiments have been performed based on Box-Behnken methodology.
b) RSM analysis provides the best regression equation supported by the ANOVA table. ANOVA table also provided the information about the fitness of the experimental data.
c) The 3D surface plots, along with contour plot, provided the idea about the interaction effect of the process parameters. The fitness data statistics tables were used to decide that for MRR the quadratic model is suitable as R^2 values were above 90%. Also adjusted R^2 and predicted R^2 are quite good (above 85%). For surface roughness, the R^2 value is above 90% for the linear model.
d) The developed regression equations using the best-suited coefficients provides the basis for further multi objective optimisation.
e) Material removal rate (MRR) increases with increase of depth of cut, cutting speed and feed rate but it changes very slowly with flow rate that means the flow rate is one of the important factors that need to be optimized.
f) Surface roughness increases linearly with increase of depth of cut, cutting speed and feed rate. Ra also changes linearly but very slowly with flow rate.

References

1. Das A, Patel S.K, Biswal B.B., Sahoo N, Pradhan A, Performance evaluation of various cutting fluids using MQL technique in hard turning of AISI 4340 alloy steel, Measurement, 150, (2020).
2. Valeria H. Y, Bhavsara S. N, Experimental Investigation of Surface Roughness and Power Consumption in Turning Operation of EN31 Alloy Steel, Procedia Technology, (14) 528 – 534, (2014).
3. Abhanga L B, Hameedullaha M, Parametric investigation of turning process on en-31 steel, Procedia Materials Science, (6), 1516 – 1523, (2014).
4. Miaa M., Morshedb M.S., Kharshiduzzamana Md, Razia M. H, Mostafaa M. R., Rahmana S. M.S., AhmadaI. , Hafizc M. T., KamalaA. M., Prediction and optimisation of surface roughness in minimum quantity coolant lubrication applied turning of high hardness steel, Measurement, (118), 43–51, (2018).
5. Sen B., Mia M, Krolczyk G. M, Mandal U. K, Mondal S. P., Eco-Friendly Cutting Fluids in Minimum Quantity Lubrication Assisted Machining: A Review on the Perception of Sustainable Manufacturing, International Journal of Precision Engineering and Manufacturing-Green Technology, ISSN 2198-0810, (2021).
6. Kumara S.A., Yoganath V.G. , Krishna P., Machinability of Hardened Alloy Steel using Cryogenic Machining, Materials Today: Proceedings, (5), 8159–8167, (2018).
7. Chinchanikar S, Choudhury S.K., Hard turning using HiPIMS-coated carbide tools: Wear behaviour under dry and minimum quantity lubrication (MQL), Measurement, S0263-2241(14)00263-2, (2014).
8. Deiaba I., Razaa S. W., PervaizaS.,Analysis of Lubrication Strategies for Sustainable Machining during Turning of Titanium Ti-6Al-4V alloy, Procedia CIRP (17), 766 – 771, (2014).
9. Stanforda, M.., Lister P.M.,Morgana C., Kibble K.A., Investigation into the use of gaseous and liquid nitrogen as a cutting fluid when turning B.S. 970-80A15 (En32b) plain carbon steel using W.C.–Co uncoated tooling, journal of materials processing technology (209), 961–972, (2009).
10. Behera B C, Ghosh S, Rao PV, 2017, modelling of cutting force in MQL machining environment considering chip tool contact friction, Tribology International, (117), 283-295, (2018).
11. Prasath K.M., Pradheep T, Suresh S., Application of Taguchi and Response Surface Methodology (R.S. M) in Steel Turning Process to Improve Surface Roughness and Material Removal Rate, Materials Today: Proceedings (5), 24622–24631, (2018).
12. Ravuri M., Y. Reddy S. K., Vardhan D. H., Parametric optimisation of face turning parameters for surface roughness on EN31 material using RSM and Taguchi method, Materials Today Proceedings, (2020).
13. Mia M., Mathematical Modelling and optimisation of MQL assisted end milling characteristics based on RSM and Taguchi method, Measurement, S0263-22241(18)30110-6, (2021).
14. Davoodi B., Eskandari B., Tool wear mechanisms and multi-response optimisation of tool life and volume of material removed in turning of N-155 iron–nickel-base superalloy using RSM, Measurement (68), 286–294, (2015).
15. Aslan A., Optimisation and analysis of process parameters for flank wear, cutting forces and vibration in turning of AISI 5140: A comprehensive study, Measurement (163), 107959, (2020).
16. Roy A., Kumar N., Das S., Bandyopadhyay A., Optimisation of Pulsed Nd:YVO4 Laser Marking of AISI 304 Stainless Steel Using Response Surface Methodology, Materials Today: Proceedings, (5) 2, 5244-5253, (2018).

New Generation Forming & Welding Technology

Micro-Friction Stir Welding (μFSW) of Aluminum Alloys Using Pinless Tool

Meghnath Sen[1*] and Asit Baran Puri[1]

[1] Department of Mechanical Engineering, National Institute of Technology Durgapur, Durgapur-713209, West Bengal, India
*meghnath001@gmail.com

Abstract. Micro-friction stir welding is a highly demanding technology adopted in various industries because it is cost-effective, energy-efficient and environment-friendly. Carrying out μFSW is challenging due to decreased parent material thickness (thickness ≤ 1mm). The current study attempts to investigate μFSW process for aluminum alloys. 0.8mm thick sheets of aluminum alloy (Al6061-T6) were joined successfully in lap configuration using μFSW process. A pinless tool was used in this process to eliminate exit hole defect. Welding was performed with a consistent traverse speed of 250 mm/min, while the tool's spinning velocities varied at 2000 rpm, 2500 rpm and 3000 rpm. The plunge depth for the process was maintained at 0.2 mm. The maximum strength of the weld joint was achieved 239 MPa, equivalent to 76% of the parent material's strength. Defects like little amount of flash and irregular shoulder marks were found in the weld region. Finally, microhardness has been measured in weld region to assess the mechanical characteristics and quality of the weld.

Keywords: Micro-Friction Stir Welding, Aluminum alloys, Pinless Tool, Lap Joint, Lap-shear Test, Microhardness, Weld Defects

1 Introduction

The development of solid-state welding offers important prospects for fulfilling the demands of numerous industries like aerospace, automobile, electronics, marine, packaging and so on. Micro-friction stir welding (μFSW) process is comparatively a newly developed process to join thin sheets (thickness ≤ 1mm). A non-consumable spinning tool is utilized in this process to join parent materials below their melting point temperature. The rotating tool is inserted at one end of the parting line and made to travel along the weld line. Thus, welding is done due to the combined effect of frictional heat and intermixing of softened material. Aluminum (Al), the third largest element in earth's surface, is well known due to its excellent strength, sound workability, good recyclability and great corrosion resistance properties. But there are certain challenges associated with welding of aluminum alloys. One of the main reasons is the high thermal conductivity and low melting point of aluminum. Due to high thermal conductivity, heat is quickly conducted away from the weld zone. This makes it challenging to maintain a consistent and localized high temperature needed for successful welding. Further due to low melting point, the material melts quickly and flows away before a proper weld bead is formed [1-3]. In the year 2008, Scialpi et al. [4] successfully joined 0.8 mm thick similar Al alloys (Al2024-T3) and 0.8mm thick dissimilar Al alloys (Al2024-T3 and Al6082-T6) in butt configuration without any defects. The authors reported that the highest strength of the weld joint achieved was 91% of parent material (Al2024-T3) strength for similar joints and 69% of base material (Al6082-T6) strength for dissimilar joints. The weld joint failure occurred within the weld region, caused by a reduction in thickness at that specific area. Sattari et al. [5] joined 0.8mm thick aluminum 5083-H323 sheets using μFSW process taking into account the heat loss with a modified fixturing. A roll was employed in front of the tool to evade fixturing issues and a heat-resistant material plate was used as backing plate to reduce heat loss. The authors concluded that the weld joint was defect free in an operating temperature range 410°C - 510°C, and further increase in heat input resulted in hardness degradation in weld region. Ahmed et al. [6] joined 0.5mm thick aluminum 6061-T6 sheets with a lever type developed fixture in a CNC milling machine to avoid fixturing issues and asbestos sheets were used below cover plates to reduce heat loss during the process. Ultimate tensile strength of the butt joint was obtained as 74% of the base material's strength. The optimum welding condition was obtained at a spinning velocity or tool rotational speed of 2000 rpm and traverse speed of 150 mm/min. In addition, wang et al. [7] studied μFSW with 0.254 mm thick, 1100-O aluminum sheets at an extremely fast spinning velocity upto 30,000 rpm using CNC milling machine. Defects like surface flash, tunnels and semicircular hooks were found within the weld region. The optimal condition for a sound weld joint was reported at a spinning velocity of 20,000 rpm, a traverse speed of 3mm/s and a plunge depth of 0.85mm. High tool rotational speed improves frictional heat generation, which helps in good stirring and material mixing during μFSW process. Some researchers [8-11] used pinless tool in μFSW process to enhance the quality of the weld joints and eliminate

the exit hole problems, and consequently studied mechanical attributes of the weld. Huang et al. [12] investigated the weld quality, surface formation, thickness reduction in weld zone and its mechanical properties during µFSW process. The authors reported that increased tool rotational speed led to good weld surface without defect. Weld joint formation is also influenced by tool plunging depth. A proper plunging leads to good material mixing with adequate heat generation [12-15]. Presently, most of the studies are focused on µFSW process with different tool configurations, different process parameters, mechanical attributes or qualities and microstructure of the weld zone and process parameter optimizations. Although some studies have been done for butt configuration with tool pin primarily, a very few research works have been reported for lap configuration with pinless tool. Hence, the present research work attempts to investigate the impact of pinless tool in µFSW process while making lap joints. Thus, in the present study, Al6061-T6 (aluminum alloy) sheets of 0.8mm thickness were joined in lap configuration using a pinless tool with an 8mm diameter. The mechanical attributes or qualities of the lap joint like lap-shear strength and microhardness were determined. The effects process parameters on weld surface formation using pinless tool were also investigated in this study.

2 Experimental Details

In present study, µFSW process was performed in a conventional vertical milling machine (model: M3; Serial No: 22712; make: KMT, India). A fixture was designed and fabricated in this regard to provide appropriate clamping pressure and to avoid slipping and tearing of thin sheets during operation. The complete setup for the µFSW process is illustrated in Fig. 1(a). A pinless tool, made from H13 tool steel with 8 mm diameter, was used in this process, as presented in Fig. 1(b). This tool material shows excellent strength at high temperature during welding. It has excellent thermal shock resistance, wear resistance, good hardenability, high strength and hot toughness. Aluminum alloy (Al6061-T6) sheets with thickness 0.8mm has been used as base material in the present research. The sheet dimension was 110mm in length and 50mm in width. The chemical composition of aluminum alloy (Al6061-T6) sheet is provided in Table 1. Three different tool rotational speeds, or spinning velocities of the tool were selected for this process: 2000 rpm, 2500 rpm and 3000 rpm. Other parameters like welding speed or traverse speed (250mm/min), Plunge depth (0.2mm), tool inclination angle (0°) and dwell time (5 sec) were kept constant. The welding is done at room temperature.

After welding, rectangular lap-shear test specimens of 80mm ×10 mm (as illustrated in Fig. 2) was prepared for each weld joint to analyze mechanical properties as well as quality of the joints [16]. Lap-shear tests were carried out at ambient or room temperature using a precise UTM machine (model: Instron-8516, capacity: 100kN) with a constant speed of crosshead fixed at 0.2mm/min. Microhardness of the joints were determined on a hardness tester (model: MMT-X7B, make: Matsuzawa, Japan) at a fixed load of 1000g for a dwell time of 15sec. Additionally, to analyze the interface of the lap joint, a sample was prepared for observation under a field emission scanning microscope (FESEM, Zeiss-SIGMA). The sample was polished with sandpapers up to 2000 grits, followed by 0.5 µm diamond paste and then etched using Keller's reagent (190 ml. distilled water, 5 ml. HNO_3, 3 ml. HCl, and 2 ml. HF).

Table 1. Chemical composition of Al6061-T6

Element	Al	Mg	Si	Ti	Cr	Mn	Fe	Cu	Zn
Weight (%)	96.4	1.9	0.4	0.1	0.2	0.1	0.6	0.3	0.1

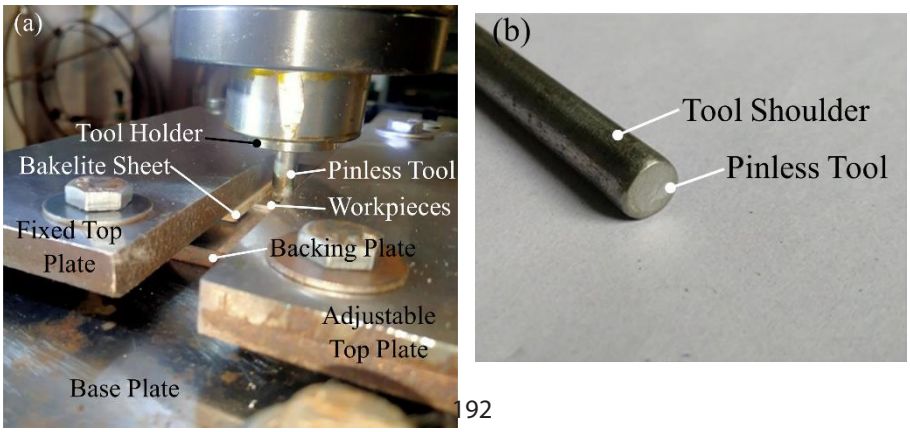

Fig. 1. (a) Complete setup of µFSW process; (b) µFSW tool

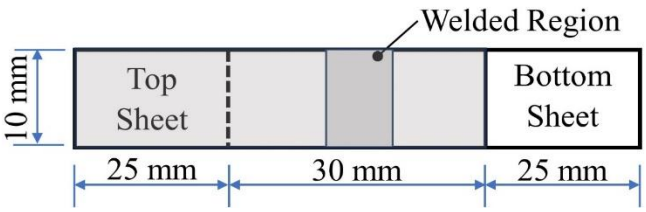

Fig. 2. Lap-shear test samples

3 Results and discussion

3.1 Surface appearance

Welding surface formation using pinless tool at different spinning velocities are shown in Fig. 3. It is clearly visible that surface appearance improves noticeably, becoming smoother and more uniform with an increase in tool rotational speed. Higher spinning velocities facilitate better heat generation and more effective material mixing, which contribute to the production of a smooth and uniform surface finish. In addition, as the spinning velocity of the tool increased from 2000 rpm to 3000 rpm, there was a notable enhancement in frictional heat generation and material mixing. This increased heat input allows for improved plastic deformation and smoother transportation of the material, which helps achieve a defect-free weld. Defects like crack, tunnel voids were not present in the weld region which indicated a good transportation of plasticized materials during the process.

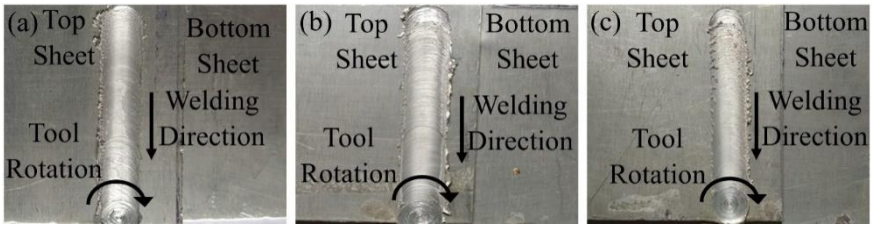

Fig. 3. Weld surface of μFSW joint: (a) 2000 rpm, (b) 2500 rpm and (c) 3000 rpm

3.2 Cross-sectional observation

Cross-sectional observation of the lap joint in μFSW is crucial for assessing the quality of the joint. The primary focus is to ensure that the base materials are properly joined at the interface and to identify any defects that might compromise the weld's performance. Fig. 4 represents the cross-sectional view of a lap joint produced at 2500 rpm, highlighting different regions [(i)–(iv)] of the weld. It was evident from the image that the central region, where the tool's action was most intense, exhibited proper material mixing, resulting in a homogeneous structure without any joining interface. However, as the distance from the weld center increased, the joining interface line became discernible. Detailed FESEM images of the four regions [(i), (ii), (iii), and (iv)] provided insights into the specific characteristics of each zone. In the first region [corresponding to Fig.4 (i)] and the fourth region [corresponding to Fig.4 (iv)], bonding ligament were clearly visible. In contrast, no such defects were found in the second and third regions [corresponding to Fig.4 (ii) and (iii)]. The cross-sectional analysis indicated that adequate heat generation and extensive material intermixing occurred in the central region and its vicinity, resulting in a defect-free and robust weld. However, as the distance from the centerline increased, heat loss occurred, leading to insufficient heat input and poor material mixing, which affected the joint quality in those areas. This resulted in a visible joining interface. The presence of bonding ligaments in the outer regions highlighted the critical role of heat input in achieving a strong joint.

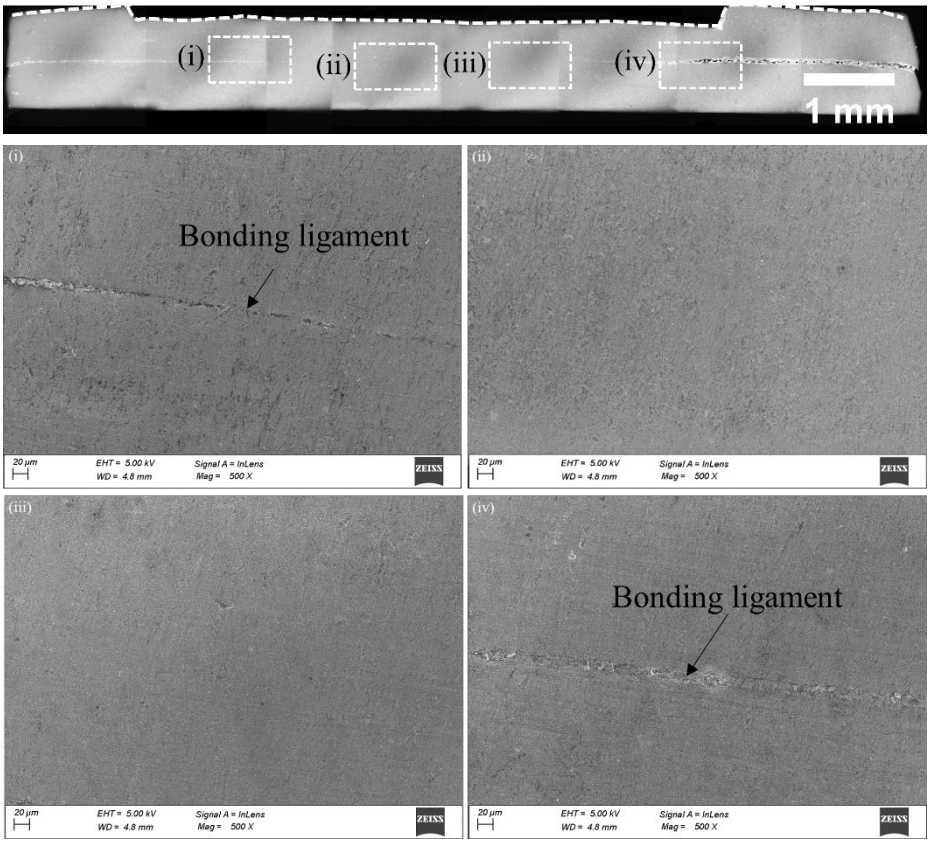

Fig. 4. Cross-sectional view of µFSW lap joint developed at 2500 rpm; (i)-(iv) FESEM images at different weld regions

3.3 Lap-shear test

Test specimens for lap-shear analysis were prepared in a rectangular shape (80mm ×10 mm), as shown in Fig. 2. Lap-shear tests were carried out using a highly precise Universal Testing Machine (UTM Model: Instron -8516, capacity: 100 kN) with a fixed crosshead speed of 0.2mm/min. Initially, the samples were held between two crossheads, one is fixed and another movable. After the load was applied, neck formation started at weld zone and finally, breaking took place. The lap-shear strengths of the weld joints were recorded as 142 MPa, 239 MPa and 173 MPa, which was 45%,76 % and 55% of the base material's strength (314MPa). The highest strength observed was 239MPa in the weld specimen, obtained at TRS of 2500 rpm. Lap-shear strength initially increased and then slightly decreased as the speed continued to rise. High rotational speeds can subject the material to rapid and intense heating, which may result in undesirable metallurgical changes, and the formation of undesirable microstructures that negatively affect the mechanical attributes or qualities of the weld joint. During testing, the locations of fractures were found in the weld region as illustrated in Fig. 5(a) and Fig. 5(b). This occurrence might be attributed to thinning in the weld zone. Fig. 6(a) and Fig. 6(b) present detailed analyses of the mechanical behavior and joint performance at varying tool rotational speeds. Fig. 6(a) illustrates the stress-strain diagrams obtained for welds produced at different rotational speeds, highlighting the material's response to applied stress and its deformation characteristics. The curves provide insights into the weld's mechanical properties, such as joint strength, which are critical indicators of joint quality. Fig. 6(b) shows the joint strength with respective percentage elongation at different tool rotational speeds. This combination of two figures provides valuable insights into the mechanical performance of the welds, highlighting how variations in rotational speed influence both the strength and ductility of the joints.

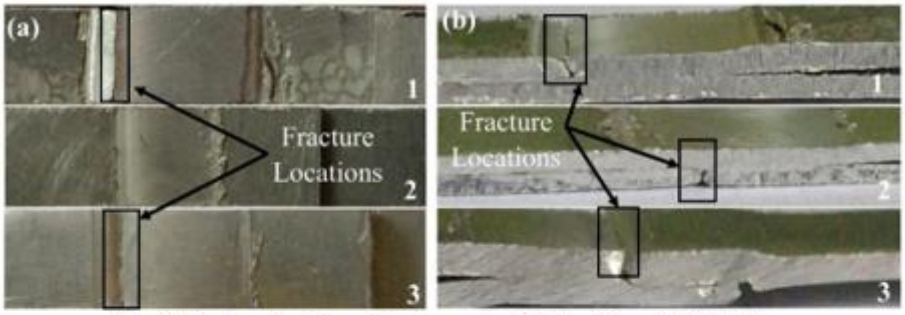

Fig. 5. Fracture locations in test samples: (a) Top View, (b) Side View

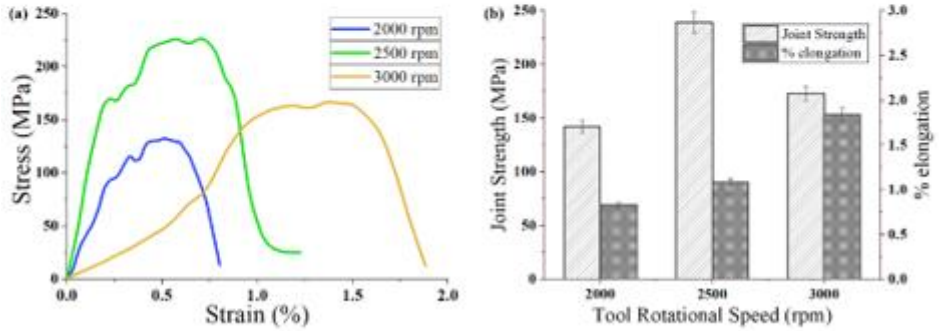

Fig. 6. (a) Stress – strain diagram; (b) joint strength and % elongation at different tool rotational speed

3.4 Micro hardness

Micro hardness tests assess the material's resistance to deformation caused by indentation. The spinning velocity of the tool, commonly defined as how fast the tool spins about its axis, is a crucial factor in μFSW. It affects the temperature during the process, which changes the material's physical properties. Variations in tool's rotational speed significantly influence the microhardness of the welded material, as illustrated in Fig. 7(a). The graph shows that as the spinning velocity increases from 2000 rpm to 3000 rpm, the microhardness value also rises. This could be due to the improvement in frictional heat generation. This additional heat softens the material, facilitating better intermixing and leading to more finer grain structure. Finer grains are typically associated with higher hardness, as they offer greater resistance to deformation. Microhardness distribution along the weld zone of μFSW joints are presented in Fig. 7(b). It is clearly evident that hardness distributions at all weld joints are almost W-shaped. During μFSW process, generation of frictional heat and intermixing of the plasticized material depends upon the faying surface of the pinless tool. Frictional heat can cause localized heating of the material, while rapid cooling after the welding tool passes results in the formation of fine-grained microstructures in the weld region, contributing to increased hardness. Further, the rotational movement and axial force applied by the tool lead to intense plastic flow, causing grain refinement and work hardening in the material, which leads to higher hardness values. Rotational speed is more important in this case. The maximum hardness across weld zone was found 70.5HV, which is lower than the base material hardness (101.2HV). This phenomenon was found as the μFSW process involves the stirring and intermixing of the material by the rotating tool. This mixing action promotes the redistribution of alloying elements within the weld zone, affecting the microstructure and contributing to changes in hardness.

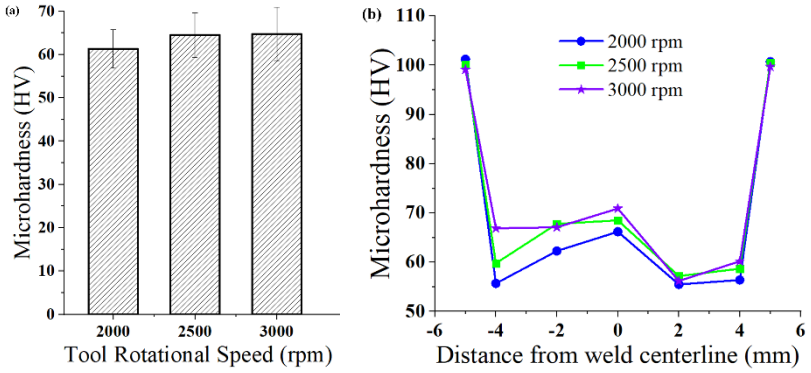

Fig. 7 Microhardness at different (a) tool rotational speed; (b) distance at weld zone

3.5 Defects

Obtaining sound weld joints using µFSW process is challenging as several parameters associated with it affect the quality of the joint in a combined and complicated manner. The literature survey shows that welding speed, tool rotational or spinning speed (TRS) and axial force have significant impacts on µFSW process. Generally, voids and tunnel defects are found in weld region due to inadequate heat and material flow during process. Sticking defects are found in case of excessive heat generation. Material thinning is mainly caused due to excessive axial forces during µFSW welding. However, in the present study, a few defects like flash generation and irregular shoulder marks were found as shown in Fig. 8. A little flash was generated due to the plunge depth. Irregular shoulder marks were found at a higher rpm of 2500 rpm. It may be caused due to tool wear and tear at high speed, as tool geometry and surface condition changes. Further, inhomogeneous material flow during process can result in irregularities in the shoulder marks. No sticking phenomenon was observed. Also, cracks, voids and tunnel defects were not found in weld region.

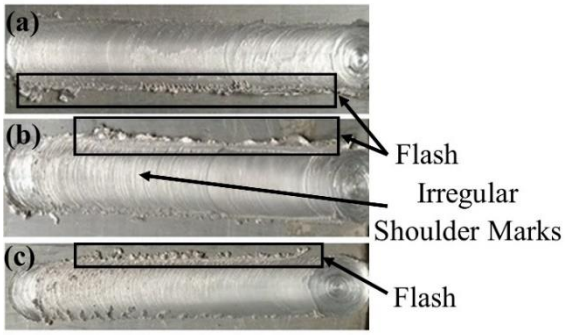

Fig. 8. Defects in µFSW weld joints: (a) 2000 rpm, (b) 2500 rpm and (c) 3000 rpm

4 Conclusions

In the current study, 0.8 mm thick aluminum (Al6061-T6) sheets were successfully joined using µFSW process. The µFSW technique proved effective in achieving strong, reliable joints with this specific alloy and thickness. The study provides insights into the performance of µFSW for thin sheet materials, highlighting its potential for precision applications in aerospace and automotive industries. The major findings from this current work led to the subsequent conclusions:

(a) Exit hole problem could be eliminated using pinless tool
(b) The highest lap-shear strength was attained in a weld sample produced with a spinning velocity of 2500 rpm and a traverse speed of 250mm/min.
(c) The fracture locations were found within the welding zone due to the weld zone thinning effect.
(d) The weld joint exhibited an optimum strength of 239 MPa, equating to 76% of the base material's strength.
(e) No significant defects except a little of flash was found at of the welding joints.

References

1. Sen, M., Shankar, S., & Chattopadhyaya, S.: Investigations into FSW joints of dissimilar aluminum alloys. Materials Today: Proceedings, 27, 2455–2462 (2019).
2. Sen, M., Shankar, S., & Chattopadhyaya, S.: Micro-friction stir welding (μFSW)-A review. Materials Today: Proceedings, 27, 2469–2473 (2019).
3. Sen, M., & Puri, A. B.: Formation of intermetallic compounds (IMCs) in FSW of aluminum and magnesium alloys (Al/Mg alloys) − A review. Materials Today Communications, 33 (2022).
4. Scialpi, A., de Giorgi, M., de Filippis, L. A. C., Nobile, R., & Panella, F. W.: Mechanical analysis of ultra-thin friction stir welding joined sheets with dissimilar and similar materials. Materials and Design, 29(5), 928–936 (2008).
5. Sattari, S., Bisadi, H., & Sajed, M.: Mechanical Properties and Temperature Distributions of Thin Friction Stir Welded Sheets of AA5083. International Journal of Mechanics and Applications, 2(1), 1–6 (2012).
6. Ahmed, S., & Saha, P.: Development and testing of fixtures for friction stir welding of thin aluminium sheets. Journal of Materials Processing Technology, 252, 242–248 (2018).
7. Wang, K., Khan, H. A., Li, Z., Lyu, S., & Li, J.: Micro friction stir welding of multilayer aluminum alloy sheets. Journal of Materials Processing Technology, 260, 137–145 (2018).
8. Ni, Y., Liu, Y., Zhang, P., Huang, J., & Yu, X.: Thermal cycles, microstructures and mechanical properties of AA7075-T6 ultrathin sheet joints produced by high speed friction stir welding. Materials Characterization, 187 (2022).
9. Simoncini, M., Ciccarelli, D., Forcellese, A., & Pieralisi, M.: Micro- And macro- mechanical properties of pinless friction stir welded joints in AA5754 aluminium thin sheets. Procedia CIRP, 18, 9–14 (2014).
10. Ni, Y., Fu, L., & Chen, H. Y.: Effects of travel speed on mechanical properties of AA7075-T6 ultra-thin sheet joints fabricated by high rotational speed micro pinless friction stir welding. Journal of Materials Processing Technology, 265, 63–70 (2019).
11. Ni, Y., Qin, D. Q., Mao, Y., Xiao, X., & Fu, L.: Influences of welding parameters on axial force and deformations of micro pinless friction stir welding. International Journal of Advanced Manufacturing Technology, 106(7–8), 3273–3283 (2020).
12. Huang, Y., Meng, X., Zhang, Y., Cao, J., & Feng, J.: Micro friction stir welding of ultra-thin Al-6061 sheets. Journal of Materials Processing Technology, 250, 313–319 (2017).
13. Huang, Y., Meng, X., Lv, Z., Huang, T., Zhang, Y., Cao, J., Zhou, L., & Feng, J.: Microstructures and mechanical properties of micro friction stir welding (μFSW) of 6061-T4 aluminum alloy. Journal of Materials Research and Technology, 8(1), 1084–1091 (2019).
14. Ni, Y., Fu, L., Shen, Z., & Liu, X. C.: Role of tool design on thermal cycling and mechanical properties of a high-speed micro friction stir welded 7075-T6 aluminum alloy. Journal of Manufacturing Processes, 48, 145–153 (2019).
15. Panchal, M., Patel, D., Vyas, H., & Mehta, K.: Ultra-thin friction stir welding on aluminum alloy. Materials Today: Proceedings, 26, 2888–2894 (2019).
16. Kimapong, K., & Watanabe, T.: Lap Joint of A5083 Aluminum Alloy and SS400 Steel by Friction Stir Welding. MATERIALS TRANSACTIONS, 46(4), 835–841 (2005).

Statements and Declarations

The authors declare that they have no known competing financial interests or personal relationships that could have appeared to influence the work reported in this paper.

Funding

The authors declare that no funds, grants, or other support were received during the preparation of this manuscript.

Acknowledgement

The authors express their gratitude to the Department of Metallurgical & Materials Engineering, NIT Durgapur, and the Centre of Excellence (COE) in Advanced Materials, NIT Durgapur, for providing the facilities for Lap-shear testing, Hardness testing and FESEM analysis (Zeiss-SIGMA).

Author Contributions

Meghnath Sen: Writing − original draft preparation, Conceptualization, Methodology, Data collection, Formal analysis and Investigation. **Asit Baran Puri:** Writing − review & editing, Supervision.

Microwave-Assisted Fusion Joining of Natural Fiber Composites

Abhijay Muliya[1], Himanshu Pathak[1], Sunny Zafar[1], Subhamoy Sen[1*]
[1]Composite Design and Manufacturing Research Group, School of Mechanical and Materials Engineering, Indian Institute of Technology, Mandi, Kamand, Mandi, Himachal Pradesh, 175075, India
*Corresponding Author E-mail: subhamoy@iitmandi.ac.in

Abstract. Nowadays, requirement of natural fiber-based polymer composites is increasing because of environmentally friendly characteristics compared to synthetic polymer-based composites. Composite materials mainly known for its light weight and high strength characteristics, are widely used in the field of aerospace and automotive industries. The need of joining of composites is often required to join complex and large structures. There are many joining techniques which are used in manufacturing industries like Mechanical, Fusion and Adhesive joining. These traditional methods have certain limitations. To address these issues, Microwave-based joining technique have been developed and implemented in this work. This paper presents joining of Sisal Reinforced Polypropylene Composites (SRPC) using Microwave-Assisted Fusion Joining (MAFJ) process as a novel joining technique for thermoplastic-based polymer composites. The composite samples were joining using heat absorbing material called susceptor. For comparison of joints, the samples also joined without susceptor material. The efficacy of joined samples was evaluated using standardized testing procedures. Specimen were also tested under the tensile loading to measure strength of base material. The results showed that MAFJ technique having high joining efficiency, which indicates potential use for structural applications.

Keywords: Microwave-assisted joining technique; Single Lap Joint; Thermoplastic-based Natural fiber Composites;

1 Introduction

In today's fast developing world, requirement of sustainable and specific work-oriented materials is increasing. The usage of composite materials is booming because they are having of high strength to weight ratio, high stiffness and corrosion resistivity. Composites are often used for manufacturing of aerospace and automobile parts [1-3]**.** There is a requirement to join these components as large structure cannot be produced in once. Amna Siddique at el. concludes that many traditional methods have been developed to join different types of composite structures according to requirement in different applications, like Mechanical joining, Fusion welding and adhesive joining. However, these joining techniques are having certain limitations. Mechanical joining techniques like bolting and riveting require a drilling or puncturing to assemble parts together, which compromises with material integrity, breaks the fibers and generate stress concentration around the joint area. This stress concertation leads sudden failure at joint area. Moreover, mechanical fasteners contribute in increment of overall weight of overall assembly, which negates lightweight advantage of composite materials. Adhesive joining, although it is good joining technique and avoids puncturing in the material, but it requires precise surface preparation and challenges to susceptibility to environmental degradation, and require long curing time, sensitivity to environmental factors such as temperature and moisture, also there is a difficulty in disassembly without damaging the parent component. On the other hand, thermal welding techniques of thermoplastic composites have also been explored for the joining of thermoplastic composites. These methods are effective in some cases but they have often some limitations like thermal degradation of natural fibers, inconsistent heat distribution, difficulties in welding of large and complex shapes [4]. Also, ultrasonic welding having constrains with thin parts and precise surface alignment for joining [5]. To overcome these challenges, MAFJ is employed as a novel joining approach [6, 7]. The novelties of joining SRPC are as mentioned below:

- SRPC single lap joint is implemented utilized natural fiber to enhance environmental sustainability.
- To stick with light weight benefits of composite materials MAFJ of single lap SRPF composite has been implemented.
- MAFJ is a versatile joining method that can be used with wide range of thermoplastic composites.

Previous study in the microwave assisted joining of natural composites highlighted significant advancement. Singh et al. explored microwave assisted joining of PLA/sisal composite concludes without filler material joint is not much efficient [8]. Bajpai et al. investigated MAFJ of Polypropylene (PP) and Polylactic Acid (PLA) with Grewia optiva (GOV) and Nettle Fibers (NF), including combination such as PLA/GOV, PLA/NF, PP/GOF and PP/NF, with the temperature variation along lap area computationally [7]. In the above-mentioned literature Teflon tap is used to develop uniform pressure and contact between

two adherend material. Also, the existing literature says that, MAFJ of Sisal-Reinforced Polypropylene Composites have not been studied using bolt operated Teflon fixture. Therefore, this technique is focusing on joining of SRPC using MAFJ.

2 Materials and Method

Sisal fiber is used as the reinforcement and Polypropylene (PP) pallets are used as matrix material. Ther PP had density of 0.901 g/cm^3 and Melting temperature of 168°C. A fixed-frequency microwave applicator is used for heating process, having maximum output frequency of 900 W at 2.45 GHz. The dimensions of Microwave cavity were 49.5L × 51W × 30.5H (in cm). The PP pallets were dried in hot air oven for 72 hours to remove moisture. Sisal fibers were alkali treated using microwave and then dried at room temperature for 24 hours [9]. To remove excess moisture from fibers they were further dried for 48 hours at 55°C. A thin sheet of thickness 2.5 mm was produced using compression moulding having mould dimensions of 17 cm × 17 cm. The moulding process had contact time of 30 minutes and then allowed to cool down at room temperature.

Single-layered SRPC plates were manufactured using compression moulding, in which sisal fibers are placed between the PP plates. The layers were further heated for 40 minutes and allowed to melt down PP Plates at 170°C and 10 MPa. The resulting SRPC had thickness of 5 mm and fiber weight fraction were 17.3 %. The samples were cut form SRPC plate using LASER cutter according to ASTM D3039 [10] and ASTM D5868 (Lap Shear Adhesion for FRP) standards [11]. The sample size was 101.6 cm × 25.4 mm. The surface preparation of overlap area was done using Grade-80 emery paper to increase the area for fusion bonding in lap joint.

3 Joining Procedure, Parameters and Results

Charcoal has a higher capacity to absorb electromagnetic waves. A paste of charcoal and acetone, which are immiscible solutions, was applied to the overlap area. The required weight of charcoal used per sample was 2 mg. Teflon, being highly transparent to microwaves, was used in a fixture to apply pressure for fusion, as shown in the Figure 1. For joining, a multimode microwave was used. Sisal-reinforced polypropylene composites (SRPC) were exposed to microwaves for 180 seconds at 360W power output. After fusion in the lap area, a 3-phase composite region developed. Additionally, SRPC without charcoal susceptors was exposed to microwaves for 300 seconds at 900W [7, 8].

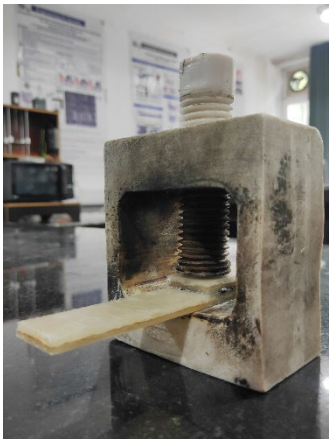

Figure 1. Bolt-Operated Teflon fixture

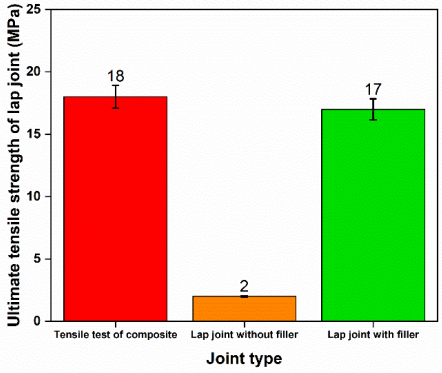

Figure 1. Comparison of Ultimate tensile strength of lap joint

The parent specimen was tested for tensile strength on a Universal Testing Machine (UTM) according to ASTM D3039 standard [10], with a displacement speed of 2 mm/min. The joined samples were also tested on the UTM. The test results are shown in the figure 2. Comparison results indicate that the joint without charcoal susceptor had a negligible effect, while the joint with charcoal susceptor exhibited significantly higher strength. The slight drop in strength compared to the parent material was attributed to the heat-affected zone.

4 Conclusion

The SRPC samples were fabricated using compression moulding and joined through a MAFJ process. The samples were tested on a Universal Testing Machine (UTM) with displacement rate of 2 mm/min at room temperature, leading to the following conclusions:

- Samples without charcoal susceptor did not achieve effective joining.
- The quantity of susceptor must be carefully controlled, as excessive amount of filler material can get overheated and damage the samples.
- A bolt-operated Teflon fixture was employed to facilitate the joining process, in the replacement of Teflon tap as it ensures consistent overlap area contact and enhances joint reliability.
- Samples incorporating a charcoal susceptor exhibited a joint efficiency of 76%.
- Adherend failure during lap shear testing was attributed to the heat-affected zone generated by the heating effect of the charcoal susceptor.

References

[1] Mazumdar, S.: *Composites Manufacturing: Materials, Product, and Process Engineering.* CRC Press, Florida (2001). https://doi.org/10.1201/9781420041989.

[2] Ismail, S. O., Akpan, E., Dhakal, H. N.: Review on natural plant fibres and their hybrid composites for structural applications: Recent trends and future perspectives. *Composites Part C: Open Access* 9, 100322 (2022). https://doi.org/10.1016/j.jcomc.2022.100322.

[3] da Costa, A. P., Botelho, E. C., Costa, M. L., Narita, N. E., Tarpani, J. R.: A review of welding technologies for thermoplastic composites in aerospace applications. *Journal of Aerospace Technology and Management* 4, 339–351 (2012). https://doi.org/10.5028/jatm.2012.04033912 .

[4] Siddique, A., Iqbal, Z., Nawab, Y., Shaker, K.: A review of joining techniques for thermoplastic composite materials. *Journal of Thermoplastic Composite Materials* 36, 2327–2352 (2023). https://doi.org/10.1177/08927057221096662 .

[5] Wang, Y., Rao, Z., Liao, S., Wang, F.: Ultrasonic welding of fiber reinforced thermoplastic composites: Current understanding and challenges. *Composites Part A: Applied Science and Manufacturing* 150, 106578 (2021). https://doi.org/10.1016/j.compositesa.2021.106578 .

[6] Siores, E., Do Rego, M. D.: Microwave Applications in Materials Joining. *Journal of Materials Processing Technology* 48, 619–630 (1995). https://doi.org/10.1016/0924-0136(94)01735-A .

[7] Bajpai, P. K., Singh, I., Madaan, J.: Joining of natural fiber reinforced composites using microwave energy: Experimental and finite element study. *Materials & Design* 35, 596–602 (2012). https://doi.org/10.1016/j.matdes.2011.10.007.

[8] Singh, I., Bajpai, P. K., Malik, D., Sharma, A. K., Kumar, P.: Feasibility study on microwave joining of 'green' composites. *Materials & Design* 32, 2263–2271 (2011). https://doi.org/10.1016/j.matdes.2011.10.007.

[9] Naik, T. P., Gairola, S., Singh, I., Sharma, A. K.: Microwave-assisted alkali treatment of sisal fiber for fabricating composite as non-structural building materials. *Construction and Building Materials* 411, 134651 (2024). https://doi.org/10.1016/j.conbuildmat.2023.134651.

[10] ASTM International: Standard Test Method for Tensile Properties of Polymer Matrix Composite Materials. *ASTM Designation: D3039/D3039M−08*, ASTM International, West Conshohocken, PA (2008). https://doi.org/10.1520/D3039_D3039M-08.

[11] ASTM International: Standard Test Method for Lap Shear Adhesion for Fiber Reinforced Plastic (FRP) Bonding. *ASTM Designation: D5868-01-2023*, ASTM International, West Conshohocken, PA (2023). https://doi.org/10.1520/D5868-01-2023.

Effect of Thermal Properties on Transport Phenomena during Laser Welding of Dissimilar Materials in Lap Configuration

Asish Tripathy, Himadri Chattopadhyay, Sudip Simlandi, Nilkanta Barman

Department of Mechanical Engineering, Jadavpur University, India
nilkantajdvu@yahoo.com

Abstract. The present work considers effect of thermal properties on transport phenomena during laser welding of Al- and Mg- alloys in lap configuration. The transport phenomena during laser welding are complex in nature as it happens in presence of a high energy density laser beam. Under such a condition, consideration on variable thermal properties and subsequent effect on welding process is essential. Accordingly, this work considers modeling of the respective laser welding based on conservation of mass, momentum and energy along with appropriate boundary conditions. The set of conservation equations is then discretized based on the finite volume method (FVM) using the power law scheme and SIMPLER algorithm. The final discretized linear equations are solved using the tri diagonal matrix algorithm (TDMA). A FORTRAN based numerical code is subsequently developed to investigate related transport phenomena during welding. This work is focused mainly on development of weld pool as well as heat affected zone (HAZ) along with the temperature distribution during welding. Since the thermal properties play an important role in laser welding, respective effect on temperature and liquid fraction distributions is presented here in details.

Keywords: Laser welding, dissimilar material, Thermal effect

1 Introduction

In recent decades, the laser welding is widely being used in various engineering applications including automobile, construction, aerospace industries [1, 2]. Use of laser welding in joining of dissimilar materials is a challenge to the researchers in this era of light-weight. It is found in the literature that thermal properties of the materials affect the welding process to a great extent. The analysis on effect of thermal properties on transport phenomena during laser welding has been reported in the literature rarely, which is the primary consideration of present work.

There are several literatures reported on laser welding of dissimilar materials, but a very few reported on effect of thermal properties on transport phenomena during laser welding, a closer after an extensive review of related literature. Some of such reviewed literatures are presented here. Mishra et al.[3] presented a numerical analysis on laser welding using a three dimensional volumetric heat source model. They reported variation of temperature, melt pool dimensions during welding. Chen et al.[4] presented an experimental analysis on effect of high-power, high-welding speed during laser welding of 316 L and GH909 dissimilar metals. Zhou et al.[5] reported an experimental investigation on joining of 5052 aluminium alloy with H62 brass in butt configuration using laser. The authors analysed effect of welding speed on microstructural characteristics and mechanical properties of weld. They also observed effect of different properties on welding. Zhang et al.[6] presented a numerical investigation of dual laser beam on heat transfer and temperature field distribution, and also analysed its effect on weld profile and weld quality. Referring to the review conducted for this work, which leads to a necessity of investigating laser welding under different thermal properties of weld materials.

In the present work, therefore, a numerical study is considered to investigate effect of thermal properties on transport phenomena during laser welding of dissimilar materials (Al- and Mg- alloys) in lap configuration. The conservation of mass, momentum and energy along with appropriate boundary conditions, is considered here to represent respective laser welding process where a volumetric heat source is considered to represent its laser beam. Subsequently, a numerical code is developed on the FORTRAN platform for necessary solution, and extended the code for detailed simulation after a grid independent study and validation.

2 Consideration of a Physical Problem Design of samples

This work considers a comparative study on laser welding of dissimilar materials in lap configuration under different thermal properties of materials. In lap configuration, joining of a Mg-alloy sheet is considered with a Al-

alloy sheet because such kind of joint is widely being used in structural, automobile and aerospace industries due to its high strength to weight ratio [1, 2]. In order to realize effect of thermal properties on transport phenomena during laser welding, different combination of properties in case of Al-alloys is considered to join separately with Mg-alloy. Since melting temperature of aluminium (660°C) is higher than that of magnesium (650°C), the Al-sheet is considered here on top of Mg-sheet as shown in Fig.1. Each of the sheets is considered with dimensions of 15mm×12mm×2mm (L×W×H) where length (L) is along the Y-axis, width (W) is along the X-axis, and height (H) is along the Z-axis. The considered thermal properties of Mg-alloy and Al-alloy are presented in Table-1. For joining of the above mentioned dissimilar materials in lap configuration, use of an Nd: YAG laser is considered here with a power of 2500W.

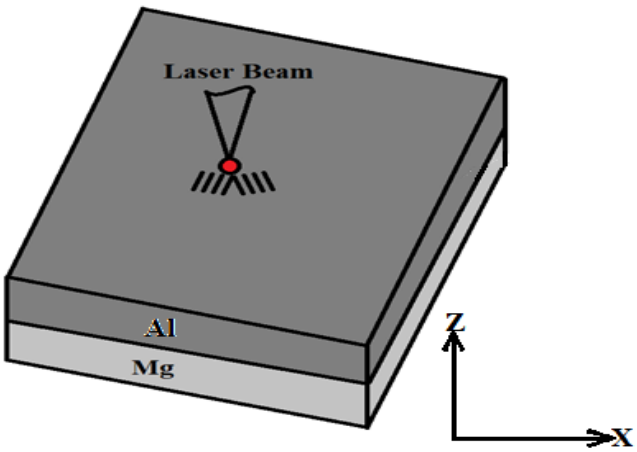

Fig. 1. A schematic of lap joint, formed by laser welding of Al- and Mg-alloy

Table 1. Thermal properties of the alloys used in present simulation [7–9]

Properties	Al-alloys				Mg-alloy
	2024 alloy	6061 alloy	5454 alloy	5754 alloy	
Density of solid (kg/m^3)	2780	2700	2070	2880	1904
Density of liquid (kg/m^3)	2375	2240	2010	2669	
Sp. heat of solid (J/kg.°C)	875	896	900	469	532
Sp. heat of liquid (J/kg.°C)	1273	1230	1340	1261	1400
Thermal conductivity (W/m.°C)	151	154	134	101	75
Solidus temperature (°C)	502	582	602	575	463
Liquidus temperature (°C)	638	652	646	638	595
Latent heat (J/kg)	390000	400000	400000	400000	370000
Thermal expansion coefficient (1/°C)	22.9×10^{-6}	22×10^{-6}	23.7×10^{-6}	24×10^{-6}	26×10^{-6}

3 Mathematical Modeling

Incorporation of a high-density laser beam in modeling of laser welding is a crucial issue, which is represented in the work as a volumetric heat source as

$$Q(x,y,z) = \frac{9\eta P e^3}{2000\pi H(e^3-1)({r_u}^2+{r_l}^2+r_u.r_l)} exp\left[\frac{-3(x^2+y^2)}{\left\{r_l+(r_u-r_l)\left(\frac{z}{2H}\right)\right\}^2}\right] \tag{1}$$

where P is power of the laser beam, η is efficiency of the laser welding, H is vertical thickness of each metal sheet, r_u and r_l are upper and lower radii of the laser beam, z is counted as depth from top surface of the joint. This laser beam is then applied steadily to join Al- and Mg-sheets, that increases temperature of weld materials to a high that results melting of weld materials. Simultaneously, there is a possibility of solidification of molten weld pool due to heat transfer in form of convection and radiation from open surfaces of the joint. Different transport phenomena such as mass, momentum and energy transfers involve in melting and solidification of dissimilar materials of the weld, those are very complex in nature. The following assumptions are made, therefore, in order to simply modeling of the laser welding.

- Both materials are considered as eutectic.
- Volume averaged properties are considered.
- Molten metals are assumed as incompressible
- Considered a 2-D computational domain

Based on above assumptions, simultaneous melting and solidification behaviour during laser welding are modeled considering the mass, momentum and energy conservation equations (3-5) along with necessary boundary conditions where volume averaged properties are represented in entire domain as

$$\varphi = f_l\varphi_l + f_s\varphi_l \tag{2}$$

where φ_l and φ_s are liquid and solid properties.

Conservation of mass [10–13]:

$$\frac{\partial}{\partial x}(\rho u) + \frac{\partial}{\partial z}(\rho w) = 0 \tag{3}$$

where ρ denotes density of weld materials; *u, v* and *w* denote velocities in *x*, *y*, z directions, respectively.

Conservation of momentum [10, 12, 13]:

$$\frac{\partial(\rho u)}{\partial t} + u\frac{\partial(\rho u)}{\partial x} + w\frac{\partial(\rho u)}{\partial z} = -\frac{\partial P}{\partial x} + \nabla.(\mu\nabla u) + S_u \tag{4a}$$

$$\frac{\partial(\rho w)}{\partial t} + u\frac{\partial(\rho w)}{\partial x} + w\frac{\partial(\rho w)}{\partial z} = -\frac{\partial P}{\partial z} + \nabla.(\mu\nabla w) + S_w + \rho g\beta_T\left(T - T_{ref}\right) \tag{4b}$$

In above equations, S_u and S_w are the Darcy source terms presented as

$$S_u = Bu \tag{4c}$$

$$S_w = Bw \tag{4d}$$

where B is defined as

$$B = -\frac{X(1-f_l)^2}{{f_l}^3 + a} \tag{4e}$$

where X is a morphological constant and a is a computational constant to avoid division by zero.

Conservation of Energy [10–12]:

$$\rho C_p \left(\frac{\partial T}{\partial t} + u\frac{\partial T}{\partial x} + w\frac{\partial T}{\partial z}\right) = \nabla.(k\nabla T) - \frac{\partial(\rho \Delta H)}{\partial t} + \mathrm{Q} \tag{5}$$

where Q is a volumetric heat source representing the energy input from the laser beam.

3.1 Boundary Conditions

A high energy density laser beam is introduced in laser welding to join work pieces of a weld, results a high temperature. Based on the situation, all bare surfaces are considered here as the surfaces those transfer convective as well as radiative heat. The respective heat transfer from the bare surfaces is presented as

$$q_s = h_C(T - T_a) + h_r(T - T_a) \tag{6}$$

where h_c is heat transfer coefficient related to convection, and h_r is denoted as equivalent heat transfer coefficient related to radiation and given as

$$h_r = \varepsilon\sigma\left(T^2 + {T_a}^2\right)(T + T_a) \tag{6a}$$

where ε is surface emissivity and σ is the Stefan-Boltzmann constant, and T_a is ambient temperature. The bottom surface is considered as an adiabatic surface also presented in Fig.2. The above governing equations are solved considering variation in thermal properties of dissimilar materials of the weld.

4 Numerical Modeling

This study considered the power law scheme to discretize governing equations along with boundary conditions on the basis of finite volume method (FVM). The source term in equation (4) that represents absorption and evolution of latent heat during melting and solidification, respectively is taken care in simulation considering enthalpy update scheme. Subsequently, liquid and solid fractions are calculated. To calculate fluid flow during melting and solidification, SIMPLER algorithm [14] is adapted, and after discretization, all the linear equations are solved by try diagonal matrix algorithm (TDMA) where convergence is declared when

$$\left|\frac{\in - \in_{old}}{\in_{max}}\right| < 10^{-6} \tag{7}$$

In equation (7), $\in$ is any variable at a grid point at present iteration, $\in_{old}$ is its corresponding value at previous iteration, $\in_{max}$ is the maximum value of that variable at present iteration in the entire domain. To solve present set of equations, a suitable uniform grid and a suitable time interval of 0.01s are considered for convergence.

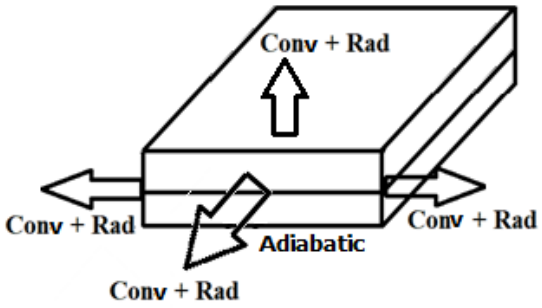

Fig. 2. Bouandary conditions for present study

5 Results and Discussion

This work presents a numerical simulation on laser welding of Al- and Mg-alloys in lap configuration. A numerical code on FORTRAN platform is developed, accordingly. In order to validate the code, a slab of Al-alloy (15mm×12mm×4mm) is considered first, initially at a very high temperature corresponds to that arises in a laser welding. It releases heat by combination of convection and radiation from its bare surfaces. Its bottom surface is assumed here as an adiabatic surface. A grid size of 82× 82 × 42 is chosen for simulation. Corresponding variation of temperature at centre of the slab with time is presented in Fig. 3, and compared it with analytical solution by Ozisik (1985) [15]. A good agreement is found between the analytical solution and the present work. For grid independent study, a separate grid size of 92× 92 × 52 is considered further where a similar variation of temperature profile is found. Therefore, a grid size of 82× 82 × 42 is considered as a suitable grid for necessary simulation with a time period of 0.01s.

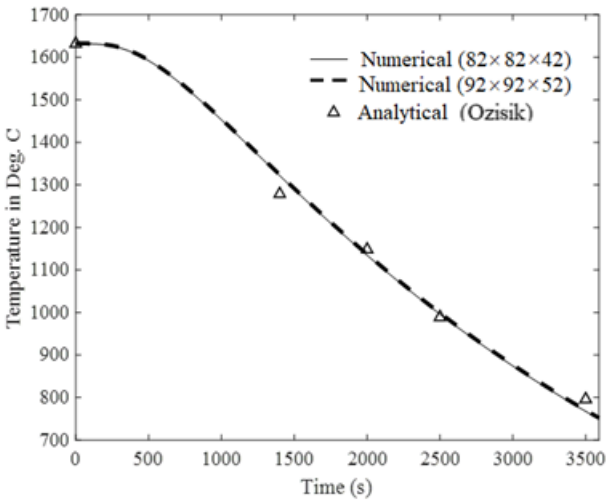

Fig. 3. Validation of the developed numerical code

5.1 Distribution of Temperature along with Weld Pool and HAZ

The validated code is then extended to predict transport phenomena during laser welding of 5754 Al-alloy with Mg-alloy in lap configuration as presented in section 2.0. In presence of laser beam, respective temperature distribution in entire computational domain is predicted considering mathematical model of simultaneous melting and solidification as presented in section 3.0. The distribution of temperature is then presented in Fig. 4 at two different times, i.e., 0.3s and 1.8s for analysis. It is found that a maximum temperature of about 750°C is attained in the entire domain during welding within a time period of about 0.05s. At this high temperature, the weld materials melt. In the simulation, the enthalpy update scheme is considered to calculate respective fraction of molten

liquid within its weld pool. A cylindrical shaped of weld pool with a diameter of about 0.86mm and a depth of about 2.2mm is found at steady state condition, also presented in Fig. 4, which depends on distribution of related high energy density laser beam. As found, this depth increases gradually to 2.2mm with a period of 0.05s approximately. It indicates a complete melting of top, i.e., Al-alloy sheet as a through hole on it and a part melting (about 0.2 mm depth) in case of bottom, i.e., Mg-alloy sheet after a time period of 0.05s. This simulation is, thus, a clear indication on the feasibility of joining Al- and Mg-alloys in lap configuration using an Nd: YAG laser with a power of 2500Wneed to apply for a period of about 0.05s.

The laser welding results is a very high temperature filled under such a condition, the weld materials undergo a heat treatment process. Prediction of respective heat affected zone (HAZ) is, thus, a consideration of this work. In this context, an average of recrystallization temperatures of the weld materials is considered as a boundary of the HAZ is represented in Fig. 4. During entire welding process, a negligible change in the HAZ profile is observed with a maximum of 3.1mm width at bottom surface of the weld.

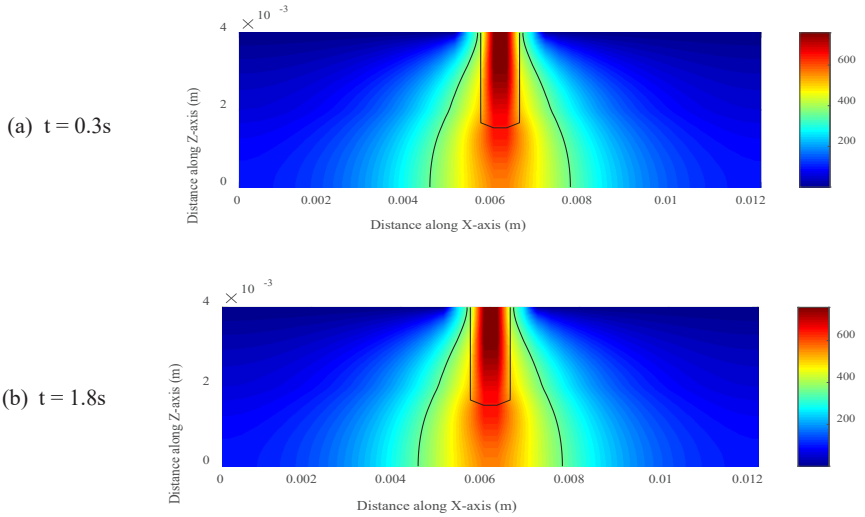

Fig. 4. Distribution of temperature along with weld pool and HAZ

5.2 Effect of Thermal Conductivity on Transport Phenomena

In this section, specifically highlighted the effect of thermal conductivity on transport phenomena. Fig. 5 shows variation of maximum temperature with time at different values (75 W/m.°C, 101 W/m.°C and 154 W/m.°C) of thermal conductivity which corresponds to Mg-alloy, 5754 Al-alloy, and 6061 Al-alloy, respectively. At a low value of thermal conductivity (75 W/m.°C), the maximum temperature in the entire domain attains to a high value about 857°C whereas it shows a low value (~690°C) at high thermal conductivity (~154 W/m.°C). The heat transfer within computational domain increases with increase in value of the thermal conductivity, and subsequent increase in heat transfer from the bare surfaces is also observed. Accordingly, respective maximum temperature decreases with increase in the thermal conductivity.

In order to know respective effect on variation in liquid fraction of the weld pool, different values of the thermal conductivity (W/m.°C) such as 75, 101, 151, and 175 are considered. Fig. 6 is a representation of corresponding variation in liquid fraction of the weld pool with time, which clearly shows that there is a drop in average liquid fraction of the weld pool with increase in value of the thermal conductivity. This oscillatory pattern is a combined effect of melting that takes place due to presence of the laser beam and simultaneous solidification that occurs due to heat transfer through the bare surfaces. The higher thermal conductivity increases heat transfer through the bare surfaces, and results in solidification to a higher extent than that in case of low thermal conductivity. Hence, a low value in liquid fraction is observed at high value of thermal conductivity. It is further observed from Fig.6 that there is a fluctuation in liquid fraction at steady state condition, and such fluctuation increases with increase in value of the thermal conductivity. This fluctuation is a cause of remelting and subsequent solidification of weld materials at steady state, which increases in case of a high value of thermal conductivity.

Such simultaneous remelting and solidification affect the joining process to a great extent under different values of the thermal conductivity. In Fig. 7, a variation in depth of weld pool is presented under different values of the

thermal conductivity. A decrease in depth of the weld pool is observed with a fluctuation on it at a high value of thermal conductivity due to simultaneous occurrence of remelting and solidification. It is also found from Fig. 7 that the depth of weld pool is less than that of the top or Al-alloy sheet at moderate thermal conductivity, and unpredictable at high value of thermal conductivity. This analysis indicates clearly that joining of Al- and Mg-sheets with 2mm thick each under the 2500W laser power may or may not be possible at a high value of thermal conductivity. Accordingly, laser welding of 5754 Al-alloy with Mg-alloy in lap configuration is a suitable selection under a laser power of 2500W than other combinations in context to only increase in the thermal conductivity.

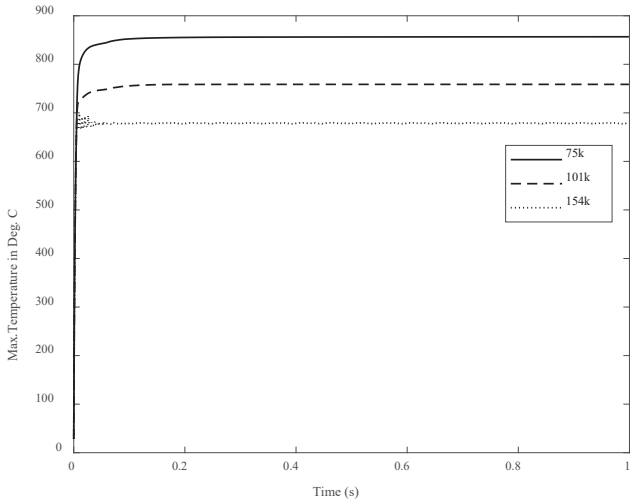

Fig. 5. Variation of maximum temperature with time, effect of thermal conductivity (k = 75 W/m.°C, 101 W/m.°C, and 154 W/m.°C)

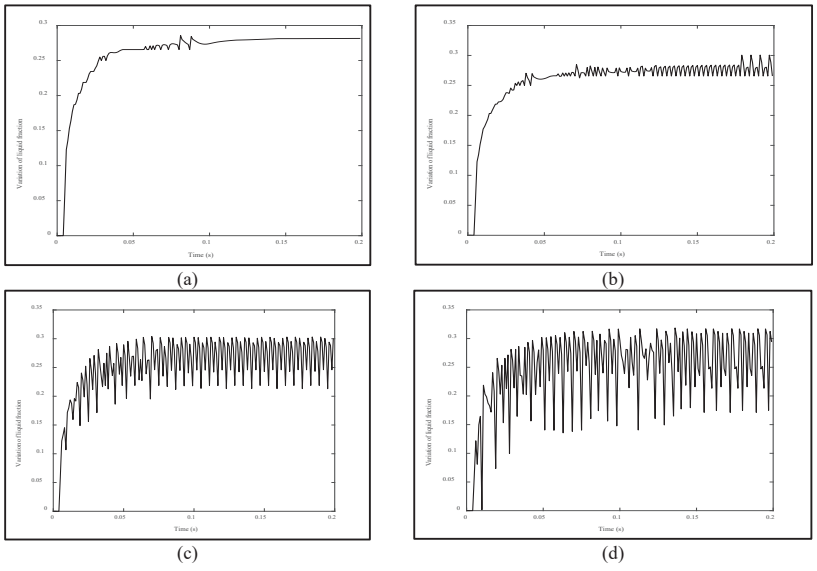

Fig. 6. Variation in liquid fraction of weld pool with time under different values of thermal conductivity. (a) k = 75W/m.°C, (b) k = 101W/m.°C, (c) k =151W/m.°C, and (d) k = 175W/m.°C

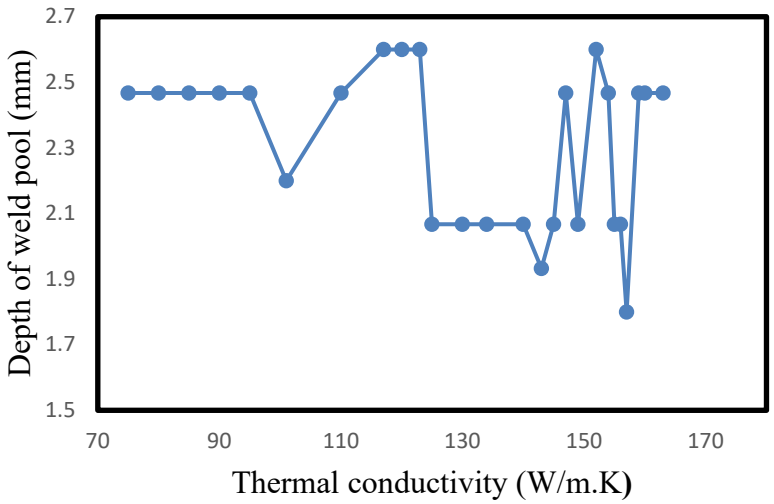

Fig. 7. Variation of depth of weld pool with increase in thermal conductivity

5.3 Effect of Different Thermal Properties on Temperature Distribution, and Size of Weld Pool and Heat Affected Zone (HAZ)

In this section, effect of heat capacity and thermal diffusivity on temperature distribution and size of the weld pool and heat affected zone (HAZ) is considered. Accordingly, joining of 5754, 5454, and 2420 Al-alloys is considered with Mg-alloy in lap configuration separately using a laser of 2500W so that their heat capacity in solid state increases in the mentioned sequence, which results a decrease in the thermal diffusivity as presented in Fig. 8 even their thermal conductivity increases. Respective effect of the thermal diffusivity represents a combination effect of all properties on transport phenomena during laser welding. A high value of thermal diffusivity allows transferring of heat at higher rate to the ambient, results a higher solidification of the liquid in weld pool. Thus, a weld pool of low depth and diameter is obtained in case of a high value of thermal diffusivity, which is presented in Fig. 8 clearly. Depth of the weld pool is found as 2.2mm in case of 5754 Al-alloy, 3.1mm in case of 5454 Al-alloy, and 3.5mm in case of 2024 Al-alloy. It is also observed from Fig. 8 that the weld pool diameter and HAZ increases with decrease in value of the thermal diffusivity. Maximum width of respective heat affected zone (HAZ) is found as 3.1mm in case of 5754 Al-alloy, 3.9mm in case of 5454 Al-alloy, and 4.0mm in case of 2024 Al-alloy. On the contrary, a high thermal conductivity in case of 2024 Al-alloy although its thermal diffusivity is less, results a high heat transfer from top surface, and subsequent a narrow weld pool diameter on near top surface.

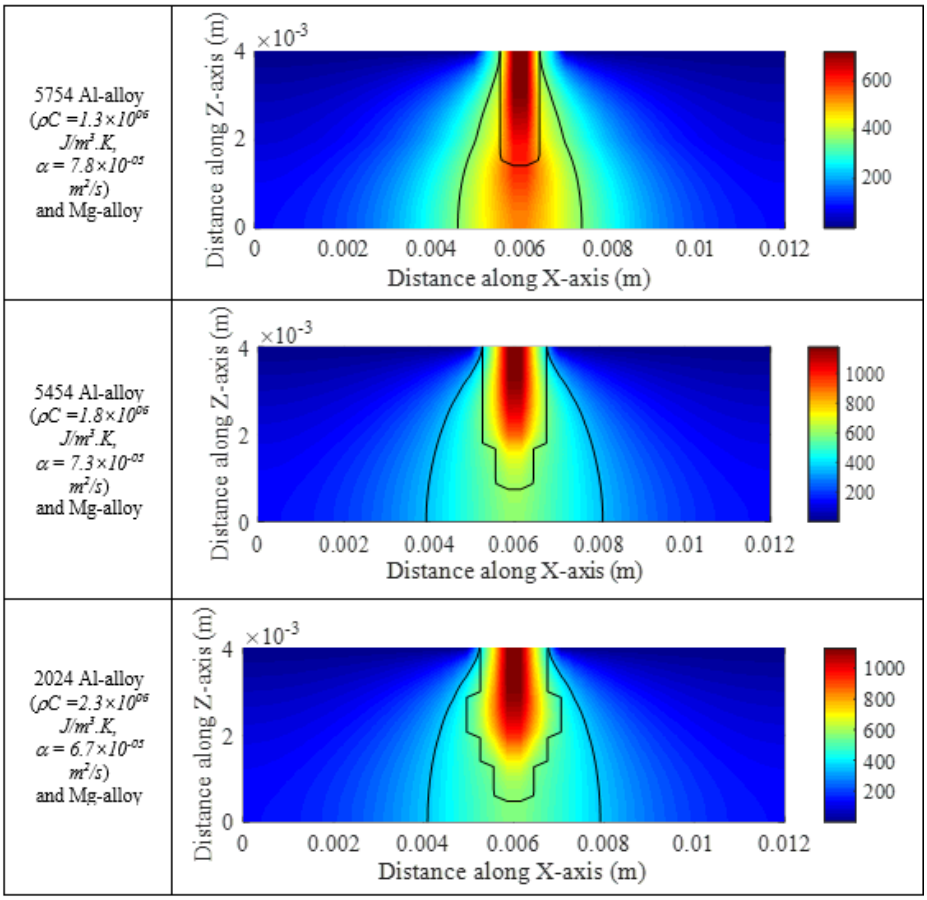

Fig. 8. Distribution of temperature along with weld pool and HAZ

6 Conclusion

Joining of dissimilar materials is a challenge in recent decades, where use of laser welding is a suitable solution. This work, thus, considered a numerical study to investigate the related transport phenomena. Accordingly, effect of thermal properties on transport phenomena during laser welding of Al- and Mg-alloys in lap configuration is considered as a primary focus of this work. In order to model the present problem, conservation of mass, momentum and energy is considered along with appropriate boundary conditions. The power law scheme, SIMPLER algorithm and TDMA are considered for discretization and subsequent solution of the governing equations. A numerical code is developed on FORTRAN platform and extended the same for simulation after a grid independent study and validation. Following major conclusions are drawn through the present work.

- A weld pool of cylindrical shaped and a HAZ of bell shaped are observed.
- Simultaneous remelting and solidification occurs during laser welding depend greatly on the value of thermal conductivity.
- Heat capacity and thermal diffusivity affect the temperature distribution significantly and size of weld pool and heat affected zone (HAZ). Wider weld pool is observed at low thermal diffusivity.

Based on present analysis, it is concluded that a numerical analysis is useful before practical application of a laser welding process in terms of power requirement, and selection of materials and their corresponding thickness in case of lap configuration.

Nomenclature

Symbols	***Description***
ρ	Density (kg/m^3)
C_p	Specific heat (J/kg.°C)
k	Thermal conductivity (W/m.°C)
L_a	Latent heat of fusion (J/kg)
β_T	Thermal expansion coefficient (1/°C)
φ_l	Liquid properties
φ_s	Solid properties
f_l	Liquid fraction
f_s	Solid fraction
u, v, w	Velocity components (m/s)
X	Morphological constant
a	Computational constant
h	Heat transfer coefficient (W/m^2 K)
P	Laser Power (W)

References

1. Hong K-M, Shin YC (2017) Prospects of laser welding technology in the automotive industry: A review. J Mater Process Technol 245:46–69. https://doi.org/https://doi.org/10.1016/j.jmatprotec.2017.02.008
2. Quazi MM, Ishak M, Fazal MA, (2020) Current research and development status of dissimilar materials laser welding of titanium and its alloys. Opt Laser Technol 126:106090. https://doi.org/https://doi.org/10.1016/j.optlastec.2020.106090
3. Mishra AK, Kumar A (2019) Numerical and experimental analysis of the effect of volumetric energy absorption in powder layer on thermal-fluidic transport in selective laser melting of Ti6Al4V. Opt Laser Technol 111:227–239. https://doi.org/https://doi.org/10.1016/j.optlastec.2018.09.054
4. Chen L, Wang C, Zhang X, Mi G (2021) Effect of parameters on microstructure and mechanical property of dissimilar joints between 316L stainless steel and GH909 alloy by laser welding. J Manuf Process 65:60–69. https://doi.org/https://doi.org/10.1016/j.jmapro.2021.03.015
5. Zhou L, Luo LY, Tan CW, (2018) Effect of welding speed on microstructural evolution and mechanical properties of laser welded-brazed Al/brass dissimilar joints. Opt Laser Technol 98:234–246. https://doi.org/https://doi.org/10.1016/j.optlastec.2017.08.004
6. Zhang LJ, Zhang JX, Gumenyuk A, (2014) Numerical simulation of full penetration laser welding of thick steel plate with high power high brightness laser. J Mater Process Technol 214:1710–1720. https://doi.org/https://doi.org/10.1016/j.jmatprotec.2014.03.016
7. Malekshahi Beiranvand Z, Malek Ghaini F, Naffakh Moosavy H, (2020) The relation between magnesium evaporation and laser absorption and weld penetration in pulsed laser welding of aluminum alloys: Experimental and numerical investigations. Opt Laser Technol 128:106170. https://doi.org/https://doi.org/10.1016/j.optlastec.2020.106170
8. Halim S Ben, Bannour S, Abderrazak K, (2021) Numerical analysis of intermetallic compounds formed during laser welding of Aluminum-Magnesium dissimilar couple. Therm Sci Eng Prog 22:100838
9. Borrisutthekul R, Miyashita Y, Mutoh Y (2005) Dissimilar material laser welding between magnesium alloy AZ31B and aluminum alloy A5052-O. Sci Technol Adv Mater 6:199–204. https://doi.org/10.1016/j.stam.2004.11.014
10. Barman N, Kumar P, Dutta P (2009) Studies on transport phenomena during solidification of an aluminum alloy in the presence of linear electromagnetic stirring. J Mater Process Technol 209:5912–5923. https://doi.org/https://doi.org/10.1016/j.jmatprotec.2009.07.008
11. Dhar M, Barman N, Mandal S, Chattopadhyay H (2014) Remelting and interface dynamics during solidification of a eutectic solution in a top-cooled rectangular cavity: A numerical study. Int J Heat Mass Transf 77:730–737. https://doi.org/https://doi.org/10.1016/j.ijheatmasstransfer.2014.05.064

12. Chakraborty S, Dutta P (2002) An analytical solution for conduction-dominated unidirectional solidification of binary mixtures. Appl Math Model 26:545–561. https://doi.org/https://doi.org/10.1016/S0307-904X(01)00073-7
13. Ghosh A, Chattopadhyay H (2013) Mathematical modeling of moving heat source shape for submerged arc welding process. Int J Adv Manuf Technol 69:2691–2701. https://doi.org/10.1007/s00170-013-5154-z
14. Patankar S V. (2018) Numerical Heat Transfer and Fluid Flow, CRC Press. CRC Press
15. Ozisik MN (1985) Heat transfer: a basic approach. McGraw-Hill

Multi-objective optimization of FSW parameters for joining dissimilar AA5230 and AA4635 aluminium alloys

Anubhab Basu[1], Ranjib Biswas[2], Nirmal Kumar Mandal[3], Dipankar Bose[3], Souren Mitra[2]

[1] Heritage Institute of Technology, Kolkata, India
[2] Jadavpur University, Kolkata, India
[3] NITTTR, Kolkata, India
anubhab.basu@heritageit.edu

Abstract. Friction stir welding (FSW) method effectively resolves multiple challenges may occur during fusion welding of similar and dissimilar aluminum alloys. The proper selection of welding parameters is responsible to achieve a good quality of weld joint in the FSW process. In the present study, 3 mm thick dissimilar aluminium alloy plates of AA5230 to AA4635 were joined in the lap configuration using the FSW process. Investigation of the ultimate shear strength (USS) and weld nugget zone hardness (NZH) of the FSW joints have been performed and optimized both separately and simultaneously utilizing response surface methodology (RSM). The welding parameters and the responses (USS and NZH) were correlated and finally, an optimum set of parameters were identified through desirability approach which may be used to obtain highest mechanical properties within the working range.

Keywords: Friction stir lap welding, AA5230, AA4635, RSM.

1 Introduction

In recent times, aluminium alloys become a popular material for various structural applications due to its high strength to weight ratio and FSW has become a prominent method to join aluminium alloys [1]. It avoids melting and filler materials, produces no fumes, and, when executed correctly, results in better weld quality compared to fusion welding [2]. It is observed that friction stir lap welding (FSLW) is unable to provide similar mechanical behaviors compared to butt joints done by FSW. In FSLW, the heat produced by the non-consumable rotating tool needs to be conducted through the upper sheet in order to reach the interface of the sheets underneath. Moreover, the tangential speed of the material surrounding the tool pin must be adequate to fill the gap created by the movement of the tool. This complexity makes it more difficult to achieve a robust lap weld than a butt weld, heavily depending on tool design, fixture configuration and welding parameters. The depth of penetration (DOP) of the tool needs to be controlled carefully to achieve a good quality weld in FSLW for both similar and dissimilar aluminium alloys. The weld zone is divided into weld nugget or stir zone (NZ), thermo-mechanically affected zone (TMAZ) and heat affected zone (HAZ) [3]. In an experiment of joining similar aluminium alloys in lap configuration it was found that both tool rotational speed (RS) and DOP should be kept at the lower end of their respective ranges to maximize the lap shear strength [4]. The welding of Aluminium alloys of grade AA2017 to AA6061 were examined to assess the impact of various pin profiles on metal flow and concluded that the threaded pin profile is the most effective pin profile of getting the optimal metal flow between the upper and lower plates [5]. In an investigation of joining AA6061 to AA1050 plates using FSW process, the strain rate at the edge of the rotation flow zone (RFZ), near to the surface of the tool, found higher compared to the middle layer [6]. The metal flow on the advancing side was more compared to the retreating side with the higher metal flow rate occurring at the nugget zone (NZ) during the FSW of dissimilar aluminium alloys [7]. During the FSW of AA6063 to AA5083, it was observed that the wormhole defect is a major concern [8]. In addition to wormhole defects, 'kissing bond' defects present a significant challenge in the dissimilar aluminum FSW process [9]. In the previous studies it has been observed that there is no study is performed on FSW of AA4635 and AA5230 aluminium alloys, further there is a very few studies were performed on FSLW of dissimilar aluminium alloys. In FSLW the effect of DOP on the weld quality is important, but there are very few studies were carried out on the effect of DOP on the weld quality during FSLW. In most of the previous studies, a dedicated FSW machine was used, but in this present work it has been shown that a CNC Vertical Machining Centre (VMC) with a proper FSW tool can also be used to perform this process. So the present work aims to experimentally investigate the quality of lap joints formed by welding dissimilar aluminum alloys using the FSLW process. To analyze the effects of three FSLW parameters, i.e. RS, welding speed (WS), and DOP, a central composite design (CCD) and response surface method (RSM)

have been employed. Weld qualities, including ultimate shear strength (USS) and nugget zone hardness (NZH), are evaluated and modeled through statistical methods. Additionally, a multi-objective optimization analysis has also been conducted using MINITAB 20.

2 Experimental Details

2.1 Experimental Work

In this study, AA4635 and AA5230 were joined using a VMC through FSLW. The 3 mm thick plates were machined into rectangular shapes measuring 120 mm × 110 mm. Table 1 and Table 2 represent the mechanical properties and chemical compositions of these alloys respectively. The dissimilar plates were arranged in lap configuration and securely clamped on the VMC table for the welding process. The study focused on developing a tool having a cylindrical shoulder with a threaded probe, featuring a concave shoulder design to contain plasticized material during welding. Constructed from high-speed steel (HSS), the tool underwent a case hardening process, achieving a hardness of 91 HRB. The tool includes an adjustable pin and a pin shoulder, with three holes on the shoulder: one for the pin and two perpendicular holes for a 6 mm Allen set screw, which secures the pin and limits relative motion. The developed tool is shown in Fig. 2 and Fig. 3.

Table 1: Mechanical Properties

Workpiece Materials	UTS (MPa)	Hardness (HRB)
AA4635	190	55
AA5230	170	33

Table 2: Chemical compositions

Workpiece Materials	Cu (%)	Si (%)	Mg (%)	Fe (%)	Mn (%)	Ni (%)	Zn (%)	Pb (%)	Ti (%)	Al (%)
AA 4635	0.1	11.2	0.4	0.52	0.6	0.1	0.1	0.1	0.2	Bal.
AA 5230	0.1	0.3	4.3	0.51	0.32	0.4	0.1	0.05	0.2	Bal.

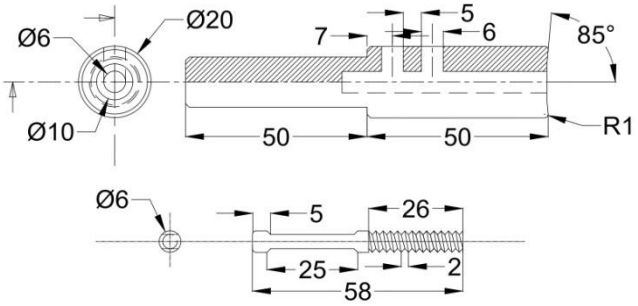

Fig. 2. Dimensions of the tool shoulder and pin. (All dimensions are in mm)

Fig. 3. Developed tool for FSW

Fig. 4. Experimental set-up for FSW

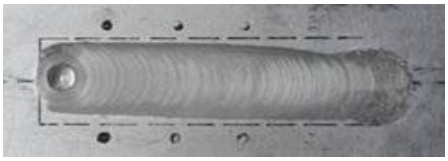

Fig. 5. Friction stir welded lap joint

The joints after welding underwent testing for shear strength and Rockwell hardness to assess the USS and NZH, respectively. The joints machined as per the ASTM E8M-04 guidelines, as shown in Fig. 6. Shear tests were conducted using a 100 kN hydraulic universal testing (UTM) machine, while hardness testing utilized a SAROJ RAB250 machine with a 100 kgf load on the "B" scale.

2.2 Design of Experiment

CCD, a RSM, optimizes processes using various experimental designs and regression techniques. In this study, a multiple linear regression model was employed to analyze the responses, i.e. USS and NZH. A CCD with 20 trials was chosen to accommodate linear, quadratic, and interaction terms within the model.

Table 3. Dimension of tool and probe

	Name	Length (mm)	Diameter (mm)
1.	Pin or probe for FSW tool	58	6
2.	Shoulder of the FSW tool	100	20

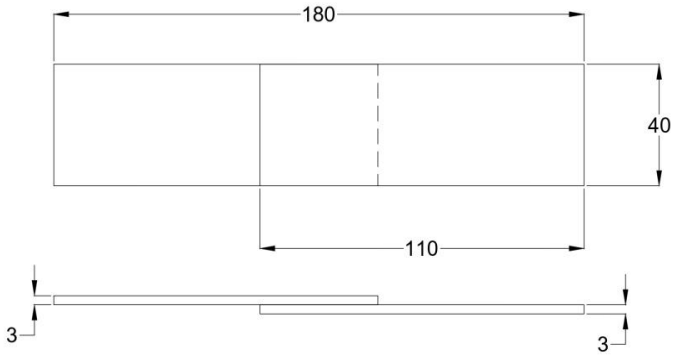

Fig. 6. Shear test specimen geometry and dimension (All dimensions are in mm)

2.3 Welding parameters

Drawing from earlier research, the selected welding parameters were RS, WS, and DOP, with their respective ranges outlined in Table 4. USS and NZH were considered as dependent variables.

Table 4. Actual values and their associated coded values.

Welding Parameters	Symbols	Units	Levels				
			-1.6818	-1	0	1	1.6818
Tool rotational speed (RS)	N	rpm	697.73	800	950	1100	1202.27
Welding speed (WS)	S	mm/min	9.77	20	35	50	60.23
Depth of penetration (DOP)	D	mm	32.5	4.0	4.5	5.0	41

3 Experimental results and analysis

A RSM based mathematical model was developed based on experimental results which represents the correlation between the welding parameters and the responses in the form of Mathematical equations. RSM and multiple regression analysis were further utilized to analyze the output, while key parameters were identified through analysis of variance (ANOVA). The general second-order polynomial RSM based model is shown in equation 2.

$$y_u = \beta_0 + \sum_{i=1}^{k} \beta_i x_{iu} + \sum_{i=1}^{k} \beta_{ii} x_{iu}^2 + \sum_{i<j} \beta_{ij} x_{iu} x_{ju} + e_u \quad (2)$$

Here, y_u = responses, e.g. USS of the welded joint, x_{iu} = coded values of the i^{th} control parameters for u^{th} experiment, k = no of control parameters, β_i, β_{ii}, β_{ij} are the 2nd order regression coefficients, e_u = experimental error of the u^{th} trial.

The obtained mathematical correlation to predict the USS and NZH is shown in equation 2a and equation 3 respectively:

Y_{USS} = - 429.9 + 0.4934 N + 3.286 S + 80.4 D - 0.000228 N*N - 0.03157 S*S - 7.18 D*D - 0.000311 N*S - 0.00548 N*D - 0.1492 S*D (2a)

Y_{NZ} = - 232.4 + 0.2811 N + 1.406 S + 43.46 D - 0.000130 N*N - 0.013766 S*S - 3.904 D*D - 0.000222 N*S - 0.00333 N*D - 0.0333 S*D (3)

Table 5. Experimental combinations of trial runs and their corresponding results

Run order	Coded values			Responses	
	RS (N)	WS (S)	DOP (D)	USS (MPa)	NZH (HRB)
1	-1	-1	-1	46.2	27
2	1	-1	-1	54.85	32
3	-1	1	-1	52.7	31
4	1	1	-1	58.35	33.5
5	-1	-1	1	53.72	31.5
6	1	-1	1	60.52	35
7	-1	1	1	55.54	34
8	1	1	1	59.75	36
9	-1.6818	0	0	46.19	28
10	1.6818	0	0	62.1	34.5
11	0	-1.6818	0	45.12	28.5
12	0	1.6818	0	51.95	33
13	0	0	-1.6818	57.83	32.5
14	0	0	1.6818	69.27	41
15	0	0	0	69.95	40
16	0	0	0	69.5	39.5
17	0	0	0	70.15	40.5
18	0	0	0	67.55	38.5
19	0	0	0	68.88	39
20	0	0	0	67.95	39.5

Table 6 presents the P values for the various welding parameters, the squared effects of those parameters, and the interactions between them. It has been observed that WS, RS, DOP, square effects of RS (i.e. $(N)^2$), WS (i.e. $(S)^2$) and DOP (i.e. $(D)^2$) are significantly affecting the USS, whereas the linear effect of RS, WS and DOP, the square effect of RS (i.e. $(N)^2$), WS (i.e. $(S)^2$) and DOP (i.e. $(D)^2$) are significantly influential for controlling the NZH as the P value of each of them is less than 0.05. The S, R-Sq and R-Sq (adj) values of the regression analysis for USS and NZH is shown in Table 6.

Table 6. P values of the welding parameters in relation to the responses.

Terms	Symbols	P values	
		USS	NZH
Constant		0.000	0.000
RS	N	0.000	0.000
WS	S	0.002	0.000
DOP	D	0.000	0.000
RS*RS	N*N	0.000	0.000
WS * WS	S*S	0.000	0.000
DOP*DOP	D*D	0.001	0.001
RS * WS	N*S	0.207	0.093
RS *DOP	N*D	0.445	0.374
WS*DOP	S*D	0.056	0.374

Table 7. S, R-Squared, and Adjusted R-Squared values.

Responses	S	R-Squared	Adjusted R-Squared	Predicted R-Squared
USS	1.46332	98.46%	97.07%	90.81%
NZH	0.760644	98.42%	96.99%	92.14%

Table 8. Results of the ANOVA for responses.

Source	USS		NZH	
	F value	**P value**	**F value**	**P value**
Model	70.96	0	69.13	0
Linear	52.02	0	67.17	0
Square	158.47	0	138.48	0
2-Way Interaction	2.38	0.131	1.73	0.224
Lack-of-Fit	2.76	0.145	1.31	0.386

It has been determined that the data for each response align well with the developed models, as indicated by the small S values and the moderately high R-Sq and R-Sq (adj) values for the responses. ANOVA, along with the P-value analysis and F-ratio test, was conducted to evaluate the adequacy of the mathematical models developed for the responses of the welded joints produced by the FSLW process on dissimilar aluminum alloys. The ANOVA analysis results for these responses are shown in Table 8. Both the P-values for the regression model sources and linear effects are significantly lower than 0.05, indicating strong significance for the developed second-order regression model. Additionally, the linear and squared effects of the parameters are also noteworthy.

4 Discussion

4.1 Impact on Ultimate shear strength

Fig. 7. Illustrates the combined effect of RS and WS on USS, with DOP held constant at 4.5 mm. Initially, USS increases with RS, then decreases in a parabolic trend. A similar trend is observed with WS. At low RS and high WS, insufficient heat leads to poor material flow and lower shear strength. Conversely, high RS and low WS result in excessive heat, causing turbulence and grain coarsening, also lowering shear strength. Thus, optimal heat input is crucial in FSLW. Fig. 8 demonstrates the effect of WS and DOP on USS, with RS fixed at 950 rpm. USS gradually increases with DOP at low WS, while high WS and low DOP yield low USS. Using Minitab software, Maximum USS has been obtained as 70.596 MPa when RS, WS and DOP are set at optimum parametric setting i.e. 1003.51 rpm, 35.76 mm/min and 4.85 mm respectively after optimization.

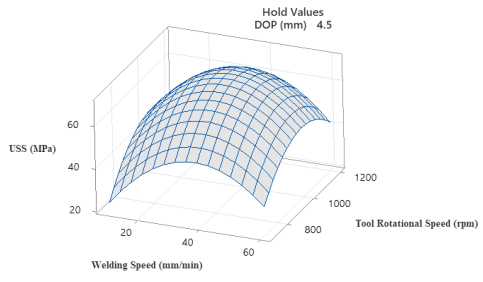

Fig. 7. Effect of RS and WS on USS.

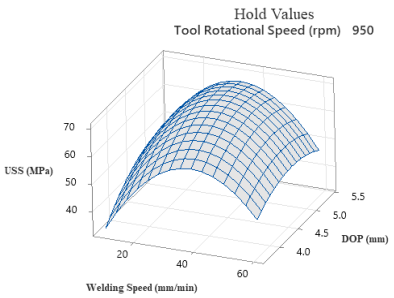

Fig. 8. Effect of WS and DOP on USS

Fig. 9. Optimization result of USS

4.2 Impact on Nugget zone hardness

Fig. 10. Illustrates the effects of RS and WS on NZH, with DOP held constant at 4.5 mm. At lower WS levels, NZH initially increases with RS before decreasing. Similarly, at higher RS, NZH rises with WS and then falls. This indicates that low RS and high WS result in insufficient heat, while high RS and low WS produce excessive heat. Figure 11 shows the impact of WS and DOP on NZH, with RS fixed at 950 rpm, NZH gradually increases with DOP at lower WS. However, high WS and low DOP lead to very low USS. On the basis of a developed mathematical model (i.e., Eq (2)), the optimization results for maximum NZH are presented in Fig. 12. Maximum NZH has been obtained as 40.77 HRB when RS, WS and DOP are set at optimum parametric settings i.e. 988.22 rpm, 37.29 mm/min and 4.98 mm respectively after optimization.

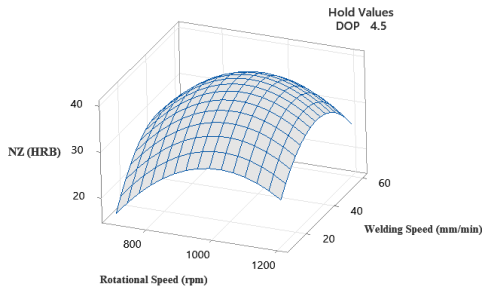

Fig. 10. Effect of RS and WS on NZH.

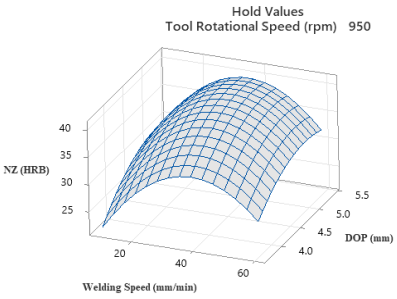

Fig. 11. Effect of DOP and WS on NZH.

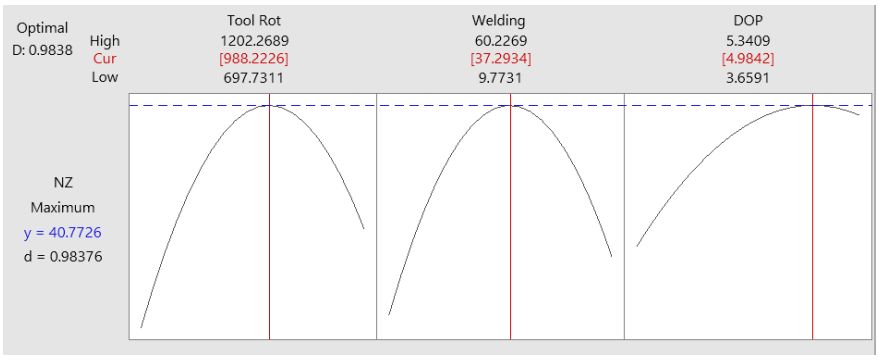

Fig. 12. Optimization result of NZH

4.3 Multi-objective optimization

A multi-objective optimization analysis for FSLW of dissimilar aluminum alloys has been conducted, with results USS and NZH shown in Fig. 13. The objective is to maximize both USS and NZH simultaneously. Fig. 13 is obtained considering current parameters along the vertical axis and the current responses along the horizontal

axis. Each column shows parameter levels, while the left side details response goals, predicted values, and desirability scores.

Current settings are: RS at 988.22 rpm, WS at 37.29 mm/min, and DOP at 4.98 mm, achieving predicted maximum USS of 70.32 MPa and NZH of 40.77 HRB. The composite desirability factor is 0.992.

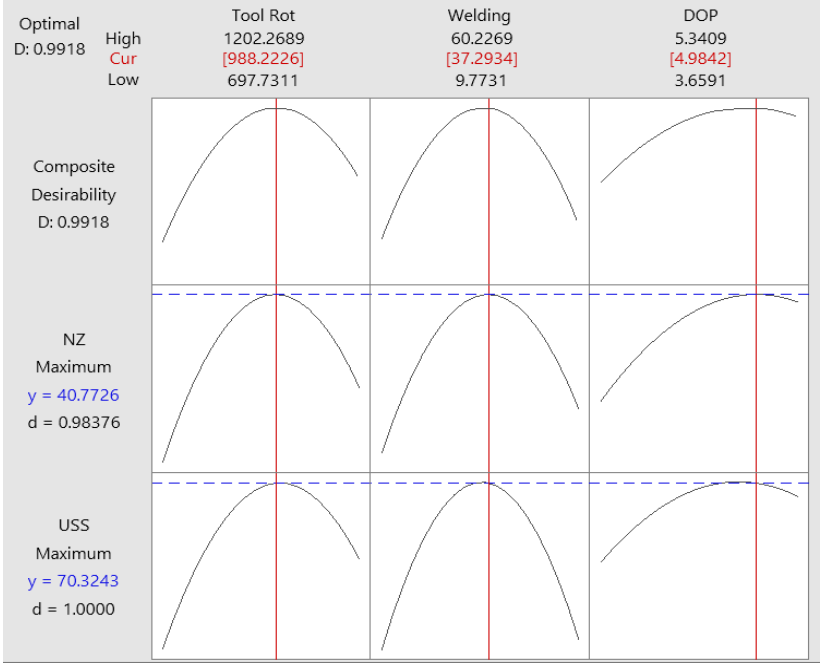

Fig. 13. Multi-objective optimization results

Table 9. Confirmation Test.

Responses	Welding Parameters Setting		Obtained Result	Predicted Result	Error %
USS (MPA)	RS (rpm)	1003.51	70.34	70.595	-0.363
	WS (mm/min)	35.76			
	DOP (mm)	4.85			
NZH (HRB)	RS (rpm)	988.22	41.5	40.77	1.759
	WS (mm/min)	37.29			
	DOP (mm)	4.98			
Maximum NZH (HRB) and Maximum USS (Mpa)	RS (rpm)	988.22	41.5 and 70.25	40.77 and 70.32	1.759 and -0.100
	WS (mm/min)	37.29			
	DOP (mm)	4.98			

5 Confirmation test results

To validate the proposed mathematical model, an additional series of tests were conducted based on the optimized parameters for USS, NZH, and both the responses combined (i.e., maximum USS and maximum NZH). The experimental outcomes were then compared to the predicted optimal results. Table 9 represents both the obtained and predicted optimum results, along with the error.

6 Conclusions

FSLW of different grades of Al alloys was carried out and a detailed investigation of the effects of welding parameters on the response variables. The optimization analyses were performed to assess weld quality, focusing on USS and NZH. The findings suggested that the RS, WS, and DOP can be optimally controlled to achieve the desired outcomes with the help of the RSM based mathematical model. ANOVA analysis was performed to determine the impact of the welding parameters to achieve the desired weld quality. The results indicate that RS and WS significantly influence both the responses. The predicted optimal values for the responses are 70.3243 MPa as maximum USS and 40.7726 HRB as maximum NZH, achievable with a RS of 988.2226 rpm, WS of 37.2934 mm/min, and DOP of 4.9842 mm. Finally, the proposed mathematical models were validated through a series of experiments on the basis of the optimized welding parameter settings, yielding satisfactory results.

References

1. Threadgill, P., Leonard, A., Shercliff, H., Withers, P.: Friction stir welding of aluminium alloys. Int. Mater. Rev. 54 (2), 49–93 (2009).
2. Akianlabi, E. T., and Akianlabi, S. A.: Friction Stir Welding process: A Green Technology, International Journal of Mechanical, Industrial Science and Engineering, 6 (11), 63-65 (2012).
3. Moreira, P., Santos, T., Tavares, S., Richter-Trummer, V., Vilaça, P., De Castro, P.: Mechanical and metallurgical characterization of friction stir welding joints of AA6061-T6 with AA6082-T6. Materials & Design. 30 (1), 180–187 (2009).
4. Scafe, A., Joaquin, A.: Friction Stir Welding of Extruded Aluminum for Automotive Applications. SAE World Congress, (2004).
5. Shinoda, T., Suzuki, J.: Observation of Metal Flow Phenomenon of Lap Joints during Friction Stir Welding, Proceedings of the 3rd International Symposium on Designing, Vol. 449–452(1), pp. 421–424. Processing and Properties of Advanced Engineering Materials, (2004).
6. Liu, X., Sun, Y., Morisada, Y., Fujii, H.: Dynamics of rotational flow in friction stir welding of aluminium alloys. Journal of Materials Processing Technology, 252, pp. 643–651 (2018).
7. Zeng, X., Xue, P., Wang, D., Ni, D., Xiao, B., Wang, K., Ma, Z., Material flow and void defect formation in friction stir welding of aluminium alloys. Science and Technology of Welding and Joining. 23 (8), pp. 677–686 (2018).
8. Khan, N.Z., Siddiquee, A.N., Khan, Z.A.: Friction Stir Welding: Dissimilar Aluminium Alloys. 1st Edition. CRC Press, (2017).
9. Khan, N.Z., Siddiquee, A.N., Khan, Z.A., Shihab, S.K.: Investigations on tunneling and kissing bond defects in FSW joints for dissimilar aluminum alloys. J. Alloys Compd. 648, pp. 360–367 (2015).

An Overview of Laser-Assisted Metal-Polymer Welding: Fundamentals, Key Parameters, Quality Attributes, and Applications

Rajesh Guria[1], Bappa Acherjee[2], Souren Mitra[1]

[1] Department of Production Engineering, Jadavpur University, Kolkata, India, 700032
[2] Department of Production and Industrial Engineering, Birla Institute of Technology, Mesra, Ranchi, India, 835215

Abstract. Laser-assisted metal-polymer (LAMP) welding has evolved as a successful way of joining metals to polymers, which is critical for lightweight material applications in automotive, aircraft, electrical, and medical equipment. LAMP welding involves selectively irradiating the metal surface with a laser, causing the melting polymer to flow into microscopic imperfections present on the metal surface and produce a bond after cooling through mechanical and chemical interlinking. LAMP welding has demonstrated excellent processing efficiency and is promising as a new welding technology for combining hybrid structures when compared to conventional adhesives, mechanical bonding techniques, and other bonding methods. Its strengths include its precision, versatility, minimal heat impact, reduced processing time, and potential for automation. This paper reviews the key elements of LAMP welding, including process fundamentals, parameters, quality attributes, and benefits over alternative joining processes. The review also includes an exploration of several applications that demonstrate the ability of LAMP welding to join polymer-metal hybrid structures.

Keywords: laser-assisted welding, LAMP welding, metal-polymer bonding, lightweight structures, multi-material applications, weld quality

1 Introduction

The automotive industry must find ways to lighten vehicles to decrease fuel consumption, enhance engine efficiency, and reduce carbon emissions. Similar challenges apply to other sectors, such as aerospace, aviation, and biomedicine, where reducing weight is crucial [1]. Due to its increased Gross Vehicle Weight (GVW), the average weight of cars rose from 1000 kg in 1970 to 1380 kg by 2015. This rise has led to greater fuel consumption, reduced engine efficiency, and higher carbon emissions, adversely affecting the environment and public health [2]. The global civil aviation sector aims to reduce aircraft emissions by 50% by 2050, with weight reduction being a vital factor in reaching this goal. Lightweight designs can improve flight performance metrics, including acceleration, structural rigidity, and safety. Current solar-powered unmanned aerial vehicle (UAV) designs face challenges with wing stiffness and low energy density. Ultralight aircraft often require a lightweight structure with targets such as an empty weight below 115 kg and a minimal fuel capacity of 19 liters. Lightweight construction enables extended flight times and improved performance. Weight reduction is also essential in rocket design [3]. In the healthcare sector, using plastic instead of metal for medical devices makes equipment lighter, more customizable, and easier to clean. Thus, lightweight solutions are advantageous in biomedicine [4]. Efforts should focus on joining polymer-to-polymer or polymer-to-metal hybrid structures to decrease the weight of heavy components [5]. Polymers offer several benefits, including low weight, high weldability, enhanced formability, vibration damping [6], impact resistance [7], high production yield, and tolerance to damage [8]. They are durable, recyclable, deformable, and repairable [9-10]. Various thermoplastics with high transparency are suitable for light-structure joints, as are certain amorphous polymers with lower transparency [1]. For metals, the manufacturing sector seeks lighter, stronger options with excellent thermal and electrical conductivity, weldability, formability, and corrosion resistance [11]. This focus is primarily on non-ferrous metals like titanium, nickel, magnesium, copper, aluminium, and their alloys [12].

Various techniques are used in industry to join polymers with metals or other polymers. One method is adhesive bonding, which requires the adhesive to cure and be shielded from air exposure. While mechanical fastening is another widely used approach, it has drawbacks, such as added weight and longer processing time. Advances in various thermal joining techniques over the past decade have accelerated the development of polymer-metal hybrid joint production. However, conventional thermal joining methods are often limited by joint type and technology, leading to lower joint strength and susceptibility to flaws. Integrating metals and polymers through thermal joining presents several challenges: (i) due to the notable variations in their physical and chemical characteristics, polymers struggle to effectively wet metal surfaces. (ii) Metallurgical bonding does not occur at the metal-polymer interface; rather, joining dissimilar materials primarily relies on physical adsorption, mechanical interlocking, and

limited chemical interactions at the interface. (iii) Heat-induced stress distribution during bonding and cooling varies because of metal-to-polymer thermal expansion coefficients and elastic modulus. This mismatch results in residual stresses that reduce bonding strength at the interface. (iv) A range of chemical bonds form, requiring distinct calibration standards for each element in new compound phases, and many lack standardized testing protocols. In resistance spot welding, for example, material conductivity must be addressed to ensure effective bonding, particularly in thermal joining applications. Achieving a continuous bond over large areas is challenging, as the bonding contact tends to be discontinuous [13]. The brazing process introduces inclusions at the interface, and overcoming the filler metal's wettability on polymers is necessary [14]. Ultrasonic welding can result in joint weakening due to material deformation and extrusion during polymer melting [15-18]. Friction stir welding, which relies on a robust stirring tool, can lead to defects such as voids or holes [19-21].

Welding is one of the most well-known processes for creating permanent joints with high strength [22]. Among recent advancements in metal-to-polymer welding, LAMP welding has gained attention. This technique uses laser radiation to melt and fuse materials at their interface, enabling the joining of both similar and dissimilar materials. In this process, the upper material must be transparent to let the laser progress and heat the absorbent substance underneath. This method is also known as Laser Transmission Welding (LTW), and it has expanded to incorporate various laser types, including diode, CO2, Nd:YAG, and fiber lasers [23]. For most opaque polymers, the upper material must absorb and transfer heat to the bottom layer, with the joining occurring at the interface where the heat is absorbed. This variant is termed laser conduction welding (LCW). LCW offers several advantages, including speed, adaptability, deep and narrow welds, minimal heat input and distortion, suitability for diverse materials and thicknesses, non-contact operation, vacuum capability, and dual-sided access. It also allows automation and the production of complex shapes [24]. Laser welding, which uses a concentrated heat source, is efficient for joining metal and polymer materials by creating strong, continuous seams. In the automotive industry, laser welding is used extensively for joining components likely roofs, doors, and filters, providing high productivity at a low cost [25]. Laser welding is also popular in the medical and jewellery industries for precise, small-scale metal joining. This technology is suitable for materials with high thermal conductivity, making it versatile for applications ranging from automotive parts to jewellery and medical devices [26]. Additionally, lightweight airplane fuselage components are increasingly fabricated using laser welding [27].

2 Process Fundamentals

The nature of the metal-polymer laser joining process depends on the thermal, optical, chemical and physical properties of the materials that are fused. To ensure there are no air gaps during the joining procedure, the components being welded should be securely pressed together using appropriate fixtures.

2.1 Materials

The main materials used in LAMP are thermoplastics, which fall into two categories: amorphous and semi-crystalline. Amorphous polymers contain long side chains, coiled or knotted molecular chains, resulting in a disordered, freely entangled state. This structure provides strong laser transmission and general transparency or translucency, allowing for transmission and thermal conduction joining. In contrast, semi-crystalline polymers are composed of long-chain molecules that organize into highly structured microcrystalline densities. However, a fully organized structure is not achieved by these molecules, leading to their classification as semi-crystalline due to the presence of some amorphous areas. Transparency is typically not observed in these polymers. Thermal conduction joining is the only possible method for laser joining due to the diffuse scattering of the laser and high absorption rate in semi-crystalline polymers. Additionally, a minimum temperature higher than the GTT (glass transition temperature) (around 100 °C) is required for the bonding of amorphous polymers, while a bonding temperature above 50 °C, corresponding to the melting point, is needed for semi-crystalline polymers. High-transparency thermoplastics that are semi-crystalline, such as polycarbonate (PC), polymethyl methacrylate (PMMA), and polyethylene terephthalate (PET) are commonly used. On the other hand, low transparency is seen in some amorphous polymers, including nylon (PA6 and PA66), polyimide (PI), acrylonitrile butadiene styrene (ABS), polystyrene (PS) and liquid crystal polymer (LCP). Increased attention is being given to food-grade polymers, such as high-density polyethylene (HDPE) and synthetic nylon, due to their lightweight and weldable characteristics [28].

Metals and polymers together offer high utility, strength, and low weight, which are essential for everyday life and technological advancement. Today, metals like steel, aluminium alloys, and titanium alloys are frequently combined with polymers due to their desirable properties. For example, titanium alloy is widely used in the marine, aerospace, and biomedical industries due to its strong resistance to corrosion, fatigue, and cracking and its

biocompatibility. Aluminium alloy is popular in the electronics, automotive, aerospace, and marine sectors for its high specific strength, low density, excellent conductivity, ease of production, and corrosion resistance. Additionally, magnesium alloys, known for their low densities and high porosity, have attracted interest from researchers [29]. Magnesium alloys' low weight makes them appropriate for the automotive, marine, and aerospace industries. Because it reacts with the atmosphere, magnesium alloys' drawbacks can be eliminated by laser lap welding between them with an appropriate polymer.

2.2 Mechanism

During LAMP welding, the laser energy is getting absorbed by the metal and melts the polymer at the polymer-metal interface. While temperature increases, part of the polymer decomposes in the molten state, forming bubbles. The high-temperature, activated polymer completely melts into the metal surface, and while it cools, it creates a permanent bond. This is aided by the internal pressure from bubble formation and expansion, along with external clamping pressure [30]. These bubbles remain within the solidified plastic region. The intimate contact between metal and polymer, which can be produced by a fastening mechanism, is essential to the bonding process, ensuring full interface contact without air gaps [31], as illustrated in Fig. 1. Thermoplastic polymers are preferred due to their melting properties. The LAMP welding process can be categorized as laser conduction welding (LCW) or laser transmission welding (LTW), depending on the type of laser irradiation. The primary difference is that in LTW, the bonding interface in the metal-polymer hybrid structure is heated by direct laser illumination when transparency is over 60% (Fig. 2a) [32]. In contrast, LCW applies the laser directly to the metal surface to join with the polymer (Fig. 2b) [32]. The LTW variant of the LAMP process is highly dependent on the polymer's transmittance and the laser wavelength [33].

The bonding process at the interface, which determines the connection between metals and polymers at a particular temperature, involves three types of mechanisms: physical, chemical, and mechanical bonding. Mechanical bonding, for instance, creates micro-level anchorage by embedding composite materials onto metal surfaces with concave and convex features. This bonding strength depends on the microstructure's size, density, and surface treatment technique. The accuracy and reliability of metal-polymer laser joining are strongly correlated with the selected laser welding procedure, process parameters, laser performance and the thermal, optical, physical and chemical characteristics of the metal-polymer materials. The appropriateness of these parameters and the procedure are reflected in the forming quality. Therefore, thorough characterization of forming quality and the monitoring method are necessary to produce structural parts with high-quality bonding.

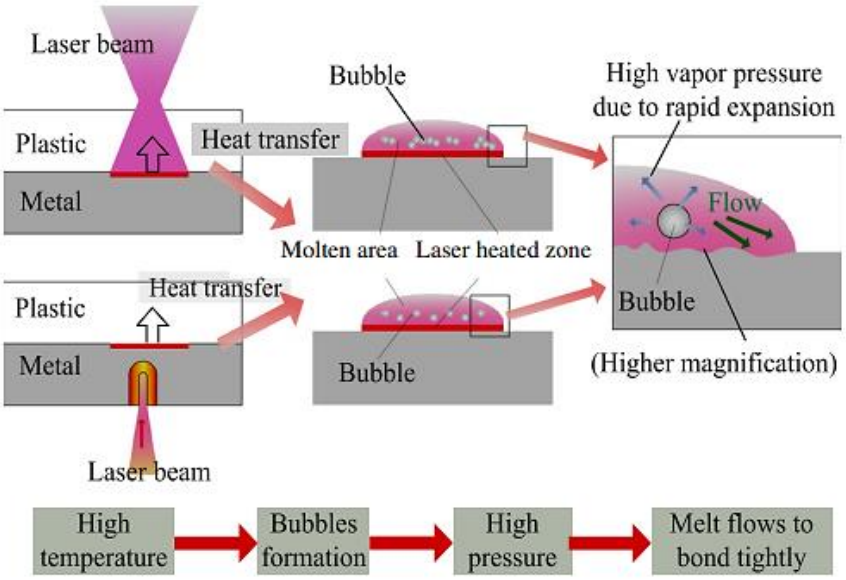

Fig. 1. Principle of LAMP joining [1]

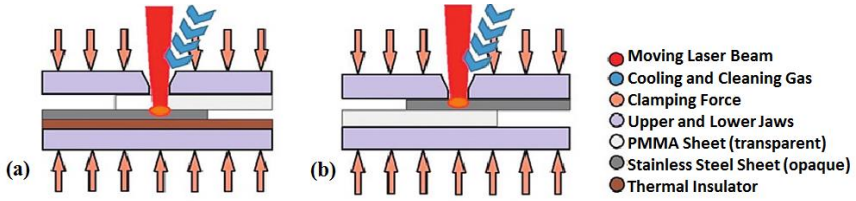

Fig. 2. (a) LAMP- transmission welding process; (b) LAMP-conduction welding process [32]

3 Process Parameters and Quality Attributes

The efficiency of laser joining is significantly influenced by the material characteristics of both components to be joined along with the process parameters. Intensity of laser power and interaction time are the most critical variables in any laser material processing application. In the case of LAMP welding, the four primary independent process parameters are recognized as laser power, welding speed, laser beam spot size on the workpiece, and clamping pressure. These parameters allow the effective management of the temperature field within the weld during the welding process. The energy density employed in welding is determined by the combination of laser power density and laser interaction time. Each of the following factors, laser power, laser beam spot size, laser irradiation time, and welding speed, plays a role in this process. Extremely low energy density is likely to result in no fusion, while excessively high energy density can lead to overheating and partial material degradation, ultimately limiting the weld strength. Optimal weld strength is achieved when laser power and welding speed are properly balanced to reach a desirable energy density. The same energy density can be obtained by combining high power with high welding speed or low power with low welding speed. However, it has been noted that at slower welding speeds, heat conduction losses are more significant, which makes heat transmission more critical due to the relatively low laser output. Conversely, at faster speeds, reduced heat loss is observed when higher laser power is utilized to maintain the same energy density, as there is less time for heat dissipation. The majority of the input energy is received by the weld zone. It was demonstrated by Bun et al. [34] that the maximum tensile shear strength exceeds 30 N/mm2 between 6061-T6 Al Alloy (2 mm thickness) and CFRTP (2 mm thickness) with an optimized laser power and welding speed through conduction joining. Various ordinary and bionic structures have been created on metal surfaces to enhance the strength between the aluminium alloy and CFRTP, with the highest strength, surpassing 30 N/mm2, being exhibited by fishbone structures (Fig. 3). Even though the experiment's design allows for higher power and slower welding speeds, the polymer or metal burns under extreme circumstances. It is evident that greater welding strength without burning may be attained at optimal parameters. Xue et al. [35] found that the maximum tensile shear force between PA6GF30 and SUS444 lap joints reached 1695.7 N with a laser power of 900 W and a scanning speed of 8 mm/s through conduction joining. However, this maximum force decreased to 1192.5 N when the welding speed increased from 8 mm/s to 12 mm/s. Additionally, tensile shear force improved from 1554.5 N to 1785.9 N while the defocus distance increased from 44 mm to 61 mm. The outcome demonstrates that the temperature between plastic melting point and decomposition point a strong link is created between metal and plastic joint surface. So, the tensile shear force is partially reflected in the width of undecomposed area of weld zone. Yuan et al. [36] conducted conduction joining between a 7075 T6 aluminium alloy (thickness: 1 mm) and CFRP-PEEK (thickness: 3 mm) using a maximum laser power of 600 W and a scanning speed of 7 mm/s. The greatest tensile force, which initially increased and then decreased, reached a maximum of 478 N at 450 W. It is evident that CFRP-PEEK's melting effect increases with laser power in the 300–450 W range, leading to an enhanced tensile force.

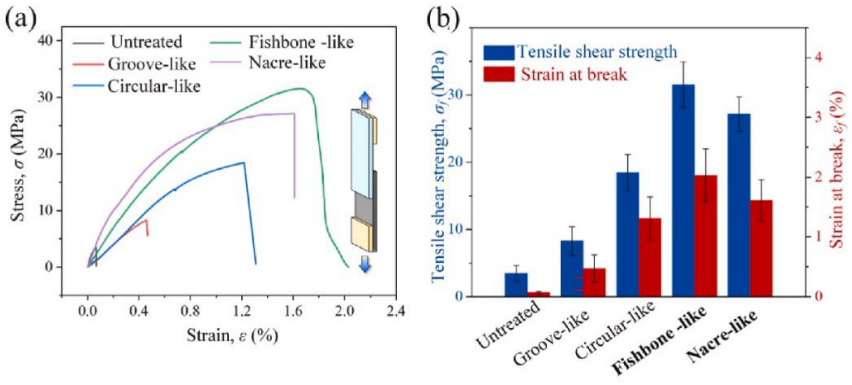

Fig. 3. Mechanical characteristics of Al 6061/CFRTP joints: (a) stress-strain diagram; (b) break point of metal polymer joint during tensile test [34].

When the laser power surpassed 450 W, it entered the aluminum alloy, carbonizing CFRP-PEEK and weakening its tensile strength as a result (Fig. 4). Xia et al. [37] demonstrated the impact of laser power on conduction welding joint quality. The peak load gradually increased at a laser power of 700 W, welding speed of 5.5 mm/s, and +95 mm defocus distance, reaching a maximum value of 3855 N. One of the primary reasons for this increase in tensile-shear load was the expansion of the bonding area with increasing laser power. However, the tensile-shear peak load dropped to 3689 N when the laser power increased to 800 W due to the burning away of the resin matrix after the laser's intensity was raised. From the result it is assumed that steel did not melt within the specific range of laser power. A small amount of CFRP was also discovered near the workpieces' edges. Jigs' pressure effect was the source of this. During the welding process, the clamping jigs held the CFRP and steel workpieces in place. Some CFRP was melted by the laser beam's heating effect. Because of its extreme fluidity, the melted CFRP poured out of the workpiece when the jigs applied pressure. Elahi et al. [38] performed conduction joining between a 1050 H24 aluminium alloy (thickness: 0.5 mm) and polyamide 6 (thickness: 4 mm) at a laser power of 400 W and a scanning speed of 2.5 mm/s, achieving a maximum tensile shear strength of 1630 N. This paper guided that the market-received aluminum surface and the molten polyamide have a very weak bond, which leads to joint failure. Surface modification, such as laser ablation or polishing on the aluminum surface, is crucial to increasing the joint strength. Feng et al. [39] presented the shear strength of conduction welding joints for CFRTP and 6061 T6 aluminium alloy at various laser powers. The shear strength improved from 900 W to 1100 W; however, further increases in laser power led to a decrease in shear strength. The highest strength recorded was 23.8 MPa (Fig. 5). The PEEK resin began to melt at an interface temperature of 341 °C, and the melting range expanded with increasing laser power, resulting in a wider melting width of CFRTP. At 1100W laser power highest shear force is achieved due to the excessive amount of heat input becomes consistent with shear strength observations. The maximum temperature varied from 353 °C to 500 °C while the laser power was changed from 900 W to 1300 W. The PEEK resin started to melt at the interface temperature of 341 °C (the melting point of PEEK resin). The higher power intensity expanded the melting range improving the shear strength of joints. However, the CFRTP resin matrix began to break down when the interface temperature surpassed 460 °C, which is the breakdown temperature for PEEK resin. Consequently, resulting in the formation of pores as defects at the junction, reducing the shear strength of the joints.

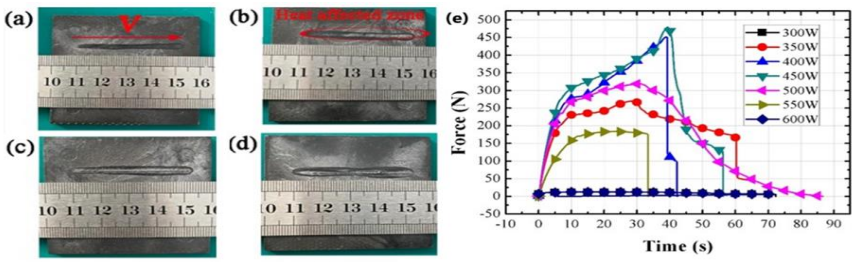

Fig. 4. Failure surface at different laser power (a) 300W (b) 350W (c) 400W (d) 450W (e) shear force diagram of welded joints at different laser power [36].

The tensile shear test is the most effective method for determining the mechanical joint strength of welded connections. The failure load or maximum joint strength depends on the optimal process parameters. Gisario et al. [40] presented the different failure load versus displacement curves for Al 50 μm and MaterBi samples under

various parameters (Fig. 6). From the paper it is seen that the welded joints' resistance was more than enough because it consistently outperformed the polymeric material's resistance in every test. It is evident that shorter laser beam-to-polymeric material interaction durations result in less heat deterioration of the polymer and, consequently, improved mechanical responsiveness in static tensile testing. Hao et al. [41] investigated the tensile characteristics and weld formation of austenitic steel and PET (Polyethylene Terephthalate). They found that, at optimized parameters of laser power (P) of 300 W, oscillation radius (r) of 2 mm, and oscillation frequency (f) of 300 Hz, along with a specified welding speed of 50 cm/min and a defocused distance of 20 mm, the challenges of thermal degradation and fusion could be discarded in transmission joining. In comparison to samples without beam oscillation, shear force increased by 26%, reaching 78% of the PET base material's strength. For samples without beam oscillation, large pores with linear connecting segments at the center and an even surface at the boundary were seen on the plastic side of the fracture surface, indicating a typical brittle failure mode. In contrast, samples with optimal parameters showed smaller pore sizes at the center, transitioning from a linear to a planar form. A plastic mode of fracture was identified, demonstrating increased deformability from the center to the edge. Additionally, due to the interaction between the plastic and steel, few steel particles were visible at the fracture surface, with higher bonding strength correlating with the presence of these particles. Liao et al. [42] improved the bonding strength of LAMP welds between stainless steel and PET by employing oscillating laser irradiation at the same parameters used by Hao et al. [41]. In the case of the LTW joint, the average shear tensile force was measured at 841.2 N, while an increased tensile shear force of 1036 N was achieved in the O-LTW (where O indicates oscillation). The shear tensile force increased by 19% for O-LTW. For the LCW joint, a tensile shear force of 1113.3 N was recorded, which increased to 1282.5 N in the O-LCW joint (Fig. 7) [41-42]. This represented a 15% increase in shear tensile force for O-LCW. In both cases of oscillating laser irradiation in metal-polymer welds, the strength achieved was 96.7% and 90% of the PET plastic, which serves as the parent material. Notably, compared to the O-LTW joint, the O-LCW joint exhibited a higher tensile force increase of 23.8%. It can be inferred that the discrete interface bubble distribution in joint O-LCW enhances performance more than the network distribution observed in joint O-LTW. Additionally, better plasticity was found in the O-LCW joint (Fig. 8). Here, "MX fracture" denotes samples with cracks in mixed mode, while "BP fracture" denotes samples with cracks along the interface [42].

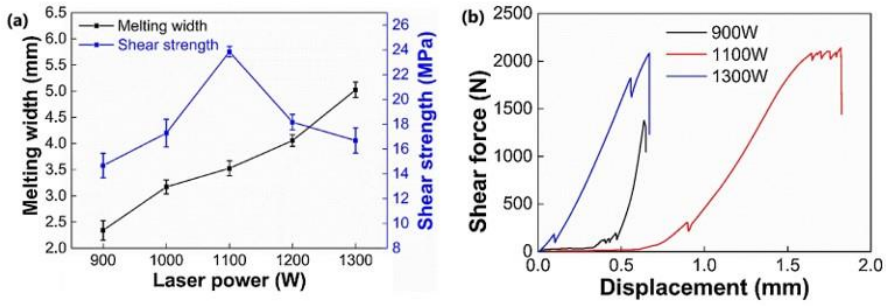

Fig. 5. Variation of shear strength and shear force as functions of laser power and displacement: (a) shear strength vsersus melting width at different laser powers; (b) shear force versus displacement at different laser powers [39].

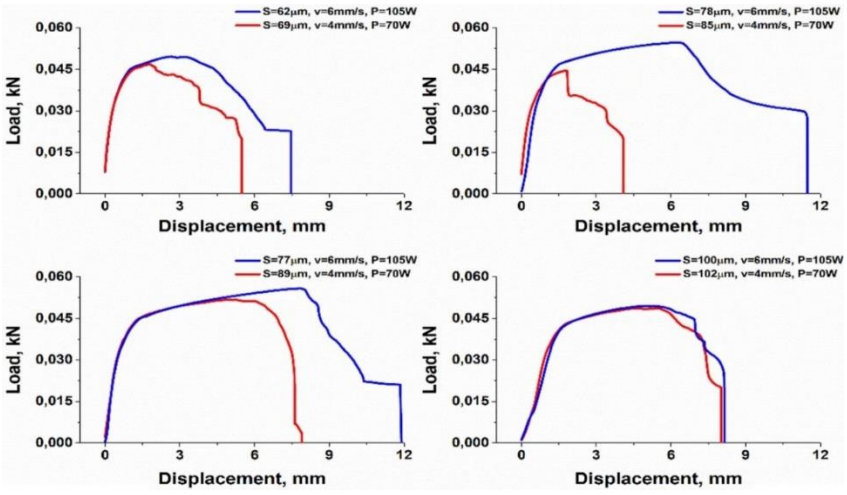

Fig. 6. Displacement variation as a function of load at different process parameters for the shear tests performed on Al 50 μm and MaterBi samples [40].

The recent challenge of LAMP hybrid structure is low mechanical strength due to weak interface bonding. Chen et al. [43] tested the laser transmission welding (LTW) of PET and ceramic with the assistance of ultrasonic vibration. They discovered that friction between the rough blind hole and the melted PET is increased due to ultrasonic vibration, which decreases the melt's viscosity and enhances fluidity. This improvement facilitates the flow of melted plastic into the blind hole and enables it to anchor mechanically to the hole's entrance and walls. The ultrasonic vibration also provided extra driving acceleration in the melted plastic, raising the blind hole's filling depth by almost 73%. The joints created by LTW and ultrasound-assisted laser transmission welding (U-LTW) were examined using optical microscopy, revealing the joints' appearance and bonding region dimensions. Three samples were measured for each welding condition, yielding average bonding areas of 85.9 mm² for U-LTW and 73.4 mm2 for LTW, indicating a 17% increase in bonding area (Fig. 9). Chen et al. [44] also demonstrated how the failure load for U-LTW and LTW specimens is affected by laser power. The bonded surface area of the joint was calculated prior to the shear test, showing an increase with rising laser power (Fig. 10). Fig. 10a was revised to more accurately depict joint performance in terms of failure stress (Fig. 10b).

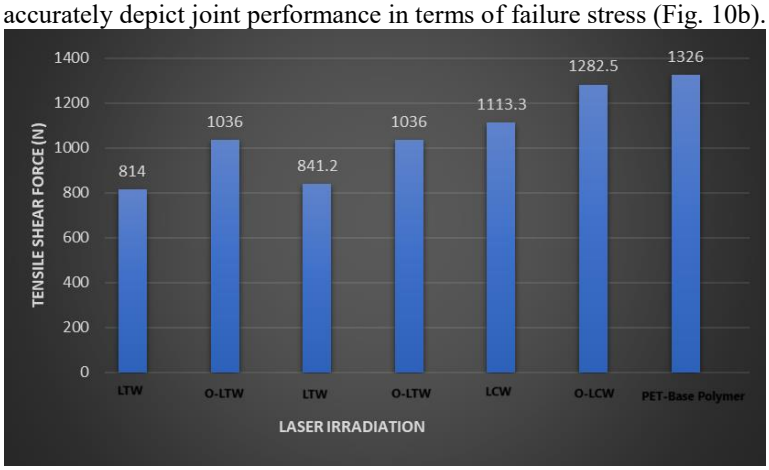

Fig. 7. Comparison of tensile shear force with respect to single pass and oscillating laser irradiation [41-42]

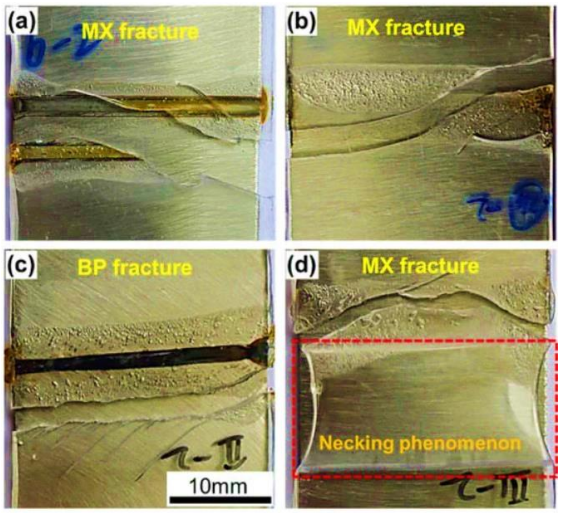

Fig. 8. Macroscopic fracture morphologies: (a) LTW, (b) O-LTW, (c) LCW, (d) O-LCW [42].

The significant fracture formation of the LTW and U-LTW specimens are displayed in Fig. 11. The U-LTW specimens broke in the parent plastic section, while the LTW specimens failed at the joining interface, causing separation of the metal and plastic parts. This indicates that the fracture processes of the LTW specimens differed, with U-LTW specimens exhibiting fracture stress at least four times higher.

Alongside the tensile or shear strength of the weld, the morphological behaviour of the weld is crucial in determining its quality. Various characterization techniques are now employed to assess failure reasons, elemental distribution, crystallographic information, and other factors. The surface morphology of LAMP welded joints can be effectively analyzed using the different characterization procedures listed in Table 1. Ideally, these methods will transform the practical application of LAMP welding in the future and be adopted by various industries where weight reduction is a top priority. Bun et al. [34] demonstrated how hybrid joints with different interfacial textures

can be analyzed using optical microscopy. The area below the weld seam, observed as the interfacial zone, shows that hybrid joints with untreated and nacre-like interfacial textures exhibit good interfacial bonding and minimal visible pores at the interface (Fig. 12).

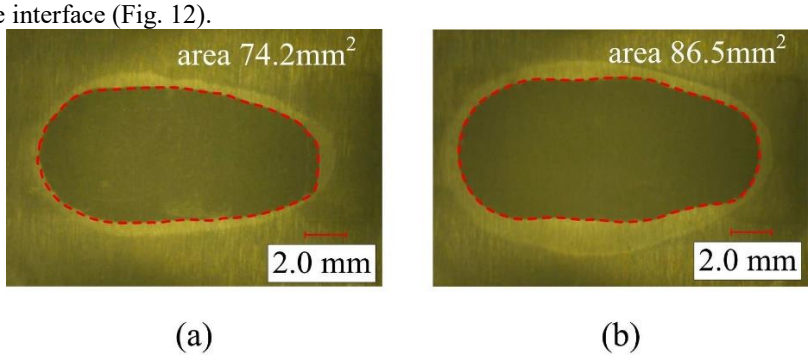

Fig. 9. Microscopic image of joint formation: (a) LTW specimen (b) U-LTW specimen [43]

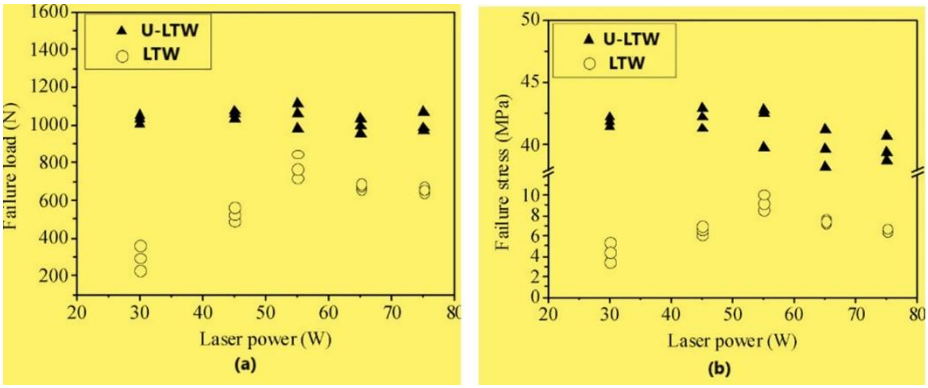

Fig. 10. The impact of laser power on (a) failure load (b) failure stress [44]

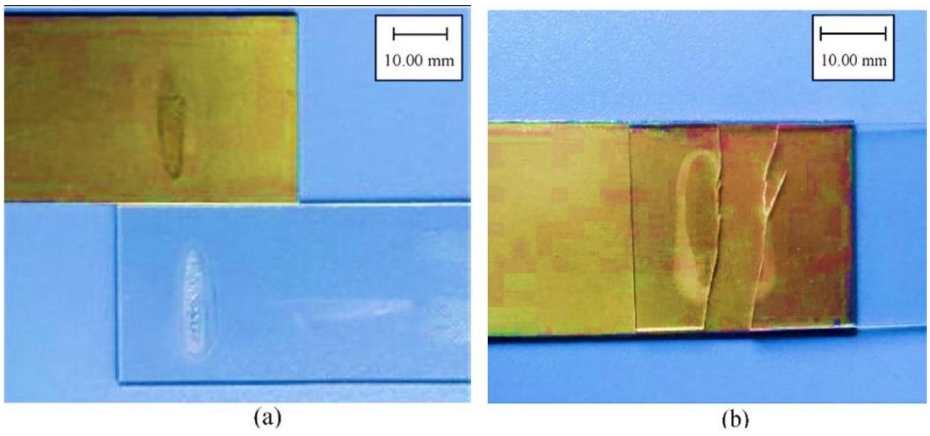

Fig. 11. Image of failure appearance of (a) a LTW specimen (b) a U-LTW specimen [44]

However, pores with textures resembling fishbones, circles, and grooves can be clearly seen around the hybrid joint interface. Notably, the interfacial pores in fishbone-textured hybrid joints exhibit less dimensional change and deformation. It is commonly accepted that interfacial pores tend to weaken the mechanical characteristics of heterogeneous joints, and a superior interface morphology is characterized by smaller, rounder pores or, ideally, no pores at all. Consequently, textures resembling nacre and fishbone structures provide comparatively better interface morphology. The larger pore size and groove-like texture, which impede bubble escape, are two potential reasons for this: improved wettability to molten PEEK and unique features that facilitate bubble escape. Xue et al. [35] displayed the fracture surface morphologies of the PA6GF30 and SUS444 joint produced at 900 W of laser power, a 44 mm defocus distance, and an 11 mm/s welding speed. Residual plastic was observed on the broken SUS444 surface (Fig. 13(a) and 13(c)), while the broken PA6GF30 surface exhibited pits and porosities (Fig. 13(b) and 13(d)). The elemental distribution of joint fracture surface is analysed at 800 W laser power, 49 mm defocus distance, and 11 mm/s welding speed, was investigated using SEM and EDS. The EDS results for

point A2 (Fig. 14(a)) indicated that the dark gray area, identified as the remaining polymer on the fractured metal surface, primarily consisted of carbon and oxygen, with trace amounts of iron and chromium. Conversely, the broken surface of polymer was composed mainly of carbon and oxygen, with a smooth, level surface. As a result, the samples failed along their plastic side, exhibiting brittle fracture as the mode of failure (Fig. 14(b)). Tana et al. [45] investigated the SEM morphologies to analyze the elemental distribution at the joint interface between carbon fiber- reinforced PEEK and titanium alloy (Fig. 15). By varying the scanning speeds to 0.6 m/min, 0.8 m/min, and 1.0 m/min, SEM morphologies near the interface were observed. The CF-PEEK melted resin permeated the uneven titanium alloy surface, leading to mechanical interlocking upon cooling at the attachment contact. EDS line scanning was employed to map the elemental distribution throughout the interface. Element diffusion of titanium, carbon, and vanadium occurred at the joint surface, indicating that a new compound layer was formed on the titanium alloy surface during the laser joining process. The thickness of this compound layer decreased as the welding speed increased, resulting in a 10 μm thick layer at a welding speed of 0.6 m/min.

It is evident from a number of studies that optimal process parameters determine the tensile shear strength of LAMP welding. One of the most crucial requirements to attain greater strength is surface changes. To assess the quality of the bonding between metal and polymer, as well as heat-affected zones, interface morphology, fracture types, and elemental distributions that can clearly reveal internal changes following the formation of bonds between metal and polymer, various characterization techniques are needed.

4 Applications of Lamp Welding Structures

A sharp increase in fuel prices drives the aircraft industry's efforts to lower the structural weight of passenger aircraft. The airbus company has demonstrated that laser beam welding is a promising and validated industrial solution for decreasing the weight and manufacturing costs of metallic fuselages in civil passenger aircraft [27]. In future developments of airplane structures, particularly for passenger aircraft fuselages, the key challenge will be to reduce weight while controlling production costs. An important objective for metallic structures is to enhance their cost advantages over CFRP structures when comparing the operational efficiency of contemporary CFRP and metallic constructions. Advancements in new production techniques, improved aluminium alloys, and structural design could facilitate this weight reduction potential (Fig. 16).

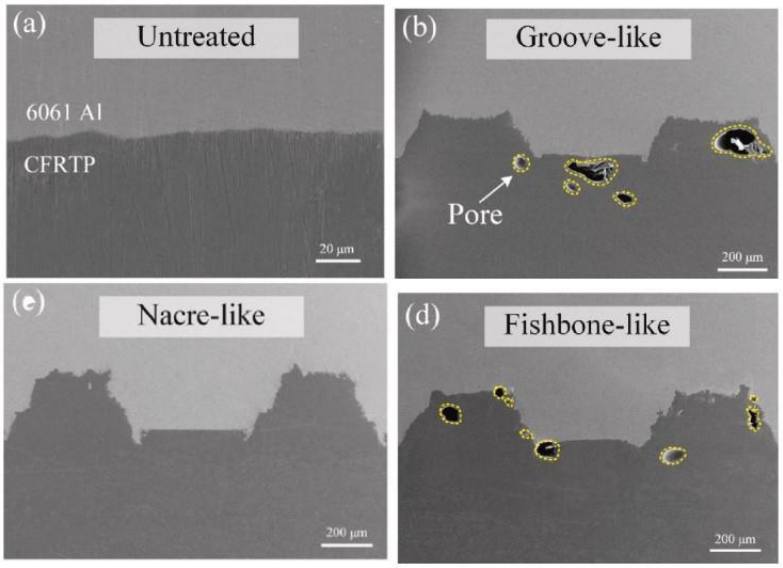

Fig. 12. Image of LAMP hybrid joints with different interfacial structures: (a–d) Interface morphology [34]

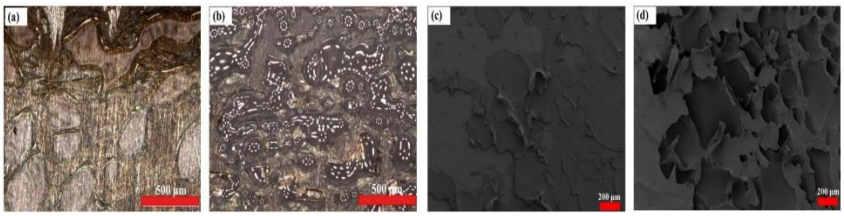

Fig. 13. Fracture surface morphologies of the PA6GF30 and SUS444 joint: (a)-(b) macrostructure of stainless-steel and plastic, (c)-(d) microstructure of stainless-steel and plastic [35]

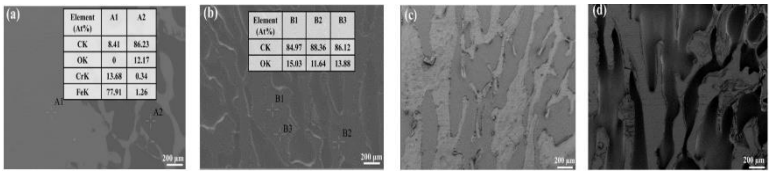

Fig. 14. SEM and EDS results of the fracture surfaces: (a) and (c) stainless steel, (b) and (d) plastic [35]

The automotive industry is facing challenges due to its large structural weight, which raises carbon emissions and contributes to global warming. Additionally, the market for automobiles is impacted by high fuel prices. These difficulties can be addressed by altering the joining techniques for lightweight materials and substituting them for heavier materials. Due to budgetary constraints, the majority of manufacturers currently rely on creating effective chassis designs using various grades of advanced high-strength steel rather than alternative materials. However, lightweight materials such as aluminium alloys, magnesium alloys, and titanium alloys are expected to gradually replace conventional materials as the limits of efficient design are identified and the costs of alternative materials decrease. Different metal-polymer couplings are also being considered to reduce the weight of vehicles. Nevertheless, the automotive industry faces additional hurdles in finding joining methods to replace conventional materials with alternative ones. Manufacturers employ spot welding and friction welding; however, both processes are associated with various drawbacks, including liquid metal cracking, surface explosions, and a high incidence of voids and cracks. Due to the numerous benefits of laser welding over spot, resistance spot, and friction welding, including non-contact welding, quick processing times, customized weld preparation, maximum structural integrity, minimal heat distortion, and suitability for mass production, it has been adopted by the automotive industry as a solution to these issues [46]. Figure 17 shows that LAMP welding can be utilized in various segments of the automotive industry [47].

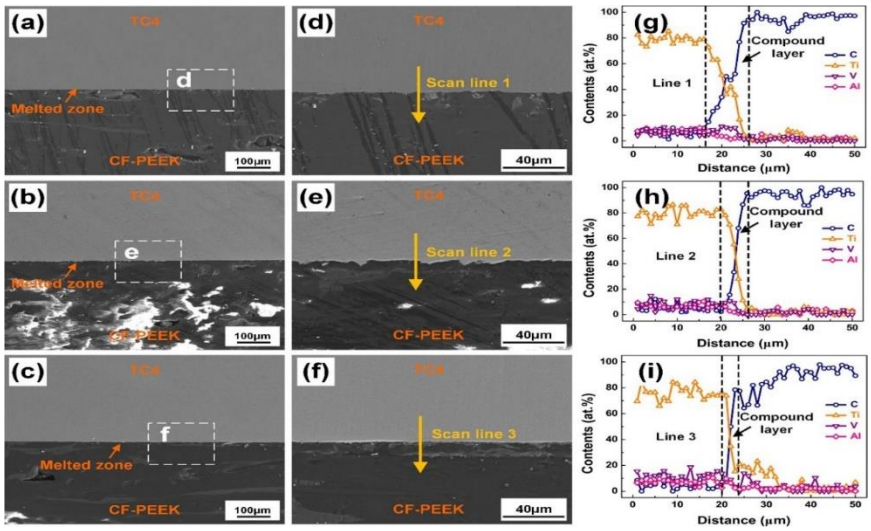

Fig. 15. SEM morphologies and element distribution at the joint surface under various welding speeds (a) 0.6 m/min, (b) 0.8 m/min, (c) 1.0 m/min, (d), (e) and (f): higher magnification of zones, (g), (h) and (i): EDS line scanning results with the scan line marked at (d), (e) and (f) [45]

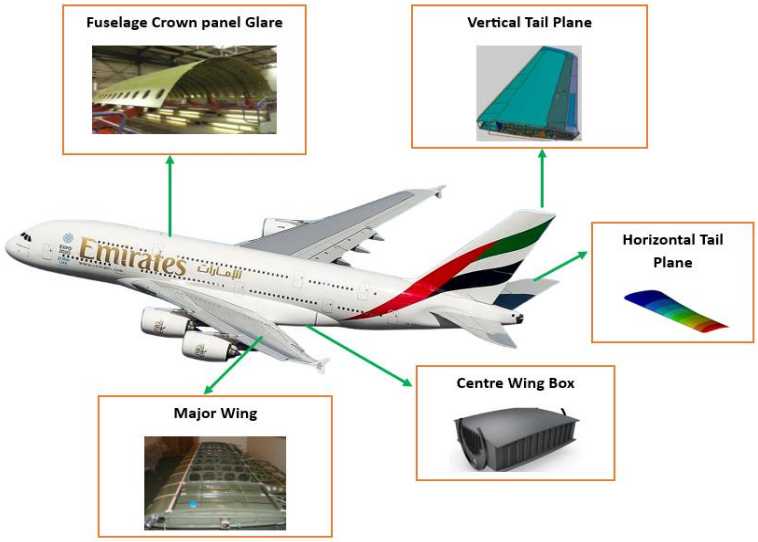

Fig. 16. Application of Al alloys-CFRP multi-material fabrication in aircraft fuselage structure

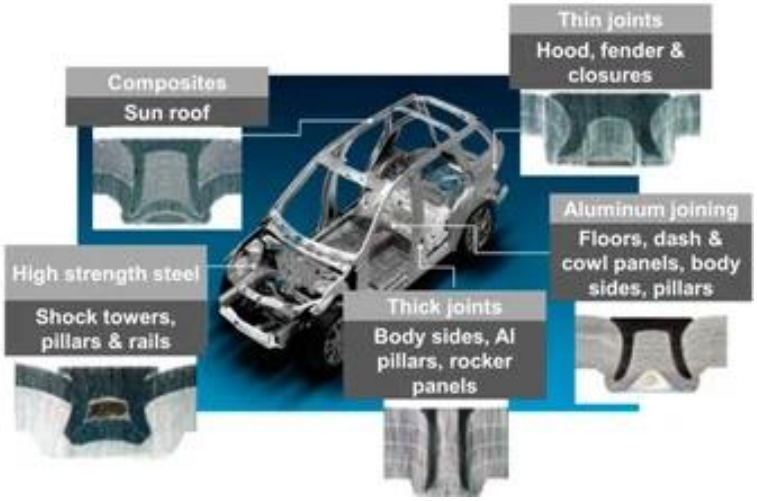

Fig. 17. Major areas where laser welding of metal polymer joints can be utilized over riveting systems [47]

Currently, only a select few conventional techniques, including brazing, welding, adhesive bonding, fastening, thermal butt fusion, and mechanical coupling, are primarily used to join metal and polymer tubes. There are significantly fewer methods available for joining tubes made of entirely different materials with radically different mechanical and physical properties. At present, structural adhesive bonding (Fig. 18(a)) and mechanical couplings (Fig. 18(b) to (e)) are the only methods for combining metal and polymer tubes [48]. In structural adhesive bonding, a thin layer of liquid or semisolid adhesive is applied between the opposing sides of the two tubes that need to be joined. This process requires careful surface preparation and stringent tolerances. The adhesive also needs time to cure, and under unfavourable weather conditions, the finished joint may become less effective. Among the various options available for mechanical couplings are compression gaskets, gasket-equipped clamping systems, threaded connections, and intricated threaded connections with gaskets and compression rings. Most of these joints are featured in simple designs, are ease to assemble and disassemble, and fits in general sizes. However, their scope of applications are sometimes limited by requirements for tightness, mechanical strength, dimensional accuracy, and aesthetics. There are not many well-tested methods for combining metal and polymer tubes that can provide robust resistance and a leak-proof design. LAMP welding can be particularly useful for joining metal and polymer tubes at their ends.

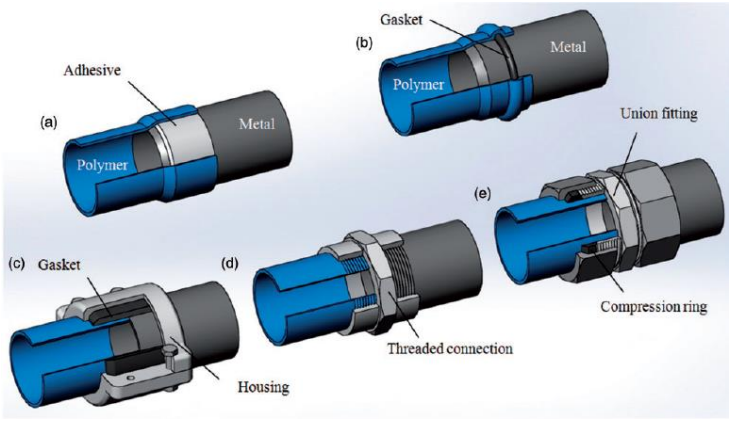

Fig. 18. Joining of polymer and metal tubes by their ends using (a) structural bonding and mechanical couplings based on (b) compression gaskets, (c) clamping systems, (d) threaded connections and (e) complex threaded connections [48]

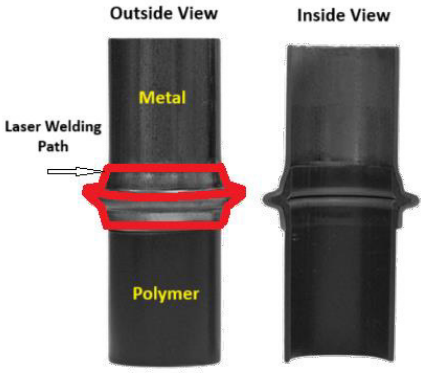

Fig. 19. Joining of polymer and metal tubes at their ends by using of laser welding

5 Conclusions

LAMP welding emerges as a promising technology for creating lightweight, multi-material structures across various industries for joining metal with polymers. The success of LAMP welding hinges on understanding the interplay of material properties and operational parameters. The effectiveness of LAMP welding is significantly influenced by the interplay of material properties and operational parameters. The selection of appropriate thermoplastics, like amorphous or semi-crystalline types, is deemed essential due to their unique structures that affect laser absorption and transmission. Proper clamping minimizes air gaps, which is critical for enhancing bond strength. Effective bonding results from physical, chemical, and mechanical interactions at the interface. Parameters like laser power, welding speed, beam spot size, and clamping pressure are vital, as they influence energy density, thermal dynamics, and, ultimately, the structural integrity of the joint. A precise balance between laser power and welding speed is necessary to achieve adequate energy density, ensuring material fusion without causing overheating or material degradation. Advanced configurations, such as bionic designs, further improve mechanical strength by optimizing the surface for better bonding. Assessing joint quality through surface morphology and interfacial bonding analysis helps determine performance reliability. As industries increasingly prioritize lighter, stronger multi-material assemblies, LAMP welding's role in enhancing multi-material structures is becoming more significant.

The future of LAMP welding presents several research opportunities aimed at expanding its effectiveness and applicability. Investigating polymer-metal pairs with enhanced laser absorption, optimized polymer flow, and greater chemical compatibility could broaden LAMP welding applications. Fine-tuning welding parameters alongside adaptive control systems could ensure higher joint quality, consistency, and operational efficiency. Developing advanced interfacial structures, like bionic patterns, may enhance mechanical strength and bonding quality. Integrating LAMP with other welding methods might achieve synergies, enhancing overall joint durability and strength. Rigorous testing of the long-term stability and environmental effects of LAMP-welded structures is necessary for validating their commercial viability. These areas collectively offer a roadmap for advancing LAMP welding, potentially unlocking greater capabilities in multi-material construction across industries.

References

1. Y. Huang, X. Gao, Y. Zhang, B. Ma: Laser joining technology of polymer-metal hybrid structures. Journal of Manufacturing Processes 79, 934–961 ((2022).
2. Light car low carbon, Federation Internationale DEL Automobile, https://www.lightcarlowcarbon.eu.
3. L. Zhu, N. Li, P.R.N. Childs: Light-weighting in aerospace component and system design. Propulsion and Power Research 7(2), 103–119 (2018).
4. https://www.solvay.com/en/article/lightweight-medical-instruments.
5. F. Lambiase, S. Scipioni, C. Lee, D. Ko, F. Liu: A State-of-the-Art Review on Advanced Joining Processes for Metal-Composite and Metal-Polymer Hybrid Structures. Materials 14(8),1890 (2021).
6. S. K. Bhudolia, P. Perrotey, S. C. Joshi: Enhanced vibration damping and dynamic mechanical characteristics of composites with novel pseudo-thermoset matrix system. Composite Structures 179, 502–513 (2017).
7. G. Anwer and B. Acherjee: Laser Welding Innovations for Polymers and Hybrid Structures. Lasers in Engineering 53, 139–170 (2022).
8. G. K. Dossou, R. M. Boumbimba, N. Bonfoh, S. G. Hernandez, D. G. Gonzalez: Innovative acrylic thermoplastic composites versus conventional composites: improving the impact performances. Composite Structures 217, 1–13 (2019).
9. M. Mehrpouya, A. Gisario, A. Rahimzadeh, M. Barletta: An artificial neural network model for laser transmission welding of biodegradable polyethylene terephthalate/polyethylene vinyl- acetate (PET/PEVA) blends. The international journal of advanced manufacturing technology 102, 1497–1507 (2019).
10. L. Shanmugam, M. Kazemi, Z. Rao, D. Lu, X. Wang, B. Wang, L. Yang, J. Yang: Enhanced mode I fracture toughness of UHMWPE fabric/thermoplastic laminates with combined surface treatments of polydopamine and functionalized carbon nanotubes. Compos Part B: Engineering 178, 107450 (2019).
11. D. Wallerstein, A. Salminen, F. Lusquiños, R. Comesaña, J. García, A. Rodríguez, A. Badaoui and J. Po: Recent Developments in Laser Welding of Aluminium Alloys to Steel. Metals 11(4), 622 (2021).
12. A. Hossein, N. Iqbal: A review on dissimilar laser welding of steel-copper, steel-aluminum, aluminum-copper, and steel-nickel for electric vehicle battery manufacturing. Optics & Laser Technology 146, 107595 (2022).
13. X. Xiong, D. Wang, J. Wei, P. Zhao, X. Cui: Resistance welding technology of fiber reinforced polymer composites: a review. Journal of adhesion science and technology 35, 1593-1619 (2021).
14. L. Dong, W. Chen, L. Hou, J. Wang, J. Song: Metallurgical and mechanical examinations of molybdenum/graphite joints by vacuum arc pressure brazing using Ti-Zr filler materials. Journal of materials processing technology249, 39-45 (2017).
15. B. Frank, W. Guntram, E. Dietmar: Ultrasonic metal welding of aluminium sheets to carbon fiber reinforced thermoplastic composites. Advanced Engineering Materials 11(1), 35–39(2009).
16. F. Lionetto, F. Balle, A. Maffezzoli: Hybrid ultrasonic spot welding of aluminum to carbon fiber reinforced epoxy composites. Journal of materials processing technology 247, 289-295 (2017).
17. F. Balle, D. Eifler: Statistical test planning for ultrasonic welding of dissimilar materials using the example of aluminum-carbon fiber reinforced polymers (CFRP) joints. Material science and engineering technology 43(4), 286-292 (2012).
18. F. Lionetto, C. Mele, P. Leo, S. D'Ostuni, F. Balle, A. Maffezzoli: Ultrasonic spot welding of carbon fiber reinforced epoxy composites to aluminum. Mechanical and electrochemical characterization. Compos Part B: Engineering 144, 134-142 (2018).
19. F. Liu, J. Liao, K. Nakata: Joining of metal to plastic using friction lap welding. Materials & Design (1980-2015) 54, 236-244 (2014).
20. K. Nagatsuka, S. Yoshida, A. Tsuchiya, K. Nakata: Direct joining of carbon-fiber-reinforced plastic to an aluminum alloy using friction lap joining. Compos Part B: Engineering 73, 82-88 (2015).
21. H. Derazkola, M. Elyasi: The influence of process parameters in friction stir welding of Al-Mg alloy and polycarbonate. Journal of manufacturing process 35, 88-98 (2018).
22. P. Kah, R. Suoranta, J. Martikainen, C. Magnus: Techniques for joining dissimilar materials: metals and polymers. Advanced Materials Science 36, 152-164 (2014).
23. A. Khayoon, A. Hubeatir, M. Mohanned, A. Khafaji: Laser Transmission Welding is a promising joining technology technique – A Recent Review. Journal of Physics: Conference Series 1973, 012023 (2021).
24. E. Moldovan, M.H. Tierean, E.M. Stanciu: Overview of joining dissimilar materials: metals and polymers. Series I: Engineering Sciences Vol. 10 (59), 39-46 (2017).
25. K.M. Hong and Y. C. Shin: Prospects of laser welding technology in the automotive industry: a review. Journal of Materials Processing Technology 245, 46-69 (2017).
26. M. Kallek, S. Ataoglu, Y. Yagci, H.N. Bozkurt, A.N. Gulluoglu: In the jewellery, brazing and laser welding with parameter optimization. Archives of Metallurgy and Materials 57(2), 525-537 (2012).
27. B. Brenner, J. Standfuss, D. Dittrich, B. Winderlich, J. Liebscher, and J. Hackius: Laser beam welding of aircraft fuselage structures. Laser Institute of America, ICALEO 2008; 27th international proceedings 1801 (2008).
28. I.S. Shyha, S.L. Soo, D. Aspinwall, S. Bradley: Effect of laminate configuration and feed rate on cutting performance when drilling holes in carbon fibre reinforced plastic composites. Journal of materials processing technology 210(8), 1023-1034 (2010).
29. F.C. Liu, P. Dong, W. Lu, K. Sun: On formation of aloc bonds at aluminum/polyamide joint interface. Applied surface science 466, 202-209 (2019).

30. K. Schricker, M. Alhomsi and J. P. Bergmann: Thermal Efficiency in Laser-Assisted Joining of Polymer–Metal Composites. Materials 13(21), 4875 (2020).
31. T. Temesi, T. Czigan: Integrated Structures from Dissimilar Materials: The Future Belongs to Aluminum–Polymer Joints. Advanced Engineering Materials 22(8), 2000007 (2020).
32. B. Acherjee: State-of-art review of laser irradiation strategies applied to laser transmission welding of polymers. Optics & Laser Technology 137, 106737 (2021).
33. B. Acherjee: Laser Transmission Welding of Polymers-A Review on Process Fundamentals, Material Attributes, Weldability, and Welding Techniques. Journal of manufacturing process 60, 227–246 (2020).
34. B. Hengchang, Li. Xiang, L. Binbin, L. Xiaodong, Z. Xiaohong: Enhanced interfacial joining strength of laser wobble joined 6061-T6 Al alloy/CFRTP joint via interfacial bionic textures pre-construction. Composites Part B 261, 110787 (2023).
35. X. Zhongliang, S. Junqi, H. Shengsun: Influence of scanning speed and defocus distance on laser welded PA6GF30/SUS444 dissimilar lap joints. Optics & Laser Technology 153, 108223 (2022).
36. G. Yuan, Z. Zhou, L. Xiang, Y. Long: Blue laser welding of 7075-T6 aluminum alloy and carbon fiber reinforced polyetheretherketone. Optics & Laser Technology 15, 108440 (2022).
37. H. Xia, M. Yunwu, C. Chen, S Jianhui, C. Zhang, T. Caiwang, L. Liqun, P. Geng, M. Ninshu: Influence of laser welding power on steel/CFRP lap joint fracture behaviours. Composite Structures 285, 115247 (2022).
38. M. A. Elahi, M. Koch, J. Bardon, F. Addiego, P. Plapper: Failure mechanism analysis based on laser-based surface treatments for aluminum-polyamide laser joining. Journal of Materials Processing Tech. 298, 117318 (2021).
39. Z. Feng, M. Guolong, S. Jianhui, T. Caiwang, H. Xiaohui, Z. Hongyun, B. Chen, X. Song: Influence of process parameters on the joint characteristics during laser joining of aluminium alloy and CFRTP. Journal of Manufacturing Processes 64, 1493–1506 (2021).
40. A. Gisario, C. Aversa, M. Barletta, S. Natali, F. Veniali: Laser joining of aluminum film coated with vinylic resin and plastic/ bioplastic films for applications in food packaging. Optics & Laser Technology 142, 107237 (2021).
41. K. Hao, W. Liao, T. Zhang, M. Gao: Interface formation and bonding mechanisms of laser transmission welded composite structure of PET on austenitic steel via beam oscillation. Composite Structures 235, 111752 (2020).
42. W. Liao, S. Zhao and M. Gao: Oscillating Laser Conduction Joining of Dissimilar PET to Stainless Steel. Polymer 14, 4956 (2022).
43. Y.J. Chen, J.X. Tang, Z. Pang, C. Yuan, T.M. Yue: Enhancement mechanism of ultrasonic vibration on interface bonding strength in laser joining of polymer to ceramic. Journal of Manufacturing Processes 112, 263–272 (2024).
44. Y.J. Chen, T.M. Yue, Z.N. Guo: Laser joining of metals to plastics with ultrasonic vibration. Journal of Materials Processing Technology 249, 441-451 (2017).
45. C. Tana, S. Jianhui, B. Zhu, L. Xiaoting, W. Laijun, B. Chen, X. Song, J. Feng: Effect of scanning speed on laser joining of carbon fiber reinforced PEEK to titanium alloy. Optics and Laser Technology 129, 106273 (2020).
46. K. M. Hong and Y. C. Shin: Prospects of laser welding technology in the automotive industry: a review. Journal of Materials Processing Technology 245, 46-69 (2017).
47. F. Lambiase, S. I. Scipioni, C. J. Lee, D. C. Ko, F. Liu: A State-of-the-Art Review on Advanced Joining Processes for Metal-Composite and Metal-Polymer Hybrid Structures. Materials 14, 1890 (2021).
48. L. M. Alves, C. M. Silva, P. A. Martins: Joining of polymer and metal tubes by cold forming. Journal of Materials: Design and Applications 0(0), 1–11 (2015).

Study of Weldability of 304H Austenitic Boiler Quality Steels by Gas Tungsten Arc Welding

Subhodwip Saha[1][0009-0004-0588-4076], Santanu Das[2][0000-0001-9085-3450] and Subrata Mondal[3][0009-0001-0907-5709]

[1,3]Jadavpur University, Kolkata, India
[1,2]Kalyani Government Engineering College, Kalyani, India
[1]Techno Main Salt Lake, Kolkata, India
[1]subhodwipsaha@gmail.com
[2]sdas.me@gmail.com
[3]sub.mondal@gmail.com

Abstract. This study aims to improve the welding process for 304H austenitic stainless steel, commonly used in boiler components due to its strength and corrosion resistance. The design of the experiment was based on Response Surface Methodology (RSM) using Central Composite Design (CCD), using three key factors: heat input, root gap and gas flow rate. Each factor was tested at three different levels to assess their impact on weld quality, with the primary goal of achieving full penetration, which is essential for strong joints. Weld experiments were conducted on 14 samples of 8mm thick 304H stainless steel plates, each measuring 50 mm by 50 mm, using Gas Tungsten Arc Welding (GTAW) with filler material to enhance weld quality. To analyze the results, bead geometry was measured by making cross-sectional cuts and examining them under a microscope. Important parameters such as reinforcement, bead width and penetration were evaluated, ensuring full penetration. Additionally, Reinforcement Form Factor (RFF) and Penetration Shape Factor (PSF) were calculated to assess weld quality.
Keywords: GTAW, Weldability, Austenitic Stainless Steel, Bead Geometry.

1 Introduction

Austenitic stainless steels, particularly SS 304H, are extensively used in high-stress and high-temperature applications, such as boiler components, due to their remarkable properties, including high-temperature strength, corrosion resistance and resistance to thermal fatigue. These steels are suitable for Advanced Ultra-Supercritical (AUSC) boiler environment where temperatures exceed 600°C, making them essential in power plants and heavy industries reliant on stable performance under extreme conditions [1, 2]. Austenitic stainless steels are especially valued for their low thermal conductivity, high creep resistance and good weldability, making them an ideal choice for structural components in advanced boiler systems [3, 4, 5]. However, the welding of SS 304H, particularly in thicker sections, requires precise control of process parameters to achieve high-quality welds with consistent penetration and minimal defects, such as distortion or cracking, which may affect the weld's performance under operational stresses [6].

The Gas Tungsten Arc Welding (GTAW) process, commonly referred to as Tungsten Inert Gas (TIG) welding, has emerged as the preferred technique for welding austenitic stainless steels due to its ability to deliver high-quality welds with fine control over heat input and minimal contamination risks. GTAW is particularly advantageous in welding SS 304H because it provides a stable arc and allows precise control over the welding parameters, which are critical when joining thick sections of material that require full penetration [7, 8]. Full penetration is particularly important in pressure-bearing components, like those in boilers, where incomplete or inconsistent welds can lead to catastrophic failures due to cyclic thermal stresses [9].

In GTAW, achieving the ideal bead geometry and weld penetration is a desirable task, as these outcomes depend on a range of interrelated welding parameters, such as current, voltage, travel speed, filler wire diameter, torch angle, root gap and gas flow rate. Studies have shown that varying these parameters can significantly impact the weld's structural characteristics, including penetration depth, reinforcement and bead width, which together define the quality and robustness of the weld [10, 11]. Excessive heat input can, for example, cause overheating, leading to grain growth in the Heat-Affected Zone (HAZ) and reducing the mechanical strength of the weld [12]. Conversely, inadequate heat input may result in partial penetration, leaving the joint susceptible to failure under high loads [13]. Selecting optimal parameters thus requires a delicate balance, as demonstrated in numerous studies focused on welding austenitic stainless steels in high-temperature applications [14].

The bead geometry characteristics- including reinforcement, width and depth of penetration- are essential indicators of weld quality and are highly sensitive to variations in root gap, heat input and gas flow rate.

Specifically, a larger root gap may facilitate improved penetration in thicker sections, but excessive root gaps can lead to underfill or excessive reinforcement that may compromise the structural integrity of the weld [15, 16]. Additionally, variations in gas flow rate affect shielding quality, which is crucial for maintaining weld integrity by minimizing oxidation and ensuring a clean fusion surface [17, 18]. In optimizing these parameters, achieving full penetration has emerged as a primary goal, as it ensures that the weld can bear loads and withstand environmental stresses effectively [19].

Given the complex interdependence of these parameters, advanced statistical methods, such as Response Surface Methodology (RSM), are employed to systematically optimize welding conditions. In welding research, RSM, combined with Central Composite Design (CCD), is commonly applied to evaluate and optimize parameters in multi-factor processes like GTAW [20]. This methodology is particularly advantageous in welding applications because it enables a detailed exploration of the parameter space, thereby identifying conditions that yield optimal weld quality while minimizing the occurrence of defects [21, 22]. Numerous studies utilizing RSM have successfully optimized welding parameters for austenitic stainless steels, identifying ideal ranges for variables such as heat input, root gap and gas flow rate that contribute to achieving high-quality, defect-free welds [23, 24]. By applying CCD within the RSM framework, this study ensures comprehensive experimental coverage, facilitating a reliable selection of process parameters for consistent and robust weld performance [25].

Additionally, the quality of GTAW welds is often evaluated based on specific metrics of bead geometry, including penetration depth, bead width and reinforcement height. These factors have a direct impact on the mechanical properties and structural integrity of the welded joints, particularly in thick austenitic stainless-steel sections, where uniform penetration is required for optimal load-bearing performance. A comprehensive understanding of how welding parameters affect bead geometry can thus provide valuable insights into producing joints with the necessary strength and durability. By studying these relationships, researchers aim to optimize the GTAW process to produce high-quality welds suitable for critical applications in high-stress environment [26].

The objective of this study is to optimize GTAW welding parameters such as heat input, root gap and gas flow rate to achieve full penetration and desirable bead geometry in 8 mm thick SS 304H austenitic stainless-steel plates. This research employs RSM with CCD to systematically investigate the influence of these parameters, with the aim of establishing optimal conditions for producing robust and reliable welds suited for high-temperature applications in boiler components. By focusing on bead geometry and penetration depth, this study aims to contribute valuable insights into the effective welding of austenitic stainless steels for enhanced performance in demanding environment.

2 Materials and Method

This study focused on optimizing the welding parameters for 304H stainless steel plates, specifically using Gas Tungsten Arc Welding (GTAW) with continuous filler supply. The welding setup included the KEMPPI K2 TIG 200 AC/DC machine, which provided precise control over current and arc stability and a MOGRA CWF 04 Cold Wire Feeder, maintaining a consistent 1.2 mm diameter filler having feed speed of 20 mm/s. Weld speed was set at 1.22 mm/s to ensure controlled deposition and heat input. The materials used consisted of 14 samples of 304H stainless steel, each 8 mm thick and measuring 50 mm x 50 mm, designed to evaluate optimal welding parameters.

The welding was performed at a torch angle of 75^{o}, maintaining a constant arc gap length of 5 mm and a welding speed of 1.22 mm/s. The experiments were conducted in the welding laboratory of Kalyani Government Engineering College.

To evaluate the effects of different parameters on weld quality, various current and voltage settings were applied. The experimental design was based on Response Surface Methodology (RSM) using Central Composite Design (CCD), which incorporated three factors- current, root gap and gas flow rate; each evaluated at three levels. The current levels were varied at 130 A, 140 A and 150 A, with the voltage adjusted accordingly. The root gap was also modified, using three settings: 1.2 mm, 1.6 mm and 2 mm. The gas flow rate of argon was controlled at three levels: 10, 12 and 14 l/min.

Each of the 14 specimens was prepared and welded according to these variations, facilitating a comprehensive analysis of the optimization parameters affecting weld quality. The specific welding joint performed was non-Autogenous butt Joint using a 3.2 mm (diameter) non-consumable Thoriated tungsten electrode. The specimen was cooled in open air after non-autogenous butt welding. Chemical composition of the austenitic stainless steel workpiece of 304H and filler of the same material (derived from spectrometry) is

given in Table 1. The cross-sectional cuts of the welded specimens are polished and etched with Carpenter's Etchant for measurement of bead geometry. Weld bead geometry parameters such as weld bead width (W), reinforcement (R) and depth of penetration (P) are measured with the help of Tool Maker's Microscope. Reinforcement form factor (RFF), penetration shape factor (PSF) and Heat Input are evaluated on the basis of equations (1), (2) and (3).

$$RFF = W/R \quad (1)$$

$$PSF = W/P \quad (2)$$

Heat Input was calculated by the following equation.

$$HI = (V \times I \times \eta)/ (1000 \times S) \quad (3)$$

Here, HI is the heat input in kJ/mm, V is the voltage in V, I is the current in A, S is the welding speed in mm/s and η is the efficiency of the welding process (0.75 taken for GTAW). Figure 1 shows the welding setup and conditions used during the experiments.

Table 1. Chemical composition of SS304H work specimen and filler wire

Element	C	Si	Mn	P	S	Cr	Ni	Fe
Wt.%	0.055	0.477	1.398	0.028	0.03	18.11	8.477	Balance

Fig 1. GTAW Machine used (torch angle 75°)

2.1 Design of Experiment by Central Composite Design

In this work, Central Composite Design (CCD) is applied with three main factors such as current (which determines heat input), root gap and gas flow rate, each tested at three levels. These levels were established based on preliminary trials to optimize welding conditions for the desired weld quality. CCD is a widely used approach in Response Surface Methodology (RSM) for investigating the effects of multiple factors on a response variable. Specifically, gas flow rates were set at 10, 12 and 14 l/min; root gap was adjusted to 1.2, 1.6 and 2.0 mm; and the current values were varied at 130 A, 140 A and 150 A, with the voltage adjusted accordingly to provide the appropriate heat input. Experimental parameters along with heat input found out using equation (3) are shown in Table 2.

Here OCC represents Open Circuit Current, CCC represents Closed Circuit Current, CCV represents Closed Circuit Voltage and HI represents Heat Input. Numbers 1 and 2 denote butt welds done on top and bottom side of the metal plates.

Table 2: Experimental Parameters during welding

Run order	Sl. No.	Gas Flow Rate (l/min)	Root Gap (mm)	OCC (A)	CCC (A)	CCV 1 (V)	CCV 2 (V)	HI1 (kJ/mm)	HI2 (kJ/mm)	Avg HI (kJ/mm)
1’	1	10	1.2	130	130	16.8	16.6	1.343	1.327	1.335
2’	2	14	1.2	130	130	16.5	16.6	1.319	1.327	1.323
3’	3	10	2.0	130	129	16.9	16.8	1.34	1.332	1.336
4’	4	14	2.0	130	129	17.0	17.2	1.348	1.364	1.356
5’	5	10	1.2	150	148	18.3	17.6	1.665	1.601	1.633
6’	6	14	1.2	150	148	18.1	17.9	1.647	1.629	1.638
7’	7	10	2.0	150	148	18.2	18.1	1.656	1.647	1.651
8’	8	14	2.0	150	148	18.3	18.2	1.665	1.656	1.660
9’	9	12	1.6	140	138	17.7	16.8	1.502	1.425	1.463
10’	10	12	1.6	140	138	17.8	17.6	1.510	1.493	1.502
11’	11	12	1.6	140	138	17.5	16.9	1.485	1.434	1.459
12’	12	12	1.6	140	138	17.4	16.8	1.476	1.425	1.451
13’	13	12	1.6	140	138	18.0	17.9	1.527	1.519	1.523
14’	14	12	1.6	140	138	18.5	17.6	1.569	1.493	1.531

3 Results and Discussion

Table 3 shows the non-presence of defects, namely uniformity, crack, blowhole, pinhole, undercut and spatter formation by visual inspection after welding.

It is found by visual inspection that all the fourteen welded specimens are uniformly welded with no visible small spatter on the surface. Neither of the specimens are found with visible defects such as crack, undercut, blowhole, or pinhole, etc. Images of few welded specimens are given in figure 2. Images of cross-sectional cuts of few welded specimens are given in figure 3. The observed bead geometry found out from the Tool Maker’s microscope is given Table 4.

Fig 2. Sample images of few welded specimens

Table 3. Visual Observations Made in Experiment Set 2

Sl. No.	Gas Flow Rate (l/min)	Root Gap (mm)	Heat Input (kJ/mm)	Spatter	Weld Uniformity	Crack	Blow hole-Pinhole	Under cut
1	10	1.2	1.335	Nil	✓	Nil	Nil	Nil
2	14	1.2	1.323	Nil	✓	Nil	Nil	Nil
3	10	2.0	1.336	Nil	✓	Nil	Nil	Nil
4	14	2.0	1.356	Nil	✓	Nil	Nil	Nil
5	10	1.2	1.633	Nil	✓	Nil	Nil	Nil
6	14	1.2	1.638	Nil	✓	Nil	Nil	Nil
7	10	2.0	1.651	Nil	✓	Nil	Nil	Nil
8	14	2.0	1.660	Nil	✓	Nil	Nil	Nil
9	12	1.6	1.463	Nil	✓	Nil	Nil	Nil
10	12	1.6	1.502	Nil	✓	Nil	Nil	Nil
11	12	1.6	1.459	Nil	✓	Nil	Nil	Nil
12	12	1.6	1.451	Nil	✓	Nil	Nil	Nil
13	12	1.6	1.523	Nil	✓	Nil	Nil	Nil
14	12	1.6	1.531	Nil	✓	Nil	Nil	Nil

Table 4. Observed bead geometry

Run order	Sl. No.	Gas Flow Rate (l/min)	Root Gap (mm)	Heat input (kJ/mm)	Penetration (mm)	Width (mm)	Reinforcement (mm)	PSF (W/P)	RFF (W/R)
1’	1	10	1.2	1.335	2.825	8.105	1.610	2.869	5.034
2’	2	14	1.2	1.323	4.630	8.610	1.180	1.860	7.297
3’	3	10	2.0	1.336	8.000	8.295	1.140	1.037	7.276
4’	4	14	2.0	1.356	8.000	7.755	2.455	0.969	3.159
5’	5	10	1.2	1.633	8.000	8.990	1.315	1.124	6.837
6’	6	14	1.2	1.638	8.000	9.650	0.665	1.206	14.511
7’	7	10	2.0	1.651	8.000	9.705	0.510	1.213	19.029
8’	8	14	2.0	1.660	8.000	9.135	0.485	1.142	18.835
9’	9	12	1.6	1.463	8.000	8.190	1.045	1.024	7.837
10’	10	12	1.6	1.502	8.000	8.615	-0.665	1.077	-12.955
11’	11	12	1.6	1.459	2.730	11.860	0.690	4.344	17.188
12’	12	12	1.6	1.451	2.980	11.805	0.380	3.961	31.066
13’	13	12	1.6	1.523	3.250	12.615	0.825	3.882	15.291
14’	14	12	1.6	1.531	8.000	9.630	1.590	1.204	6.057

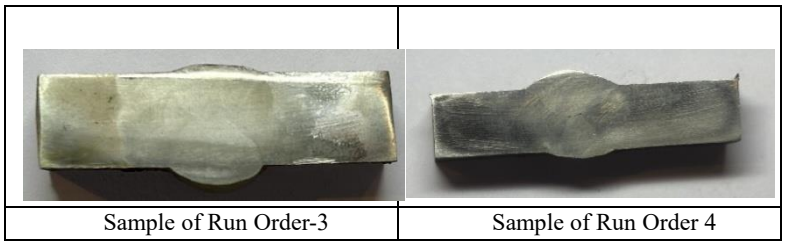

Sample of Run Order-3 | Sample of Run Order 4

Fig 3. Cross sectional cuts of few welded specimens revealing full penetration.

4 Conclusion

Most of the welding parameters resulted in fully penetrated joints, which is highly desirable for creating strong, reliable connections. Specifically, run orders 5, 6, 7, 8 and 14 showed excellent results, where a heat input around 1.5 - 1.6 kJ/mm, combined with gas flow rates of 10-14 l/min and root gaps of 1.6 to 2 mm, produced solid and uniform welds. These settings allowed for full penetration when welded from both sides, ensuring desirable joint formation. In run orders 7 and 8, a 2 mm root gap and gas flow rate of 10-14 l/min led to smooth,

stable welds with minimal reinforcement. Similarly, in run order 14, a 1.6 mm gap and 12 l/min gas flow yielded excellent penetration and uniformity. Except for a few combinations, which showed incomplete penetration likely due to insufficient heat input or mismatched gas flow rates, the majority of parameters tested resulted in fully penetrated joints for achieving strong and durable welds.

References

1. Kuo, M., Chang, C., Shiau, Y.: Optimizing parameters in GTAW for SS 304 applications using RSM. Journal of Manufacturing Processes 67, 123–132 (2021).
2. Fang, X., Chen, X., Huang, R.: Influence of heat input on bead geometry in SS 304 welding. Materials and Design 198, 109520 (2020).
3. Cheng, H., Zhang, Y.: GTAW process modeling for austenitic stainless steel. International Journal of Advanced Manufacturing Technology 105, 743–755 (2019).
4. Singh, R., Ghosh, P.: A review on the use of RSM in welding parameter optimization. Welding in the World 65, 1456–1464 (2021).
5. Saha, S., Das, S., Mondal, S.: Exploring the Weldability of Austenitic Stainless Steels in Advanced Ultra-Supercritical Power Plant Applications: An Extensive Review. Indian Welding Journal 56(4), 54–66 (2023).
6. Wang, Y., Liu, C.: Effects of root gap and gas flow rate on GTAW weld quality. Journal of Materials Processing Technology 264, 267–275 (2018).
7. Kim, S., Lee, D.: Impact of process parameters on bead geometry in TIG welding. Journal of Materials Research and Technology 17, 389–398 (2022).
8. Garcia, F., Silva, M., Biro, M.: Evaluation of GTAW bead penetration for SS 304H using CCD. Materials Today: Proceedings 11, 345–354 (2019).
9. Rahman, H., Alam, S.: GTAW techniques for high-performance austenitic stainless steels in power plants. Journal of Engineering Materials and Technology 142, 041017 (2020).
10. Gupta, K., Mukherjee, P.: Bead geometry optimization in GTAW. Procedia CIRP 105, 150–155 (2021).
11. Sun, Q., Wang, J.: Optimization of welding parameters using CCD and RSM. Materials Science and Engineering: A 823, 141716 (2021).
12. Zhou, X., Li, R.: Analysis of welding process factors in stainless steel joints. Journal of Materials Science and Technology 55, 104–110 (2020).
13. Ali, T., Zhou, J.: Evaluation of bead characteristics in TIG welding. Journal of Manufacturing Science and Engineering 142, 120310 (2019).
14. Murugan, N., Parmar, R.: Experimental study of GTAW parameters in SS 304H. Materials Characterization 156, 109825 (2019).
15. Wang, Z., Liu, P.: Application of RSM in GTAW parameter optimization for stainless steels. International Journal of Mechanical Sciences 183, 105759 (2020).
16. Goyal, A., Srivastava, R.: TIG welding practices for improved penetration in SS 304. Journal of Materials Processing Technology 255, 32–40 (2018).
17. Wu, T., Feng, L.: Penetration and bead quality assessment in stainless steel welding. Journal of Manufacturing Processes 36, 124–132 (2018).
18. Kumar, D., Chandel, S.: Impact of RSM-optimized parameters on GTAW. Journal of Manufacturing Science and Engineering 141, 081011 (2019).
19. Liu, S., Zhang, Q.: Optimization of heat input and gas flow rate in GTAW. Metallurgical and Materials Transactions A 52, 4756–4768 (2021).
20. Garcia, H., Lin, J.: TIG welding practices and parameter analysis for SS 304 in boiler applications. Materials and Design 209, 109973 (2021).
21. Qin, Y., Zhang, M.: Welding parameter optimization with CCD for enhanced weld strength. Journal of Materials Research and Technology 8, 6021–6029 (2019).
22. Tan, S., Tanaka, Y.: Microstructural analysis of SS 304 welds in TIG processes. Welding Journal 99, 181–190 (2020).
23. Li, C., Zhou, B.: Experimental study on gas flow rate effects in TIG welding. Materials Science Forum 967, 282–288 (2019).
24. Zheng, F., Wang, P.: Analysis of GTAW welding factors on penetration depth. Journal of Materials Engineering and Performance 27, 3101–3109 (2018).
25. Yang, K., Li, S.: Optimization of bead geometry in SS 304 GTAW using RSM. International Journal of Advanced Manufacturing Technology 120, 523–532 (2021).
26. Lin, S., Zhu, T.: Application of TIG welding in austenitic stainless steel boiler components. Journal of Manufacturing Processes 82, 301–315 (2022).

Optimization of Laser Welding Parameters to Minimize Heat-Affected Zone in SS304 Stainless Steel

Upama Dey[1*], Bappa Acherjee[2], Souren Mitra[3]

[1] School of Laser Science and Engineering, Jadavpur University, Kolkata, India, 700032
[2] Department of Production and Industrial Engineering, Birla Institute of Technology, Mesra, Ranchi, India, 835215
[3] Department of Production Engineering, Jadavpur University, Kolkata, India, 700032
upama@ieee.org

Abstract. This study focuses on optimizing laser welding parameters to minimize the Heat-Affected Zone (HAZ) in SS304 stainless steel. Using the Taguchi L9 experimental design, the effects of laser power, welding speed, and gas pressure on HAZ were analyzed. The results showed that higher laser power increases HAZ, while higher welding speed and gas pressure reduce it. Statistical analysis confirmed the significant impact of these parameters on HAZ. Particle Swarm Optimization (PSO) was used to find the optimal parameters, resulting in a minimum HAZ of 583.83 μm at 350 W laser power, 1.93 mm/s welding speed, and 3 bar gas pressure. This study provides valuable insights for improving weld quality in precision applications.

Keywords: Laser Welding; Heat-Affected Zone; Particle Swarm Optimization

1 Introduction

Laser welding has become an essential manufacturing process in industries requiring high-precision, low-distortion joining, particularly for metals. This technique is highly valued for its ability to produce narrow weld zones with minimal thermal impact, which is advantageous in sectors such as aerospace, automotive, and biomedical applications [1, 2]. Among various metals, stainless steel grade SS304 is widely used because of its excellent corrosion resistance, mechanical strength, and ease of fabrication [3]. Due to these properties, laser welding on SS304 has been extensively studied by researchers, who have examined both thin and thick SS304 sheets [4-6]. Their investigations focused on weld microstructure, microhardness, and tensile strength, often achieving joint strengths close to those of the base metal. However, these studies also found that increased heat input can significantly elevate residual stress levels in laser-welded SS304 [7].

A critical challenge in the laser welding of SS304 is controlling the Heat-Affected Zone (HAZ). Excessive HAZ can lead to undesired microstructural changes, elevated residual stresses, and compromised corrosion resistance, all of which can impact the durability and reliability of the welded structure [8, 9]. Therefore, identifying and optimizing the welding parameters to minimize HAZ is essential for ensuring weld quality and the long-term performance of SS304 components. For instance, researchers have focused on optimizing laser welding parameters to reduce HAZ width in SS304 [10]. Studies like those of reference [11] identified high residual stress concentrations in the HAZ. However, a comprehensive, systematic approach to parameter optimization that minimizes HAZ across various SS304 applications remains lacking.

To systematically explore the effects of different welding parameters on outcomes, the design of experiments (DOE) is a powerful tool, with the Taguchi method being particularly efficient due to its ability to minimize experimental runs without sacrificing data quality [12, 13]. The Taguchi L9 array, in particular, allows for the investigation of three factors at three levels, reducing the number of experiments needed. In addition to experimental design, optimization techniques are also essential for refining laser welding parameters. Particle Swarm Optimization (PSO), inspired by social behavior in nature, is an effective approach for solving complex, non-linear optimization problems [14-16]. In PSO, particles iteratively improve their positions in the solution space based on individual and collective experience, gradually converging toward an optimal solution.

It is evident that minimizing the HAZ is crucial, as it directly affects the structural integrity of welded joints. Therefore, a more in-depth investigation into HAZ minimization during the laser welding of SS304 is essential. This study focuses on identifying optimal welding parameters to improve joint quality and extend component lifespan. By employing robust experimental designs and advanced optimization techniques, such as Particle Swarm Optimization (PSO), this research addresses the pressing need for reliable parameter sets that enhance weld performance in SS304 applications. Specifically, the aim is to integrate PSO with experimental data obtained using the Taguchi method to develop an optimized parameter set that effectively minimizes HAZ, thereby improving the quality and durability of laser-welded SS304 components.

2 Experimental Setup

The chemical composition of the SS304 stainless steel used in this study is detailed in Table 1. Each specimen was precisely cut to a square shape, with each side measuring 50 mm and a thickness of 2 mm to ensure consistency across all test samples.

The laser welding experiments were performed in butt joint configuration using a continuous-wave fiber laser system, chosen for its high stability and precise energy delivery. This laser system has a maximum power output of 500 W and operates at a wavelength of 1064 nm, suitable for deep penetration and minimal distortion in stainless steel materials. When focused, the laser beam spot has a diameter of 500 μm, promoting consistent welding quality in all samples. Throughout the experiments, argon gas was employed as a shielding medium to prevent oxidation and contamination in the weld zone. This shielding gas was continuously supplied to the welding area, creating an inert atmosphere that preserves the integrity of the weld by preventing unwanted chemical reactions with atmospheric oxygen. The pressure of the argon gas was meticulously controlled to ensure optimal coverage and stability during the welding process.

Table 1. Chemical composition of the SS304 stainless steel.

Material	C	Mn	Si	P	S	N	Cr	Ni	Fe
Composition (%)	0.07	2.00	1.00	0.05	0.03	0.11	18.5	9.00	Remainder

3 Experimentation

This study utilizes the Taguchi L9 orthogonal array to systematically design and execute laser welding experiments on SS304 stainless steel, aiming to understand the influence of key process parameters on the Heat-Affected Zone (HAZ). The Taguchi method was selected for its efficiency in evaluating multiple variables with a reduced number of experiments, allowing a structured and comprehensive assessment of parameter impacts while minimizing experimental effort. By applying this approach, the study explores how adjustments to laser power, welding speed, and shielding gas pressure can be optimized to achieve the smallest possible HAZ, thereby improving weld quality.

For the experimental design, the L9 orthogonal array configuration enables an exploration of three critical variables, each tested at three different levels. This arrangement allows for an in-depth investigation of the combined and individual effects of each parameter on the HAZ. The variables and their respective levels were carefully chosen to represent a meaningful range of welding conditions: laser power was tested at levels of 350 W, 400 W, and 450 W; welding speed was varied across 0.8 mm/s, 1.6 mm/s, and 2.4 mm/s; and gas pressure was adjusted to 1 bar, 2 bar, and 3 bar. Table 2 presents the complete Taguchi L9 experimental design.

The laser welding experiments were carried out on SS304 samples in a butt joint configuration, following the parameters set forth by the Taguchi array. After each welding trial, samples were carefully prepared for analysis. Figure 1 shows the welded SS304 butt joint after the welding process. A sample from each experimental condition was observed under an optical microscope (OM) to evaluate the weld zone and measure the Heat-Affected Zone (HAZ). This systematic experimentation and observation method ensure a thorough understanding of how each parameter and their interactions influences HAZ, contributing valuable data for further analysis and optimization.

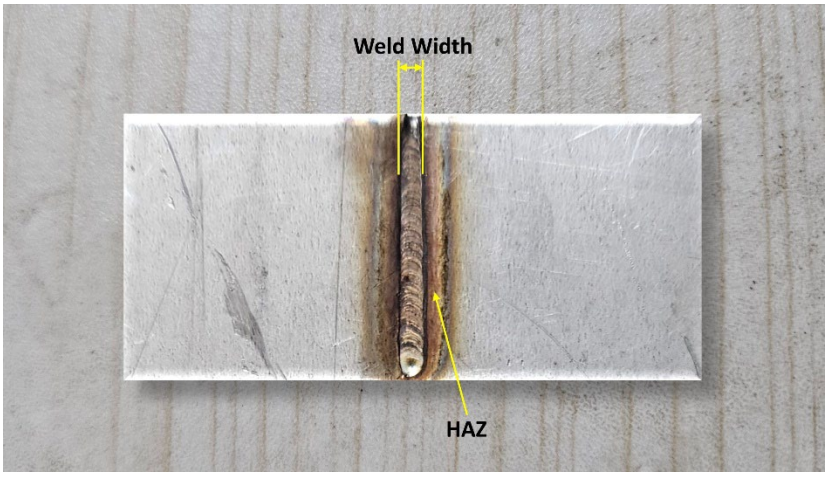

Fig. 1. Pictorial view of welded SS304 sample

4 Results and Discussions

In this study, measurements were taken for both the weld zone and the Heat-Affected Zone (HAZ). Table 2 presents the Taguchi L9 design of experimental process parameter combinations and the corresponding measured response values. Since the primary objective of this study is to minimize the HAZ, the discussion will focus specifically on this aspect. The investigation was conducted in two parts: one focused on the statistical analysis of welding parameters and their effects on HAZ, and the other on optimization using Particle Swarm Optimization (PSO).

Table 2. Designed process parameter combinations and response values

Sl No.	Power (W)	Welding Speed (mm/sec)	Gas Pressure (bar)	Weld Zone (µm)	HAZ (µm)
1	350	0.80	1	1316.83	948.42
2	350	1.60	2	1169.52	725.88
3	350	2.40	3	1021.2	670.24
4	400	0.80	2	1331.71	1086.02
5	400	1.60	3	1189.38	821.10
6	400	2.40	1	1164.82	979.69
7	450	0.80	3	1407.32	1280.86
8	450	1.60	1	1354.25	1410.26
9	450	2.40	2	1197.26	1171.96

4.1 Effect of Welding Parameters on HAZ

The influence of laser welding parameters such as, laser power, welding speed, and shielding gas pressure on the Heat-Affected Zone (HAZ) was analyzed in this study. A mean effect plot (Figure 2) was generated to visualize the relationship between each parameter and the HAZ. The mean effect plot shows a positive correlation between laser power (P) and HAZ width. As laser power increases, there is a corresponding increase in HAZ. This can be attributed to the higher energy input, which generates more heat in the material and subsequently enlarges the HAZ. Higher laser power results in a larger volume of material affected by the thermal cycle, which can negatively impact weld quality by increasing residual stresses and potentially altering microstructure.

Conversely, the mean effect plot indicates that HAZ decreases with an increase in welding speed (S). A higher welding speed reduces the time that the material is exposed to the laser, leading to a smaller thermal footprint and hence a narrower HAZ. This effect is beneficial for maintaining weld quality, as a reduced HAZ can minimize unwanted microstructural changes and residual stress concentrations.

The mean effect plot also shows that increasing the shielding gas pressure (G) reduces the HAZ. Higher gas pressure provides a more effective protective layer, reducing the interaction between the weld area and atmos-

pheric gases. Additionally, higher gas pressure can facilitate faster cooling, which limits heat spread and thereby restricts the HAZ.

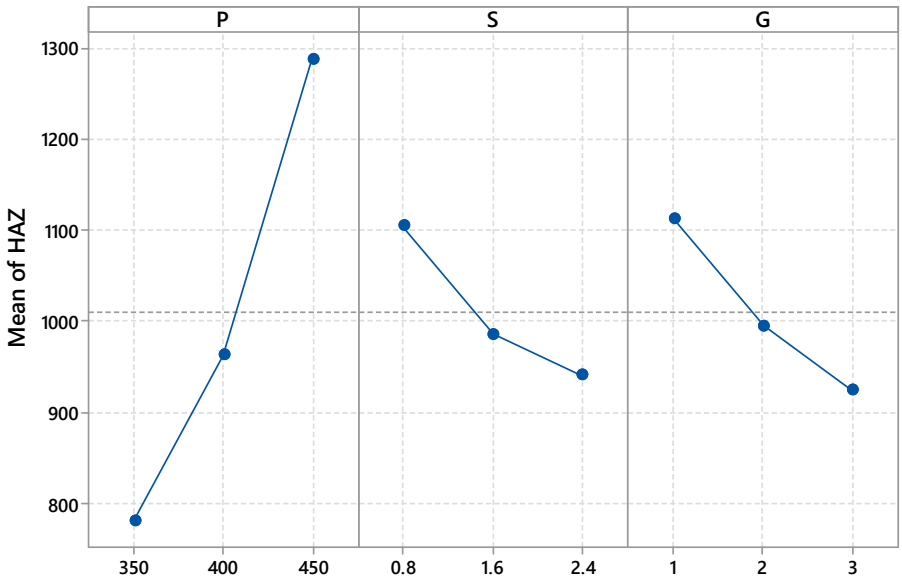

Fig. 2. Main effects of process variables on HAZ

To quantify the effects of these parameters and determine their statistical significance, regression analysis and Analysis of Variance (ANOVA) were performed.

Regression Analysis: A regression model was developed to relate the HAZ to the three primary factors laser power (P), welding speed (S), and gas pressure (G). The model fit was evaluated using key statistics, revealing a high degree of predictive accuracy. The R-squared (R^2) value of 95.26% indicates that the model explains 95.26% of the variability in HAZ, reflecting strong agreement between the predicted and actual data. The adjusted R-squared value, at 92.41%, confirms that the model remains robust even after adjusting for the number of predictors. Additionally, the predicted R-squared value of 81.20% suggests that the model has good predictive capability when applied to new data.

The regression equation of HAZ,

$$-661 + 5.062 * P - 102.8 * S - 94.4 * G \qquad (1)$$

ANOVA Results: ANOVA was conducted to determine the statistical significance of each parameter, as shown in Table 3. The results indicate that laser power, welding speed, and gas pressure are all significant factors influencing the HAZ (p-value < 0.05 for each parameter). This significance indicates that variations in each of these factors lead to measurable changes in HAZ, validating the impact of parameter selection on weld quality.

Table 3. Analysis of variance of HAZ

Source	DF	Adj SS	Adj MS	F-Value	P-Value
Regression	3	478328	159443	33.48	0.001
P	1	384327	384327	80.71	0.000
S	1	40576	40576	8.52	0.033
G	1	53425	53425	11.22	0.020
Error	5	23809	4762		
Total	8	502136			

4.2 Optimization Using Particle Swarm Optimization (PSO)

The PSO Algorithm

Particle Swarm Optimization (PSO) is an optimization technique inspired by the social behaviors observed in swarms, such as flocks of birds. It efficiently searches for an optimal solution by using a population of candidate

solutions, referred to as "particles". Each particle represents a potential solution and navigates through the search space by adjusting its position based on its own best-known location and the best-known positions of other particles in the swarm. This approach enables PSO to balance exploration (searching broadly across the space) and exploitation (refining the best solutions) [17]. The movement of each particle is influenced by an inertia weight, which controls the particle's tendency to continue in its current direction, as well as cognitive and social components, which draw each particle toward both its personal best position and the swarm's best-known position. For this study, the PSO algorithm was configured with a particle size of 100 and allowed to run for 100 iterations. An inertia weight of 0.7 was chosen to promote convergence while still allowing adequate exploration of the solution space.

Optimization of Weld Parameters for Minimizing HAZ

The primary objective of this study is to determine the optimal combination of laser welding parameters specifically, laser power, welding speed, and gas pressure to minimize the Heat-Affected Zone (HAZ) during SS304 welding. Each parameter was constrained within defined bounds, and the objective function for the PSO algorithm was set to minimize HAZ, as described by a regression equation (Eq. 1) derived from experimental data. By defining HAZ as the objective function, PSO was able to systematically adjust parameter values and converge on an optimal solution that reduces HAZ to a minimum. MATLAB R2020B was used to implement the PSO algorithm, facilitating precise control over particle movement and solution evaluation.

After 100 iterations, PSO successfully identified an optimal parameter set with a global best position at a laser power of 350 W, a welding speed of 1.9253 mm/s, and a gas pressure of 3 bar. This combination yielded a minimized HAZ, with a global best objective value of 583.8343 µm. The optimization results were consistent with the findings from the parametric analysis, which indicated that lower laser power, higher welding speed, and increased gas pressure contribute to HAZ reduction. Additionally, a fitness versus iteration plot (Figure 3) demonstrated the convergence behavior of PSO, showing a gradual improvement in fitness values over iterations. A 3D scatter plot of particle distribution at the final iteration shown in Figure 4 was also generated, illustrating how particles clustered around the optimal solution. This distribution verifies PSO's effectiveness in efficiently locating and converging on the ideal welding parameters to achieve minimal HAZ.

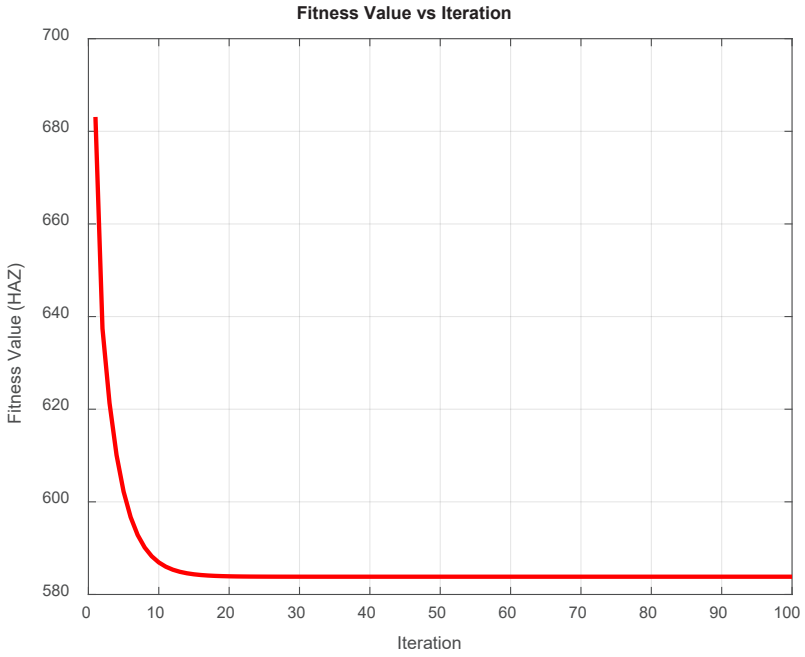

Fig. 3. Variation of Fitness Value over Iterations

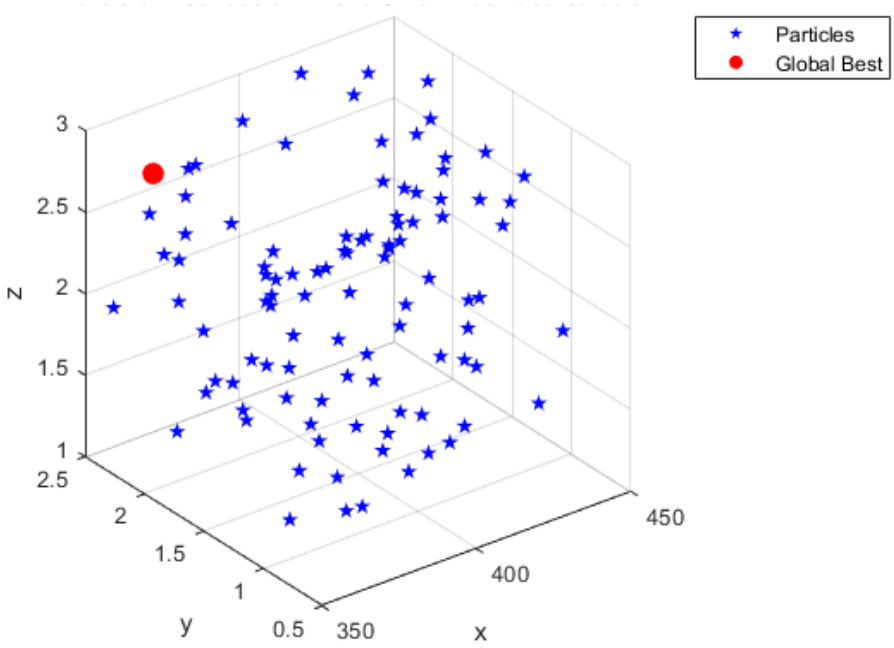

Fig. 4. Particle distribution in the swarm at last iteration

5 Conclusions

- This study has effectively demonstrated the use of laser welding on SS304 stainless steel, with a primary focus on minimizing the Heat-Affected Zone (HAZ) to enhance weld quality. Through a design of experiments based on the Taguchi L9 orthogonal array, the impacts of laser power, welding speed, and shielding gas pressure on HAZ were systematically investigated. The results indicated that increased laser power leads to a larger HAZ, while higher welding speeds and gas pressures contribute to HAZ reduction. This behavior aligns with theoretical expectations, as lower power and increased cooling reduce thermal spread, thus preserving the material's structural integrity.
- Regression modeling and ANOVA, confirmed the significant influence of each parameter on HAZ. The regression model exhibited strong predictive accuracy, with an R-squared of 95.26%, adjusted R-squared of 92.41%, and the Predicted R-squared value of 81.20%. The ANOVA results also verified that all factors laser power, welding speed, and gas pressure are statistically significant in determining HAZ, validating the relevance of the selected process parameters.
- Furthermore, Particle Swarm Optimization (PSO) was employed to identify an optimal parameter combination that minimizes HAZ, using the regression model as the objective function. The PSO algorithm efficiently converged to an optimal solution with a global best HAZ value of 583.8343 µm, achieved at a laser power of 350 W, welding speed of 1.9253 mm/s, and gas pressure of 3 bar. The convergence plot and 3D scatter plot of particle distribution confirm the effectiveness of PSO in identifying optimal parameter sets for complex, nonlinear welding processes.

References

1. Katayama, S. (Ed.). Handbook of laser welding technologies. Elsevier (2013).
2. Hong, K. M., & Shin, Y. C. Prospects of laser welding technology in the automotive industry: A review. Journal of Materials Processing Technology, 245, 46-69 (2017).
3. Dewangan, S., & Chattopadhyaya, S. RESEARCH PAPER ANALYSING EFFECT OF QUENCHING AND TEMPERING INTO MECHANICAL PROPERTIES AND MICROSTRUCTURE OF 304-SS WELDED PLATES. Acta Metallurgica Slovaca, 28(3), 140-146 (2022).
4. Jamaludin, M. N., Quazi, M. M., Aiman, M. H., & Ishak, M. Distortion in laser micro welding of stainless steel SS304 foils. *Materials Today: Proceedings* (2023).
5. Patel, S., Aggrawal, A., & Kumar, A. Micro laser lap welding of thin SS304 sheet. Proceedings of the LiM, 24-27 (2019).

6. 3. Bhargava, P., Paul, C. P., Mundra, G., Premsingh, C. H., Mishra, S. K., Nagpure, D., ... & Kukreja, L. M. Study on weld bead surface profile and angular distortion in 6 mm thick butt weld joints of SS304 using fiber laser. Optics and Lasers in Engineering, 53, 152-157 (2014).
7. Kumar, B., Bag, S., Mahadevan, S., Paul, C. P., Das, C. R., & Bindra, K. S. On the interaction of microstructural morphology with residual stress in fiber laser welding of austenitic stainless steel. CIRP Journal of Manufacturing Science and Technology, 33, 158-175 (2021).
8. Perka, A. K., John, M., Kuruveri, U. B., & Menezes, P. L. Advanced high-strength steels for automotive applications: arc and laser welding process, properties, and challenges. Metals, 12(6), 1051 (2022).
9. Vemanaboina, H., Purushotham, A., Reddy, K. S., Reddy, P. N., Prakash, C., Kumar, R., & Mehdi, H. Optimization of process parameters of CO2 laser beam butt joints of SS321. International Journal on Interactive Design and Manufacturing (IJIDeM), 1-13 (2024).
10. Selvaperumal, S., & Thangaraju, D. B. K. Experimental studies and optimization of process parameters in laser welding of stainless steel 304 H. Proceedings of the Institution of Mechanical Engineers, Part E: Journal of Process Mechanical Engineering, 238(1), 171-179 (2024).
11. Shevchenko, V., Korzhyk, V., Gao, S., Khaskin, V., Cai, D., Luo, Z., ... & Perepichay, A. Formation of Stainless Steel Welded Joints Produced with the Application of Laser and Plasma Energy Sources. Metals, 14(6), 706 (2024).
12. Chellu, P. K., Padmanaban, R., Vignesh, R. V., Menon, A. S., Shariff, S. M., & Padmanabham, G. Experimental Study on Laser Welding of AISI 304 Steel with Design of Experiments Approach. In IOP Conference Series: Materials Science and Engineering (Vol. 577, No. 1, p. 012117). IOP Publishing (2019, November).
13. Hisam, M. W., Dar, A. A., Elrasheed, M. O., Khan, M. S., Gera, R., & Azad, I. The Versatility of the Taguchi Method: Optimizing Experiments Across Diverse Disciplines. Journal of Statistical Theory and Applications, 1-25 (2024).
14. Das, D., Jaypuria, S., Pratihar, D. K., & Roy, G. G. Weld optimisation. Science and Technology of Welding and Joining, 26(3), 181-195 (2021).
15. Qiao, J., Wang, G., Yang, Z., Luo, X., Chen, J., Li, K., & Liu, P. A hybrid particle swarm optimization algorithm for solving engineering problem. Scientific Reports, 14(1), 8357 (2024).
16. Acherjee, B. Modern optimization techniques for performance enhancement in welding. Advanced Welding and Deforming, 265-290 (2021).
17. Jain, M., Saihjpal, V., Singh, N., & Singh, S. B. An overview of variants and advancements of PSO algorithm. Applied Sciences, 12(17), 8392 (2022).

Precision & Micro-Manufacturing

An Experimental Investigation into the Top Burr Formation in Micro-milling using Bulk Metallic Glass

Debajyoti Ray[1][0000-0003-2095-2431] and Asit Baran Puri[2][0000-0001-8152-1585]

[1] Sanaka Educational Trust's Group of Institutions, Durgapur - 713212, India
[2] National Institute of Technology Durgapur, Durgapur - 713209, India
debajyoti_ray2002@yahoo.co.in

Abstract. Proper functionality of micro-parts depends largely on the quality of the micro-cut features. Quality of micro-cut features includes surface roughness, micro-structural integrity, form and dimensional accuracy and machined edge quality. Formation of burrs is inevitable in almost all machining processes. As this burr formation cannot be avoided, so minimisation of burrs on the generated edges becomes essential to achieve the compliance to the required quality. Micro-cutting is an effective process to fabricate micro-features cost-effectively. Micro-milling represents a flexible micro-cutting process used commonly to fabricate intricate micro-features. This paper presents an experimental study on the formation of top burrs in mechanical micro-milling of bulk metallic glass, a unique class of lightweight amorphous metallic alloy. The influence of the cutting conditions under different combinations of the cutting parameters on the formation of the top burrs is analysed and explanations for the observed trends are presented. The experimental results indicated that width of top burrs was higher at low feed rates than at higher feed rates. Experimental results also showed that increase in axial depth of cut resulted in increased burr width. However, increase in cutting speed showed a decreasing trend in the width of the burrs.

Keywords: Micro-milling, Bulk metallic glass, Cutting edge radius, Ploughing, Micro-burrs.

1 Introduction

Development of miniature components with reduced size, cost, and increased performance in different application areas has earned enormous scientific interest. Materials used in micro-components need to have suitable properties that meet the specific functional requirements. Amongst several materials utilized in the fabrication of micro-parts that have emerged over the past decades, bulk metallic glass (BMG) represents a unique class of lightweight amorphous metallic material. BMG possesses superior strength to weight ratio and improved properties than many other commonly known crystalline metallic materials. Use of BMG in recent days is expanding in various areas of application ranging from sports goods to biomedical devices. Many of these micro-devices or micro-parts have micro-features [1]. Micro-cutting, particularly micro-milling is a reliable, cost effective micro-machining process that can be suitably used to fabricate these micro-features [1, 2]. Quality of these micro-cut features is the most important aspect with regard to its proper application. Quality of micro-cut features includes surface roughness and micro-structural integrity, form and dimensional accuracy and machined edge quality. Formation of burrs on the machined edges is inevitable in all machining processes. However, the extent of burr formation depends upon the cutting conditions, work material microstructure and property, cutting tool geometry, etc. Burrs are residual material overhanging on the machined edge and form at different locations depending upon the underlying mechanisms and cutting geometry. Burrs are preferably formed in machining ductile materials. Formation of burrs on the edges of micro-machined features (e.g., micro-channels) creates undesirable edge quality and poses problem during its use. Removal of micro-burrs at post machining stage is a difficult task to handle. Minimization and control on the formation of burrs through proper selection of cutting conditions is an effective way to handle the problem and avoid rectification effort [3].

Several studies related to machinability and burr formation in macro- and micro-scale cutting of different materials have been reported. All these studies have a guiding significance in understanding the machinability and burr formation at different locations for different conditions of cutting. Nakayama and Arai [4] experimented with brass in orthogonal cutting process and found that burr size could be reduced by reducing uncut chip thickness and selecting cutting conditions that reduce shear strain of the deforming work material. Their experimentation also indicated that large uncut thickness, low cutting speed and low rake angle of the cutting tool developed small sized roll-out burrs in brittle materials. Zhang et al. [5] analysed burr heights of entrance, side and exit burrs in orthogonal face turning of carbon steel under different cutting conditions. Their study showed that for entrance and side burrs, burr dimensions increased marginally with the increase in feed

rate when the uncut chip thickness was more than the cutting edge radius. Wu et al. [6] investigated the formation of side burrs in micro-planing process and top burrs in micro-milling process. They reported that maximum interacting stress between the cutting tool and the work material shifted from the rake face side to the bottom segment (adjacent to the flank side) of the rounded cutting edge as the ratio of uncut chip thickness to the cutting edge radius was decreased. Mamedov [7] investigated the applicability of micro milling method in processing of glass material. The effect of cutting parameters, such as cutting speed, feed rate, depth of cut and lead angle on generated surface quality and cutting forces was evaluated via surface examination under an optical microscope and cutting force measurements with dynamometer. Lawn et al. [8] analysed the micromechanics of machining and wear in hard and brittle Materials. The studies available in literature were mostly concerned with machining of crystalline metallic materials. Limited studies were reported in the literature regarding formation of burrs in micro-milling amorphous metallic substances, such as bulk metallic glass. The present work undertakes a study on burr formation on bulk metallic glass, and examines the influence of the cutting parameters on the formation of top burrs in fabricating micro-channels on a bulk metallic glass sample in full immersion mechanical micro milling process.

1.1 Mechanism of Top Burr Formation in Micro Milling

A micro-channel created in full immersion micro-milling is shown in Fig. 1. As shown in this Figure, the tool starts to cut the material with an uncut layer of thickness zero (at point A). The uncut layer thickness gradually increases as the tool rotates with more material getting engaged with the tool. Thus, the inflowing material toward the cutter edge gets severely ploughed at point A, and plastic flow of the material underneath the stagnation point on the cutter edge causes upward bulging of the work material, thereby, forming top burrs adhering to the top machined edges. This occurs on both the edges, namely the edges on the up-milling and down-milling sides as the cutting edge engages or disengages from the cut respectively. During the tool's travel from A to B and then to C, burrs are also formed with different sizes on the top edge of the transient machined surface depending on the work material properties, cutting conditions and tool edge condition. However, the burrs formed in the transient machined edges are removed in subsequent cuts.

The extent of bulging out of the work material on the edge and correspondingly the burr size depends on the work material properties and the pressure developed due to the radial force applied by the micro-cutter edge on the sidewall work material. The cutting parameters influence the forces applied on the sidewall. Burr formation in micro-milling is influenced by the micro-cutting mechanics, cutting parameters, work material microstructure, such as grain size, micro tool condition etc. Reduced grain size may reduce burr size due to increased hardness and strengthening. At the same time, it may cause increase in the cutting force, which in turn may increase the indenting pressure on the side wall. Micro-cutting using cutting tool having low cutting edge radius results in reduced cutting forces and burr size due to the reduced effect of indentation and ploughing. However, progressive tool wear causes increase in cutting edge radius. Studies [6] reported increase in burr size with increase in the cutting edge radius. Amorphous metallic alloy, such as bulk metallic glass is brittle solid, but may exhibit increased ductility in micro-scale deformation that happens in micro-cutting due to formation of secondary shear bands. Increased ductility of the work material enhances ploughing and indentation leading to increased lateral bulging and development of burrs. The extent and intensity of burr formation is quantified by the burr size in micro-milling of bulk metallic glass. The width of top burrs represents the burr size in the present study.

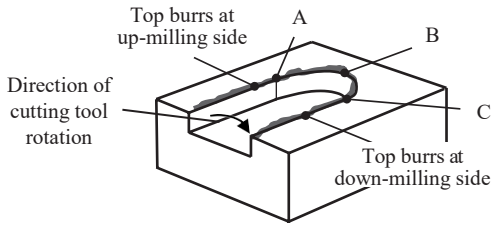

Fig. 1. Schematic of micro-channel geometry created in micro-milling.

2 Experimentation

The experimental work was conducted on a Zr-based bulk metallic glass ($Zr_{68}Cu_{12}Ni_9Ti_{11}$) cylindrical shaped specimen. The specimen diameter was 10 mm with thickness of 5 mm. Different properties of the bulk metallic

glass specimen are hardness of 4805 MPa (Vickers: 490 kgf/mm^2), yield strength of 1600 MPa and Modulus of elasticity of 80 GPa. Micro-milling experiments were conducted on a micro-milling set-up with precision stages of resolution 1 µm and high accuracy motion controllers. The work sample was firmly placed on the machine table using rigid and suitably designed fixture device. The schematic of the micro-milling of the work sample is shown in Fig. 2. Uncoated two fluted micro-milling carbide (Code: SC2FEM E9661; Make: Axis) cutter of 300 µm diameter was used in the experiment. Different dimensions of the cutter are summarized in Table 1. Fig. 3 depicts the schematic of the micro-milling cut geometry and cross-sectional geometry (exaggerated) of the top burrs formed in the micro-channel, where, W_b, h_b, t_b, a_p represents the burr width, burr height, burr root thickness and axial depth of cut respectively

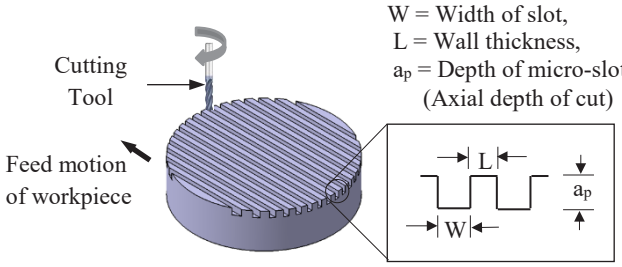

Fig. 2. Schematic of micro-milling of the work sample.

Table 1. Dimensions of the micro-milling cutter

Dimensions	Values
Diameter (µm)	300
Rake angle (Deg.)	15
Clearance angle (Deg.)	10
Helix angle (Deg.)	30
Cutting edge radius (µm)	3
Effective flute length (mm)	0.6
Shank diameter (mm)	3
Overall length (mm)	38

The present study examines the influence of the cutting parameters namely, cutting speed (v_c), feed per tooth (f_t), and depth of cut (a_p) on the width of the top burrs formed at the top horizontal edges of the micro-channel. The parametric study was carried out under different combinations of the cutting parameters. The micro-channels on the work sample have width equal to the diameter of the cutter and height equal to the axial depth of cut. The micro-channels were separated by a narrow wall thickness. The values of the factors used in this study were chosen with the consideration of the effects of ploughing and cutting edge radius applicable in micro cutting. The cutting conditions are summarized in Table 2.

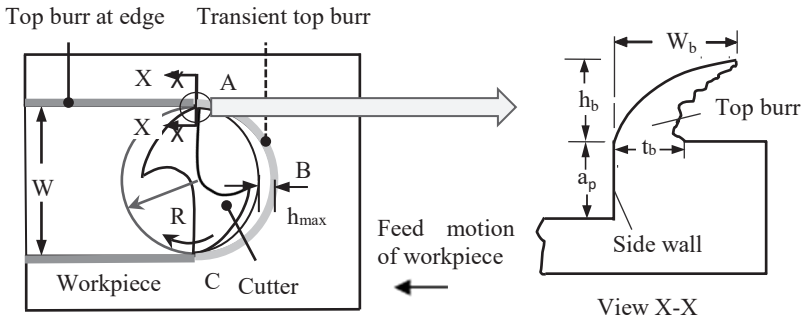

Fig. 3. Schematic of micro-milling cut geometry and cross-sectional geometry of top burr (view X-X) [W = width of micro-channel; h_{max} = Maximum uncut chip thickness].

. **Table 2.** Summary of cutting conditions

Cutting conditions	Description
Workpiece material	Zr-based BMG ($Zr_{68}Cu_{12}Ni_9Ti_{11}$)
Cutting tool	Uncoated WC micro-end mill (Ø 0.3 mm)
Cutting speed (v_c)	0.031-0.094 m/s
Feed rate (f_t)	3-7 µm/tooth
Axial depth of cut (a_p)	12-28 µm
Radial depth of cut (a_r)	Full immersion
Cutting environment	Dry

3 Results and Analysis

The present experimental work investigated the influence of cutting parameters on the width of top burrs formed in up-milling and down-milling sides of the micro-channels. Experimental findings of the study with suitable cutting conditions applicable in micro-cutting domain are analyzed to explore the influence of the cutting parameters on the formation of top burrs. However, several aspects in cutting, such as low ratio of uncut chip thickness to the cutting edge radius and associated ploughing effect, unrestricted free surface providing plane strain deformation, mode of cutting, etc. played critical underlying role on the top burr formation.

3.1 Analysis of the effect of feed rate on the burr size

Fig. 4 presents the variation of the width of the top burrs in the up-milling and the down-milling sides of the fabricated micro-channels at different feed rates for cutting speed and axial depth of cut of 0.063 m/s and 20 µm respectively. The values of the width of top burrs indicated are the average of the values of the width of top burrs obtained in the respective up-milling and down-milling sides. The results clearly show that width of the top burrs developed in down-milling side was lower than in up-milling side. However, the results show that the difference is reduced at higher feed rates. Width of burrs might have been influenced by the strategy of milling (up-milling or down-milling). Some studies on the burr formation in micro-planning and micro-milling experiments [6] reported wider burrs in down-milling side than in up-milling. They opined that a portion of the chip that was supposed to be clearly separated out from the material in cutting might have torn-out and got adhered with the burr formed in the down-milling side. This tearing and adhering of the chip remnants or unseparated chips resulted in the observation of wider burrs. However this tearing effect may be a random phenomenon and occurs primarily as the cutting tool gradually gets blunt while cutting ductile work material. During the end of cut, instead of a portion of the chip getting into the burr, the chip may also detach out some portion of burr resulting in less wider burr. The results from this study indicated that a lower feed rate resulted in higher top burr size. It is also seen that the increase in burr size with the decrease in feed rate showed a linear trend for up-milling side burrs. However, for down-milling side burrs the tendency of increase in burr size was higher at lower range of feed rate while the feed rate (feed per tooth) was lower than the cutting edge radius. In this work the average cutting edge radius was estimated to be 3 µm. With reference to Fig. 3, burrs formed at point A of the work sample got adhered to the sidewall top edge. At low feed rates, for short duration contact of the cutting edge to the sidewall work material, ploughing occurred for a longer time than at higher feed rates. Increased ploughing and indenting pressure at low feed rate augmented the bulging out of the work material to occur more intensely. For higher feed rates, cutting action with chip formation started earlier than at lower feed rates in the up-milling side (A to B) with reduced ploughing due to which action of lateral deformation at the sidewall diminished quickly resulting in lower sized burrs. The burr size formed around point B (mid-point of the rotating tool pass) increased with the decrease in the feed per tooth when feed per tooth was less than the cutter edge radius. For feed per tooth more than the cutter edge radius, burr size decreased with the decrease in the feed per tooth. The uncut layer thickness at point B was at maximum value and was closely equal to feed per tooth value. However, the burrs formed around point B were at the transient machined edge and were removed

in subsequent passes. So, analysis of burrs in this area is of little importance. For higher feed rates, cutting action in the down-milling side (B to C), continued to occur till the tool edge was very near to the end of the cut (point C), whereas, for low feed rates, ploughing started to play much earlier before it reached point C. This led to higher sized burrs at the sidewall for lower feed rates at the exit end.

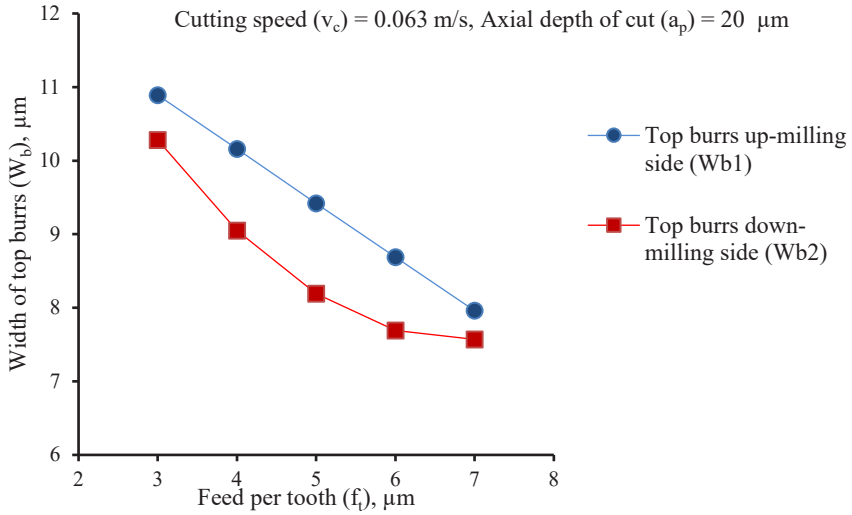

Fig. 4. Variation of width of top burrs (W_b) at different feed rates.

3.2 Analysis of the effect of depth of cut on the burr size

Fig. 5 presents the variation of the width of the top burrs in the up-milling and the down-milling sides of the fabricated micro-channels at different depths of cut for cutting speed and feed per tooth of 0.063 m/s and 5 µm respectively. The up-milling side burrs exhibited larger size than the down-milling side burrs. Experimental results showed that increase in axial depth of cut resulted in the increase of burr size. This may be due to larger engagement of the side wall with the cutter edge and the presence of unrestricted top work surface. Furthermore at lower axial depth of cut the cutting force was low and the radial indenting force on the sidewall was also low. This might have reduced the plastic side flow and top burr formation. The difference in the burr size between up-milling and down-milling side burrs widens up at higher axial depths of cut.

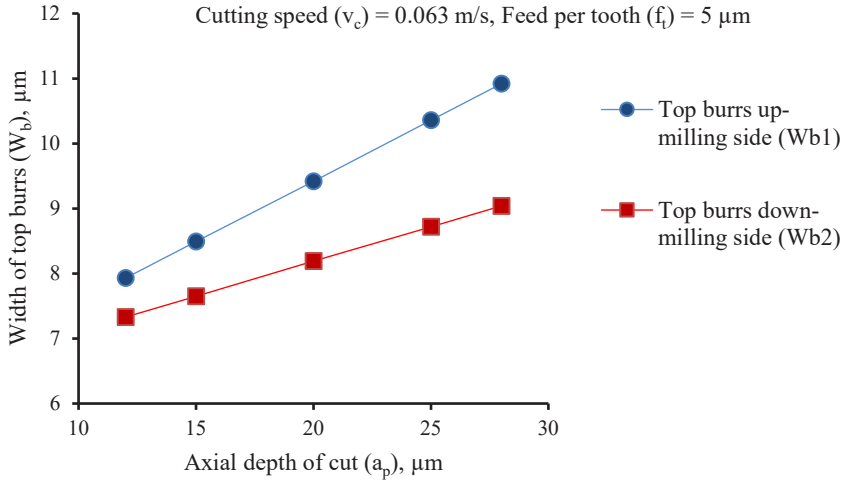

Fig. 5. Variation of width of top burrs (W_b) at different axial depths of cut.

3.3 Analysis of the effect of cutting speed on the burr size

Fig. 6 presents the variation of the width of the top burrs in the up-milling and the down-milling sides of the fabricated micro-channels at different cutting speeds for feed per tooth and axial depth of cut of 5 µm and 20 µm respectively. The experimental results indicated that increase in cutting speed showed a decreasing trend in the size of the burrs. For increased cutting speed the contact time of the cutting edge with the sidewall material is reduced resulting in reduced indenting and ploughing effect on the sidewall. This further reduced the amount of plastic side flow of the work material and thus, burr formation with less size was obtained. Furthermore, at higher cutting speeds chip removal was easy than at lower cutting speeds due to increased temperature in the cutting zone which resulted in reduced effect on side flow. Fig, 7 depicts some scanning electron microscope (SEM) images of the top burrs obtained in this study.

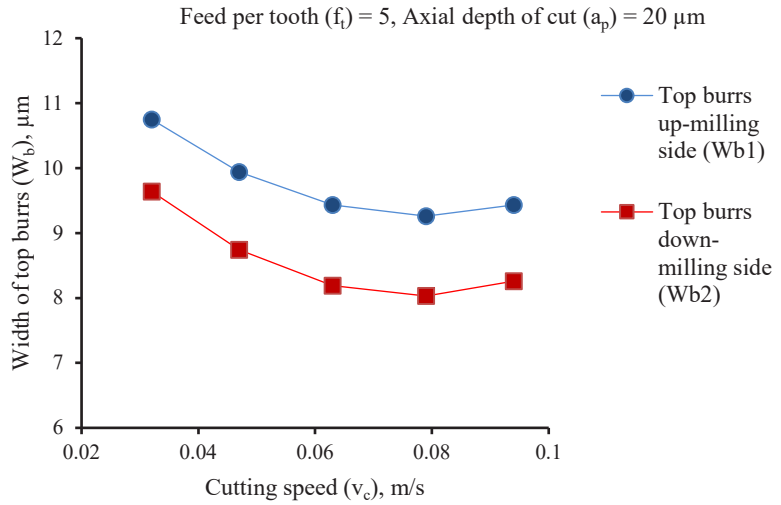

Fig. 6: Variation of width of top burrs (W_b) at different cutting speeds.

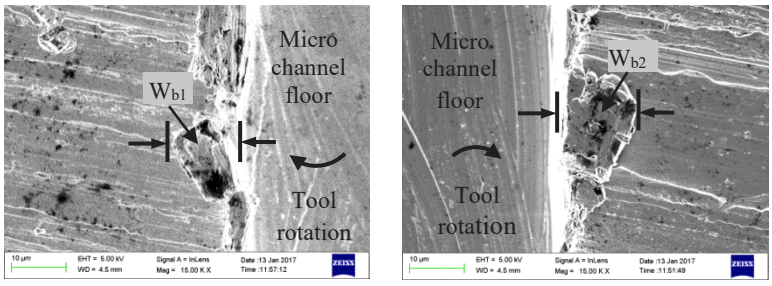

Fig. 7. Burr formation at (a) up-milling side with v_c = 0.079 m/s, f_t = 5 µm, a_p = 15 µm; (b) down-milling side with v_c = 0.063 m/s, f_t = 4 µm, a_p = 20 µm.

4 Conclusions

This paper presents an experimental investigation on the formation of top burrs in micro-milling of bulk metallic glass. Critical issues that influence the burr formation on the top machined edges in micro-end milling and the mechanism of its formation are discussed. Proper strategies in machining are of ardent importance in getting good edge quality of the micro-feature with minimum burr size. For cutting a particular material without any option of altering the material grain size or ductility and limitation in the cutting geometry, the only cost effective option could be to select cutting conditions that yield least sized burrs. The results obtained in the study indicated several important aspects, such as,

- Up-milling side burrs were higher than the down-milling side burrs.

- Feed rate influences the top burr formation characteristics significantly. Width of top burrs at low feed rates was found to be higher than at higher feed rates. Increased ploughing and upward plastic flow resulted in higher burr size at low feed rates.
- Increase in axial depth of cut resulted in increased burr width due to larger engagement of the side wall with the cutter edge and unrestricted top work surface. Increase in cutting speed showed a decreasing trend in the width of the top burrs.
- Adopting feed rate (feed per tooth) larger than the cutting edge radius and higher cutting speed may be an appropriate strategy to obtain minimum sized burrs. However, as the surface roughness increases with the feed rate, the feed rate should not be chosen so high such that surface roughness is compromised.
- For peripheral end milling, cutting with minimum axial depth of cut in down-milling mode would have more beneficial effects in terms of generation of lower burr width than in up-milling mode. For cutting a particular depth, multi-pass runs may be carried out.

References

1. Dornfield, D., Min, S., Takeuchi, Y.: Recent Advances in Mechanical Micromachining, CIRP Ann. 55 (2), 745-768 (2006).
2. Chae, J., Park, S.S., Freiheit, T.: Investigation of micro-cutting operations, Int. J. Mach. Tools Manuf. 46 (3-4), 313-332 (2006).
3. Aurich, J.C., Dornfield, D., Arrazola, P.J., Franke, V., Leitz, L., Min, S.: Burrs–Analysis, control and removal, CIRP Ann. 58 (2), 519-542 (2009).
4. Nakayama, K., Arai, M.: Burr Formation in Metal Cutting, CIRP Ann. 36 (1), 33–36 (1987).
5. Zhang, T., Liu, Z., Xu, C.: Influence of size effect on burr formation in micro cutting. Int. J. of Adv. Manuf. Technol. 68, 1911-1917 (2013).
6. Wu, X., Li, L., Ning, H.: Investigation on the burr formation mechanism in micro cutting. Precis. Eng. 47, 191-196 (2017).
7. Mamedov, A.: Machining of brittle materials: micro milling of glass. Journal of Mechanical Science and Technology 35(9), 1-6 (2021).
8. Lawn, B.R., Lopez, O.B., Huang, H., Zhang, Y.: Micromechanics of machining and wear in hard and brittle materials, Journal of the American Ceramic Society 104(1), 5-22 (2020).

Experimental Investigation on the dielectric effect during electro discharge machining of TiN-Al_2O_3 composites

Goutam Paul[1], Soumya Sarkar[2], Nagahanumaiah[3] and Souren Mitra[2]

[1] Institute of Engineering and Management (IEM), University of Engineering and Management Kolkata., Kolkata, India
[2] Jadavpur University, Kolkata, India
[3]CMTI, Bengaluru, India
goutamju04@mail.com

Abstract. Among the various types of non-contact type processes electro-discharge machining (EDM) plays a major role in the field of machining advanced composites like TiN-Al_2O_3 which was indigenously developed for the application of cutting tool material. High chemical stability, low friction coefficient and high hardness etc. are the key properties responsible for its application in component of complex shapes. Here in the current research, the application of various dielectric media was experimentally investigated during machining of the composites by micro EDM. The two responses i.e. Material removal rate (MRR) and circularity (the difference between maximum and minimum ferret diameters of the drilled holes) were under the investigation and it were observed that though the air dielectric possesses many advantages over oil medium but circularity is better in case of oil dielectric medium. Air medium can produce hazard free environment but due to small spark generations and sometime short-circuiting conditions the productivity as well as product quality were hampered.

Keywords: Micro-EDM, Tin-Al_2O_3, Dielectric media.

1 Introduction

Electro discharge machining (EDM) is an electro-thermal process that uses electrical discharges to erode electrically conductive materials. EDM being a non-contact type process, EDM can be used for making complex and miniaturized shapes, micro holes, micro fluidic channels etc. on any electrically conductive materials irrespective of its hardness and brittleness. In fact, EDM was originated for die making because any complex shapes can be formed on hard materials. The voyage of EDM began with the discovery of electric discharges. Apart from the natural discharges phenomena, namely lightening, there are productions of artificial discharges which are closely related to the development of electrical energy sources. First investigations of electrostatic phenomena were started with frictional machines during the first half of the 18th century. After that, the first sparks and pulsed arcs were produced with “Leyden jars”, an early form of capacitor invented in Germany and in the Netherlands around 1745 [1]. Then Joseph Priestley, an English theologian and chemist, discovered erosion craters left by electric discharges on the cathode surface in 1766.

Developing very large voltaic batteries, the first continuous carbon arc was produced by Vasilii Petrov in St-Petersburg in 1802. His discovery remained disclosed for over a century. So the discovery of electric arcs was accredited to Humphry Davy. Unacquainted of Petrov’s work, he re-discovered carbon arcs around 1808, using the huge voltaic battery of the Royal Institution of London. With complexity of electric sources and industrialization, Auguste de Meritens developed in 1881 in France a second major application using electric arcs. He used the heat produced by an arc for joining lead plates, inventing the principle of arc welding. Nowadays, electric arcs are also used for coating deposition, metal processing, plasma spraying and as high power switches, for example [2]. The history of EDM began in 1943, with the invention by Russian scientists Boris and Natalya Lazarenko in Moscow. They investigated the wear caused by sparking between tungsten electrical contacts, a problem which was particularly critical for maintenance of automotive engines during the Second World War. Keeping the electrodes in oil, they observed that the sparks were more uniform and predictable than in air. They then used controlled sparking as an erosion method [3]. Lazarenko developed during the war the first EDM machines, which were very useful to erode hard metals such as tungsten or tungsten carbide. The “Lazarenko circuit” remained the standard EDM generator for years. In the 1950’s, progress was made on understanding the erosion phenomenon [4-6].

To control pollution associated with traditional wet wire EDM, Jia et. al., 2009 [7], investigated the feasibility of near-dry wire EDM of PCD-coated WC cutting tool material using deionized water and air mist. A parametric study on spark cycle and spark duration was carried out, and the effect of these two important wire EDM process parameters on machining performance in terms of material removal rate (MRR) and surface roughness (Ra) was

analysed. Compared with conventional wet wire EDM, near-dry wire EDM consistently produced better Ra values on the PCD-coated WC work piece, but near-dry wire EDM produces lower MRR than wet wire EDM under some conditions.

In the current work, parametric analysis of the process has been performed with tubular copper tool electrode and mild steel work piece by Saha and Choudhury, 2009 [8]. Experiments have been conducted using air as the dielectric medium to study the effect of gap voltage, discharge current, pulse-on time, duty factor, air pressure and spindle speed on material removal rate (MRR), surface roughness (Ra) and tool wear rate (TWR). First, a set of exploratory experiments has been performed to identify the optimum tool design and to select input parameters and their levels for later stage experiments. Empirical models for MRR, Ra and TWR have then been developed by performing a designed experiment based on the central composite design of experiments. Response surface analysis has been done using the developed models. Analysis of variance (ANOVA) tests were performed to identify the significant parameters. Current, duty factor, air pressure and spindle speed were found to have significant effects on MRR and Ra. However, TWR was found to be very small and independent of the input parameters.

Dry electrical discharge machining is one of the novel EDM variants, which uses gas as dielectric fluid. Experimental characterization of material removal in dry electrical discharge drilling technique is presented by Govindan and Joshi, 2010 [9]. It was based on six-factor, three-level experiment using L27 orthogonal array. All the experiments were performed in a 'quasi-explosion' mode by controlling pulse 'off-time' so as to maximize the material removal rate (MRR). Furthermore, an enclosure was provided around the electrodes with the aim to create a backpressure there by restricting expansion of the plasma in the dry EDM process. The main response variables analyzed in this work were MRR, tool wear rate (TWR), oversize and compositional variation across the machined cross-sections. Conducting statistical analysis of the results it was shown that discharge current (I), gap voltage (V) and rotational speed (N) significantly influence MRR. TWR was found close to zero in most of the experiments. A predominant deposition of melted and eroded work material on the electrode surface instead of tool wear was evident. Compositional variation in the machined surface has been analyzed using EDAX; it showed migration of tool and shielding material into the work material. In the study it was also analyzed erosion characteristics of a single-discharge in the dry EDM process vis-a-vis the conventional liquid dielectric EDM. It was observed that at low discharge energies, single-discharge in dry EDM could give larger MRR and crater radius as compared to that of the conventional liquid dielectric EDM. For high precision application of EDM the machining must be carried out in low level of discharge energy [10, 11]. The mechanism of material removal is bit complicated in low discharge energy domain [12, 13]. Nevertheless, the physics of the micro-EDM of diverse class of engineering materials using different types of dielectric are very much complex and not fully understood. So far very some research studies have been carried out on EDM for micro machining application but that too also restricted to machining of very common limited materials [14, 15, 16]. Till date no research work has so far been reported on machining characteristics of different new generation engineering materials in the field of high precision application. In the present research, TiN-Al2O3 composites have been considered as work piece material in view of their varieties of successful engineering applications and also due to their poor machinability by conventional methods. There is no reported research study on electrical discharge machining of this advanced engineering materials particularly in the domain of low discharge energy machining.

2 Materials and experimental setup

2.1 Materials

In recent years there have been remarkable strides in development of engineering materials for wide applications in many fields, such as high-temperature structural applications in heat engines, heat exchangers, nozzles, automotive and aerospace industries, precision bearings, cutting tools and seal parts in machinery industries, nuclear industries and others. Metallurgists have been developing a large range of super alloys and heat resistant materials like ceramics and composites. Metal matrix composites are newly advanced materials having the properties of light weight, high specific strength, good wear resistance and a low thermal expansion coefficient. Again, the incorporation of a hard and brittle ceramic phase offers the potential for significant improvements in the mechanical performance of the composite over that of the monolithic metal or alloy. Titanium nitride-aluminum oxide (TiN-Al2O3) is a new generation composite material having potential for many industrial applications as it possesses high resistance to thermal degradation, anti-wear and anti-abrasion properties. Titanium nitride-aluminum oxide (TiN-Al2O3) have high resistance to thermal degradation and can be used for heat shielding. Moreover, as TiN and Al2O3 are highly wear and abrasion resistant materials, this composite has a good potential to be used as cutting tool material. High chemical stability, low friction coefficient and high hardness etc. are the key properties responsible for its application in component of complex shapes. Although titanium nitride-aluminum oxide

composite has many potential industrial application areas, conventional machining of such type of advanced composites is difficult to perform as they possess some peculiar properties like anisotropy, low thermal conductivity and abrasive nature of the reinforcing phases.

Table 1. Mechanical Properties of TiN-Al2O3 composite (provided by CSIR-CGCRI Lab)

Property	Unit	Value
TiN content	[Mol %]	66
Density	[kg.m^{-3}]	4342
Strength (Flexural) 4 points	[MPa]	440
Vicker's Hardness	[GPa]	20
Young' s Modulus	[GPa]	270
DC Resistivity	[Ω.m]	0.25
Thermal conductivity	[W.m^{-1}.K^{-1}]	21±1
Thermal expansion	[K^{-1}]	8.78 E-6
Specific heat capacity	[J/gm-°C]	0.75

As a result, a full-scale application of these advanced materials is hindered by high cost of conventional machining. In the present study, titanium nitride-aluminum oxide (TiN-Al2O3) composite has been chosen in view of the promise of application of this material in several engineering components and for the development of suitable technology guideline and optimal parameter settings for electro discharge machining. No guidelines or technology settings are available in the literature for this material. The mechanical and electrical properties of the work material are furnished in Table 1.

2.2 Micro-EDM Setup

The experimental setup shown in Fig. 1 has been developed by the researchers of Micro Systems Laboratory, CSIR-CMERI, Durgapur.

2.2.1 Work Table and its Control Unit

Physic Instrument stages [415.CG] are used for Z–axis servo drive. For Horizontal and Vertical Movement X and Y stages are also controlled through the same controller. Lab View Control Program were written to operate the Z–Stage for preliminary experiments in single discharge of micro EDM and in the hole making. For the single discharge experiment Lab View was used to run the Z stage through GPIB with Motion Assistant. For a single discharge three steps are required.

Firstly, straight line move, Z stage will move forward (say 100 revolutions) with a constant velocity and acceleration. Then secondly a delay for 500ms is set and third step is same as in the first step i.e. straight line move in a reverse direction. At the time of delay, the material is removed by means of the constant spark discharges. Third step requires just to avoid the short condition and to maintain the spark gap voltage. The Z–stage is fed down, moving the tool closer to the work piece, until the oscilloscope triggered, registering the discharge and record the voltage and current pulses across the machine gap. When the oscilloscope shows short circuit the Z–stage is ordered to stop and retract.

2.2.2 Power Supply Unit

In the precision EDM setup EP3010 EDM power supply is used. EP3010 is specially designed to generate micro pulse power for micro electro-discharge machining (micro-EDM). EP3010 provides high performance micro pulse generation which is needed for micro EDM process. EP3010 also provides a simple and easy solution to establish an interface with various motion controllers. EP3010 is controlled through RS232 serial communication protocol, which provides an easy way for users to develop various application programs on top of their machine tool control program.

Fig. 1. Experimental setup for precision EDM [17,18]

3 Experimental Investigation on TiN-Al2O3 Composite

In this study TiN-Al2O3 composite has been used as a work material. The applications and characteristics of TiN-Al2O3 composite has been described in section 2.1 Making holes in this material is very difficult by conventional machining. After some preliminary experiments, it was noticed that micro-EDM could be a significant process for producing holes in the composite and it was also noticed that electrode wear was high when copper electrodes were used. Therefore, steel rod of diameter 200μm and circularity of 0.02 μm was used as an electrode in these experimental investigations.

3.1 Plan of Experiment

Based on literature review on micro-EDM of multiple materials, preliminary experiments were conducted on TiN-Al2O3 composite and through voltage and current signals recorded in oscilloscope it was found that the Open circuit voltage (Vo), Capacitance (C), Pulse Frequency (f), and Pulse on time (Ton) play significant role for a given spark gap. Although change in spark gap also play significant role, selecting appropriate spark gap for different conditions was difficult, as often it could end up with either no spark or short circuit condition. Therefore, experiments were conducted at two different spark gaps (8 μm and 4 μm) by varying other four variables at three levels. On the basis of these process variables, an orthogonal array (L18) consisting of 18 experiments (as shown in Table 2) has been performed for both the spark gaps on micro-EDM setup (Figure 1) in absence of dielectric. For each experimental run, the number of machining steps (loops in Lab View program) was kept constant at 1000 steps. The discharge voltage (Vd), discharge current (Id), spark on time (td) were measured with the help of the oscilloscope. In this study the responses are MRR (μm2/sec), ROC (μm) and circularity (μm). The experimental results for both dielectric media are given in Table 2.

Table 2. Experimental Results of micro-EDM of TiN-Al2O3 Composite in oil dielectric

	Air Dielectric		Oil Dielectric	
Sl. No.	MRR (μm^3/min)	Circularity (μm)	MRR (μm^3/min)	Circularity (μm)
1	0.391	0.269	1.191	0.969
2	0.54	0.379	1.25	1.079
3	0.57	0.489	1.51	1.179
4	0.477	0.589	1.377	0.989
5	0.495	0.789	1.585	1.089
6	1.002	0.956	1.513	1.199
7	1.327	1.091	2.455	1.291
8	2.009	1.192	3.189	1.392
9	2.086	1.291	3.463	1.491
10	0.892	1.394	1.991	1.696
11	0.792	1.496	1.997	1.796
12	1.192	1.597	2.087	1.897
13	0.915	1.394	2.995	1.696
14	0.992	1.497	1.898	1.797
15	1.303	1.597	2.505	1.897
16	0.941	1.497	3.117	1.797
17	2.062	1.599	3.823	1.899
18	2.276	1.699	2.567	1.999

Table 3. F-value and % contribution of different factors on responses as obtained by ANOVA for TiN-Al_2O_3 Composite in oil dielectric medium

Input Parameters	Measured Responses			
	MRR		Circularity	
	F value	% Contribution	F value	% Contribution
Spark Gap (micron)	10.0872	32.69	219.033	84.78
Open Voltage (volt)	37.6124	55.67	15.355	10.41
Capacitance (nF)	0.0439	0.07	11.958	4.63
Frequency (kHz)	0.6604	0.98	0.004	0.01
Pulse-on-Time (microsec)	7.1562	10.59	0.000	0.01

Table 4. F-value and % contribution of different factors on responses as obtained by ANOVA for TiN-Al_2O_3 Composite in air dielectric medium

Input Parameters	Measured Responses			
	MRR		Circularity	
	F value	% Contribution	F value	% Contribution
Spark Gap (micron)	2.2900	33.7	71.3027	67.96
Open Voltage (volt)	22.5542	53.18	17.8196	28.42
Capacitance (nF)	5.2510	12.38	3.7025	3.53
Frequency (kHz)	0.2803	0.66	0.0801	0.08
Pulse-on-Time (microsec)	0.0325	0.08	0.0064	0.01

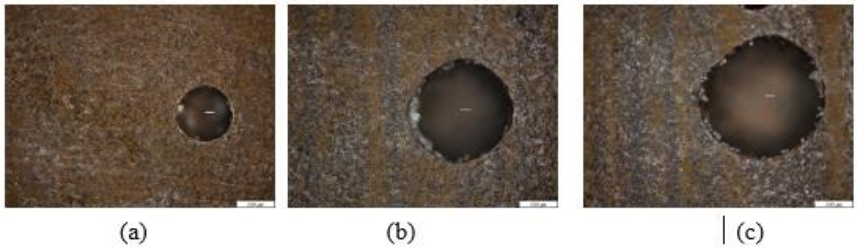

Fig. 2. Optical microscopic images of craters for (a) experiment no. 2, (b) experiment no. 6 and (c) experiment no. 9 at 8 μm spark gap in oil media

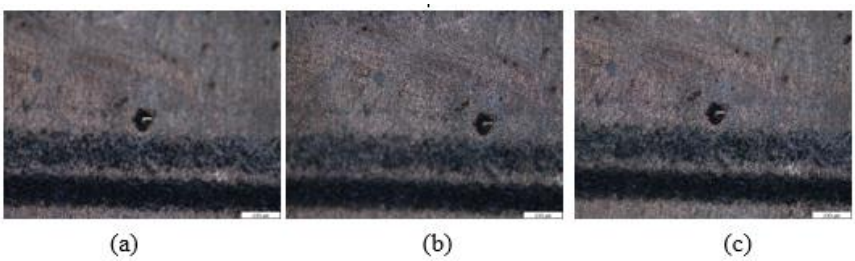

Fig. 3. Optical microscopic images of craters for (a) experiment no 2, (b) experiment no 6 and (c) experiment no 9 at 4 μm spark gap in air media

3.2 Analysis of the Experimental Result

The performance of micro-EDM is analyzed by the MRR, and circularity (CIR) of the formed μ-hole. Each experiment was repeated thrice and the crater diameters were measured under optical microscope. The images were further analyzed using in Olympus Image Analysis-5 software to measure the micro-hole. Circularity was measured by the difference of maximum and minimum ferret diameter as obtained by analyzing the Optical photograph of the craters with the help of Olympus Image Analysis-5 software. The lower values in response (CIR) functions were considered as desired values. Therefore, the signal to noise ratio (η (CIR)) have been calculated under the category of 'smaller-the-better' type problem as explained in Eqn. (1). Since the MRR is a larger-the-better type problem the signal to noise ratio (η (MRR)) has been measured by the formula as given in Eqn. (2).

$$S/N(\theta) = -10\log_{10}\left[\frac{\sum_{i=1}^{n} Y_i^2}{n}\right] \qquad \text{Eqn (1)}$$

$$S/N(\theta) = -10\log_{10}\left[\frac{\sum_{i=1}^{n} \frac{1}{Y_i^2}}{n}\right] \qquad \text{Eqn (2)}$$

3.3 Comparative Study of Response parameters of Micro-EDM on TiN-Al2O3 composite in oil and air dielectric

It has been observed from the optical microscopic images, as shown in Figure 2 and Figure 3 that at the same combination of discharge energy and spark on time the MRR for oil dielectric was higher compared to that produced in air dielectric medium. Also for same number of machining steps the depth of crater is more in oil medium. From the S/N ratio plots, as shown in Figure 4, it has been observed that maximum MRR can be obtained at spark gap= 4μm, Vo = 125 volt, C= 100 nF, F = 90 kHz and ton = 10 μs for both oil and air dielectric media. Analyzing the oscilloscope readings, it has been observed that at higher level settings of the process variables the discharge energies (Eqn 3) as well as energy densities are increased. As discharge energy and energy density becomes more than 100 μJ and 20 W/m2 respectively, the oxidation and/or decomposition along with melting and/or evaporation

of the composite. This oxidation and melting phenomenon might have increased the material removal rate. At higher level settings of the process variables more oxidation and/or decomposition of the composite materials occurs and these generated oxides melt and/or evaporate rapidly.

$E = 0.5\ C\ V_d^2$ Eqn. (3)

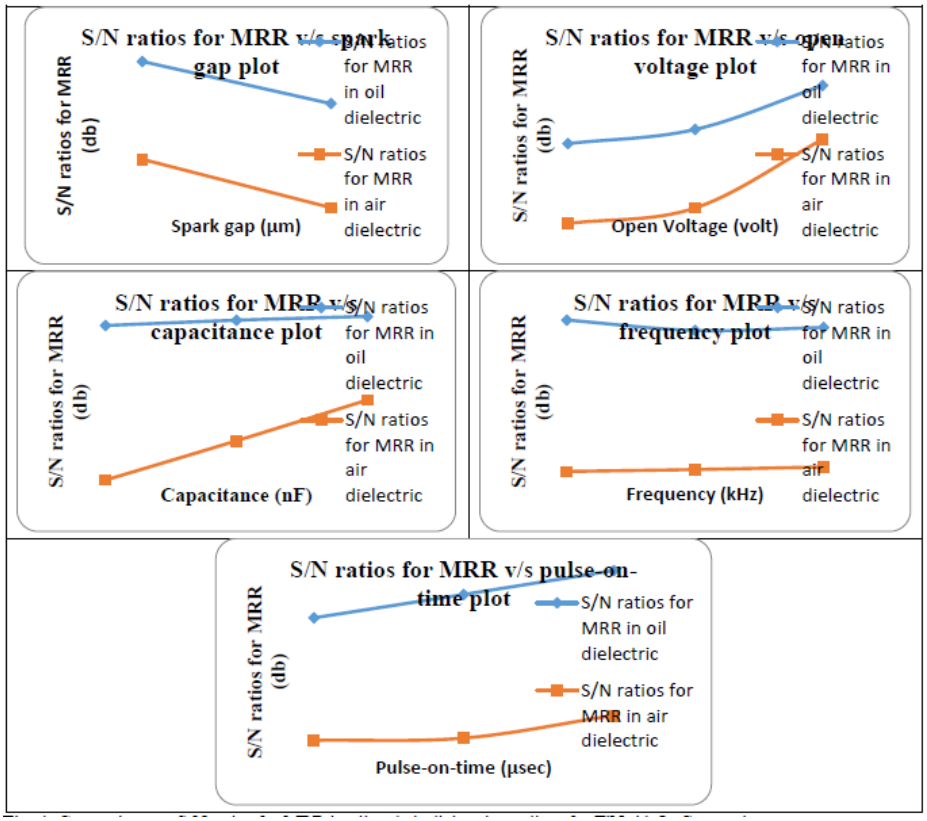

Fig. 4. Comparison on S-N ratios for MRR in oil and air dielectric medium for TiN-Al_2O_3 Composite

This melting phenomenon is supported by the formation of spherical shaped debris. The MRR is also higher in oil medium in comparison to air medium. This might be due to the fact that at oil medium the surface area to volume ratio of the melting isotherm is more than that of air medium. So, the oxidation and/or decomposition of the composites is more in oil medium and these oxides melt rapidly and the MRR become higher in oil medium. From ANOVA as depicted in Table 3 and Table 4, it is observed that factors spark gap and open voltage have more percent of contribution. So spark gap and open voltage are the most significant factors for MRR in micro drilling of TiN-Al2O3 composite both in oil and air dielectric media. Micro EDM is mainly developed to produce micro features where the accuracy of the product is more important than the production rate. The accuracy of the micro hole generation is measured by two important responses i.e. radial overcut and circularity. Now the S/N ratio plots, as shown in Fig. 5, indicates that minimum circularity are obtained at The optimum level settings for circularity has been obtained as spark gap = 8 µm, Vo = 75 volt, C = 1nF, F = 30kHz and ton = 2 µs both in oil and air dielectric medium. The results of ANOVA test performed for the response function are depicted in Table 3 and Table 4. These results show that spark gap, open voltage and capacitance contribute significantly in case of ROC and circularity of the formed µ-hole in oil dielectric.

So, it is clear from the S/N ratio plots that at lower level settings of the process variables radial overcut and circularity are also less. This might be due to the fact that at lower level settings of the process variables short pulses are generated and these short pulses help to create short sparks with smaller diameters. The spark duration (td) is also small, as evident from oscilloscope readings, for lower level settings. as a result, the radius of spark (Eqn 3.1) is also small. This short spark reduces the radial overcut and so, short sparks are essential to generate accurate hole i.e. holes with lower overcut. Now at the higher-level settings of the process parameters even due to small noise in the sparks gap, a huge change in the sparks occurs resulting in inaccurate hole. At lower level settings, short sparks are generated and the process can be kept under control in spite of presence of some noise like debris particles. So, short sparks reduce the radial overcut and generate circular holes.

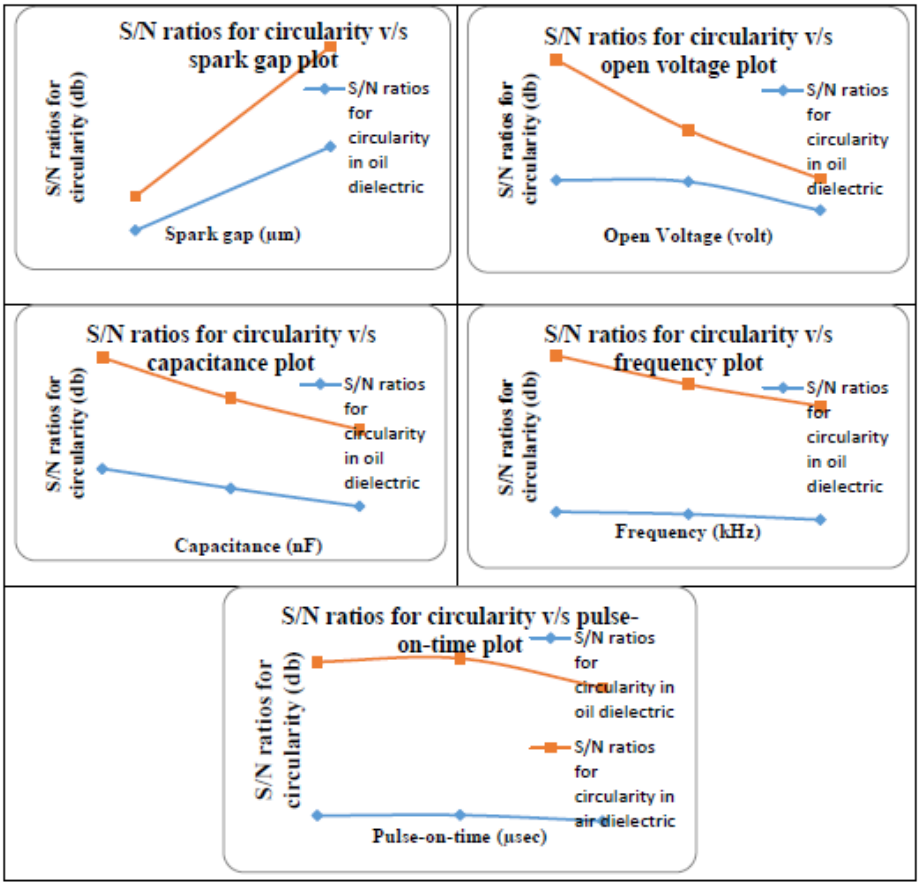

Fig. 5. Comparison on S-N ratios for circularity in oil and air dielectric medium for TiN-Al_2O_3 Composite

So the circularity is lower when oil dielectric is used. It has been obtained that the brittle fracture is less in oil medium in comparison to air medium and the surface area to volume ratio of the isotherms corresponding to the melting temperature is less in oil medium. So, the spherical shaped debris is more in oil medium than air medium. Material removal occurs in the form of smooth spherical balls. So, the obtained accuracy of the product during micro EDM of TiN-Al2O3 Composite is better in oil medium than air medium. In case of air dielectric, the brittle fracture might be more and the material is removed from the work piece as irregular shaped debris with perforated edges. This irregular shaped debris is sometimes removed in a chunk form. So, the accuracy of the product is poor in air dielectric.

3.4 Development of regression model for response parameters

The regression model to represent the relationship among responses and various controllable machining parameters of micro-EDM process has been developed by regression analysis. The regression equations are as follows:

For air dielectric medium:

MRR = -0.555361 - 0.0585556 Spark Gap + 0.03108 Open Voltage + .00464489 Capacitance - 0.00195833 Frequency + 0.005 Pulse-on-time Eqn (4)

(S = 0.384404 R-Sq = 71.70% R-Sq (adj) = 89.91%)

Circularity = 1.26758 - 0.186806 Spark Gap + 0.00915 Open Voltage + 0.00190465 Capacitance + 0.000511111 Frequency - 0.00108333 Pulse-on-time

Eqn (5)

(S = 0.187717 R-Sq = 88.56% R-Sq (adj) = 83.80%)

For oil dielectric medium:

MRR = 0.000777778 - 0.151306 Spark Gap + 0.0286267 Open Voltage +0.000446697 Capacitance - 0.00316111 Frequency + 0.0780417 Pulse-on-time

Eqn (6)

(S = 0.404237 R-Sq = 82.24% R-Sq (adj) = 74.84%)

Circularity = 1.99146 - 0.161 Spark Gap + 0.00417667 Open Voltage + 0.00168318 Capacitance + 5.27778e-005 Frequency - 2.08333e-005 Pulse-on-time

Eqn (7)

(S = 0.0923076 R-Sq = 95.36% R-Sq (adj) = 93.42%)

4 Discussion on the Effect of Dielectric on Micro-EDM

In order to study the effect of two dielectric media (i.e. kerosene oil and air) on micro-EDM of TiN-Al2O3 composites, experiments were carried out at different level settings of the process parameters. It was observed that air dielectric reduces the fumes generated in oil medium and produces a clean and hazard free environment. Also, if air dielectric medium can be used, machining can be done in any hazardous position e.g. overhead machining. Again, since the viscosity of air is lower than the oil so, air can flow through micro holes easily and able to remove debris at micro holes. This is one of the great advantages of air which makes it to select an effective medium in micro EDM.

Though in case of micro EDM of TiN-Al2O3 composites the material removal mechanism is a little different, MRR was more in oil medium. Here, the reason might be due to the fact that in oil medium the surface area to volume ratio of the isotherms corresponding to the melting temperature was quite less than that in air medium and as a result the oxidation and/or melting effect dominated the brittle fracture. This rapid oxidation and/or melting of the composites enhance MRR.

The analysis on micro EDM of TiN-Al2O3 composites indicated that ROC and circularity were lower when oil dielectric had been used. This might be related to the fact that in oil medium oxidation and/or melting of the composite were more and material removal in the form of spherical shaped debris was more.

5 Conclusions

So, it has been concluded at all from the above analysis that though air medium has many advantages in micro EDM of the above materials, oil medium helps to produce more accurate product than air medium. If nitrogen gas assisted dry air or air with a little moisture content can be used as a dielectric medium, then greater accuracy of the product can be obtained. Still, it requires an exhaustive research with major changes in the existing experimental setup. So, it is out of scope of this research study.

Acknowledgement

The authors acknowledge the gracious contribution towards the scientist group of CSIR-CGCRI for providing the composite material for machining and the CSIR-CMERI for providing the developed micro-EDM setup under the guidance of one of the authors of the paper.

References

1. A. Anders, , Tracking down the origin of arc plasma science, I. Early pulsed and oscillating discharges, IEEE Trans. Plasma Sci., 31(4), pp: 1052–1059(2003).
2. R. L. Boxman, D. M. Sanders and P. J. Martin, 1995, Handbook of vacuum arc science and technology, fundamentals and applications, Noyes publications, Park Ridge.
3. B. R. Lazarenko, 1943, About the inversion of metal erosion and methods to fight ravage of electric contacts, WEI-Institute, Moscow (in Russian).
4. L. H. Germer and F. E. Haworth, Erosion of electrical contacts on make, J. Appl. Phys., 20(11), pp: 1085–1109 (1949).
5. J. D. Cobine and E. E. Burger, Analysis of electrode phenomena in the high-current arc, J. Appl. Phys., 26(7), pp: 895–900(1955).
6. A. S. Zingerman, , The effect of thermal conductivity upon the electrical erosion of metals, Sov. Phys. Tech. Phys., 1, pp: 1945–1958(1956).

7. Weiliang Zeng, Zhenlong Wang, Qiang Gao, Wenzhuo Li and Wansheng Zhao, 2006, Study on Technology of Micro-EDM with Lower Working Voltage, Materials Science Forum, volumes, volumes 532-533, pp: 225-228 (2006).
8. Philip Allen and Xiaolin Chen, Process simulation of micro electro-discharge machining on molybdenum, Journal of Materials Processing Technology, volume 186, pp: 346-355(2007).
9. Asit Kumar Khanra, L. C. Pathak, M. M. Godkhindi, Microanalysis of debris formed during electrical discharge machining (EDM), J Material Science, Volume 42, pp: 872–877(2007).
10. B.X. Jia, W.S. Zhao, Z.L. Wang and F.Q. Hu, Study to Enhance the Precision of Micro-EDM, Key Engineering Materials, volume 339, pp: 26-31(2007).
11. Y Jia, B S Kim, D J Hu, and J N, Parametric study on near-dry wire electro discharge machining of polycrystalline diamond-coated tungsten carbide material, IMechE, Vol. 224 Part B (2009).
12. Sourabh K. Saha and S.K.Choudhury, 2009, Experimental investigation and empirical modeling of the dry electric discharge machining process, International Journal of Machine Tools & Manufacture, volume 49, pp: 297–308 (2009).
13. P. Govindan and Suhas S. Joshi, Experimental characterization of material removal in dry electrical discharges drilling, International Journal of Machine Tools & Manufacture, volume 50, pp: 431–443 (2010).
14. Fuzhu Han, Yuji Yamad, Taichi Kawakami, Masanori Kunieda, 2006, Experimental attempts of sub-micrometer order size machining using micro-EDM, Precision Engineering, volume 30, pp: 123–131 (2006).
15. D. M. Cao, J. Jiang, W. J. Meng, J. C. Jiang and W. Wang, Fabrication of high-aspect-ratio microscale Ta mold inserts with micro electrical discharge machining, Microsystem Technology, volume 13, pp: 503–510 (2007).
16. Jung-Chou Hung, Wei-Chieh Wu, Biing Hwa Yan, Fuang Yuan Huang and Kun-Ling Wu, Fabrication of a micro-tool in micro-EDM combined with co-deposited Ni–SiC composites for micro-hole machining, Journal of Micromechanical Microengineering, volume 17, pp: 763–774 (2007).
17. G. Paul, S. Roy, S.Sarkar, Nagahanumaiah and S.Mitra, , 'Investigations on Influence of Process Variables on Crater Dimensions in Micro- EDM of γ -Titanium Aluminide Alloy in Dry and Oil Dielectric Media', International Journal of Advanced Manufacturing Technology, Vol.- 65, pp.-1009-1017(2013).
18. G.Paul, M.Das, S.Ghatak, S.Sarkar, Nagahanumaiah, S.Mitra, , 'Investigation on the effect of spark gap in dry μ- electro discharge machining of SiC-10BN Nano-composite', International Journal of Manufacturing Technology and Management, Vol.-24, No.-1/2/3/4, pp.- 71-87(2011).

Emerging Manufacturing Technologies

Bibliometric Analysis of Emerging Manufacturing Technologies: A sustainable Review

Ajoy Kumar Bhowmick[1], Nipu Modak[1]

[1] Department of Mechanical Engineering; Jadavpur University; Kolkata 700032; India

Abstract. From Bibliographic analysis, by the visual representation of different type of data, acquired from the database like Scopus, Web of Science, Pub Med etc, researchers are intended to find out the scope and depth of existing research on a particular topic. From the representation of different figures and tables with the stipulated criteria of searched data, most suitable and prolific data comes into focus that helps to identify the hotspots and track trends of the present research area. It also helps to the research scholar to find out the research gap and necessary direction to the future scope of the research on the selected area. The aim of this paper is to make a panoramic analysis of 2780 articles on emerging manufacturing technologies from scopus database during the period of 2015 to 2025 limited to "English" language and "Articles" only documents. The citation as well as visualization analysis has been made by the VOSviewer 1.6.20 and Biblioshiny 2.0 software aiming to assign the rank of most prolific and significant articles and authors in reference of citation numbers, total number of articles, average citations and link strength. To work out the present trend, hotspot and research gap on emerging manufacturing technologies, different keywords model has been studied. The article "Industry 4.0: state of the art and future trends" by Xu, L. D., Xu, E. L., & Li, L. published in the journal "International Journal of Production Research" , USA, has been selected as the most prolific and significant article in view of citation and total link strength. In light of bibliometric analysis, different term like "additive manufacturing", "industry 4.0", "3d printing" etc. has been selected as the most occurrence term that leads a clear perception to the researcher those who are working on it. On the contrary, different terms like "regenerative medicine" emerges as the probable research gap in the field of emerging manufacturing technologies.

Keywords: Bibliometric analysis, Biblioshiny, VOSviewer, industry 4.0, additive manufacturing

1 Introduction

The First Industrial Revolution started from England during the period 1750-1760, probably one of the remarkable changes made in the human history when technology developed to transform human and animal labour into machinery [1]. After the improvement of steam engine by James Watt (1776) enabled factories to operate machineries efficiently [2]. In the Second Industrial Revulsion (late 19th century) the people realize the mass production system by introducing assembly line in the automotive industry for high volume production [3, 4]. Electrification started to improve the factories with efficient complex machineries [5]. After 2nd World War, a surge in demand came in the industry to scale out the production efficiently, specially in context of the labour shortage, when many people return from the military services [6]. Since 1968, PLC (Programmable Logic Control) dominated the industrial automation and replaced the relay logic circuit to increase quality, production and decrease cost [7]. Since then robots are also started to achieve quality and continuous product. During the Information Age (1970s-1990s), Computer Numerical Control (CNC) enhanced the precision machining and automation. Whereas Lean Manufacturing introduced the Just-In-Time (JIT) concept to reduce waste and improve efficiency in the manufacturing field [8]. The day by day improvement of the manufacturing as well as other industries with the innovative technologies, Industry 4.0 revealed as the new era in the year of 2011. The Internet of Things (IoT) created the smart interconnected network throughout the manufacturing units that transformed traditional manufacturing system into modern digitalized system [9]. 3D printing in Additive Manufacturing allowed rapid photocopying and customized products that changed the total product development system [10]. Today human and robot both performing together as a cobot enhancing productivity and safety [11, 12]. Virtual models are using now to simulate and optimize the production process as digital twins [13]. To balance the environmental impact with the industrial growth in the manufacturing system innovative sustainability practice also increased. All together manufacturing technologies are emerging rapidly to enter into the new era of Industry 5.0.

Citation analysis exposed the present trends in manufacturing by defining frequently referred studies and emerging research areas. Observing the most cited papers; researchers can determine the cutting edge technologies and its approaches towards the innovation of techniques in the modern industry as high citation counts often leads the significance and relevance of the topic in the selected research field. The data driven approach of citation

analysis shifts the focus into the sustainability, automation as well as digital manufacturing to understand the evolving landscape of manufacturing. In this paper in context of emerging manufacturing technologies, bibliometric analysis has been implemented to find out the research hotspot in many fields like Internet of Things, Cobot, Industrial Research etc. The review of literature of emerging manufacturing technologies provided a significant response in bibliometric analysis. But it is not adequately characterized the overall framework of emerging manufacturing technologies. To fulfill this both, bibliometric and visualization review has been made. This study focused only on the selected database from the scopus in the stipulated criteria from 2015 to 2025

2 Materials and Methods

To analyze document citation, research trends, keywords and content analysis of emerging manufacturing technologies, VOSviewer 1.6.20 and Biblioshiny 2.0 software has been used.

Research Data Collection Methodology on Emerging Manufacturing Technologies

The research data has been collected from scopus database system that consists of peer-reviewed journals and conferences for primary citation sources. The data collection has been completed on 21st October 2024. The database of documents on emerging manufacturing technologies extracted from the scopus system by the title key given in the step 1 in the Table 1. It was found 10241 documents initially, which are then filtered by limited to the year between 2015 to 2025 and data reduced to 7201 documents. In turn further filtered by "Article" only and documents of articles only reduced to 2955 in step 3. A further filter limited to "English" language only in step 4, database of 2780 articles obtained finally.

Table 1. Data collection steps on Scopus search engine

Search Steps	Query on Scopus	Description	Number of Documents
1	TITLE-ABS-KEY	(("emerging") AND ("manufacturing") AND ("technologies"))	10241
2	AND LIMIT-TO PUBYEAR	2015 to 2025	7201
3	AND LIMIT-TO	("Article")	2955
4	AND LIMIT-TO	("English")	2780

3 The Most Significant and Dominant Articles, Sources, Authors, Institutions and Countries in Emerging Manufacturing Technologies

3.1 The Most Significant and Dominant Article-Citation Analysis

This section shows and analyzed the most cited article on emerging manufacturing technologies [14]. Citation analysis has been done in scopus data on emerging manufacturing technologies articles. Considering 50 minimum number of citation per document, 447 documents out of 2780 documents meets the threshold. For each of 447 documents, the number of citation link will be calculated. The document with the largest number of link will be selected. Some of the 447 documents are not connected to each other. The largest set connected to each other's is 73 that showed in 12 clusters in the document network visualization in Figure 1. The node size in the Figure 1 signifies the frequency of occurrences. The co-occurrences between the two node linked with the line signifies the link strength. More the concurrences more will be the link strength. Different link strength has shown in the Table 2. As per the highest link strength of 8 and 2120 citations the article "Industry 4.0: state of the art and future trends" by Xu, L. D. et al. , USA (2018) considered as the Rank 1 link strengthen document [16]. The second rank holding article in the above context is "The role of renewable energy in the global energy transformation", article published by Gielen, D. et al. (2019) in the journal Energy Strategy Review having 2916 total citations, 7 link strength [15]. Based on the above citation criteria rank 3rd to rank 10th articles showed in the Table 2 [17-24].

All these papers has more than 800 citations as per the stipulated date of collection of data on emerging manufacturing technologies.

Table 2. Top 10 documents or articles of emerging manufacturing technologies based on citations

Documents	TCi	Rank on TCi	TLS	Rank on TLS	SYoY	CiY	TCi/Y	Rank on TCi/Y	Ref.
GIELEN D, 2019, ENERGY STRATEG REV	2916	1	1	7	2019	6	486.00	1	[15]
XU LD, 2018, INT J PROD RES	2120	2	8	1	2018	7	302.86	3	[16]
FRANK AG, 2019, INT J PROD ECON	1798	3	6	2	2019	6	299.67	4	[17]
DWIVEDI YK, 2021, INT J INF MANAGE	1542	4	0	9	2021	4	385.50	2	[18]
DALENOGARE LS, 2018, INT J PROD ECON	1391	5	4	4	2018	7	198.71	6	[19]
WANG J, 2018, J MANUF SYST	1201	6	3	5	2018	7	171.57	7	[20]
FULLER A, 2020, IEEE ACCESS	1195	7	3	6	2020	5	239.00	5	[21]
KUSIAK A, 2018, INT J PROD RES	922	8	6	3	2018	7	131.71	9	[22]
CHEN B, 2017, IEEE ACCESS	875	9	1	8	2017	8	109.38	10	[23]
DUTTA P, 2020, TRANSP RES PART E LOGIST TRANSP REV	835	10	0	10	2020	5	167.00	8	[24]

Total citations: TCi, total link strength: TLS, start year of article: SYoY, citation year: CiY

3.2 The Most Significant and Dominant Author-Citation Analysis

This section depicts the author's productivity in context of emerging manufacturing technologies. Considering 3 minimum numbers of documents of an author and 20 minimum number of citation of an author, out of 11809 authors, 136 authors meet the threshold. Some of the 136 authors are connected to each other and the largest set is 30 that depicted in the density visual network mode in the Figure 2. The authors rank is designated based on the total number of citations, articles, and total link strength and average yearly citations. Nripendra P. Rana, Queen's University Belfast UK secured the rank 1 author who have 1757 citations, 4 articles, 4 link strength in context of emerging manufacturing technologies.

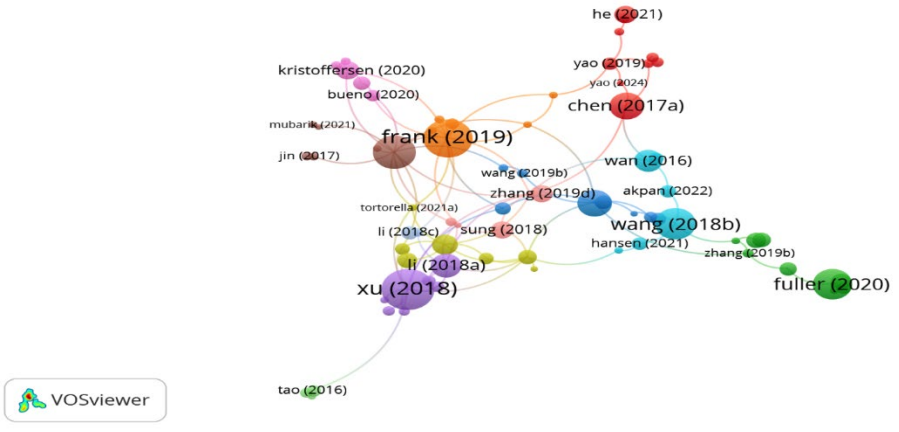

Fig. 1. Document network visualization based on citation

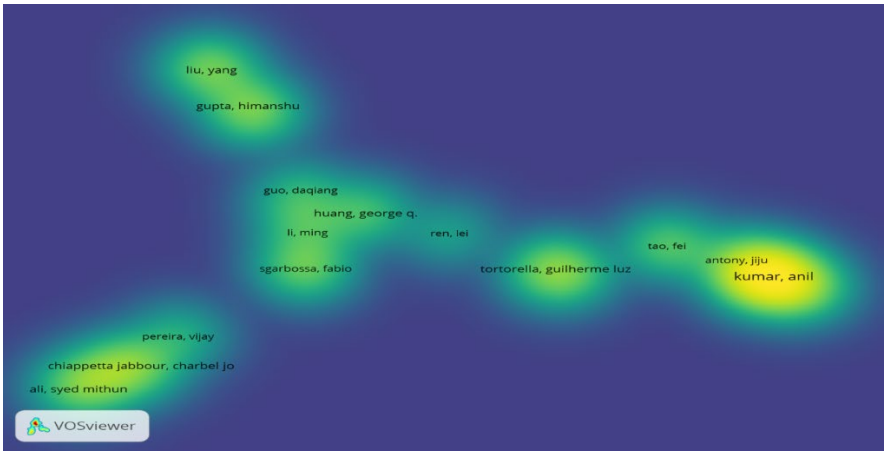

Fig. 2. Author density network visualization based on 20 citations and 3 documents per author

4 Co-occurrence of Keywords and Content Analysis

When few of the words or phrases appear together in different articles, it is often referred as the occurrence phenomenon of the articles showing certain relationship between the concepts. The entities may consist of title, organization, keywords or authors and many more. These characteristics are significant in different fields like linguistics, data interpreting and ordinary language processing. To find out regular research hotspot and research growth keywords can be explored in the study periphery.

4.1 Co-occurrence Analysis of Author keywords of Emerging Manufacturing Technologies

This section analyzes the concurrence of author's keywords in context of emerging manufacturing technologies. Considering 5 minimum number of occurrence of a keyword from 8815 keywords 269 keywords are selected to analysis the data in context of emerging manufacturing technologies. A author's keyword network visualization based on co-occurrences shown in the Figure 3. From each of the keywords, the total link strength of the co-occurrence link with other keywords will be calculated. The keywords with the greatest total link strength and co-occurrences are selected for the "Top 15 Co-occurrence Keywords" and excluding few of the keywords like "digital", "competitiveness", "adoption" and focusing on the keywords for the research perspective and very low co-occurrences and link strength, 15 keywords are selected for the "Selected Least Co-occurrence Keywords" shown in the Table 3.

Table 3. Co-occurrence author's keywords: top 15 and least 15 selected occurrences

Top 15 Co-occurrence Keywords				Selected Least Co-occurrence Keywords		
keyword	**occurrences**	**total link strength**		**Keyword**	**Occurrences**	**Total Link Strength**
additive manufacturing	306	357		emerging pollutants	5	0
industry 4.0	221	474		carbon nanotubes	5	2
3d printing	167	231		regenerative medicine	5	5
manufacturing	74	171		biodegradable	5	6
sustainability	72	150		biomanufacturing	5	6
innovation	58	117		wire arc additive manufacturing	5	6
smart manufacturing	54	129		carbon emissions	5	7
artificial intelligence	51	107		distributed manufacturing	5	7
emerging technologies	51	79		laser	5	7
digital twin	49	87		synthetic biology	5	7
internet of things	49	87		aerospace	5	8
block chain	46	101		construction industry	5	8
machine learning	45	95		rfid	5	8
circular economy	40	68		network analysis	5	8
digital transformation	31	77		life cycle assessment (lca)	7	8

4.2 Co-occurrence Analysis of Index- keywords of Emerging Manufacturing Technologies

The index keywords are extracted from the scopus data on emerging manufacturing technologies aiming to find out the core theme of the articles that analyze and explains the co-occurrences of the research area during the period of 2015 to 2025 in the stipulated conditions i.e. limited to the language “English” and “Article” only documents. In Figure 4 considering maximum concurrences from 16467 keywords top 30 index keywords are shown in the tree plot to analysis the effect of most co-occurrences keywords in the research area of emerging manufacturing technologies. “3d printers”, “emerging technologies”, “manufacture” and others are the top most co-occurrences index keywords that shown in the Figure 4.

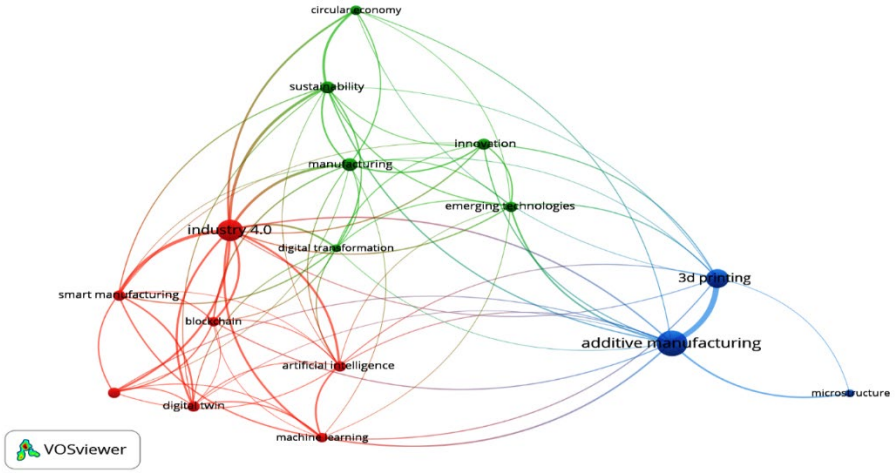

Fig. 3. Author keyword network visualization based on co-occurrences

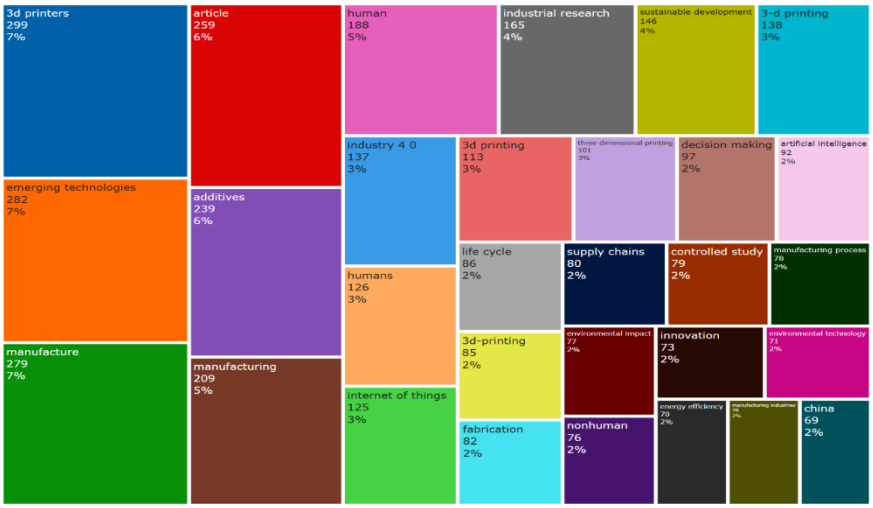

Fig. 4. Tree plot of top 30 Index Keyword

5 Thematic Area and Research Hotspot of Emerging Manufacturing Technologies

The thematic area classified documents in different fields. The Figure 5 shows the thematic area of all the documents on emerging manufacturing technologies. The major contribution from the field “Engineering” is 27.7% followed by “Computer Science” 11.2%, Material Science 10.5% and others. 18.6% of “Others” category contributed by the fields “Economics, Econometrics and Finance”, “Pharmacology”, “Toxicology and Pharmaceutics”, “Mathematics”, “Biochemistry, Genetics and Molecular Biology” and others. This thematic area provides the concise idea in the research field of emerging manufacturing technologies vividly.

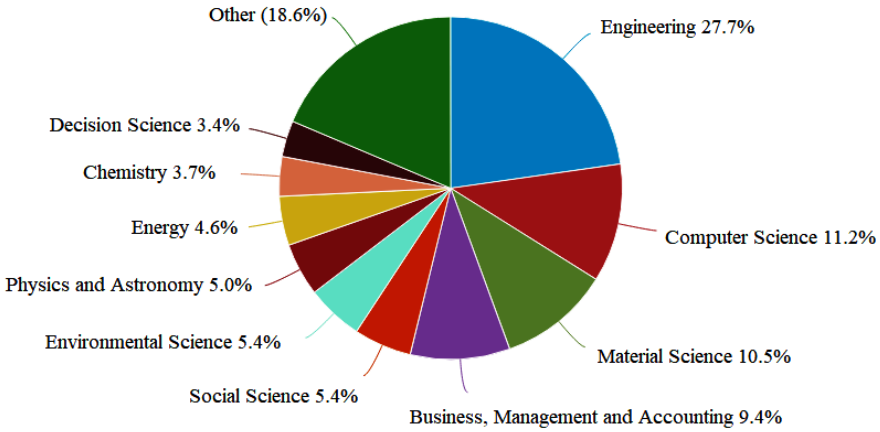

Fig. 5. Classification of Articles on Thematic Area

6 Hotspots and Research Gap

From bibliometric analysis in context of emerging manufacturing technologies, different hotspot and research trend can be predicted like “additive manufacturing”, “industry 4.0”, “green innovation”, “3d printing”,” sustainability”, “smart manufacturing”, “artificial intelligence”, “digital twin” and many more which are vividly depicted in different figures and tables. For example if we observe the tree plot of top 30 index keyword in Figure 4 we can easily understand the biggest plot in the figure is “3d printing” of 7% contribution in the 30 keywords tree plot which exist in the Table 3 with 167 co-occurrence and 231 link strength and also in the Figure 3 of author keyword network, associated with the biggest node of keywords “additive manufacturing” that consist of 306 co-occurrences and 357 link strength in the Table 3. For more example like “Industry 4.0” exist in the Table 3 with 221 co-occurrences and 474 link strength and contributing 3% of the total top 30 index keywords of Figure 4 also remarkably exists in the author’s keyword network of Figure 3. From this analysis we also observed that two broad sense of review emerges namely smart manufacturing and sustainable manufacturing. The first one associated with the modernization of technologies including the terms like “additive manufacturing”, “industry 4.0”, “3d printing” , “smart manufacturing”, “artificial intelligence”, “digital twin” etc and the second one associated with the goal of sustainability of manufacturing containing the keywords “green innovation”, ” sustainability” , “circular economy” etc. Moreover, if outcomes are compared with the similar such studies, it is observed that other researchers those who are working on the same area are concluding almost same as the paper culminated here [25].

On the contrary, from the Table 3, voices of keywords are evolving to the scholars as resonance of ideas for the research gap and their future work in context of emerging manufacturing technologies. The keywords like “synthetic biology” exists with 5 co-occurrences and 7 link strength whereas keywords like “additive manufacturing” exists with 221 co-occurrences and 357 link strength showing a huge difference of their application in the research area of manufacturing technologies. Synthetic Biology has significant role in health care, sustainable materials and agriculture field and as per the report by BCC Publishing (report code: BIO066H), Aug 2024 already valued to $ 15.4 billion in 2023 in the world economy, projecting the market growth of $ 19.3 billion to $ 61.7 billion at the end of 2029. The keyword like “life cycle assessment (lca)” in context of emerging manufacturing technologies has very poor co-occurrence of 7 and 8 link strength exist in the Table 3. LCA i.e. life cycle assessment is not only a methodology to quantify environmental impact of products but it has also the potential as an analysis and design tool for processes, and stresses that one of the biggest challenges of this decade in the field of process systems engineering (PSE) is the development of tools on the basis of environmental considerations [26]. But the amount of work on “lca” in reference to bibliometric analysis of emerging manufacturing technologies shows very poor which is a research gap and more work is expected on it. “Regenerative medicine” is one of the key field in the advanced manufacturing technology to transform production process in light of “3D bioprinting”, stem cell therapy, tissue engineering and different bio medical emerging field [27]. But it’s unfortunate poor existence in the co-occurrence Table 3 with 5 co-occurrences and link strength may lead to the scholar as a research gap. Manufacturing of composite materials for aerospace and automotive applications are enhancing rapidly due to the strength and light weight properties of carbon nanotubes (CNTs) that also leads the advancements in the electronics field for its application of faster transistor and efficient batteries [28]. But its existence of 2 link strength and 5 co-occurrences in the author’s keywords in the Table 3 indicates the research gap in the manufacturing field.

Emerging pollutants from different manufacturing units like pharmaceuticals, micro plastics required proper treatment like green chemistry in the level of nano filtration to minimize the environmental impact. In context of sustainability of the manufacturing technologies more research demands in the field of “emerging pollutants” when it shows that only 2 link strength and 5 co-occurrences, the keyword exits in the Table 3.

7 Conclusions

The motto of this bibliometric analysis is to focus on the research area on emerging manufacturing technologies so that in the light of bibliometric tools all the trend of the researches in the world may come out and what is the gap of the research which will also revealed to the scholar to work more on it. To do so a database has been collected from the scopus system with the stipulated conditions like limited to year 2015 to 2025, “Article” ony and “English” language. Then citation analysis has been made in context of authors, sources, countries, documents which depicted the most cited authors, journals, articles and countries. After that different Keywords, and their co-occurrence and relevance analysis has been made by the different type tables and graphs obtained by VOSviewer and biblioshiny software. This analysis helps to find out different trends and hotspot like “additive manufacturing”, “industry 4.0”, “green innovation”, “3d printing”,” sustainability” , “smart manufacturing”, “artificial intelligence”, “digital twin” and others. Different research gaps are also revealed from the analysis like “synthetic biology”, “regenerative medicine”, ”carbon nanotubes”, “life cycle assessment” and others which demands more work in the research area on emerging manufacturing technologies. It is expected that this analysis will help to the researcher to sketch out their work in the future in context of emerging manufacturing technologies.

References

1. Mohajan, H. (2019). The first industrial revolution: Creation of a new global human era.
2. Spear, B. (2008). James Watt: The steam engine and the commercialization of patents. World patent information, 30(1), 53-58.
3. Jevons, H. S. (1931). The second industrial revolution. The Economic Journal, 41(161), 1-18.
4. Mokyr, J., & Strotz, R. H. (1998). The second industrial revolution, 1870-1914. Storia dell’economia Mondiale, 21945(1), 219-245.
5. Hughes, T. P. (1993). Networks of power: electrification in Western society, 1880-1930. JHU press.
6. Engelberger, J. F. (1999). Historical Perspective and role in automation. Handbooks of Industrial Robotics.
7. Alves, T. R., Buratto, M., De Souza, F. M., & Rodrigues, T. V. (2014, October). OpenPLC: An open source alternative to automation. In IEEE Global Humanitarian Technology Conference (GHTC 2014) (pp. 585-589). IEEE.
8. Voss, C. A., & Robinson, S. J. (1987). Application of just-in-time manufacturing techniques in the United Kingdom. International Journal of Operations & Production Management, 7(4), 46-52.
9. Mourtzis, D., Vlachou, E., & Milas, N. J. P. C. (2016). Industrial big data as a result of IoT adoption in manufacturing. Procedia cirp, 55, 290-295.
10. Berman, B. (2012). 3-D printing: The new industrial revolution. Business horizons, 55(2), 155-162.
11. Weiss, A., Wortmeier, A. K., & Kubicek, B. (2021). Cobots in industry 4.0: A roadmap for future practice studies on human–robot collaboration. IEEE Transactions on Human-Machine Systems, 51(4), 335-345.
12. Djuric, A. M., Urbanic, R. J., & Rickli, J. L. (2016). A framework for collaborative robot (CoBot) integration in advanced manufacturing systems. SAE International Journal of Materials and Manufacturing, 9(2), 457-464.
13. Leng, J., Wang, D., Shen, W., Li, X., Liu, Q., &Chen, X. (2021). Digital twins-based smart manufacturing system design in Industry 4.0: A review. Journal of manufacturing systems, 60, 119-137.
14. Van Eck, N., & Waltman, L. (2010). Software survey: VOSviewer, a computer program for bibliometric mapping. scientometrics, 84(2), 523-538.
15. Gielen, D., Boshell, F., Saygin, D., Bazilian, M. D., Wagner, N., & Gorini, R. (2019). The role of renewable energy in the global energy transformation. Energy strategy reviews, 24, 38-50.
16. Xu, L. D., Xu, E. L., & Li, L. (2018). Industry 4.0: state of the art and future trends. International journal of production research, 56(8), 2941-2962.
17. Frank, A. G., Dalenogare, L. S., & Ayala, N. F. (2019). Industry 4.0 technologies: Implementation patterns in manufacturing companies. International journal of production economics, 210, 15-26.
18. Dwivedi, Y. K., Hughes, L., Ismagilova, E., Aarts, G., Coombs, C., Crick, T., ... & Williams, M. D. (2021). Artificial Intelligence (AI): Multidisciplinary perspectives on emerging challenges, opportunities, and agenda for research, practice and policy. International journal of information management, 57, 101994.
19. Dalenogare, L. S., Benitez, G. B., Ayala, N. F., & Frank, A. G. (2018). The expected contribution of Industry 4.0 technologies for industrial performance. International Journal of production economics, 204, 383-394.

20. Wang, J., Ma, Y., Zhang, L., Gao, R. X., & Wu, D. (2018). Deep learning for smart manufacturing: Methods and applications. Journal of manufacturing systems, 48, 144-156.
21. Fuller, A., Fan, Z., Day, C., & Barlow, C. (2020). Digital twin: Enabling technologies, challenges and open research. IEEE access, 8, 108952-108971.
22. Kusiak, A. (2018). Smart manufacturing. International journal of production Research, 56(1-2), 508-517.
23. Chen, B., Wan, J., Shu, L., Li, P., Mukherjee, M., & Yin, B. (2017). Smart factory of industry 4.0: Key technologies, application case, and challenges. Ieee Access, 6, 6505-6519.
24. Dutta, P., Choi, T. M., Somani, S., & Butala, R. (2020). Blockchain technology in supply chain operations: Applications, challenges and research opportunities. Transportation research part e: Logistics and transportation review, 142, 102067.
25. Tiwari, S., Bahuguna, P. C., & Srivastava, R. (2023). Smart manufacturing and sustainability: a bibliometric analysis. Benchmarking: An International Journal, 30(9), 3281-3301.
26. Bakshi, B. R., & Fiksel, J. (2003). The quest for sustainability: Challenges for process systems engineering. AICHE journal, 49(6), 1350-1358.
27. Vijayavenkataraman, S., Yan, W. C., Lu, W. F., Wang, C. H., & Fuh, J. Y. H. (2018). 3D bioprinting of tissues and organs for regenerative medicine. Advanced drug delivery reviews, 132, 296-332.
28. Zhang, Q., Huang, J. Q., Qian, W. Z., Zhang, Y. Y., & Wei, F. (2013). The road for nanomaterials industry: A review of carbon nanotube production, post-treatment, and bulk applications for composites and energy storage. small, 9(8), 1237-1265.

A Comprehensive Review of Cryogenic Treatment Effects on Tool Hardness, Wear Resistance, and Microstructural Transformations

Mr Mohan L Chanpur and Dr Sandeep H Wankhade

AISSMS College of Engineering, Pune – 01

mlchanpur@aissmscoe.com
shwankhade@aissmscoe.com

Abstract. Cryogenic treatment is a complex method for processing materials that is known to greatly improve the mechanical qualities of tools used in many industrial settings. This thorough review looks at how cold treatment changes the microstructures of tools and how hard they are, as well as how resistant they are to wear. This study looks at both shallow and deep cryogenic treatments. It considers soaking duration, temperature ranges, and cooling or warming rates to improve treatments. Tests are done on high-speed steels (HSS), carbide inserts, and powder metallurgy (PM) steels to see how these techniques influence them. The paper details how freezing causes tools to harden, such as austenite loss and fine carbide formation. Vickers and Rockwell hardness scales are often used to quantify hardness variations. Comparative investigations of treated and raw tool hardness may also aid. The potential for carbide density and distribution to enhance wear resistance is also investigated. Real-world studies have shown that these changes can make a big difference in high-wear areas like the aircraft, automobile, and machine industries. In addition, the study talks about how tool materials change at the microstructural level, such as how residual austenite changes into martensite and fine eta-carbides are made. The use of Scanning Electron Microscopy (SEM), X-Ray Diffraction (XRD), and Transmission Electron Microscopy (TEM) to look at these changes in the structure of the material and how they affect its dynamic features. The significance of artificial intelligence, particularly machine learning models such as Adaptive Neuro-Fuzzy Inference System (ANFIS) and Artificial Neural Networks (ANN), is emphasized in determining the optimal approach to conduct the procedure and forecasting the effectiveness of treatments. A comparison with regular heat treatments shows the pros and cons of mixed systems that use both types of heat treatment. The last part of the paper talks about how cryogenic treatment can be used in industry and how it can help the economy and the environment. It also suggests areas for future research that will focus on sustainability, new materials, and better modelling methods to make these treatments even better for use in industry.

Keywords: Cryogenic Treatment, Tool Hardness, Microstructural Transformations, Artificial Intelligence Optimization, Mechanical Property Enhancement

1 Introduction

Cryogenic treatment is a complex method used to work with materials that is at the heart of improving the mechanical qualities of tools used in many fields. During this process, tools are heated to very low temperatures, usually below -190 degrees Celsius, to smooth out their grain and make them work better in ways like strength, wear resistance, and general life span. An important benefit of cold treatment is that it can greatly increase the useful life of tools, which lowers costs and improves the efficiency of production [1]. The goal of this review is to go into great detail about how cold treatment changes the hardness, wear resistance, and microstructural changes of tools. This will give us a full picture that could help us come up with new ways to build and maintain tools in the future. In factories, the performance of the tools is very important because the speed and quality of production rely on how reliable and long-lasting the tools are. The main things that affect how long a tool lasts are its hardness and its resistance to wear. The hardness of a tool decides how well it resists bending and wear, which is important for keeping the accuracy of cutting and shaping processes. The tool's wear resistance, on the other hand, refers to how well it can handle normal wear and tear over time, ensuring steady performance and reducing the number of times it needs to be replaced. The microstructure of tool materials is very important in these areas because it determines how tools react to forces and situations outside the tool. The use of cryogenic treatment can completely change the way tools are improved. The treatment changes the crystalline structure of the material by putting tools through very low temperatures, usually in two steps: first they are cooled to below zero temperatures, and then they are slowly warmed back up. When steel is heated, one of the main results seen is the change from residual austenite, a soft and unstable phase, to martensite, a much harder and more stable

phase. These changes are made even better by the creation of fine carbides inside the steel core, which makes it harder and more resistant to wear.

The specifics of cryogenic treatment depend on the type of treatment used (shallow or deep cryogenic treatment) and the conditions used, such as how long the material is exposed to the cryogenic environment and how fast it is heated during the cooling phase. These factors are very important because they decide how big and even the changes in the microstructure are, which in turn affects the tool's mechanical features. Also, cryogenic treatment has different effects on different materials, such as high-speed steels, carbide inserts, and powder metallurgy steels. This means that picking the right process settings is very important, taking into account the tool material and the qualities that are wanted. In addition to changing the way the material looks, cold treatment also changes how the carbides are distributed and how dense they are in the material. Because a more even spread of carbides helps fight wear and keep cutting edges sharp and precise, this rearrangement is very important for making the tools last longer. Advanced measuring methods, like Vickers and Rockwell hardness tests, scanning electron microscopy (SEM), X-ray diffraction (XRD), and transmission electron microscopy (TEM), are used to find out how much these improvements are and to show that cold treatment works.

1.1 Background and Importance of Tool Performance

The performance of industrial tools is pivotal across various applications, significantly impacting productivity, efficiency, and cost-effectiveness. Tool hardness, wear resistance, and microstructure play crucial roles in determining the longevity and functionality of these tools.

A. Tool hardness: It is essential because it directly influences a tool's ability to maintain its shape and sharpness under stress, making it resistant to deformation and penetration. This characteristic is especially crucial in cutting and machining operations where exactness is foremost for keeping up the quality of the work piece and the speed of generation.
B. Wear resistance: It is another critical attribute, as it determines how well a tool can withstand the constant friction and abrasion it encounters during operation. Higher wear resistance deciphers into less visit instrument substitutions, decreased downtime, and lower upkeep costs. This property is particularly profitable in businesses such as mining, development, and metal creation, where apparatuses are subjected to unforgiving working conditions and materials that can quickly corrupt their surfaces.
C. The role of microstructure in tool materials: The tool material's toughness, hardness, impact resistance, and wear resistance depend on grain arrangement and size. Fine-tuned microstructures, accomplished by cryogenic treatment, may give denser carbides and more homogenous micro-constituents. Through microstructural optimization of hardness and wear resistance, apparatuses gotten to be more tough and proficient and can work beneath troublesome circumstances in a wide assortment of mechanical applications. The combination of these criteria ensures that tools match application needs and streamline and reduce industrial costs.

1.2 Overview of Cryogenic Treatment

Cryogenic treatment improves metal microstructure hardness, wear resistance, and toughness. Depending on the material and desired attributes, the tool material is stored at cryogenic temperatures for a few hours to over 24 hours after progressive cooling. This step is significant because it converts remaining austenite to martensite, a harder, more stable phase. This enhances tool wear and durability. The material is progressively warmed to room temperature after soaking, and post-tempering is typically done to reduce thermal tensions and stabilize the new microstructures.
In homogenizing the tool's microstructure, cryogenic treatment excels. This technique increases martensite volume and refines carbide dispersion in the metal. The mechanical properties of the tool are greatly influenced by these microstructural changes. Fine carbides that precipitate throughout the matrix enhance hardness and density, improving wear resistance and toughness. This treatment works well on high-speed steels, carbide, titanium, and other alloy steels. Every material reacts differently to cryogenic treatment, therefore optimizing treatment conditions for each application is necessary. Cryogenic treatment is used in automotive, aerospace, and industrial sectors where tools must survive extreme wear and stress.
Also, cryogenic therapy is a complement to heat treatment. Combining it with quenching and tempering stabilizes the steel structure and improves its mechanical qualities. Due to tool longevity and industrial downtime savings, cryogenic treatment typically pays for itself. Cryogenic treatment's applicability and effectiveness are expanding as molecular knowledge improves. As companies seek to increase tool efficiency and durability, cryogenic treatment is a fundamental material science approach that improves important component quality and

performance. Figure 1 shows a basic setup for a cryogenic treatment system. It has a tank of liquid nitrogen that is linked to a cryogenic room by a solenoid valve. A temperature controller connected to a thermometer controls this setup. An airflow fan makes sure that the temperature is the same all over the room

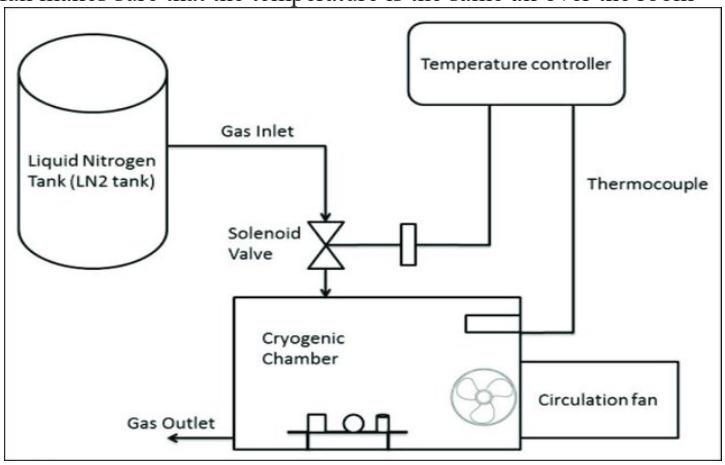

Fig. 1. Representation of Process for cryogenic process

The complete examination of cryogenic treatment on device materials appears impressive mechanical property enhancements, eminently in hardness and wear resistance. Cryogenic treatment, which includes cooling materials to cryogenic temperatures and after that warming to room temperature, causes microstructural changes like held austenite to martensite and fine carbides, agreeing to considers. These enhancements are fundamental for instrument toughness and execution in mechanical applications [2, 3, 4]. Solid experimental information underpins cryogenic treatment's convenience in expanding instrument life and making strides wear resistance. High-Speed Steel (HSS) and tungsten carbide devices function better with reduced wear rates and increased hardness following cryogenic handling. These developments will benefit the automotive, mechanical, and aviation industries, which rely on the accuracy and durability of their equipment [5, 6, 7]. AI and machine learning models like ANNs and ANFIS can expect and optimize cryogenic treatment comes about by modifying temperature and dousing length. AI integration may progress cryogenic instrument generation exactness and viability [8, 9]. The financial and natural impacts of cryogenic treatment are noteworthy. Figure 2 shows the various types of cryogenic treatment.

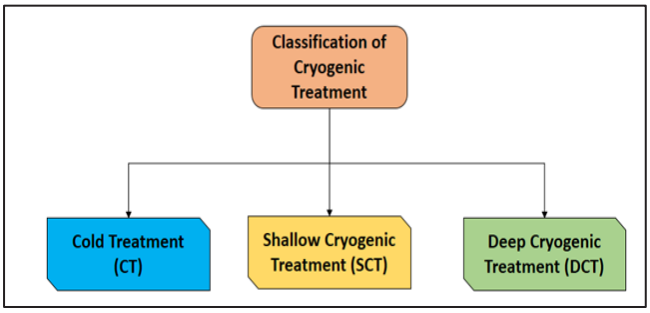

Fig. 2. Type of Cryogenic Treatment

1.3 Research Objectives

The following describes the study goals of this thorough analysis of how cryogenic treatment affects tools:

- Examine Tool Hardness Improvements: To methodically assess the effects of cryogenic treatment on the hardness of different tool materials, such as carbides, high-speed steels, and other alloyed metals. Investigating the degree to which hardness, durability, and performance under operating pressures are increased is part of this goal.
- Examine Improvements in Wear Resistance: To investigate how cryogenic treatment might increase wear resistance. This entails analysing how the treatment affects tool wear rates in various operating scenarios and comprehending how these improvements might result in extended tool life and lower maintenance expenses.
- Examine Microstructural Transformations: To examine the microstructural alterations brought about by cryogenic treatment, with an emphasis on the creation and dispersion of fine carbides as well as the conversion

of retained austenite to martensite. Correlating these microstructural changes with enhanced mechanical performance and characteristics is the goal of this mission.

• Comparative Analysis of Conventional therapy Methods: To assess how cryogenic therapy differs from traditional thermal treatment techniques. This entails assessing the synergistic effects of applying both treatments and determining the circumstances in which cryogenic therapy may be more advantageous or, conversely, in which conventional techniques may still be more effective.

2 Cryogenic Treatment Processes

2.1 Types of Cryogenic Treatments

A. Shallow Cryogenic Treatment (SCT): Shallow Cryogenic Treatment cools material to -80°C to -145°C. The material and usage determine how long the procedure takes, from a few hours to a day. Light metals and certain polymers that cannot withstand deep cryogenic treatments are treated with SCT [10]. SCT reduces material tensions without altering its architecture. This method is often used to treat aluminum alloys and plastic molds, where even small changes to the microstructure can make the shapes more stable and relieve stress. Even though SCT doesn't improve strength and wear resistance as much as Deep Cryogenic Treatment (DCT) does, it still successfully increases the useful life of tools by lowering the chances of stress corrosion cracking and failure before its time, as process illustrate in figure 3.

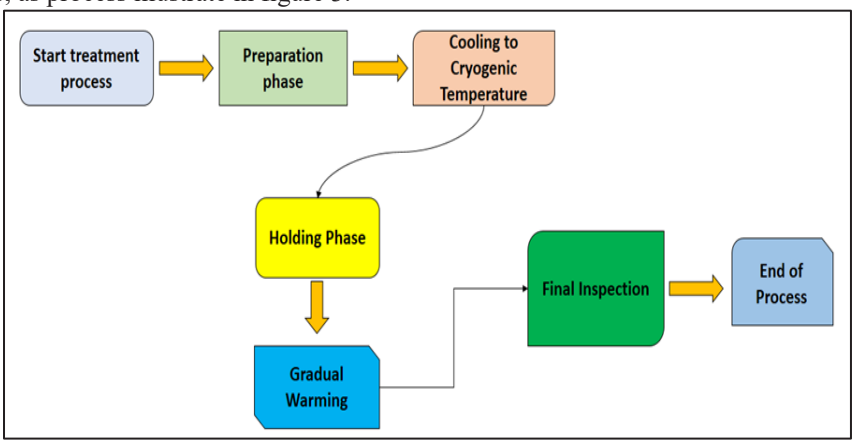

Fig. 3. Process for SCT

B. Deep Cryogenic Treatment (DCT): With Deep Cryogenic Treatment, the temperature of the material drops close to -190°C, which is below the point at which liquid nitrogen boils. The treatment can last anywhere from 24 to 72 hours. After that, the material is slowly heated up to room temperature. DCT [11] is more intense and is mostly used for carbide, high-speed steels, and other strong tool steels. The main thing that DCT does is change the remaining austenite into martensite. This makes the tool much harder and improves the density and spread of fine carbides throughout its matrix. As a result, the wear resistance, impact power, and general longevity all get a big boost. DCT is especially popular in fields that need tools that can handle a lot of wear and tear, like heavy-duty drilling, cutting, and grinding. Because DCT has a significant impact on tool performance, it is the most effective method for extending tool life and improving tool performance in demanding industrial environments.

2.2 Process Parameters

Several process variables, such as soaking time, temperature range, and cooling and warming rates, have a big effect on how well cryogenic treatment works. Controlling every element very carefully is needed to make the tool work better as wanted. Table 1 shows the summary of cryogenic treatment and their impact on the effectiveness of the treatment, following parameters are used for comparison;

Soaking Time: Soaking time is the amount of time that the tool material is kept at its coldest possible state. The length of this time is very important because it decides how much microstructural changes can happen, like residual austenite turning into martensite. If you soak for less time, you might not be able to fully change, which would make the treatment less useful. On the other hand, soaking for too long might not add any benefits and could waste energy. Depending on the material and the level of treatment (shallow vs. deep), soaking times can be anywhere from a few hours to 24 hours or more. For example, deep cold treatments often need longer soak-

ing times to make sure that the whole material of the tool is changed, which is necessary to get the best strength and wear resistance.

Range of Temperatures: The range of temperatures used during cryogenic treatment is another important factor that affects how the process turns out. Deep cryogenic treatments use temperatures close to -190°C, while shallow cryogenic treatments use temperatures between -80°C and -145°C. The temperature must be low enough to cause the microstructural changes that are wanted without making the material weak or causing thermal shock [16]. The type of material and its original texture determine the exact temperature range that is used. For metals like high-speed steel and carbide, which are used in high-performance tools, to get their features much better, they usually need to be cooled to much lower temperatures.

Cooling and Warming Rates: How quickly the material is cooled and then brought back up to room temperature is also very important to the success of cryogenic therapy. Controlling the rate of cooling helps keep thermal stresses from happening, which could cause cracks or other damage to the structure. Usually, the rate of cooling should be slow enough to let the material's temperature drop evenly, so there aren't any thermal differences that could damage the tool. It is also important to carefully control the rate of heat after soaking to keep the newly formed microstructures, especially the martensite, from becoming unstable. Rapid heat could cause uneven growth, which could put new pressures on the material.

Table 1. Summary of cryogenic treatment and their impact on the effectiveness of the treatment

Aspect	Description	Impact on Treatment
Soaking Time	Cryogenic temperatures are maintained for the duration tool.	Longer soaking times allow for more complete microstructural transformations, enhancing hardness and wear resistance. Shorter times may be insufficient for full benefits [12].
Temperature Range	Range within which the tool is cooled.	Shallow treatments use -80°C to -145°C; deep treatments approach -190°C. Deeper temperatures are necessary for significant transformations in robust materials like high-speed steel and carbide.
Cooling Rate	Speed at which the tool is cooled to cryogenic temperatures.	Must be controlled to prevent thermal stresses and ensure uniform temperature reduction, avoiding structural damage or cracks.
Warming Rate	Speed at which the tool is warmed back to room temperature.	Controlled warming is crucial to stabilize new microstructures and prevent uneven expansion or new stress introductions.

2.3 Material Compatibility

More and more businesses are using cryogenic treatment to make tool materials work better by making them harder, more resistant to wear, and more stable at the microstructural level. Cryogenic treatment affects different materials in different ways. To get the best results from the treatment, it is important to know how each type of material works with others and how it reacts to the treatment. Table 2 shows the response of various tool materials to cryogenic treatment, considering key parameters listed below;

- High-Speed Steel (HSS): This type of steel is used to make drill bits, milling tools, and taps. Cryogenic treatment makes HSS harder and more resistant to wear by changing the austenite that is still present into martensite and smaller carbide patterns [14].
- Carbide Inserts: These are commonly used in cutting and grinding processes. They are usually made from tungsten carbide and have better grain development and spread of carbides, which makes them last longer and work better.
- Powder Metallurgy (PM) Steels - Cryogenic processing improves the microstructural consistency and performance of PM steels, which are used in precision tools and parts. This makes their wear qualities and physical stability even better.
- Tool Steels - Tool steels are used to make dies, punches, and cutting blades. They come in types like D2, A2, and M2. The cryogenic process helps to harden things more deeply and make them more resistant to wear.
- Stainless Steels: These are used in medical equipment and tools for handling food. Cryogenic treatment makes them more resistant to wear and gives them a more stable microstructure.
- Titanium Alloys: These are often used in medical and military settings. When treated with cryogenics, they become stronger and less likely to wear down because the microstructural features are fine-tuned.
- Aluminum Alloys: Despite their rarity, shallow cold procedures can improve the thermal stability of aluminium alloys by reducing residual pressures.
- Copper Alloys: Copper alloys are used in heat and electrical wires. Cryogenic treatment can make them a little harder and more resistant to wear.

• Nickel Alloys: Nickel alloys can be used in high-temperature situations and can become more resistant to wear and rust after being frozen.

Table 2. Response of various tool materials to cryogenic treatment, considering key parameters

Tool Material	Enhanced Properties	Typical Applications	Benefits of Cryogenic Treatment
High-Speed Steel (HSS) [11]	Wear resistance, Hardness	Drills, Milling cutters, Taps	Increases hardness and wear resistance through transformation of austenite to martensite and carbide refinement.
Carbide Inserts [12]	Grain refinement, Durability	Machining operations	Enhances durability and performance with better grain and carbide distribution.
Powder Metallurgy (PM) Steels [14]	Wear properties, Dimensional stability	Precision tools and components	Optimizes microstructural uniformity for superior wear properties and dimensional stability.
Tool Steels [17]	Hardening depth, Wear resistance	Dies, Punches, Shearing blades	Deep hardening effects improve wear resistance and tool longevity.
Stainless Steels [18]	Wear resistance, Microstructural stability	Food processing tools, Medical instruments	Increased wear resistance and stability suitable for hygienic and sterile applications.
Titanium Alloys [19]	Strength, Wear resistance	Aerospace and medical applications	Enhanced strength and wear resistance for critical, high-performance applications.
Aluminum Alloys [20]	Thermal stability, Reduced stresses	Less common applications	Improves thermal stability and reduces residual stresses for specific applications.
Copper Alloys	Hardness, Wear resistance	Electrical and thermal conductors	Slight improvements in hardness and wear resistance enhance performance in conductive applications.
Nickel Alloys [21]	Wear and Corrosion resistance	High-temperature applications	Improves resistance to wear and corrosion under extreme conditions.
Bearing Steels [22]	Hardness, Wear rate	Roller and ball bearings	Increases hardness and reduces adhesive wear, extending bearing life.

3 Impact on Tool Hardness

3.1 Mechanisms of Hardness Improvement

Cryogenic treatment significantly enhances the hardness of tool materials primarily through two key mechanisms: residual austenite is reduced and fine carbides are formed. Retained austenite is a softer part of steel that can make it less hard and less stable in its shape. When this austenite is frozen, it changes into martensite, which is a solid structure that is much harder and more rigid. The change happens because the temperatures below zero make the transfer more thorough than what can be done with normal cooling. The hardness and structural stability of the material both get better with this change [13].

Also, treating something with cryogenics makes tiny carbides form in the material's matrix. These carbides are very hard bits that are spread out in the metal and stop dislocations from moving. Dislocation movement is a key way that materials change shape when they are stressed. This spreading out makes the metal's grid structure stronger, which makes it much harder. Studies have shown that the shape, mass, and spread of these carbides are very important for making the tools harder and more resistant to wear. Because cryogenic treatment smooths out the nanoscale in such great detail, it makes sure that tools can handle more operating stress and last longer.

3.2 Measurement and Quantification

Several measurement methods are used to figure out how the changes in hardness caused by cold treatment are felt. The Vickers and Rockwell hardness tests are the most popular. These tests give us numbers that we need to figure out how well cold methods work on different types of tool metal.

• Vickers Hardness Test: This test is very popular because it can be used to find out how hard any metal is and give a constant scale of hardness. To do this, a given force is applied to a diamond pyramid indenter that is pushed into the substance. The size of the resulting depression is then measured, and the hardness value is found by using the measurement and the force that was used to make the depression. When measuring hardness, the

Vickers test is very helpful for materials that have different amounts of hardness or when accuracy is very important.

• Rockwell Hardness Test: The Rockwell test is another well-known way to compare how profound an indenter can go into a fabric when it is beneath a huge stack and when it is beneath a little stack to begin with. This test is speedier than the Vickers test and is ordinarily utilized on materials that are greater and heavier or when speed is exceptionally imperative. It gives readings of hardness on various scales, such as C, B, A, etc., based on the type of indenter used and the measuring load. This method is helpful because it works quickly and doesn't require much preparation of the material.

3.3 Comparative Studies

A research found that cryogenics works by comparing tool hardness before and after treatment. These investigations examine PM, HSS, and carbide insert tool materials. Regular cold treatment makes these materials tougher, making tools operate better and last longer. Here is a list of the most important research findings:

• High-Speed Steel (HSS): An important study on HSS tools found that deep cold treatment made them much harder by changing the austenite that was still there into martensite and causing smaller carbides to form in the steel matrix. Rockwell and Vickers hardness tests were used to measure the changes in hardness. Compared to samples that had not been handled, the hardness numbers went up by about 7 to 10%. These improvements made the tools last longer and fight wear better in tough cutting jobs.

• Carbide Inserts: Studies with carbide tools, especially tungsten carbide, showed that freezing them improved the structure of the grains and made more carbide crystals form. Vickers hardness testing was used in the studies, and the results showed that the tools were much harder than raw carbide tools, usually by 5 to 15%. When it came to high-precision cutting, this improvement made the tools much better.

• Powder Metallurgy (PM) Steels: Research on PM steels that were treated with cold methods showed that they became harder because the composition of the material became more uniform and the carbide distribution improved. Both the Rockwell and Vickers hardness tests showed that PM steels that had been cryogenically treated had better wear resistance and a higher total hardness profile by about 8 to 12% more than steels that had not been treated.

• Comparative Analysis of Different Types of Tools: One thing that all of the studies agree on is that tools that go through deep cold treatment get much harder and perform better as a result than tools that go through shallow or no treatment. The long cooling times at very low temperatures are very important for changing austenite completely into martensite and getting the most carbide to form.

4 Enhancement of Wear Resistance

4.1 Factors That Affect Wear Resistance

The wear resistance of tools is greatly improved by freezing them. This is because the freezing process changes the distribution and quantity of carbides in the material. Carbides are hard bits that can make a material much more resistant to wear if they are spread out very finely. During the cold process, the change of residual austenite into martensite and the following formation of carbides happen more completely and evenly. This even spread of small carbides throughout the matrix of the tool stops dislocations from moving, which is one of the main ways that materials change shape when they are loaded. In addition, these carbides lower the size of the material's grains, which makes it harder and, as a result, more resistant to wear. Overall, this makes a tool that can handle higher working loads and last longer without wearing down. This is especially helpful for cutting, drilling, and other tasks that involve a lot of friction.

4.2 Studies Based on Real Life on Wear Resistance

The use of cold treatment to make tools more resistant to wear has been shown in many real-world studies. For example, a research using cryogenically treated HSS drills revealed that they wore significantly less during demanding drilling operations, with wear resistance increasing by up to 50% when compared to untreated drills. In another investigation, the cold treatment of carbide inserts that were used to mill hard metals resulted in a reduction of approximately thirty percent in the amount of tool wear. This made the tools last longer and meant they needed to be replaced less often. Standardized grinding and cutting tests are usually used in these studies to

measure wear resistance. The amount of material lost from treated and untreated tools under the same working conditions is compared.

4.3 Applications in High-Wear Environments

Cryogenic treatment can make things more resistant to wear, which has big effects in many high-wear areas, like the aircraft, automobile, and machine industries. More wear resistance means fewer tool changes, better accuracy, and a more efficient machining process as a whole. This is because tools in machining are constantly in touch with hard surfaces. This is very important for keeping the surface finish and accuracy of machined parts, especially those with complicated shapes or made from materials that are hard to machine.

In the car business, tools that are used to cut and shape engine parts must be able to handle high temperatures and pressures. This makes wear resistance a very important feature. Tools that have been frozen make production lines more reliable, which cuts down on downtime and repair costs. In the same way, tools that can keep their cutting edge and structural stability under high stress are important in the aircraft business, which uses a lot of materials like titanium and high-strength metals. Cryogenic treatment makes things more resistant to wear, which makes production more uniform. This is important for meeting the aircraft industry's strict safety and quality standards. Table 3 shows the summary of key aspects of wear resistance enhancement through cryogenic treatment.

Table 3. Summary of key aspects of wear resistance enhancement through cryogenic treatment

Aspect	Details	Impact on Wear Resistance	Industry Applications
Mechanisms Affecting Wear Resistance	Changes in carbide distribution and density, transformation of austenite to martensite [15].	Improved barrier to dislocation movement, reduced grain size enhances hardness and wear resistance.	Applicable across all industries using metal tools.
Empirical Studies on Wear Resistance	Studies show significant reductions in tool wear; HSS drills and carbide inserts tested.	Up to 50% improvement in HSS drills, 30% in carbide inserts.	Useful for evaluating treatment effectiveness and guiding industrial applications.
Applications in High-Wear Environments	High wear resistance critical in machining, automotive, and aerospace industries.	Fewer tool changes, higher precision, and greater efficiency.	Machining: Maintains accuracy and finish; Automotive: Ensures reliability of production lines; Aerospace: Meets stringent safety and quality standards.

5 Microstructural Transformations

5.1 Transformation Mechanisms

Microstructural transformations are central to the effectiveness of cryogenic treatment in improving tool performance. The primary transformations involve the reduction of retained austenite to martensite and the formation of fine eta-carbides and other hard phases.

A. Reduction of Retained Austenite to Martensite: Tools that need high hardness and wear resistance should avoid retained austenite, a softer and more ductile phase in steel and other alloys. Cryogenic treatment turns residual austenite into martensite, a tougher, more stable crystalline structure. The cryogenic process's ultra-low temperatures enable austenite in steel to become martensite. This new martensite greatly boosts the material's hardness and strength. The entire transformation also lowers volume changes from subsequent phase transformations under operating stress, improving tool dimensional stability.

B. Formation of Fine Eta-Carbides and Other Hard Phases: In addition to martensitic transformation, cryogenic treatment promotes the precipitation of fine eta-carbides within the tool's microstructure. These carbides are incredibly troublesome little particles that reliably scatter all through the metal organize, giving staying centers that hinder separation advancement. This prevention contributes to the material's extended hardness and basically updates its wear resistance. The formation of these carbides fills the interstitial spaces within the martensite lattice, further stabilizing the structure against deformation under load.

5.2 Microstructural Analysis Techniques

Understanding and documenting these microstructural changes require sophisticated analysis techniques that can observe these changes at the microscopic level:

Scanning Electron Microscopy (SEM): SEM offers high-resolution imaging that helps in visualizing surface morphologies and microstructural features, such as carbide distribution and martensitic structures. It is instrumental in analyzing wear patterns and the efficacy of cryogenic treatments.

X-Ray Diffraction (XRD): XRD is crucial for identifying the phases present in the material after cryogenic treatment. It can quantitatively measure phase transformations, such as the conversion of austenite to martensite, and detect the presence of various carbides and other phases.

Transmission Electron Microscopy (TEM): TEM provides even greater magnification than SEM, allowing for the observation of the material's internal structure at the atomic level. This is particularly useful for identifying the size, distribution, and nature of carbides and other precipitates formed during cryogenic treatment.

6 Role of Artificial Intelligence in Cryogenic Treatment Optimization

6.1 Models for Machine Learning

It is very important to use artificial intelligence, especially machine learning models like Artificial Neural Networks (ANN) and Adaptive Neuro-Fuzzy Inference System (ANFIS), to predict and improve the results of cold treatment methods. These AI models can see at tremendous sums of information from prior medications to discover patterns and figure how changes to the method will influence the materials' quality and resistance to wear.

Artificial Neural Networks (ANN) are extraordinary for modelling complicated, nonlinear connections, just like the ones between the parameters of a cold treatment and the qualities of the instrument that comes out of it. By gaining experience on datasets that include variables such as time, temperature, fabric type, and previous mechanical features, artificial neural networks (ANNs) can learn to make extremely accurate predictions regarding the functioning of potential treatments. This capacity to anticipate long-term is exceptionally supportive for arranging and moving forward treatment rounds because it lets changes be made some time recently the method begins, which spares time and resources.

The Adaptive Neuro-Fuzzy Inference System (ANFIS) may be a demonstration that uses neural networks and fuzzy reasoning to make sense of information in a manner similar to how humans do it, successfully handling instability and the need for accuracy. The ANFIS modelling method can be used to fine-tune the cold treatment processes by adapting to the specifics of different tool materials and the results that are wanted. It can, for instance, guess how small changes in the cooling rate or soak time might impact the hardness and texture of certain types of steel, which makes it possible to create very specific treatment methods.

6.2 Case Studies

Artificial intelligence in cryogenic treatment techniques has improved tool material properties across industries. Here are numerous case examples showing how AI has improved various treatments:

1. Optimizing Automotive Component Cryogenic Treatment: A major automaker optimized cryogenic treatment of high-speed steel engine components using AI, especially an ANN model. The AI model was trained using prior treatment settings and wear resistance measurements. The business was able to accurately anticipate the appropriate soaking time and temperature for maximum hardness and wear resistance using this model. This improvement increased engine component longevity by 20%, lowering maintenance costs and improving vehicle performance.

2. ANFIS Improves Aerospace Tooling: The Adaptive Neuro-Fuzzy Inference System (ANFIS) improved cryogenic treatment of aerospace tooling titanium alloys. Based on toughness and wear resistance, the AI system automatically adjusted treatment settings. Real-time data and AI predictions helped the business fine-tune the process to give treated alloys a more homogeneous microstructure, improving their performance in high-stress situations. This increased tool life by 30%, lowering aerospace production tooling costs and downtime.

3. AI-driven Cryogenic Cutting Tool Processing: Machine learning was used to improve cryogenic treatment for carbide inserts by a metal fabrication cutting tool maker. The company found the best cooling rate and temperature to improve wear resistance without sacrificing tool integrity by utilizing a machine learning model to examine process variables and tool performance. AI-enabled optimization reduced tool wear, improved cutting accuracy and efficiency, and reduced tool replacements.

4. Academic Research Application: A university research team studied powder metallurgy steels after cryogenic treatment using machine learning. The researchers used regression models to estimate how cooling rates and soaking durations affected steel hardness and microstructure. The AI analysis helped build a better cryogenic treatment technique, which industrial partners used to improve PM steel component performance in high-wear applications.

These case studies show that AI can optimize cryogenic treatment methods for various materials and industries. Companies may save money and increase operational efficiency by using predictive models and adaptive learning systems to improve tool durability and performance.

7 Comparison with Conventional Heat Treatment

7.1 Advantages of Cryogenic Treatment

There are several reasons why cryogenic treatment is better than traditional heat treatment, especially when it comes to enhancing the mechanical and physical qualities of tool materials:

Lower Tool Wear Rates: Cryogenic treatment lowers tool wear rates by a large amount. Tools last longer under practical pressures because they change the austenite that is still present into the more solid martensite and cause fine carbides to form. In industries where tools are used often, this means that the tools last longer and require fewer replacements.

Increased Hardness: The changes in the microstructure that happen during cold treatment, especially the rise in martensitic content and carbide density, make the material much harder. This increased hardness is good for cutting and high-stress situations where keeping the edge straight and not deforming is important.

Microstructural Refinement: The microstructure of metals can be made more regular with cryogenic treatment than with normal heat treatment alone. This improvement raises mechanical qualities like toughness and tensile strength. This makes the tools not only stronger but also better at handling changing loads.

7.2 Limitations and Considerations

There are many good things about cryogenic treatment, but there are also some things that mean traditional heat treatment might still be better:

Cost: The energy and cooling equipment required to reach extremely low temperatures make cryogenic treatment more expensive. Conventional heat treatment is still a cheaper option for some uses, especially when the small improvement in tool performance doesn't make up for the extra cost.

Material Compatibility: Cryogenic treatment doesn't work the same way on all materials. For example, materials that don't have a lot of residual austenite might not get much better after the process. If the qualities of the material don't work well with the benefits of cold treatment, normal heat processes might work better.

Complexity of the Process: Compared to traditional heat treatments, cryogenic treatments are more difficult to understand and need more careful control over the treatment settings. Sometimes, this level of complexity can get in the way of smaller tasks or uses where exact control doesn't provide a sufficient benefit.

7.3 Hybrid Approaches

To get the most out of both cold and regular heat processes, combined ways have been created that improve the performance of tools by using both:

Sequential Treatment: Usually, tools are heated in a normal way to make them stronger and tougher, and then they are frozen to make them even harder and more resistant to wear. This step-by-step process makes sure that the tools get the benefits of both treatments, like how hardening makes them tougher and how cryogenic processing makes them more resistant to wear.

Integrated Treatment Cycles: Some newer treatment cycles combine several steps of heat treatment with cold treatment. As an example, a tool could be cooled, frozen, and then heated again. This unified method can help get a smoother microstructure and get rid of any stresses that were added during the initial cooling.

These combined methods make it possible to optimize tool materials in a more personalized way. They offer a balanced solution that takes advantage of the unique benefits of both cryogenic and traditional heat treatments. This adaptability is especially helpful for high-performance uses in the aircraft, automobile, and precise machining fields.

8 Applications and Industrial Relevance

8.1 Case Applications

Cryogenic treatment has been used successfully in many fields, all of which benefit from the better qualities of tools and parts that have been through this advanced process:

In the metal cutting and drilling industry, tools that have been treated with cryogenically show a big increase in their strength and resistance to wear. This directly leads to more efficient and accurate cutting operations. For example, drill bits and end mills that have been treated with cold processes wear less and last longer, which means that they don't need to be replaced as often during high-volume manufacturing processes. In fields like making cars and heavy machinery, where downtime for tool changes can have a big effect on production times and prices, this is especially helpful.

Aerospace: Because aircraft parts have to work very well, the automotive business gains from cold treatment. The tools that are used to make things out of high-strength metals and composites must be able to handle a lot of stress and wear without breaking. Tools that have been treated with cryogens are better able to keep their shape under these high-stress situations, making sure that aircraft parts are precise and reliable. Also, aerospace-grade materials like titanium and nickel-based metals have better toughness and wear resistance, which can make parts last longer and make planes safer and more reliable.

Automotive: When making cars, the accuracy and dependability of the tools used are very important to meet the high standards of the business. When cutting tools are used to make engine parts, transmission parts, and other important parts, freezing them can make the bounds more tightly and the surfaces flatter. The process also helps tools last longer, which is important for keeping production lines running smoothly and reducing the amount of time spent on repair.

8.2 Economic and Environmental Implications

Cryogenic treatment has big effects on the economy and the environment, helping to save money and make businesses more ecologically friendly:

Cost Savings: The biggest clear economic benefit of cold treatment is that it makes tools last longer, which lowers the costs of replacing and maintaining them by a large amount. Tools might be used for extended periods of time before needing to be changed thanks to cryogenic treatment, which also improves their resistance to wear. This saves money and speeds up production. Being able to keep accuracy for longer periods of time also lowers the number of faulty goods, which cuts down on trash and costs even more.

Environmental Benefits: Cryogenic treatment is good for the environment in a number of ways. In the first place, the treatment makes tools last longer, which means that they don't have to be made as often, which saves resources and energy. Additionally, less tool wear and tear means less metal chips and other waste is made during cutting processes. This can help reduce the damage that getting rid of waste does to the environment. Lastly, tools that are more efficient and last longer use less energy per unit of production. This helps lower the carbon footprint of industrial activities.

9 Future Research Directions

9.1 Emerging Materials and Techniques

There is a chance to use cold treatment in more areas because tool materials and treatment methods are always changing. In the future, researchers might look into brand-new tool materials like advanced ceramics, ultra-high-strength steels, and composite materials that are being used more and more in technological domains like aviation and biology. Finding out how these materials react to being frozen could lead to new ways to improve their features even more. It might also be possible to make mixed treatments that improve tool performance by combining cold treatment with other surface improvement methods like Physical Vapor Deposition (PVD), Chemical Vapor Deposition (CVD), and laser treatment. These mixtures could make tools and parts harder, more resistant to wear, and less likely to rust, which would help them meet the complex needs of modern industrial settings.

9.2 Enhanced Modelling and Simulation

Advancements in AI and computational methods offer promising avenues for optimizing cryogenic treatment processes. More accurate AI models and re-enactments are needed in order to predict the outcomes of cryogenic drugs under various settings more precisely. Understanding the intricate relationship between various treatment parameters and textural reactions might be aided with progressed illustrations. Future explore need to middle on making overwhelming prescient models that connect machine learning and restricted component examination to recreate the physical changes that happen in the midst of cryogenic treatment. These models can be invaluable for optimizing treatment traditions custom fitted to specific materials and pined for properties, diminishing exploratory costs and speeding up the headway of present day applications. Furthermore, real-time monitoring and adaptive control systems based on AI could be developed to dynamically adjust treatment parameters, ensuring optimal outcomes consistently.

9.3 Sustainability Considerations

As global emphasis on sustainability grows, the environmental impact of manufacturing processes, including cryogenic treatment, is becoming increasingly significant. Future inquire about ought to investigate ways to form cryogenic medications more energy-efficient and naturally inviting. This seem incorporate creating unused advances or forms that lower the vitality utilization required to attain ultra-low temperatures or reusing the vitality utilized within the cooling prepare. Moreover, exploring the lifecycle impacts of cryogenically treated apparatuses, from fabricate to transfer, may offer assistance in understanding and moderating the natural impression of these forms.

10 Conclusion

The in-depth study of cold treatment shows that it has a big effect on making tools harder, more resistant to wear, and changing their microstructure, which makes it an important process in many industrial settings. The study looks into both shallow and deep cryogenic treatments to see how they improve the performance of tools by finding the best soaking time, temperature range, and cooling rates. These processes work especially well on materials like powder metallurgy steels, high-speed steels, and carbide inserts, which are important in fields that need things to last a long time and do a good job. The study also shows how advanced techniques like SEM, XRD, and TEM can be used to look at these microstructural changes. It confirms that retained austenite changes to martensite and that fine eta-carbides are formed, which are essential for the improved mechanical properties seen in tools that have been treated. Aside from that, the study shows how important artificial intelligence is for predicting treatment outcomes and finding the best process parameters. This is a significant step in the direction of more technologically focused and successful manufacturing methods. By contrasting cold treatment with regular heat treatment, the advantages of a mixed method are stressed, indicating that mixing these treatments can lead to better tool performance. The review doesn't shy away from talking about the economic and environmental effects. They could have lesser of an impact on the environment since they use less energy and produce less waste, and they will last longer, which will save money. The study also makes recommendations for future lines of inquiry that center on sustainability issues, improved simulation and modelling, and new materials. These areas promise to refine and expand the applications of cryogenic treatment, pushing forward the boundaries of current manufacturing capabilities and leading to innovations in tool design and maintenance. This ongoing evolution will likely provide substantial benefits across multiple industries, making cryogenic treatment a cornerstone of modern material science.

References

1. Yao, Enze, Huijie Zhang, Kang Ma, Conggang Ai, Qiuzhi Gao, and Xiaoping Lin. "Effect of deep cryogenic treatment on microstructures and performances of aluminum alloys: A review." Journal of Materials Research and Technology, vol. 26, 2023, pp. 3661-3675. https://doi.org/10.1016/j.jmrt.2023.08.140.
2. Nadig, D. S., M. R. Bhat, Pavan V. K., and Chandan Mahishi. "Effects of Cryogenic Treatment on the Strength Properties of Heat Resistant Stainless Steel." IOP Conference Series: Materials Science and Engineering, 2017.
3. Kumar, M., D. Panda, S. K. Behera, and R. K. Sahoo. "Experimental investigation and performance prediction of a cryogenic turboexpander using artificial intelligence techniques." Applied Thermal Engineering, vol. 162, 2019, art. no. 114273.

4. Kumar, S., N. K. Khedkar, and B. Jagtap. "The Effects of Cryogenic Treatment on Cutting Tools." IOP Conference Series: Materials Science and Engineering, 2017.
5. Kumar, M. C., P. Vijayakumar, and B. Narayan. "Optimization of cryogenic treatment parameters to maximize the tool wear of HSS tools by Taguchi method." International Journal of Modern Engineering Research, vol. 2, no. 5, 2012, pp. 3051-3055.
6. Sharma, N., A. Singh, and R. Sharma. "Modeling the WEDM Process Parameters for Cryogenic Treated D-2 Tool Steel by Integrated RSM and GA." Procedia Engineering, vol. 97, 2014, pp. 1609-1617.
7. Gaddi, P., S. V. Mudakappanavar, B. Arya, and S. Manjunath. "Cryogenic treatment effect on tool tip temperature during milling process." Materials Today: Proceedings, 2021.
8. Shandilya, P., P. K. Jain, and N. K. Jain. "RSM and ANN Modeling Approaches for Predicting Average Cutting Speed During WEDM of SiCp/6061 Al MMC." Procedia Engineering, vol. 64, 2013, pp. 767-774.
9. Jadhav, P., S. Kumar, and A. Bongale. "Optimization of cutting forces by cryogenic treatment on tungsten carbide inserts during dry turning of the P 20 tool steel." Materials Today: Proceedings, 2020.
10. Uz, D., M. M. Solomon, H. Gerengi, M. Sahin, and M. Yıldız. "Shallow cryogenic treatment: Effect on the corrosion resistance and hardness properties of AA5083-H111 alloy in chloride-ion-enriched medium." Materials Research Express, vol. 8, no. 7, 2021, art. no. 076516. [https://doi.org/10.1088/2053-1591/ac144d] (https://doi.org/10.1088/2053-1591/ac144d).
11. Yao, Enze, Huijie Zhang, Kang Ma, Conggang Ai, Qiuzhi Gao, and Xiaoping Lin. "Effect of deep cryogenic treatment on microstructures and performances of aluminum alloys: A review." Journal of Materials Research and Technology, 2023. https://doi.org/10.1016/j.jmrt.2023.08.140.
12. Yao, Enze, Huijie Zhang, Kang Ma, Conggang Ai, Qiuzhi Gao, and Xiaoping Lin. "Effect of deep cryogenic treatment on microstructures and performances of aluminum alloys: A review." Journal of Materials Research and Technology, 2023. https://doi.org/10.1016/j.jmrt.2023.08.140.
13. Snopiński, P., A. Woźniak, and M. Pagáč. "Microstructural Evolution, Hardness, and Strengthening Mechanisms in SLM AlSi10Mg Alloy Subjected to Equal-Channel Angular Pressing (ECAP)." Materials, vol. 14, no. 7598, 2021. https://doi.org/10.3390/ma14247598.
14. Kim, Myungjae, Hyokyeong Kim, Jinyong Lee, Jiho Kim, Sooah Kyung, Jongwook Kwak, and Jiwoong Kim. "Effects of Secondary Carbide Addition on the Mechanical Properties of (Ti1-xTMx)C-Based 20Ni Cermets (TM = V, Mo, and W): A Study Combining Ab Initio Calculation and Experimental Results." Materials Technology, vol. 38, no. 1, 2023.
15. Bhadauria, N., S. Pandey, and P. M. Pandey. "Wear and enhancement of wear resistance – A review." Materials Today: Proceedings, 2020. https://doi.org/10.1016/j.matpr.2020.02.616.
16. Gupta, S., G. Parande, and M. Gupta. "Comparison of Shallow (−20 °C) and Deep Cryogenic Treatment (−196 °C) to Enhance the Properties of a Mg/2wt.%CeO2 Nanocomposite." Technologies, vol. 12, no. 2, 2024, pp. 14. https://doi.org/10.3390/technologies12020014.
17. Prasad, S. V. S., S. B. Prasad, K. Verma, R. K. Mishra, V. Kumar, and S. Singh. "The Role and Significance of Magnesium in Modern Day Research-A Review." Journal of Magnesium and Alloys, vol. 10, 2022, pp. 1-61.
18. Liu, L., X. Chen, and F. Pan. "A Review on Electromagnetic Shielding Magnesium Alloys." Journal of Magnesium and Alloys, vol. 9, 2021, pp. 1906-1921.
19. Shang, Y., C. Pistidda, G. Gizer, T. Klassen, and M. Dornheim. "Mg-Based Materials for Hydrogen Storage." Journal of Magnesium and Alloys, vol. 9, 2021, pp. 1837-1860.
20. Lopes, V., H. Puga, I. V. Gomes, N. Peixinho, J. C. Teixeira, and J. Barbosa. "Magnesium Stents Manufacturing: Experimental Application of a Novel Hybrid Thin-Walled Investment Casting Approach." Journal of Materials Processing Technology, vol. 299, 2022, art. no. 117339.
21. Yu, Z., J. Chen, H. Yan, W. Xia, B. Su, X. Gong, and H. Guo. "Degradation, Stress Corrosion Cracking Behavior and Cytocompatibility of High Strain Rate Rolled Mg-Zn-Sr Alloys." Materials Letters, vol. 260, 2020, art. no. 126920.
22. Jia, J., M. Meng, Z. Zhang, X. Yang, G. Lei, and H. Zhang. "Effect of Deep Cryogenic Treatment on the Microstructure and Tensile Property of Mg-9Gd-4Y–2Zn-0.5Zr Alloy." Journal of Materials Research and Technology, vol. 16, 2022, pp. 74-87.

Green Technology & Sustainable Manufacturing

Transforming Plastic Waste into Eco-Friendly Bricks: A Sustainable Approach to High-Density Polyethylene Recycling

Abu Supian Gazi* · Ziyauddin Seikh · Mukandar Sekh

Department of Mechanical Engineering, Aliah University, Kolkata-700160, India.
*Corresponding author's Email id: abumechanical99@gmail.com

Abstract. In today's world, plastic waste especially dangerous kinds like high-density polyethylene (HDPE) along with polyethylene terephthalate (PTE) is a major problem. One efficient mode of plastic waste is to recycle it into new materials like mortar or concrete. Plastic waste (PW) addition in brick fabrication is one way to generate high-strength, lighter-weight bricks as well as good sound qualities in an economical and environmentally responsible manner. Additional benefits of plastic sand brick include resource and economic efficiency as well as a decrease in greenhouse gas emissions. Eco-friendly Bricks, often referred to as plastic sand bricks, are constructed from plastic waste that would otherwise be detrimental to all living things. In contrast to regular clay bricks, it improves the compressive strength (CS). As an environmentally responsible substitute for conventional bricks, the study aims to explore the viability of reusing PW as a reinforcement in brick manufacturing. Four plastic bricks are developed with 0, 5, 10, and 15 wt. % HDPE. Several tests, like compressive strength tests, soundness, water absorption tests, and hardness, are performed on developed brick samples and found significant results. A comparison study between conventional bricks as well as PW bricks was carried out in order to meet the needs of the industry.

Keywords: Plastic Bricks, Waste, HDPE, Building Material.

1 Introduction

Building energy usage has significantly increased during the past ten years. Population expansion, longer periods of indoor activity, increased demand for construction services, indoor ecofriendly value, along with worldwide climate variation are some of the reasons contributing to this increase. The United States, the European Union, and also a greater global framework all exhibit this pattern, with building energy surpassing more than 40% of overall key energy routine. However, concentrating on building design, houses, and operation offers significant potential for energy conservation [1]. Consuming local, ground-based materials should be given priority because transportation is a major factor in the poor environmental performance of building materials. For any future thermal insulation or other covering enhancement, it is crucial to forecast the building envelope's thermal performance [2]. Thorough energy research is not as important to a building's performance as choosing the best wall structures. A building thermal investigation must interpret the impact of moisture-resistant materials. It is found that employing energy-efficient materials lowers energy expenses and improves building heat exchange [3]. One study used low thermal conductivity materials like cellular concrete and expanded polystyrene (EPS) insulation and also sensible thermal conductivity constituents, which enhanced the insulation act of the building [4-6]. Thermal performance is also influenced by the direction of the structure, and it can be enhanced by the right orientation, courtyard design, and shading elements. In building, insulation has been made from a variety of materials. PET is considered a potential substitute for concrete because of its lower thermal conductivity [7-8]. One strategy to lessen pollution and protect natural resources is to use textile waste in building, for example, for thermal and acoustic insulation [9, 10]. Compared to conventional building materials, these materials are said to have superior mechanical and thermal qualities [11]. As a result, it was proposed that utilizing waste materials in building is a novel idea that provides a sustainable substitute for conventional building materials [12]. The study investigated the feasibility of incorporating used plastic bottles as a limited replacement for conventional brick, demonstrating their capacity to prevent cracks from spreading after the initial block construction [13]. Furthermore, a different study using plastic sand bricks [14] found that they were a suitable substitute for traditional clay bricks because they were lightweight and also had a suitable compressive strength. Furthermore, it is noteworthy that plastic sand bricks absorb less water than clay bricks, ranging from 0.9% to 4.5%, which makes them a more insulating building material than clay bricks, which absorb 15% to 20%. As far as the author is aware, a large portion of the study concentrated on the plastic waste brick's mechanical strength rather than its insulating capabilities. The production of plastic bricks has already been the subject of much research, according to earlier studies. Thus, the purpose of

this work is to study how the amount of HDPE affects the created plastic bricks' compressive strength, water absorption, soundness, and hardness characteristics.

2 Review of Research on Building Waste Plastic

Some experiments have been lately performed on recycling PW to building constituents. In one study it is found that the use of recycled polyethylene terephthalate (PET) bottles loaded with aggregates for wall-building purposes. In one study, fine sand-filled waste plastic bottles of five different sizes improved the mechanical quality of PW. It is stated that the compressive value of the largest one is 17.44 MPa [15]. Besides manufacturing a plastic brick-making machine, In one study bricks are test using a new method. In addition, it has been found that plastic-based composite bricks are more effective than bricks made of clay and cement. In another study, fly ash and plastic beads were used as materials for plastic brick fabrication. Bricks were found to be lighter, highly water-absorbing, and showed more compressive strength than red clay bricks. Researcher has been actively producing plastic bricks as well as tiles using fly ash and waste plastics. According to their findings, plastic sand brick has a compressive strength of 5.6 MPa and has no water absorption. From another investigation [19], the feasibility of using torn-out PW to make compressed earth brick. When prepared using shredded plastic trash without additives, the compressive strength was just 0.45 MPa. To increase durability and compressive strength, it is recommended that adhesive binders be added to soil and also PW shreds throughout the brick-making process. The CS of plastic paver blocks is the same as that of concrete paver blocks, as concluded [20] on the use of PW in paver blocks. Some researchers conducted a number of experiments on the properties of plastic sand bricks. According to reports, plastic bricks have been shown to be more efficient than fly ash and third-class red bricks. In an investigation, different types of soil, such as plastic bottles, PET, were used to manufacture plastic bricks: rock crusher, red clay, and river sand. Plastic bricks have been manufactured using three materials: crushed plastics and stone, river sand, and red clay. The CS of this specimen mixture is greater than plastic with red clay and river sand [21-22]. In other study the effect of mix design ratio for sand-based plastic brick are performed. They reported that the mix proportion of 1:2 is ideal as it increases compressive strength with higher values up to 203.56 kg/cm² than the traditional bricks. The water absorption (WA) rate is also superior and ranges between 0.949 and 1.227%. It is reported that burnt clay brick is significantly replaced with recycled cumulative occupied plastic bottles. CS of 25 MPa is developed when bottles used have 10 percent crushed aggregate as well as coarse stone aggregates. Researcher developed eco-bricks using recycled PET bottles; they found that the performance of their eco-bricks outperformed the performance of the red clay bricks. Researcher also examined [26] the effect of brick production on India's agricultural output. India is the world's second major brick maker with a 2-5% yearly growth rate. Brick kilns now occupy about 0.7 million hectares of farming land, which produce approximately 250 billion bricks annually. India's growing brick kilns use topsoil, which is farm-productive, to make bricks, lowering agricultural productivity by 60%–90%. Private farmed land ownership decreased from 0.48 hectares in 1951 to 0.14 hectares in 2013 and 0.08 hectares in 2035, as per a 2010 report. To save agricultural land, alternative building materials need to be developed. HDPE and PP plastic are used for the production of plastic bricks based on physical recycling techniques [27]. The physical, mechanical as well as thermal properties of the bricks produced were examined. According to them, HDPE-based plastic bricks act like typical red clay bricks. Plastic bricks prepared using waste plastics and river sand were also studied for their behaviour [28-29]. The compressive strength was reported to be higher when compared with conventional bricks. Maria Idrees et al. used various proportions of plastic dust in burnt clay bricks for the study of variations in mechanical and physical properties. Final observations showed that an increase in percent plastic dust resulted in lower compressive strength but increased water absorption. It is also reported that WA and CS are within acceptable building standard limits. Ground High-Density Polyethylene (HDPE) was employed by Sabiha Sarwar et al. [30] to prepare plastic bricks and studied their mechanical and physical properties. Bricks with up to 35% HDPE meet the specifications of the building industry. The traditional brick preparation process, being on natural materials, is used in the construction business [31]. Compared to clay bricks, plastic bricks have lower water absorption, stronger compressive strength, lower cost, and less thermal shrinkage; bricks encased in aluminium have a higher fire ignition value [32]. Because of its reduced heat conductivity, PET is being considered as a potential substitute for concrete [33]. In comparison to plastic sand, fly ash bricks, often referred to as ecological plastic sand bricks, have a lower compressive strength. When reinforced with polyethylene terephthalate, they can be utilized in construction. In tests of compression and water absorption, they perform better [34-36]. The building industry seeks alternative sustainable bricks in the requirement to decrease the use of natural resources, which includes clay, sand, and shale, in brick making. LDPE plastic bricks are suitable solutions to the shortage of conventionally produced and environmentally friendly building materials needed by the construction industry. Plastic waste provides all the general properties of building materials, including strength, durability, impermeability, lightweight, easy formability, and recyclability. These wastes can be

converted into sustainable resources that greatly reduce pollution in the environment. Further research is needed to fully understand the properties of the newly developed sustainable bricks from plastic waste. Consequent to this realization, more materials scientists and researchers are currently investigating the performance of plastic waste in different construction techniques. From the literature survey, it is evident that numerous works have been done on the manufacturing process of bricks from several types of plastic waste. In addition to this, findings from previous research are also in favor of decent mechanical properties of bricks prepared from plastic waste. The key objectives of this study are to study the properties of produced bricks and convert single-use (LDPE) PW into bricks along with M-sand. Road construction and plastic bricks have gradually started to use plastic waste as basic raw materials. Therefore, the consumption of raw material in the construction business has two advantages. It reduces environmental pollution on one hand and could lead to the production of inexpensive bricks on the other. Both parties can attain sustainable goals. It entails less usage of natural raw materials and less ecological contamination.

3 MATERIAL & METHODOLOGY

Masonry construction uses bricks as a type of building material for walls, pavements, and other components. Historically, bricks were mostly composed of clay soil, but today they are commonly used to indicate that a brick stands for a masonry element composed of clay, concrete, lime, and also fly ash. Sand and ash. Our project's primary goal is to create affordable, environmentally friendly bricks and find effective ways to repurpose waste plastic. Thus, the readily available items listed below are acquired and utilized in our experiments.

3.1 Plastic waste (HDPE)

Reducing plastic waste and using it efficiently is our primary goal for this research project. As a result, we combined recycled High-Density Polyethylene (HDPE) plastic in varying proportions with other materials to create granules. HDPE was utilized in place of LDPE has a high Melting Flow Index (MFI) and can attain higher compressive strength. The local company is the source of the plastic granules.

3.2 Sand

The river sand is collected from the local river, and after removing unwanted particles with the help of a sieve shaker, it is used to make plastic sand bricks.

3.3 Cement

One of the most crucial components is cement, which provides a binding matrix that enhances the CS of the brick, making it sturdier and more suitable for structural use. Waste plastic, particularly melted plastic, can be used with cement and other aggregates (such as gravel or sand) to form a solid composite. The plastic particles are uniformly dispersed and "locked in" within the brick structure thanks to the binding qualities of cement. Better thermal insulating qualities may be provided by bricks made from cement and plastic. In addition to adding mass that may improve energy efficiency, cement helps preserve the inherent insulating qualities of plastic.

3.4 Water

One of the vital components of construction is water, which is needed for curing work, making mortar, mixing cement concrete, as well as making bricks, among other things. The strength of the cement concrete and mortar during construction is directly impacted by the superiority of the water utilized. Concrete must be mixed with potable water. The maximum amount of suspended solid matter in water is 200 mg/l. The water's pH must not be less than six. The IS Code Recommendations provide the necessary water quantity and quality: Building Construction Water Quality (IS 456:2000).

4 Fabrication of Plastic Waste Brick

The initial step in creating the plastic waste brick was to shred the waste plastic into tiny bits that ranged in diameter from 5 to 10 mm. The discarded plastic utilized in this HDPE, which was obtained from discarded materials such as milk jugs, shampoo bottles, plastic bottles, bottles, bleach cutting boards, and also more, HDPE

uses plastic. Next, the waste plastic that has been shredded is combined with three distinct ratios of sand aggregates: 5:95, 10:90, and 15:85. A mixture of sand and cement is made in a 1:6 ratio, after which water is added to make cement. mortar. The compositions of four developed plastic bricks are given in Table 1. HDPE plastic waste (0.5, 10, 15 wt.%) is heated in a container, and then river sand and cement are mixed. The final mixture was put into the mold box to dry into a length, breadth, and depth brick mold 190, 90, and 90 mm in size. The developed brick sample is given in Fig. 1.

Table 1. Plastic bricks compositions

HDPE (Wt.%)	HDPE plastic (kg)	River Sand (kg)	Cement (kg)
0	0	2.6240	0.4373
5	0.1312	2.4928	0.4155
10	0.2624	2.3616	0.3936
15	0.3936	2.2304	0.3717

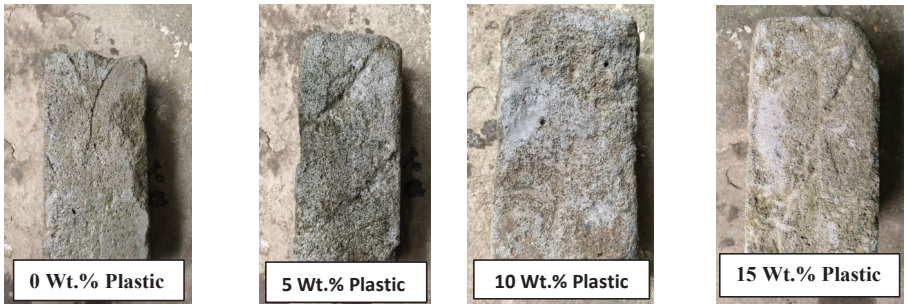

Fig. 1. Developed plastic brick samples

The first step in our historical overview of technique was to examine research that was done both inside and outside of India. Next, in accordance with that, we have acquired and gathered raw materials such as cement, sand, and HDPE plastic, and we have moved on to the production of bricks in conventional dimensions (19 cm x 9 cm x 9 cm). While making bricks, the ratios of sand to plastic are reviewed. Once brick production is complete, the brick The quality of plastic sand bricks is examined and evaluated in detail by executing different tests as per brick manufacturing standard [37-39].

4.1 Preparation of sand and plastic waste for brick production

The collection of sand and plastic waste is the first phase towards the generation of sustainable materials or for the construction of eco-friendly items, for instance, ‘eco-bricks’ or ‘plastic roads.’ The procedure is basically as follows:

Collection: Plastic waste is sourced through dumpsites, oceans, and communities, while sand is obtained from virgin or recycled sources. Plastic waste consists of bottles, bags, packaging, and other one-time-use plastics. Sorting and Cleaning: Plastic waste is categorized into different types, including PET, HDPE, and LDPE, because of the different characteristics and heat melting points of different plastics. After sorting, it is cleaned to get rid of soil, labels, and impurities. Shredding and Granulating: Clean plastic is reduced in size by either being shredded or being granulated into small particles that are less difficult to work with. The use of smaller particles increases the efficiency of mixing with sand. Mixing and Heating: In the case of plastic roads, reduced plastic is first heated up to its own optimal temperature before it is mixed with sand or other aggregates in order to improve bond

formation. It is the melted plastic that bonds sand particles together to produce a composite that is more durable and flexible.

Mixing. Collect water, cement, and sand. Mix the cement and sand together in a mixing container until thoroughly combined. Make sure to uniformly distribute the plastic or shreds in the sand-cement mixture. Small amounts of water should be added gradually until the mixture has a thick, cohesive consistency. Don't get it too moist. To create sturdy, dense bricks, pour the mixture into molds and crush hard.

Moulding. The third step, molding, is carried out using a conventional brick mold (190 x 90 x 90 mm), with the sample placed on a vibrator machine to ensure complete mixing.

Drying. After molding, sand bricks are placed in an environment with room temperature for a period of 24 hours. The purpose of this initial drying process is to remove most of the surface water from the sand bricks while ensuring that no cracks develop, and it also allows for the effective curing of the bricks in the subsequent stage.

5 Results and Discussion

The following tests were conducted in both the lab and the field in accordance with the Indian Standard Code (ISC) to determine the quality of plastic sand bricks. Brick quality is assessed and discussed based on the findings from the several tests. Every test result obtained for plastic sand bricks is contrasted with those of regular clay bricks.

5.1 Compressive strength test

Compressive strengths are measured by a universal testing machine (UTM) as shown in Fig. 2. The primary determination of the test was to determine the compressive strength value. Typically, a large number of brick specimens are brought to the lab and examined one at a time. Plastic sand bricks were placed on a compressive testing apparatus for this test, and pressure was applied until the sample broke. After tasting each sample of PSB with varying ratios of plastic to sand, it was discovered that one sample had a high compressive strength rating. Additionally, that figure for compressive strength is contrasted with that of regular clay bricks. The effect of plastic waste percentage on the CS of plastic brick is stated in fig. 3.

$$\text{Compressive Strength (CS)} = \frac{Maximum\ load\ (P)}{Area\ of\ specimen\ (A)}$$

Where,
P: Maximum load (KN)
A: Area of specimen (mm^2)

Fig. 2. Compression test of developed Brick Sample

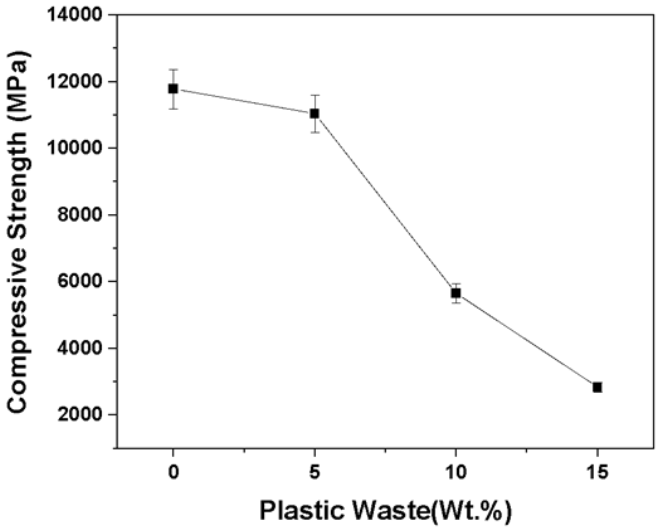

Fig. 3. Plot for Plastic waste (%) Vs Compressive Strength.

5.2 Water Absorption Test

Bricks are weighed dry before being submerged in fresh water for a whole day as part of this test. Following a full day of submersion (See Fig 4), bricks are removed from the water and cleaned by a cloth. After that, a wet brick is weighed. The water that brick absorbs accounts for the weight difference. Next, the water absorption percentage is computed. Brick is of higher grade the less water it absorbs. A high-quality brick won't absorb more than 20 % of its own weight in water. From WA test it is found that with the increase of HDPE percentage water absorption is reducing.

$$\text{Water Absorption} = \{[W2 - W1] / W1\} \times 100$$

Where, W1 = Weight of dry brick (kg)
W2 = Weight of wet brick (kg)

Fig. 4. Water absorption test of developed brick

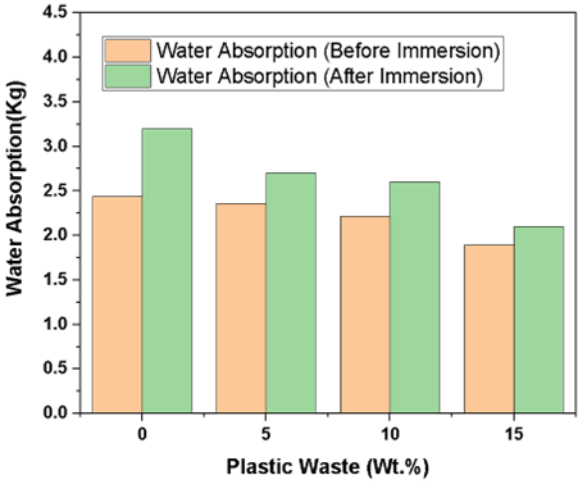

Fig. 5. Plot for waster absorption Vs plastic waste ratio

5.3 Soundness test

The brick is kept in the air for two days after creation. Then the bricks are made to collide with each other for a sound test (see Fig. 6). When a good brick is hit, it rings. A ringing sound produced when the bricks are hit against each other marks the presence of high-quality bricks.

Fig. 6. Soundness test

5.4 Hardness Test.

The ability to withstand local plastic deformation brought on by abrasion or mechanical indentation is slow by hardness. A good brick should be resistant to scratches from sharp things. Harness test (see 7) is performed by scratching the bricks' surface with fingernails or a sharp instrument. The brick is sufficiently hard and suitable for usage if the surface shows no signs of a scratch. This is an indirect test to determine the brick's compressive strength and kilning quality. This is tested by scratching against the brick surface with a sharp instrument or fingernail. The bricks are referred to as hard bricks because they do not leave any scratches on their surface when scratch them with your fingernail or nail.

Fig. 7. Hardness test

6 Conclusion

Plastic bricks have been successfully manufactured with weight percentages of 5, 10, and 15% HDPE plastic waste along with sand and cement. The compressive strength as well as waster absorption quality decreasing with the increase of plastic weight percentage. The soundness and hardness properties of plastic brick are good compare to clay bricks. The WA presence of alkalis was significantly decreased by using plastic sand bricks. Given their many benefits, more study would enhance the durability and quality of plastic sand bricks. The following conclusion was reached based on the experimental investigation's results: Bricks made from sand and waste plastics might serve as a substitute for the conventional clay bricks now in use. In comparison to regular clay or sand plastic bricks exhibit reduced water absorption good sound quality and lighter weight. Plasic brick also have a higher CS than regular clay bricks, and waste plastics, which are widely accessible, can be effectively used to make bricks. Sand plastic bricks can contribute to a cleaner, healthier environment by lowering pollution levels. Eco-bricks are an economically viable and energy-efficient innovation. Thus, plastic bricks, often known as eco-bricks, have several advantages over regular clay bricks. Waste Plastic are commitment to protect the environment by using plastic bricks for pavement and building.

References

1. P. Wang, Y. Yang, C. Ji, and L. Huang, “Influence of Built Environment on Building Energy Consumption: A Case Study in Nanjing, China,” Environ. Dev. Sustain., no. 0123456789, 2023, doi: 10.1007/s10668-023- 02930-w.
2. S. Rhee-Duverne and P. Baker, “Research into the thermal performance of traditional brick walls,” English Herit. Res. Rep., p. 34, 2013, [Online]. Available: https:// research.historicengland.org.uk/Report.aspx?i=15741 2020)
3. H. Boostani and P. Hancer, “A Model for External Walls Selection in Hot and Humid Climates,”Sustainability, vol. 11, no. 1, p. 100, 2018, doi: 10.3390/su11010100.
4. T. B. de Souza, M. H. F. Medeiros, F. W. C. Araújo, and A. A. de Melo Neto, “The influence of expanded polystyrene granules on the properties of foam concrete,” Mater. Struct., vol. 56, no. 1, 2023, doi:10.1617/s11527-023- 02109-9.
5. Q. Al-Yasiri and M. Szabó, “Building envelope-combined phase change material and thermal insulation for energy-effective buildings during harsh summer: Simulation-based analysis,” Energy Sustain. Dev., vol. 72, no. November 2022, pp. 326–339, 2023, doi: 10.1016/j. esd.2023.01.003.
6. Á. Lakatos, “ Thermal insulation capability of nanostructured insulations and their combination as hybrid insulation systems,” Case Stud. Therm. Eng., vol. 41, no. November 2022, 2023, doi: 10.1016/j. csite.2022.102630.
7. K. A. Tarabieh, K. Nassar, and M. Sharkass, “A Comparative Study of the Thermal Performance of Plastic Bottle Wall against Traditional Composite Brick Wall Typologies,” J. Constr. Res., vol. 2, no. 1, pp. 1–8, 2021, doi: 10.30564/jcr.v2i1.2653.
8. Y. Arsandrie, D. Mutiari, N. R. Syamsiyah, Suharyani, and S. A. Himmah, “Thermal insulation of plastic waste brick composite with rice husk and sawdust,” Civ. Eng. Archit., vol. 8, no. 6, pp. 1283–1289, 2020, doi: 10.13189/cea.2020.080612.
9. T. Samardzioska, M. Jovanoska, and V. Grujoska, “Sustainable Thermal Insulation Derived from Recycled Textile Waste,” Adv. Environ. Eng. Res., vol. 04, no. 01, pp. 1–8, 2023, doi: 10.21926/aeer.2301004.

10. N. P. Tran, C. Gunasekara, D. W. Law, S. Houshyar, and S. Setunge, "Repurposing of blended fabric waste for sustainable cement-based composite: Mechanical and microstructural performance," Constr. Build. Mater., vol. 362, no. November 2022, p. 129785, 2023, doi: 10.1016/j.conbuildmat.2022.129785.
11. K. J. O. Grings, F. R. Carneiro Ribeiro, D. V. A. Junior, A. R. G. de Azevedo, and M. P. Kulakowski, "Evaluation of Light Cementitious Matrix with Composite Textile Reinforcement from Garment Waste," Materials (Basel)., vol. 16, no. 2, 2023, doi: 10.3390/ma16020733.
12. S.L. Platt, P. Walker, D. Maskell, A. Shea, F. Bacoup, A. Mahieu, H. Zmamou, and R. Gattin, "Sustainable bio & waste resources for thermal insulation of buildings," Constr. Build. Mater., vol. 366, no. November 2022, p. 130030, 2023, doi: 10.1016/j. conbuildmat.2022.130030.
13. D. K. Dadzie, A. K. Kaliluthin, and D. Raj Kumar, "Exploration of waste plastic bottles use in construction," Civ. Eng. J., vol. 6, no. 11, pp. 2262–2272, 2020, doi: 10.28991/cej-2020-03091616.
14. Muyen, T.N. Barna, M.N. Hoque, Strength properties of plastic bottle bricks and their suitability as construction materials in Bangladesh, Progress. Agric. 27 (3) (2016) 362–368, https://doi.org/10.3329/pa.v27i3.30833.
15. C.G. Mohan, J. Mathew, J.N. Kurian, J.T. Moolayil, C. Sreekumar, Fabrication of plastic brick manufacturing machine and brick analysis, Int. J. Innov. Res. Sci. Eng. Technol. 2 (2016).
16. A. Daftardar, R. Shah, P. Gandhi, H. Garg, et al., Use of waste plastic as a construction material, Int. J. Eng. Appl. Sci. 4 (11) (2017), https://doi.org/ 10.15406/mojce.2017.03.00082.
17. Arvind Singhal, Omprakash Netula, Utilization of plastic waste in manufacturing of plastic sand bricks, 3rd International Conference on New Frontiers of Engineering, Science, Management and Humanities (ICNFESMH2018) At: Pune, 2018.
18. I.I. Akinwumi, A.H. Domo-Spiff, A. Salami, Marine plastic pollution and affordable housing challenge: Shredded waste plastic stabilized soil for
19. J. Ghuge, S. Surale, B.M. Patil, S.B. Bhutekar, Utilization of waste plastic in manufacturing of paver blocks, System 6 (04) (2019) 1967–1970.
20. R. Kognole, K. Shipkule, M. Patil, L. Patil, U. Survase, Utilization of plastic waste for making plastic bricks, Int. J. Trend Sci. Res. Dev. 3 (2019) 878–880, https:// doi.org/10.22214/ijraset.2022.42336.
21. R. Bhushaiah, S. Mohammad, D.S. Rao, Study of plastic bricks Made from waste Plastic, J. Eng. Technol. 6 (4) (2019) 6.
22. S.S. Chauhan, B. Kumar, P.S. Singh, A. Khan, H. Goyal, S. Goyal, Fabrication and testing of plastic sand bricks, in: IOP Conference Series: Materials Science and Engineering, 2019, vol. 691, no. 1, p. 12083, DOI 10.1088/1757-899X/691/1/ 012083.
23. P.L. Paihte, A.C. Lalngaihawma, G. Saini, Recycled Aggregate filled waste plastic bottles as a replacement of bricks, Mater. Today: Proc. 15 (2019) 663–668, https://doi.org/10.1016/j.matpr.2019.04.135.
24. D. Ariyani, N. Warastuti, R.N. Arini, Ecobrick Method To Reduce Plastic Waste In Tanjung Mekar Village, Karawang Regency, Civ. Environ. Sci. J. 4 (1) (2020) 22–29, https://doi.org/10.21776/ub.civense.2021.00401.3.
25. .J. Nath, R. Lal, A.K. Das, Fired bricks: CO2 emission and food insecurity, Glob. Challenges 2 (4) (2018) 1700115, https://doi.org/10.1002/gch2.201700115.
26. P. Kulkarni, V. Ravekar, P.R. Rao, S. Waigokar, S. Hingankar, Recycling of waste HDPE and PP plastic in preparation of plastic brick and its mechanical properties, Clean. Mater. (2022).
27. M. Idrees, A. Akbar, F. Saeed, M. Gull, S.M. Eldin, Sustainable production of Low-Shrinkage fired clay bricks by utilizing waste plastic dust, Alexandria Eng. J. 68 (2023) 405–416.
28. A. Barman, T. Dutta, G. Mazumdar, Testing and Characterization of Plastic Bricks, Ref. Modul. Mater. Sci. Mater. Eng. (2022), https://doi.org/10.1016/ B978-0-12-820352-1.00211-X.
29. J. Yang, W.M. Shaban, K. Elbaz, B.S. Thomas, J. Xie, L. Li, Properties of concrete containing strengthened crushed brick aggregate by pozzolan slurry, Constr. Build. Mater. 247 (2020).
30. S. Sarwar et al., Preparation of environmental friendly plastic brick from highdensity polyethylene waste, Case Stud. Chem. Environ. Eng. 7 (2023).
31. B. of I. Standards, Indian Standard Methods of Tests of Burnt Clay Building Bricks (Third Revision), IS 3495 (Parts 1 to 4), 1992.
32. Biradar, S. V.; Kumar, A. S.; Gowri, T. V.; Alisha, S. S. Comparative Study on Properties of Plastic Bricks with Conventional Bricks. Journal of Physics Conference Series 2024, 2779 (1), 012088. https://doi.org/10.1088/1742-6596/2779/1/012088.
33. K. A. Tarabieh, K. Nassar, and M. Sharkass, "A Comparative Study of the Thermal Performance of Plastic Bottle Wall against Traditional Composite Brick Wall Typologies," J. Constr. Res., vol. 2, no. 1, pp. 1–8, 2021, doi: 10.30564/ jcr.v2i1.2653.
34. Raza ST, Wu J, Rene ER, Ali Z, Chen Z. Reuse of agricultural wastes, manure, and biochar as an organic amendment: a review on its implications for vermicomposting technology. J Clean Prod. 2022. https://doi.org/10.1016/j.jclepro.2022.132200.
35. Xu Y, et al. Suitability analysis of consensus protocols for blockchain-based applications in the construction industry. Autom Constr. 2023. https://doi.org/10.1016/j.autcon.2022.104638.
36. Nayaka RR, Alengaram UJ, Jumaat MZ, Yusof S, Ganasan R. Performance evaluation of engineering properties, radiation shielding, and sustainability of hollow masonry blocks produced using a high volume of industrial by-products. J Mater Civ Eng. 2021. https://doi.org/ 10.1061/(ASCE)MT.1943-5533.0003558.

37. A.A. Solomon, G. Hemalatha, Characteristics of expanded polystyrene (EPS) and its impact on mechanical and thermal performance of insulated concrete form (ICF) system, Structures 23 (2020) 204–213, https://doi.org/10.1016/j.istruc.2019.10.019.
38. P.C. Varghese, Building Materials, PHI Learning, 2005.
39. B. of I. Standards, Indian Standard Common Burnt Clay Building Bricks - Specification (Fifith Revision), IS 1077 :1992 (Reaiffirmed 2007).

Safety Engineering & Management

IoT Based Radiation Monitoring for Safe Operation of Industrial Radiography (IR) Facilities

M. K. Pathak[1*], A. Pathak[2], Prof. S. Sarkar[3]

[1]Atomic Energy Regulatory Board, Kolkata India
[2] Edelwiss Global Market, Mumbai, India
[3]Production Engineering, Jadavpur University, Kolkata, India

*mkpaathak@aerb.gov.in

Abstract. Industrial radiography (IR) is a well-established non-destructive testing technique that uses ionizing radiation, such as gamma rays and x-rays. Exposure to high dose of ionizing radiation can lead to severe health effects, including radiation injury. Efficient radiation monitoring is needed for safe radiography operation. Currently, manual radiation survey meters are used, which do not provide continuous monitoring necessary to ensure safe operation. Accidents resulting in overexposure and injuries often occur either due to non-use or faulty use of the manual radiation survey meters. To address the issue, an IoT-based radiation monitoring system has been developed, using a GM counter, microcontroller, Wi-Fi module, and IoT analytics platform for real-time radiation measurement in industrial radiography operation. The device has been tested in field and results have been compared with other standard radiation survey meters. Test result demonstrates the reliability & accuracy of the system and thus its usefulness in industrial radiography operation. Continuous radiation monitoring by the system will lower the risk of overexposure and injuries. This paper brings out materials and methods used for development of the IoT based radiation monitoring system with test results of the system.

Keywords: Ionising Radiation, RSM, GM Tube

1 Introduction

One of the longest established applications of ionising radiation is industrial radiography, which uses both x- ray and gamma ray to investigate the integrity of equipment and structures [1]. Industrial radiography uses intense radiation sources which can expose people at work to significant amounts of radiation. Radiation monitoring in industrial radiography is crucial to ensure the safety of workers, the public, and the environment. Radiation Survey Meter (RSM) is the most important safety tool of radiographer which is used to confirm the return of the source into the shielded position in the gamma exposure device following each exposure and also to confirm the integrity of shielding of the exposure device before transport or use [2]. In spite of stringent control and procedures, there have been accidents in industrial radiography resulting in significant radiation exposures and in some cases, injuries to radiographers. There have been numbers of radiation accidents in this field and a few of them resulted in radiation injuries to the exposed individuals [3]. Large number of over-exposure incidents have happened in industrial radiography because a radiographer did not use his or her survey meter [4] or the survey meter was not calibrated and functioning properly [5]. Traditional radiation monitoring is performed manually to locate radiation sources or radioactive materials, on the other hand online radiation monitoring will allow continuous, real-time measurement and monitoring of radiation levels during IR operation. This ensures immediate detection of any abnormal radiation level enabling prompt action to mitigate risks and to ensure safety of the workers. The online radiation monitoring is done using an IoT based approach. Greengard, mentioned that the IoT was proposed in the year of 1999 by Kevin Ashton and is intended to exchange information [6]. IoT is a network of interrelated devices that connect and exchange data with other IoT devices and the cloud. IoT devices are typically embedded with technology such as sensors and software and can include mechanical and digital machines and consumer objects [7]. Over the past two decades, IoT has different modes of operations, such as access points, Wi-Fi devices, Bluetooth devices, infrared devices, smart trash bins, monitoring environment, IoT-centered irrigation systems, smart traffic control, and healthcare systems [8]. IoT based radiation monitoring system will substantially assist in taking preventive measures and alleviate the risk of over exposure to industrial radiographers. This paper brings out materials and methods used for development of an IoT based radiation monitoring system in order to prevent radiation related injury and overexposure of industrial radiographers, test results and discussions along a conclusion.

2 Materials and Methods

2.1 Literature Review

Although not for industrial radiography, some studies have been conducted on internet of things-based radiation monitoring for other radiation applications, such as radon concentration measurement, background radiation detection, nuclear emergency preparedness, and doses from artificial and natural radioisotopes. A smart electronic device for radiation protection and nuclear security was made to measure radon concentration, temperature, and relative humidity in indoor spaces [9]. Micro controller based system was developed for background radiation measurement [10]. The microcontroller system measures the level of radiation, analyses the received data and transmits them to the PC. It sends the alarm signal when the level of radiation exceeds. The data collection is implemented using a gas-discharge Geiger–Mueller SBM-20 meter. An IoT based area radiation monitoring device was developed using micro-controller and GM detector to support radiological emergency preparedness system in the yogyakarta nuclear area [11]. The IoT based radiation monitor was designed to analyze nuclear emergency potential in the nuclear emergency response and preparedness system. IoT-based radiation monitoring system comprised of a Geiger counter, Wemos microcontroller, and a temperature, humidity, and light ambient sensor was developed to study correlation between temperature/ humidity and radiation in an area [12]. Further, an IoT enabled intelligent system was implemented for radiation monitoring and warning by classifying radiations and their corresponding effects on infants using infrared sensors, ultraviolet sensors, electromagnetic sensors, and gamma radiation sensors, connected to arduino [8]. The system was used to alert through an android mobile application when the intensity level of rays becomes dangerous.

2.2 System Design

Ionising radiation like beta particles and gamma rays are detected and measured most commonly using a GM counter. Inert gas like helium, argon is filled inside the tube which turns electrically conductive when a high-energy particle strikes it [14]. For radiation measurement in IR operation, an assembled GM tube has been used. The GM tube is capable of detecting gamma rays within the range of 20 mR/hr to 120 mR/hr. It can also detect soft beta rays within the range of 100 to 1800 counts per minute (cpm) per square centimeter. It requires 5V power supply. The maximum count rate of the tube is 25 times/min and life is greater than 1 x 10^9 pulse. The module is compatible with arduino micro controller. A microcontroller, often referred to as an embedded controller, is a single chip computer. As compared to a microprocessor, a microcontroller has the various components such as memory, I/O module, clock module all built into a single chip. This reduced dependence on external chips enable them work at a very low power consumption [15]. Among the various microcontrollers available today, the Arduino microcontrollers are especially popular. For the IoT System, Arduino UNO Rev 3 microcontroller board has been used. It is based on the ATMega328P – Atmel's 8 Bit AVR microcontroller with 32KB of programmable flash memory [16]. The large programmable flash memory allows for a larger and more complicated application logic to be deployed as required in the case of the IoT based radiation monitoring system. The square wave pulses sent by the GM tube are received in the microcontroller as counts. The number of counts recorded is then used for calculating the counts per minute (CPM). To add wireless functionalities to the radiation monitoring system, an ESP8266 Wi-Fi module has been used which receives data from microcontroller and uploads to IoT platforms. ESP8266 is Wi-Fi enabled system on chip (SoC) module ad is mostly used for development of IoT embedded applications. Microcontroller communicate with the ESP8266 module using set of AT commands [17]. Thingspeak is an open source platform for Internet of Things devices, enables users to upload and log data, analyse, retrieve, and store findings by graphical representation with Matlab support [18]. This cloud based data storage would enable facility to keep a track of radiation exposures during industrial radiography and take necessary steps as deemed to be fit. Block diagram of the IoT based radiation monitoring system developed for industrial radiography operation has been shown in Fig. 1.

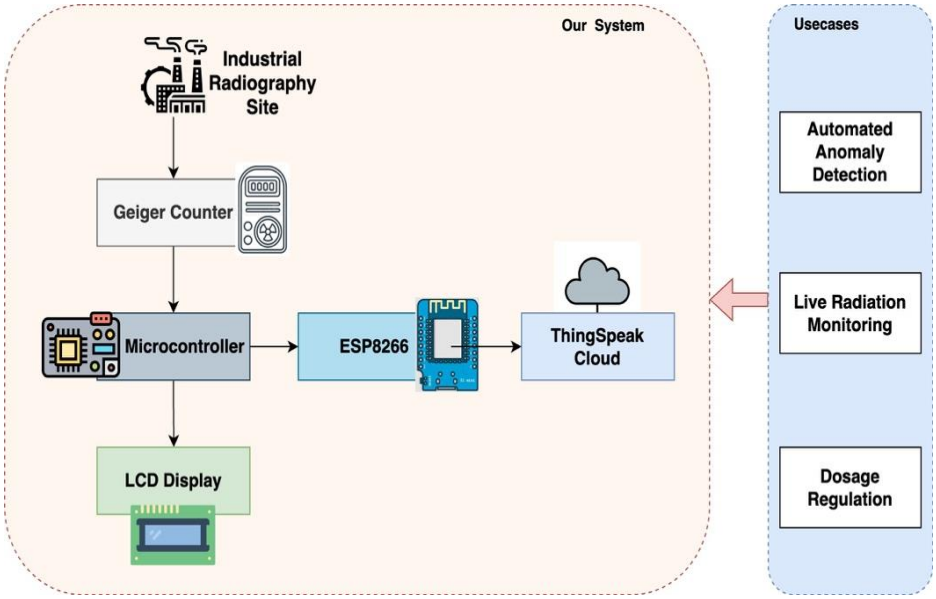

Fig. 1. Block diagram of the IoT based radiation monitoring system

The square wave pulses sent by the GM tube are received in the microcontroller as counts. The number of counts recorded is then used for calculating the counts per minute (CPM). In the Arduino microcontroller the pulses are received in the form of interrupts and handled by an interrupt handler responsible for incrementing the counts. As per characteristic of the tube, counts per minutes is converted to µSv/hr with the index 151 CPM equals to 1 µSv/hr. The radiation readings update is done periodically, according to intervals set at start up, and are displayed on the LCD. The Wi-Fi module uploads the live radiation measurements to ThingSpeak, an IoT analytics platform allowing users to aggregate, visualize, and analyze live data streams in the cloud. ThingSpeak provides instant visualizations of data posted by ESP 8266 module. This cloud based data storage would enable facility to keep a track of radiation exposures during industrial radiography and take necessary steps as deemed to be fit.

3 Results and Discussion

The system was tested on field using a ROLI-3 portable IGRED containing an Ir-192 radioactive source of activity 9.7 Ci. Radiation levels were measured at different distances ranging from 0.05 m to 4.5 m from the ROLI-3 device during "No Exposure" condition (i.e. the source is inside shielded enclosure of the device) and at 20 m, 25 m and 30 m distances during "Exposure" condition. Two radiation survey meters (RSM)s; one Thermo Scientific RadEye PRD and another Pulsecho Minirad were also used simultaneously side by side to record the radiation levels at the same location for comparison of the effectiveness of the developed system. Fig. 2 (i) & 2 (ii) given below present comparative results of radiation level measured during 'No Exposure' (source is in shielded position) and 'Exposure' condition respectively using three different RSMs.

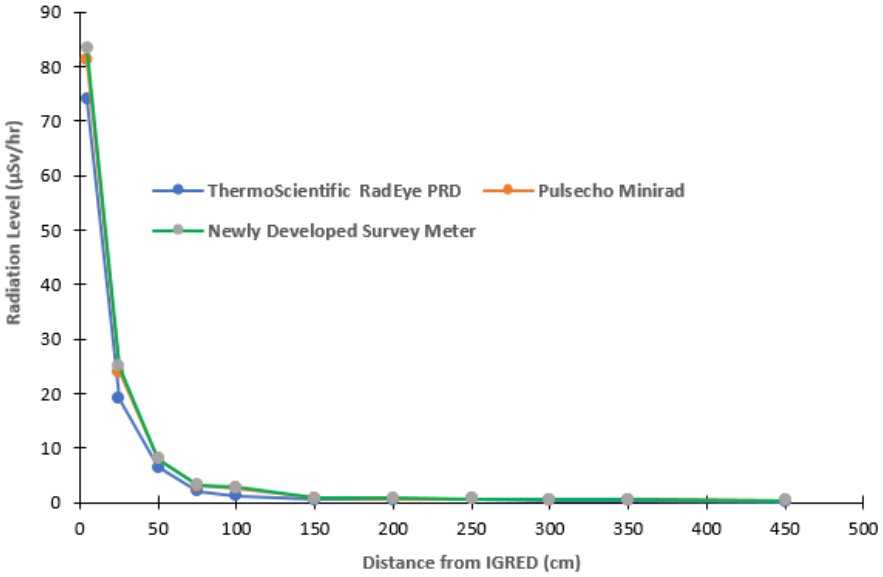

Fig. 2 (i)

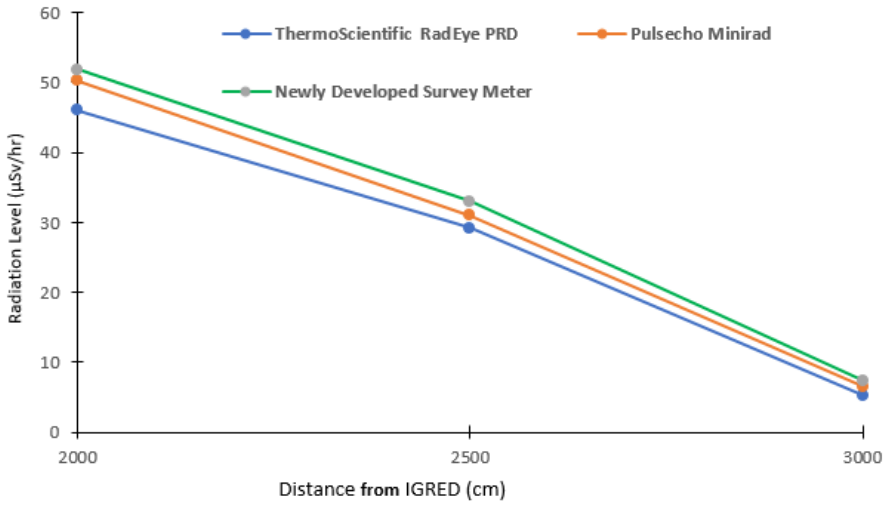

Fig. 2 (ii)

Fig. 2 (i) & (ii). Radiation levels measured during 'No Exposure' and 'Exposure' Condition using three RSMs

The accuracy of the developed IoT based radiation monitoring system was checked by comparing Mean Absolute Error (MAE) of the developed system with that of two standard calibrated RSMs (Pulsecho Minirad and the Thermo Scientific RadEye PRD used for industrial radiography using the following formula:

$$MAE = \frac{\sum_{i=0}^{n} |x_i - \hat{x}_i|}{n}$$

Here x_i refers to the radiation measurement obtained at a certain distance from the system developed, $\hat{x}_i$ refers to the radiation measurement obtained at the same location by the standard RSM and n is number of observations. It is seen that the developed radiation survey meter had a MAE of 0.58 µSv/hr and 2.31 µSv/hr with respect to the Pulsecho Minirad and the Thermo Scientific RadEye PRD respectively where comparatively higher differences are observed during exposure situation. This indicates that the prototype device developed is working accurately in radiography operation. The ThingSpeak channel where the outputs recorded by the developed system are transmitted and analyzed as shown in Fig. 3. Apart from displaying the current radiation measurement, historical readings are also available. This thus enables facility to constantly monitor the radiography operation and detect any abnormal radiation level. Cost involved to make the IOT based radiation monitoring system comes around

Rupees seven thousand whereas minimum cost of manual RSM used by the IR facilities generally comes at around rupees thirty thousand in India.

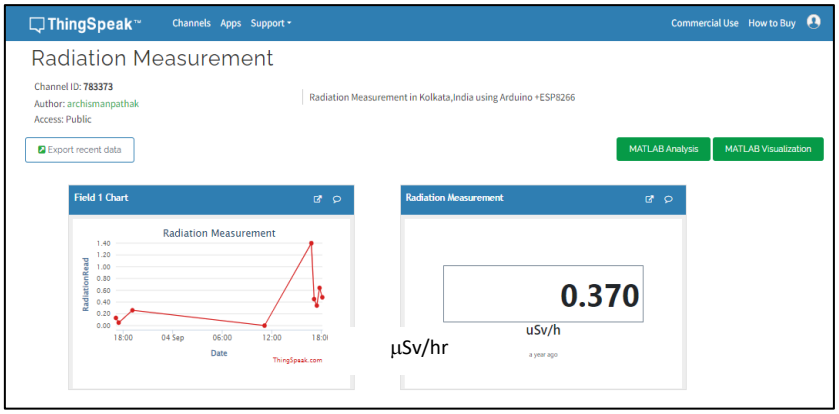

Fig. 3. Portal for visualization and analyzation of measured radiation data

4 Conclusion

In this work, an Internet of Things-based radiation monitoring system for industrial radiography is developed and tested in the field. The system makes use of an arduino microcontroller for data processing, a geiger-müller (GM) tube for radiation detection, and an ESP8266 Wi-Fi module for real-time transmission to the ThingSpeak IoT platform. Extensive field testing showed a number of important findings and proved its efficacy.

The system's accuracy and dependability were demonstrated by its Mean Absolute Error (MAE), when compared to the manual RSMs used in industrial radiography. High radiation levels under "Exposure" settings showed somewhat larger disparities, suggesting possible regions for additional calibration. Furthermore, it's a very cost-effective substitute for commercially available radiation survey meters, which start at about Rs. 30,000 in India, due to its low development cost of about Rs. 7,000. This cost advantage is further complemented by the system's automation capabilities, which eliminate the need for manual measurements while enabling real-time monitoring. By enabling cloud-based storage, historical trend analysis, and continuous data visualisation, the system's connection with the ThingSpeak IoT platform increases its usefulness. These characteristics offer strong radiation safety assistance and enable prompt actions during anomalous radiation incidents.

In conclusion, the IoT-based radiation monitoring system offers a cost-effective, accurate, and efficient solution for real-time monitoring in industrial radiography. The system holds significant potential to replace traditional manual systems in compliance with regulatory standards. Future work could focus on optimizing its calibration for high radiation levels and exploring its applicability in different environmental conditions.

References

1. IAEA Safety Reports Series No. 13: Radiation Protection and Safety in Industrial Radiography, ISBN 92-0-100399-4 (1999).
2. Canadian Nuclear Safety Commission: Working Safely with Industrial Radiography, PWGSC catalogue number CC172-105/2014E-PDF, ISBN 978-1-100-23558-5 (2014).
3. Kumar A., Subramanya M. J., Raghavendran C.P., Murthy B.K.S., Vishwakarma R. R., Kannan R.: Safety of Radiation Sources and Security of Radioactive Materials, IAEA Conference France, 14-18 September 1998.
4. IAEA Safety Reports Series No. 7: Lessons Learned from Accidents in Industrial Radiography. ISBN 92-0-103098-39 (1998).
5. Ballard J. S.: Radiation Safety, ISBN 13: 9781636350219. Open Oregon Educational Resources.
6. Greengard S.: The Internet of Things, 232 pp. ISBN: 9780262527736. MIT Press (2020).
7. Gillis A. S.: Definition - Internet of Things (IoT), https://www .techtarget.com/.
8. Saifullah M., Bajwa I. S., Ibrahim M., and Asghar M.: IoT-Enabled Intelligent System for the Radiation Monitoring and Warning Approach. Hindawi Mobile Information Systems. Volume 2022. Article ID 2769958 (2022).
9. Jacob M. T., François K., Souffit G. D., Modibo O. B., Abba H. Y., Michaux K. N., Saïdou, Tokonami S.: Low-cost radon monitoring with validation by a reference instrument. Instrumentation Science & Technology. Volume 51. Issue 1 (2023).

10. Holovatyy A., Teslyuk V., Kryvinska N., Kazarian A.: Development of Microcontroller-Based System for Background Radiation Monitoring Sensors, doi: 10.3390/s20247322, PMCID: PMC7765999, PMID: 33419256 (2020).
11. Muhtadan, Abimanyu A., Akmalia R., Salam M.: Design of IoT-based Radiation Monitor Area for Nuclear and Radiological Emergency Preparedness System in Yogyakarta Nuclear Area. The 4th International Conference on Applied Physics and Materials Application Journal of Physics: Conference Series 1428 (2020)
12. Mahatab T. A., Muradi M. H., Ahmed S. and Kafi A.: Design and Analysis of IoT Based Ionizing Radiation Monitoring System. Proceedings of the International Conference on Innovations in Science. Engineering and Technology, pp. 432–436 (2018).
13. Navarro R. B., Hoyos F. T., Rios C. U., Quintero R. F. C.: Design and Assembly of an IoT Based Device to Determine the Absorbed Dose of Gamma and UV Radiation. Applied Radiation and Isotopes. vol. 166. Article ID 109359 (2020).
14. Iovine J,: Nuclear Experiments Using A Geiger Counter. ISBN: 9781623850081. 1623850088 (2020).
15. Dogan I.: PIC Microcontroller Projects in C Basic to Advanced, Second Edition Newnes Publication. ISBN-13: 978-0-08-099924-1.
16. Product Reference Manual: SKU: A000066. Arduino Uno Rev3 (2023).
17. Schwartz M. : Internet of Things with ESP 8266. PACKT Publishing Ltd. ISBN: 978-1-78646-802-4 (2016).
18. Pasha S.: Thingspeak Based Sensing and Monitoring System for IoT with Matlab Analysis. International Journal of New Technology and Research (IJNTR). ISSN: 2454-4116. Volume-2. Issue-6. June 2016 Pages 19-23 (2016).

Optimisation of Production Systems

Multi-response optimization of design for tibia fracture fixation plate using Taguchi grey relational analysis

Drupad Roy[1] · Manik Chandra Das[2] · Raja Dhason[3] · Shubhabrata Datta[3]

[1]Department of Mechanical Engineering, MCKV Institute of Engineering, Liluah, Howrah711204, West Bengal, India
[2]Department of Industrial Engineering and Management, Maulana Abul Kalam Azad University of Technology,West Bengal, Haringhata, Nadia 741249, West Bengal, India
[3]Department of Mechanical Engineering, SRM Institute of Science and Technology, Kattakulathur, Chengalpattu Dist. 603203, Tamil Nadu, India
drupadroy@gmail.com

Abstract. The fracture plate should have enhanced axial movement with less twisting angle at the fracture site, as well as evenly distributed stress between the plate and the bone, to facilitate healing process of a tibia fracture. To achieve these purpose, carbon/epoxy fiber reinforced laminated composite bone plates are studied on a transversely cracked human tibia shaft with a 3 mm fracture gap. The design of experiment (DOE) guided finite element analysis results of the L32 orthogonal array have been employed to do Multi Response optimization, such as Taguchi gray relational analysis (GRA), to achieve the desired stress distributions and motions. 32 simulations are ranked using the grey relational grades. Stacking sequence of [-45/0/0/0/0/0/0/0]s and with 0.2 mm lamina thickness gives best multi response optimization result. The design with a 0.2 mm layer thickness and a [-45/-45/-45/-45/-45/-45/-45/-45]s stacking sequence achieved the best results for axial movement and plate stress, while [90/90/0/-45/45/-45/45/90/0]s with a 0.25 mm layer thickness addressed the optimum twisting angle and bone stresses..

Keywords: Composite fixation plate, tibia fracture, Taguchi GRA, finite element analysis

1 Introduction

The fixation of tibia fracture is essential to prevent malunion [1] and non-union [2]. The fixation types are depending on the type of injuries. Intramedullary nailing (IMN) and plating are still used for this purpose. Both have some advantages and limitations. Plating is popular fixation technique for achieving anatomical reduction but can cause significant trauma, soft tissue complications and wound infection. The reasons behind the popularity if IMN's are minimum invade in bone with a capability of handling the torsional stress and less stress shielding [3].

For tibia, mostly all diaphyseal fracture may be fixed by bone plate. Biocompatibility of materials are very much essential for plate material. Metallic plates are used since long era for its availability and manufacturability. Those are mostly SS and Ti. Both have proved biocompatibility. But even Ti has much more elastic modulus than bone and after implantation in tibia, during standing, the metal plates absorb most of the stress for their axial rigidity and bone experiences low stress. Lowering of long bone's mechanical stresses causes gradual bone resorption near the implant; this phenomenon is known as "stress shielding" [4]. This disorder increases the risk of refracture in the bone, which is regarded as a challenging plating complication [5]. This challenge may be addressed by using more flexible bone plate material but may resist the twisting of the bone plate. So, it would be a solution for suitable bone plate material which has lower axial stiffness but higher stiffness in transverse direction. Few researches indicated that anisotropic fiber reinforced polymer matrix composite material is capable to replace the isotropic metal bone plates in aspect of lowering axial stiffness and increased transverse stiffness [6].

Carbon fiber/epoxy (CF/epoxy) composite material has proven biocompatibility. CF/epoxy composite material has epoxy polymer matrix and carbon fiber reinforcement. The mechanical property can be controlled by implying suitable fiber orientation and laminated thickness. Laminate thickness can be calculated by multiplying thickness of individual layers by the number of layers. This study is aiming to find a CF/epoxy bone plate material for 3 mm gap diaphyseal tibia fracture [7] under 700N load [8]. The outcomes are selected to check the suitability of the bone plate materials are axial movement, twisting angle, stress on the cortical bone, cancellous bone and the bone plates. DOE guided FEA experimental results are used for Taguchi GRA [9,10] to determine the rank of combination of input parameters used in the FEA.

2 Materials and methods

2.1 Modelling

An intact and dried human tibia bone served as the main focus of this investigation. A high-precision portable coordinate measuring device, was used to record the tibia's measurements and surface characteristics. Fig.1 represents tibia-CMM (portable) setup. Following that, reduction of surface noise was done to ensure a more accurate representation.

Then, an extensive three-dimensional model of the tibia has been generated. This model consists of the tibia's cortical and cancellous regions. A 3 mm transverse fracture gap is created at the midshaft. A carbon fiber/epoxy composite plates were used and a bone-plate-bolts assembled model has been generated for Finite Element Analysis (FEA). The FEA has been done using Ansys 2022 R1 software. Fig. 2 represents the stress distribution of an exp no. 1 of L32 Orthogonal array which is the suitable Design of Experiment in this study. The bone plates were supposed to span the fracture gap. The plate with dimensions of 103 mm length, 15 mm width, thicknesses of 3.6 and 4.5 mm and curvatures of 13.6 mm has been considered. Every plate would also have six holes in it.

There were 18 layers of lamina along the thickness, in total 3.6 mm and 4.5 mm, respectively, where the layers thickness are 0.2 mm and 0.25 mm, respectively. Screws' diameters are 4.5 mm as solid bodies [11]. All interface contacts were applied. The material of the plate is Carbon fiber/epoxy (CF/epoxy) composite material.

All material properties have been assigned [4,12,13]. Only the immediate post-operative (IPO) phase was taken into account during the simulation. 700N force was axially applied to the assembled model in downward direction. A mesh sensitivity analysis was performed to confirm the accuracy of the results. It is checked that the model's optimal mesh is within 5%.

Fig. 1. Tibia-CMM (portable) setup

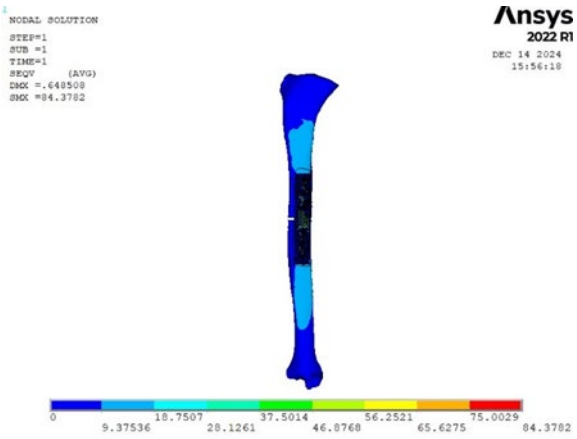

Fig. 2. Stress distribution in Finite Element Analysis

2.2 Hybrid Taguchi/GRA Approach for MCDM:

Taguchi Method. The orthogonal arrays (OAs) serve as the basis for experiments that are designed using the Taguchi method. Taguchi orthogonal designs, require few tests to examine the entire parameter space. The

Taguchi approach employs the signal-to-noise (S/N) ratio, a statistical performance metric, to analyze the data. A performance metric used to create regulated insensitivity to noise elements in products or processes is the S/N ratio. Uncontrollable elements that affect process or product uncertainty are known as noise factors. The S/N ratio in the Taguchi method can be determined in three distinct ways, depending on the goal.

(1) Smaller the better (2) Larger the better (3) Nominal the better

In order to create a CF/Epoxy tibia bone plate, symmetrical nine layers are selected for the laminate. For each lamina, a layer orientation (LO) is selected from -45°, 0°, 45°, and 90°. Two types of lamina thickness (LT) are used (0.2 mm and 0.25 mm) to create laminates with thicknesses of 3.6 mm and 4.5 mm. The factors for a suitable orthogonal array are layer thickness and fiber orientation. Layer thickness has two levels i.e. 0.2 mm and 0.25 mm, whereas layer orientation has four levels, i.e. the aforesaid angles. L32 orthogonal array is the appropriate for this mixed level optimization. Hence, the no. of experiment or run in this study is 32.

In this study the outcomes require are higher axial movement and lower twisting angle, von Mises stresses on the cortical bone, cancellous bone.

GRA. An adequate mathematical model is constructed to quality features of the CF/Epoxy composite tibia fracture plates in the case study. The GRA approach calculates the degree of correlation between variables depending on how similar or different they are from one another. GRA is distinguished by its multifactor analysis and minimal data requirements.

The process of grey relational creation entails preprocessing and calculating data based on quality characteristics. In this study, grey relational values are calculated based on the Signal to noise ratios which have been taken as criteria for different outcomes. Then, the normalization of S/N ratios have been done to scale the values in between 0 to 1. The deviational sequence has been calculated by subtracting the respective normalized value from the maximum value of same output parameters. Calculation of grey relational coefficient t (GRC) have been done by considering an identification coefficient of 0.5 followed an expression constructed by the maximum and minimum value i.e. 0 & 1 and the identification coefficient. Then the grey relational grade (GRG) has been calculated by the means of GRC's.

Depending on the value of GRG ranking of different experiments, i.e. 32 nos. plate designs of different layer thickness and layer orientation, have been done for design optimization.

3 Results and discussions

3.1 Finite Element Analysis

In this study, finite element analysis has been done for producing data of 5 different outcomes used for Taguchi-GRA analysis to optimize design parameters. The von Mises stresses on the cortical, cancellous, and plate bones as well as axial and shear movement are the outcomes.

Highest axial movement and lowest von Mises stress on the plate are the design criteria fulfilled by the first experiment's parameters which is 0.2 mm thickness's having LOs in [-45°,-45°,-45°,-45°,-45°,-45°.-45°.-45°.-45°]s. The lowest twisting angle and von Mises stress on bones are found in the Exp. no.32 in which 18 layers of 0.25 mm consists of LOs [90/ 90/ 0/ -45/ 45/-45/ 45/ 90/ 0]S.

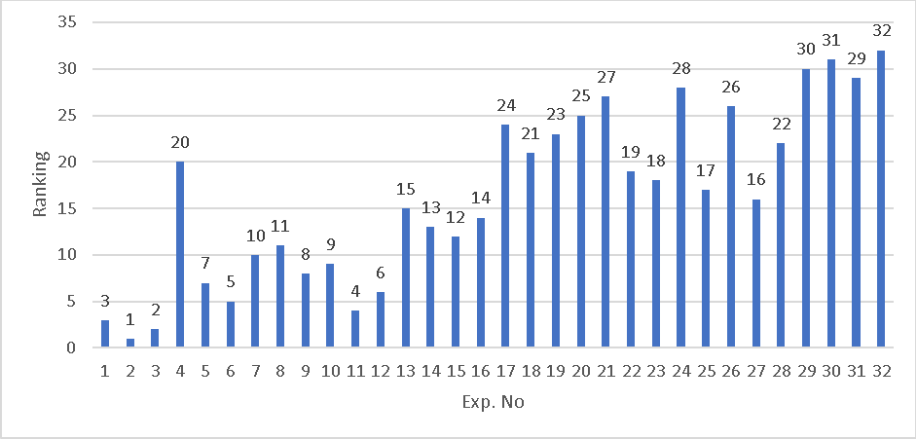

Fig. 3. Ranking as per the Exp. Nos.

3.2 Multi Criteria Decision Making (MCDM)

In this study, Taguchi- GRA approach is used for MCDM using S/N ratios of all designed experiment. Then the ranking of all 32 nos. of experimental criterial has been done. Fig.3 is representing the experiment number wise ranking of design parameter. For raking of the experiments, the following Steps of Grey relational analysis (GRA) has been done.

Step 1 Signal to noise ratio generation by the FEA results of all outcomes
Step 2 Normalisation of all data
Step 3 Calculation of deviational sequences
Step 4 Considering the identification coefficient as 0.5
Step 5 Grey relational coefficient (GRC) calculation
Step 6 Finding the grey relational grades of all experiments (GRG)
Step 7 Ranking the experiments based on GRGs

Fig. 4 represents comparisons between the best results of particular outcome from FEA with the same outcome in the optimized multi-response parameter. The exp. 2 have optimized multi-response parameters where the axial movement is 0.273 mm but best result found in the exp. No. 1 with 0.291 mm. Similarly, von Mises stress in plate is found 186.043 MPa in experiment number 2 which is 101.665 MPa higher than the exp. No.1.

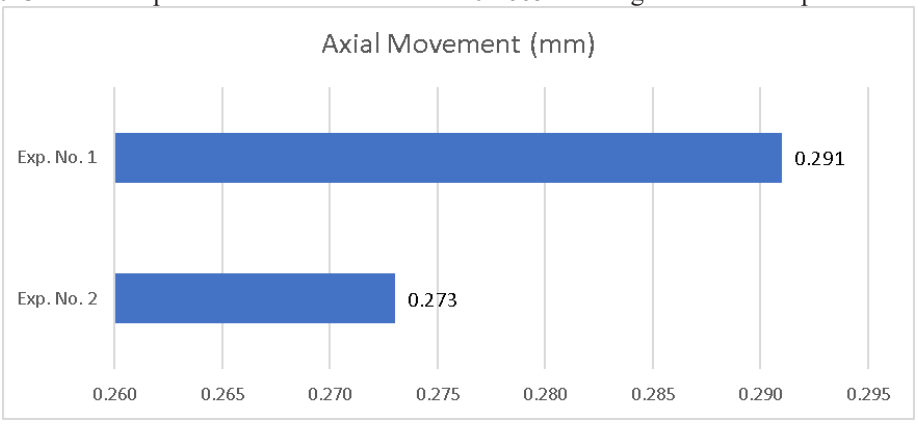

(a)

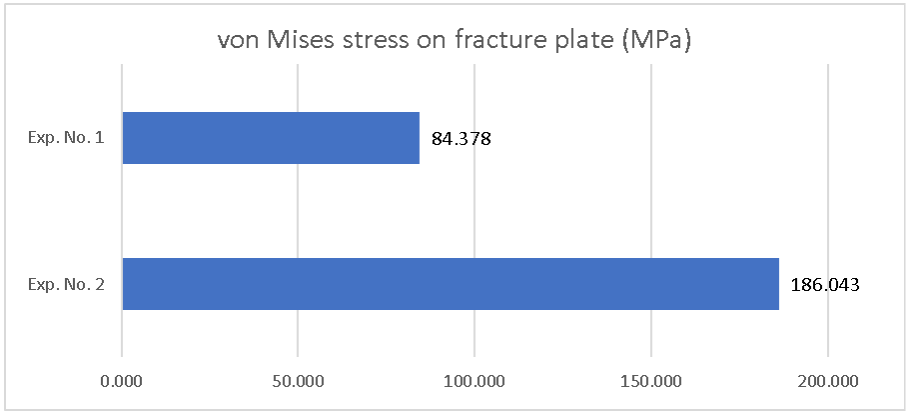

(b)

Fig. 4. Comparison of results between exp. no. 1 and 2

4 Conclusion

The following results can be drawn from the Taguchi DOE guided FE simulations of the tibia fracture composite plates, which were followed by the Taguchi GRA hybrid MCDM technique:

• A transversely fractured human tibia shaft with a 3 mm fracture gap that is fixed with a bone plate constructed of CF/Epoxy composite material is simulated using finite element analysis.

• The axial load equivalent to adult human body weight is applied to the cancellous bone, cortical bone and plates.

• The solutions are ranked using the Multi Criteria Decision Making (MCDM) technique, which integrates Taguchi- GRA hybrid approach.

• Out of the 32 simulations with a stacking sequence of [-45/0/0/0/0/0/0/0]S, the simulation with the largest axial movement and a 0.2 mm lamina thickness ranks best when taking into account the average performance index.

References

1. Patel, I., Young, J., Washington, A., & Vaidya, R. (2022). Malunion of the tibia: a systematic review. Medicina, 58(3), 389.
2. Antonova, E., Le, T. K., Burge, R., & Mershon, J. (2013). Tibia shaft fractures: costly burden of nonunions. BMC musculoskeletal disorders, 14, 1-10.
3. Mukherjee, S., Arambam, M. S., WaikhOM, S., Masatwar, P. V., & Maske, R. G. (2017). Interlocking nailing versus plating in tibial shaft fractures in adults: a comparative study. Journal of Clinical and Diagnostic Research: JCDR, 11(4), RC08.
4. Dhason, R., Roy, S., & Datta, S. (2020). A biomechanical study on the laminate stacking sequence in composite bone plates for vancouver femur B1 fracture fixation. Computer Methods and Programs in Biomedicine, 196, 105680.
5. Dhason, R., Roy, S., & Datta, S. (2022). Metal and composite bone plates for B1 periprosthetic femoral fracture in healthy and osteoporotic condition: A comparative biomechanical study. The International Journal of Artificial Organs, 45(8), 704-714.
6. Dhason, R., Roy, S., & Datta, S. (2022). The influence of composite bone plates in Vancouver femur B1 fracture fixation after post-operative, and healed bone stages: A finite element study. Proceedings of the Institution of Mechanical Engineers, Part H: Journal of Engineering in Medicine, 236(9), 1288-1296.
7. Mehboob, A., & Chang, S. H. (2019). Effect of initial micro-movement of a fracture gap fastened by composite prosthesis on bone healing. Composite Structures, 226, 111213.
8. Roy, D., Das, M. C., Dhason, R., Roy, S., & Datta, S. (2024). Effect of matrix material property on the composite tibia fracture plate: a biomechanical study. Biomed. Physics & Eng Express, 10(3), 035026.
9. Qazi, M. I., Akhtar, R., Abas, M., Khalid, Q. S., Babar, A. R., & Pruncu, C. I. (2020). An integrated approach of GRA coupled with principal component analysis for multi-optimization of shielded metal arc welding (SMAW) process. Materials, 13(16), 3457.
10. Mehat, N. M., Kamaruddin, S., & Othman, A. R. (2014). Hybrid integration of taguchi parametric design, grey relational analysis, and principal component analysis optimization for plastic gear production. Chinese Journal of Engineering, 2014(1), 351206.
11. Kim, S. H., Chang, S. H., & Jung, H. J. (2010). The finite element analysis of a fractured tibia applied by composite bone plates considering contact conditions and time-varying properties of curing tissues. Composite Structures, 92(9), 2109-2118.
12. Sylajakumari, P.A., Ramakrishnasamy, R., & Palaniappan, G. (2018). Taguchi grey relational analysis for multi-response optimization of wear in co-continuous composite. Materials, 11(9), 1743.
13. Samiezadeh, S., Avval, P. T., Fawaz, Z., & Bougherara, H. (2015). On optimization of a composite bone plate using the selective stress shielding approach. Journal of the Mechanical Behavior of Biomedical Materials, 42, 138-153.
14. Beirami, S., Nikkhoo, M., Hassani, K., & Karimi, A. (2021). A comparative finite element simulation of locking compression plate materials for tibial fracture treatment. Computer methods in biomechanics and biomedical engineering, 24(10), 1064-1072.

Infusion of Holonomy in Multi Criteria Decision Making

Bikash Bepari# and Bipradas Bairagi
Haldia Institute of Technology, Haldia, India
#bikashbepari@gmail.com
bipradasbairagi79@mail.com

Abstract. In this paper, the authors proposed a novel HMCDM (Holonomic Multi Criteria decision making) technique which includes pair-wise Euclidean Deviation Quotient (DQ) between criteria-holons to determine the relative suitability of the alternatives. Problems in which the interactions of criteria-holons are predominant, this method obtains the disagreement measure for all the pairs and forms the Disagreement Matrix (DM). Then the disagreement indices (DI) were determined for each criteria-holons by aggregating the deviation quotients and the criteria-holon having minimum sum was considered as nodal-holon. After determining the nodal-holon, the relative importance of the criteria-holons was determined. Then the composite scores for all the alternatives were calculated using the above determined weights and initial decision matrix. Higher the composite score implies higher the suitability of the competing alternative. An illustrative example was solved by the proposed method and results were compared with the results of the existing methodologies and legitimate degree of correlation was found.

Keywords: HMCDM, Euclidean Deviation Quotient, Disagreement Matrix, Criteria-Holons, Composite Scores.

1 Introduction

In today's dynamic business scenario, in order to sustain the unprecedented global economical turmoil there should be a tremendous coalition between market pull and technological push. Owing to the extirpation of monopoly, the business and sustenance has eventually become mutually dependent on the utility of goods and choice of the customer. Therefore, to exist in this milieu, proper decision, foresightedness and business trend analysis play a significant role. To substantiate these components, researchers and scientists are extending their untiring endeavour to develop different expert systems. Decision science being one of the inevitable components for business prosecution, prediction and prevention has already established itself as an emergent avenue to envisage the business spectrum.

Biologically, decision is an internal desire encapsulated by the cognitive aspects to judge good over bad, best over better and which is a time and instinct variant hierarchical phenomena amalgamated with cognitive layers of mind namely sensing, generation and interpretation. Contrastingly, the external decision making refers to formulating a decision under abundance of alternatives based on number of adjudging parameters known as 'criteria'. Therefore, Multi Criteria Decision Making (MCDM) explicitly evaluates the relative suitability of the alternatives based on a set of criteria (Hwang & Yoon, 1981). . Over and above, one should be chary in defining the criteria and their conflicts because MCDM reveals the decision as a whole subjected to a set of criteria which are in non-commensuration by virtue of their considerations.

The concept of "holon" was first coined by Koestler (Koestler, 1967). Holons are self deployed entities with distinct characteristics within a biological and/or social hierarchy to emulate functionality of a larger whole. Nevertheless, the interaction between the holons dictates the performance of the whole and the mode of interaction forms a structured architecture which is known as holarchy. Now, if a MCDM problem is analyzed with the eyes of holonomy, unequivocally they are analogous with respect to criteria-holons poised up with unique characteristics which when interacts in a synergistic manner within the decision making holarchy determines the relative suitability of the alternatives. Moreover, criteria-holons are adroit enough to evaluate the goodness or badness of each alternative but it leads to mono-criteria decision making. Therefore, MCDM is assemblage of decisions laid by different criteria-holons whose consensus ascertains unanimous decision as shown in Fig.1.

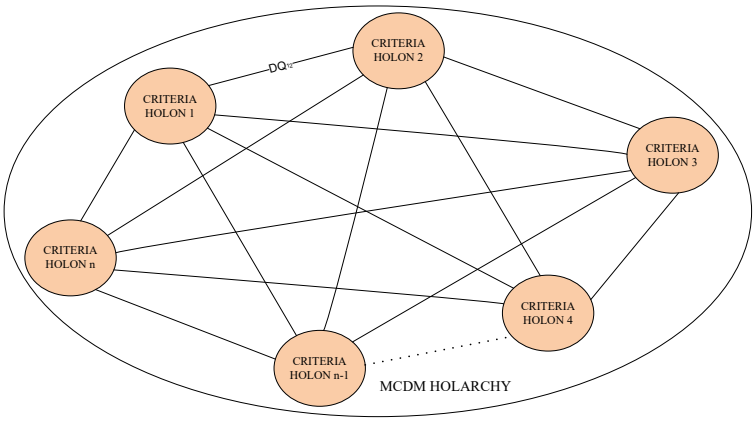

Fig.1. The Holonomic MCDM Architecture

Literature survey reveals several MCDM techniques to rank or quantify alternatives based upon Pareto optimal selection which can be categorized into two distinct types, Multi-Attribute (MA) methods and Outranking methods (Hodgett, 2016). MA methods follow a standalone mathematical protocol in the form of a mathematical function which results into assignment of a numerical score to each alternative. Whereas, outranking methods adjudges pair wise preferential assessments of the alternatives to determine the rank order (Malczewski, 1999). Evidence of conflicts between objectives and criteria was sought which seldom requires trade-off amongst decisive factors i.e. criteria (Chatterjee & Chakraborty, 2012).

Over the past few decades, certain MCDM methods like AHP (Dweiri & Al-Oqla, 2006), MUAT (Roth, Field & Clark, 1993), TOPSIS (Jee & Kang, 2000; Edwards, 2011), GTMA (Rao, 2006), ELECTRE (Shanian & Savadogo, 2006; Shanian & Savadogo, 2006), VIKOR (Rao, 2008), evaluation of mixed data method (Chatterjee et al, 2011), COPRAS (Chatterjee et al, 2011), GRA (Chan, 2006; Chan & Tong, 2007), PSI (Maniya & Bhatt, 2010) and LA method (Jahan et al, 2010), were extensively deployed to solve MCDM problems arising in wide range of engineering applications. Although, there exists methods which are unique with their respective mathematical foundations substantiated with tremendous logical background, but they lack with dexterity to prop up the characteristics that defines MA and outranking methods simultaneously. Hence, the objective of the present investigation includes a holonomic approach to entail the agreements of the criteria-holons through a pair-wise consensus map to ascertain the weights of the criteria which is dynamic and case variant also rational in formative protocol. The proposed methodology therefore, integrates both the MA and Outranking fraternities in an authentic manner to emanate an alternate avenue to solve MCDM problems diffused with Holonomy.

2 Mathematical Formulations

This section circumscribes the explanation of the projected methodology bit by bit. The sequential propositions are as follows:

Step 1: MCDM Problem Formulation:

For MCDM problem, let A = $\{A_1, A_2, \ldots\ldots A_k\}$ ($k \geq 2$) be a discrete set of 'k' feasible Alternatives, and C = = $\{C_1, C, \ldots\ldots C_n\}$ be a finite set of 'n' Criteria-holons. Let, $i \in k$, $j \in n$. If 'k' alternatives are evaluated with respect to the 'n' Criteria, the values constitute a decision matrix shown in equation 1.

$$DM = \begin{array}{c} \\ A_1 \\ \dots \\ A_i \\ \dots \\ A_k \end{array} \begin{array}{c} \begin{array}{ccccc} C_1 & \dots & C_j & \dots & C_n \end{array} \\ \begin{bmatrix} x_{11} & \dots & x_{1j} & \dots & x_{1n} \\ \dots & \dots & \dots & \dots & \dots \\ x_{i1} & \dots & x_{ij} & \dots & x_{in} \\ \dots & \dots & \dots & \dots & \dots \\ x_{k1} & \dots & x_{kj} & \dots & x_{kn} \end{bmatrix} \end{array} \quad (1)$$

Step 2: Data Pre Processing:

When the target value of the original sequence is infinite, then it has a characteristic of the "higher is better". The original sequence is normalized through:

$$r_{ij} = \frac{x_{ij} - \min x_{ij}}{\max x_{ij} - \min x_{ij}} \quad (2)$$

When the "lower the better" is the feature of the original sequence, then this is normalized as follows:

$$r_{ij} = \frac{\max x_{ij} - x_{ij}}{\max x_{ij} - \min x_{ij}} \quad (3)$$

Where, i =1,…..,k; j = 1,…..,n. m is the number of experimental data set, n is the number of responses. x_{ij} denotes the original sequence, r_{ij} is known as comparability sequence which is had after pre-processing, $\max x_{ij}$ and $\min x_{ij}$ are the largest and smallest value of x_{ij} respectively. After pre-processing or normalization, the dimensionless sequences were compensated to obtain the compensated normalized decision matrix. The grey relational coefficient for jth criteria for ith alternative is expressed by:

$$\varepsilon_{ij} = \frac{\Delta_{\min} + \zeta.\Delta_{\max}}{\left(1 - r_{ij}\right) + \zeta.\Delta_{\max}} \quad (4)$$

Where, $\Delta_{\min} = 0.00$ $\Delta_{\max} = 1.00$. 'ζ'is the distinguishing or identification coefficient whose value is confined within the range of $0 \le \zeta \le 1$ and the value may be tweak based on the practical requirements of the system (Abhang & Hameedullah, 2012). Here this value has been taken as 0.5.

Step 3: Calculation of Deviation Quotient

For calculating the deviation measure, the grey coefficients down by any two criteria holons Ci, Cj' are taken and mathematically Euclidean distance can be determined equation (5).

$$DQ_{j,j'} = \sqrt{\sum_{i=0}^{i=k} (\varepsilon_{ij} - \varepsilon_{ij'})^2} \text{ Where,} j \neq j' \quad (5)$$

In a very similar way the deviation quotients for all the pairs were derived and tabulate in the form of a Disagreement Matrix (DM) which has been shown in (6).

$$[DM]_{n\times n} = \begin{array}{ccccc|c} C_1 & \dots & C_j & \dots & C_n & \\ \hline 0 & \dots & DQ_{j,1} & \dots & DQ_{n,1} & C_1 \\ \dots & 0 & \dots & \dots & \dots & \dots \\ DQ_{1,j'} & \dots & DQ_{j,j'} & \dots & DQ_{n,j'} & C_{j'} \\ \dots & \dots & \dots & 0 & \dots & \dots \\ DQ_{j,n} & \dots & DQ_{j,n} & \dots & 0 & C_n \end{array} \quad (6)$$

Step 4: Determination of Disagreement Index (DI):

Herein the Disagreement Index (DI) for jth criteria-holon has been expressed as the summation of deviation-quotient with the remaining criteria-holons and it is mathematically expressed by (7).

$$\mathrm{DI_j} = \sum_{j=1}^{n} \mathrm{DQ_{j',j}}\,;\ \forall j, j' \in n \tag{7}$$

Step 5: Determination of Nodal Criteria-Holon:

Nodal criteria-holon seems to have the least value of Disagreement Index (DI). Logically, the same has been expressed by the following logic statement.

$$j \rightarrow \text{nodal, if } \min\{\mathrm{DI_j}\} = \mathrm{DI_j};\ j \in n \tag{8}$$

Step 6: Determination of Weights of Criteria-Holons:

Once the nodal criteria-holon is determined, the deviation from the same in terms of disagreement indices with the other criteria-holons can be processed to generate the relative weights of importance amongst them.

$$l_j = \frac{\mathrm{DI_{jmin}}}{\mathrm{DI_{j,}}};\ \text{where } j \in n \tag{9}$$

Weight of jth criteria-holon is then calculated as

$$w_j = \frac{l_j}{\sum_{j=1}^{n} l_j} \tag{10}$$

Step 7: Determination of Composite Score

Composite Score of each Alternative's is calculated as

$$CS_i = \sum_{j=1}^{n} w_j \times r_{ij} \tag{11}$$

Alternatives are then ranked according to the descending order of the composite score.

3 Illustrative Example

To reveal the usefulness and effectiveness of the proposed method, the authors took up a material selection problem of mass-produced non-heat-treatable cylindrical cover has been shown in Table 1. (Shanian & Savadogo, 2006). Eight number of different materials were taken into consideration based on thirteen selection criteria, namely Density (C1), Compressive stress (C2), Ultimate tensile stress (C3), Spring back index (C4), Bend force index (C5), Static load index (C6), Hardness (C7), Yield stress (C8), Elastic modulus (C9), Thermal diffusivity(C10), Thermal conductivity (C11), Thickness (C12) and Cost of base material(C13).

Table 1 Decision matrix for selection problem

Material	C1	C2	C3	C4	C5	C6	C7	C8	C9	C10	C11	C12	C13
Mat1	8.25	560	940	0.78	15183	2916	380	560	138	465	105	5.207	18.64
Mat2	8.65	460	600	0.71	12472	2395	220	460	125	465	205	5.207	13.99
Mat3	8.94	50	210	0.08	1355	260	45	50	122	460	398	5.207	3
Mat4	8.95	340	380	0.48	9218	1770	115	340	135	460	390	5.207	3.46
Mat5	2.67	190	295	0.25	20317	1966	87	191	73.59	741	152	10.238	2.81
Mat6	8.06	690	1030	1.55	5909	2174	350	800	190	189	17	2.7178	5.99
Mat7	8.63	95	270	0.17	2711	520	63	100	116	174	185	5.207	3.32
Mat8	7.08	267	355	0.49	1957	720	110	265	205	329	50	2.7178	1.04

The decision matrix is then normalized to make dimensionless and comparable through equation (1) and equation (3) depending upon their orientation and the compensation normalization decision matrix as shown in Table 2.

Table 2 Compensation normalized decision matrix

Material	C1	C2	C3	C4	C5	C6	C7	C8	C9	C10	C11	C12	C13
Mat1	0.360	0.711	0.820	0.512	0.407	0.333	1.000	0.610	0.495	0.507	0.394	0.602	0.333
Mat2	0.344	0.582	0.488	0.538	0.460	0.383	0.511	0.524	0.451	0.507	0.497	0.602	0.405
Mat3	0.334	0.333	0.333	1.000	1.000	1.000	0.333	0.333	0.442	0.502	1.000	0.602	0.818
Mat4	0.333	0.478	0.387	0.648	0.547	0.468	0.387	0.449	0.484	0.502	0.960	0.602	0.784
Mat5	1.000	0.390	0.358	0.812	0.333	0.438	0.364	0.381	0.333	1.000	0.436	0.333	0.833
Mat6	0.368	1.000	1.000	0.333	0.676	0.410	0.848	1.000	0.814	0.339	0.333	1.000	0.640
Mat7	0.345	0.350	0.350	0.891	0.875	0.836	0.346	0.349	0.425	0.333	0.472	0.602	0.794
Mat8	0.416	0.431	0.378	0.642	0.940	0.743	0.383	0.412	1.000	0.408	0.354	1.000	1.000

Employing equation (5) pair-wise deviation Quotients were calculated and the disagreement indices were calculated through equation (7). It may be observed that 8th criteria-holon (C8) is having least DI values which indicate C8 in the nodal-holon having highest weights as shown in Table 3.

Table 3 Disagreement Matrix, Disagreement Index and weights of criteria-holons

	C1	C2	C3	C4	C5	C6	C7	C8	C9	C10	C11	C12	C13	*DI*	l_j	w_j
C1		0.99	1.02	0.99	1.26	1.06	1.04	0.94	1.03	0.33	1.10	1.23	1.04	12.04	0.80	0.069
C2	0.99		0.18	1.21	1.10	1.15	0.35	0.12	0.67	0.94	1.12	0.70	1.16	9.68	1.00	0.086
C3	1.02	0.18		1.27	1.16	1.19	0.24	0.23	0.75	1.00	1.19	0.79	1.26	10.27	0.94	0.081
C4	0.99	1.21	1.27		0.68	0.50	1.26	1.21	1.07	0.82	0.72	1.03	0.58	11.35	0.85	0.074
C5	1.26	1.10	1.16	0.68		0.37	1.20	1.08	0.74	1.18	0.90	0.63	0.60	10.91	0.89	0.077
C6	1.06	1.15	1.19	0.50	0.37		1.22	1.11	0.87	0.99	0.74	0.88	0.64	10.72	0.90	0.078
C7	1.04	0.35	0.24	1.26	1.20	1.22		0.42	0.82	0.97	1.19	0.87	1.30	10.88	0.89	0.077
C8	0.94	0.12	0.23	1.21	1.08	1.11	0.42		0.65	0.93	1.10	0.72	1.15	9.66 *	1.00	0.086
C9	1.03	0.67	0.75	1.07	0.74	0.87	0.82	0.65		1.02	1.10	0.37	0.82	9.90	0.98	0.084
C10	0.33	0.94	1.00	0.82	1.18	0.99	0.97	0.93	1.02		1.09	1.52	1.34	12.13	0.80	0.069
C11	1.10	1.12	1.19	0.72	0.90	0.74	1.19	1.10	1.10	1.09		1.11	0.92	12.28	0.79	0.068
C12	1.23	0.70	0.79	1.03	0.63	0.88	0.87	0.72	0.37	1.52	1.11		0.78	10.64	0.91	0.078
C13	1.04	1.16	1.26	0.58	0.60	0.64	1.30	1.15	0.82	1.34	0.92	0.78		11.58	0.83	0.072

*Minimum DI

Once the criteria weights are determined by the present methodology, the composite score is evaluated in accordance with equation (11). The result reveals the priority of the alternatives as M6 $\succ$ M8 $\succ$ M4 $\succ$ M1 $\succ$ M3 $\succ$ M2 $\succ$ M7 $\succ$ M5.

Table 4 Composite Score and Ranks

wj	0.07	0.09	0.08	0.07	0.08	0.08	0.08	0.09	0.08	0.07	0.07	0.08	0.07		
Mi	C1	C2	C3	C4	C5	C6	C7	C8	C9	C10	C11	C12	C13	Score	Ri
M1	0.11	0.80	0.89	0.52	0.27	0.00	1.00	0.68	0.49	0.51	0.23	0.67	0.00	0.49	4
M2	0.05	0.64	0.48	0.57	0.41	0.20	0.52	0.55	0.39	0.51	0.49	0.67	0.26	0.45	6
M3	0.00	0.00	0.00	1.00	1.00	1.00	0.00	0.00	0.37	0.50	1.00	0.67	0.89	0.48	5
M4	0.00	0.45	0.21	0.73	0.59	0.43	0.21	0.39	0.47	0.50	0.98	0.67	0.86	0.49	3
M5	1.00	0.22	0.10	0.88	0.00	0.36	0.13	0.19	0.00	1.00	0.35	0.00	0.90	0.37	8
M6	0.14	1.00	1.00	0.00	0.76	0.28	0.91	1.00	0.89	0.03	0.00	1.00	0.72	0.62	1
M7	0.05	0.07	0.07	0.94	0.93	0.90	0.05	0.07	0.32	0.00	0.44	0.67	0.87	0.41	7
M8	0.30	0.34	0.18	0.72	0.97	0.83	0.19	0.29	1.00	0.27	0.09	1.00	1.00	0.56	2

4 Results and Discussion

Table 5 reveals the rank orders of the competing materials as per existing methods like Block-TOPSIS, VIKOR, MOORA, COPRAS and SAW by (Shanian & Savadogo, 2006) alongwith the rank order revealed by the proposed methodology. It is noteworthy to observe that the rank orders laid down by the different methodologies are having mostly the same extremities i.e. the most desired and less desired materials are the

same which indicates the alignment of the rank band width of the proposed methodology over the existing methodologies. Moreover, the rank order laid by the proposed methodology has 88% compliance in terms of spearman's correlation coefficient with methodologies like B-TOPSIS, MOORA and SAW and also the compliance of the proposed methodology is sufficiently high with methods like VIKOR and COPRAS as shown in Table 6.

Table 5 Rank orders by different methods

Material	Block-TOPSIS	VIKOR	MOORA	COPRAS	SAW	Proposed Methodology
M1	5	7	5	3	5	4
M2	6	5	6	6	6	6
M3	3	3	3	1	3	5
M4	2	1	2	5	2	3
M5	8	8	8	8	8	8
M6	1	2	1	2	1	1
M7	7	6	7	7	7	7
M8	4	4	4	4	4	2

Table 6 Composite Score and Ranks

	Block-TOPSIS	VIKOR	MOORA	COPRAS	SAW
PM	0.88	0.71	0.88	0.69	0.88

5 Conclusion

As the objective of the present investigation was to diffuse holonomic approach in MCDM and in that pursuit a novel technique namely HMCDM (Holonomic Multi Criteria decision making) was proposed, implemented and validated through a materials selection problem. The proposed methodology is not only limited to materials selection problem, rather it has got a generic spectrum of usage pertinent to any kind of MCDM problem which deals with crisp data. This proposed method is also applicable for of fuzzy environment having uncertainty subject to data conversion from fuzzy to crisp using suitable defuzzification technique.

In general as coda the following are the outcomes of the present investigation:

- A novel MCDM technique has been proposed, implemented and validated.
- Infusion of Holonomy in MCDM has been addressed.
- The novelty of proposed method encompasses determination of the criteria weights.
- The method is capable of determining Rank orders of alternatives with diversified multiple criteria.
- Rank order laid by the proposed methodology has higher correlation coefficient with existing conventional methodologies.
- The method can be effectively used for managerial decision making process.

References

Abhang, L. B., & Hameedullah, M., (2012). Determination of optimum parameters for multi-performance characteristics in turning by using grey relational analysis. *The International Journal of Advanced Manufacturing Technology*. 63(1-4), 13-24, https://doi.org/10.1007/s00170-011-3857-6

Chan, J. W. K., (2006). Application of grey relational analysis for ranking material options. *International Journal of Computer Applications in Technology,* 26(4), 210–217. doi: 10.1504/IJCAT.2006.010766

Chan, J. W. K., & Tong, T. K. L., (2007). Multi-criteria material selections and end-of-life product strategy: grey relational analysis approach. *Materials & Design,* 28(5), 1539–1546. doi: https://doi.org/10.1016/j.matdes.2006.02.016

Chatterjee, P., Athawale, V. M., & Chakraborty, S., (2011). Materials selection using complex proportional assessment and evaluation of mixed data methods. *Materials & Design,* 32, 851-860. doi: https://doi.org/10.1016/j.matdes.2010.07.010Get

Chatterjee, P., & Chakraborty, S. (2012). Material selection using preferential ranking methods. *Materials and Design,* 35, 384–393, doi:10.1016/j.matdes.2011.09.027

Dweiri, F., & Al-Oqla, F. M. (2006). Material selection using analytical hierarchy process. *International Journal of Computer Applications in Technology*, 26(4), 182-189. doi:10.1504/IJCAT.2006.010763

Edwards, K. L. (2011). Materials influence on design: a decade of development. *Materials and Design,* 32, 1073–1080.

Hodgett, R.E., (2016). Comparison of multi-criteria decision-making methods for equipment selection. *The International Journal of Advanced Manufacturing Technology*. 85(5-8), 1145-1157, https://doi.org/10.1007/s00170-015-7993-2

Hwang, C.L. Yoon, K. (1981). *Multiple Attribute Decision Making: Methods and Applications*. New York: Springer-Verlag.

Jahan, A., Ismail, M.Y., Mustapha, F., & Sapuan, S. M. (2010). Material selection based on ordinal data. *Materials and Design*, 31(7), 3180–3187. doi: https://doi.org/ 10.1016/ j.matdes.2010.02.024

Jee, D-H., & Kang, K-J. (2000). A method for optimal material selection aided with decision making theory. *Materials & Design,* 21, 199–206. doi: https://doi.org/10.1016/S0261-3069(99)00066-7

Koestler, A. (1967). *The Ghost in the Machine*. London: Arkana.

Malczewski, J. (1999). *GIS and multi-criteria decision analysis*. New York: Wiley.

Maniya, K., & Bhatt, M. G., (2010). A selection of material using a novel type decision making method: preference selection index method. Materials & Design, 31(4), 1785–1789. doi: https://doi.org/10.1016/j.matdes.2009.11.020

Rao, R.V. (2006). A material selection model using graph theory and matrix approach. *Material Science and Engineering A*, 431, 248–255. doi: https://doi.org/10.1016/j .msea.2006.06.006

Rao, RV. (2008). A decision making methodology for material selection using an improved compromise ranking method. *Materials & Design*, 29, 1949–1954. doi: https://doi.org/ 10.1016/j.matdes.2008.04.019

Roth, R., Field, F., & Clark, J. (1993). Materials selection and multi-attribute utility analysis. *Journal of Computer Aided Materials Design*, 1(3), 325–342. doi: https://doi.org /10.1007/BF00712855

Shanian, A., & Savadogo, O. (2006). TOPSIS multiple-criteria decision support analysis for material selection of metallic bipolar plates for polymer electrolyte fuel cell. *Journal of Power Sources*, 159, 1095–1104. doi: https://doi.org/10.1016/j.jpowsour.2005.12.092

Shanian, A., & Savadogo, O. (2006). A material selection model based on the concept of multiple attribute decision making. *Materials & Design*, 27, 329–337. doi: https://doi.org /10.1016/j.matdes.2004.10.027

Shanian, A., & Savadogo, O. (2006). A non-compensatory compromised solution for material selection of bipolar plates for polymer electrolyte membrane fuel cell (PEMFC) using ELECTRE IV. *Electrochimica Acta,* 51(25), 5307–5315. doi: https://doi.org/10.1016/j.electacta.2006.01.055

Design and optimization of two stage gear reducer using real coded genetic algorithm for multiple gear ratios

Paridhi Rai[1] and Asim Gopal Barman[2]

[1] Department of Mechanical Engineering, Bhagalpur College of Engineering, Bhagalpur, Bihar India
[2] Department of Production Engineering, Jadavpur University Kolkata, West Bengal India

raiparidhi25@gmail.com

Abstract. Design optimization of multi-stage gear reducer has always been an area of concern since these high power gear reducers demand high efficiency and low volume. This paper presents an application of real coded genetic algorithm(RCGA) for minimizing volume of a two-stage helical gearbox. The results obtained using RCGA are compared with previously published result. It is observed that RCGA perform well and produces good results for different gear ratios. The research outcomes are good and can aid design engineers to exploit minimum material and cost by achieving high efficiency, smooth operation and other performance requirements.

Keywords: Two stage helical gearbox, Minimum volume, Helix angle, Real coded genetic algorithm, Gear ratios.

1 Introduction

Among all machine components, gears are the most complex mechanical units. They find their applications in almost all types of machinery and vehicles for power transmission such as aerospace, automobile and many more[1]. Designing a multi-stage gearbox is very complicated task as they involve complex empirical formulas and geometry. But it is an area of great interest for researchers and designers. Various approaches for gear design optimization have been proposed by the designers. It has been observed that conventional methods of optimization do not perform well over a wide range of design problems. Furthermore, conventional methods are not robust in nature. They are not suitable for problems that are complex in nature. In contrast to this, non-conventional methods of optimization consider objective function instead of functional derivatives, so they prove to be more robust and practical. Therefore, researchers are continuously searching for such evolutionary algorithms which provide more optimal and accurate solution with faster convergence to optimum. Different approaches are used by the researchers to obtain optimal gear design. A computer aided strategy to design a compact spur gear set have been developed[2]. Involute interference, bending stress and Hertzian stress are the design constraints considered while designing the spur gear set. Jog and Pande [3] optimized the volume of helical gear set using interior penalty method along with Powell's method. Helix angle, diametrical pitch, addendum ratio and number of teeth are the design variables for the optimization problem. A preliminary design of gearbox computing the number of shafts and number of teeth on each gear was done using Genetic Algorithm (GA)[4]. Number of teeth on gear, maximum transmission ratio and maximum number of shafts are the design constraints formulated. A design problem related to minimization of weight of gear pair system using GA has been formulated [5]. Design constraints used are bending strength of gear, torsional strength of shaft and each gear dimension acts as non-linear problem. A single stage gear pair was optimized by employing GA by Marcelin [6]. The objective of this design problem was to minimize the volume of gear by reducing the centre distance of gear pairs and other parameters like transmitting power and reduction ratio. Golabi et al.[7] used MATLAB program for optimization of one-, two- and three- stage gearbox with an objective to minimize the volume of gearbox. Variation in gearbox ratio, hardness and power is done to demonstrate practical graphs from the results obtained after optimization. Panda et al. [8] proposed differential evolution (DE) algorithm for minimization of weight of single stage spur gear set. Results obtained proved to be much better when compared to other heuristic algorithm like GA, Simulated Annealing (SA) and Particle Swarm Optimization (PSO). In addition to this, stress analysis is done using ANSYS V-12 workbench by preparing CAD model using obtained geometric variables. Recently, Abderazek et al. [9] presented a new evolutionary algorithm called adaptive mixed differential equation (AMDE) for obtaining an optimal spur gear profile. Equalizing the maximum bending stress and specific sliding stress at the extreme paths were the objectives formulated for the study. The optimization results obtained show that AMDE give significantly better solution in comparison to previously used algorithms. Other conventional methods [10;11] have been used by the researchers in order to improvise gear performance. A multi-optimization model has been developed in order to minimize

volume and maximize efficiency of K-H-V cycloid gear reducer by Wang et al. [12] The optimization technique proposed was based on genetic algorithm. The optimization result showed more reduction in volume when compared to results from traditional algorithm. Miler et al. [13] analysed the effect of profile shift on spur gear optimization. Results with and without profile shifts are compared and verified with commercial gear optimization software. Gologlu and Zeyveli [14] used stochastic approach for optimizing volume of a parallel axis two stage helical gear train. While perform the optmizaation procedure, static and dynamic procedure have also demonstrated. The results have been compared with the deterministic design procedure and found to be better than that. Achari and Daivagna[15] optimized the design of non-standard centre distance helical gear pair using multi-objective optimization using genetic algorithm. Balancing tooth root strength for carrying maximum load, optimizing specific sliding ratio and maximizing the sum of addendum modification factor are the objective of the study conducted. To further validate the FEM results, strain gauge method have been employed. Buiga et al.[16] used genetic algorithm for minimizing mass of helical gear mechanism employed for automatic power transmission in hybrid vehicle. Seventeen design constraints and five design variables are used while performing design optimization. There was overall 24.2% mass reduction was obtained when compared to traditional method.

In the present paper, an attempt have been made to minimize volume of multi stage helical gear[14] using RCGA so as to have any possible improvement. Geometric constraint, also known as interference constraint and has not been used in past, along with other twelve design constraints have been employed in the design problem. RCGA is used to optimize the modified design problem to produce optimal solutions. Different gear ratios have been used to validate the results obtained. Along with this, various value of cross-over probabilities and mutation probabilities have been studied to opt for the correct value while performing design optimization of multi-stage helical gear. To validate the results, a CAD model of gear for a particular gear ratio while using the optimized design values is developed and stress analysis have been done using ANSYS.

2 Design Problem

To solve an optimization design problem, it starts with formulation of objective function, set of design variables and constraints mathematically using basic gear concepts. The current study has been discussed below.

2.1. Design Variables and Objective function

A two stage gearbox optimization model proposed by Gologlu and Zeyveli [14] is discussed in this section. Various design variables considered for optimization are face width (b), module (m_n) and number of teeth on pinion $(z_1; z_3)$ and the bounds imposed on them are shown in Table 1. This paper do not consider larger value of modules, since this will not help in achieving the objective function considered for optimization [14] formulated at first. For a two stage helical gearbox, the objective function can be stated as

$$f(x) = \left(\frac{\pi}{4}\left(((m_{n1}z_1)^2 + (m_{n1}z_1)^2\, b_1) + ((m_{n2}z_1)^2 + (m_{n2}z_2)^2\, b_2)\right)\right) \quad (1)$$

Here, m_{n1} and $m_{n2}$are the normal module for first and second stage gears respectively. The face widths of gear pair at two stages are b_1 and b_2.

Table 1 Range of Design Variables used in Optimization

Design Variable	Lower Bound	Upper Bound
Module, mm	1	5.5
Number of teeth on pinion	17	24
Face width ratio, b/mn	20	40

2.2. Constraints

To formulate design constraints, bending stress (Eq. 2) and contact stress (Eq. 3), for performing optimization of two-stage helical gearbox, the following formulas

$$\sigma_b = K_d K_{fe} \frac{F_t}{\varepsilon b m_n} \leq \frac{\sigma_D}{K_c} \quad (2)$$

$$P_{max} = K_m K_\alpha K_\beta K_\varepsilon \sqrt{\frac{K_d F_t}{bd}\frac{i+1}{i}} \leq P_{alw} \quad (3)$$

where σ_b is the bending stress. The allowable stress can be expressed as

$\sigma_b = {}^{\sigma_D}/_{K_c}$ where dynamic stress, $\sigma_D = 0.55\sigma_K$. P_{max} is the maximum surface pressure.

The face width, b, is usually defined early in the design process and can be expressed with respect to face width factor as,

$$20 \leq \varphi_m \leq 40 \tag{4}$$

where $\varphi_m = {}^{b}/_{m_n}$

This can be further utilized to obtain face width constraint for the design problem. All the other terms used in the above formula are explained below.

2.2.1. Design Constraints

Constraints considered for the optimization of a two-stage helical gearbox are as follows

$$g_1(x) = K_d K_c K_{fe} F_{t1} - \varepsilon b m_{n1}(0.55\sigma_K) \leq 0 \tag{5}$$

$$g_2(x) = K_d K_c K_{fe} F_{t2} - \varepsilon b m_{n2}(0.55\sigma_K) \leq 0 \tag{6}$$

$$g_3(x) = K_d\left(K m K_\alpha K_\varepsilon K_\beta\right)^2 F_{t1}\left(\frac{z_1+z_2}{z_1}\right) - (z_1 b m_{n1}(P_{allw})^2) \leq 0 \tag{7}$$

$$g_4(x) = K_d\left(K m K_\alpha K_\varepsilon K_\beta\right)^2 F_{t2}\left(\frac{z_3+z_4}{z_3}\right) - (z_3 b m_{n2}(P_{allw})^2) \leq 0 \tag{8}$$

Since this is a helical gearbox so pitch circle diameter is given as

$$d = \frac{m_n z}{\cos\beta} \tag{9}$$

where β is helix angle. Here, the allowable surface pressure is denoted by P_{allw} and can be expressed as, $P_{allw} = 0.25HB$ where HB is the Brinell hardness. K_d and K_{fe} are the dynamic velocity and form factor for the gears [14]. F_{t1} and F_{t2} are the transmitted force in gears for first and second stage respectively. K_c and K_m is the stress concentration factor and material factor for the problem respectively. Factors like K_α, K_ϵ and K_β are the flank transverse coefficient, tooth overlap factor and tooth slope factor for gears.

2.2.2. Control Constraints

Various control parameters used while performing design optimization are face width constraint and number of teeth on pinion and gear. Eq. (10) to Eq. (13) are used. Eq. (14) to Eq. (17) represent constraints on number of teeth for pinion and gear.

$$g_5(x) = 20m_{n1} - b_1 \leq 0 \tag{10}$$
$$g_6(x) = b_1 - 40m_{n1} \leq 0 \tag{11}$$
$$g_7(x) = 20m_{n2} - b_2 \leq 0 \tag{12}$$
$$g_8(x) = b_2 - 40m_{n2} \leq 0 \tag{13}$$
$$g_9(x) = 17 - z_{1,3} \leq 0 \tag{14}$$
$$g_{10}(x) = z_{1,3} - 24 \leq 0 \tag{15}$$
$$g_{11}(x) = 35 - z_{2,4} \leq 0 \tag{16}$$
$$g_{12}(x) = z_{2,4} - 145 \leq 0 \tag{17}$$

2.2.3. Geometric constraint

To avoid interference in gear pairs, a geometric constraint has been introduced in the Case II. Minimum number of teeth required by the gear pair on pinion to avoid interference can be expressed as [17] where i is the gear ratio and ∅ is the pressure angle.

$$g_5(x) = \frac{{}^{2a}/_{i}}{1-\sqrt{(\cos\emptyset)^2+\left({}^{1}/_{i}+1\right)^2(\sin\emptyset)^2}} \tag{18}$$

The value for ∅ is 22.5° for this design problem. Here, a represents the addendum and its value is taken as per AGMA. However, geometric constraint has not been considered in earlier study [14]. All the constraints mentioned above are inequality constraints. No equality constraints are used in the design problem.

3. Optimization Procedure

The mathematical model established is associated with non-linear programming problem. The design problem is solved using program codes developed for RCGA in MATLAB. The optimization methodology used in this paper is based on GA. GA is an evolutionary optimization algorithm with the working principle of survival of the fittest. RCGA usually requires

- a real-coded representation of possible solutions,
- a fitness to evaluate these solutions.

The algorithm starts with initialization of population consisting of randomly generated individuals (Fig.2). This is an iterative process with population of solution in each iteration termed as generation. To measure the quality of solution, fitness function is evaluated for each individual which is the value of objective function in optimization problem. The solutions are further improved using three genetic operators, selection, crossover and mutation. Hence, a new population is generated in each iteration with elite preservation of good solutions [18]. The algorithm stops when maximum number of generations has been reached. RCGA is used to perform the design optimization of gearbox. Selection for reproduction is done using tournament selection as roulette wheel procedure has certain disadvantages [14]. Simulated binary crossover (SBX) is used for better results [19].

Instead of static or dynamic penalty approach, parameter less approach is utilized to improve the result [18,19]. The initial parameters for the study includes, maximum generations as 100, 150, 200 and 250; probabilities of crossover as 0.5, 0.7 and 0.9, population size as 50; probabilities of mutation as 0.1, 0.01 and 0.001; distribution index for SBX as 2 and distribution index for polynomial mutation as 20. As number of generation rises, there is drop in objective function value. But after a certain value, the difference is minimum and that value is considered as maximum generation. Here maximum generation is 250. The material considered for both pinion and gear is cementite steel (16MnCr5). The values for input coefficients and some other gear parameters such as gear ratio, input speed etc. are given in Table 2.

Table 2 Value of working conditions and coefficient for design problem[14]

Design Parameters	Value
Transferred power,kW	7.5
Input speed	1800
Usuage	Electricity motor
Manufacturing process	Fine work
Brinell's hardness	1460
Ultimate tensile strength	1100
Working factor, K_o	1.25
Flank transverse coefficient, K_α	1.76
Stress concentration factor, K_c	1.5
Tooth overlap factor, K_ϵ	0.79
Tooth slope factor,K_β	1
Material factor,K_m	271.11
Overlap Ratio,ϵ	1.6

Different probabilities of cross-over and mutation operator have been used to obtain optimal solution for the design problem [14]. It can be seen in Table 3 that these operators have direct influences on the solution. For carrying out the tests, a PC compatible with Intel core i5, a 2.4 GHz processor and 4 GB RAM was used.

4. Results & Discussion

RCGA has successfully been implemented to automate the design procedure for helical gearbox with different gear ratios. Search power of RCGA with SBX operator is significantly adequate in continuous search space [18]. Solution points for module are assumed to lie in continuous search space like other design variables. RCGA with SBX crossover operator produces real values in decimal. However, the obtained design values can be approximated to the nearest standard design values. As mentioned earlier, the module values greater than 5.5 are not taken into consideration since they do not have any impact on reduction in volume of gearbox [14]. Therefore, higher value of face width are only considered for significant contribution in objective function. The result of design problem solved at various gear ratios using RCGA at varying mutation and cross-over probabilities is recorded and shown in Table 3.

Table 3. Minimum Vol. of Gearbox for different Cross-over and Mutation Probability

Gear Ratio	Cross-over probability	Mutation probability		
		0.1	0.01	0.001
21	0.5	6164.1	6148.8	15858.8
	0.7	6097.3	6209.5	6086.0
	0.9	6070.6	6039.5	6150.8
	0.5	2724.8	2082.8	3138.5
11	0.7	2691.4	2726.3	2805.6
	0.9	2688.2	2845.8	3148.7
	0.5	3972.6	3985.97	4125.22
16	0.7	3975.13	4028.38	4142.43
	0.9	4066.65	4325.16	4085.96
	0.5	1840.28	1864.67	1929.23
6	0.7	1805.95	1828.68	1908.57
	0.9	1823.89	1847.23	2060.57

The finding are explained below.

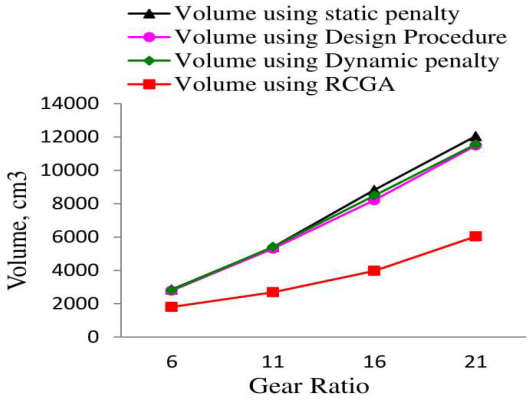

Fig. 1 Comparision of Volume using RCGA and other GA [14]

The results obtained at various gear ratios show that there is significant improvement in the results obtained using RCGA. It is observed that with the increase in gear ratio there is increase in volume at a particular given input speed and transmitted power (Fig.1).

Table 4 Gear Design Values for Case I

Gear ratio	Stages	Module, mm	Number of teeth	Face width, mm	Volume, cm^3
21	1st	1.96	20	78.5	
			141		6039.5
	2nd	2	23	60	
			70		
16	1st	2.19	19	78.5	
			95		3972.6
	2nd	2.20	21	64.8	
			66		
11	1st	2	22	73	
			74		2688.2
	2nd	2.5	20	64	
			60		
	1st	2.15	22	73.3	
6			74		1805.9
	2nd	2	20	54.3	
			66		

There is significant amount of reduction in the gear volume for different gear ratio. When the results are compared, RCGA with parameter-less approach gives better results than other approaches used earlier. As the generation increases, the best and average fitness converges to give the minimum volume of the gearbox for gear ratio 11 and gear ratio 21 is shown (Fig. 2 and Fig. 3).

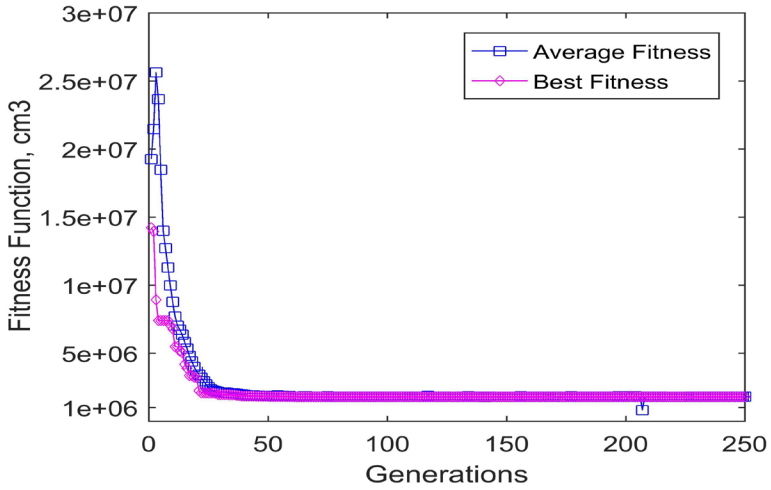

Fig 2. Best and Average Fitness value for gear ratio 11

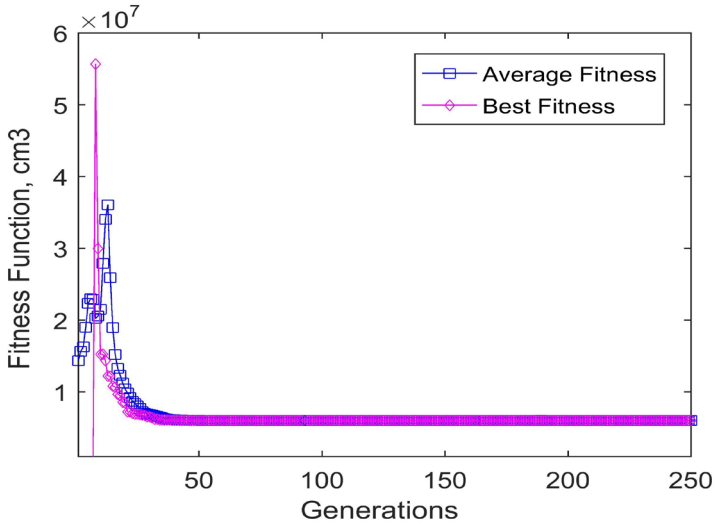

Fig 3. Best and Average Fitness value for gear ratio 21

The reason is that initially some of the design constraints are not satisfied. The value of design parameters obtained after optimization at various gear ratio are illustrated in Table 4. These values satisfy all the constraints considered in the design problem. It is observed that as gear ratio decreases volume reduces, showing a linear relationship between them. Thus, it is clear that RCGA and an optimal solution in short interval of time for a specified objective function.

Table 5 Comparison of values of objective function [14]

Gear ratio	Design procedure	RCGA with static penalty	BCGA with dynamic penalty	RCGA with parameter less approach
6	2780.9	2849.6	2806.4	1805.9
11	5297.8	5395.6	5405.4	2688.2
16	8211.8	8826.9	8494.6	3972.6
21	11488.3	12052.5	11557.2	6039.5

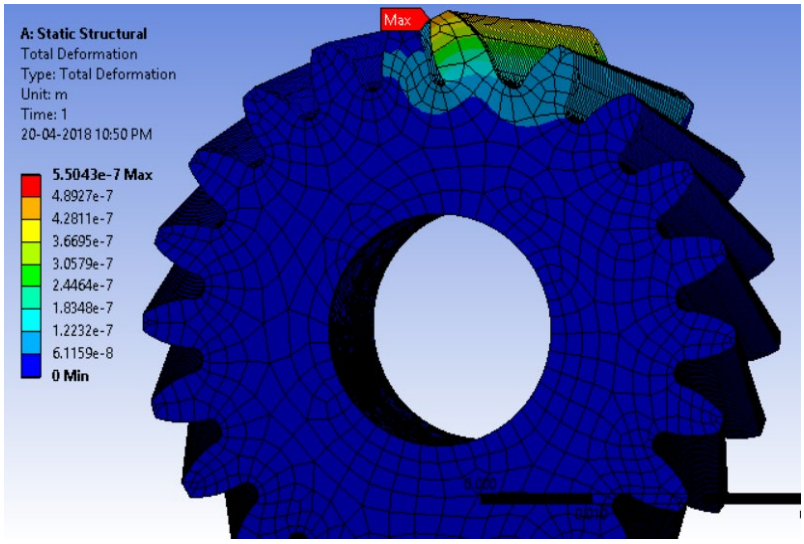

Fig 4. Stress analysis for pinion of 1st stage gearbox for gear ratio 6

To further validate the optimized gear design obtained using RCGA, finite element analysis is done to analyze the stress region by generating CAD model on CATIA package. Torque applied on the pinion is 39.79 N-m with gear ratio 6. For stage I, deformation and stress analysis has been done on pinion and gear respectively for demonstrating the efficiency of results.

5. Conclusions

In this paper, the objective function taken for optimization is minimization of volume of gearbox. Bending strength, contact strength of gear, face width and number of teeth on pinion and gear are the constraints used for design optimization. In addition to this, interference has been added as design constraint in the second case. The range of design variables are taken as per AGMA standards. RCGA has been employed to automate the design procedure for helical gearbox. Results obtained are compared and validated with the results of other methods published earlier. It has been concluded that RCGA produces good results for two stage helical gearbox design. In order to validate the optimized values of design variables attained, a CAD model was developed using CATIA package. Stress analysis has been performed on the gear model using ANSYS and it has been found that the stress developed is within the allowable limit of the material for both the stages. The current research results are able to exploit minimum material and cost significantly by attaining high efficiency and other performance requirements. More number of stages of gearbox and objectives can be considered for further study.

References

1. Radzevich S P: Dudley's handbook of practical gear design and manufacture. CRC Press. (2012)
2. Carroll R and Johnson G: Optimal design of compact spur gear sets. Journal of Mechanisms, Transmissions, and Automation in Design, 106(1):95-01 (1984).
3. Jog C and Pande S: Computer-aided design of compact helical gear sets. Journal of mechanisms, transmissions, and automation in design, 111(2):285-289 (1989).
4. Pham D and Yang Y: Optimization of multi-modal discrete functions using genetic algorithms. Proceedings of the Institution of Mechanical Engineers, Part D: Journal of Automobile Engineering 207(1):53-59 (1993).
5. Yokota T, Taguchi T, and Gen M: A solution method for optimal weight design problem of the gear using genetic algorithms. Computers & industrial engineering, 35(3-4):523-526 (1998).
6. Marcelin J L: Genetic optimisation of gears. The International Journal of Advanced Manufacturing Technology, 17(12):910-915 (2001).
7. Golabi S, Fesharaki J J and Yazdipoor M: Gear train optimization based on minimum volume/weight design. Mechanism and Machine Theory, 73:197-217(2014).
8. Panda S, Biswal B, Jena, S., and Mishra, D: An approach to weight optimization of a spur gear. Proceedings of the Institution of Mechanical Engineers, Part J: Journal of Engineering Tribology, 231(2):189-202(2017).
9. Abderazek H, Ferhat D and Ivana A: Adaptive mixed differential evolution algorithm for bi-objective tooth profile spur gear optimization. International Journal of Advanced Manufacturing Technology.1-11 (2016).
10. Tong B and Walton D: The optimisation of internal gears. International Journal of Machine Tools and Manufacture, 27(4):491-504(1987).

11. Daidie A et al.: Dimensionnement optimal d'ultrain d'engrenages _a l'aide d'un logiciel cao. In ActesColloque Primeca, Ecole Centrale Paris, 24, 25-26 Novembre(1993).
12. Wang J, Luo S, and Su D: Multi-objective optimal design of cycloid speed reducer based on genetic algorithm. Mechanism and Machine Theory, 102:135-148 (2016).
13. Miler D, Loncar A, Zezelj D and Domitran Z: Influence of profile shift on the spur gear pair optimization. Mechanism and Machine Theory, 117:189-197 (2017).
14. Gologlu C and Zeyveli M: A genetic approach to automate preliminary design of gear drives. Computers & Industrial Engineering, 57(3):1043-1051(2009).
15. Achari A. S. and Daivagna U M: Genetic algorithm-based optimization of helical gear pair with non-standard center distances: validated through FEA and strain gauge technique. Journal of the Brazilian Society of Mechanical Sciences and Engineering, 46:1-23 (2024).
16. Buiga O, Haragâș S and Tudose L: Helical gears pair optimal design using Genetic Algorithms. In 2023 10th International Conference on Modern Power Systems, pp. 1-6 IEEE (2023).
17. Maitra G M: Handbook of gear design. Tata McGraw-Hill Education (1994).
18. Deb, K. and Agrawal, S: niched-penalty approach for constraint handling in genetic algorithms. In Artificial Neural Nets and Genetic Algorithms, 235-243. Springer (1999)..
    Agrawal R B, Deb K and Agrawal R: Simulated binary crossover for continuous search space Complex systems, 9(2):115-148 (1995).
19. Deb K and Deb D: Analysing mutation schemes for real-parameter genetic algorithms. International Journal of Artificial Intelligence and Soft Computing, 4(1):1-28(2014).

Miscellaneous

A Numerical Study on Evolution of Heat Flow during Solidification of A356 Alloy

Joydip Paul[1] · Sudip Simlandi[1] · Nilkanta Barman[1*]

[1]Deptartment of Mechanical Engineering, Jadavpur University, Kolkata, India
* Corresponding author, e-mail: nilkantajdvu@yahoo.com

Abstract. The direction of heat flow is a measure in formation of microstructure during solidification. This work accordingly investigates related heat flow during solidification of A356 alloy numerically in a cylindrical cavity based the finite volume method (FVM) using the volume-averaged properties where a set of governing equations is used to represent the solidification process includes conservation of mass, momentum, energy and species. The respective numerical simulation is performed based on the SIMPLER algorithm and TDMA solver to investigate the solidification behaviour under different degree of superheats, i.e., 90°C, 135°C and 185°C. It is found that the development of solid-liquid interface is delayed at higher degree of superheat. Subsequently, the heat flow in the domain during solidification is investigated. At the solid-liquid interface, the latent heat evolution results a value about 175-225 W/m^2 to the heat flux that flows normal to it in both the directions towards the solid and liquid phases. The buoyancy driven fluid flow also carries the latent heat within the domain, which results an accumulation of heat following the fluid flow in the domain. In the liquid state, a high value to the heat flux is observed, it reaches to a value about 200 W/m^2 during phase change and decreases in completion of the solidification process. This direction of heat flow at the interface is a possible direction of the dendritic growth.

Keywords: Solid-liquid interface, latent heat evolution, heat flow.

1 Introduction

In this era of light-weight engineering, use of A356 is one of the most suitable selections in various applications such as automobile, construction, aerospace etc. Effective casting of such a material is in progress and reported in the literature since long past, where it is reported that both mechanical and metallurgical properties of the cast depend on respective formation of microstructures during solidification of the alloy. In solidification, different microstructures are formed such as columnar, dendrite, equiaxed etc. depending on prevailing conditions like temperature, cooling rate, thermal and solutal under-cooling etc. In this context, Yang *et al.* [1] studied variation of the temperature during solidification of aluminum alloy at high heat transfer condition. Liu *et al.* [2] presented the behaviour of recalescence during solidification. Roh [3] presented basic mechanism of the solidification in details. It is found that prediction of solidification phenomena is complex in nature, depend on various process parameters. Numerical solution is a suitable one to understand such phenomena than conducting an experiment. Prakash *et al.* [4] conducted a review, accordingly, on different numerical methods for their suitable application in solidification and melting processes, and reported that the volume-averaged single-domain finite volume method is suitable for numerical investigations. In this context, Soliman *et al.* [5] considered enthalpy based single domain numerical model to present solidification and melting phenomena, and subsequently the model is validated with respective experiments. Liu and Li [6] considered a volume averaged numerical model to present directional columnar growth during solidification of Sn-10 wt% Pb alloy based on evolution of related transport phenomena. Kumar *et al.* [7] presented a FVM based benchmark numerical model to predict the segregation during columnar alloy solidification. It is reported that the solidification involves formation of microstructures. In this regard, Jegatheesan and Bhattacharya [8] presented enthalpy-based numerical model to predict microstructural evolution during solidification of binary alloy. Tang and Xue [9] also reported formation of microstructures during directional solidification under different boundary conditions. It is found that the heat flux condition is a responsible parameter in formation of the microstructure during solidification, which accelerates the microstructural growth in the direction of heat flow.

In brief, a research on such a measure (evolution of heat flux) during solidification is very essential in order to enhance the metallurgical as well as mechanical properties of the cast, and is very rarely been cited in the literature. In this context, Sabau [10] investigated heat transfer behaviour at metal-mold interface using a sensor for direct measurement of the heat flux. Dhar *et al.* [11] explored an option using heatline to study the heat flow direction during solidification. However, rare citation of related research and a necessity to understand the basic behaviour

of heat flow during solidification demand a systematic study. However, there is hardly any literature represented on the heat flow direction during solidification in order to investigate growth direction of the microstructure. This work, thus, considers a numerical investigation on evolution of the heat flow during solidification of A356 alloy since Al-alloys are widely being used in the engineering applications due to their high strength to weight ratio.

2 Consideration of the Physical Problem

The present study considers solidification of A356 Al-alloy, with compositions as presented in Table 1, in a cylindrical cavity vertically placed on a slab. The molten A356 alloy with a degree of superheat ($T-T_L$) is then poured into the cavity. Periphery of the cavity is considered here as a water-cooled surface, whereas its top surface is considered as a free surface. Based on geometry of the cavity, a 2-D axisymmetric computational domain is considered as presented in Fig. 1 where its left surface represents axisymmetric condition, bottom surface is adiabatic, convection is assumed on its right surface that represents water cooling, and its top surface is free that considers convection and radiation to the atmosphere.

In this work, then a numerical study on transport phenomena and related heat flow during solidification of A356 alloy in the cavity is presented. The thermophysical properties of A356 alloy used in the simulation are listed in Table 2.

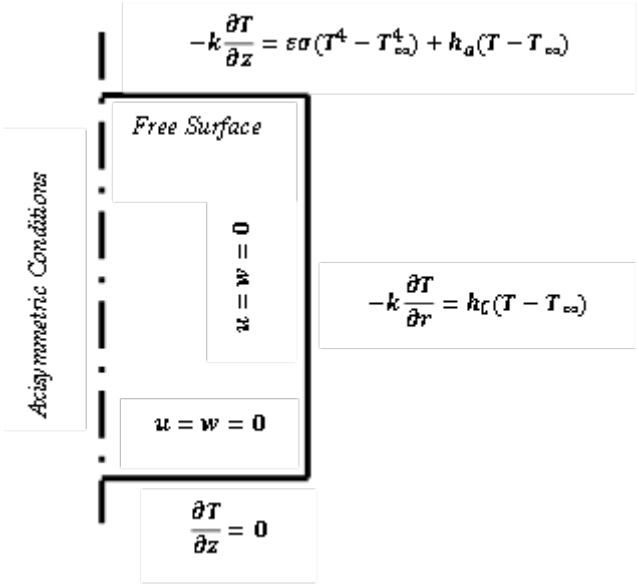

Fig. 1. Schematic of the computational domain

Table 1. Compositions of A356 Al-alloy (Kund and Dutta, [12])

Alloying elements	Si	Mg	Fe	Mn	Cu	Ti
Wt (%)	7.32	0.31	0.086	< 0.1	< 0.2	0.157

Table 2. Thermophysical properties of A356 alloy (Simlandi et al., [13])

Properties	**Values**	**Units**
Solid density (ρ_s)	2698	kg/m^3
Liquid density (ρ_l)	2532	kg/m^3
Solid thermal conductivity (k_s)	191	W/m.K
Liquid thermal conductivity (k_l)	88	W/m.K
Specific heat of liquid (c_{pl})	1049	J/kg.K
Specific heat of solid (c_{ps})	1089	J/kg.K
Latent heat of fusion (L_a)	3.75×10^5	J/kg
Thermal expansion coefficient (β_T)	1.7×10^{-4}	K^{-1}
Solutal expansion coefficient (β_C)	-0.73	-
Viscosity (μ)	1.3×10^{-3}	Pa.s

Partition coefficient (k_p)	0.1015	-
Liquid diffusivity (D)	3×10^{-9}	m^2/s

3 Mathematical Modelling

The present work considered a fixed-grid single-domain approach (Barman *et al*., [14]) to represent solidification process of molten A356 alloy in the cavity assuming

(i) all properties follow continuum in the entire domain,
(ii) a laminar, Newtonian and incompressible fluid,
(iii) the fluid satisfies the Boussinesq approximation,
(iv) the solid phase is free of internal stresses, and
(v) there is no solidification shrinkage.

Accordingly, a set of volume-averaged single phase governing equations includes mass, momentum, energy and species conservations, is used to represent present solidification process. The volume-averaged properties are considered here as

$$\rho = f_l\rho_l + f_s\rho_s \tag{1a}$$

$$k = f_l k_l + f_s k_s \tag{1b}$$

$$c_P = f_l c_{Pl} + f_s c_{Ps} \tag{1c}$$

where ρ, k, c_p are the volume-averaged density, thermal conductivity and specific heat, respectively. f_l and f_s are the liquid and solid fractions in the domain. Respective governing equations are given here as:

Mass conservation equation *(Barman et al.,* [14]*)*:

$$\frac{\partial\rho}{\partial t} + \frac{1}{r}\frac{\partial}{\partial r}(\rho r u) + \frac{\partial}{\partial z}(\rho w) = 0 \tag{2}$$

Momentum conservation equation *(Barman et al.,* [14]*)*:

$$\frac{\partial}{\partial t}(\rho u) + \frac{1}{r}\frac{\partial}{\partial r}(\rho r u u) + \frac{\partial}{\partial z}(\rho w u) = -\frac{\partial P}{\partial r} + \frac{1}{r}\frac{\partial}{\partial r}\left(\mu r\frac{\partial u}{\partial r}\right) - \frac{\mu u}{r^2} + \frac{\partial}{\partial z}\left(\mu\frac{\partial u}{\partial z}\right) + Au \tag{3a}$$

$$\frac{\partial}{\partial t}(\rho w) + \frac{1}{r}\frac{\partial}{\partial r}(\rho r u w) + \frac{\partial}{\partial z}(\rho w w) = -\frac{\partial P}{\partial z} + \frac{1}{r}\frac{\partial}{\partial r}\left(\mu r\frac{\partial w}{\partial r}\right) + \frac{\partial}{\partial z}\left(\mu\frac{\partial w}{\partial z}\right) S_b + Aw \tag{3b}$$

where $S_b = \rho g\beta_T(T - T_\infty) + \rho g\beta_C(C - C_\infty)$ represents both thermal and solutal buoyancies. During solidification, the molten A356 alloy changes to a mush which is referred here as a solid-liquid interface. The last term in each of the equations (3a,b) is used to take care about the fluid flow under such a condition where A is defined as

$$A = -C\frac{(1-f_l)^2}{(f_l^3+b)} \tag{3c}$$

where f_l represents liquid fraction in the domain, C is a morphological constant with an approximate value of 1.6×10^6, and b is a computational constant assumed a value of 1×10^{-6}, which uses in the simulation to prevent division by zero. In case of liquid phase, i.e., f_l = 1.0, A provides a zero resistance to the liquid flow whereas it provides a very high resistance when f_l = 0.0 and ceases the flow.

Energy conservation equation (Barman *et al.,* [14]):

$$\frac{\partial}{\partial t}(\rho T) + \frac{1}{r}\frac{\partial}{\partial r}(\rho r u T) + \frac{\partial}{\partial z}(\rho w T) = \frac{1}{r}\frac{\partial}{\partial r}\left(\frac{k}{C_p}r\frac{\partial T}{\partial r}\right) + \frac{\partial}{\partial z}\left(\frac{k}{C_p}\frac{\partial T}{\partial z}\right) + S_h \tag{4a}$$

where latent heat evolution during solidification is represented by S_h, a heat source term, given as

$$S_h = -\frac{1}{C_p}\left[\frac{\partial}{\partial t}(\rho \Delta H) + \frac{1}{r}\frac{\partial}{\partial r}(\rho r \Delta H u) + \frac{\partial}{\partial z}(\rho \Delta H w)\right] \tag{4b}$$

In order to evaluate the latent heat content (ΔH) in a cell, the enthalpy update scheme (Brent *et al*., [15]) is considered here, given as

$$[\Delta H_P]_{n+1} = [\Delta H]_n + \frac{a_P}{a_P^0}\lambda\left(\left[h_p\right]_n - c_P F^{-1}[\Delta H]_n\right) \tag{4c}$$

$$\begin{aligned} \Delta H &= 0 \quad \text{when} \quad T < T_S \\ &= L_a \quad \text{when} \quad T > T_L \end{aligned}$$

where a_p and $a_P^0 = \frac{\rho\, \Delta V}{\Delta t}$ are the coefficients of T and T_o in discretized energy equation. ΔV is volume of respective cell, h_p is sensible enthalpy at the nodal point P, and λ is a relaxation factor. The inverse function of the latent heat (F^{-1}) is given according to Kumar *et al.* [16] as

$$F^{-1} = T_M - (T_M - T_L)\left(\frac{\Delta H}{L_a}\right)^{(k_P - 1)} \tag{4d}$$

The liquid and solid fractions in the domain are then calculated as

$$f_l = \frac{\Delta H}{L_a} \tag{4e}$$

$$f_s = 1 - f_l \tag{4f}$$

The present work mainly focuses on heat flow during solidification in the entire computational domain. Respective heat fluxes in the domain are calculated as

$$q_r = \rho C_p u T - k\frac{\partial T}{\partial r} \tag{5a}$$

$$q_z = \rho C_p w T - k\frac{\partial T}{\partial z} \tag{5b}$$

Conservation of species *(Barman et al.,* [14]*)*:

The conservation of species equation is considered here as

$$\frac{\partial}{\partial t}(\rho C_l) + \frac{1}{r}\frac{\partial}{\partial r}(\rho r u C_l) + \frac{\partial}{\partial z}(\rho w C_l) = \frac{1}{r}\frac{\partial}{\partial r}\left(Dr\frac{\partial C_l}{\partial r}\right) + \frac{\partial}{\partial z}\left(D\frac{\partial C_l}{\partial z}\right) - \frac{\partial(\rho_s f_s C_s)}{\partial t} \tag{6}$$

in which Schiel equation is used to calculate C_s.

4 Boundary Conditions

Solidification of A356 alloy in a cylindrical cavity is considered here as discussed in section 2. Left face is an axisymmetric condition. Other boundary conditions are approximated here as follows:

Top/free surface:

$$-k\frac{\partial T}{\partial z} = \varepsilon\sigma(T^4 - T_\infty^4) + h_a(T - T_\infty) \tag{7a}$$

Bottom surface:

$$\frac{\partial T}{\partial z} = 0 \tag{7b}$$

$$u = w = 0$$

(7c)

Right surface:

$$-k\frac{\partial T}{\partial r} = h_C(T - T_\infty) \tag{7d}$$

$$u = w = 0 \tag{7e}$$

5 Solving Methodology

In accordance with the SIMPLER algorithm (Patankar, [17]), the set of mass, momentum, energy and species conservation equations coupled with the boundary conditions are discretized considering the finite volume method (FVM) and power law scheme. Thereafter, the obtained simultaneous linear algebraic equations are solved using the line-by-line tri-diagonal matrix algorithm (TDMA). A convergence is declared when a variable satisfies the following relation.

$$\left|\frac{\varphi-\varphi_{\text{old}}}{\varphi_{\max}}\right| < 10^{-4} \tag{8}$$

In equation (8), φ is any of the variables at any node at present iteration, φ_{old} is its corresponding value at previous iteration, and φ_{max} is maximum value of the variable at present iteration in the entire domain. The present simulation considered a suitable uniform grid 62×62 after a suitable grid independent study includes consideration of 52×52, 62×62 and 72×72, and a time interval of 0.01s for better convergence.

6 Results and Discussion

A FORTRAN based numerical code is developed to simulate solidification of A356 Al-alloy in a cylindrical cavity as discussed in section 2, where initial and boundary conditions are furnished according to those available in the research paper reported by Egole *et al.* [18]. A variation of temperature at mid-point of the axis in the cavity is evaluated with time as presented in Fig.2 in order to compare it with that predicted experimentally by Egole *et al.* [18]. In both the cases, the molten A356 alloy is poured into the cavity with same initial temperature, and cooled for a period of about 500s. As temperature of molten alloy falls below its liquidus temperature, solidification begins and continues until the temperature reaches to its solidus temperature. A similar variation of the present prediction is found with that reported by Egole *et al.* [18]. However, there is a deviation in the present prediction due to numerical errors and consideration of an averaged-melting temperature than consideration of the liquidus and solidus temperatures of the alloy.

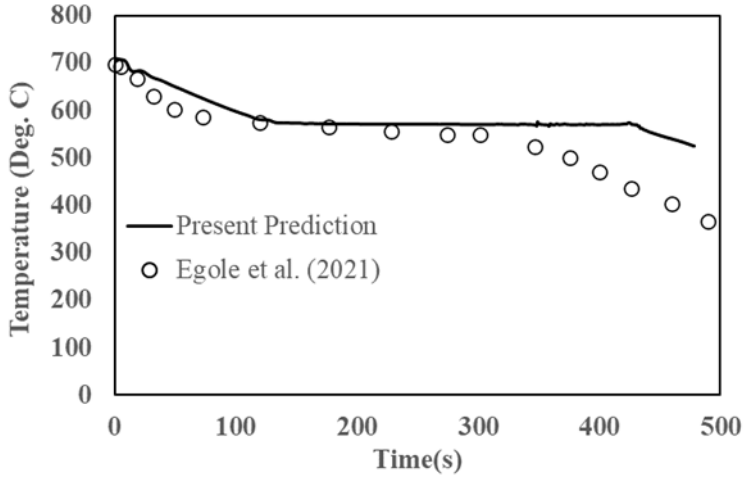

Fig. 2. Variation of temperature at mid-point of the cylindrical cavity with time

This work is then considered a study on solidification behaviour of the A356 alloy in the cylindrical cavity to investigate the effect of degree of superheat ($T-T_L$), which is presented in Fig. 3. In Fig. 3, evolution of the solid-

liquid interface during solidification is shown under different degree of superheats, i.e., 90°C, 135°C and 185°C as solidification time increases. In all cases, the solidification begins at bottom corner of the periphery depending on the employed boundary conditions where a high value (~2000 W/m^2.K) is considered for the heat transfer coefficient at periphery represents the peripheral water cooling. In addition to the peripheral cooling, a thermal buoyancy induces in the cavity that carries cold molten liquid towards bottom corner of the periphery. Accordingly, development of the solid-liquid interface starts at bottom corner of the periphery. The solid-liquid interface is then starts moving towards axis of the cylinder. Due to the buoyancy induced circulation, the lower part of the interface moves fast towards axis compare to that of the top surface even it releases heat by convection and radiation.

It is also found that the degree of superheat affects the solidification rate significantly. With increase in the degree of superheat, the solidification rate decreases. In case of a higher degree of superheat, the molten alloy takes a longer time to reach to its liquidus temperature than that at a low degree of superheat. Accordingly, the solid-liquid interface develops later and grows slowly towards axis of the cylinder at higher degree of superheat, as presented in Fig.3 in details.

This work is extended further to study the heat flow direction during solidification in context to know the growth of microstructure. The respective heat fluxes are calculated using the equations (5a, b). During solidification, the presence of maximum heat flux in the entire cavity is evaluated with increasing time under different degree of superheats (ΔT_{SH}) as presented in Fig. 4. In Fig. 4, a high value to the maximum heat flux is observed at higher degree of superheat. This indicates a condition of high heat transfer initially during cooling of the molten alloy under a higher degree of superheat. This high value of maximum heat flux is continued for a long period of time in case of higher degree of superheat, which results convective and radiative heat transfers of the molten alloy. The molten alloy accordingly takes a long time to reach its liquidus temperature. Subsequent development of the solid-liquid interface takes a long time at higher degree of superheat, also presented in Fig. 3. As time increases, value of the maximum heat flux decreases and reaches to a value about 200 W/m^2 per unit circumferential length and maintains the same value for a long period of time. This value of the maximum heat flux is same for all the cases. It represents a condition of the phase change and movement of the respective solid-liquid interface in the cavity until completion of the solidification process. The value of maximum heat flux then decreases, which represents a condition of solid-state heat transfer in the cavity.

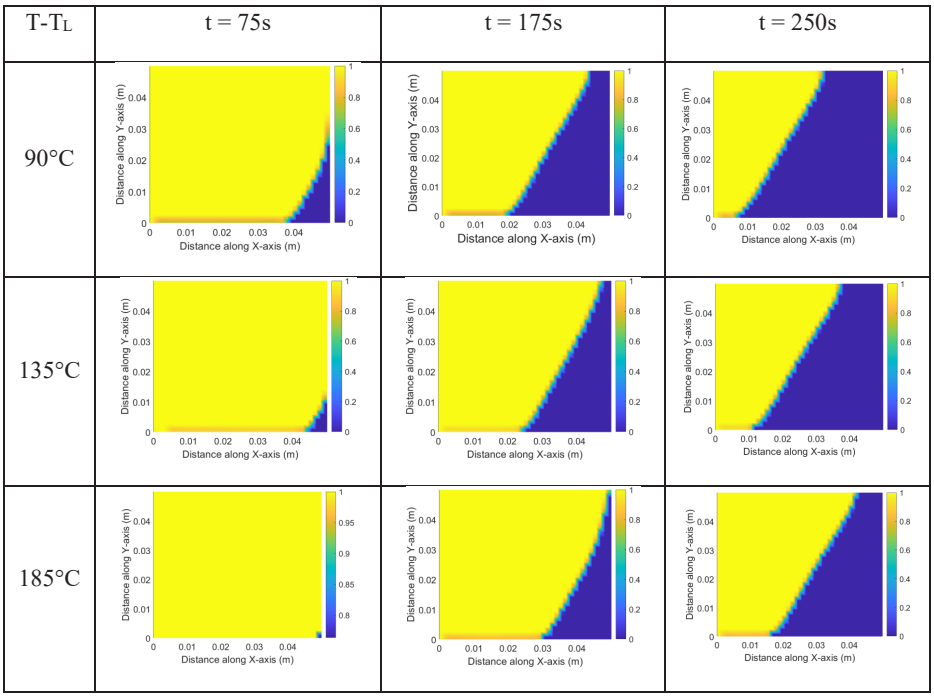

Fig. 3. Effect of degree of superheat on growth of solid-liquid interface

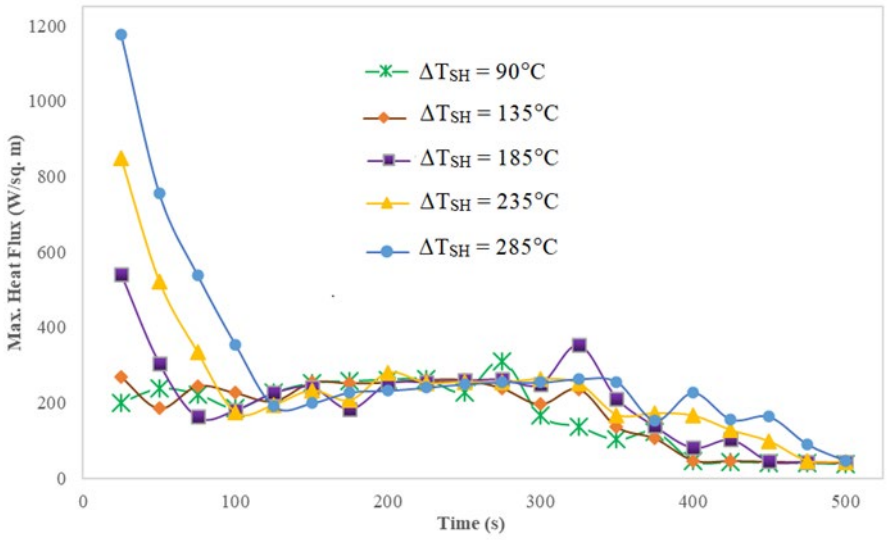

Fig. 4. Variation of the maximum heat flux with time

This work then presented distribution of heat flow in the entire domain as shown in Fig. 5 under different degree of superheat conditions. Solidification of an alloy involves evolution of latent heat, which is observed clearly at solid-liquid interface for all the cases. A high flux density with a value of about 175-225 W/m^2 is observed at the solid-liquid interface that leads to a heat flow to its surroundings, i.e., towards the solid phase as well as to the liquid phase in opposite direction. It is observed from Fig. 5 that direction of heat flow is always normal to the solid-liquid interface during alloy solidification, which is a possible direction of the dendritic growth. It is also observed that the latent heat of the interface is carried out by the fluid flow developed during solidification in the domain. Accordingly, there is accumulation of heat flux in some places of the domain, as presented in Fig. 5. Depending on the distribution of heat flux, heat transfer from all cavity surfaces is varied with time. It is observed that the peripheral heat transfer is very high in beginning of the cooling, and decreases with time as molten liquid transforms to solid. Further, it is observed that the molten liquid transfers more heat than that of the solid; this fact is clearly presented on top surface of the cavity in all the cases. Hence, the study on heat flow during solidification is an insight of the related transport phenomena.

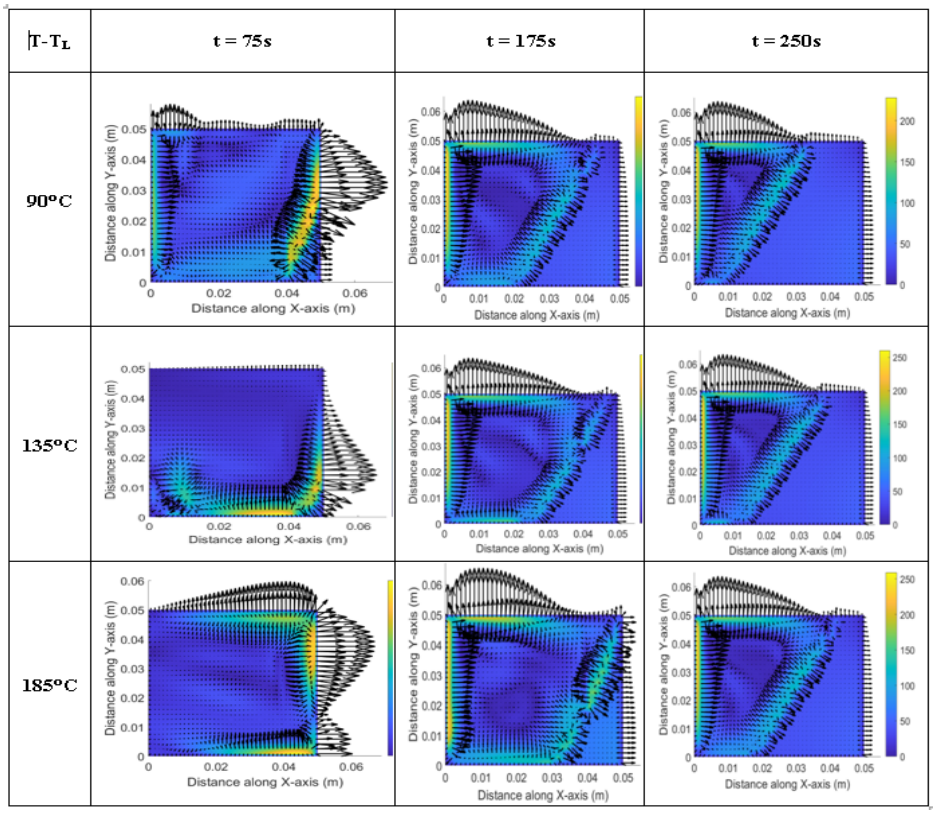

Fig. 5. Distribution of heat flux in the computational domain under different degree of superheat

7 Conclusions

In this work, a FVM based numerical study is considered to investigate the heat flow behaviour during solidification of an Al-alloy (A356) in a cylindrical cavity. A volume-averaged single-domain model is considered here to represent the respective solidification process, which uses conservation of mass, momentum, energy and species equations. A numerical code is developed accordingly to simulate the solidification process under different degree of superheats, i.e., 90°C, 135°C and 185°C. It is found that the degree of superheat influences growth of solid-liquid interface significantly during solidification. Subsequent evolution of the solid-liquid interface is presented here first under different degree of superheats, followed by the heat flow direction. At solid-liquid interface, the latent heat evolution results a value about 175-225 W/m^2 to the heat flux that flows normal to it in both the directions towards the solid and liquid phases. The buoyancy driven fluid flow also carries the latent heat within the domain, results an accumulation of heat following the fluid flow. In the liquid state, a high value to the heat flux is obtained, that reaches to a value about 200 W/m^2 during phase change, and it decreases in completion of the solidification process. In brief, the heat flow direction evaluated in the present work is very helpful in determining the growth of dendrites in solidification. Such evolution of heat flow during solidification is a new approach to understand the growth of microstructures.

References

1. H. Yang, Z. Shan, Y. Wang, and L. Liu: Simulation of temperature field of A356 aluminum alloy in freeze casting. Journal of Physics Conference Series 1600(1), 012045 (2020).
2. Y. Liu, W. Wang, F. Ma, and H. Zhang: Study of Solidification and Heat Transfer Behavior of Mold Flux Through Mold Flux Heat Transfer Simulator Technique: Part I. Development of the Technique. Metallurgical and Materials Transactions B 46(3), 1419 (2015).
3. H.-S. Roh: Heat transfer mechanisms in solidification. International Journal of Heat and Mass Transfer 68, 391 (2013).
4. S. A. Prakash, C. Hariharan, R. Arivazhagan, R. Sheeja, V. A. A. Raj, and R. Velraj: Review on numerical algorithms for melting and solidification studies and their implementation in general purpose computational fluid dynamic software. Journal of Energy Storage 36, 102341 (2021).

5. A. S. Soliman, A. A. Sultan, P. Cheng, and M. A. Sultan: Comparison of simplified and solidification-melting model: Numerical simulation with experimental validation. Journal of Energy Storage 84, 110837 (2024).

6. C. Wang, Z. Liu, and B. Li: A three-phase volume-averaged solidification model considering the growth direction of columnar crystal axis. International Journal of Heat and Mass Transfer 194, 122974 (2022).

7. A. Kumar, A. Singh, and A. Kumar: Development and benchmarking of numerical model in OpenFOAM® for the prediction of channel segregation during columnar alloy solidification. Thermal Science and Engineering Progress 35, 101464 (2022).

8. M. Jegatheesan and A. Bhattacharya: An enthalpy based model for microstructure evolution during binary alloy solidification. Computational Materials Science 186, 110072 (2020).

9. J. Tang and X. Xue: Phase-field simulation of directional solidification of a binary alloy under different boundary heat flux conditions. Journal of Materials Science 44(3), 745 (2009).

10. A. S. Sabau: Measurement of heat flux at metal/mould interface during casting solidification. International Journal of Cast Metals Research 19(3), 188 (2006).

11. M. Dhar, N. Barman, H. Chattopadhyay, and S. Simlandi: Heatline Visualization During Solidification of a Eutectic Solution in a Rectangular Cavity. Transactions of the Indian Institute of Metals 68(6), 1187 (2015).

12. N. K. Kund and P. Dutta: Numerical study of solidification of A356 aluminum alloy flowing on an oblique plate with experimental validation. Journal of the Taiwan Institute of Chemical Engineers 51, 159 (2015).

13. S. Simlandi, N. Barman, and H. Chattopadhyay: Studies on Transport Phenomena during Continuous Casting of an Al-Alloy in Presence of Electromagnetic Stirring. Transactions of the Indian Institute of Metals 66(2), 141 (2012).

14. N. Barman, P. Kumar, and P. Dutta: Studies on transport phenomena during solidification of an aluminum alloy in the presence of linear electromagnetic stirring. Journal of Materials Processing Technology 209(18–19), 5912 (2009).

15. A. D. Brent, V. R. Voller, and K. J. Reid: Enthalpy-porosity technique for modeling convection-diffusion phase change: Application to the melting of a pure metal. Numerical Heat Transfer 13(3), 297 (1988).

16. G. Kumar, S. Hegde, and K. N. Prabhu: Heat transfer and solidification behaviour of modified A357 alloy. Journal of Materials Processing Technology 182(1–3), 152 (2006).

17. S. V. Patankar: Numerical Heat Transfer and Fluid Flow (2018).

18. C. P. Egole, H. E. Mgbemere, G. M. Sobamowo, and G. I. Lawal: Micro-macro model for the transient heat and fluid transport in solidification structure evolution during static casting processes. Materials Today Communications 28, 102613 (2021).

Recent Advancements in Manufacturing Technology & Management (RAMTM–II 2025)

The Recent Advancements in Manufacturing Technology & Management (RAMTM–II 2025) conference was successfully held at the Department of Production Engineering, Jadavpur University, Kolkata, India, on January 16–17, 2025. The event served as a vibrant collaborative platform for experts from manufacturing industries, along with participants from academic institutions and R&D organizations. The conference fostered meaningful interactions and the exchange of innovative ideas, while also facilitating valuable networking opportunities among institutions, organizations, and industries. RAMTM–II continued its legacy as a dynamic forum for manufacturers, researchers, and academics to stay abreast of the latest advancements in manufacturing technology.

Jadavpur University Press